Dedicated to our families and to our colleagues for their support over many years

Compliant Offshore Structures

Minoo H Patel BSc(Eng), PhD, FRINA, FIMechE, CEng
Head, Department of Mechanical Engineering, University College London

Joel A Witz BSc(Eng), PhD, ACGI, MRINA, CEng
Lecturer, Department of Mechanical Engineering, University College London

BUTTERWORTH
HEINEMANN

Butterworth-Heinemann Ltd
Linacre House, Jordan Hill, Oxford OX2 8DP


PART OF REED INTERNATIONAL BOOKS

OXFORD LONDON BOSTON MUNICH
NEW DELHI SINGAPORE SYDNEY
TOKYO TORONTO WELLINGTON

First published 1991

British Library Cataloguing in Publication Data
Patel, Minoo H.
Compliant offshore structures.
1. Offshore structures. Design & construction
I. Title II. Witz, Joel A.
627.98

ISBN 0 7506 1070 0

Library of Congress Cataloging in Publication Data
Patel, Minoo H.
Compliant offshore structures/Minoo H. Patel, Joel A. Witz.
p. cm.
Includes bibliographical references and index.
ISBN 0-7506-1070-0
1. Compliant platforms. I. Witz, Joel A. II. Title.
TC1700.P37 1991
627'.98—dc20 90-19626

Typeset by TecSet Ltd, Wallington, Surrey
Printed in Great Britain at the University Press, Cambridge

Preface

Over the last two decades, exploitation of the United Kingdom's offshore oil and gas reserves has prompted a substantial level of research activity in marine technology. This work has been directed towards the development of offshore structures designed to provide cost-effective platforms for operation in the hostile ocean environment found on the United Kingdom continental shelf.

A common element of many of the offshore structures being developed for application in the North Sea and other offshore locations is that they exhibit some degree of compliance to ameliorate the effects of wave loading and to reduce structural weight and cost. The compliant nature of these structures, through their capability to deform significantly due to wave action and mooring loads, means that structural dynamics plays an important role in their operational behaviour. Examples of compliant structures range from floating production systems, crane vessels and offshore work vessels to articulated tower type loading buoys, guyed towers and tensioned buoyant platforms.

An unusual feature of research and development in the offshore industry over the last two decades has been the fact that designs with substantial innovative features have been seriously researched and those with sufficient technical merit have mostly found an application. A leading example of this is the Hutton tensioned buoyant platform, but other examples are crane vessels with pneumatic compliance and hybrid floating production systems based on articulated joints between compliant bottom-emplaced towers and floating vessels. This close collaboration between technological development and practical application provides stimulating and rewarding challenges for the engineers involved in both the background research and in the construction, installation and operation phases of development. It is hoped that the contents of this book will convey to the reader some of the fascinating technical problems that are being encountered and solved. There is every indication that the kind of technology developments outlined above will continue and indeed increase in intensity over the next two decades.

The authors feel that it is timely, therefore, that some of the developments in the analysis of compliant structures over the last two decades are brought together in a single text book. Most of the material described has originated from work carried out in the Department of Mechanical

Engineering at University College London (UCL). This Department, in association with the Department of Civil Engineering at UCL and Imperial College of Science and Technology, has worked since 1978 within the London Centre of Marine Technology. The Centre has been financially supported by the United Kingdom government, its Department of Energy and consortia of oil companies and offshore contractors to carry out work on the structural, hydrodynamic and material aspects of offshore structures. This book presents some aspects of the mechanics of compliant structures researched by one small group within the London Centre. The London Centre has also been engaged in other relevant research work on compliant structures which has not been presented in this book.

The first four chapters of the book present an account of the various conventional and newly emerging methods of hydrostatic and hydrodynamic analysis that are available for characterizing compliant marine structures. This is followed by the use of the analysis methods for a variety of conventional and novel compliant structures. Semisubmersibles, ship forms, tensioned buoyant platforms, crane vessels and vertical marine risers are considered among the conventional structures. However, more attention is focused on those newer compliant structures which are believed to have a future application or, alternatively, are useful in illustrating an interesting performance feature. Among such structures are those with articulated joints, pneumatic compliances and tandem hull marine vehicles.

It is important to point out that this list of structures is by no means complete, but is, firstly, representative of promising compliant structure types and, secondly, consists of structures which the authors and colleagues have researched at University College London. The majority of the material presented in this book is concerned with analysis methods for determining the hydrostatic and hydrodynamic behaviour, at wave frequencies only, of conventional and novel compliant structure types. The contribution of hull configuration for tandem hull vessels and of pneumatic compliances for ship shape and semisubmersible vessels has also been emphasized. On the other hand, the treatment of second order wave forces and structural behaviour has been left out entirely, although much excellent work has been carried out on the former at the London Centre by Professor Rodney Eatock-Taylor (now at the Department of Engineering Science, Oxford University) and his research group.

This text book is aimed at a range of readers from second- and third-year undergraduates in Mechanical Engineering as well as Naval Architecture and Ocean Engineering, and postgraduates reading for Masters' degrees and carrying out research. However, care has been taken to ensure that the book contains additional material of interest to practising engineers who, it is believed, have a need for a text which brings together analysis methods and their implementation for a range of conventional and novel compliant marine structures.

The authors have many acknowledgements to make to all the colleagues who have contributed to the research and technical developments described in this book. First among these are our research colleagues Dr D T Brown, Dr G J Lyons, Dr F B Seyed, Dr J H Harrison and Mr B A Hogan. Many other former colleagues have also contributed to developing

the analysis methods and model testing described in the book; among these are Dr E R Jefferys and Mr E O Lynch. Our thanks also go to Professor T H Lambert for his guidance over the years and to Professor R Eatock-Taylor for his steady support and encouragement of our work. A special acknowledgement must also be made to the late Mr M Adye of the Marine Technology Directorate whose ideas for joint industry and government funded research on compliant structures contributed in some part to the success of the research on which this book is based. Finally, the authors wish to acknowledge the efforts made by Mrs V Clark, Miss S Collins and Mr K Pickering in the typing and preparation of the manuscript, and of Mrs J Pilbeam in the preparation of the Figures. It should be noted that the upright symbols used in the Figures are printed in italics in the text in order to improve presentation and readability.

Minoo H Patel
Joel A Witz

Chapter 1

Introduction

The introduction of a compliant mechanism into an engineering structure serves two purposes. It provides the structure with a degree of mobility and it provides a means to alleviate destructive loads. To illustrate the point, take the example of alternative forms of the jetty or landing pier. One form consists of a rigid structure fabricated out of a framework of supporting members and piles. This structure must react all the environmental forces. An alternative form consists of floating pontoons which yield to the changing water levels and wave induced fluid motions. This compliance ensures a simple and inexpensive structure.

The first compliant marine structures, ships, are almost as old as human civilization itself. Man's development has been closely entwined with the use of ships for fishing, transportation, trade, exploration and warfare. As these maritime activities developed, the skills associated with ship design and construction came to encompass an understanding of the use of hull form, and methods of propulsion and materials to achieve acceptable performance.

The compliance in a ship rests within its ability to ride the continuously moving ocean surface through its rigid body motions. Thus, the hull of a ship is essentially rigid where structural flexibilities generate deflections which are orders of magnitude less than the motions of the vessel in waves. Over the last century, the crafts of ship design and construction have been supplemented by the science of naval architecture which has laid a mathematical and experimental foundation for ship design. This has led to the development of a wide variety of marine vehicles.

However, recent scientific advances suggest that incorporating compliance into a marine vehicle can yield substantial performance advantages to the designer. The required compliance can be defined as a means of incorporating a deliberate flexibility in the submerged volume of the structure through structural articulations or interactions with trapped air volumes, or by other means such that the vessel's submerged shape alters in reaction to wave forces and vessel motions. Thus, a compliant vessel, unlike its rigid counterpart, can undergo 'structural' deformations which are of the same order of magnitude as vessel motions in waves or the wave fluid motions themselves. This consideration of compliance begins to draw man made marine vehicles closer to those developed by nature through the

evolution of marine life which uses compliance in satisfying the needs for locomotion and structural efficiency.

The use of compliance in man made marine systems has been most thoroughly investigated during the development of wave energy devices where the need for a power take off requires that wave forces be associated with some prescribed wave induced relative motion between two parts of a wave energy device. Count (1978, 1980) and Evans (1982) present details of key aspects of wave energy machines, whereas Salter (1974) gives an overall description of one such device called a Salter duck.

The requirements of the offshore oil and gas industry are promoting exploration drilling and hydrocarbon production operations in progressively deeper and more hostile waters. These requirements need to be met by more efficient marine vehicles designed to satisfy hitherto unusual performance demands. In this context, compliant marine vehicles are being researched and engineered into systems which offer significantly better performance than rigid alternatives.

The purpose of any compliant marine structure is to satisfy a specific functional requirement. This functional requirement will include social, economic and environmental factors as well as technical factors. The general design principles for compliant marine structures must embody the goal of finding the optimum solution to the functional requirement. The structure and all its subsystems must satisfy the highest standards of safety and reliability. A compliant marine structure must survive extreme wave, wind and current conditions associated with its design life. All potential failure modes must be identified, together with their probability of occurrence. The consequences of failure also need to be examined.

Compliant marine structures are complex systems consisting of a number of subsystems which closely interact with each other. The designer must be aware of all the interacting subsystems and the effect that each subsystem has on the design. The general design principles for compliant marine structures are addressed below.

The compliant marine structure is a working platform which must support all envisaged payload requirements. A significant proportion of the weight of the structure will be fixed during its design life. This weight will consist of primary and secondary structural weight, together with plant weight. The structure must also support the range of variable loads anticipated in its working life. The designer must foresee all potential weight variations during the structure's design life and incorporate these weight variations into the design. This procedure will often dictate the general overall dimensions of the structure. These dimensions will require further optimization during the design cycle.

Many compliant marine structures utilize buoyancy of the submerged hull to support the payload. Hydrostatics, therefore, is a fundamental design consideration. The buoyancy and hydrostatic stability requirements often determine vessel dimensions. The vessel must have adequate hydrostatic characteristics to remain afloat and, also, it must have sufficient hydrostatic stability to prevent capsize. Damage considerations are important. The compliant marine structure may be damaged by collision, explosion, fire or accidental flooding. In its damaged condition, the

structure must have adequate buoyancy and hydrostatic stability to prevent capsize in the prevailing sea state.

Station keeping is an important consideration in the design of a compliant marine structure. The mooring system must be able to maintain the structure on location within specified limits for all sea states. The mooring system must have sufficient redundancy so that failure of a mooring system component does not result in a significant deterioration of station keeping ability.

Wave induced motions are also fundamental to the successful operation of a compliant marine structure. The designer must optimize the dynamic response of the structure to waves in order to maximize operability and minimize structural loads. It is the responsibility of the designer to ensure that structural integrity is always maintained. A major problem for most marine structures is significant levels of cyclic fatigue damage associated with oscillatory wave loading. The designer must address this issue.

The above considerations are representative of some of the challenges faced by designers of compliant marine structures. Design is an iterative procedure. Hopefully the process converges to an optimum solution.

1.1 Historical development

This century has seen rapid growth in the exploration of the oceans, particularly in the search for hydrocarbons. In the last two-and-a-half decades, the demands for the offshore oil and gas industry have been met with a number of different types of marine structure. Some of these structures have been rigid, but, as exploration has moved into moderate to large water depths and more hostile environmental conditions, compliant marine structures in the form of drill ships and semisubmersibles have been utilized. Hydrocarbon production is still dominated by the use of fixed structures.

The oil industry began its move offshore in the late 1940s. The first offshore operations were in the United States where a gradual move was made from the swamps and marsh lands of Louisiana into the Gulf of Mexico. Exploration in shallow waters ($\sim$ 20 m) was carried out from submersible drilling units which were floated onto location and then ballasted to rest on the sea bed. Experience obtained with submersible ballasting operations and the requirement for exploration in deeper waters led to the development of the semisubmersible.

One of the earliest semisubmersibles was the *Blue Water I* which was converted in 1961 from a submersible by adding vertical columns for flotation. *Blue Water I* started drilling off Louisiana in 90 m of water in 1962. The semisubmersible had arrived. This type of vessel has seen considerable development since then but has maintained its essential form. Figure 1.1 illustrates the evolution of the semisubmersible.

The 1960s also saw the emergence of the drill ship. As the name implies, it is simply a monohull vessel used for drilling purposes. The early drill ships were usually converted from barges, ore carriers, tankers or supply vessels. Drill ships are the most mobile of all drilling units but they are the

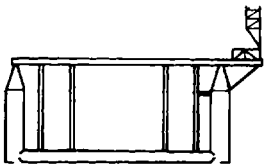

(a) 1962

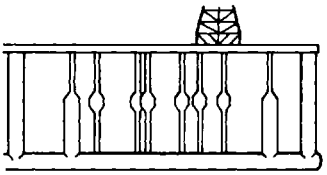

(b) 1963

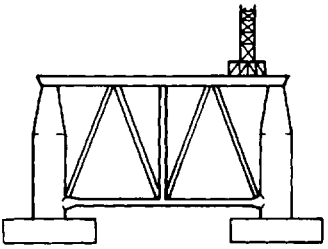

(c) 1965

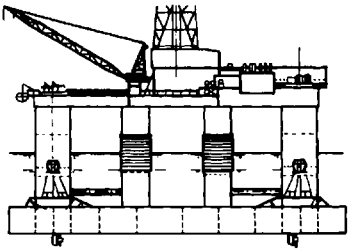

(d) 1975

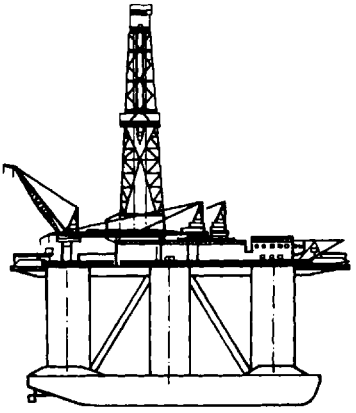

(e) 1983

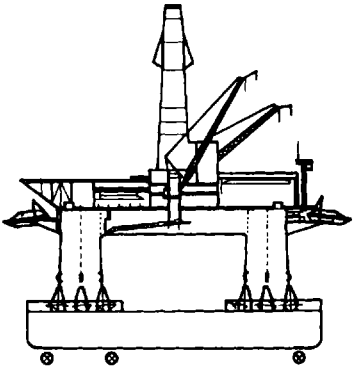

(f) 1985

Figure 1.1. The evolution of the semisubmersible

least productive because of their relatively poor sea keeping characteristics. One important development associated with the drill ship is the concept of the turret mooring system. This system allows the vessel to weather vane. Figure 1.2 shows a typical drill ship with a turret mooring. Despite their poor sea keeping characteristics, drill ships are still used because of their mobility and high payload capacity. Advances in dynamic positioning systems have allowed drill ships to work in deep waters without a conventional mooring spread.

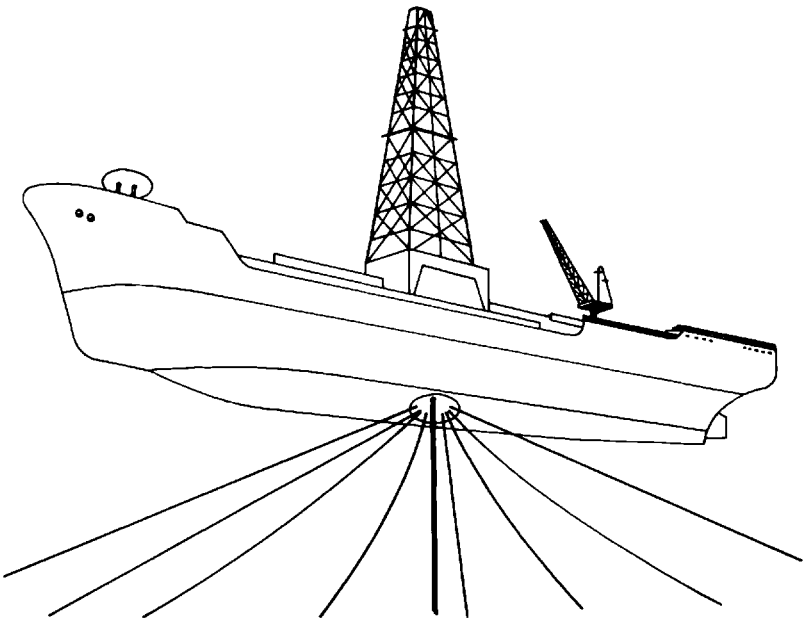

Figure 1.2. Drill ship with turret mooring

The needs of hydrocarbon production differ from those of exploration drilling. Hydrocarbon production requires a stable platform which must be able to carry large amounts of development drilling and oil processing equipment along with support and maintenance services. These requirements have been satisfied with the development of the fixed jacket structure. A typical fixed offshore drilling and production platform is illustrated in Figure 1.3.

Fixed marine structures have evolved considerably from the early timber frame constructions located in a few metres' water depth to the steel structures sited in hostile environments with water depths in the region of 200 m. The largest water depth to date for a fixed jacket structure is 412 m. This is the Bullwinkle platform in the Gulf of Mexico.

However, hydrocarbon reservoir size and characteristics as well as location and water depth raise technical and economic constraints for the feasibility of utilizing fixed platforms. This has led to increased interest in using floating production systems for the exploitation of offshore oil and

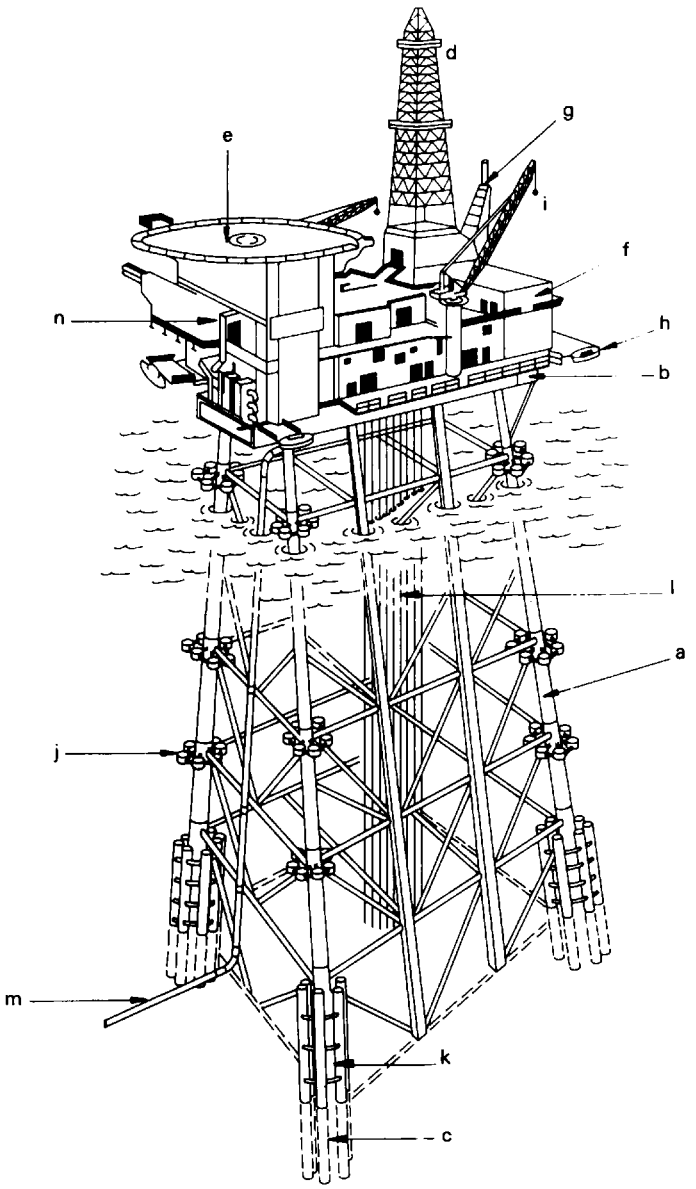

Figure 1.3. Typical offshore drilling and production platform. *Key*: a – jacket; b – module support frame; c – piles; d – drilling derrick; e – helicopter pad; f – drilling and production equipment; g – flare stack; h – survival craft; i – revolving cranes; j – pile guides; k – pile sleeves; l – drilling and production risers; m – export pipes; n – accommodation

gas fields. Many oilfield developments have used tankers for oil storage and export, but with production facilities installed on fixed platforms.

The first floating production system came on stream in June 1975 at the Argyll Field in the UK sector of the North Sea. This system consisted of a

semisubmersible production unit with oil export using shuttle tankers via a single point mooring. Figure 1.4 illustrates the Argyll Field development. This early development has provided considerable experience in operating floating production systems (Blair and Smith, 1988).

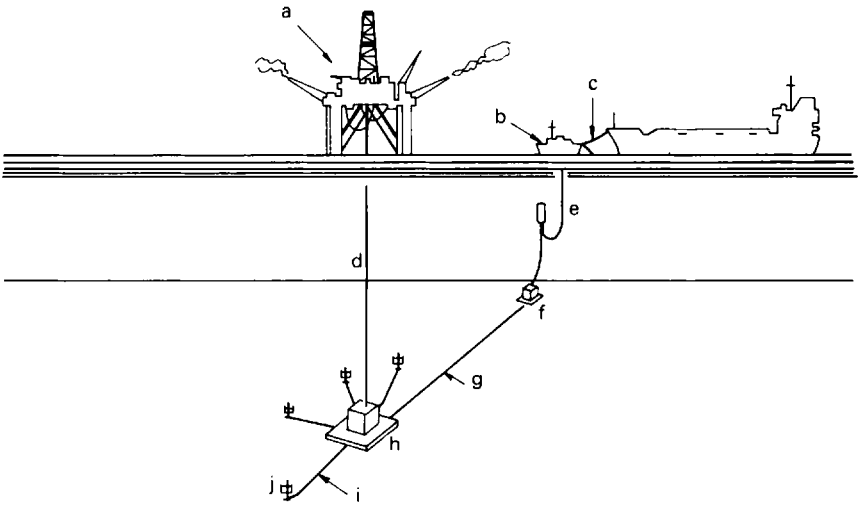

Figure 1.4. Initial Argyll field development concept (Blair and Smith, 1988). *Key*: a – Transworld 58 semisubmersible; b – catenary anchor leg mooring buoy; c – loading hose; d – hard pipe riser system; e – 12″ flexible riser; f – pipeline end module; g – 10″ export pipeline; h – Argyll base manifold and mass anchor; i – 4″ subsea flowline; j – subsea tree

Several oilfield developments have used a combination of fixed and floating production facilities. An example of this approach is the Hondo Field in California's Santa Barbara Channel. The Hondo Field development includes one of the deepest single anchor leg moorings (SALMs) in the world in over 150 m of water. The SALM is made up of a piled base; a double articulated riser (consisting of an upper buoy body and a lower riser section); a triaxial joint joining the yoke to the buoy and a truss type yoke which is hinged to the ship. The terminal moors a 50 000 t deadweight storage and process tanker which receives, processes and stores raw crude from the Hondo platform via the SALM terminal piping. The Hondo field development is shown in Figure 1.5.

The introduction of articulations into a marine structure has led to the development of the Lena guyed tower which was installed in 1983 in over 300 m water depth offshore Louisiana, USA – see Boening and Howell (1984). The guyed tower is similar in structure to a fixed jacket structure but is allowed to rock about its base to give significant horizontal deflections at deck level. These horizontal deflections are restrained by guy lines designed to have differing stiffness responses in operating and extreme weather conditions. The Lena guyed tower is shown in Figure 1.6.

The early 1970s saw considerable interest in the tensioned buoyant platform concept, or the tension leg platform as it is otherwise known. This concept involves a buoyant surface platform which is held in position by

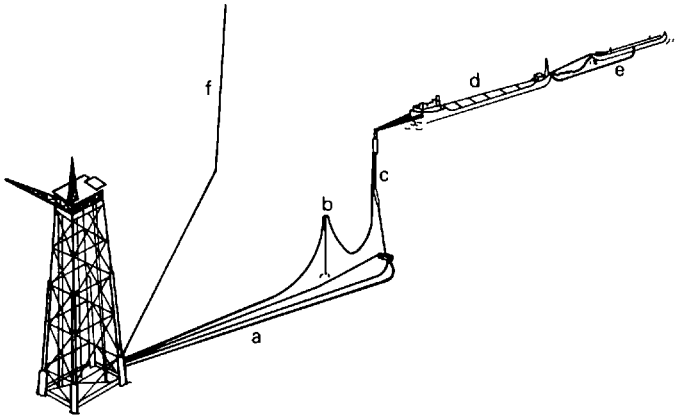

Figure 1.5. Hondo field development (*Offshore Engineer*, 1986). *Key*: a – pipelines; b – power cable; c – single anchor leg mooring; d – offshore storage and treatment vessel; e – shuttle tanker; f – gas pipeline

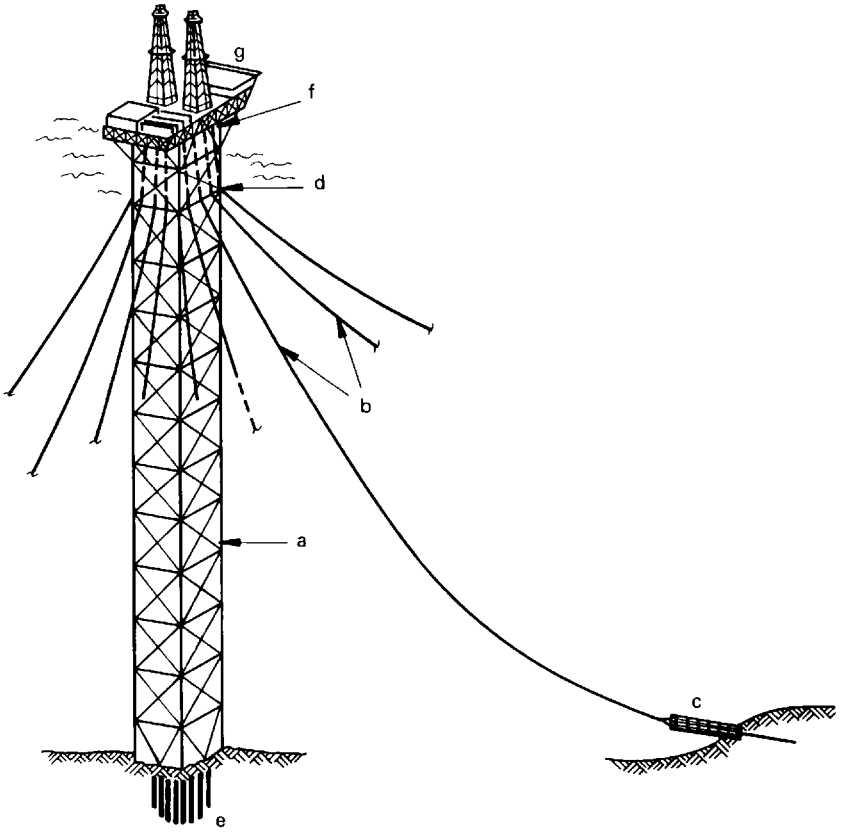

Figure 1.6. Typical guyed tower. *Key*: a – tower; b – guylines; c – clump weight; d – fairleads; e – foundation; f – guyline terminations; g – platform deck

tensioned tethers. The platform's vertical motions are restrained by the tethers while the platform is compliant in its horizontal degrees of freedom. A sea-test programme of a test tension leg platform was carried out in 1975 by Deep Oil Technology, Inc. on behalf of a consortium of oil company sponsors (Horton, 1975). The tension leg platform was on station for a three-month period in 60 m water depth on the seaward side of Santa Catalina Island, offshore California. This test tension leg platform with an operating displacement of 645 t was designated the *Deep Oil X-1* and is shown in Figure 1.7.

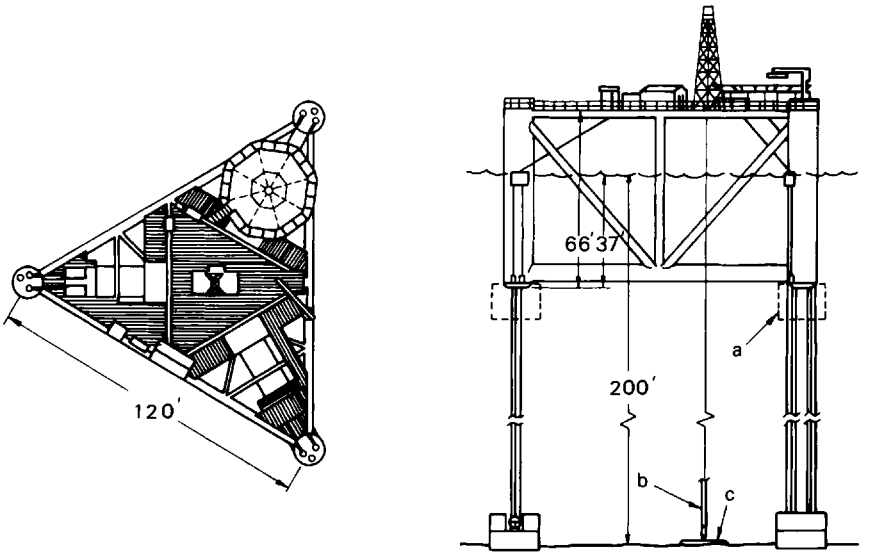

Figure 1.7. *Deep Oil X-1 TLP* (Horton, 1975). *Key*: a – anchor position for tow; b – test riser; c – template

The first oil producing tension leg platform for hydrocarbon production came into operation in 1984 in the North Sea (Mercier, 1982) and can be regarded as a direct descendant of the *Deep Oil X-1*. The platform is located on the Hutton Field in 147 m of water. The displacement of the Hutton tension leg platform is 63 300 t at its operating draught of 33.2 m. This platform is illustrated in Figure 6.1.

Table 1.1 presents an overview of the many other floating production platforms that are in operation or under development.

1.2 Types of structures

The wide variety of compliant marine structures is remarkable. New ideas and developments seem to appear every day. There are, however, general classes of compliant marine structures. These are as follows:

(a) semisubmersibles;
(b) tensioned buoyant platforms;

Table 1.1 The world's floating production systems in order of on-stream date*

Field	*Country*	*Operator*	*On-stream*	*Water depth*	*Max wave*	*Production unit*	*Mooring system*	*Diag.†*
Argyll	UK	Hamilton	Jun 75	79 m	25 m	Conv. semi–TW58	Anchor spread	D
Casablanca	Spain (Med)	Eniepsa	Feb 77	161 m	16 m	Conv. semi	Anchor spread	E
Castellon	Spain (Med)	Shell	Aug 77	117 m	16 m	Conv. tanker	Leg. buoyant yoke	B
Enchova	Brazil	Petrobras	Aug 77	190 m	15 m	Conv. semi–Penrod 71	Anchor spread	E
Dorada	Spain (Med)	Eniepsa	May 78	93 m	13 m	Conv. semi–Sedco 1	Anchor spread	D
Garoupa	Brazil	Petrobras	Feb 79	118 m	15 m	Conv. tanker–P.P. Moraes	Buoyant single leg	C
Nilde	Italy	Agip	Sept 80	95 m	18 m	Conv. tanker	Leg. buoyant yoke	B
Garoupinha	Brazil	Petrobras	Nov 80	120 m	15 m	Conv. semi–Sedco 135F	Anchor spread	E
S. Pampo	Brazil	Petrobras	Dec 80	120 m	15 m	Conv. semi–Sedco Staflo	Anchor spread	E
Hondo	US (Calif)	Exxon	Apr 81	151 m	13 m	Conv. tanker	Buoyant single leg	C
Buchan	UK	BP	May 81	117 m	27 m	Conv. semi	Anchor spread	D
Cadlao	Philippines	Amoco	Aug 81	97 m	17 m	Conv. tanker	Calm yoke	A
Linguado	Brazil	Petrobras	Dec 81	100 m	15 m	Conv. semi–Petrobras 12	Anchor spread	E
Bicudo	Brazil	Petrobras	Feb 82	145 m	15 m	Conv. semi–Sedco 135D	Anchor spread	E
Tazerka	Tunisia	Shell	Nov 82	145 m	10 m	Conv. tanker	Leg. buoyant yoke	B
Corvina	Brazil	Petrobras	Aug 83	226 m	15 m	Conv. semi–Petrobras 14	Anchor spread	E
Pirauna	Brazil	Petrobras	Dec 83	244 m	15 m	Conv. semi–Petrobras 15	Anchor spread	E
Trilha	Brazil	Petrobras	Jun 84	105 m	15 m	Conv. semi–Transworld 61	Anchor spread	E
Duncan/Argyll	UK	Hamilton	Nov 84	79 m	25 m	Conv. semi–Deepsea Pion.	Anchor spread	D
Parati	Brazil	Petrobras	Dec 84	107 m	15 m	Conv. semi–Pentagone 81	Anchor spread	E
Viola	Brazil	Petrobras	Dec 84	127 m	15 m	Conv. semi–Ocean Zephyr	Anchor spread	E
Innes	UK	Hamilton	Jan 85	78 m	25 m	Conv. semi–Transworld 58	Anchor spread	D
Geisum	Egypt (G.Suez)	Conoco	Nov 85	45 m	6 m	Conv. tanker	Anchor spread	F
Mila	Italy (Sicily)	Montedison	Dec 85	55 m	14 m	Conv. tanker–Acqua Blu	Calm yoke	A
Akam	Nigeria	Ashland	Jan 86	42 m	10 m	Conv. tanker	Fixed jacket	G
Kakap	Indonesia	Marathon	Apr 86	85 m	11 m	Conv. tanker	Calm yoke	A
White Tiger	Vietnam	Sudoimport	–	55 m	16 m	Conv. tanker	Calm yoke	A
Kepiting	Indonesia	Conoco	Jun 86	90 m	12 m	New barge	Anchor spread	F
Jabiru	Aust. (Timor S.)	BHP	July 86	119 m	16 m	Conv. tanker	Buoyant riser	C
Weizhou	China	Total	Mid 86	37 m	19 m	Conv. tanker	Fixed tower (EMH)	G
Petrojarl	Norway	For N. Hydro	Sept 86	110 m	29 m	New ship	Turret & dp	F
Balmoral	UK	Sun Oil	Feb 87	143 m	29 m	New semi	Anchor spread	E
Green Canyon	US (G. Mex.)	Placid	Mid 87	500 m	22 m	Conv. semi–Penrod 72	Anchor spread	E
Swops/Cyrus	UK	BP	Mid 87	112 m	29 m	New ship	dp	F
Bohai	China	JCODC	Late 87	23 m	10 m	New barge	Fixed tower	G
Ivanhoe	UK	Amerada	Aug 88	125 m	28 m	Conv. semi–Sedco SS?	Anchor spread	E
Snorre	Norway	Saga	1989	350 m	31 m	Conv. tanker?	–	–
Emerald	UK	Sovereign	1989	150 m	31 m	Conv. semi?	–	–

Riser	*Oil transport*	*Eng. contr.*	*Tanker dwt*	*Wells*	*Oil capy.*	*Storage (bbls)*	*Remarks*	*Field*
Rigid	Shuttle, spm		–	7	40 000 b/d	–	£125mn project. TW58 moves 84 (see Duncan).	Argyll
Flex	Shuttle/pipe		–	2	20 000 b/d	–	Bideford Dolphin to May 78, then Afortunada.	Casablanca
Flex	Shuttle, side	SBM Inc	60 000 t	2	20 000 b/d	350 000	£32mn project. Linked bars leg, clamped riser.	Castellon
Flex	Shuttle, spm		–	11	60 000 b/d	–	Started with one well and built up.	Enchova
Rigid	Shuttle, direct		–	3	20 000 b/d	–	Was extended well test, to Dec 85.	Dorada
Flex	Shuttle, spm	Canocean	55 000 t	6	50 000 b/d	350 000	Now replaced by platform.	Garoupa
Rigid	Shuttle, side	SBM	84 000 t	1	20 000 b/d	550 000		Nilde
Rig/Flex	Shuttle		–	3	10 000 b/d	–		Garoupinha
Rig/Flex	Shuttle, spm		–	4	40 000 b/d	–		S. Pampo
Rigid	Shuttle	Imodco	50 000 t	–	37 000 b/d	250 000	Limited processing on vessel. Wells at jacket.	Hondo
Rigid	Spm (pipe 87)		–	8	72 000 b/d	–	£280mn project.	Buchan
Flex	Shuttle, tandem	SBM	127 000 t	2	30 000 b/d	72 000	Leased system. Steep S riser.	Cadlao
Rig/Flex	Shuttle, spm		–	10	40 000 b/d	–		Linguado
Rig/Flex	Shuttle, spm		–	5	20 000 b/d	–	Platform replacing soon.	Bicudo
Rigid	Shuttle, side	SBM	210 000 t	8	30 000 b/d	–	$190mn project. High pressure swivel	Tazerka
Rig/Flex	Shuttle, spm		–	6	40 000 b/d	–		Corvina
Flex	Shuttle, spm		–	8	30 000 b/d	–	Deepest subsea well is 383m.	Pirauna
Rig/Flex	Shuttle, spm		–	4	10 000 b/d	–		Trilha
Rig/Flex	Shuttle, spm	RJBA	–	11	70 000 b/d	–	£110mn project. Flex riser for water (60,000b/d).	Duncan/Argyll
Rig/Flex	Shuttle		–	6	20 000 b/d	–		Parati
Flex	Shuttle		–	5	18 000 b/d	–		Viola
Rigid	Shuttle, spm	RJBA	–	1	10 000 b/d	–	£15mn project. Via Argyll spm.	Innes
Flex	Heated shuttle	Imodco	227 000 t	8	20 000 b/d	1 mn	Shut in, March 86. Lazy wave riser.	Geisum
Flex	Shuttle, tandem	Bluewater	70 000 t	2	20 000 b/d	–	Leased system.	Mila
Rigid	Shuttle, tandem	SBM	285 000 t	–	80 000 b/d	1.75 mn	Two more fields to be tied in. Up to 20 wells.	Akam
Flex	Shuttle, side	SBM/Modec	140 000 t	8	22 000 b/d	55 000	Now on stream.	Kakap
Flex			150 000 t				Installed. Delays in going on stream.	White Tiger
Flex	Heated shuttle	Comb. Eng.	–	2	10 000 b/d	72 000	Leased system.	Kepiting
Flex	Shuttle	SBM	160 000 t	1	30 000 b/d	1 mn	A$60mn project. Disconnectable in cyclone.	Jabiru
Rigid	Shuttle, side		174 000 t	6	30 000 b/d	600 000	Trial production. Disconnectable.	Weizhou
Rig/Flex	Shuttle, tandem	(Golar Nor)	52 000 t	1	30 000 b/d	190 000	Vessel cost £75mn. Operator Golar Nor.	Petrojarl
Flex	Pipeline		33 000 t	19	60 000 b/d	–	£400mn plus project. Built-in workover.	Balmoral
Rig/Flex	Pipeline		–	24	15 000 b/d	–	Will gain world depth record.	Green Canyon
Rigid	Itself	BP/H&W/MH	76 000 t	3	15 000 b/d	300 000	Vessel cost £110mn.	Swops/Cyrus
Rigid	Shuttle, side	(Bluewater)	75 000 t	4	10 000 b/d	–	Disconnectable.	Bohai
Flex	Pipeline	Brown & Root	–	8	50 000 b/d	–	£375mn project.	Ivanhoe
–	–		–	–	–	–	Decision July 86 on extended pilot.	Snorre
–	–	Global Eng.	–	–	–	–	Still at conceptual stage.	Emerald

* This list is strictly limited to *production*; no 'storage only' floaters are included, nor is the single operational tension leg platform Hutton on it, nor other prospective TLPs

† Basic layout diagrams, shown on p. 12, are generalized; for example, Hondo and Jabiro, both classed as 'C', differ markedly in reality

Table 1.1 (continued)

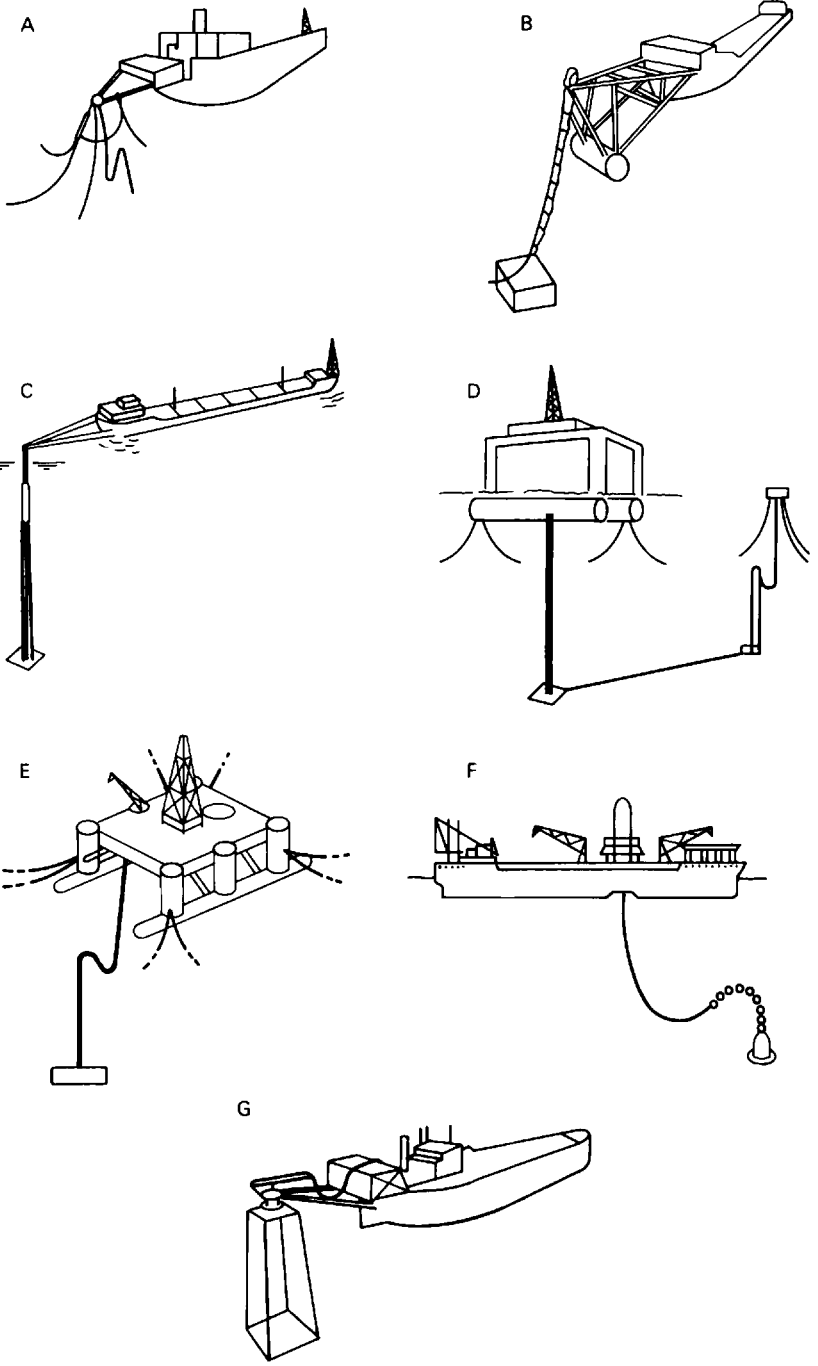

(c) articulated structures;
(d) single point moorings;
(e) monohull vessels;
(f) multi-hull vessels.

Each of the above classifications of compliant marine structures is briefly discussed below.

Semisubmersibles are floating platforms with a geometry that is considerably different from conventional ship, or monohull, forms. Such vessels are widely used by the offshore oil industry because of their relatively low wave induced motion response – a perspective view of a semisubmersible is shown in Figure 1.8. The low motions of a semisubmersible are a consequence of its hull form which consists of deeply submerged pontoons connected to an elevated deck by several large diameter water surface piercing columns together with bracing members. Thus, a large proportion of the vessel's submerged volume is at a deep draught where wave pressures have decayed rapidly with depth. The small water plane area of a semisubmersible and its large submerged volume yields long natural periods in heave, roll and pitch. These periods are well above the range of periods observed for ocean gravity waves, further contributing to reduced motions.

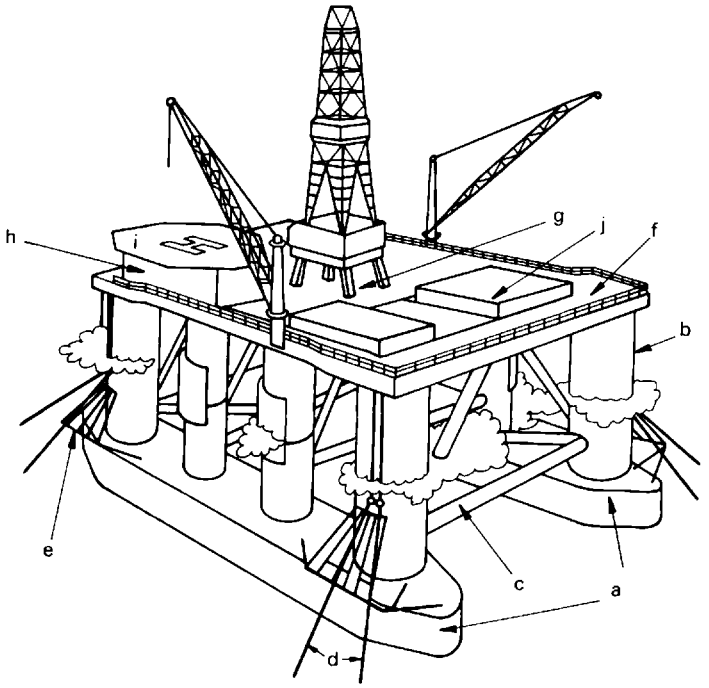

Figure 1.8. Typical semisubmersible vessel. *Key*: a – submerged pontoons; b – surface piercing deck support column; c – bracing members; d – mooring lines; e – anchor racks; f – deck structure; g – moonpool; h – accommodation; i – helicopter pad; j – drill pipe racks

The main limitation of semisubmersibles is their relatively low payload capacity. This is primarily due to their small water plane area and large displacement. As a consequence semisubmersible designs often represent a balance between wave induced motions and payload capacity. The quest for the optimum compromise between heave motions and payload capacity has led to complex semisubmersible designs. One latest example is the Trendsetter class semisubmersible *Zane Barnes* (Allan, 1988) which has a central caisson and pontoons with variable cross-section, as shown in Figure 1.9. Nevertheless, the heave motion of a semisubmersible is still a significant factor in curtailing marine operations such as drilling or hydrocarbon production. Therefore, it is desirable to reduce heave motion in order to reduce the down-time of the vessel.

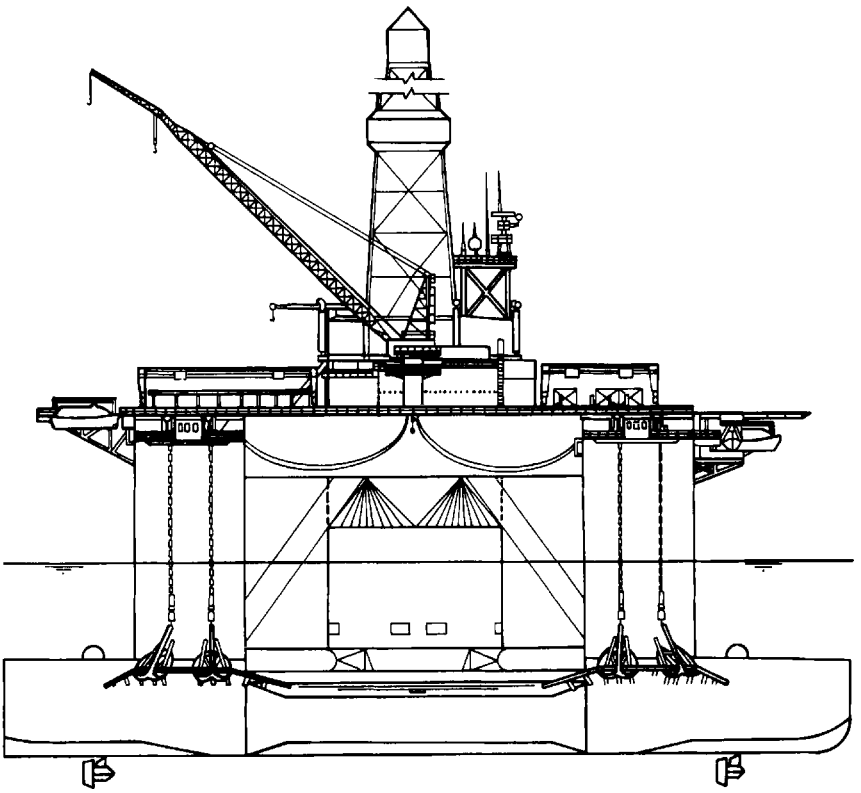

Figure 1.9. *Trendsetter Zane Barnes*

This has led to the development of passive motion suppression devices. One such device is in the form of open bottom tanks which are known as motion suppression tanks. These tanks are attached to the vessel at the water line and extend some distance above and below still water level. Each tank is open to the sea at its base and traps a volume of air above the internal water level. On semisubmersibles, the tanks take the form of annular volumes surrounding some or all of the surface piercing columns.

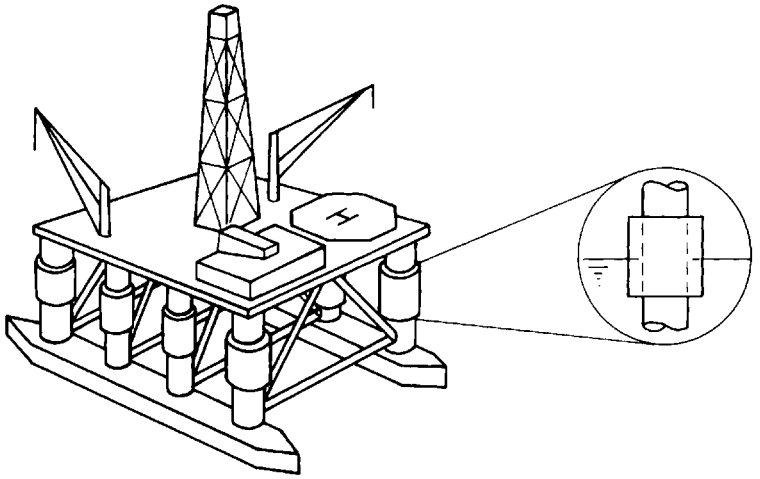

Figure 1.10. Semisubmersible with motion suppression tanks

Figure 1.10 shows a schematic view of an annular motion suppression tank attached to a semisubmersible column. The trapped air mass inside the tank introduces a pneumatic 'compliance' between wave action and the motions of the vessel. This device helps reduce wave induced motions.

Another approach to increase the payload capacity of a semisubmersible while maintaining low wave induced motions is to introduce structural articulations into the semisubmersible's structure. This allows the vessel to maintain a large span and draught without the corresponding increase in structural weight. One such design is the articulated column semisubmersible shown in Figure 9.1.

The tensioned buoyant platform (or tension leg platform) has evolved from the semisubmersible concept. The platform structure is similar to that of a semisubmersible. However, the platform has excess buoyancy over self weight and is held in position at its operating draught by tensioned tethers anchored to the sea bed. Figure 6.1 shows a typical tensioned buoyant platform. The tensioned buoyant platform vertical motions are now constrained but the platform retains its compliance in the horizontal modes of motion.

The articulated tower shown in Figure 1.11 is the simplest illustration of a compliant marine structure. The tower is connected to a subsea base by a universal joint which allows free movement in all vertical planes. The subsea base may be piled into the sea bed or be of sufficient submerged weight to remain stationary on the sea bed. The articulated tower is held upright by a level of excess buoyancy over self weight in its structure. Thus, the universal joint at the base coupled with an angular stiffness due to excess buoyancy yields a compliant structure which will tilt due to wave action or other horizontal forces.

The performance advantage of an articulated tower over an equivalent rigid alternative arises from the fact that the tower tilts in waves, thus reducing wave induced surge forces on itself due to reduced relative

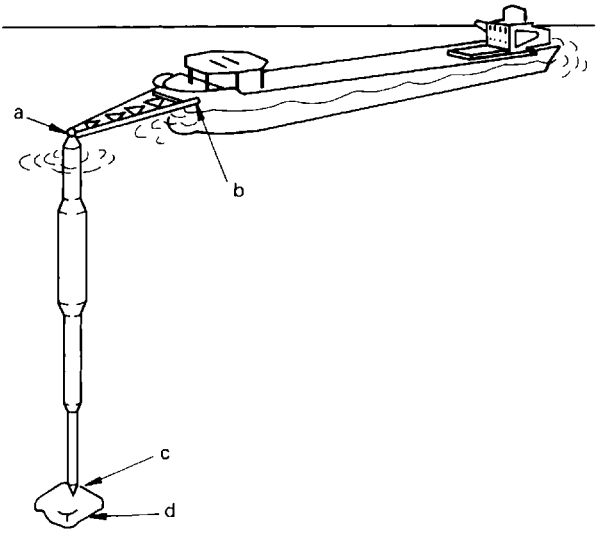

Figure 1.11. Articulated tower. *Key*: a – mooring yoke, universal-joint and swivels; b – hinge; c – universal-joint; d – base

velocities and accelerations between the tower and surrounding wave fluid. The same principle resists the effects of the hawser loads due to a tanker moored at the tower. The overturning moment due to such hawser loads is balanced by a resisting moment due to the tower angular stiffness and tilt angle. Design of an articulated tower must, therefore, ensure that the natural period in tilting motion is above the range of predominant wave periods. This minimizes the effects of dynamic magnification in tilt motions and is consistent with the requirement that the tower should be as compliant to oscillating wave forces as possible but capable of resisting steady forces from tanker mooring tension, wind and current.

A variation on the articulated tower is the guyed tower. The guyed tower has mooring lines which provide a restoring force, thus restraining the horizontal motions of the tower to a certain degree.

Single point moorings are probably the most common type of permanently installed compliant marine structures. There are numerous variations, some of which are illustrated in Figure 1.12. Many of these designs are currently in operation.

Monohull vessels are often used in association with single point moorings for hydrocarbon processing, storage and export. These vessels are usually converted tankers with the main differences being in the functional layout, mooring systems and propulsion. The primary advantage of using a monohull vessel is its high payload capacity – the principal drawback is the relatively high motion in moderate sea states. This is alleviated to a certain extent by the design of a mooring system which allows the vessel to weather vane, and by incorporating motion suppression devices. Figures 1.13 and 5.2 show representative modern monohull vessels typical of those that can be used for well testing and hydrocarbon production in the North Sea.

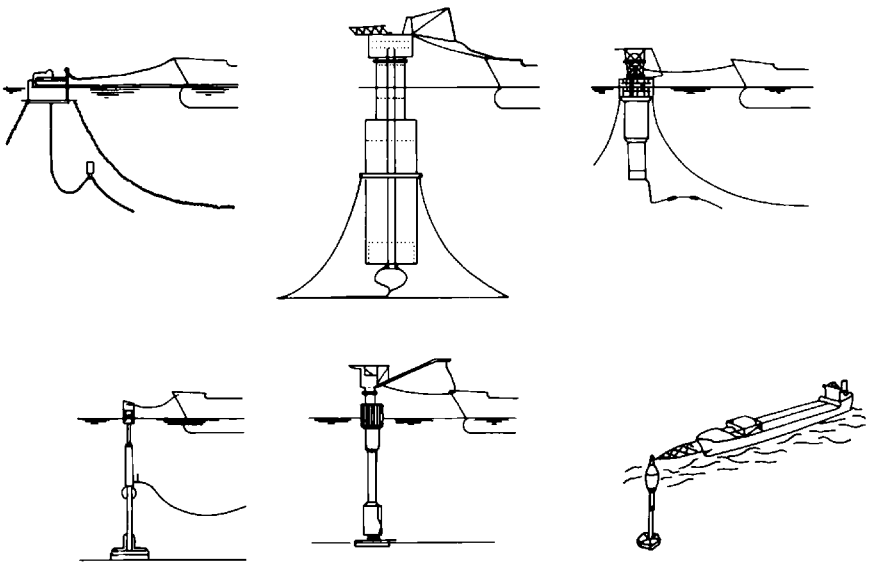

Figure 1.12. Typical North Sea single point moorings. Top left – CALM (catenary anchor leg mooring); top centre – SPAR (single point anchor reservoir); top right – ELSBM (exposed location single buoy mooring); bottom left – SALM (single anchor leg mooring); bottom centre – ALT (articulated loading tower); bottom right – YMS (yoke moored storage)

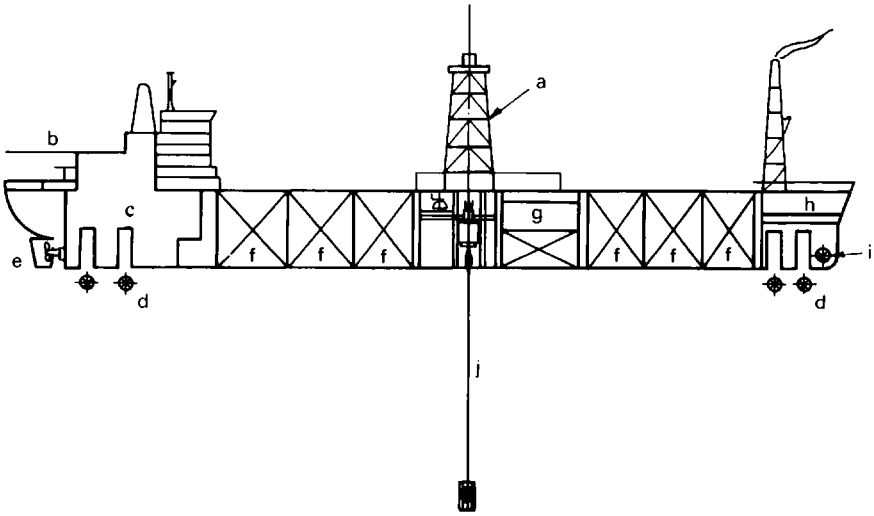

Figure 1.13. Monohull floating production vessel. *Key*: a – riser carrier; b – helicopter deck; c – machinery; d – retractable thrusters; e – two fixed thrusters; f – cargo; g – process; h – machinery; i – tunnel thruster; j – riser

The relatively large length of some modern tankers has led to the development of placing a structural articulation in the centre of the ship. This is illustrated in Figure 1.14. The purpose of this hinge is to alleviate the midships bending moment.

The extension of the monohull vessel to a multi-hull vessel such as a catamaran or trimaran has yet to find application in exposed offshore locations, although these vessels have been used as crane vessels in sheltered waters because of their high hydrostatic stability. A different kind of multi-hull vessel which is of considerable interest is the tandem hull barge shown in Figure 8.1. The tandem hull concept consists of a lower hull, which is totally submerged, separated from an upper hull by interhull columns. The objective of this design is to combine the best features of both semisubmersible and monohull vessels – low wave induced motions and high payload capacity.

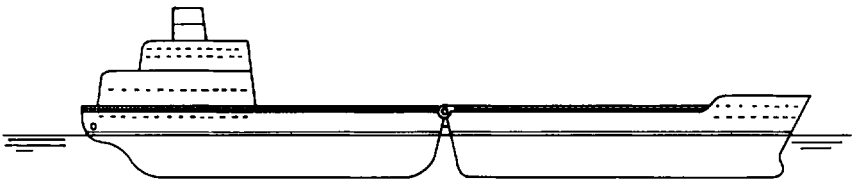

Figure 1.14. Hinged ship

1.3 General analysis and design requirements

The analysis and design of compliant marine structures has rapidly advanced in the last two decades, with numerous techniques being currently available to evaluate and predict their operating performance. A compliant marine structure consists of a number of subsystems which are highly interactive. These subsystems can be classified into the surface platform and process plant, the mooring system, flexible or rigid marine risers, product storage and export facilities.

Technical assessments of each of the above systems tend to be isolated into different disciplines such as naval architecture, structural design, process equipment design, and so on. However, the interactive behaviour of the whole system is such that design and specification of each subsystem must account for potential effects on other subsystems or the whole facility.

The general design criteria for a compliant marine structure are listed below in a perceived order of importance:

1. The structure must be fit for the purpose of being operated safely in a generally hostile marine environment.
2. It must have sufficiently high payload for all reasonable processing, marine systems and possible oil storage options.
3. Wave induced motions must be sufficiently low to allow plant, marine equipment and crew to function with an economically viable low down-time.

4. Mooring system loads in extreme sea states must be acceptable but exhibit sufficiently low vessel offsets to allow a riser system to function with low down-time.
5. The system must survive extreme sea states with or without remedial actions such as pulling risers or slackening moorings.
6. All certification, inspection and maintenance requirements must be satisfied.
7. Initial and running costs as well as construction and installation timescales should be financially viable for the field to be developed.

The assessment of a compliant marine structure's ability to satisfy the above design criteria requires analysis capabilities in the following areas:

(a) modelling of the marine environment;
(b) hydrostatics;
(c) environmental loading;
(d) hydrodynamics in waves;
(e) structural design and analysis;
(f) moorings and risers.

The state of knowledge in each of the above areas has advanced considerably since the 1960s. This book describes typical analysis methods which cover most of the above areas but with special emphasis on the determination of hydrostatic and hydrodynamic characteristics. Applications of these analysis methods to a range of compliant marine structures are illustrated by specific treatment of selected conventional and novel structure types.

References

Allan, R. J. (1988) Integrated motion, stability and variable load design of the Trendsetter class semisubmersible *Zane Barnes*. *Proceedings of the Offshore Technology Conference*, OTC 5625

Blair, E. A. and Smith, C. A. (1988) An overview of Argyll area operation. *Proceedings of the Offshore Technology Conference*, OTC 5688

Boening, D. E. and Howell, E. R. (1984) Lena guyed tower project overview. *Proceedings of the Offshore Technology Conference*, OTC 4649

Count, B. M. (ed.) (1980) *Power from Sea Waves*. Academic Press, London

Count, B. M. (1978) On the dynamics of wave power devices. *Proceedings of the Royal Society of London*, **A**, 363, 559–579

Evans, D. V. (1981) Power from water waves. *Annual Review of Fluid Mechanics*, **13**, 157–187

Horton, E. (1975) *Deep Oil X-1* tension leg platform prototype completes Pacific Coast test. *Ocean Industry*, September, 244–247

Mercier, J. A. (1982) Evolution of tension leg platform technology. *Proceedings of the Third International Conference on the Behaviour of Offshore Structures (BOSS82)*, 2–5 August

Salter, S. H. (1974) Wave power, *Nature*, **249**, 720–724

Chapter 2

Ocean wave excitation

Compliant marine structures have to be designed to withstand the static and dynamic forces exerted by environmental phenomena which include wind, current, tidal action and waves. In addition, structures in cold regions have to withstand ice impacts and icing loads, and structures with sea bed connections need to be designed for the effects of seismic activity.

Of these environmental phenomena, ocean gravity waves generally induce the largest oscillatory forces on marine structures and do so throughout its life time. Most of the analysis and design associated with compliant structures is, therefore, based on their displacement and stress response to dynamic wave excitation. The analysis methods presented in this book are, consequently, directed solely at these wave induced responses. Work on the response of compliant structures to wind, current and earthquake loading is also relevant to design. Such work is available in the offshore engineering research literature and is not covered within this book.

2.1 Ocean waves as a random process

Consideration of the gravity wave loading of compliant marine structures requires physical and statistical descriptions of the mechanics of ocean waves. The physical description of ocean waves is available at various levels from linear theory embodying infinitesimal wave height and other related assumptions to Stokes' fifth order theory offering a series based solution for waves of finite height. There is an extensive body of research literature on these various wave theories – Patel (1989) and Sarpkaya and Isaacson (1981) give overviews of the various wave theories used for the analysis of offshore structures. These theories are not described in great detail here.

However, the statistical description of the occurrence of ocean waves on a wave-by-wave basis or as discrete storms needs to be well understood for evaluating compliant marine structure designs. These two levels of statistical descriptions differ fundamentally with the first making use of a description of wave elevations, velocities, accelerations and pressures within a set of waves of given (known) severity. The second level involves

the prediction of overall extreme storm events over a specified long time period. Such an extreme event is defined as one which occurs, on average, once in a specified number of years – the time period being known as the return period.

The most common approach for selection of wave design criterion for marine structures is to estimate an extreme value parameter (such as the maximum wave height) associated with a return period which equals or exceeds the expected service life of the marine structure. The choice of the design return period is determined on the basis of the expected life of the marine structure and the accepted level of risk of structural damage within that time.

Compliant marine structures are required to survive a nominal 50 (or 100) year return period storm. This storm is represented by applying 50 year return period values of all the environmental parameters (i.e. wind, currents and waves) simultaneously and, for vectorial quantities, in the same direction. This representation is much more severe than a real 50 year event. It does, however, have the advantage of including an additional safety margin and it is a convenient device for designers who would otherwise have to adopt a more complex approach.

A more realistic approach would be to evaluate the joint probability of occurrence of all the environmental parameters and to establish the combined 50 year event. This would result in a large variety of combinations of environmental conditions which would give rise to different dynamic responses and structural loads. Also, the more realistic combined 50 year event may not impose loads of sufficient severity for use as design limits and, therefore, an increase in the design return period may be required.

The use of the joint probability of occurrence of environmental parameters for the prediction of design criteria is a complex procedure and is inherently more difficult to carry out. This approach is also hindered by the absence of sufficient environmental data. It is for this reason that the simpler design principle of worst case simultaneous occurrence generally finds application.

The problem then becomes one of estimating the required 50 year values using all the data available. The parameters which are generally required to define the static design load condition for a fixed marine structure are the one minute mean wind speed; the significant wave height, H_s; and the mean zero-crossing period, T_z; the 'maximum' wave height, H_{max} and its associated period, T_{max}; the vertical profile of total current speed; and the maximum and minimum water levels. Directions are also required for vector parameters.

The above approach has been successfully used for the selection of environmental design criteria for fixed offshore structures. However, it is inadequate on its own for the assessment of compliant marine structures.

The dynamic characteristics of compliant marine structures are such that extreme structural loads and responses may occur in wave conditions which are less severe than the design return period values. As a consequence of the potential problems of dynamic amplification occurring with compliant marine structures, the design criteria must include sets of wave parameters together with their energy – frequency – direction distributions and the

corresponding probabilities of occurrence. This data is also required for the assessment of cumulative fatigue damage. The selection of wave design parameters requires short term and long term statistical models of the physical parameters in question. Both these models will be described below.

The sea surface in a storm exhibits chaotic behaviour. The water heaves and tosses in an apparently random manner in the general downwind direction. Individual waves are short crested and preserve their identities for relatively short periods of time. This behaviour appears to the observer to be far removed from the long crested waves of permanent form which are implied by most deterministic mathematical theories for ocean waves (Weigel, 1964; Stoker, 1957; Cokelet, 1977; Lamb, 1975).

Analysis of ocean waves requires a statistical model based on our knowledge of surface gravity waves. One such model is to assume that the sea surface is composed of a large number of superimposed simple harmonic progressive waves propagating in different directions with different amplitudes and phases. This approach is illustrated in Figure 2.1.

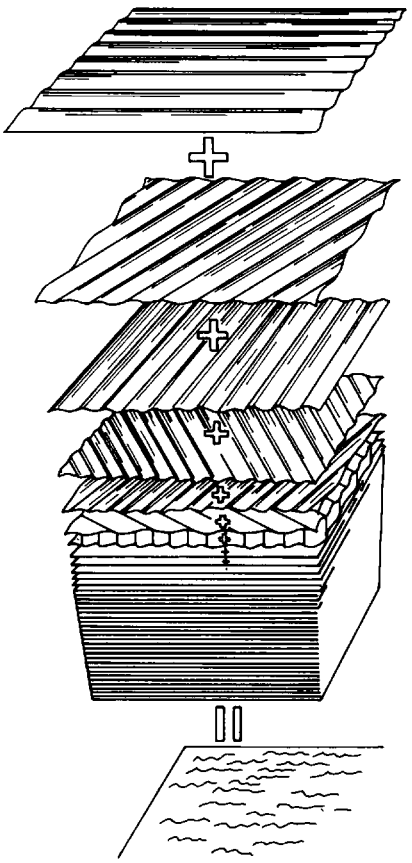

Figure 2.1. Structure of a random sea (Pierson *et al.*, 1958)

Consider the progressive wave travelling along the x_0 direction in Figure 2.2 with wave speed (or celerity), c. The water surface elevation, η, is given by

$$\eta(x_0, t) = a \cos(kx_0 - \omega t) \tag{2.1}$$

where a is the wave amplitude; k is the wave number; and ω is the angular frequency in radians per second.

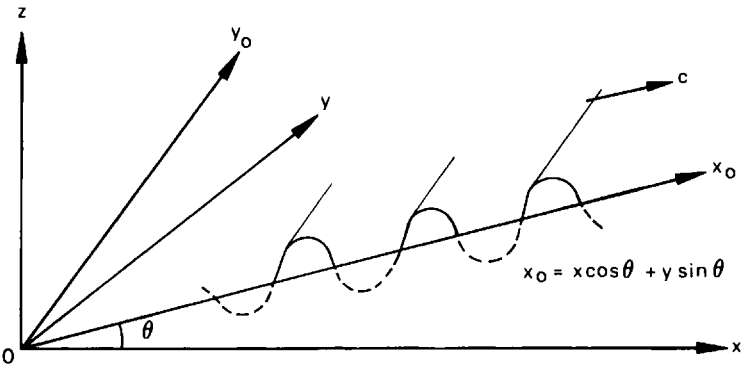

Figure 2.2. Definition of progressive waves moving in an arbitrary direction

In terms of the general axis system:

$$\eta(x, y, t) = a \cos(k\{x \cos\theta + y \sin\theta\} - \omega t + \epsilon) \tag{2.2}$$

where θ is the angle between the x and x_0 axes measured in a counterclockwise direction with respect to the x axis; and ϵ is the phase of the wave at $x = y = t = 0$.

The wave number, k, is related to the angular frequency, ω, by the dispersion relationship.

$$c^2 = \frac{\omega^2}{k^2} = \frac{g}{k} \tanh(kd) \tag{2.3}$$

where d is the water depth. The general results for linear wave theory are given in Appendix I. The principal interest is in deep water ocean waves where the dispersion relationship becomes

$$kg = \omega^2 \tag{2.4}$$

Wind generated waves at a deep water location may be described by a linear superposition of simple harmonic waves propagating in various directions. The sea surface may be described by

$$\eta(x, y, t) = \sum_i a_i \cos\left[\frac{\omega_i^2}{g}(x \cos\theta_i + y \sin\theta_i) - \omega_i t + \epsilon_i\right] \tag{2.5}$$

That is, the wave surface at time t is given by the sum of an infinite number of component waves for all directions, θ_i, and for all frequencies, ω_i, covering the range $0 \leqslant \theta_i \leqslant 2\pi$ and $0 \leqslant \omega_i < \infty$ respectively. The phase,

ϵ_i, is assumed to be a random variable distributed uniformly over the range $0 \leqslant \epsilon_i \leqslant 2\pi$ and its magnitude depends on ω_i and θ_i.

The amplitude, a_i, is also a random variable with a range $0 \leqslant a_i < \infty$. For any frequency and direction interval, $\Delta\omega\Delta\theta$, the average wave energy is $1/2\ \rho g a_i^2$. Ignoring the factor ρg, the sum of $\frac{1}{2}\ a_i^2$ defines the single sided directional spectral density function $G(\omega, \theta)$:

$$G(\omega, \theta)\ d\omega\ d\theta = \sum_{\Delta\omega} \sum_{\Delta\theta} \tfrac{1}{2}\ a_i^2 \tag{2.6}$$

where $G(\omega, \theta)$ is defined over the frequency range $0 \leqslant \omega < \infty$.

Pierson (1955) makes use of the above definition (Equation (2.6)) to express the profile of a random sea surface by the following stochastic integral representation:

$$\eta(x, y, t) = \int_{-\pi}^{\pi} \int_{0}^{\infty} \cos\left[\frac{\omega^2}{g}(x\cos\theta + y\sin\theta) - \omega t + \epsilon(\omega, \theta)\right] \times \sqrt{[2G(\omega, \theta)\ d\omega\ d\theta]} \tag{2.7}$$

Equation (2.7) is not an integral in the Riemann sense but should be interpreted as the limit of the partial sum

$$\eta(x, y, t) = \sum_{j=-m}^{m} \sum_{i=0}^{n} \cos\left[\frac{\omega_{2i+1}^2}{g}(x\cos\theta_{2j+1} + y\sin\theta_{2j+1}) - \omega_{2i+1}t + \epsilon(\omega_{2i+1}, \theta_{2j+1})\right] \times \sqrt{[2G(\omega_{2i+1}, \theta_{2j+1})(\omega_{2i+2} - \omega_{2i})(\theta_{2j+2} - \theta_{2j})]} \tag{2.8}$$

with the limits

$\omega_{2n} \rightarrow \infty$

$\omega_{2i+2} - \omega_{2i} = 0$

$\theta_{2m+1} \rightarrow \pi$

$\theta_{-2m-1} \rightarrow -\pi$

$\theta_{2j+2} - \theta_{2j} = 0$

Equation (2.7) represents a stationary normal random process in three dimensions. The mathematical proof of this fact is given by Pierson (1955, pp. 126–129).

A measure of the total energy in the wave field is given by the integral

$$\int_{0}^{\infty} \int_{-\pi}^{\pi} G(\omega, \theta)\ d\theta\ d\omega = E \tag{2.9}$$

Often, interest is focused on the energy–frequency distribution in the wave field. A measure of this energy–frequency distribution is given by the spectral density, $G(\omega)$. The total energy, E, is given by

$$E = \int_0^\infty G(\omega)\, d\omega = E[\eta^2] \tag{2.10}$$

where $E[\,.\,.]$ is the expectation operator. The directional spectral density and the power spectral density are related by

$$\int_{-\pi}^{\pi} G(\omega, \theta)\, d\theta = G(\omega) \tag{2.11}$$

which states that the total energy at frequency ω is the sum of the energy at that particular frequency over all directions of travel. A more detailed discussion of the mathematical description of random wave profiles may be found in Pierson (1955), Kinsman (1965), Phillips (1966) and Borgman (1972).

2.2 Short term wave statistics

The designer is not directly interested in the wave elevation process itself, but, rather, in its statistics such as average wave height or maximum wave height. In many severe sea states most of the energy in the wave field propagates in one general direction. Statistical descriptions of unidirectional (or long crested) irregular waves may be made using random process theory. The following assumptions are generally made:

1. Ocean waves are taken to be a weakly stationary, ergodic, normal random process with zero mean.
2. Wave spectral density functions are narrow banded.
3. Wave crest elevations (maxima) are statistically independent.
4. The statistical properties of ocean waves are homogeneous, that is, they are independent of local position.

The assumption that the sea state is represented by a stationary process is only valid for short periods of time – typically 20 minutes to 3 hours.

Figure 2.3 shows a representative wave elevation time history. This diagram illustrates some of the possible definitions of wave height and period. Fortunately, the situation is simplified with narrow banded wave spectral density functions since the wave energy is concentrated in a narrow frequency band and there is effectively only one maximum and minimum between successive up crossings of the mean water level.

Predictions made under the above assumption are known as short term statistics. The sea state is described by its spectrum and its spectral moments.

The kth moment of the wave spectrum, m_k, is defined as

$$m_k = \int_0^\infty \omega^k G(\omega)\, d\omega \tag{2.12}$$

The probability distribution function, $P(\eta)$, for the wave elevation is the probability that a realization of the wave elevation, $\eta(t_0)$, is less than the value η. In notation form:

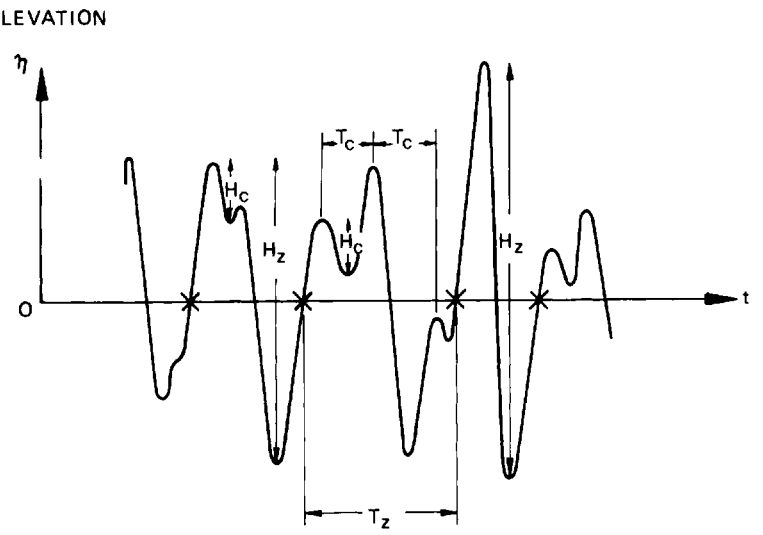

Figure 2.3. Definitions of wave heights and periods

$$P(\eta) = \text{Prob}\,[\eta(t_0) \leqslant \eta] \tag{2.13}$$

$P(\eta)$ is given by

$$P(\eta) = \int_{-\infty}^{\eta} p(z)\,\mathrm{d}z \tag{2.14}$$

or

$$\frac{\mathrm{d}P(\eta)}{\mathrm{d}\eta} = p(\eta) \tag{2.15}$$

where $p(\eta)$ is the probability density function.

For a Gaussian (or normal) wave elevation process with zero mean, $p(\eta)$ is given by

$$p(\eta) = \frac{1}{\sqrt{(2\pi)}\sigma} \exp(-\eta^2/2\sigma^2) \tag{2.16}$$

where σ^2 is the variance of the wave elevation process. The Gaussian probability density function is illustrated in Figure 2.4.

The variance is obtained from the wave spectral density, $G(\omega)$, using the relationship

$$\sigma^2 = \int_0^{\infty} G(\omega)\,\mathrm{d}\omega = m_0 \tag{2.17}$$

The probability distribution for wave amplitude or height is obtained from a crossing analysis and the wave elevation probability density function. Cartwright and Longuet-Higgins (1956) describe the procedure. They also

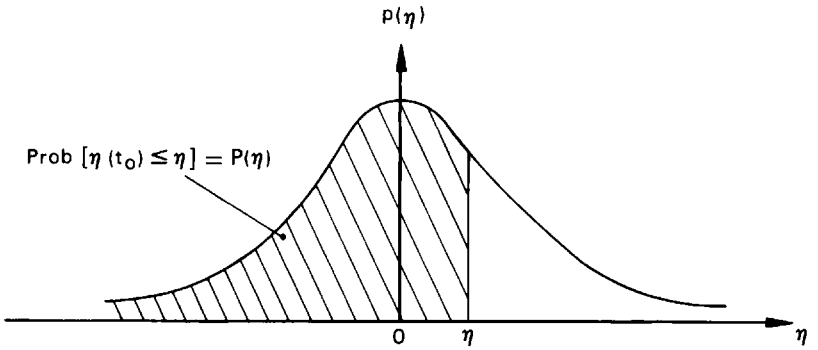

Figure 2.4. Gaussian probability density function with zero mean

show that the distribution of maxima for a Gaussian process depends on the bandwidth of the frequency spectrum. The bandwidth of the frequency spectrum is the frequency range which contains most of the energy in the spectrum. This concept is illustrated in Figure 2.5.

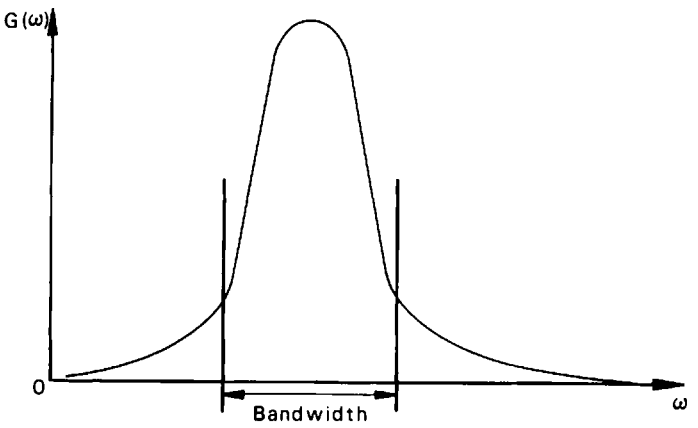

Figure 2.5. Concept of bandwidth for a frequency spectrum

One measure of the bandwidth of the wave frequency spectrum is the bandwidth parameter which is defined in moments of the frequency spectrum. The bandwidth parameter, ϵ, is given by

$$\epsilon^2 = \frac{m_0 m_4 - m_2^2}{m_0 m_4} \tag{2.18}$$

The two limits of ϵ are zero and unity where $\epsilon = 0$ represents a narrow band spectrum and $\epsilon = 1$ indicates a wide band spectrum.

Cartwright and Longuet-Higgins (1956) show that the probability density function of maximum, η_{max}, is given by

$$p(\mu) = \frac{1}{\sqrt{(2\pi)}}[\epsilon \exp(-\mu^2/2\epsilon^2) + \sqrt{(1-\epsilon^2)}\,\mu \exp(-\mu^2/2) \int_{-\infty}^{\mu\sqrt{(1-\epsilon^2)}/\epsilon} \exp(-x^2/2)dx] \tag{2.19}$$

where $\mu = \eta_{max}/\sqrt{(m_0)}$. Figure 2.6 shows this probability density function for a range of bandwidth parameters. For narrow band spectra ($\epsilon = 0$),

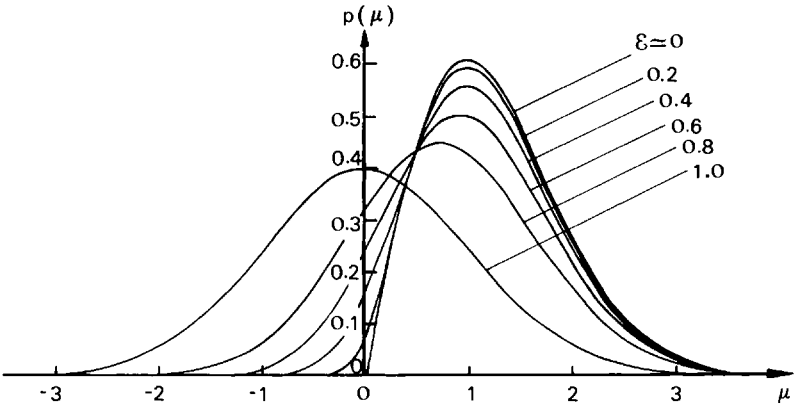

Figure 2.6. Graphs of $p(\mu)$, the probability distributions of the heights of maxima ($\mu = \eta_{max}/m_0^{1/2}$), for different values of the bandwidth parameter ϵ

Equation (2.19) reduces to the Rayleigh probability density function

$$p(a) = \frac{a}{\sigma^2} \exp\left(\frac{-a^2}{2\sigma^2}\right) \qquad 0 \leqslant a < \infty \tag{2.20}$$

where a is the wave amplitude. For narrow banded wave spectra we are interested in the wave height, H, which is twice the wave amplitude. In terms of wave height, H, the Rayleigh probability density function is given by

$$p(H) = \frac{H}{4\sigma^2} \exp\left(\frac{-H^2}{8\sigma^2}\right) \qquad 0 \leqslant H < \infty \tag{2.21}$$

The probability that the wave height exceeds a value H_0 is given by

$$\text{Prob}\,[H > H_0] = P(H_0) = \exp\left(\frac{-H_0^2}{8\sigma^2}\right) \tag{2.22}$$

The Rayleigh probability density function for wave height is shown in Figure 2.7. The Rayleigh distribution is used to predict wave height statistics. For example, the mean wave height, H, is given by

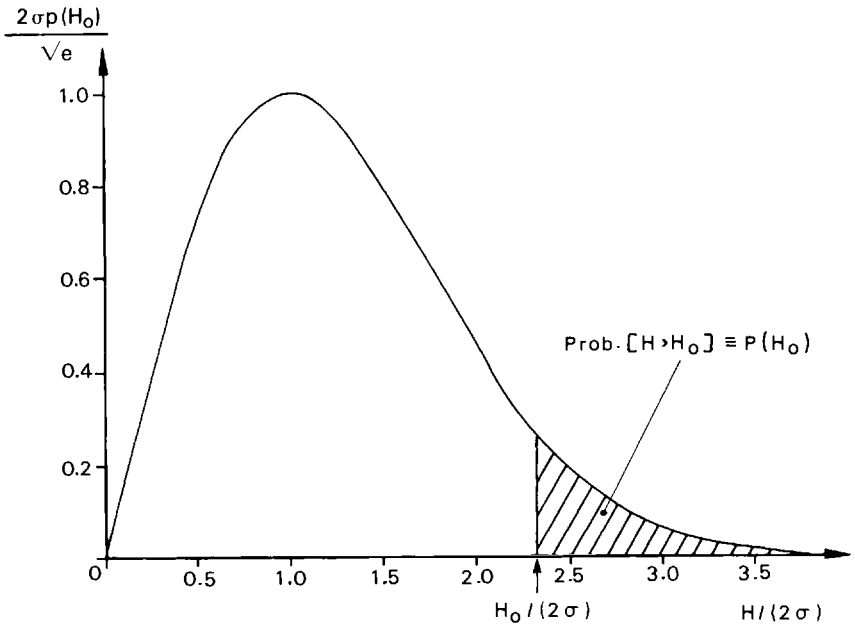

Figure 2.7. Rayleigh probability density function (Ochi, 1982)

$$\bar{H} = \int_0^\infty Hp(H)\,\mathrm{d}H = \sqrt{(2\pi)}\sigma \tag{2.23}$$

and the root mean square wave height H_{rms} is given by

$$H_{\mathrm{rms}} = \sqrt{\left[\int_0^\infty H^2 p(H)\,\mathrm{d}H\right]} = 2\sqrt{(2)}\sigma \tag{2.24}$$

The most widely used wave height statistic which describes the severity of a sea state is the significant wave height. The significant wave height, H_S, is defined as the average of the highest one-third of the wave heights. For this reason the notation $H_{1/3}$ for significant wave height is sometimes found in the literature.

If H_* is the lower limit of the highest one-third of a sample of wave heights then

$$\text{Prob}\,[H > H_*] = \int_{H_*}^\infty p(H)\,\mathrm{d}H = \tfrac{1}{3} \tag{2.25}$$

This is illustrated in Figure 2.8.

If the wave height probability density function is given by the Rayleigh probability density function (Equation 2.21) then

$$\begin{aligned} H_* &= 2\sqrt{(2\ln 3)}\sigma \\ &\simeq 1.048\,\sigma \end{aligned} \tag{2.26}$$

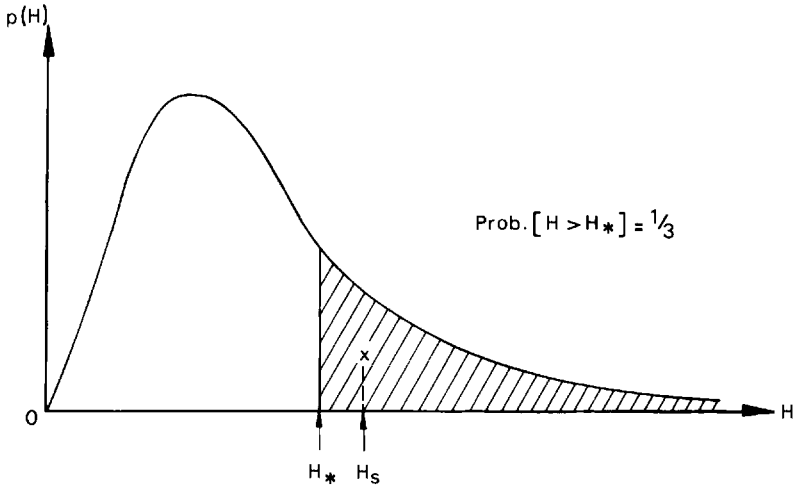

Figure 2.8. Sketch showing the location of significant wave height

Now, H_s is found from (see Figure 2.8)

$$\tfrac{1}{3} H_s = \int_{H_*}^{\infty} H\, p(H)\, dH \tag{2.27}$$

$$= \int_{H_*}^{\infty} \frac{H^2}{4\sigma^2} \exp\left(\frac{-H^2}{8\sigma^2}\right) dH$$

$$= H_* \exp\left(\frac{-H_*^2}{8\sigma^2}\right) + 2\sqrt{(2\pi)}\sigma \left[1 - \Phi\left(\frac{H_*}{2\sqrt{(2)}\sigma}\right)\right] \tag{2.28}$$

where $\Phi(u)$ is the Gaussian Error Integral and is given by

$$\Phi(u) = \frac{1}{\sqrt{(2\pi)}} \int_{-\infty}^{u} \exp(-u^2/2) du \tag{2.29}$$

Substituting $H_* = 2\sqrt{(2 \ln 3)}\ \sigma$ into Equation (2.28) gives

$$H_s \simeq 4.01\ \sigma = 4.01\ \sqrt{(m_0)} \tag{2.30}$$

The significant wave height is related to the area under the 'narrow banded' wave spectrum.

The above arguments may be extended to consider the average of the highest $1/N$th wave heights, $H_{1/N}$

$$H_{1/N} = [\sqrt{(\ln N)} + N\sqrt{(\pi)}\ (1 - \Phi\ (\sqrt{(2 \ln N)}))]\ 2\sqrt{(2)}\sigma \tag{2.31}$$

When N is large, the second term in Equation (2.31) is small compared with the first term and so

$$H_{1/N} \simeq 2\sqrt{(2 \ln N)}\ \sigma \tag{2.32}$$

Table 2.1 Wave height relations based on the Rayleigh distribution

Characteristic height		$\frac{H}{H_{rms}}$	$\frac{H}{\sqrt{(m_0)}}$	$\frac{H}{H_s}$
Standard deviation of free surface	$\sigma_\eta = \sqrt{(m_0)}$	[1/2√(2) =] 0.354	1.0	0.250
Root mean square height	H_{rms}	1.0	[2√(2) =] 2.828	0.706
Mode	$H(p = \max)$	[1/√(2) =] 0.707	[2 =] 2.0	0.499
Median height	$H\left(P = \frac{1}{2}\right)$	[√(ln2) =] 0.833	[2√(ln2) =] 2.355	0.588
Mean height	$\bar{H} = H_1$	[√(π)/2 =] 0.886	[√(2π) =] 2.507	0.626
Significant height	$H_s = H_{1/3}$	1.416	4.005	1.0
Average of 10 highest waves	$H_{1/10}$	1.800	5.091	1.271
Average of 100 highest waves	$H_{1/100}$	2.359	6.672	1.666

Table 2.1 summarizes the wave height relations based on the Rayleigh distribution.

The question remains as to how restrictive is the assumption that the wave spectrum is narrow banded. The effect of the bandwidth parameter, ϵ, on the wave amplitude statistics is illustrated in Figure 2.9. The diagram shows that the narrow band wave spectrum assumption only starts to introduce significant errors in the statistics when ϵ is greater than 0.6 to 0.8. The mean wave amplitude is most in error, with the smallest errors associated with the extreme statistics. For example, the error in significant wave height is overestimated by approximately 8% for ϵ equal to 0.8. Figure 2.9 also shows that the narrow band wave assumption is conservative as it generally overpredicts the wave amplitude statistics. Most sea states observed in the ocean have a bandwidth parameter which lies in the range 0.4–0.8.

The prediction of wave periods is also of importance to compliant marine structures. The wave spectrum already gives information on the energy–frequency distribution. The mean frequency, $\bar{\omega}$, is given by the zero and first moments of the wave spectrum:

$$\bar{\omega} = \frac{m_1}{m_0} \tag{2.33}$$

or in terms of mean wave period, $\bar{T}$:

$$\bar{T} = 2\pi \left(\frac{m_0}{m_1}\right) \tag{2.34}$$

The wave period in a long crested irregular sea is normally defined as the time interval between successive up crossings (or, alternatively, down

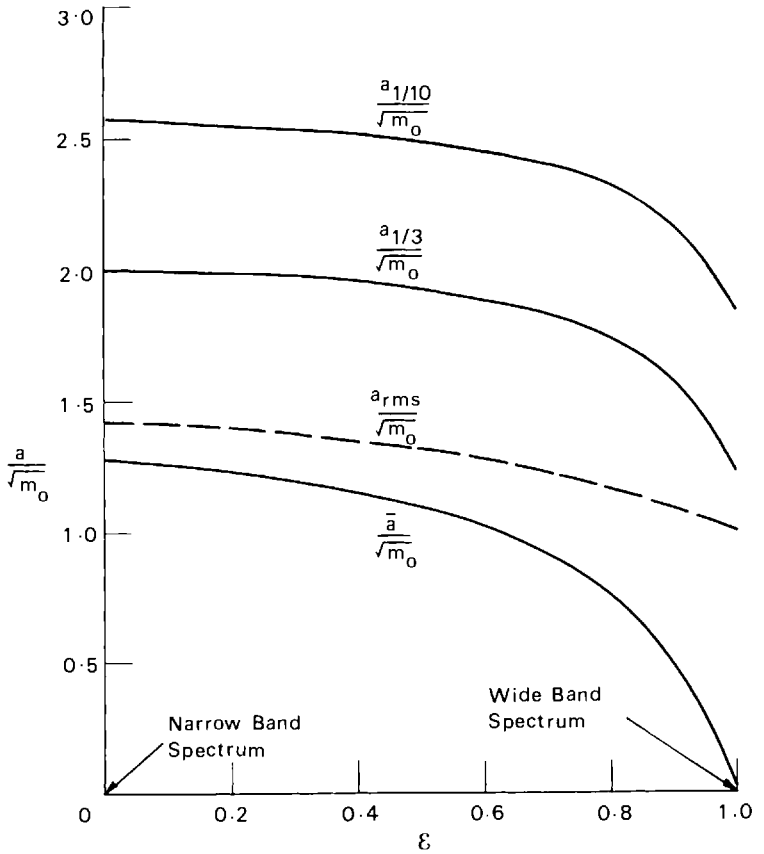

Figure 2.9. Wave amplitude statistics as functions of bandwidth parameter ϵ

crossings) of the zero mean level. If the narrow band wave spectrum assumption is made then the average zero-crossing frequency ω_z and the average zero-crossing period T_z are given by

$$E[\omega_z] = \sqrt{\left(\frac{m_2}{m_0}\right)} \tag{2.35}$$

and

$$E[T_z] = 2\pi \sqrt{\left(\frac{m_0}{m_2}\right)} \tag{2.36}$$

The average time interval, T_c, between successive crests is sometimes used and is given by

$$E[T_c] = \sqrt{\left(\frac{m_2}{m_4}\right)} \tag{2.37}$$

For narrow band processes where the bandwidth parameter tends to zero, T_c is equal to T_z.

The pioneering work of Rice (1944, 1945) set the basis for the prediction of the short term statistics of ocean waves. Rice's work was developed further by Pierson (1952) and Longuet-Higgins (1952, 1956), among others, for the analysis of ocean waves. Ochi (1982) and Carter *et al.* (1986) present excellent reviews of the development of the stochastic analysis of random seas. Comparison between the above theory and observation of ocean waves generally demonstrate good agreement providing confidence in the short term statistical models.

2.3 Wave spectra

Short term predictions of wave height and period may be made once the wave spectrum is known. The wave spectrum may be estimated from wave measurements (Jenkins and Watts, 1968; Bendat and Piersol, 1986; Priestley, 1981). Alternatively, models of the wave spectrum may be selected based on the general environmental conditions and the offshore location. Considerable work has been carried out in the development of spectral models of the sea. These models are presented by Ochi (1982). The wave spectral models generally used for design criteria of marine structures are presented below. One of the earliest spectral models was proposed by Pierson and Moskowitz (1964) and is still widely used. From observations of ocean waves taken in the North Atlantic, Pierson and Moskowitz developed a spectral formulation representing fully developed wind-generated seas. In the derivation of this formulation the wave spectra were first expressed in a dimensionless form. The average line of the measured dimensionless spectra yielded the following spectral formulation in terms of frequency ω:

$$G(\omega) = \frac{\alpha g^2}{\omega^5} \exp\left[-\beta \left(\frac{g/U}{\omega} \right)^4 \right] \qquad 0 \leqslant \omega \leqslant \infty \tag{2.38}$$

where $\alpha = 0.0081$; $\beta = 0.74$; and U is the wind speed at an elevation of 19.5 m above the mean sea level.

The shape of the wave spectrum depends only on the wind speed U and, therefore, this spectral formulation is known as a single parameter spectrum. Figure 2.10 shows Pierson–Moskowitz wave spectra for various wind speeds. The Pierson–Moskowitz is part of a family of wave spectra which have the form

$$G(\omega) = \frac{A}{\omega^5} \exp\left(-\frac{B}{\omega^4} \right) \tag{2.39}$$

where, in the case of the Pierson–Moskowitz wave spectrum, $A = \alpha g^2$ and $B = \beta(g/U)^4$.

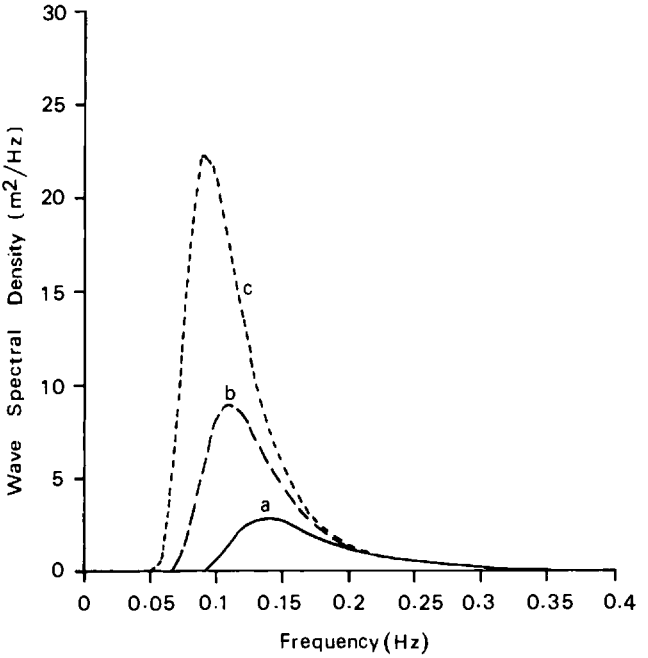

Figure 2.10. Pierson–Moskowitz wave spectrum: (a) 10.0 m/s (Beaufort 5); (b) 12.5 m/s (Beaufort 6); (c) 15.0 m/s (Beaufort 7)

The spectral moments of the Pierson–Moskowitz spectrum are given by

$$m_0 = A/4B$$

$$m_1 = \frac{\Gamma(3/4)}{4}\frac{A}{B^{3/4}} \simeq 0.306\frac{A}{B^{3/4}} \tag{2.40}$$

$$m_2 = \frac{\sqrt{(\pi)}}{4}\frac{A}{\sqrt{(B)}}$$

$$m_4 = \infty$$

where Gamma function, $\Gamma(n)$, is given by

$$\Gamma(n) = \int_0^\infty x^{n-1}\,\mathrm{e}^{-x}\,\mathrm{d}x \tag{2.41}$$

Note that the fourth moment is infinite. This is a general feature of wave spectra with a ω^{-5} tail. This results in the bandwidth parameter, ϵ, defined by Equation (2.18) being equal to unity, the value of a wide band spectrum. Many researchers regard this situation as being more a mathematical quirk than a true reflection of the physical situation since most of the energy is concentrated around the modal frequency, ω_m. This is illustrated in Figure 2.11 which shows the amount of energy in the wave spectrum from zero frequency up to an upper frequency limit, ω_u. Virtually

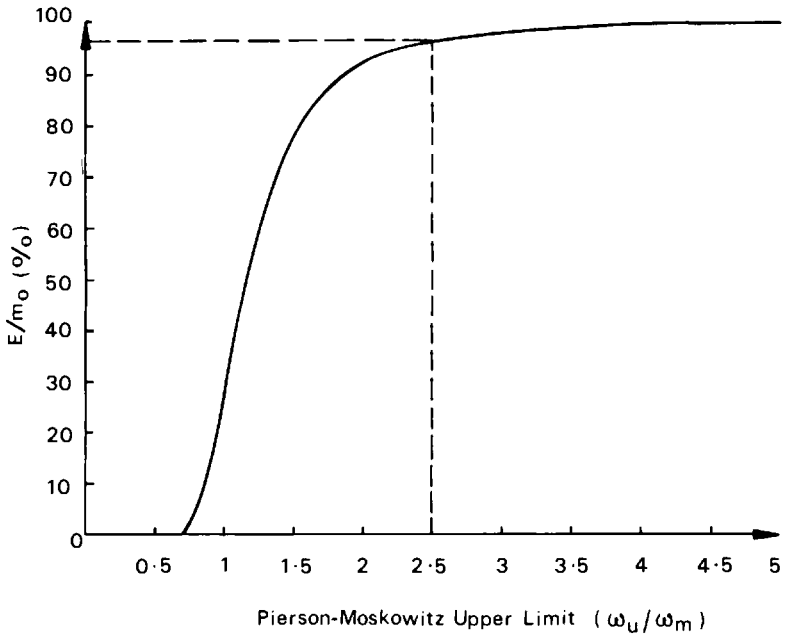

Figure 2.11. Percentage energy in Pierson–Moskowitz spectrum as function of ω_u/ω_m

all the energy occurs below 2.5 ω_m. One approach is to truncate the frequency range by applying an upper frequency limit. One realistic representation of wind waves is to make the upper frequency limit equal to $g/(2\pi U)$; this corresponds to assuming that waves cannot be generated with a phase velocity exceeding the local wind speed, U. Longuet-Higgins (1983) has proposed an alternative measure of bandwidth by the parameter, ν, given by

$$\nu = \frac{m_0 m_2}{m_1^2} - 1 \tag{2.42}$$

The value of ν is zero for a narrow banded sea. It has no upper limit but is approximately 0.42 for a Pierson–Moskowitz spectrum.

The narrow band spectrum assumption is often used for predicting wave height in the seas described by the Pierson–Moskowitz spectrum, even though this spectrum is not, strictly speaking, a narrow band spectrum. This contradiction is inherent in the use of the one parameter spectral formulation (Equation (2.39)). If this spectrum is assumed to be narrow banded then the following relationships exist:

Significant wave height:

$$H_s = (4A/B)^{1/2}$$

Average wave height:

$$\bar{H} = (\pi A/2B)^{1/2}$$

Ratio of the significant and average wave heights:

$$H_s/\bar{H} = \sqrt{(8/\pi)} = 1.60$$

Modal frequency and period:

$$\omega_m = (4B/5)^{1/4}$$

$$T_m = 2\pi(4B/5)^{-1/4}$$

Average frequency and period:

$$\bar{\omega} = m_1/m_0 = \Gamma(3/4)B^{1/4} = 1.23B^{1/4}$$

$$\bar{T} = [2\pi/\Gamma(3/4)]B^{-1/4} = 5.13B^{-1/4}$$

Average zero-crossing frequency and period:

$$\omega_0 = \sqrt{(m_2/m_0)} = (\pi B)^{1/4}$$

$$T_0 = 2\pi^{3/4}/B^{1/4}$$

Ratio of frequencies and periods:

$$\omega_m/\omega_0 = (4/5\pi)^{1/4} = 0.71$$

$$\bar{\omega}_m/\omega = [(4/5)^{1/4}/\Gamma(3/4)] = 0.77$$

$$T_m/T_0 = (5\pi/4)^{1/4} = 1.41$$

$$T_m/\bar{T} = [\Gamma(3/4)/(4/5)^{1/4}] = 1.30$$

(2.43)

The general application of one-parameter Pierson–Moskowitz wave spectrum is limited by the fact that the sea state seldom reaches the fully developed situation. This is particularly true for severe wind speeds where the duration must be sufficiently long over the fetch before the sea reaches its fully developed state. Bretschnieder (1959) has derived a spectral formulation suitable for partially developed seas.

The development of a sea is also limited by the fetch. An extensive wave measurement program, known as the Joint North Sea Wave Project (JONSWAP), was carried out in the North Sea. From the analysis of the measured data, the JONSWAP spectral formulation was derived (Hasselmann *et al.*, 1973). The JONSWAP spectral formulation is representative of wind-generated seas with a fetch limitation. The JONSWAP spectrum is given by

$$G(f) = \alpha \frac{g}{(2\pi)^4} \frac{1}{f^5} \exp\left[-1.25 \left(\frac{f_m}{f}\right)^4 \right] \gamma^{\exp[-(f-f_m)^2/2\sigma^2 f_m^2]} \tag{2.44}$$

where

γ = peak enhancement parameter

$$\sigma = \begin{cases} \sigma_a & \text{for } f \leq f_m \\ \sigma_b & \text{for } f > f_m \end{cases}$$

α = scale parameter

f_m = modal frequency in Hz

f = frequency in Hz

The peak enhancement parameter, γ, in Equation (2.44) is defined as the ratio of the maximum spectral energy to the maximum of the corresponding Pierson–Moskowitz spectrum for the same values of α and f_m. It can be seen that the spectrum formulation (Equation (2.44)) is given by multiplying the Pierson–Moskowitz spectrum by the following peak enhancement factor:

$$\gamma^{\exp[-(f-f_m)^2/2\sigma^2 f_m^2]} \tag{2.45}$$

In terms of circular frequency, the JONSWAP spectrum is given by

$$G(\omega) = \alpha \frac{g}{\omega^5} \exp\left[-\frac{5}{4}\left(\frac{\omega_m}{\omega}\right)^4 \right] \gamma \exp[-(\omega - \omega_m)^2/2\sigma^2\omega_m^2] \tag{2.46}$$

where $\omega_m = 2\pi f_m$.

The JONSWAP spectral formulation has five parameters: $\gamma, f_m, \alpha, \sigma_a$ for $f \leq f_m$ and σ_b for $f > f_m$. The values of these parameters change from one spectrum to another, although some parameters show fairly consistent trends in relation to wind speed and fetch. Hasselmann *et al.* (1973) provide average values for each parameter based on the measured data. The average values of the parameters are

$$\begin{aligned} \gamma &= 3.30 \\ \sigma_a &= 0.07 \text{ and } \sigma_b = 0.09 \\ \alpha &= 0.076\,(\bar{x})^{-0.22} \\ f_m &= 3.5(g/U)(\bar{x})^{-0.33} \end{aligned} \tag{2.47}$$

where $\bar{x}$ is the dimensionless fetch; $\bar{x}$ is given by

$$\bar{x} = gx/U^2 \tag{2.48}$$

where x is the fetch; and U is the wind speed. The use of these average parameters in Equation (2.44) gives the mean JONSWAP spectrum, which is a function of two parameters: the wind speed and the location where the fetch is known.

Figure 2.12 illustrates a typical JONSWAP spectrum and a corresponding Pierson–Moskowitz spectrum with the same zero-crossing period and significant wave height.

The above spectral formulations are not the only available one dimensional wave spectral models. Examples of other models are Neumann (1953), Bretschnieder (1956), Darbishire (1961) and Scott (1965). Ochi and Hubble (1976) present a multi-parameter spectral model which can be used to model bimodal seas which can occur in sea states comprising local wind-generated waves and swell.

The above wave spectra are frequency or point spectra. These spectra represent energy at a point which is an accumulation of all the energy propagating in different directions. No consideration has been given to the dispersion of wave energy with direction. It is often assumed that the sea is long crested. That is, the waves propogate in only one direction and the associated wave spectrum is known as the unidirectional spectrum.

Observations of wind-generated waves show that they do not necessarily propagate in only one direction such as the wind direction. The wave energy is usually distributed over a range of directions. The situation that is

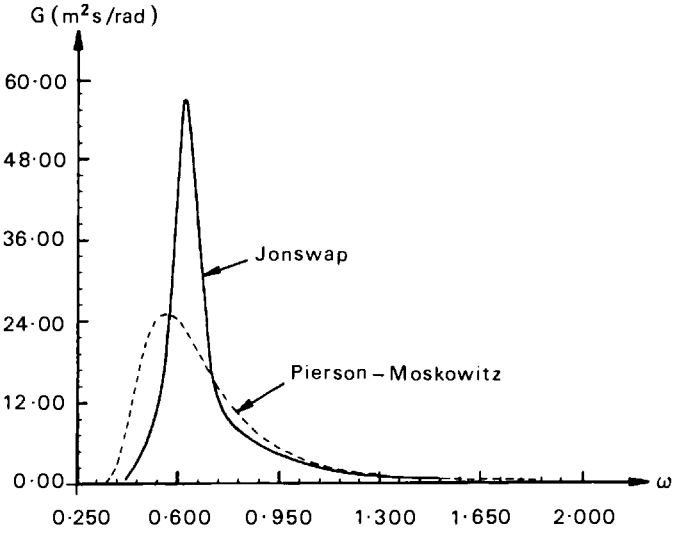

Figure 2.12. JONSWAP and Pierson–Moskowitz spectra for H_s = 5.0 m, T_z = 8 s

often encountered is one where wave energy associated with frequencies close to the modal frequency generally propagates in the direction of the wind, whereas wave energy associated with frequencies above or below the modal frequency is generally distributed over a range of directions (Mitsuyasu, 1975). It is evident that information on the directional dispersion of wave energy is required for a more accurate description of random seas.

In addition, information on wave directionality is needed for predicting the excitation of compliant marine structures because the forces are associated with coupled motions induced by waves travelling in different directions.

Directional wave spectra, $G(\omega, \theta)$, are normally expressed in terms of the frequency or point spectrum, $G(\omega)$, and the angular spreading function, $D(\omega, \theta)$, of the wave energy:

$$G(\omega, \theta) = G(\omega)\, D(\omega, \theta) \tag{2.49}$$

where

$$\int_{-\pi}^{\pi} D(\omega, \theta)\, d\theta = 1 \tag{2.50}$$

The separation of the directional spectra into the product of a spreading function and a frequency spectra is particularly convenient for evaluating the response of marine structures in a short crested seaway where correlations between different modes of motion need to be considered.

Several spreading functions have been proposed. These are outlined below:

The spreading function for the special case of unidirectional waves propagating in the direction $\bar{\theta}$ is given by

$$D(\theta) = \frac{1}{2\pi}\,\delta\,(\theta - \bar{\theta}) \tag{2.51}$$

where $\delta(..)$ is the Dirac delta function.

The cosine square spreading function is given by

$$D(\theta) = \begin{cases} (2/\pi)\cos^2(\theta-\theta_0) & \text{for } -\pi/2 < \theta - \theta_0 < \pi/2 \\ 0 & \text{otherwise} \end{cases} \tag{2.52}$$

where θ_0 is the mean wave direction. The cosine square function is extremely simple. Its limitation is that it is independent of both frequency and wind speed.

A more advanced spreading function is the Stereo Wave Observation Project (SWOP) formulation, which was derived from analysis of measured data (Cote *et al.*, 1960) and is a function of angle and dimensionless frequency. The SWOP energy spreading function is given by

$$D(\theta, \bar{\omega}) = \begin{cases} 1/\pi\ (1 + a\cos 2\theta + b\cos 4\theta) \text{ for } -\pi/2 < \theta < \pi/2 \\ 0 \qquad \text{otherwise} \end{cases} \tag{2.53}$$

where

$$a = 0.50 + 0.82\exp(-1/2\,\omega^{-4})$$

$$b = 0.32\exp(-1/2\,\omega^{-4})$$

$\bar{\omega}$ is the dimensionless frequency given by

$$\bar{\omega} = U\omega/g \tag{2.54}$$

where U is the wind speed at 19.5 m above the mean sea level. Note that the SWOP spreading function is not equal to zero at $\pm\pi/2$ but is truncated at these limits.

The Mitsuyasu formulation for directional distribution has been developed from work reported in Mitsuyasu *et al.* (1975) and modified by Goda and Suzuki (1975). The equation can be written as

$$D(\theta, \omega) = N_0 \cos^{2s}\left(\frac{\theta - \theta_0}{2}\right)$$

where θ_0 is the mean wave direction

$$N_0 = \left\{\int_{\theta\min}^{\theta\max} \cos^{2s}\left(\frac{\theta - \theta_0}{2}\right) d\theta\right\}^{-1}$$

$$G = \begin{cases} G_{\max} \cdot (\omega/\omega_p)^5 & \text{for } \omega \leqslant \omega_p \\ G_{\min} \cdot (\omega/\omega_p)^{-2.5} & \text{for } \omega > \omega_p \end{cases} \tag{2.55}$$

$$\omega_p = 2\pi/1.05\ T_z$$

and

T_z is an average zero crossing period

Other more complex directional distributions have been proposed by Longuet-Higgins *et al.* (1961) and Hasselmann *et al.* (1976) but are not

presented here because of the difficulty of using them in design calculations.

2.4 Long term wave statistics

The assumptions underlying the short term stochastic models of ocean waves no longer apply over long periods of time. The general approach to modelling the ocean environment over a long period of time is to regard the behaviour of the ocean as a set of sea states with each sea state being described by its short term statistics (significant wave height and zero-crossing period). Each sea state will also have an associated probability of occurrence. One of the primary requirements in the evaluation of a compliant marine structure is the choice of a design wave and period. The design wave is often associated with the extreme sea state which will occur once on average in the design return period.

An estimate of extreme wave heights is normally based on the extrapolation of instrumentally measured waves over a period of one to three years. This procedure is empirical and there is inevitably an element of error in the extrapolation process. However, no alternative method of estimating the extreme conditions is known.

Long term wave data is usually obtained from records of wave elevation taken typically every three hours for a period of 15 or 20 min. Each sample is reduced to two representative parameters, significant wave height, H_s, and average zero-crossing period, T_z, by using the methods previously described. Data for a long period of time is then represented by a bivariate histogram (or scatter diagram) of H_s and T_z, as shown in Figure 2.13. This scatter diagram summarizes data for three years of measurements at the Stevenson Station in the North Sea. Each box in the scatter diagram denotes the number of occurrences of wave conditions, with significant wave heights and zero-crossing periods denoted by the range in the height and width of the box respectively. The diagram has a total of 1000 events recorded on it and so, for example, waves with significant wave height in the range 1.5 to 2 m and zero-crossing period in the range from 6 to 7 s occurred for 46/1000 of the three year period covered by the diagram.

Now the maximum wave heights that are most likely to occur over a very long period of time (from 5 to 100 years) can be predicted if the probability of occurrence of H_s measured over relatively short time scales (from 1 to 3 years) is plotted using distribution functions that yield straight lines. Three such distributions have been identified. They are as follows:

(a) the logarithmic normal distribution by Jasper (1956);
(b) the Weibull distribution by Weibull (1951);
(c) the Gumbel distribution by Gumbel (1958) and Saetre (1974).

There is little theoretical justification for these distributions other than that observed data generally plots on to straight lines through their use. The first two of the above distributions suffer from the slight disadvantage that they give a larger emphasis to the effects of smaller waves.

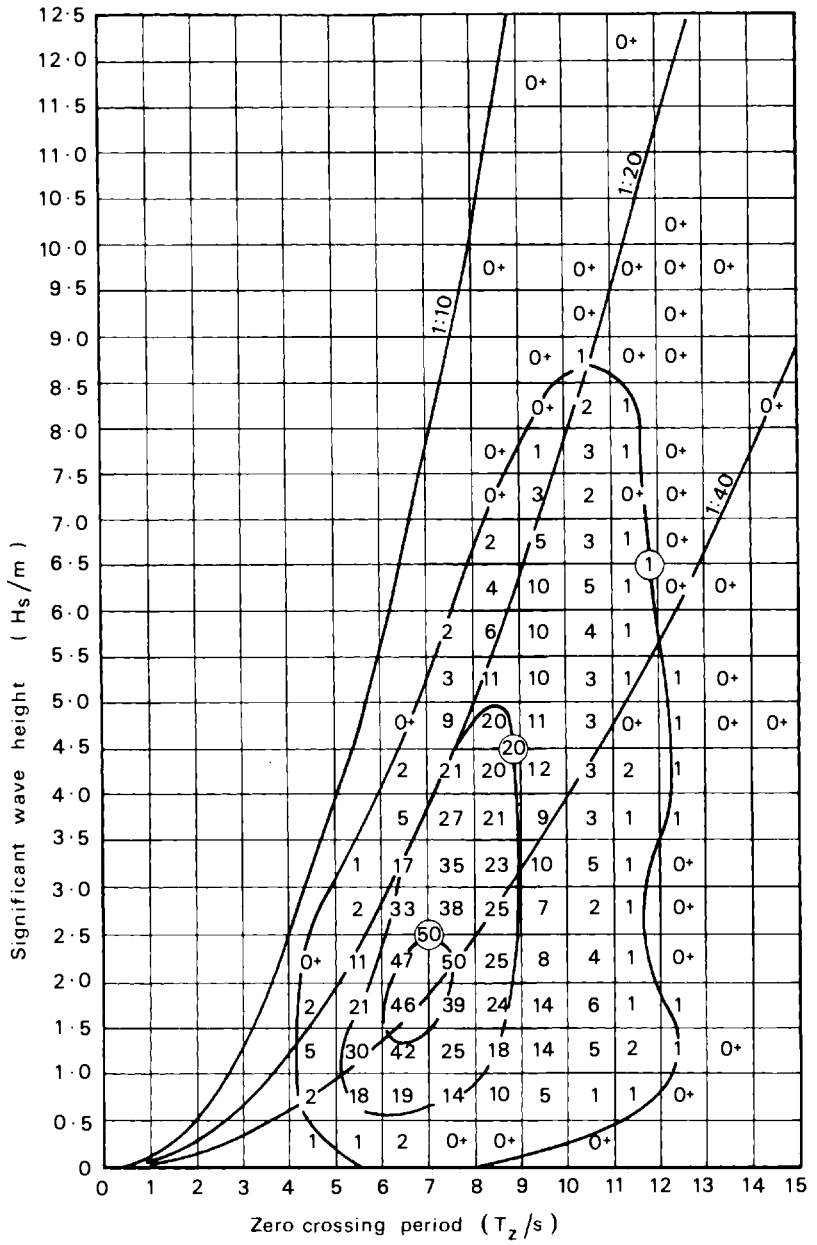

Figure 2.13. Wave scatter diagram (units indicated in parts per thousand, 0+ denotes value less than 0.5 parts per thousand)

Wave height data from scatter diagrams can be used in these distributions in two ways. In the first, more common, approach, significant or maximum wave height data are plotted against a function of their probability of occurrence for every record in the available data set where the wave height exceeds a small threshold value. In some cases this threshold value can be set to zero. An alternative method utilizes the highest wave height in a fixed small time interval plotted against a function of its probability of occurrence.

The detailed form of the three distributions are described below:

1. The logarithmic normal distribution

This distribution assumes that the natural logarithm of wave heights has a normal distribution. The probability distribution function is, therefore, described by the equation

$$P_L(H) = \frac{1}{2\pi\sigma H} \exp\left[\frac{-(\ln H - \mu)^2}{2\sigma^2}\right] \tag{2.56}$$

where σ and μ are constants dependent on the characteristics of the data set. Thus a plot of cumulative probability distribution against significant wave height, say, on normal probability paper should be a straight line. Measured data often deviates from a straight line, particularly at large wave heights where the linearity is necessary for accurate predictions of long term significant wave heights.

2. The Weibull distribution

The Weibull cumulative probability distribution of wave height is described by the equation

$$\text{Prob}\,[H > H_m] = P_{CL}(H) = 1 - \exp\left[\frac{-H^\gamma}{\beta}\right] \tag{2.57}$$

where $P_{CL}(H)$ is the probability that any wave height chosen at random, H_m, is less than wave height H; and β, γ are constants. By rearranging and taking logarithms, Equation (2.57) can be written as

$$\ln[\ln\{1 - P_{CL}(H)\}^{-1}] = \gamma \ln H - \gamma \ln \beta \tag{2.58}$$

Tests of the Weibull distribution with long term wave data has shown that the distribution gives better fits to a straight line if the wave height H on the right hand side of Equation (2.58) is replaced by $(H - a')$ where a' is a threshold wave height value below which wave activity is never expected to fall. In sheltered waters a' may be taken to be zero or very small, with a large value (from 0.5 to 2.0 m) being usual for more exposed locations.

Long term wave data can be used with the equation for the Weibull distribution by plotting $\ln[\ln\{1 - P_{CL}(H)\}^{-1}]$ against $\ln(H - a')$ and using a straight line fit on the plotted points to extrapolate probabilities of occurrence of larger wave heights. This graph may also be plotted directly on to specially prepared Weibull probability paper.

3. The Gumbel distribution
This is defined as

$$\left.\begin{aligned} &\text{Prob}\,[H \leqslant h] = P_{CL}(H) = \exp\,[-\exp\,(-a\{H-\beta\})] \\ &\text{or} \\ &-\ln\,[-\ln P_{CL}(H)] = a(H-\beta) \end{aligned}\right\} \tag{2.59}$$

The application of these long term distributions is illustrated by using the data of Figure 2.13 through a Weibull distribution to predict significant wave heights for 1, 10 and 100 year return periods for wave rider buoy data recorded at the Stevenson Station in the North Sea.

Taking H as the significant wave height, the terms of the Weibull distribution equation are evaluated in Table 2.2 using a threshold value of $a' = 1.0$ m. Figure 2.14 presents plotted data from the fourth and third columns of the table which fits a straight line apart from one anomalous

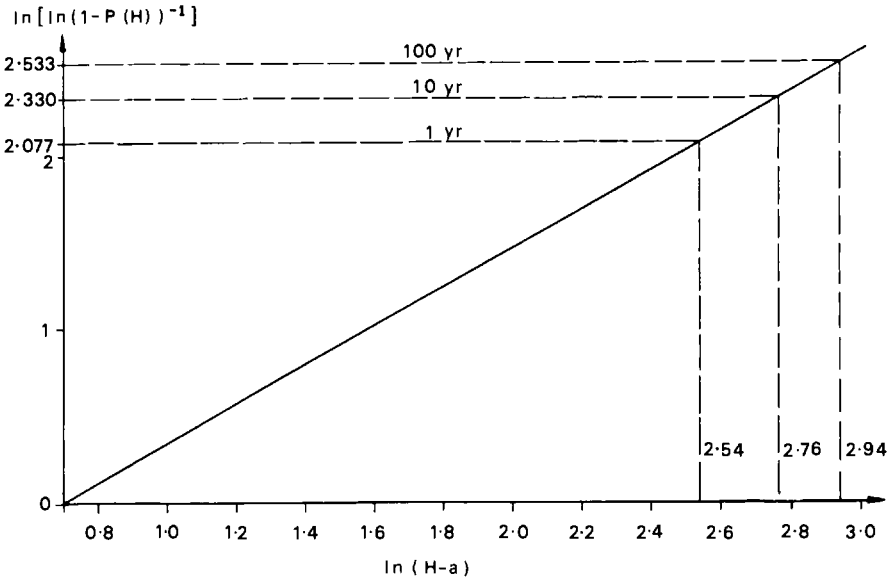

Figure 2.14. Weibull plot

point due probably to insufficient occurrences recorded in the scatter diagram for high significant wave height. The 100 year return period significant wave height is predicted by taking the probability of $H < H_{100}$ to be

$$P_{100}(H) = P[H < H_{100}] = 1 - \frac{3}{100 \times 365.25 \times 24} = 0.999\,996\,58$$

Then

$$\ln\left\{\ln\left[\frac{1}{1 - P_{100}(H)}\right]\right\} = 2.533$$

Table 2.2 Weibull distribution data

H/m	$P_{C1}(H)$	$\ln[H - 1.0]$	$\ln\left\{\ln\left[\frac{1}{1 - P_{C1}(H)}\right]\right\}$
2	0.370	0	−0.772
3	0.624	0.693	−0.022
4	0.783	1.099	0.424
5	0.888	1.386	0.784
6	0.940	1.609	1.034
7	0.971	1.792	1.264
8	0.981	1.946	1.377
9	0.984	2.079	1.420

gives $\ln [H_{100} - a] = 2.94$ from the graph, with H_{100} thus being 19.9 m. Similarly, the 1 year and 10 year return periods' significant wave heights can be obtained as 13.7 m and 16.8 m respectively.

A comparative evaluation of the prediction from the log normal, Weibull and Gumbel distributions has been carried out by Saetre (1974), using three years' data; the results are listed in Table 2.3. The Gumbel probability distribution gives the highest extrapolated values although

Table 2.3 Comparison of long term predictions from Gumbel, Weibull and log normal distributions

		Extrapolated wave heights (m)		
Wave parameter	*Return period* (years)	*Gumbel*	*Weibull*	*Log normal*
$H_{1/3}$	10	14.4	13.6	12.5
	50	16.3	15.2	14.6
H_{max} (3 hrs)	10	26.8	24.5	23.2
	50	30.6	27.8	27.0

(From Saetre, 1974)

Saetre concluded that the Gumbel gives the best fit to this particular set of data. The Weibull distribution offers a prediction that is midway between the three and tends to be the distribution that is used most often in the offshore industry. However, the recommended approach would be to use all three methods and assess the 'goodness-of-fit' to the particular data invoved. The Weibull and Gumbel distributions generally show a better fit to data than the log normal distribution. Further improvements to long term predictions can only be achieved by continuous sets of observed data which cover periods of 10–20 years. Unfortunately, such data sets are generally unavailable at present.

2.5 Wind and current

The effects of wind and current must also be considered in the design of compliant marine structures. Wind and currents need to be specified in terms of their strength, direction and spatial variation. Long term statistical methods such as those described in the preceding section are used to determine extreme wind and current conditions in order to establish environmental design conditions. Spectral techniques have been used to describe wind gusts. Patel (1989) gives further details on wind and currents in the ocean environment.

One important feature of both wind and currents is the presence of a significant mean component over a specified period of time. This mean component is usually evaluated either over a period of one minute or one hour. The choice of the averaging period depends on the problem under consideration. For example, the one minute mean wind speed is normally used when considering wind heeling effects associated with hydrostatic stability considerations.

Mean wind and current components have an important effect on compliant marine structures as they provide a source of steady environmental loading on the structure. This will influence many aspects of the design such as station keeping. Steady wind and current may also result in important dynamic phenomena such as vortex induced vibration. This is an important consideration for structures such as marine risers.

2.6 Application of environmental spectra

The long term statistical methods such as those described in Section 2.4 form the basis for determining extreme environmental conditions for the design of compliant marine structures. The extreme sea state, or indeed any other sea state, is best described as a random process. This requires the application in the design process of the methods presented in Sections 2.2 and 2.3. However, much of the analysis of compliant marine structures is based on deterministic methods. For example, the behaviour of a marine structure is often evaluated in response to regular wave excitation. At first sight these deterministic methods appear incompatible with the random nature of the wave loading. Fortunately this is not the case for many compliant marine structure system models. This is best illustrated by examining the response of a single degree of freedom dynamic system to random excitation.

Consider the mass – damper – spring system.

$$m\ddot{y} + b\dot{y} + ky = x(t) \tag{2.60}$$

where m is the mass; b is the damping; k is the stiffness; x is the excitation; and y is the response. If the excitation is harmonic at frequency ω, then $x(t)$ has the form

$$x(t) = X(\omega)e^{i\omega t} \tag{2.61}$$

and the response will be of the form

$$y(t) = Y(\omega)e^{i\omega t} \tag{2.62}$$

where $X(\omega)$ and $Y(\omega)$ are the complex amplitudes of the excitation and the response respectively. Substituting Equations (2.61) and (2.62) into Equation (2.60) gives

$$Y(\omega) = H(\omega)\, X(\omega) \tag{2.63}$$

where

$$H(\omega) = \frac{1}{k - \omega^2 m + i\omega b} \tag{2.64}$$

$H(\omega)$ is the frequency response function of the dynamic system.

If the excitation is a stationary random process with spectrum, $G_{xx}(\omega)$, then the frequency response function, $H(\omega)$, governs the transmission of the random excitation. It can be shown that the relationship between the excitation–response cross-spectrum, $G_{xy}(\omega)$, and the excitation spectrum, $G_{xx}(\omega)$, is given by (Newland, 1984; Bendat and Piersol, 1986)

$$G_{xy}(\omega) = H(\omega)G_{xx}(\omega) \tag{2.65}$$

The response spectrum, $G_{yy}(\omega)$, is related to the excitation spectrum, $G_{xx}(\omega)$, by

$$G_{yy}(\omega) = H^*(\omega)H(\omega)G_{xx}(\omega) \tag{2.66}$$

or

$$G_{yy}(\omega) = |H(\omega)|^2 G_{xx}(\omega) \tag{2.67}$$

These results readily extend to multiple input–multiple output systems. Bendat and Piersol (1986) give further details.

The important point is that once the frequency response functions of the dynamic systems under consideration have been established then response spectra and statistics may be determined from the excitation spectra. For example, the reponse of interest may be wave induced motions. Knowledge of the wave spectra and the response of the structure to regular wave loading would allow the calculation of the statistics on the determination of the frequency response functions for many types of compliant marine structure. The constraint on this theory is that the dynamic system is linear. Alternative methods must be considered if the dynamic system is highly non-linear. One commonly applied approach is to carry out time domain numerical simulations. These, however, are generally expensive in terms of computation.

References

Bendat, J. S. and Piersol, A. G. (1986) *Random Data: Analysis and Measurement Procedures.* Wiley Interscience, USA

Borgman, L. E. (1972) *Statistical Models for Ocean Waves and Wave Forces. Advances in Hydroscience*, Academic Press, NY

Bretschneider, C. L. (1959) Wave Variability and Wave Spectra for Wind-Generated Gravity Waves. *Technical Memo No 118*. Beach Erosion Board US Army Corps of Engineers, Washington, DC

Carter, D. J. T., Challenor, P. G., Ewing, J. A., Pitt, E. G., Srokosz, M. A. and Tucker, M. J. (1986) *Estimating Wave Climate Parameters for Engineering Applications*, OTH 86 228, Department of Energy, HMSO, London

Cartwright, D. E. and Longuet-Higgins, M. S. (1956) The statistical distribution of the maxima of a random function. *Proceedings of the Royal Society, London*, **A237**, 212–232

Cokelet, E. D. (1977) Steep gravity waves in water of arbitrary depth. *Philosophical Transactions of the Royal Society of London*, **A286**, 183–230

Cote, J. J., Davis, J. O., Marks, W., Mcghough, R. J., Mehr, E., Pierson, W. J., Ropek, J. F., Stephenson, G. and Vetter, R. C. (1960) The directional spectrum of a wind generated sea as determined from data obtained by the stereo wave observation project. *Meteorological Papers*, **2**(6), 1–88. New York University, College of Engineering USA

Darbyshire, J. (1961) The one-dimensional wave spectrum in the Atlantic Ocean and in coastal waters. *Proceedings of the Conference on Ocean Wave Spectra* (1961), pp. 27–31, Prentice Hall, Englewood Cliffs, NJ

Goda, Y. and Suzuki, Y. (1975) Computation of Refraction and Diffraction of Sea Waves with Mitsuyasu's Directional Spectrum, Port and Harbour Research Institute. *Japan, Technical Note No. 155*, 33 pp.

Gumbel, E. J. (1958) *Statistics of Extremes*. Columbia University Press, USA, 371 pp.

Hasselman, K. *et al.* (1973) Measurements of wind wave growth and swell decay during the joint North Sea wave Project (JONSWAP). Herausgegeben vom Deutsch. Hydrograph. Institut., Reihe A, no. 12, 95pp

Hasselman, K., Ross, D. B., Muller, P. and Sell, W. (1976) A parametric wave prediction model. *Journal of Physical Oceanography*, **6**, 200–228

Jasper, N. R. (1956) Statistical distribution patterns of ocean waves of wave induced ship stresses and motions with engineering applications. *Transactions of the Society of Naval Architects and Marine Engineers*, **64**, 375–432

Jenkins, G. M. and Watts, D. G. (1968) Spectral Analysis and its applications, Holden-Day, SF

Kinsman, B. (1965) *Wind Waves*. Prentice Hall, Englewood Cliffs, NJ

Lamb, H. (1975) *Hydrodynamics*. Cambridge University Press, Cambridge

Longuet-Higgins, M. S. (1952) On the statistical distribution of the heights of sea waves. *Journal of Marine Research*, **11**(3), 245–266

Longuet-Higgins, M. S., Cartwright, D. E. and Smith, N. D. (1961) Observations of the directional spectrum of sea waves using the motions of a floating buoy. *Proceedings of the Conference on Ocean Wave Spectra*, Prentice Hall, Englewood Cliffs, NJ, USA, pp. 111–132

Longuet-Higgins, M. S. (1983) On the joint distribution of wave periods and amplitudes in a random wave field. *Proceedings of the Royal Society of London*, **A389**, 241–258

Mitsuyasu, H., Tasai, F., Sabara, T., Mizuno, S., Okusu, M., Honda, T. and Rikiishi, K. (1975) Observation of the directional spectrum of ocean waves using a clover leaf buoy. *Journal of Physical Oceanography*, **5** (4), 750–760

Neumann, G. (1953) On Ocean Wave Spectra and a New Method of Forecasting Wind-Generated Sea, *Technical Memo No 43*. Beach Erosion Board, US Army Corps of Engineers, Washington DC

Newland, D. E. (1984) *An Introduction to Random Vibrations and Spectral Analysis*, 2nd edn, Longman

Ochi, M. K. (1982) Stochastic analysis and probabilistic prediction of random seas, V. T. Chow (ed.). *Advances in Hydroscience*, **13**, 217–375

Ochi, M. K. and Hubble, E. N. (1976) On six-parameter wave spectra. *Proceedings of the 15th Conference on Coastal Engineering*, Vol. 1, pp. 301–328

Patel, M. H. (1989) Dynamics Of Offshore Structures. Butterworths, London

Phillips, O. M. (1966) *Dynamics of the Upper Ocean*. Cambridge University Press, Cambridge

Pierson, W. J. (1952) *A Unified Mathematical Theory for the Analysis, Propagation and Refraction of Storm Generated Ocean Surface Waves*, Parts I and II. NYU, College of Engineering, Research Division, Department of Meteorology and Oceanography. Prepared for the Beach Erosion Board, Department of the Army, and Office of Naval Research, Department of the Navy, 461 pp

Pierson, W. J. (1955) Wind generated gravity waves. *Advances in Geophysics*, **2**, 93–177

Pierson, W. J. and Moskowitz, L. (1964) A proposed spectral form for fully developed wind seas based on the similarity theory of S. A. Kitaigorodskii. *Journal of Geophysical Research*, **69**(24), 5181–5190

Priestley, M. B. (1981) Spectral Analysis and Time Series, Academic Press, London

Rice, S. O. (1944) Mathematical analysis of random noise. *Bell System Technical Journal*, **23**, 282–332

Rice, S. O. (1945) Mathematical analysis of random noise. *Bell System Technical Journal*, **24**, 46–156

Saetre, H. J. (1974) On High Wave Conditions in the Northern North Sea. *Institute of Oceanographical Sciences, NERC Wormley, Report No 3*

Sarpkaya, T. and Isaacson, M. (1981) *Mechanics of Wave Forces on Offshore Structures*. Van Nostrand Reinhold, NY, USA

Scott, J. R. (1965) A sea spectrum for model tests and long-term ship prediction. *Journal of Ship Research*, **9**, No 3, 145–152

Stoker, J. J. (1957) *Water Waves*. Interscience, NY, USA

Weibull, W. (1951) A statistical distribution of wide applicability. *Journal of Applied Mechanics*, **18**, 293–297

Wiegel, R. L. (1964) *Oceanographical Engineering*. Prentice Hall, Englewood Cliffs, NJ, USA

Chapter 3

Hydrostatic analysis

The hydrostatic stability of compliant floating marine structures plays an important role in their design and operating effectiveness. In the case of conventional rigid floating structures replacing fixed bottom emplaced platforms, the hydrostatic stability is the limiting criterion for deck payload capacity. For compliant structures with articulated joints or those that are tethered to the sea bed, however, the hydrostatic stability is substantially modified by the effects of the compliance. At the same time, the stiffness associated with the hydrostatic stability of a compliant vessel can have a major effect on its dynamic response in waves. This occurs for the case of a semisubmersible with articulated columns (see Chapter 9) where a non-monotonically increasing hydrostatic righting moment with angle of heel leads to the presence of a catastrophic dynamic instability in the damaged condition. It is important, therefore, to consider the hydrostatic stability of a compliant structure very carefully for its impact on its payload performance and on its dynamic response in waves.

For certification purposes, the hydrostatic stability of a compliant vessel is usually considered using criteria set down for conventional floating rigid structures. Typical such certifying agency requirements are presented by Patel (1989) and in certifying authority publications. However, care has to be taken to ensure that the conventional criteria for floating rigid structures are applied with proper account being taken of the behaviour of compliant features of the structure. Again, hydrostatic stability calculations for the semisubmersible with articulated columns of Chapter 9 illustrates types of interaction that can take place between the hydrostatics and compliance.

The above considerations invariably require that the hydrostatic stability of a compliant vessel be examined from first principles as far as is possible. This is the approach taken in this chapter with the introduction of a new pressure integration technique for hydrostatic stability calculations.

3.1 Theoretical background to pressure integration technique for hydrostatic analysis

Consider the arbitrary body shown in Figure 3.1(a) floating at the free surface between a 'heavy' and a 'light' fluid such as an air–water interface.

The light fluid is at a constant pressure equal to the free surface pressure. The pressure is assumed to be constant across the free surface. The pressure, p, of the stationary heavy fluid with respect to the free surface at any point $\mathbf{x}(x, y, z)$ below the free surface is

$$p = \rho g (d - z) \tag{3.1}$$

The position and orientation of the global $Oxyz$ axis system shown in Figure 3.1 is arbitrary. In Figure 3.1(a) it has been placed, for convenience, at the bottom of the floating body but this fact is not of major significance.

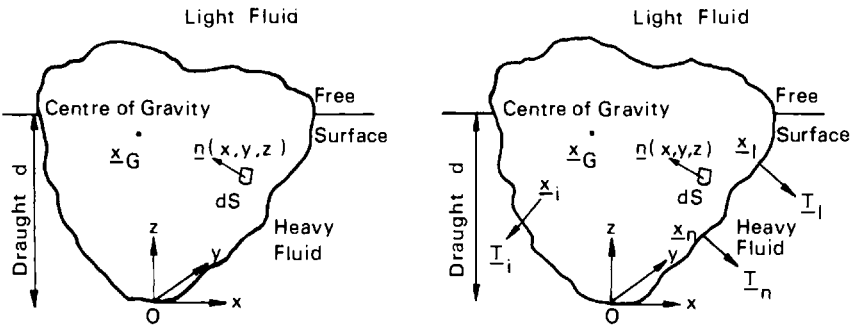

Figure 3.1(a). Free floating body equilibrium. **(b)** Floating body equilibrium with attached loads

There are two forces acting on the body. The first force is the weight of the body acting vertically downwards. The second force is due to the fluid pressure acting on the body's submerged surface.

The incremental force, $\mathbf{dF}$, acting on the body due to fluid pressure is

$$\mathbf{dF} = \rho g (d - z)\, \mathbf{dS} \tag{3.2}$$

By integrating over the submerged surface the total force, $\mathbf{F}$, is

$$\mathbf{F} = \int_S \rho g (d - z)\, \mathbf{n}(\mathbf{x})\, dS \tag{3.3}$$

where $\mathbf{n}$ is the unit normal vector acting into the body and is a function of position, $\mathbf{x}$. Similarly, the incremental moment $\mathbf{dM}$ is

$$\begin{aligned} \mathbf{dM} &= \mathbf{x} \times \mathbf{dF} \\ &= \mathbf{x} \times \rho g (d - z)\, \mathbf{dS} \end{aligned} \tag{3.4}$$

Integrating Equation (3.4) over the submerged surface gives

$$\mathbf{M} = \int_S \mathbf{x} \times \rho g (d - z)\, \mathbf{n}(\mathbf{x})\, dS \tag{3.5}$$

Resolving forces and moments due to body weight gives

$$\mathbf{F} = W\mathbf{k} \tag{3.6}$$

and

$$\mathbf{M} = \mathbf{x}_G \times W\,\mathbf{k} \tag{3.7}$$

where W is the weight of the body; and $\mathbf{x}_G$ is the centre of gravity.

For static equilibrium, Equations (3.6) and (3.7) must be satisfied since the fluid exerts an upward thrust on the body equal and opposite to the body's weight. This upward thrust, called the buoyancy force, F_B, lies on the same line of action as the weight.

Now the divergence theorem states that

$$-\int_S \mathbf{f}\cdot\mathbf{n}\,dS = \int_V \nabla\cdot\mathbf{f}\,dV \tag{3.8}$$

where $\mathbf{f}$ is the vector field; and ∇ is the gradient operator (Kreyszig, 1988). The negative sign arises because the divergence theorem is normally defined by a unit normal vector acting out of the surface. From Equation (3.3) the buoyancy force is given by

$$F_B = \int_S \rho\, g\,(d - z)\mathbf{k}\cdot\mathbf{n}(\mathbf{x})\,dS \tag{3.9}$$

Using the divergence theorem (Equation 3.8), Equation (3.9) becomes

$$F_B = -\rho\, g \int_V \frac{\partial}{\partial z}(d - z)\,dV = \rho g V \tag{3.10}$$

This is Archimedes' principle – the buoyancy force acting on a freely floating body is equal to the weight of the volume of fluid displaced by the body.

The solutions of Equations (3.6) and (3.7) determine the magnitude of the buoyancy force and the horizontal coordinates of the centre of buoyancy. The vertical centre of buoyancy can not be determined from these equations since the solution of Equation (3.7) only gives the line of action. The solution for the vertical centre of buoyancy is given from the fact that it lies at the centroid of the submerged volume. Thus

$$\mathbf{x}_B\cdot\mathbf{k} = d - \frac{1}{V}\int_V (d - z)\,dV \tag{3.11}$$

Relating the right hand side of Equation (3.11) to the right hand side of the divergence theorem (Equation (3.8)) gives

$$\nabla\cdot\mathbf{f} = d - z \tag{3.12}$$

The solution to Equation (3.12) is

$$\mathbf{f} = -\frac{(d - z)^2}{2}\mathbf{k} \tag{3.13}$$

Substituting Equation (3.13) into Equation (3.11) via Equation (3.7) results in

$$\mathbf{x}_B\cdot\mathbf{k} = d - \frac{\rho\, g}{F_B}\int_S \frac{(d - z)^2}{2}\mathbf{k}\cdot\mathbf{n}(\mathbf{x})\,dS \tag{3.14}$$

Now all the hydrostatic properties have been determined in terms of surface integrals. The advantage of these surface integrals is that they do not have to be evaluated over the waterplane area as they are zero on that surface.

Solutions to Equations (3.6), (3.7) and (3.14) give the body's equilibrium position. However, nothing is known about the stability of the body in this position. The classical approach to stability is to apply a small linear or rotational displacement to a body and test whether it returns to its equilibrium position of its own accord or if it goes to another equilibrium position. In the theory described here, a small rotation is applied to the body. The point of rotation may be anywhere in space, provided that the buoyancy force remains constant. The centre of buoyancy moves to a new position, $\mathbf{x}'_B$ and the centre of gravity moves to $\mathbf{x}'_G$. Note that the centre of gravity does not move relative to the rigid body but it does move in a fixed global frame of reference.

Taking moments gives

$$\begin{aligned}\mathbf{M}_R &= (-\mathbf{x}'_G \times W\mathbf{k}) - (\mathbf{x}'_B \times [-W\mathbf{k}]) \\ &= W(\mathbf{x}'_B - \mathbf{x}'_G) \times \mathbf{k}\end{aligned} \tag{3.15}$$

where $\mathbf{M}_R$ is the restoring moment vector. If $\mathbf{M}_R$ is greater than zero in the direction of rotation, then the body is stable. If $\mathbf{M}_R$ is less than zero, the body is unstable and will find a new equilibrium position.

In many floating vessels the centre of gravity does not remain fixed relative to the rigid body. This is due to movements in load such as suspended crane loads and movement of liquids within the hull. These mechanisms lead to a loss in stability which is reflected in the restoring moment, $\mathbf{M}_R$. If the centre of gravity moves to a new position, $\mathbf{x}''_G$, with rotation then the loss in restoring moment, $\Delta\mathbf{M}_R$, is given by

$$\Delta\mathbf{M}_R = W(\mathbf{x}'_G - \mathbf{x}''_G) \times \mathbf{k} \tag{3.16}$$

Floating vessels often have attached loads as a result of tethers, mooring lines and other systems. These loads will influence the hydrostatics of the vessel. Figure 3.1(b) shows a floating vessel with n attached loads. The loads, $\mathbf{T}_i$, are located on the surface of the vessel at positions, $\mathbf{x}_i$. In this case the equilibrium equations of the body are given by:

$$\mathbf{F} = W\mathbf{k} + \sum_{i=1}^{n} \mathbf{T}_i \tag{3.17}$$

and

$$\mathbf{M} = \mathbf{x}_G \times W\mathbf{k} + \sum_{i=1}^{n} \mathbf{x}_i \times \mathbf{T}_i \tag{3.18}$$

The implication of Equation (3.17) is that the horizontal components of the attached loads are in equilibrium and that the buoyancy force is equal to the weight of the body plus the vertical components of the attached loads.

This gives:

$$F_B - W = \sum_{i=1}^{n} \mathbf{T}_i \cdot \mathbf{k} \tag{3.19}$$

In considering the stability of a floating vessel with attached loads the previously described procedure of applying a rotation to the vessel and determining the restoring moment may be used. However, the problem may be relatively complex since, in general, the attached loads $\mathbf{T}_i$ will change in magnitude and orientation with rotation. This is best illustrated by considering the influence of a catenary mooring line where rotation of the vessel will cause a change in line tension and line orientation with respect to the vessel.

The pressure integration method for evaluating the hydrostatic stability of floating rigid vessels also gives the same results as those associated with submerged volume calculations of the classical approach. The classical hydrostatic stability results will be presented here for free floating bodies which are totally submerged or pierce the free surface.

3.2 Classical hydrostatics

A free submerged body, such as that illustrated in Figure 3.2 will be in vertical equilibrium if its weight, W, acting through its centre of gravity, G, is equal to the buoyancy force, ρgV, acting through the centre of buoyancy (or volume) B, where V is the body's submerged volume. However, the relative positions of points G and B will govern the body's stability in roll and pitch. The body will be in stable, neutral or unstable equilibrium if the

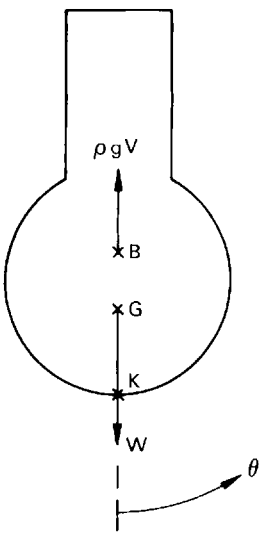

Figure 3.2. Submerged body

centre of buoyancy B, is above, coincides with or is below the centre of gravity G. A body in stable equilibrium will, if given a small displacement and then released, return to its original position. If the equilibrium is unstable, the body will not return to its stable position but will move further from it. In neutral equilibrium, the body will neither return to its original position nor increase its displacement following the initial disturbance, but, rather, will simply adopt a new position. The condition for stable equilibrium requires a restoring couple to return the vessel to its original position following angular perturbation.

This restorinng couple can be written as

$$M = \rho g V(KB - KG)\sin\theta = W(KB - KG)\sin\theta \tag{3.20}$$

where θ is the rotation angle of the body from its equilibrium position; and K is a reference point on the vessel keel.

Now, for a fully submerged rigid body without free surfaces in internal tanks, the positions of points B and G relative to the body will remain fixed and the stability will be fully defined by the above considerations. However, for a freely floating body at the free surface, the shape of the submerged volume, and hence the position of the centre of volume (or buoyancy), will shift with inclination of the body.

This aspect complicates consideration of the stability of a floating body at the free surface and requires the problem to be examined from first principles. Consider the arbitrary body in Figure 3.3 floating at the free surface with submerged volume V. The shape of the surface boundary of

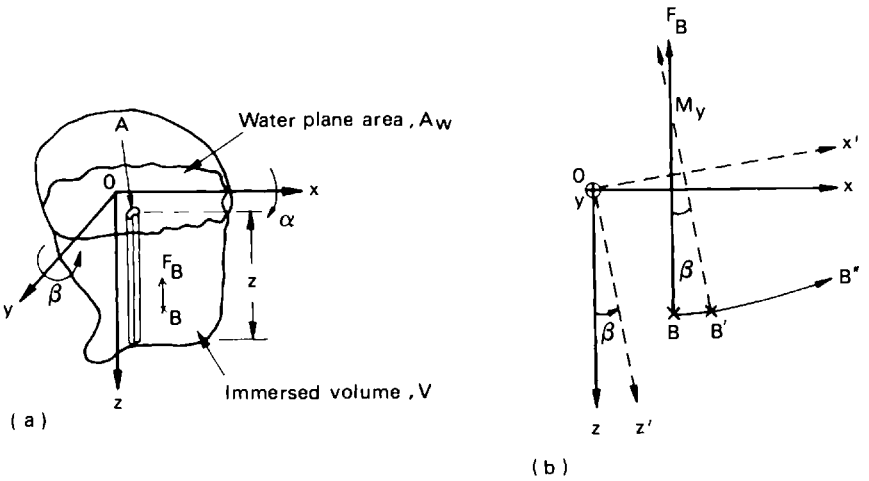

Figure 3.3. Arbitrary body floating freely at water surface

this volume is described with respect to Cartesian axes $Oxyz$ that are fixed in the body with Oxy initially in the water plane. At equilibrium, the constant body weight, W, will be equal to the buoyancy force, $\rho g V$, with the latter acting through the centre of buoyancy, B. Now, if the body is

given a small inclination, β, about the Oy axis, the condition that the submerged volume must remain constant before and after inclination is

$$V = \int_A S\mathrm{d}A = \int_A (S - x\beta)\mathrm{d}A \tag{3.21}$$

where the function $S = f(x, y)$ describes the z co-ordinate of the submerged body surface relative to axes $Oxyz$. Simplifying Equation (3.21) and carrying out a similar procedure for rotation about the x axis leads to the conditions

$$\int_A x\mathrm{d}A = 0, \int_A y\mathrm{d}A = 0 \tag{3.22}$$

which prove that rotation of the body at constant submerged volume, and, therefore with equilibrium maintained, can only take place about axes through the centroid of the water plane. This point is defined as the centre of flotation.

The co-ordinates of the centre of buoyancy before inclination, $(\bar{x}, \bar{y}, \bar{z})$, can be defined by the equations

$$\begin{aligned} \bar{x} &= \frac{1}{V}\int_A Sx\mathrm{d}A \\ \bar{y} &= \frac{1}{V}\int_A Sy\mathrm{d}A \\ \bar{z} &= \frac{1}{V}\int_A \frac{1}{2}S^2\mathrm{d}A \end{aligned} \tag{3.23}$$

After an inclination of β about the Oy axis, the centre of buoyancy shifts to co-ordinates (x', y', z'):

$$\begin{aligned} \bar{x}' &= \frac{1}{V}\int_A (S - x\beta)x\mathrm{d}A \\ \bar{y}' &= \frac{1}{V}(S - x\beta)y\mathrm{d}A \\ \bar{z}' &= \frac{1}{V}\int_A \frac{1}{2}(S - x\beta)(S + x\beta)\mathrm{d}A \end{aligned} \tag{3.24}$$

with the moments being taken about the initial co-ordinate axes. The movement of the centre of buoyancy parallel to the y axis can then be obtained as

$$\bar{y} - \bar{y}' = \frac{\beta}{V}\int_A xy\mathrm{d}A \tag{3.25}$$

This equation indicates that if the cross-product of area of the water plane about Ox and Oy is zero, that is, Oxy are principal axes of the water plane

area, then the centre of buoyancy will move parallel to the Oxz plane during inclination about the y axis. The condition of zero cross-product of water plane area is satisfied if either Ox or Oy are lines of symmetry of the water plane. Since this condition is satisfied for the majority of floating vessels used in offshore operations, $\bar{y} = \bar{y}'$ and $\bar{x} = \bar{x}'$ are taken to be valid for inclination about the Oy and Ox axes respectively. These conditions also imply that rotation about the Ox and Oy axes can be treated independently in hydrostatic analysis if Oxy are principal axes of the water plane area. On the other hand, if the cross-product of water plane area is non-zero, it is recommended that the hydrostatic analysis is carried out from first principles without the use of the relationships derived in this section.

The vertical movement of the centre of buoyancy can be written as

$$\bar{z} - \bar{z}' = \frac{1}{2V} \beta^2 \int_A x^2 \, dA \tag{3.26}$$

with the β^2 indicating that the movement is small or of second order. Also, the horizontal movement of the centre of buoyancy is given by

$$\bar{x} - \bar{x}' = \frac{\beta}{V} \int_A x^2 \, dA \tag{3.27}$$

The effect of this is illustrated by Figure 3.3(b) where $BB'B''$ indicates the locus of centre of buoyancy as β increases. The upward shallow curvature of the line is due to the vertical movement in B being of second order compared to the horizontal movement. Furthermore, for small β the vertical through the centre of buoyancy (B') goes through a fixed point M_y whose position can be defined by using triangle BM_yB' in Figure 3.3(b) to obtain

$$BM_y = \frac{BB'}{\beta} = \frac{\bar{x} - \bar{x}'}{\beta} = \frac{1}{V} \int_A x^2 \, dA = \frac{I_{yy}}{V} \tag{3.28}$$

with I_{yy} being the second moment of water plane area about Oy. Using a similar derivation for rotation about the Ox axis, the relationship

$$BM_x = \frac{I_{xx}}{V} \quad \text{where} \quad I_{xx} = \int_A x^2 \, dA \tag{3.29}$$

can be obtained. Therefore, for small rotations about the Ox and Oy axes, the centre of buoyancy will move along a surface which is concave upwards but with different curvatures in the Oy and Ox directions – the centres of curvatures being the metacentres M_x and M_y respectively. These M_x and M_y metacentre positions are given by Equations (3.28) and (3.29) and may be considered as the effective point of application of the buoyancy force after rotations about the Ox and Oy axes respectively. At any inclination of the body, the tangent plane to the surface of buoyancy will be parallel to the water plane. Note also that if the axes Oxy are not principal axes of the water plane, that is

$$\int_A xy \, dA \neq 0,$$

the metacentre positions cannot in general exist since the lines through B and B' in Figure 3.3(b) will not necessarily intersect.

For stable equilibrium, the metacentre positions must both lie above the centre of gravity, although the centre of buoyancy need not do so. The righting moments in the Oyz and Oxz planes, RM_x and RM_y, can then be written as

$$\left.\begin{aligned} RM_x &= \rho g V \cdot GM_x \cdot \sin\alpha = \rho g V \cdot GZ_x \\ \mathrm{RM_y} &= \rho g V \cdot GM_y \cdot \sin\beta = \rho g V \cdot GZ_y \\ GZ_x &= GM_x \cdot \sin\alpha,\ GZ_y = GM_y \cdot \sin\beta \end{aligned}\right\} \tag{3.30}$$

where GM_x, GM_y are metacentre heights; α and β are inclinations about the Ox and Oy axes, respectively; and GZ_x , GZ_y are moment arms of the restoring couples.

Calculations for initial stability of a freely floating vessel are carried out by identifying the position of five points within or around the vessel. The lower most point on the vessel vertical centre line, denoted by K (for keel level), is conventionally used as a reference. The positions of vessel centre of gravity, G, centre of buoyancy, B, and the longitudinal and transverse metacentres M_y and M_x are defined with respect to the keel reference K and using the Ox axis pointing forwards and Oz vertically downwards. The longitudinal and transverse metacentric heights are given by

$$\left.\begin{aligned} GM_y &= KB + BM_y - KG \\ &\text{and} \\ GM_x &= KB + BM_x - KG \end{aligned}\right\} \tag{3.31}$$

since BM_x and BM_y can be directly calculated from Equations (3.29) and (3.28) respectively. The above classical theory is described in further detail by Ramsey (1961), Rawson and Tupper (1976) and Clayton and Bishop (1982).

These classical theory results may also be determined in terms of surface integrals. If the axes Oxy of Figure 3.1 coincide with the principal axes of the waterplane, then the second moments of waterplane area I_{xx} and I_{yy} are

$$I_{xx} = \int_S (\mathbf{x} \cdot \mathbf{i})^2\, \mathbf{n} \cdot \mathbf{k}\, dS \tag{3.32}$$

and

$$I_{yy} = \int_S (\mathbf{x} \cdot \mathbf{j})^2\, \mathbf{n} \cdot \mathbf{k}\, dS \tag{3.33}$$

The waterplane area is given by

$$A_w = \int_S \mathbf{n} \cdot \mathbf{k}\, dS \tag{3.34}$$

The centre of flotation (x_F, y_F) is given by

$$x_F = \frac{1}{A_w} \int_S (\mathbf{x} \cdot \mathbf{i})\mathbf{n} \cdot \mathbf{k}\, dS \tag{3.35}$$

and

$$y_F = \frac{1}{A_w} \int_S = (\mathbf{x} \cdot \mathbf{j})\mathbf{n} \cdot \mathbf{k}\, dS \tag{3.36}$$

There are a number of physical effects which can contribute to a loss in the hydrostatic stability of a vessel. These effects arise from the fact that the mass distribution of a vessel can change with angle of inclination and the resultant centre of gravity shift is invariably such as to reduce the hydrostatic restoring moment arm, GZ. The stability reductions can occur due to the effects of tanks of fluids with free surfaces inside a vessel, due to freely suspended loads from cranes and also due to loads applied by catenary moorings or riser pipe connections between the floating platform and sea bed. Calculation of these stability losses is essential during definition of the hydrostatic stability of a floating vessel.

The most common source of stability loss is the so-called free surface effect. Consider a floating vessel which has partially filled tanks with free surfaces on board. Inclination of the vessel causes these free surfaces to move such that the fluid in the tanks 'piles' up towards the side of tanks closest to the submerging part of the ship. This causes the centre of gravity of the tank fluid contents, and therefore of the vessel, to shift in the direction of movement of the vessel hull's centre of buoyancy as it inclines. There is a consequent reduction in the magnitude of the restoring couple between vessel weight and the buoyancy force. An expression for this stability loss is obtained as follows.

Consider a tank, A, with fluid contents of weight w on board a vessel, B, of weight W, as shown in Figure 3.4. When the vessel inclines through a small angle, β, the horizontal shift in centre of gravity of the tank contents, gg', induces a horizontal shift GG', in the vessel centre of gravity such that

$$W \cdot GG' = w \cdot gg' \tag{3.37}$$

But gg' is identical to the centre of buoyancy shift that would occur if the shape of the tank fluid contents were to be considered as the submerged volume of a freely floating body. Then Equation (3.37) can be written as

$$W \cdot GG' = w \frac{I_1}{V_1} \beta \tag{3.38}$$

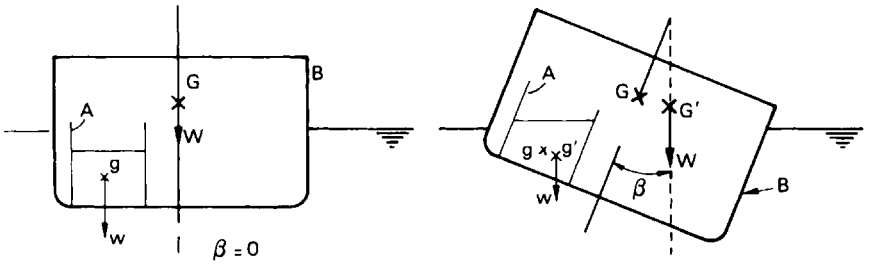

Figure 3.4. Free surface effect

where I_1 is the second moment of area of the fluid free surface about an axis through the centroid of the free surface parallel to the axis of rotation of the ship, and V_1 is the volume of liquid in the tank. Converting the centre of gravity shift as a loss in metacentric height, taking $w = \rho_1 g V_1$, where ρ_1 is the density of fluid in the tank, and $W = \rho g V$ where ρ is the density of sea water and V is the submerged volume of the vessel, the metacentric height loss is obtained as

$$\Delta(GM) = \frac{GG'}{\beta} = \frac{\rho_1 I_1}{\rho V} \tag{3.39}$$

For a ship with a large number of internal tanks (say N) with free surfaces, the total metacentric height loss is

$$\Delta(GM) = \frac{1}{\rho V} \sum_{i=1}^{N} \rho_i I_i \tag{3.40}$$

where ρ_i is the fluid density for the contents of the ith tank; and I_i is its free surface second moment of area about an axis through the free surface's own centroid and parallel to the vessel's axis of rotation.

Note that the free surface effect is independent of the volume of fluid in the tanks and would disappear if a tank was completely full – in this case the mass of fluid would act as a rigid body during vessel rotation. Free surface effects are normally reduced in the design of a floating offshore vessel by compartmentation of tanks to reduce the value of I_i substantially for each of the tanks. The loss of metacentric height or free surface correction is then subtracted from the rigid vessel metacentric height to give a net value to be considered for vessel evaluation.

Freely suspended masses on board a vessel have a similar effect to free surfaces in that the centre of gravity is shifted in the same horizontal direction as the centre of buoyancy and, therefore, tends to reduce stability. For a vessel with N suspended masses on board, each of mass m_i and with free suspension lengths L_i, the centre of gravity shift is

$$GG' = \beta \frac{1}{W} \sum_{i=1}^{N} m_i g L_i \tag{3.41}$$

Using the same approach as before, the metacentric height loss can be written as

$$\Delta(GM) = \frac{1}{\rho V} \sum_{i=1}^{N} m_i L_i \tag{3.42}$$

This correction to metacentric height can be applied by subtracting it from the rigid vessel metacentric height. Alternatively, the centre of gravity calculation of the vessel can be carried out by placing the masses m_i at the top end of the suspension lengths L_i. This has the same effect as the correction defined above.

The forces applied on a vessel by a catenary mooring spread can vary with angle of inclination of the vessel to contribute to either some gain or loss in stability, but such corrections are usually small and are neglected for

hydrostatics calculations. The generally constant downward force applied by a marine riser to a drilling or production vessel usually has little effect on vessel hydrostatic stability. However, both moorings and the riser apply net downward forces on the vessel which have to be accounted for in the weight and buoyancy force balance of the vessel.

3.3 Pressure integration technique

The calculation of the large angle stability can be carried out by a volumetric approach which makes use of submerged volume and water plane area properties. The volumetric method is an extension of the classical method (see Ramsey, 1961; Rawson and Tupper, 1976; and Clayton and Bishop, 1982). Practical difficulties have been experienced in applying this method to the calculation of the large angle hydrostatic stability of complex hull forms often associated with compliant marine structures. A more fundamental approach uses an integration of the pressure distribution acting over the submerged body surface to yield all the necessary hydrostatic characteristics.

The method is computationally more efficient when transformed into a programmed set of instructions for an arbitrary structure at any orientation. Mathematically, the surface integral of pressure can be transformed into a volume integral such that numerical quantities used in conventional naval architecture can be derived from the surface integrals. The computational requirement to divide all the vessel surface into panels is analogous to a requirement for surface panels in potential flow boundary integral techniques (see Section 4.2).

The problem is now one of solving the previously given surface integral equations, Equations (3.3), (3.5) and (3.14). Consider a body that has been modelled by a set of m surface elements covering its submerged surface. This allows complex vessel geometries to be modelled by a set of simple and easily defined plate elements. Equations (3.3) and (3.5) now become

$$\mathbf{F} = \sum_{i=1}^{m} \mathbf{F}_i \tag{3.43}$$

and

$$\mathbf{M} = \sum_{i=1}^{m} \mathbf{M}_i \tag{3.44}$$

where $\mathbf{F}_i$ and $\mathbf{M}_i$ are the forces and moments acting on the ith surface element; $\mathbf{F}_i$ and $\mathbf{M}_i$ are given by

$$\mathbf{F}_i = \int_{S_i} \rho\, g(d - z)\, \mathbf{n}_i \, \mathrm{d}S_i \tag{3.45}$$

and

$$\mathbf{M}_i = \int_{S_i} \mathbf{x} \times \rho\, g(d - z)\, \mathbf{n}_i \, \mathrm{d}S_i \tag{3.46}$$

The advantage of the above is that a complex surface integral has been reduced to a summation of a set of known surface integrals. Depending on the type of surface element, Equations (3.45) and (3.46) may be evaluated analytically, numerically or by a partially analytic/partially numerical method.

Two alternative methods are adopted here for the solution of these equations. The first is a complete numerical summation over the element's surface. The element is treated as a region and is subdivided into a set of rectangular subelements. Equations (3.45) and (3.46) now become

$$\mathbf{F}_i = \sum_{p=1}^{M_p} \sum_{q=1}^{M_q} \rho g \, (d - \mathbf{x}_{pq} \cdot \mathbf{k}) \, \mathbf{n}_{pq} \, \Delta h \Delta v \tag{3.47}$$

and

$$\mathbf{M}_i = \sum_{p=1}^{M_p} \sum_{q=1}^{M_q} \mathbf{x}_{pq} \times \rho g \, (d - \mathbf{x}_{pq} \cdot \mathbf{k}) \, \mathbf{n}_{pq} \, \Delta h \Delta v \tag{3.48}$$

where $\mathbf{x}_{pq}$ is the co-ordinate of the centroid of the rectangular subelement with dimensions Δh and Δv and a unit normal $\mathbf{n}_{pq}$. There are M_p of these subelements along the submerged edge of the element and M_q along the other.

The second method is a numerical summation of a series of line integrals of finite width. Equations (3.45) and (3.46) now become

$$\mathbf{F}_i = \sum_{p=1}^{M_p} \rho g \, \Delta h \int_0^L (d - \mathbf{x} \cdot \mathbf{k}) \, \mathbf{n} \, \mathrm{d}l$$

and (3.49)

$$\mathbf{M}_i = \sum_{p=1}^{M_p} \rho g \, \Delta h \int_0^L \mathbf{x} \times (d - \mathbf{x} \cdot \mathbf{k}) \, \mathbf{n} \, \mathrm{d}l$$

where L_p is the submerged length of the pth line element. This reduction of a complete surface integral to a sum of element surface integrals is equally applicable to all the surface integral equations. This solution method is preferred because it is more accurate and computationally faster.

The line element has unit width, a submerged length defined by the two end vectors, $\mathbf{x}_1$ and $\mathbf{x}_2$, and a constant normal vector $\mathbf{n}$. Figure 3.5 illustrates this and also gives some definitions. The force acting on element $\mathrm{d}l$ is

$$\mathrm{d}\mathbf{F} = \rho \, g \, (d - z) \, \mathrm{d}l \, \mathbf{n} \tag{3.50}$$

Integration gives

$$\mathbf{F} = \left[\int_{\mathbf{x}_1}^{\mathbf{x}_2} \rho \, g \, (d - z) \, \mathrm{d}l \right] \mathbf{n}$$

$$= F \, \mathbf{n} \tag{3.51}$$

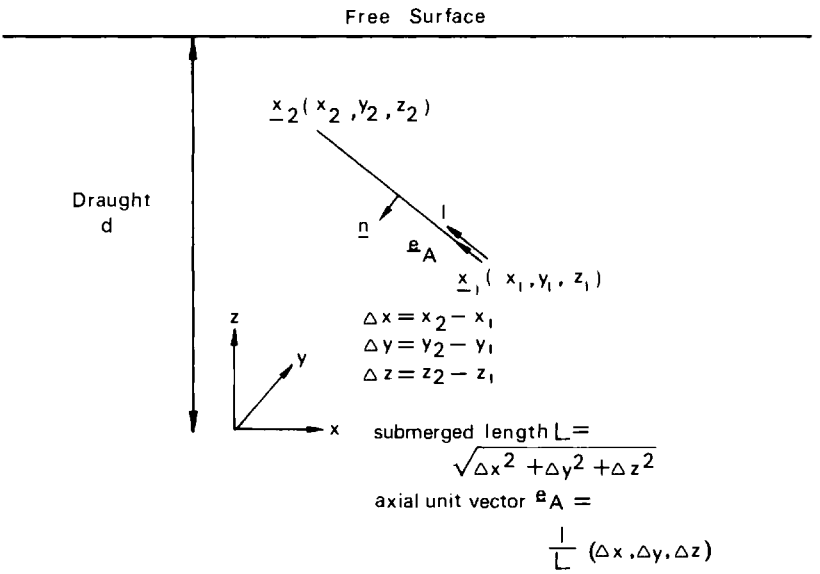

Figure 3.5. A line element

Now F is a line integral from $\mathbf{x}_1$ to $\mathbf{x}_2$. In global axes $\mathrm{d}l$ becomes

$$\begin{aligned} \mathrm{d}l &= \mathbf{e}_{Ax}\,\mathrm{d}x + \mathbf{e}_{Ay}\,\mathrm{d}y + \mathbf{e}_{Az}\,\mathrm{d}z \\ &= \frac{\Delta x}{L}\,\mathrm{d}x + \frac{\Delta y}{L}\,\mathrm{d}y + \frac{\Delta z}{L}\,\mathrm{d}z \end{aligned} \tag{3.52}$$

For any point on a straight line

$$\frac{x - x_1}{\Delta x} = \frac{y - y_1}{\Delta y} = \frac{z - z_1}{\Delta z} \tag{3.53}$$

or, in terms of a variable l,

$$\begin{aligned} x &= \frac{\Delta x\, l}{L} + x_1 \\ y &= \frac{\Delta y\, l}{L} + y_1 \\ z &= \frac{\Delta z\, l}{L} + z_1 \end{aligned} \tag{3.54}$$

F now becomes

$$F = \int_{z_1}^{z_2} \frac{\rho\, g\, (d - z)}{L} \left[x \frac{\mathrm{d}x}{\mathrm{d}z} + y \frac{\mathrm{d}y}{\mathrm{d}z} + z \right] \mathrm{d}z \tag{3.55}$$

The relations for dx/dz and dy/dz are found by differentiating the equations in (3.53). Substituting into Equation (3.55) gives

$$F = \int_{z_1}^{z_2} \frac{\rho\, g\, (d - z)\, \mathrm{d}z}{L} = \rho\, g \left[d - \frac{(z_2 + z_1)}{2} \right] \tag{3.56}$$

The force acting on the line element is

$$\mathbf{F} = \rho\, g \left[d - \frac{(z_2 + z_1)}{2} \right] \mathbf{n} \tag{3.57}$$

The moment **M** is given by

$$\mathbf{M} = \int_{x_1}^{x_2} \mathbf{x} \times \rho\, g\, (d - z)\, \mathbf{n}\, \mathrm{d}l \tag{3.58}$$

$$\mathbf{M} = \rho\, g \int_0^L (d - z) \begin{bmatrix} yn_z - zn_y \\ zn_x - xn_z \\ xn_y - yn_x \end{bmatrix} \mathrm{d}l \tag{3.59}$$

where $\mathbf{n} = (n_x, n_y, n_z)$.

Let $I_x = \dfrac{1}{L} \displaystyle\int_0^L (d - z)\, x\, \mathrm{d}l$

$$I_y = \frac{1}{L} \int_0^L (d - z)\, y\, \mathrm{d}l \tag{3.60}$$

and

$$I_z = \frac{1}{L} \int_0^L (d - z)\, z\, \mathrm{d}l$$

Substituting Equations (3.54) into (3.60) gives

$$\begin{aligned} I_x &= \frac{d}{2}(x_2 + x_1) - \frac{(x_1 z_2 + z_1 x_2)}{2} - \frac{\Delta x \Delta z}{3} \\ I_y &= \frac{d}{2}(y_2 + y_1) - \frac{(y_1 z_2 + z_1 y_2)}{2} - \frac{\Delta y \Delta z}{3} \\ I_z &= \frac{d}{2}(z_2 + z_1) - z_1 z_2 - \frac{\Delta z^2}{3} \end{aligned} \tag{3.61}$$

The moment **M** becomes

$$\mathbf{M} = \rho g L \begin{bmatrix} I_y n_z - I_z n_y \\ I_z n_x - I_x n_z \\ I_x n_y - I_y n_x \end{bmatrix} \tag{3.62}$$

This method can be developed for a wide range of surface elements such as rectangular, triangular and curved plates and Coon's patches. Further details are given by Witz and Patel (1985) and Harrison, Patel and Witz (1990).

Figure 3.6 presents a comparison of the restoring moment of a uniform 10 m by 10 m by 4 m box of 205 t mass and a draught of 2 m calculated using the above pressure integration technique and by the wall sided formula (Rawson and Tupper, 1976). This box offers a special case where the wall sided formula provides an exact analytical result for the restoring moment over the entire 180° of rotation. Figure 3.6 shows that the pressure integration technique is in excellent agreement with the analytic result.

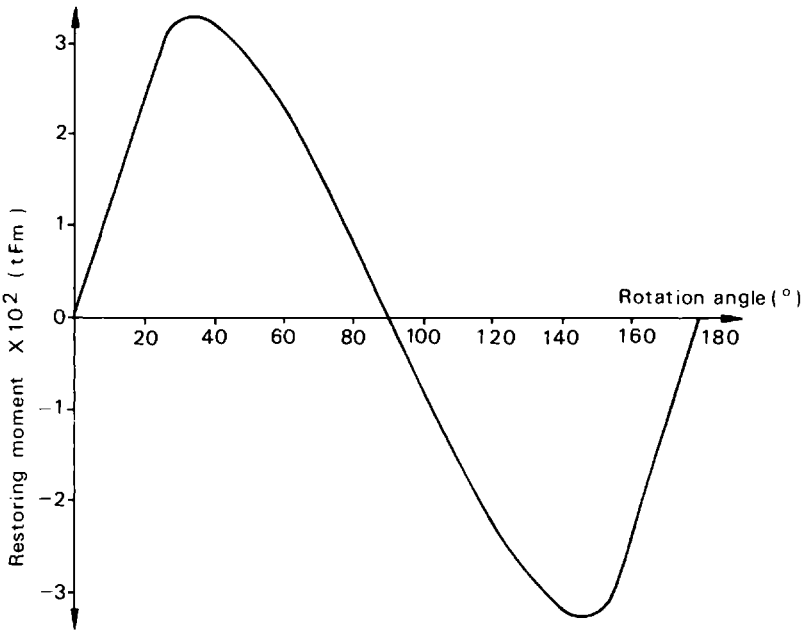

Figure 3.6. Restoring moment of a 10 m × 10 m × 4 m box of 205 t mass and draught of 2 m

Figure 3.7 shows the large angle hydrostatic stability of a naval vessel calculated by the pressure integration technique and the volumetric method. The results are presented in terms of a variation of GZ with angle of heel where G is the centre of gravity position and Z is the base of the perpendicular from G to the vertical through the metacentre M. They show good agreement between the two methods for this relatively simple hull form. The pressure integration technique is computationally more efficient than the volumetric method and is more accurate for complex hull geometries.

A final note on the presentation of large angle hydrostatic stability of marine vessels. In practical terms, the large angle stability characteristics of a hull form can be defined by tabulated or plotted data presented in various

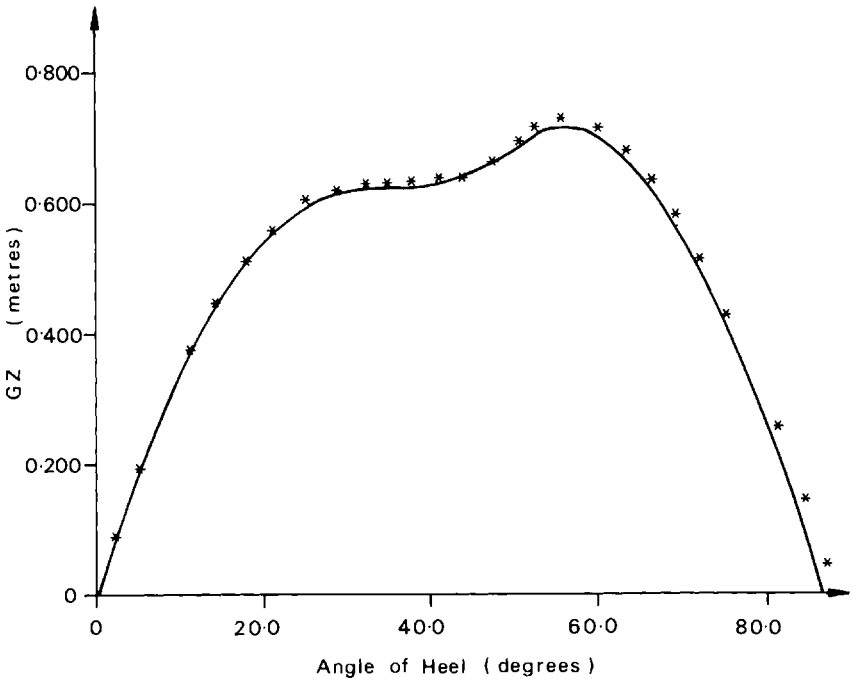

Figure 3.7. GZ curve for naval hull (— volumetric method; * pressure integration technique)

ways. Cross-curves of stability (see Figure 3.8(a)) present stability moment arms (GZ) against vessel displacement for a range of heel angles. In some cases, the variability of centre of gravity position, G, is removed from GZ by replacing it with SZ, where S is an arbitrary fixed point or pole on the vessel vertical centre line; SZ can readily be related to GZ if the positions of S and KG are known. Statical stability curves define the variation of GZ, SZ or righting moment against angle of heel (see Figure 3.8(b)). Statical stability curves are often drawn on the same axes as wind heeling curves to check that the vessel has sufficient hydrostatic restoring moment to recover from a heeling moment due to wind and to estimate the angle of heel that will be induced by wind. The area under either of these curves is a measure of the work done to heel the vessel over to any particular angle. A practical means of ensuring stability under wave induced motions is to require that the area under the restoring moment curve exceeds the area under the wind heeling curve by a specified fraction at least.

Curves of form can be used to define the values of displacement, KB, KM_y, KM_x, BM_y, BM_x as functions of vessel draught – see Figure 3.8(c). Safe vessel loading conditions can be defined by allowable KG curves (Figure 3.8(d)) which give the highest permissible centre of gravity heights above the keel as a function of vessel draught. All these curves are usually presented in tabulated and graphical form in the stability manual of a floating offshore vessel.

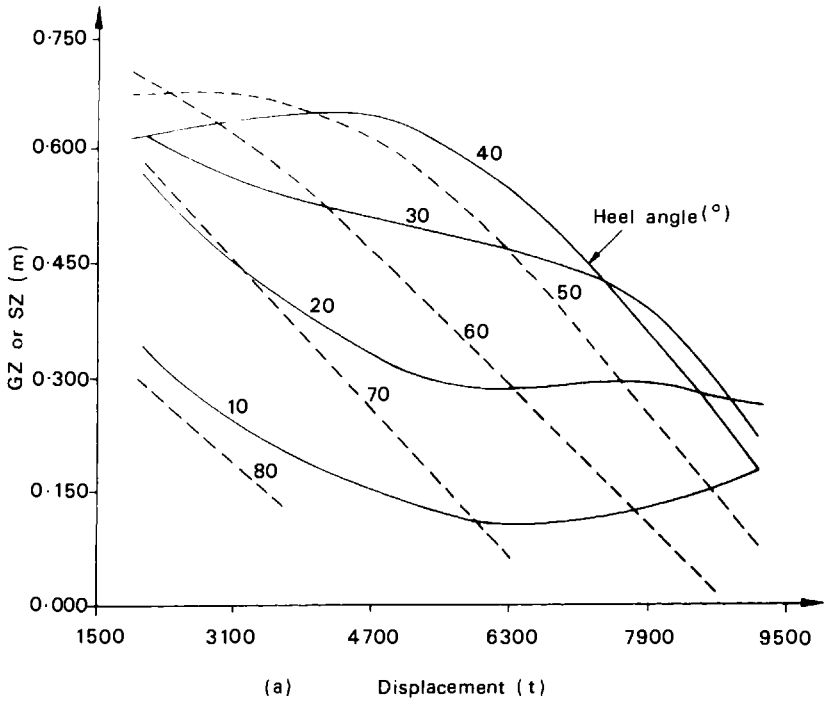

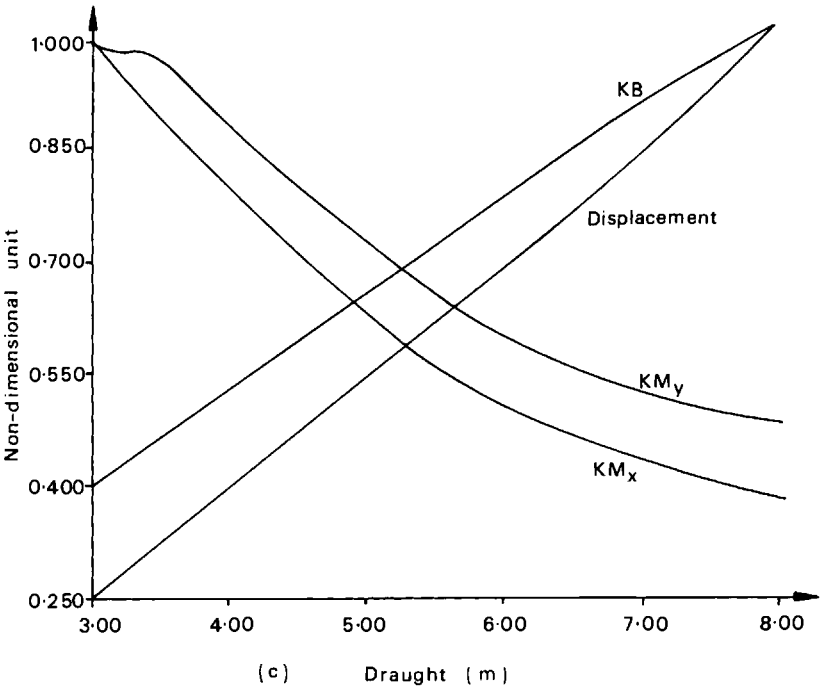

Figure 3.8. Hydrostatic stability curves: (a) cross-curves of stability; (b) static stability curve; (c) curve of form; (d) allowable KG curve

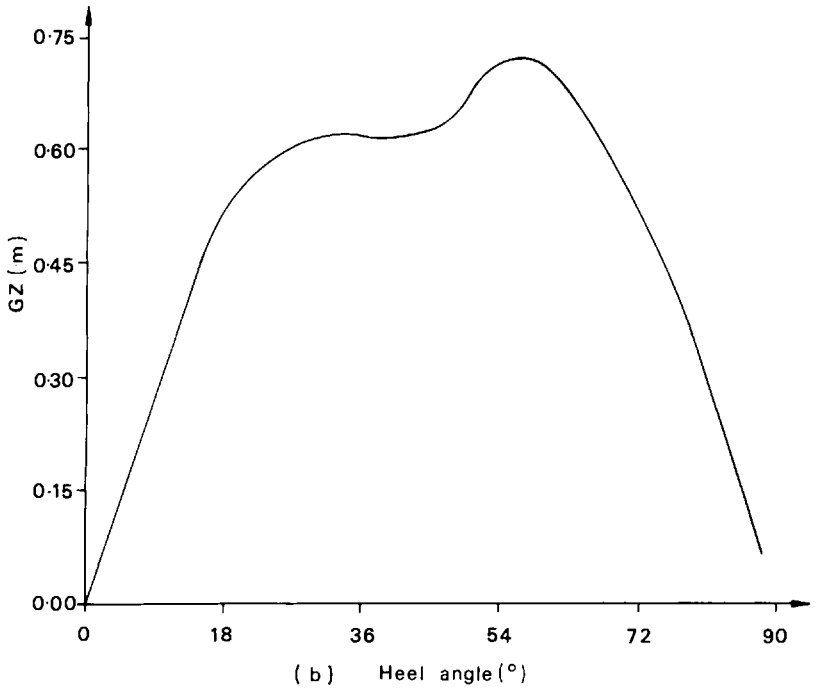
0·75
0·60
0·45
0·30
0·15
0·00
GZ (m)
0
18
36
54
72
90
(b) Heel angle (°)

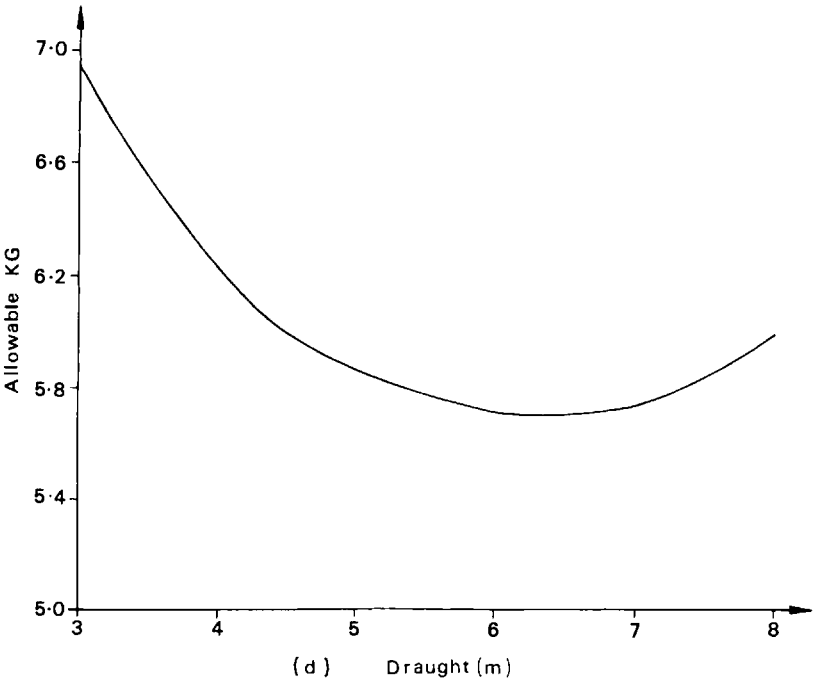
7·0
6·6
6·2
5·8
5·4
5·0
Allowable KG
3
4
5
6
7
8
(d) Draught (m)

The hydrostatic stability of floating compliant marine structures remains an important element of their operational success. Specific features of such hydrostatics are covered at appropriate points in the rest of this book.

References

Clayton, B. R. and Bishop, R. E. D. (1982) *Mechanics of Marine Vehicles*. E. and F. N. Spon, London

Harrison, J. H., Patel, M. H. and Witz, J. A. (1990) Hydrostatic analysis of naval hull forms using pressure integration. *Transactions of the Royal Institution of Naval Architects*, **132**, 141–151

Kreysig, E. (1988) *Advanced Engineering Mathematics*, 6th edn. J. Wiley & Sons

Patel, M. H. (1989) *Dynamics of Offshore Structures*, Butterworths, London

Ramsey, A. S. (1961) *Hydrostatics*, 2nd edn. Cambridge University Press

Rawson, K. J. and Tupper, E. C. (1976) *Basic Ship Theory*, Volume 1. Longman, London

Witz, J. A. and Patel, M. H. (1985) A pressure integration technique for hydrostatic analysis. *Transactions of the Royal Institution of Naval Architects*, **127**, 285–294

Chapter 4

Dynamic response analysis

Compliant marine structures are dynamic systems which interact with the surrounding fluid medium. This fluid–structure interaction plays an important part in characterizing their response. This chapter is concerned with presenting typical methods for deriving the dynamic response of compliant marine structures once their equations of motion have been formulated. The evaluation of coefficients or coefficient matrices for the governing equations are covered in later sections for each class of compliant marine structure.

Compliant marine structures are complex systems with numerous functional components. It is an almost impossible task to analyse the compliant marine structure using a complete system model which gives all relevant design information. A more practical approach is to identify system models which provide the relevant design parameters. For example, a designer is interested in the wave induced motions and stresses of a compliant marine structure. A full hydroelastic model to identify these design parameters would be very complex and difficult to utilize within a design cycle. A more practical approach would be to determine the wave induced motions by considering the marine structure to be a floating, rigid body. The next stage would be to use the computed wave induced motions and loads for a structural analysis in order to determine the stress distribution within the structure. The use of two separate system models for different but related design parameters is feasible within the design process. The designer must, of course, ensure that no significant errors are introduced, i.e. the system models applied are appropriate.

Another related approach is to reduce the complete system into a number of subsystems and to analyse each subsystem separately. Many of these subsystems will interact and therefore the analysis may be iterative. For example, a different system model is required for the analysis of the dynamics of an individual mooring line compared with the system model used for the analysis of the wave induced motions of a moored compliant marine structure. Yet both these systems interact and therefore their analysis may have to be carried out in an iterative procedure where output from one system model is required for input for the other system model and vice versa.

This chapter examines the analysis of the dynamic system models encountered in later chapters.

4.1 Formulation of governing equations

The transformation of a problem concerned with fluid–structure interactions of a floating body into the governing equation of a second order dynamic system is best illustrated by considering a simple linearized system with one degree of freedom. An example of such a system is the cylindrical buoy of Figure 4.1 where coordinate η denotes vertical motion of the water surface and z denotes the resultant buoy vertical motion. The total force acting on the buoy will be due to added mass, damping and hydrostatic stiffness induced forces due to differential motion between the buoy and surrounding fluid. The net force due to these effects will serve to accelerate the buoy. Thus the equation of motion can be written as

$$m\ddot{z} = A(\ddot{\eta} - \ddot{z}) + B(\dot{\eta} - \dot{z}) + C(\eta - z) \tag{4.1}$$

where m is the buoy mass; and A, B, C are coefficients expressing the added mass, damping and hydrostatic stiffness induced forces on the buoy.

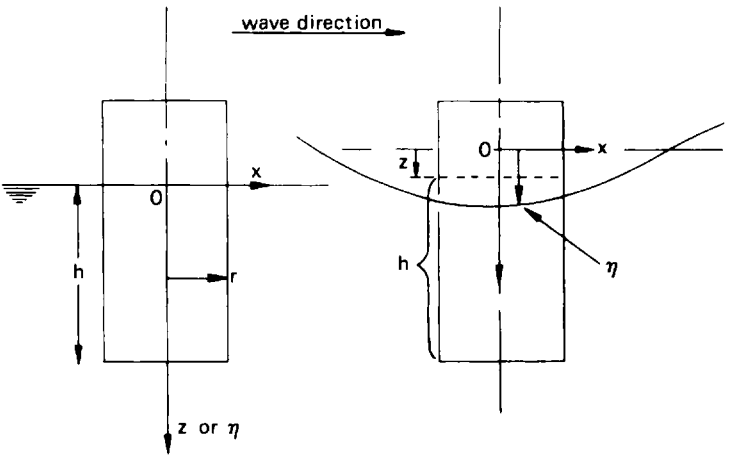

Figure 4.1. Heave motion of a buoy

Here the damping force is taken to be linear and the Froude–Krylov force – applying through dynamic wave pressure on the buoy base – is given by the stiffness term, $C\eta$, for a buoy geometry where draught, h, is very small compared to incident wave lengths.

Rearranging Equation (4.1) to bring unknown buoy motion terms to the left hand side gives

$$(m + A)\ddot{z} + B\dot{z} + Cz = F(t) \tag{4.2}$$

where

$$F(t) = A\,\ddot{\eta} + B\,\dot{\eta} + C\,\eta \tag{4.3}$$

Thus, there are two equations governing the behaviour of the buoy in waves. Equation (4.3) is concerned with the mechanism of wave elevation motion, η, exerting an exciting force $F(t)$ on the buoy, whereas Equation (4.2) is a second order linear ordinary differential equation which describes the dynamic response of the buoy. The form of the above equations is typical of that obtained for all floating bodies in that two transfer functions (from wave elevation to force and from wave force to motion) are involved in deriving a body motion response from wave elevation.

This concept can readily be extended to multiple degrees of freedom to obtain an equation of motion in matrix form as

$$\mathbf{M}\,\ddot{\mathbf{X}} + \mathbf{B}\,\dot{\mathbf{X}} + \mathbf{K}\,\mathbf{X} = \mathbf{F}(t) \tag{4.4}$$

where the $(n \times 1)$ column vector of displacement $\mathbf{X}$ holds the n degrees of freedom that characterize the response of the structure; and $\mathbf{F}(t)$ denotes the $(n \times 1)$ column vector of applied forces. All the coefficients of the n equations of motion implied in Equation (4.4) are incorporated in $(n \times n)$ matrices of mass, damping and stiffness ($\mathbf{M}$, $\mathbf{B}$ and $\mathbf{K}$). The magnitude and distribution of coefficients in these matrices reflect the dynamic characteristics of each degree of freedom and of the couplings between them.

For the floating systems described in this book, the degrees of freedom are concerned with rigid body motions of structural elements or bulk motions of water masses. The application of these equations of motion to structural deformation degrees of freedom is not considered, with the exception of the dynamics of marine risers in Chapter 11. However, many systems exhibit a quadratic form of damping arising from drag forces. Inclusion of this drag force damping for a simple single degree of freedom system yields an equation of motion of the form

$$(m + A)\,\ddot{z} + B_v\,|\dot{z}|\,\dot{z} + C\,z = F(t) \tag{4.5}$$

where m is the physical mass; A is the added mass; B_v is the quadratic damping coefficient; C is the stiffness and F is the exciting force.

One approach that permits solution of Equation (4.5) is to use a linearized equivalent damping coefficient B that is selected so that the non-linear and equivalent linear damping coefficients dissipate the same energy at resonance. For a linear damping term of the form given in Equation (4.2), the energy dissipated at resonance can be written as

$$W_L = 2\int_{-R}^{R} B(R\,\omega_0\,\sin\omega_0 t)\,dz \tag{4.6}$$

where $z = R\,\sin(\omega_0 t - \pi/2)$ is the resonant motion at frequency ω_0. Writing the integral in terms of time gives

$$W_L = 2\int_0^{\pi} B\,\omega_0\,R^2\,\sin^2\omega_0 t\,d(\omega_0 t)$$

$$= \pi B\omega_0 R^2 \tag{4.7}$$

For non-linear drag induced damping, the work, W_D, done becomes

$$W_D = 2\int_{-R}^{R} B_v(R^2\,\omega_0^2\sin^2\omega_0 t)\,dz$$

$$= 2\int_0^{\pi} B_v\,\omega_0^2\,R^3\sin^3\omega_0 t\,d(\omega_0 t)$$

$$= \tfrac{8}{3}\,B_v\,\omega_0^2\,R^3 \tag{4.8}$$

Equating the work done by linear and non-linear damping yields

$$B = \frac{8}{3\pi}\left[\omega_0 R\right]B_v$$

$$= \frac{8}{3\pi}\left[\dot{z}_{max}\right]B_v \tag{4.9}$$

Equation (4.5) can be solved by replacing $B_v\,|\dot{z}|$ by B from Equation (4.9). The equation has, therefore, to be solved by iteration in that a value of $\dot{z}_{max}$ has to be determined which satisfies the equation. The first solution for the iteration is usually found by assuming that the damping is linear and 10% of critical. The new value of $\dot{z}_{max}$ obtained from this initial solution is then placed in the damping term and the procedure repeated until successive values of $\dot{z}_{max}$ are within a small value of each other. This interaction converges very quickly away from resonance and within approximately ten solutions at resonance. The resultant solution for z will now also be a function of the amplitude of the applied force, F_a, and of wave amplitude, a.

All the above formulation features are illustrated further in Section 5.1.

4.2 Solution techniques

This section briefly describes solution techniques commonly employed in the analysis of compliant marine structures. More comprehensive treatments of the methods presented here are to be found in the literature (see, for instance, Bathe, 1982; Meirovitch, 1986; and Thomson, 1988).

4.2.1 Free response

This technique is used to derive the undamped natural periods and corresponding modes of vibration (eigen values and eigen vectors) for a marine system responding to initial conditions in still water. If the matrix equation of free undamped motion for a marine system is

$$\mathbf{M}\,\ddot{\mathbf{q}} + \mathbf{K}\,\mathbf{q} = \mathbf{0} \tag{4.10}$$

where $\mathbf{q}$ is the $(n \times 1)$ displacement vector containing the n degrees of freedom of the system, $\mathbf{M}$ is the mass matrix and $\mathbf{K}$ is the stiffness matrix.

Assuming a solution of the form

$$\mathbf{q} = \mathbf{q}_0\,e^{-i\omega t} \tag{4.11}$$

and substituting into Equation (4.10) yields

$$(\mathbf{K} - \omega^2 \mathbf{M})\, \mathbf{q}_0 = \mathbf{0} \tag{4.12}$$

Apart from the trivial solution of $\mathbf{q}_0 = 0$, Equation (4.12) has solutions given by

$$\text{Det } |\mathbf{K} - \omega^2 \mathbf{M}| = 0 \tag{4.13}$$

which leads to a polynomial of degree n where n is the number of degrees of freedom in the governing equation, Equation (4.4). Solution of the determinant yields n values of ω^2 which are the natural frequencies of the system. Each natural frequency, ω_r, has a corresponding set of values of $\mathbf{q}_{0r}$ given by

$$(\mathbf{K} - \omega_r^2 \mathbf{M})\, \mathbf{q}_{0r} = \mathbf{0} \tag{4.14}$$

although the elements of vector $\mathbf{q}_{0r}$ are only defined relative to each other rather than in absolute terms. For systems with many degrees of freedom, the determination of the eigen values ω_r and the eigen vectors $\mathbf{q}_{0r}$ requires a considerable computational effort although modern computer based algorithms make the task simpler than it would be otherwise – see Bathe and Wilson (1973) for a survey of available techniques.

It can also be shown that the eigen vectors for any two vibration modes satisfy an orthogonality condition. Consider vibration modes r and s. From Equation (4.14) these can be written as

$$\mathbf{K}\, \mathbf{q}_{0r} = \omega_r^2\, \mathbf{M}\, \mathbf{q}_{0r} \tag{4.15}$$

and

$$\mathbf{K}\, \mathbf{q}_{0s} = \omega_s^2\, \mathbf{M}\, \mathbf{q}_{0s} \tag{4.16}$$

Taking the transpose of Equation (4.15) gives

$$(\mathbf{K}\, \mathbf{q}_{0r})^{\mathrm{T}} = \omega_r^2\, (\mathbf{M}\, \mathbf{q}_{0r})^{\mathrm{T}}$$

or

$$\mathbf{q}_{0r}^{\mathrm{T}}\, \mathbf{K} = \omega_r^2\, \mathbf{q}_{0r}^{\mathrm{T}}\, \mathbf{M} \tag{4.17}$$

since $\mathbf{K}$ and $\mathbf{M}$ are symmetric and $\mathbf{K} = \mathbf{K}^{\mathrm{T}}$ and $\mathbf{M} = \mathbf{M}^{\mathrm{T}}$. If Equation (4.17) is postmultiplied by $\mathbf{q}_{0s}$ and Equation (4.16) is premultiplied by $\mathbf{q}_{0r}^{\mathrm{T}}$, then

$$\mathbf{q}_{0r}^{\mathrm{T}}\, \mathbf{K}\, \mathbf{q}_{0s} = \omega_r^2\, \mathbf{q}_{0r}^{\mathrm{T}}\, \mathbf{M}\, \mathbf{q}_{0s} \tag{4.18}$$

and

$$\mathbf{q}_{0r}^{\mathrm{T}}\, \mathbf{K}\, \mathbf{q}_{0s} = \omega_s^2\, \mathbf{q}_{0r}^{\mathrm{T}}\, \mathbf{M}\, \mathbf{q}_{0s} \tag{4.19}$$

Subtraction of (4.19) from (4.18) yields

$$(\omega_r^2 - \omega_s^2)\, \mathbf{q}_{0r}^{\mathrm{T}}\, \mathbf{M}\, \mathbf{q}_{0s} = 0 \tag{4.20}$$

so that for $\omega_r \neq \omega_s$, the orthogonality conditions for the modes of vibration are obtained as

$$\mathbf{q}_{0r}^{\mathrm{T}}\, \mathbf{M}\, \mathbf{q}_{0s} = 0 \tag{4.21}$$

and

$$\mathbf{q}_{0r}^{\mathrm{T}}\, \mathbf{K}\, \mathbf{q}_{0s} = 0 \tag{4.22}$$

The eigen vectors are often normalized by using a version of Equation (4.21) with $r = s$ so that for the rth normalized eigen vector $\boldsymbol{\phi}_r$, the condition

$$\boldsymbol{\phi}_r^{\mathrm{T}} \mathbf{M} \boldsymbol{\phi}_r = 1 \tag{4.23}$$

holds. This can be achieved by calculating the scale factor

$$S_r = \mathbf{q}_{0r}^{\mathrm{T}} \mathbf{M} \mathbf{q}_{0r} \tag{4.24}$$

and obtaining the normalized eigen vector as

$$\boldsymbol{\phi}_r = \frac{\mathbf{q}_{0r}}{\sqrt{(S_r)}} \tag{4.25}$$

With this normalization procedure, if all the eigen vectors, $\boldsymbol{\phi}_r$, are collected in an $n \times n$ square matrix, $\boldsymbol{\Phi}$, then the condition

$$\boldsymbol{\Phi}^{\mathrm{T}} \mathbf{M} \boldsymbol{\Phi} = \mathbf{I} \tag{4.26}$$

where $\mathbf{I}$ is the $n \times n$ identity matrix with unit diagonal terms and zero off diagonal terms.

4.2.2 Forced response

4.2.2.1 Frequency domain methods

The matrix equation of motion (4.4) for dynamic response can be solved in either the frequency or time domains. For solution in the frequency domain, it is necessary to use linear wave theory to obtain wave properties and to linearize the drag force term. Once these simplifications are made, a frequency domain solution offers readily usable transfer functions of structure displacements, internal forces and stresses which can be applied to deriving statistical response results.

The frequency domain solution can be obtained in two ways. A direct substitution of the form of solution

$$\mathbf{q} = \mathbf{q}_0 \, \mathrm{e}^{-\mathrm{i}\omega t} \tag{4.27}$$

in a governing equation of the form

$$\mathbf{M} \ddot{\mathbf{q}} + \mathbf{C} \dot{\mathbf{q}} + \mathbf{K} \mathbf{q} = \mathbf{F} \tag{4.28}$$

will yield the unknown displacement through matrix inversion of the term in square brackets in the equation

$$[\mathbf{K} - \omega^2 \mathbf{M} - \mathrm{i}\omega \mathbf{C}] \mathbf{q}_0 = \mathbf{F}_0 \tag{4.29}$$

where the exciting force is

$$\mathbf{F} = \mathbf{F}_0 \, \mathrm{e}^{-\mathrm{i}\omega t} \tag{4.30}$$

with amplitude $\mathbf{F}_0$ and frequency ω, $\mathbf{q}$ is the displacement vector and $\mathbf{M}$, $\mathbf{C}$ and $\mathbf{K}$ are mass, damping and stiffness matrices. For systems with non-linear loading, $\mathbf{F}$ is the linearized form of the wave exciting force. Solution of Equation (4.29) requires the inversion of a large matrix with

complex number elements. This is a numerically cumbersome operation and has prompted the development of computationally more efficient solution techniques.

One such method uses modal superposition. This technique relies on the fact that despite the large number of degrees of freedom of a typical offshore structure, its dynamic response is limited to only a few modes of vibration. The modal superposition technique uses this feature to reduce the solution computation time. This is because the eigen vectors or mode shapes can be said to be building blocks of the dynamic response of a general n degree of freedom system to the extent that it is efficient to describe the response in terms of these mode shapes. The method initially requires determination of the undamped natural frequencies and vibration modes of the structure, as is described earlier.

Thus the displacement vector, $\mathbf{q}$, of an n degree of freedom dynamic system described by the matrix equation

$$\mathbf{M}\,\ddot{\mathbf{q}} + \mathbf{C}\,\dot{\mathbf{q}} + \mathbf{K}\,\mathbf{q} = \mathbf{F}(t) \tag{4.31}$$

can be written in terms of eigen vectors (or mode shapes) through the matrix equation

$$\mathbf{q} = \mathbf{\Phi}\,\mathrm{Y} \tag{4.32}$$

where $\mathbf{\Phi}$ is the $n \times n$ matrix of normalized eigen vectors ϕ_i; and $\mathbf{Y}$ is the $(n \times 1)$ column vector of modal amplitudes. Thus Equation (4.32) transforms from geometric variables, $\mathbf{q}$, to generalized co-ordinates, $\mathbf{Y}$, which describe the amplitudes of excited modes during dynamic response. These generalized co-ordinates are called normal co-ordinates.

Equation (4.31) can be written in terms of the normal co-ordinates, $\mathbf{Y}$, by substitution of Equation (4.31) and premultiplying by the transpose of the eigen vector matrix, ϕ^{T}, to give

$$\mathbf{\Phi}^{\mathrm{T}}\,\mathbf{M}\,\mathbf{\Phi}\,\ddot{\mathbf{Y}} + \mathbf{\Phi}^{\mathrm{T}}\,\mathbf{C}\,\mathbf{\Phi}\,\dot{\mathbf{Y}} + \mathbf{\Phi}^{\mathrm{T}}\mathbf{K}\,\boldsymbol{\phi}\,\mathbf{Y} = \mathbf{\Phi}^{\mathrm{T}}\,\mathbf{F}(t) \tag{4.33}$$

Now, as a consequence of the orthogonality condition, all components except for the ith column vector term vanish in the mass and stiffness terms. The orthogonality does not apply to the damping term but the modal superposition technique assumes that terms other than in the ith mode also vanish in the terms of Equation (4.33) that are derived from the damping matrix. Thus the ith normal mode is entirely decoupled and satisfies the equation

$$M_i\,\ddot{Y}_i + C_i\,\dot{Y}_i + K_i\,Y_i = F_i(t)$$

where

$$\begin{aligned} M_i &= \boldsymbol{\phi}_i^{\mathrm{T}}\,\mathbf{M}\,\boldsymbol{\phi}_i \\ K_i &= \boldsymbol{\phi}_i^{\mathrm{T}}\,\mathbf{K}\,\boldsymbol{\phi}_i \\ C_i &= \boldsymbol{\phi}_i^{\mathrm{T}}\,\mathbf{C}\,\boldsymbol{\phi}_i \end{aligned} \tag{4.34}$$

and

$$F_i(t) = \boldsymbol{\phi}_i^{\mathrm{T}}\,\mathbf{F}(t)$$

Equation (4.34) can be solved for all the normalized co-ordinates, Y_i, and the geometric co-ordinates, $\mathbf{q}$, can be recovered from Equation (4.32). The major advantage of this modal superposition technique is that the structure dynamic response is usually made up of the superposition of only a few of all the modes that are likely to be excited. The number of times Equation (4.34) needs to be evaluated can, therefore, be reduced for computational efficiency by evaluating it only for significant modes. On the other hand, this technique requires that eigen frequencies and vectors be evaluated prior to obtaining a solution.

It can be shown that a conventional damping matrix of the form given by

$$\mathbf{C} = \alpha \mathbf{M} + \beta \mathbf{K} \tag{4.35}$$

where α and β are constants, will satisfy the orthogonality condition, since the mass and stiffness matrices will each satisfy this condition also. Thus, if the damping matrix is approximated to the form of Equation (4.35), the modal superposition technique will uncouple the damping term without resorting to the approximation of neglecting off diagonal terms in Equation (4.33).

Note that the uncoupled equations of motion in normal co-ordinates given by Equation (4.34) can be solved by any method in the frequency or time domain.

4.2.2.2 Time step integration

Solution of the equation of motion by frequency domain and modal superposition techniques as described above is only applicable to linear systems with harmonic excitation, whereas the equations of motion for drag dominated structures can have a substantial non-linear character, as illustrated by Equation (4.5), for wave forces. This non-linear nature can be preserved by solving the equations of motion through a time step procedure. This also permits the wave kinematics to be more accurately represented by Stoke's fifth order theory for regular waves at least. The disadvantage of this approach is its complexity and the fact that output results are available only as time histories. Time domain solutions are also computationally expensive.

Two methods for time step integration are described here. The first, called the central difference method, is an explicit algorithm which is based on a Taylor series expansion.

The equation of motion in a matrix form is taken as

$$\mathbf{M}\ddot{\mathbf{x}} + \mathbf{C}\dot{\mathbf{x}} + \mathbf{K}\mathbf{x} = \mathbf{F} \tag{4.36}$$

in the usual notation; $\mathbf{x}_i$ and $\mathbf{x}_{i+1}$ are taken to be the values of vector $\mathbf{x}$ at times i and $i+1$ such that $\Delta t = t_{i+1} - t_i$. Then expanding $\mathbf{x}_{i+1}$ and $\mathbf{x}_i$ as a Taylor series gives

$$\left.\begin{aligned} \mathbf{x}_{i+1} &= \mathbf{x}_i + (\Delta t)\,\dot{\mathbf{x}}_i + \tfrac{1}{2}(\Delta t)^2\,\ddot{\mathbf{x}}_i + \ldots \\ \mathbf{x}_{i-1} &= \mathbf{x}_i - (\Delta t)\,\dot{\mathbf{x}}_i + \tfrac{1}{2}(\Delta t)^2\,\ddot{\mathbf{x}}_i - \ldots \end{aligned}\right\} \tag{4.37}$$

By subtracting and adding Equations (4.37) and neglecting terms of power $(\Delta t)^3$ and higher gives

$$\left.\begin{aligned} &\dot{\mathbf{x}}_i = (\mathbf{x}_{i+1} - \mathbf{x}_{i-1})/(2\Delta t) \\ &\text{and} \\ &\ddot{\mathbf{x}}_i = \{\mathbf{x}_{i+1} - 2\mathbf{x}_i + \mathbf{x}_{i-1}\}/(\Delta t)^2 \end{aligned}\right\} \tag{4.38}$$

Direct substitution in Equation (4.36) with $\mathbf{x} = \mathbf{x}_i$ gives

$$[\mathbf{M} + \tfrac{1}{2}(\Delta t)\,\mathbf{C}]\,\mathbf{x}_{i+1} = (\Delta t)^2\,\mathbf{F}_i + [2\mathbf{M} - (\Delta t)^2\,\mathbf{K}]\,\mathbf{x}_i + [\tfrac{1}{2}(\Delta t)\,\mathbf{C} - \mathbf{M}]\,\mathbf{x}_{i-1} \tag{4.39}$$

Equation (4.39) is used for successive time steps to derive the displacement of time $i + 1$ from displacements at time i and $i - 1$. The central difference method requires the condition

$$\frac{\Delta t}{T_n} \leqslant 0.318 \tag{4.40}$$

to be satisfied for numerical stability where T_n is the period of the highest vibration mode of the system.

The second time step integration method considered here is the Newmark-β technique which assumes that the displacement and velocity at the end of a time interval can be related to the displacement, velocity and acceleration at the beginning of the time interval by the equation

$$\left.\begin{aligned} &\dot{\mathbf{x}}_{i+1} = \dot{\mathbf{x}}_i + \tfrac{1}{2}(\Delta t)\,[\ddot{\mathbf{x}}_i + \ddot{\mathbf{x}}_{i+1}] \\ &\text{and} \\ &\mathbf{x}_{i+1} = \mathbf{x}_i + (\Delta t)\,\dot{\mathbf{x}}_i + (\tfrac{1}{2} - \beta)\,(\Delta t)^2\,\ddot{\mathbf{x}}_i + \beta\,(\Delta t)^2\,\ddot{\mathbf{x}}_{i+1} \end{aligned}\right\} \tag{4.41}$$

The variable β does have physical significance, in that $\beta = 1/4$ in Equation (4.41) corresponds to a constant acceleration variation from i to $i + 1$ whereas $\beta = 1/6$ converts the equation to apply for linearly varying acceleration.

Writing Equation (4.36) for time periods $i - 1$, i and $i + 1$ gives

$$\mathbf{M}\,\ddot{\mathbf{x}}_{i-1} + \mathbf{C}\,\dot{\mathbf{x}}_{i-1} + \mathbf{K}\,\mathbf{x}_{i-1} = \mathbf{F}_{i-1} \tag{4.42}$$

$$\mathbf{M}\,\ddot{\mathbf{x}}_i + \mathbf{C}\,\dot{\mathbf{x}}_i + \mathbf{K}\,\mathbf{x}_i = \mathbf{F}_i \tag{4.43}$$

$$\mathbf{M}\,\ddot{\mathbf{x}}_{i+1} + \mathbf{C}\,\dot{\mathbf{x}}_{i+1} + \mathbf{K}\,\mathbf{x}_{i+1} = \mathbf{F}_{i+1} \tag{4.44}$$

Multiplying Equations (4.42) and (4.44) by $\beta(\Delta t)^2$, Equation (4.43) by $(1 - 2\beta)(\Delta t)^2$ and adding gives

$$\begin{aligned} &(\Delta t)^2\mathbf{M}\,[\{\beta\ddot{\mathbf{x}}_{i+1} + (\tfrac{1}{2} - \beta)\,\ddot{\mathbf{x}}_i\} - \{\beta\ddot{\mathbf{x}}_i + (\tfrac{1}{2} - \beta)\,\ddot{\mathbf{x}}_{i-1}\} \\ &+ \{\tfrac{1}{2}\ddot{\mathbf{x}}_i + \tfrac{1}{2}\ddot{\mathbf{x}}_{i-1}\}] + (\Delta t)^2\,\mathbf{C}\,[\{\tfrac{1}{2}\dot{\mathbf{x}}_i\} + \{\tfrac{1}{2}\dot{\mathbf{x}}_{i-1}\} \\ &+ \{\beta\,(\dot{\mathbf{x}}_{i+1} - \dot{\mathbf{x}}_i)\} + \{(\tfrac{1}{2} - \beta)\,(\dot{\mathbf{x}}_i - \dot{\mathbf{x}}_{i-1})\}] \\ &+ (\Delta t)^2\,\mathbf{K}\,[\beta\,\mathbf{x}_{i+1} + (1 - 2\beta)\,\mathbf{x}_i + \beta\,\mathbf{x}_{i-1}] \\ &= (\Delta t)^2\,[\beta\,\mathbf{F}_{i+1} + (1 - 2\beta)\,\mathbf{F}_i + \beta\,\mathbf{F}_{i-1}] \end{aligned} \tag{4.45}$$

Substituting from Equation (4.41), simplifying and rearranging gives

$$[\mathbf{M} + \tfrac{1}{2}(\Delta t)\,\mathbf{C} + \beta(\Delta t)^2\,\mathbf{K}]\,\mathbf{x}_{i+1}$$
$$= (\Delta t)^2[\beta\,\mathbf{F}_{i+1} + (1 - 2\beta)\,\mathbf{F}_i + \beta\,\mathbf{F}_{i-1}]$$
$$+ [2\mathbf{M} - (\Delta t)^2(1 - 2\beta)\,\mathbf{K}]\,\mathbf{x}_i$$
$$- [\mathbf{M} - \tfrac{1}{2}(\Delta t)\,\mathbf{C} + \beta(\Delta t)^2\,\mathbf{K}]\,\mathbf{x}_{i-1} \tag{4.46}$$

Thus the displacements at time $i + 1$ can be obtained from the displacement at times i and $i - 1$. Displacement $\mathbf{x}_1$ at time Δt can be obtained by a special case of Equation (4.46) obtained from Equations (4.43), (4.44) and (4.41) as

$$[\mathbf{M}\,\tfrac{1}{2}(\Delta t)\,\mathbf{C} + \beta(\Delta t)^2\,\mathbf{K}]\,\mathbf{x}_1$$
$$= (\Delta t)^2\,\beta\,\mathbf{F}_1 + (\Delta t)^2[(\tfrac{1}{2} - \beta)\,\mathbf{I} + (\tfrac{1}{4} - \beta)\,\Delta t\,\mathbf{C}\,\mathbf{M}^{-1}]\,\mathbf{F}_0 \tag{4.47}$$

with $\mathbf{x}_0 = \dot{\mathbf{x}}_0 = \mathbf{0}$ at $t = 0$.

Comparison of Equations (4.29) and (4.47) shows that the central difference and Newmark β methods are equivalent for $\beta = 0$. It can be shown from stability analysis that the Newmark β method is unconditionally stable for $\beta > 1.4$. For $\beta > 1/4$, the stability conditions are given by the equations

$$\frac{\Delta t}{T_n} = \begin{cases} 0.318 \text{ for } \beta = 0 \\ 0.450 \text{ for } \beta = \tfrac{1}{8} \\ 0.551 \text{ for } \beta = \tfrac{1}{6} \end{cases} \tag{4.48}$$

Once the condition for stability is met for either method, the accuracy of the solution must be investigated to ensure that a sufficiently small value of Δt is used for accuracy but is yet not too small that computation time is prohibitive.

Felippa and Park (1978) present more information on these and other time step integration techniques, whereas Godeau *et al.* (1977) present some results for non-linear behaviour of a fixed offshore structure in irregular waves.

Despite the more exact solution of structural dynamics offered by a time step integration, research has continued to examine ways in which frequency domain solutions can be extended to predict the effects of the drag force non-linearity by using an iterative procedure based on minimization of mean square error (see Penzien and Tseng, 1978; and Taudin, 1978). Eatock–Taylor and Rajgopalan (1982) present a perturbation technique to examine the higher harmonics generated due to the drag force non-linearity.

References

Bathe, K. J. (1982), *Finite Element Procedures in Engineering Analysis*. Prentice Hall, Englewood Cliffs, NJ

Bathe, K. J. and Wilson, E. L. (1973), Solution methods for eigen-value problems in engineering, *International Journal for Numerical Methods in Engineering*, **6**, pp. 213–215

Eatock-Taylor, R. and Rajgopalan, A. (1982), Dynamics of offshore structures, *Journal of Sound and Vibration*, **83**, pp. 401–431

Felippa, C. A. and Park, K. C. (1978), Computational aspects of time integration procedures in structural dynamics, *Journal of Applied Mechanics*, **45**, pp. 596–611

Godeau, A. J., Deleuil, G. and Heas, J. Y. (1977), Statistical analysis of nonlinear dynamic response of fixed structures to random waves, *Proceedings of the Offshore Technology Conference*, OTC 3030

Meirovitch, L. (1986), *Elements of Vibration Analysis*. McGraw-Hill, NY

Penzien, J. and Tseng, W. S. (1978), Three dimensional dynamic analysis of fixed offshore platforms, *Numerical Methods in Offshore Engineering*, eds. O. C. Zienkiewicz, R. W. Lewis and K. G. Stagg. Wiley-Interscience, Chichester

Taudin, P. (1978), Dynamic response of flexible structures to regular waves, *Proceedings of the Offshore Technology Conference*, OTC 3160

Thomson, W. T. (1988), *Theory of Vibration with Applications*, 3rd edn. Unwin Hyman, London

Chapter 5

Semisubmersible and ship forms

5.1 Introduction

The use of semisubmersibles as offshore work platforms has developed considerably in the past two decades. There are over 120 units world wide operating primarily as exploration drilling vessels, although several semisubmersibles are now dedicated to other tasks such as diver support and fire fighting and as the surface vessels for offshore hydrocarbon production systems. Indeed, for marginal fields in deeper water, a semisubmersible based production system may be the only viable economic alternative to conventional bottom standing structures.

Semisubmersibles differ from conventional ship shape forms in several fundamental ways. The deep submergence of the main buoyancy chambers in a semisubmersible causes significant reductions in the wave induced heave, roll and pitch motions compared with those of monohull ships. The small water plane area of the deck support structure further ensures low dynamic response to heave forces. However, the largest contribution to low wave induced motion response comes from the wave force cancellation effect which arises because at a certain frequency the instantaneous upward wave force caused by the vertical columns can be cancelled out almost exactly by the downward wave force on horizontal members such as pontoons. The designer of a semisubmersible has to choose the geometry of the vessel such that wave force cancellation occurs at the most advantageous frequency in the motion response transfer function of the vessel.

The features outlined above and illustrated in Figure 5.1 make it essential that the design and evaluation of a semisubmersible vessel takes proper account of the interactions which influence wave induced motions of the structure. This is important because the down-time or workability of a semisubmersible vessel is dependent on its motion response to waves, particularly in heave. Reliable performance evaluation of a vessel in a specific wave climate depends on accurate motion response calculations.

The development of modern semisubmersible designs directed at filling an increasingly diverse range of applications is tending towards vessels which have larger columns and pontoons than their predecessors but with fewer bracing members. This is partly due to the desire to maintain structural integrity while reducing construction costs, and also due to the

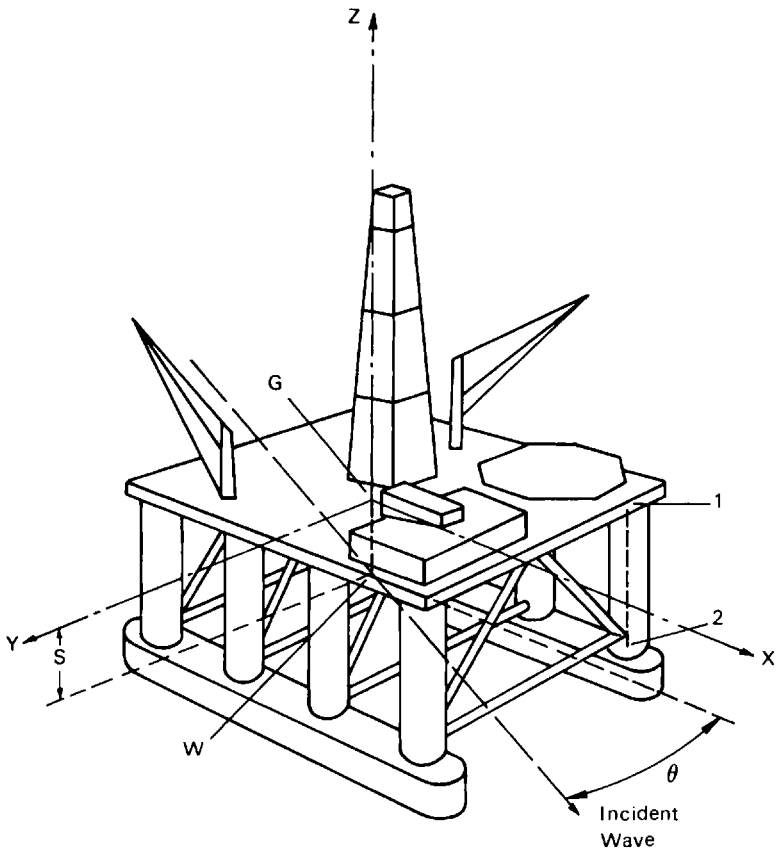

Figure 5.1. Typical semisubmersible hull and reference axes system. W is the still water level, vertically below the centre of gravity G

modern requirement for larger deck payload capabilities for such systems. Similarly, semisubmersible crane vessels are required to lift significantly heavier loads and hence must be designed with column and pontoon dimensions of sufficient size to maintain hydrostatic stability and small heel angles during lifts.

Traditionally, calculations of semisubmersible wave induced motions have been carried out using a Morison equation formulation with drag and inertia coefficients found from experiment and certifying authority rules. The assumptions and approximations associated with the use of this equation are valid for the earlier slender member rig designs, but wave diffraction effects have to be considered when calculating motions for modern, bulkier, large displacement vessels. Conversely, methods based on diffraction theory which are used to derive semisubmersible wave motion predictions do not consider drag forces on bracing members or non-linear damping effects; both phenomena significantly influence vessel motions, particularly near resonance. On the other hand, diffraction analysis will account for member interactions with incident waves and

interaction due to adjacent members, both of which are ignored by the Morison equation.

Monohull floating production systems are also becoming attractive for offshore oil floating production systems in the North Sea and offshore Brazil as well as other areas of the world. These designs have evolved from established conventional ship designs. In fact, most monohull designs for hydrocarbon production and storage are based on conventional oil product tankers. The main departures from a conventional tanker design are in the moorings, propulsion units, and in the existence of a moonpool. The propulsion units normally include thrusters in addition to stern propellers. These units improve manoeuvrability and also allow for dynamic positioning. The moorings are usually bow hawsers on turret moorings which permit weather vaning. The moonpool is an opening in the hull through which certain operations are conducted. Monohull designs traditionally take the form of a typical production tanker shown in Figure 5.2. However, recent designs to emerge include the tandem hull vessel, described further in Chapter 8.

Both semisubmersible and ship shape hull forms need to be analysed for their hydrodynamic response in waves to determine wave induced motions, survivability and operability. From a designer's view point, such analyses need to be used to arrive at the best possible hull form to yield minimum wave induced motions coupled with the maximum deck payload. The vessels must have a mooring system that will maintain station to a defined horizontal offset (expressed as a percentage of water depth) over a subsea well head. Clearly, the vessel and moorings must have sufficient structural

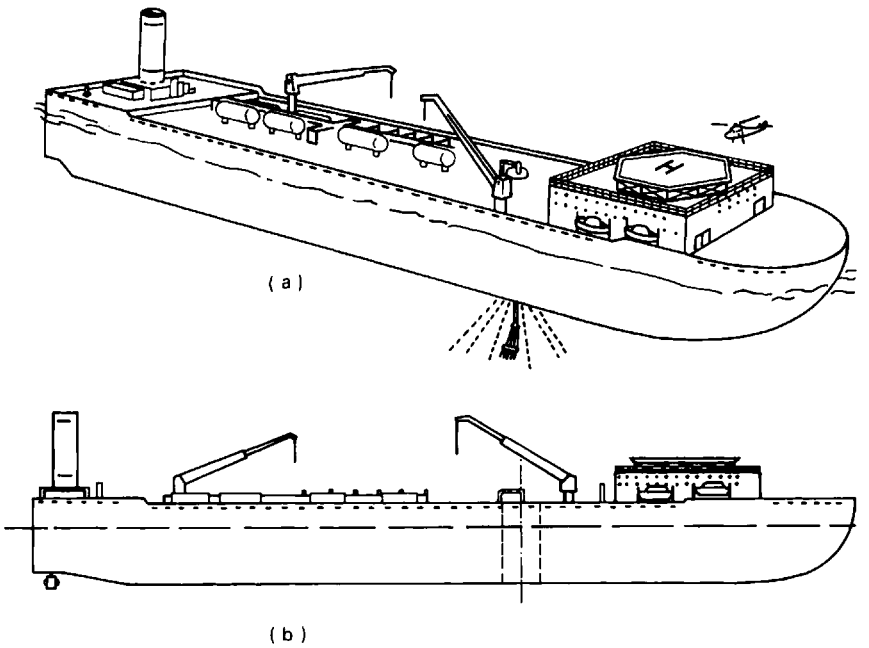

Figure 5.2. Monohull floating production system

strength and fatigue tolerance to survive extreme storms and to have acceptably long service lives.

The above requirements are substantial and only achievable by accepting design compromises which improve one aspect of the design at the expense of others.

This chapter is concerned with the hydrodynamic analysis methods used to determine the wave induced motion responses of conventional semisubmersible and ship shape hull forms. For semisubmersibles with very slender members a Morison equation based formulation is used to calculate motions in all six degrees of freedom. However, modern semisubmersibles with more massive columns and pontoons need to be analysed using diffraction theory, as do all ship shape hull forms. The basic methodology for hydrodynamic analysis of these more massive hull forms using diffraction theory is also presented.

The second half of the chapter is concerned with two specific design issues. These are the viscous damping of roll motions of a monohull and considerations of vessel operability. Monohull vessels tend to exhibit a high level of viscous damping of roll motions which cannot be predicted by diffraction theory with its inviscid, irrotational flow assumptions. Methods for determining the corrections to inviscid, irrotational theory predictions due to viscous damping are presented in Section 5.4. Furthermore, the ultimate aim of the analysis methods given in this chapter is to provide calculation methods for vessel design – principally aimed at achieving a high level of operability (low down-time) due to wave induced motions for vessels working in the oceans. Section 5.5 gives calculations for operability based on motions and for structural fatigue at typical offshore locations.

5.2 Morison equation based analysis

Several research investigations related to predictions of semisubmersible wave induced motions using the Morison equation have been reported in the technical literature over the last two decades. Some of these (Burke, 1969; Ochi and Vuolo, 1971; and Hooft, 1971) have been concerned with developing the hydrodynamics of motion response calculations and validating these against model scale experimental data. Oo and Miller (1977) employ such a computation to survey the wave induced heave motion response of a variety of semisubmersible hull configurations. These basic hydrodynamic motion response calculations have also been extended to consideration of the applied loads, strength analysis and structure dynamics of the vessel hull configuration by researchers such as Pedersen *et al.* (1974), Pincemin *et al.* (1974), van Opstal *et al.* (1974) and Paulling (1974). On the other hand, Natvig and Pendered (1977) present a more sophisticated approach to the hydrodynamic motion response computations. A linearized solution of the equations of motion in the frequency domain is compared with a time domain computation incorporating several sources of non-linearity. The two techniques agree quite well and confirm the validity of the linearization process which assumes equal energy dissipation at resonance to deduce an equivalent linear damping.

Consider a semisubmersible hull form of the type shown in Figure 5.1 with the cylindrical columns and bracing and the rectangular pontoon being of small diameter in relation to the vessel's overall length and also in relation to the wave length of incident gravity waves. Figure 5.1 shows the reference axis system used in the calculations. The *Gxz* axes are taken in the vessel's fore and aft vertical plane of symmetry, with the centre of gravity taken as the origin and the *Gz* axis vertically upwards. For vessels with lateral symmetry about the *Gxz* plane, these correspond to principal axes. The structure data required by the computation includes the total platform displacement, the radii of gyration in roll, pitch and yaw and the centre of gravity position. The hull configuration is idealized into individual members (such as member 1–2 in Figure 5.1) described by their member type (circular cylinder, rectangular cylinder or non-elongated member), and co-ordinates (of points 1 and 2 relative to reference axes *Gxyz*), cross-sectional dimensions and relevant drag and inertia coefficients.

A routine hydrostatics calculation is performed as a prelude to the dynamic calculation – see Chapter 3 for details. The vessel structure description is used to compute the contributions of water plane area, displaced volume, centre of buoyancy and second moments of water plane area for each of the members in the structure. This information is used, together with an assumed draught, to compute the buoyancy force on the structure. If this buoyancy force differs from the required displacement, the draught is adjusted accordingly and the buoyancy force recomputed. This procedure is repeated until the vessel's weight equals the buoyancy force. The draught value obtained from the above calculation is then used to determine the structure's overall centre of buoyancy position, the metacentric heights in roll and pitch and the z co-ordinate ($= s$) in Figure 5.1, of the water surface relative to the origin at the centre of gravity.

From first principles, the semisubmersible vessel equation for rigid body motions in six degrees of freedom can be written as

$$\mathbf{M}\,\ddot{\mathbf{X}} = \Sigma\mathbf{M}_A(\ddot{\boldsymbol{\eta}} - \ddot{\mathbf{X}}) + \Sigma\mathbf{M}_{FK}\,\ddot{\boldsymbol{\eta}} + \Sigma\mathbf{B}\,|\,\dot{\boldsymbol{\eta}} - \dot{\mathbf{X}}\,|\,(\dot{\boldsymbol{\eta}} - \dot{\mathbf{X}}) - \mathbf{K}\,\mathbf{X} - \mathbf{K}_m\mathbf{X} \tag{5.1}$$

where $\mathbf{X}$, $\dot{\mathbf{X}}$ and $\ddot{\mathbf{X}}$ are the six component column vectors of displacement, velocity and acceleration in surge, sway, heave, roll, pitch and yaw respectively; $\mathbf{M}$, $\mathbf{M}_A$ and $\mathbf{M}_{FK}$ are the (6×6) matrices of structure physical mass, added mass and the Krylov added inertia respectively; $\mathbf{B}$ is a (6×6) matrix representing non-linear drag force contribution; $\mathbf{K}$ and $\mathbf{K}_m$ are the semisubmersible (6×6) stiffness matrices contributed by the hydrostatic and mooring restoring forces respectively. The mooring stiffness can be provided by a catenary system (described further by Patel, 1989) or by taut tethers, as described in Chapter 6.

The wave particle velocities and accelerations are denoted by vectors $\dot{\boldsymbol{\eta}}$ and $\ddot{\boldsymbol{\eta}}$, respectively, with the summation signs in the wave force terms indicating a numerical integration over the submerged members to take account of spatial variations in wave properties. The small contribution of a potential damping term due to wave diffraction effects is neglected in the analysis for vessels with very slender members.

Equation (5.1) incorporates the Morison equation for wave loading on slender cylinders (see Morison *et al.*, 1950). The first term is the added inertia due to relative accleration between the fluid and vessel, whereas the second term is the contribution of the fluid acceleration induced pressures acting on vessel members. This latter force is called the undisturbed pressure force or the Froude–Krylov force. The third term on the right hand side of Equation (5.1) is the drag force in the Morison equation which is proportional to the square of the relative velocity between fluid and vessel with a modulus sign to ensure reversal of force with reversal of velocity.

Equation (5.1) can be rewritten to give

$$(\mathbf{M} + \mathbf{M}_A)\ddot{\mathbf{X}} + \mathbf{B} \mid \dot{\mathbf{X}} \mid \dot{\mathbf{X}} + (\mathbf{K} + \mathbf{K}_m)\mathbf{X}$$
$$= \Sigma(\mathbf{M}_A + \mathbf{M}_{FK})\ddot{\boldsymbol{\eta}} + \Sigma\mathbf{B} \mid \dot{\boldsymbol{\eta}} - \dot{\mathbf{X}} \mid (\dot{\boldsymbol{\eta}} - \dot{\mathbf{X}}) + \mathbf{B} \mid \dot{\mathbf{X}} \mid \dot{\mathbf{X}} \tag{5.2}$$

with a $\mathbf{B} \mid \dot{\mathbf{X}} \mid \dot{\mathbf{X}}$ term added to both sides of the equation to obtain a conventional form for the left hand side. Equation (5.2) would be difficult to solve in its present form due to the presence of $\mathbf{X}$ in the wave force on the right hand side of the equation. However, two features of this wave force expression suggest a useful simplification. These are concerned with the relatively large magnitude of the $\Sigma\mathbf{M}_{FK}\ddot{\boldsymbol{\eta}}$ term in the wave force and the decay with depth of wave particle velocities which makes the $\Sigma\mathbf{B} \mid \dot{\boldsymbol{\eta}} - \dot{\mathbf{X}} \mid (\dot{\boldsymbol{\eta}} - \dot{\mathbf{X}}) + \mathbf{B} \mid \dot{\mathbf{X}} \mid \dot{\mathbf{X}}$ term small for members with significant submergence below still water level. It should be pointed out that this approximation was first used by Tasai *et al.* (1970) for a single degree of freedom system. A similar formulation to that presented below has also been repeated by Matsushima *et al.* (1982).

With these approximations in mind, Equation (5.2) can be simplified to

$$(\mathbf{M} + \mathbf{M}_A)\ddot{\mathbf{X}} + \mathbf{B} \mid \dot{\mathbf{X}} \mid \dot{\mathbf{X}} + (\mathbf{K} + \mathbf{K}_m)\mathbf{X}$$
$$= \Sigma(\mathbf{M}_A + \mathbf{M}_{FK})\ddot{\boldsymbol{\eta}} + \Sigma\mathbf{B} \mid \dot{\boldsymbol{\eta}} \mid \dot{\boldsymbol{\eta}} \tag{5.3}$$

with the $\Sigma\mathbf{B} \mid \boldsymbol{\eta} - \mathbf{X} \mid (\boldsymbol{\eta} - \mathbf{X}) + \mathbf{B} \mid \dot{\mathbf{X}} \mid \mathbf{X}$ term replaced by a $\Sigma\mathbf{B} \mid \dot{\boldsymbol{\eta}} \mid \dot{\boldsymbol{\eta}}$ term. In order to explore the effects of this simplification, a residue wave force fraction, R, for a particular motion (heave, say) can be defined as

$$R = \frac{\mid \Sigma\mathbf{B} \mid \dot{\boldsymbol{\eta}}\,\dot{\mathbf{X}} \mid (\dot{\boldsymbol{\eta}} - \dot{\mathbf{X}}) + \mathbf{B} \mid \dot{\mathbf{X}} \mid \dot{\mathbf{X}} - \Sigma\mathbf{B} \mid \dot{\boldsymbol{\eta}} \mid \dot{\boldsymbol{\eta}} \mid}{(K'H/2)} \tag{5.4}$$

The residue force is non-dimensionalized with respect to the wave force amplitude at zero frequency by using the hydrostatic stiffness, K', in the mode of motion being considered and the wave height, H.

Results presented later demonstrate that, after drag force linearization, the residue wave force that remains unaccounted for due to the simplification is negligible at wave frequencies even for large wave heights where the drag forces will be greater. The drag force linearization used here is based on the well-known technique of specifying equal energy dissipation at resonance between the non-linear damping forces and their equivalent linear values – see Chapter 4 for further details. However, it should be pointed out that this linearization is a fundamentally different assumption

from that implied in the reformulation of Equation (5.1) into (5.3) which is quantified by residue factor R.

The assumptions used in the equation formulation and solution are formally stated below:

1. The semisubmersible vessel structure is assumed to be an assembly of cylindrical elements, horizontal rectangular pontoons and non-elongated members. The cylindrical members and rectangular pontoons are assumed to have small ratios of cross-sectional dimension to length. The non-elongated elements are assumed to have comparable dimensions in three orthogonal directions, all these dimensions being small when compared to incident wavelengths.
2. The motion amplitudes of the platform and waves are assumed to be small. As a consequence linear wave theory is used.
3. Wave forces on individual elements of the structure are computed as though other members were not present, that is, hydrodynamic interference between members is ignored.
4. The forces associated with sinusoidal wave motions are computed independently of the forces associated with absolute motions of the structure.
5. The non-linear drag damping term is linearized by assuming an effective linear damping which would dissipate the same energy at resonance as the non-linear damping. The contribution of wave radiation effects to the damping terms is assumed to be negligibly small.

We turn now to evaluating the coefficient matrices in Equation (5.3) prior to its solution.

Since the reference axes chosen are principal axes, the physical mass matrix, **M**, is diagonal. The total hydrodynamic added mass of the semisubmersible hull is computed as a sum of the added masses of each individual submerged or partly submerged structural member. Since the structure is assumed to be a collection of circular cylinders, rectangular cylinders and non-elongated members, the added mass for each element type needs to be evaluated separately.

The general added mass matrix of a circular cylinder with arbitrary end co-ordinates can be calculated by assuming that only the components of acceleration normal to the cylinder axis are significant. Thus, given the cylinder end co-ordinates, diameter and applicable normal flow added mass coefficient, a generalized added mass matrix for the cylinder can be readily evaluated.

Consider an arbitrary cylinder, FG, in a system of Cartesian co-ordinates, as shown in Figure 5.3. The point F has co-ordinates (x_1, y_1, z_1) and G has co-ordinates (x_2, y_2, z_2). The cylinder has a diameter d with an added mass coefficient of C_m for flow normal to the cylinder axis. Thus the cylinder length and direction cosines are given by

$$\left.\begin{aligned} L &= \sqrt{\{(x_2 - x_1)^2 + (y_2 - y_1)^2 + (z_2 - z_1)^2\}} \\ \cos\alpha &= \frac{x_2 - x_1}{L},\ \cos\beta = \frac{y_2 - y_1}{L},\ \cos\gamma = \frac{z_2 - z_1}{L} \end{aligned}\right\} \tag{5.5}$$

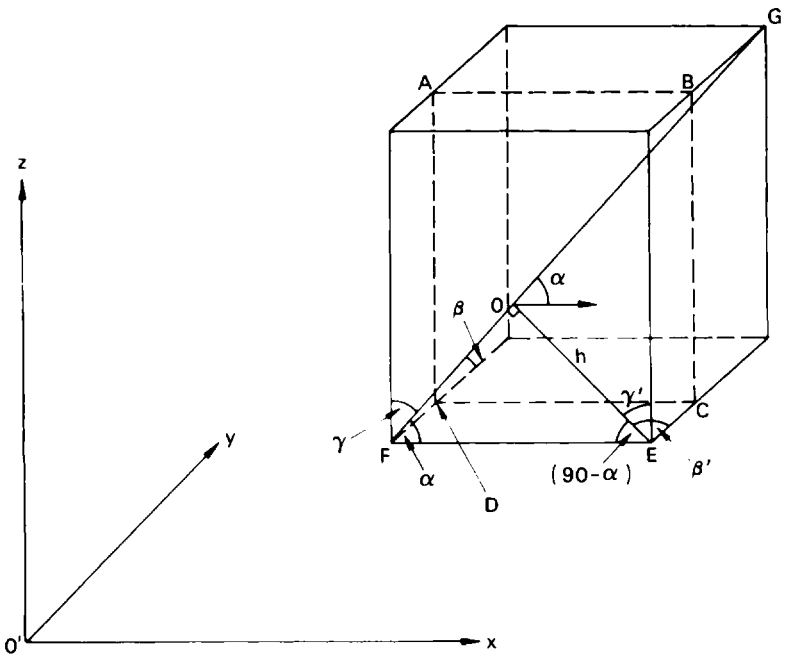

Figure 5.3. Definition diagram for added mass of a circular cylinder

Now a unit acceleration parallel to the x axis will yield acceleration components parallel and perpendicular to the cylinder axis. Only the acceleration component perpendicular to the cylinder axis will have a significant added mass force. The components of this normal flow added mass force in the three co-ordinate directions and the moments of this force about Ox, Oy, Oz make up the first (left hand) column of the added mass matrix. Note that added mass equals added mass force for unit acceleration.

Thus for unit acceleration parallel to Ox, the component perpendicular to the cylinder axis is $\sin\alpha$ and the resultant added mass force in this direction is $k_1 \sin\alpha$ where $k_1 = \rho C_m \pi d^2 L/4$. Then the component force $k_1 \sin\alpha$ in the x direction is $k_1 \sin^2\alpha$ and the component of $k_1 \sin\alpha$ in the y direction is

$$\left.\begin{aligned} &(k_1 \sin\alpha)\cos\beta' = k_1 \sin\alpha(-\cot\alpha \cos\beta) = -k_1 \cos\alpha \cos\beta \\ &\text{and in the } z \text{ direction is} \\ &(k_1 \sin\alpha)\cos\gamma' = k_1 \sin\alpha(-\cot\alpha \cos\gamma) = -k_1 \cos\alpha \cos\gamma \end{aligned}\right\} \quad (5.6)$$

The angles β' and γ' are defined in Figure 5.3 and are related to angles β and γ through the equations

$$OF = h \cot\alpha$$

$$DF = CE = h \cot\alpha \cos\beta$$

$$\cos\beta' = -\cot\alpha \cos\beta$$

$$\cos\gamma' = -\cot\alpha \cos\gamma$$

Thus the added masses due to linear accelerations parallel to the x, y and z axes are

$$m_{ij} = \begin{bmatrix} k_1\sin^2\alpha & -k_1 \cos\alpha \cos\beta & -k_1 \cos\alpha \cos\gamma \\ -k_1\cos\alpha \cos\beta & k_1\sin^2\beta & -k_1 \cos\beta \cos\gamma \\ -k_1 \cos\alpha \cos\gamma & -k_1 \cos\beta \cos\gamma & k_1 \sin^2 \gamma \end{bmatrix} \tag{5.7}$$

The matrix components m_{ij} for $i = 4$ to 6 and $j = 1$ to 3 consist of added mass force induced moments about Ox, Oy, Oz due to linear accelerations along the x, y and z axes. These moments are computed by integrating the moments due to added mass forces along the cylinder length. Note that the above matrix (Equation (5.7)) is symmetric.

Unit acceleration parallel to Ox results in forces

$$\frac{m_{11}\,\mathrm{d}l}{L}, \frac{m_{21}\,\mathrm{d}l}{L}, \frac{m_{31}\,\mathrm{d}l}{L}$$

in the x, y and z directions, respectively, on a cylinder element of length $\mathrm{d}l$. The total moment of the forces about the x axis is

$$m_{41} = \frac{m_{31}}{L}\int_0^L y\,\mathrm{d}l - \frac{m_{21}}{L}\int_0^L z\,\mathrm{d}l$$

But

$$\frac{1}{L}\int_0^L y\,\mathrm{d}l = \frac{y_1 + y_2}{2} = y_\mathrm{m}$$

and

$$\frac{1}{L}\int_0^L z\,\mathrm{d}l = \frac{z_1 + z_2}{2} = z_\mathrm{m} \tag{5.8}$$

for

$$y = y_1 + \frac{y_2 - y_1}{L}\,l$$

and

$$z = z_1 + \frac{z_2 - z_1}{L}\,l$$

Thus

$$m_{41} = m_{31}\,y_\mathrm{m} - m_{21}\,z_\mathrm{m}$$

Similarly,

$$\left.\begin{aligned} m_{51} &= m_{11}\, z_m - m_{31}\, x_m \\ m_{61} &= m_{21}\, x_m - m_{11}\, y_m \\ m_{42} &= m_{32}\, y_m - m_{22}\, z_m \\ m_{52} &= m_{12}\, z_m - m_{32}\, x_m \\ m_{62} &= m_{22}\, x_m - m_{12}\, y_m \\ m_{43} &= m_{33}\, y_m - m_{32}\, z_m \\ m_{53} &= m_{31}\, z_m - m_{33}\, x_m \\ m_{63} &= m_{32}\, x_m - m_{31}\, y_m \end{aligned}\right\} \quad (5.9)$$

Now m_{ij} for $i = 1$ to 6 and $j = 4$ to 6 are added mass matrix terms due to angular accelerations about the Ox, Oy and Oz axes. In the same way as before, for unit angular accelerations about Ox, the linear accelerations of element P with co-ordinates (x, y, x) are 0, $-z$ and $+y$ along the Ox, Oy and Oz axes respectively.

Then the added mass force components on an element of length dl due to the acceleration of $-z$ are

$$-m_{12}\, z\mathrm{d}l/L,\ -m_{22} z\mathrm{d}l/L,\ -m_{32} z\mathrm{d}l/L$$

parallel to the Ox, Oy and Oz directions, and the force components due to acceleration y are

$$m_{13} y\mathrm{d}l/L,\ m_{23} y\mathrm{d}l/L,\ m_{33} y\mathrm{d}l/L.$$

The integrated sum of these forces along the Ox, Oy and Oz axis will give terms m_{14}, m_{24}, m_{34} which are identical to the m_{41}, terms given by Equations (5.9) above – thus confirming the matrix symmetry.

Also the summed moment of these forces about the x axis gives

$$\begin{aligned} m_{44} &= -\int_0^L -\frac{m_{22} z^2}{L}\,\mathrm{d}l - \int_0^L \frac{m_{23}\, yz}{L}\,\mathrm{d}l \\ &\quad + \int_0^L -\frac{m_{32}\, zy}{L}\,\mathrm{d}l + \int_0^L \frac{m_{33}\, y^2}{L}\,\mathrm{d}l \\ &= m_{22}\int_0^L \frac{z^2}{L}\,\mathrm{d}l - 2\, m_{23}\int_0^L \frac{yz}{L}\,\mathrm{d}l + m_{33}\int_0^L \frac{y^2}{L}\,\mathrm{d}l \end{aligned}$$

Now

$$\left.\begin{aligned} \frac{1}{L}\int_0^L y^2\,\mathrm{d}l &= y_n = \tfrac{1}{3}\,(y_1^2 + y_1 y_2 + y_2^2) \\ \frac{1}{L}\int_0^L z^2\,\mathrm{d}l &= z_n = \tfrac{1}{3}\,(z_1^2 + z_1 z_2 + z_2^2) \end{aligned}\right\} \quad (5.10)$$

and

$$\frac{1}{L}\int_0^L yz\,\mathrm{d}l = (yz)_n = \tfrac{1}{6}\,[2y_1z_1 + 2y_2z_2 + y_1z_2 + z_1y_2]$$

using the functions of y and z given in Equation (5.8). Then

$$m_{44} = m_{22}\,z_n - 2m_{23}\,(yz)_n + m_{33}\,y_n \tag{5.11}$$

Taking moments about the Oy and Oz axes also yields

$$\left.\begin{aligned} m_{54} &= -m_{21}\,z_n - m_{33}\,(xy)_n + m_{31}(yz)_n + m_{32}(zx)_n \\ &\text{and} \\ m_{64} &= -m_{31}\,y_n + m_{32}(xy)_n + m_{21}(yz)_n - m_{22}(zx)_n \end{aligned}\right\} \tag{5.12}$$

where

$$\left.\begin{aligned} (xy)_n &= \tfrac{1}{6}\,(2x_1y_1 + 2x_2y_2 + x_1y_2 + x_2y_1) \\ &\text{and} \\ (zx)_n &= \tfrac{1}{6}\,(2z_1x_1 + 2z_2x_2 + z_1x_2 + z_2x_1) \end{aligned}\right\} \tag{5.13}$$

Repeating the process of imposing unit angular accelerations about the Oy and Oz axes yields the remaining results of

$$\left.\begin{aligned} m_{55} &= m_{33}x_n - 2m_{31}(zx)_n + m_{11}\,z_n \\ m_{66} &= m_{11}y_n - 2m_{21}(xy)_n + m_{22}\,x_n \\ m_{65} &= -m_{32}x_n - m_{11}\,(yz)_n + m_{21}\,(zx)_n + m_{31}(xy)_n \end{aligned}\right\} \tag{5.14}$$

where

$$x_n = \tfrac{1}{3}\,(x_1^2 + x_1x_2 + x_2^2) \tag{5.15}$$

with the remaining terms known from matrix symmetry.

A simplified form of the added mass matrix can be obtained for a non-elongated body. The derivation given below applies for an arbitrary non-elongated body that has different added mass forces for acceleration components parallel to the three reference axes directions. For a non-elongated body in a reference system $Oxyz$, the first three diagonal terms of the added mass matrix can be written as

$$\left.\begin{aligned} m_{11} &= \rho\,C_{m1}\,V \\ m_{22} &= \rho\,C_{m2}\,V \\ m_{33} &= \rho\,C_{m3}\,V \end{aligned}\right\} \tag{5.16}$$

where ρ is fluid density, V is the body volume and C_{m1}, C_{m2} and C_{m3} are added mass coefficients for body accelerations parallel to the Ox, Oy and Oz axes respectively. For a spherical body of radius a, however,

$$V = \tfrac{4}{3}\,\pi\,a^3 \text{ and } C_{m1} = C_{m2} = C_{m3} = 0.5$$

The remaining terms of the added mass matrix are obtained by calculating the acceleration reaction forces due to unit linear and angular acceleration

along the reference axes. For a body with centre of volume (x_1, y_1, z_1), this yields

$$\left.\begin{aligned}
m_{12} &= m_{13} = m_{23} = 0 \\
m_{14} &= m_{25} = m_{36} = 0 \\
m_{15} &= m_{11}z_1,\ m_{16} = -m_{11}y_1 \\
m_{24} &= -m_{22}z_1,\ m_{26} = m_{22}x_1 \\
m_{34} &= m_{33}y_1,\ m_{35} = -m_{33}x_1 \\
m_{44} &= m_{22}z_1^2 + m_{33}y_1^2 \\
m_{55} &= m_{33}x_1^2 + m_{11}z_1^2 \\
m_{66} &= m_{11}y_1^2 + m_{22}x_1^2 \\
m_{45} &= -m_{33}\,x_1y_1 \\
m_{46} &= -m_{22}\,x_1z_1 \\
m_{56} &= -m_{11}\,y_1z_1
\end{aligned}\right\} \qquad (5.17)$$

A special case of the above derivation is used to obtain the hydrodynamic added mass matrix for horizontal rectangular pontoons.

The fluid damping matrix, **B**, for the structure is evaluated in a similar manner to the added mass matrix – as a sum of the contributions from each individual member. The derivation of the generalized damping matrix for an arbitrarily oriented circular cylinder depends on the assumption that only drag forces normal to the cylinder axis are significant. Unlike the added mass matrix, the non-linear velocity square proportionality generates an asymmetric damping matrix. Only the results of the damping matrix for circular cylinders and non-elongated members are presented here for brevity.

The damping matrix relates the velocity square dependent drag force on an immersed circular cylinder to the fluid–structure relative velocity vector. An equation of the form

$$F_i' = b_{ij} \mid \dot{x}_j \mid \dot{x}_j \qquad (5.18)$$

describes the relation. The column vector $\dot{x}_j$ of surge, sway and heave velocity and angular velocities about these axes appear as individual vector element square terms. The modulus sign exists to ensure that negative velocity corresponds to a negative drag force. The notation is identical to that used before, with b_{ij} being the (6×6) damping coefficient matrix. The velocity squared non-linearity generates a non-symmetric matrix where all 36 elements need to be evaluated.

For a circular cylinder at an arbitrary orientation, taking an effective drag coefficient of C_D for flow normal to the cylinder axis, a constant k_3 given by

$$k_3 = \tfrac{1}{2}\,\rho\, C_D L d \qquad (5.19)$$

and other notation as above; it can be shown that

$$\left.\begin{aligned}
b_{11} &= k_3 \mid \sin^3\alpha \mid \\
b_{21} &= -k_3 \cos\alpha \cos\beta \mid \sin\alpha \mid \\
b_{31} &= -k_3 \cos\gamma \cos\alpha \mid \sin\alpha \mid \\
b_{12} &= -k_3 \cos\alpha \cos\beta \mid \sin\beta \mid \\
b_{22} &= k_3 \mid \sin^3\beta \mid \\
b_{32} &= -k_3 \cos\beta \cos\gamma \mid \sin\beta \mid \\
b_{13} &= -k_3 \cos\alpha \cos\gamma \mid \sin\gamma \mid \\
b_{23} &= -k_3 \cos\beta \cos\gamma \mid \sin\gamma \mid \\
b_{33} &= k_3 \mid \sin^3\gamma \mid \\
b_{41} &= b_{31}\, y_m - b_{21} z_m \\
b_{51} &= b_{11}\, z_m - b_{31}\, x_m \\
b_{61} &= b_{21}\, x_m - b_{11}\, y_m \\
b_{42} &= b_{32}\, y_m - b_{22}\, z_m \\
b_{52} &= b_{12}\, z_m - b_{32}\, x_m \\
b_{62} &= b_{22}\, x_m - b_{12}\, y_m \\
b_{43} &= b_{33}\, y_m - b_{23}\, z_m \\
b_{53} &= b_{13}\, z_m - b_{33}\, x_m \\
b_{63} &= b_{23}\, x_m - b_{13}\, y_m
\end{aligned}\right\} \quad (5.20)$$

A set of further expressions have to be defined for the remaining terms. Now

$$\left.\begin{aligned}
x_p &= \mathrm{sgn}(x_m)(x_1^2 + x_1x_2 + x_2^2)/3 \qquad \text{for } x_1x_2 \geqslant 0 \\
&\text{and} \\
x_p &= \frac{\mathrm{sgn}(x_2)(x_1^3 + x_2^3)}{3(x_2 - x_1)} \qquad \text{for } x_1x_2 < 0
\end{aligned}\right\} \quad (5.21)$$

where $\mathrm{sgn}(x_2)$ is a function which returns the sign of x_2 multiplied by 1. Similarly,

$$\left.\begin{aligned}
y_p &= \mathrm{sgn}(y_m)(y_1^2 + y_1y_2 + y_2^2)/3 \qquad \text{for } y_1y_2 \geqslant 0 \\
y_p &= \frac{\mathrm{sgn}(y_2)(y_1^3 + y_2^3)}{3(y_2 - y_1)} \qquad \text{for } x_1x_2 < 0 \\
&\text{and} \\
z_p &= \mathrm{sgn}(z_m)(z_1^2 + z_1z_2 + z_2^2)/3 \qquad \text{for } x_1x_2 \geqslant 0 \\
z_p &= \frac{\mathrm{sgn}(z_2)(z_1^3 + z_2^3)}{3(z_2 - z_1)} \qquad \text{for } z_1z_2 < 0
\end{aligned}\right\} \quad (5.22)$$

The numerical problems associated with $(x_2 - x_1)$, $(y_2 - y_1)$, or $(z_2 - z_1)$ being equal to zero is eliminated by adding an offset to one co-ordinate if a zero is detected.

Also,

$$\left.\begin{aligned}
I_x &= \operatorname{sgn}(x_m)(x_1^3 + x_1^2x_2 + x_1x_2^2 + x_2^3)/4 \qquad \text{for } x_1x_2 \geqslant 0 \\
I_x &= \operatorname{sgn}(x_2)\frac{(x_1^3 + x_1^2x_2 + x_1x_2^2 + x_2^3)}{4} + \frac{x_1^4}{2(x_2 - x_1)} \qquad \text{for } x_1x_2 < 0 \\
I_y &= \operatorname{sgn}(y_1^3 + y_1^2y_2 + y_1y_2^2 + y_2^3)/4 \qquad \text{for } y_1y_2 \geqslant 0 \\
I_y &= \operatorname{sgn}(y_2)\frac{(y_1^3 + y_1^2y_2 + y_1y_2^2 + y_2^3)}{4} + \frac{y_1^4}{2(y_2 - y_1)} \qquad \text{for } y_1y_2 < 0 \\
I_z &= \operatorname{sgn}(z_m)(z_1^3 + z_1^2z_2 + z_1z_2^2 + z_2^3)/4 \qquad \text{for } z_1z_2 \geqslant 0 \\
I_z &= \operatorname{sgn}(z_2)\frac{(z_1^3 + z_1^2z_2 + z_1z_2^2 + z_2^3)}{4} + \frac{z_1^4}{2(z_2 - z_1)} \qquad \text{for } z_1z_2 < 0
\end{aligned}\right\} \quad (5.23)$$

The description of a number of other terms is simplified if variables q and r can each denote either x, y or z. Thus, the expression

$$I_{qr\,|\,r\,|} = \tfrac{1}{12}\,[q_2(r_1^2 + 2r_1r_2 + 3r_2^2) + q_1(3r_1^2 + 2r_1r_2 + r_2^2)] \text{ if } r_1r_2 \geqslant 0 \quad (5.24)$$

$$= \tfrac{1}{12}\,q_2(r_1^2 + 2r_1r_2 + 3r_2^2) + q_1(3r_1^2 + 2r_1r_2 + r_2^2) + \frac{r_1^3(4q_1r_2 - 3q_1r_1 - q_2r_1)}{6(r_2 - r_1)^2} \qquad \text{if } r_1r_2 < 0 \quad (5.24)$$

can be used to create values for terms such as $I_{zx\,|\,x\,|}$ if $z_1 = q_1$, $z_2 = q_2$, $x_1 = r_1$ and $x_2 = r_2$.

Then, the remaining coefficients in the matrix are

$$\left.\begin{aligned}
b_{14} &= -b_{12}\,z_n + b_{14}\,y_n \\
b_{24} &= -b_{22}\,z_n + b_{23}\,y_n \\
b_{34} &= -b_{32}\,z_n + b_{33}\,y_n \\
b_{44} &= b_{33}\,I_y - b_{32}\,I_{yz\,|\,z\,|} - b_{23}\,I_{yz\,|\,y\,|} + b_{22}\,I_z \\
b_{54} &= b_{13}\,I_{yz\,|\,y\,|} - b_{12}\,I_z - b_{33}\,I_{xy\,|\,y\,|} + b_{32}\,I_{zx\,|\,z\,|} \\
b_{64} &= b_{23}\,I_{xy\,|\,y\,|} - b_{22}\,I_{zx\,|\,z\,|} - b_{13}\,I_y + b_{12}\,I_{yz\,|\,z\,|} \\
b_{15} &= b_{11}\,z_n - b_{13}\,x_n \\
b_{25} &= b_{21}\,z_n - b_{23}\,x_n \\
b_{35} &= b_{31}\,z_n - b_{33}\,x_n \\
b_{45} &= b_{31}\,I_{zy\,|\,z\,|} - b_{33}\,I_{xy\,|\,x\,|} - b_{21}\,I_z + b_{23}\,I_{zx\,|\,x\,|} \\
b_{55} &= b_{11}\,I_z - b_{13}\,I_{zx\,|\,x\,|} - b_{31}\,I_{zx\,|\,z\,|} + b_{33}\,I_x \\
b_{65} &= b_{21}\,I_{zx\,|\,z\,|} - b_{23}\,I_x - b_{11}\,I_{yz\,|\,z\,|} + b_{13}\,I_{xy\,|\,x\,|}
\end{aligned}\right\} \quad (5.25)$$

$$
\left.
\begin{aligned}
b_{16} &= b_{12}\,x_n - b_{11}\,y_n \\
b_{26} &= b_{22}\,x_n - b_{21}\,y_n \\
b_{36} &= b_{32}\,x_n - b_{31}\,y_n \\
b_{46} &= b_{32}\,I_{xy\,|\,x\,|} - b_{31}\,I_y - b_{22}\,I_{zx\,|\,x\,|} + b_{21}\,I_{yz\,|\,y\,|} \\
b_{56} &= b_{12}\,I_{zx\,|\,x\,|} - b_{11}\,I_{yz\,|\,y\,|} - b_{32}\,I_x + b_{31}\,I_{xy\,|\,y\,|} \\
b_{66} &= b_{22}\,I_x - b_{21}\,I_{xy\,|\,y\,|} - b_{12}\,I_{xy\,|\,x\,|} + b_{11}\,I_y
\end{aligned}
\right\}
$$

The corresponding matrices for the rectangular cylinder and non-elongated body are evaluated as special cases of the circular cylinder. Results are presented here for a non-elongated body with faces parallel to the Oxy, Oxz, Oyz planes. Taking the co-ordinates (x_1, y_1, z_1) as the centre of volume of the body; and p', q' and r' as equivalent rectangular body dimensions in the x, y and z directions gives

$$
\left.
\begin{aligned}
b_{11} &= \tfrac{1}{2}\,\rho\,C_{dx}\,q'r' \quad b_{22} = \tfrac{1}{2}\,\rho\,C_{dy}\,p'r' \\
b_{33} &= \tfrac{1}{2}\,\rho\,C_{dz}\,p'r' \\
b_{21} &= b_{31} = b_{12} = b_{32} = b_{13} = b_{23} = 0 \\
b_{51} &= b_{11}\,z_1 \quad b_{61} = -b_{11}\,y_1 \\
b_{42} &= -b_{22}\,z_1 \quad b_{62} = b_{22}\,x_1 \\
b_{43} &= b_{33}\,y_1 \quad b_{53} = -b_{33}\,x_1 \\
b_{41} &= b_{52} = b_{63} = 0 \\
b_{24} &= -b_{22}\,z\,|\,z_1\,| \quad b_{34} = b_{33}\,y_1\,|\,y_1\,| \\
b_{44} &= b_{33}\,|\,y_1\,|^3 + b_{22}\,|\,z_1\,|^3 + b_{22}\,|\,z_1\,|^3 \\
b_{54} &= -b_{33}\,x_1\,y_1\,|\,y_1\,| \\
b_{64} &= -b_{22}\,x_1\,z_1\,|\,z_1\,| \\
b_{15} &= b_{11}\,z_1\,|\,z_1\,| \quad b_{35} = -b_{33}\,x_1\,|\,x_1\,| \\
b_{45} &= -b_{33}\,yx\,|\,x\,| \\
b_{55} &= b_{11}\,|\,z_1\,|^3 + b_{33}\,|\,x_1\,|^3 \\
b_{65} &= -b_{11}\,y_1 z_1\,|\,z_1\,| \\
b_{16} &= -b_{11}\,y_1 \quad b_{26} = b_{22}\,x_1 \\
b_{46} &= -b_{22}\,z_1 x_1\,|\,x_1\,| \\
b_{56} &= -b_{11}\,z_1 y_1\,|\,y_1\,| \\
b_{66} &= b_{11}\,|\,y_1\,|^3 + b_{22}\,|\,x_1\,|^3 \\
b_{14} &= b_{25} = b_{36} = 0
\end{aligned}
\right\} \qquad (5.26)
$$

Contributions to the hydrostatic stiffness matrix **K**, will only arise in the heave, roll and pitch degrees of freedom due to buoyancy forces in the water plane cutting members of the hull. If, for member number, n, A_{wn} denotes the water plane area, (x_w, y_w) are the co-ordinates of this water

plane area centroid, then the stiffness elements k_{ij} can be written as the summations

$$\begin{aligned} k_{33} &= \rho g \Sigma A_{wn} \\ k_{43} &= \rho g \Sigma y_w A_{wn} \\ k_{53} &= -\rho g \Sigma x_w A_{wn} \\ k_{54} &= \rho g \Sigma A_{wn} x_w y_w \\ k_{44} &= \rho g \nabla (GM)_P \\ k_{55} &= \rho g \nabla (GM)_R \end{aligned} \tag{5.27}$$

where ∇ is the vessel displacement by volume and $(GM)_R$, $(GM)_P$ are metacentric heights in roll and pitch, respectively, while all other stiffness terms are zero.

The wave force calculation is based on the reduction of the terms on the right hand side of Equation (5.3) into an oscillating force column vector by summing the effects of wave particle velocities, accelerations and pressures on all structural members of the semisubmersible. The equation for the vertical wave surface elevation, η, relative to still water level is

$$\eta = \eta_0 \exp[i(kx \cos\theta + ky \sin\theta - \omega t)] \tag{5.28}$$

for a wave oriented at angle θ to the x axis (Figure 5.1), k is the wave number ($k = 2\pi/\lambda$ where λ is the wave length), ω is the wave frequency and η_0 is the wave amplitude.

Taking,

$$\psi = \exp[i(kx \cos\theta + ky \sin\theta)] \tag{5.29}$$

as a complex spatial description of the wave direction, Equation (5.28) can be written as

$$\eta = \eta_0 \psi e^{-i\omega t} \tag{5.30}$$

Then the wave surface vertical velocities and accelerations are

$$\dot{\eta} = i\omega\psi\eta_0 e^{-i\omega t} \tag{5.31}$$

and

$$\ddot{\eta} = -i\omega^2\psi\eta_0 e^{-i\omega t}. \tag{5.32}$$

In order to account for the decay of the vertical wave velocities and accelerations with depth below the sea surface, a depth attenuation factor is defined as

$$\sigma_1 = \frac{\sinh k(h - s + z)}{\sinh kh} \tag{5.33}$$

for water of depth h. Thus the vertical veolcity component due to the wave at any depth is

$$w = -i\omega\psi\sigma_1\eta_0 e^{-i\omega t} \tag{5.34}$$

and the acceleration is

$$\dot{w} = -\omega^2\psi\sigma_1\eta_0 e^{-i\omega t} \tag{5.35}$$

Similarly, for the horizontal velocities and accelerations, an attenuation factor of

$$\sigma_2 = \frac{\cosh k(h - s + z)}{\sinh kh} \tag{5.36}$$

is used. After the effect of wave orientation is accounted for, horizontal wave velocities and accelerations along structure axes can be written as

$$\left.\begin{aligned} u &= \omega\psi\sigma_2 \cos\theta\ \eta_0 e^{-i\omega t} \\ v &= \omega\psi\sigma_2 \sin\theta\ \eta_0 e^{-i\omega t} \\ \dot{u} &= -\omega^2\psi\sigma_2 \cos\theta\ \eta_0 e^{-i\omega t} \\ \dot{v} &= -\omega^2\psi\sigma_2 \sin\theta\ \eta_0 e^{-i\omega t} \end{aligned}\right\} \tag{5.37}$$

This completes the specification of the wave velocity and acceleration at any point around the semisubmersible submerged members.

For a semisubmersible with elongated circular and rectangular cylinders and other non-elongated members, the wave force calculations can be split into two categories. Wave forces on elongated members are computed by segmenting the member into sections and applying local wave velocity and acceleration to compute the wave force on the segment. These forces are then summed to obtain the total member wave force. The spatial variation of wave particle velocities and accelerations and particularly the wave decay due to depth are accounted for in this manner. The drag force on the right hand side of Equation (5.3) is computed after applying an equivalent linearization given by

$$\mathbf{B} \mid \dot{\boldsymbol{\eta}} \mid \dot{\boldsymbol{\eta}} = \underbrace{\left\{ \mathbf{B} \frac{8}{3\pi} \mid \dot{\boldsymbol{\eta}}_{\max} \mid \right\}}_{\text{equivalent coefficient}} \dot{\boldsymbol{\eta}} \tag{5.38}$$

This result can be derived by assuming equal work done at resonance by the non-linear and equivalent linear damping (see Chapter 4). The Froude–Krylov (or undisturbed wave dynamic pressure) force on elongated members is computed taking due account of water plane cutting members for which the axial component of this force will apply at one member end only.

Wave forces on elongated rectangular members are calculated by assuming that such members are generally pontoons which are always submerged for all draughts except the transit draught. Non-elongated members are not segmented – the wave conditions applying at the centre of volume are regarded as uniform in the vicinity of the structure for the drag, added mass and Froude–Krylov force calculations.

Once all the coefficient matrices and wave force vector, $\mathbf{F}(t)$, have been evaluated for Equation (5.3) the vessel's response is computed by using an iterative technique to account for the non-linear damping term. A first approximation diagonal linear damping coefficient matrix is obtained by ignoring all non-diagonal terms in the total mass and stiffness matrices and assuming damping of 10% of critical. The equation of motion is then solved with the first approximation to the damping value and the column

vector of resultant velocities is substituted into the modulus sign in the damping terms such that the equation

$$(\mathbf{M} + \mathbf{M}_A)\ddot{\mathbf{X}} + \mathbf{B}\frac{8}{3\pi} \mid \dot{\mathbf{X}}_{\text{last approx}} \mid \dot{\mathbf{X}} + (\mathbf{K} + \mathbf{K}_m)\mathbf{X} = \mathbf{F}(t) \qquad (5.39)$$

is being solved to obtain a better approximation for the displacement vector, **X**. The iteration is only significant in the vicinity of resonant frequencies. Thus, the equation solution is dependent on amplitude so that the wave height is a necessary part of the overall computation.

The complete motion response calculation outlined above is implemented in a program called UCLRIG (see Patel and Badi, 1980).

An interesting series of model tests and their comparison with many different methods of hydrodynamic analysis offers a useful means of validating the Morison equation based analysis described above. Takagi *et al.* (1985) have carried out comprehensive series of tests on a 1:64 scale model of an eight column semisubmersible in a wave tank of 3 m (192 m full scale) depth. Takagi and his colleagues compared their experimental data with theoretical estimates based on the Morison equation and potential flow methods from 34 different sources including program UCLRIG in a study reported by the 17th International Towing Tank Conference (ITTC) of Japan.

The prototype vessel had pontoons of length, beam and height of 115 m, 15 m and 8 m, respectively, with eight circular columns of 35 m and 24 m height, 60 m longitudinal and transverse spacing, the inner two columns being of 8 m diameter, the outer two of 10 m diameter. Full dimensions and hydrostatic data for the vessel are given in lines 1a of Tables 5.1 and 5.2. A schematic of the vessel is shown in Figure 5.4.

The model tests were used to determine wave induced rigid body motions in 6 degrees of freedom with the vessel in 0°, 45° and 90° orientation to waves (90° being beam seas). Testing was carried out with long crested regular waves of 2.944 m and 10.24 m full scale wave height over a wave period range from 6 to 28 s. A variety of irregular wave tests was also performed, though, for the sake of brevity, these will not be commented on.

The main conclusions from the study were as follows:

1. For constant water depth, most of the programs indicated surge and sway motions in excellent agreement with each other and with the experimental data.
2. There was considerable scatter predicted in the heave motion close to the heave natural period. Methods based on three dimensional potential flow were in good agreement with each other, but overpredicted the natural period by approximately 10%, the resonant heave amplitude being overestimated significantly. Calculations using the Morison equation gave heave estimates in closer agreement to the test data if the drag and inertia coefficients, C_D and C_m, were chosen carefully.
3. Variations in wave height had virtually no effect on either the experimental or theoretical wave induced motions, except for heave motion above wave periods of 20 s in the region of the heave natural period.

Table 5.1 Prototype semisubmersible dimensions

	Pontoon dimensions			*Column spacing*		*Column diameter** (m)	*No. of bracing members*
	Length (m)	*Breadth* (m)	*Height* (m)	*Longitudinal* (m)	*Transverse* (m)		
1a	110.0	15.0	8.0	24.0	60.04	10.0 & 8.0	16
1b	110.0	15.0	8.0	24.0	60.04	10.0 & 8.0	16
2	80.56	16.0	7.5	46.7	50.7	12.9	2
3	120.0	30.0	10.0	70.0	76.0	23.4	6
4	140.8	32.0	14.0	72.0	66.0	39.0	4

Notes:
Vessel descriptions
1a: Takagi model test semisubmersible 8 circular columns;
1b: Takagi semisubmersible (vessel 1) 8 circular columns;
2: Small displacement semisubmersible (vessel 2) 4 circular columns;
3: Medium displacement semisubmersible (vessel 3) 4 circular columns;
4: Large displacement semisubmersible (vessel 4) 4 rectangular columns.

* For vessel 4 the column diameter is replaced by the column side length in longitudinal direction.

Table 5.2 Dynamic and hydrostatic data for the semisubmersible vessels at prototype scale (vessel key as in Table 5.1)

No.	$\frac{d^*}{L}$	*Displ. in sea water* (t)	*Draught* (m)	*GM values*		*Radii of gyration*			*No. of facets in mesh*
				Roll (m)	*Pitch* (m)	*Roll* (m)	*Pitch* (m)	*Yaw* (m)	
1a	0.064	35011	20.0	2.88	2.36	34.3	35.5	40.6	–
1b	0.064	35638	20.0	2.88	2.36	34.3	35.5	40.6	376
2	0.080	24960	20.0	6.50	4.40	26.4	28.9	27.7	408
3	0.150	100000	24.0	8.40	4.80	32.0	40.0	40.0	416
4	0.250	160478	25.0	4.0	10.25	32.0	52.0	52.0	440

Notes:
Vessel key as in Table 5.1.
*d/L is defined as largest column diameter (or column side length in longitudinal direction for rectangular columns) divided by wavelength in 10 s deep water wave

4. In general, theoretical estimates of pitch and roll motions agreed with experimentally measured values to within 15%, results being closer for lower wave periods.

In the work presented here the experimental data obtained by Takagi and colleagues are examined in conjunction with theoretical estimates from the Morison equation using program UCLRIG in two water depths and wave heights. Motions are calculated for waves of 2.944 m height in 192 m corresponding to experimental conditions at full scale. Results are also presented for waves of 10.24 m height in deep water. The calculated motions in deep water are also compared with estimates made from

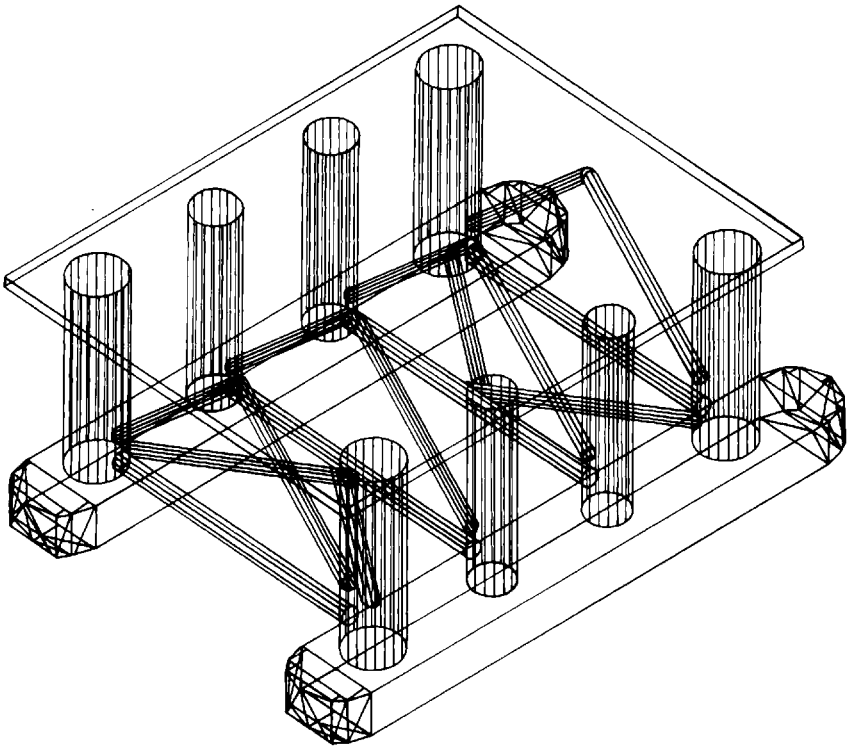

Figure 5.4. Hydrostatic mesh of Takagi semisubmersible

potential flow diffraction theory with non-linear drag and damping corrections applied as described in Section 5.3.

Before performing the Morison or diffraction theory based calculations, it is necessary to obtain various hydrostatic characteristics of the vessel using the method outlined in Chapter 3. Knowing the vessel draught, pressure integration on the vessel surface element array is used to compute the water plane area, displaced volume, centre of buoyancy and second moment of water plane area of the structure, from which the metacentric heights in pitch and roll are found. This hydrostatic pressure integration technique is described in further detail in Chapter 3. The hydrostatic characteristics of the eight column vessel are given in line 1b of Table 5.2.

Results are calculated from the Morison equation based method described above. For the Takagi semisubmersible, drag and added mass coefficients of 1.2 and 1.0 for fluid flow perpendicular to the vessel cylindrical members were used. For the pontoons, added mass and drag coefficients for horizontal flow perpendicular to the pontoon fore and aft centre lines were 0.55 and 0.43 respectively. The added mass and drag coefficients for vertical fluid motion around the pontoons were taken as 1.72 and 1.49. These values were obtained from recommendations made by Det Norske Veritas (1981).

Potential flow estimates of motions of the Takagi semisubmersible have also been found using the method outlined in Section 5.3. The mesh describing the submerged body boundary consisted of 376 facets. As

described in Section 5.3, the diffraction theory method has been enhanced to include the effect of drag forces on vessel bracing members though the wave diffraction effects of such members has been ignored. Drag damping coefficients calculated from the Morison based method are also used and are shown to significantly modify estimated linear motions near resonance, particularly for large wave heights.

The model test data, together with the Morison and diffraction theory based estimates for motions and forces, are presented in Figures 5.5 and 5.6 – natural period and added mass values are given in Table 5.3. The motion and force results in the figures have been divided by wave amplitude for direct comparison with the experimental data, though the values only apply for motions to the wave heights given in the diagrams due to non-linear drag effects. Unless indicated, the values presented are those calculated in deep water to waves of large amplitude (10.24 m wave height). In the following discussion of results it should be borne in mind that the experimental data were measured in waves of 2.944 m height in a relatively shallow water depth of 192 m (full scale values), whereas some of the theoretical runs correspond to a wave height of 10.24 m.

Figure 5.5(a) presents the surge motions of the Takagi semisubmersible in head seas. There are discrepancies in deep water surge motions predicted by the Morison and potential flow based methods for the Takagi vessel over the complete wave period range examined. The differences are due to the fact that the potential flow method does not include bracing members. It is felt that much closer agreement would be obtained between the two methods if the potential flow analysis included the influence of bracing. This is of particular importance for the Takagi vessel as it has 16 bracing members of 2068 t displacement, 6% of the total displacement of the vessel. The sway motions predicted by the two methods are in much closer agreement. Many of the bracing members have axes in the transverse direction and, therefore, have little influence on sway motions. The inclusion of non-linear drag and damping effects in the potential flow calculation does not alter the predicted motions.

Figure 5.5(b) presents heave motions in head seas. At wave periods below 16 s experimental data agree well with theoretical estimates from both methods, with the effects of water depth and wave height being negligible.

At wave periods from 11 to 18 s the heave results are broadly in agreement for both head and beam seas, though theoretical estimates underpredict the test data. Conversely, in the region of the heave force cancellation at approximately 22 s the theoretical methods significantly overpredict the test data, with results from the shallow water Morison based method being closest, overestimating the experimentally measured heave values by approximately 80%. It is anticipated that this discrepancy would be reduced if the residue force function representing the relative wave particle to body motion drag force terms, ignored in the analysis, were included in the method. It was shown earlier that the residue force is negligible when compared to the total heave force amplitude over the complete wave period range, except at heave force cancellation where the magnitude of the residue is of the same order as the total force. However, in practice it would be difficult to include the residue term in either analysis method due to the extensive numerical iteration required for solution.

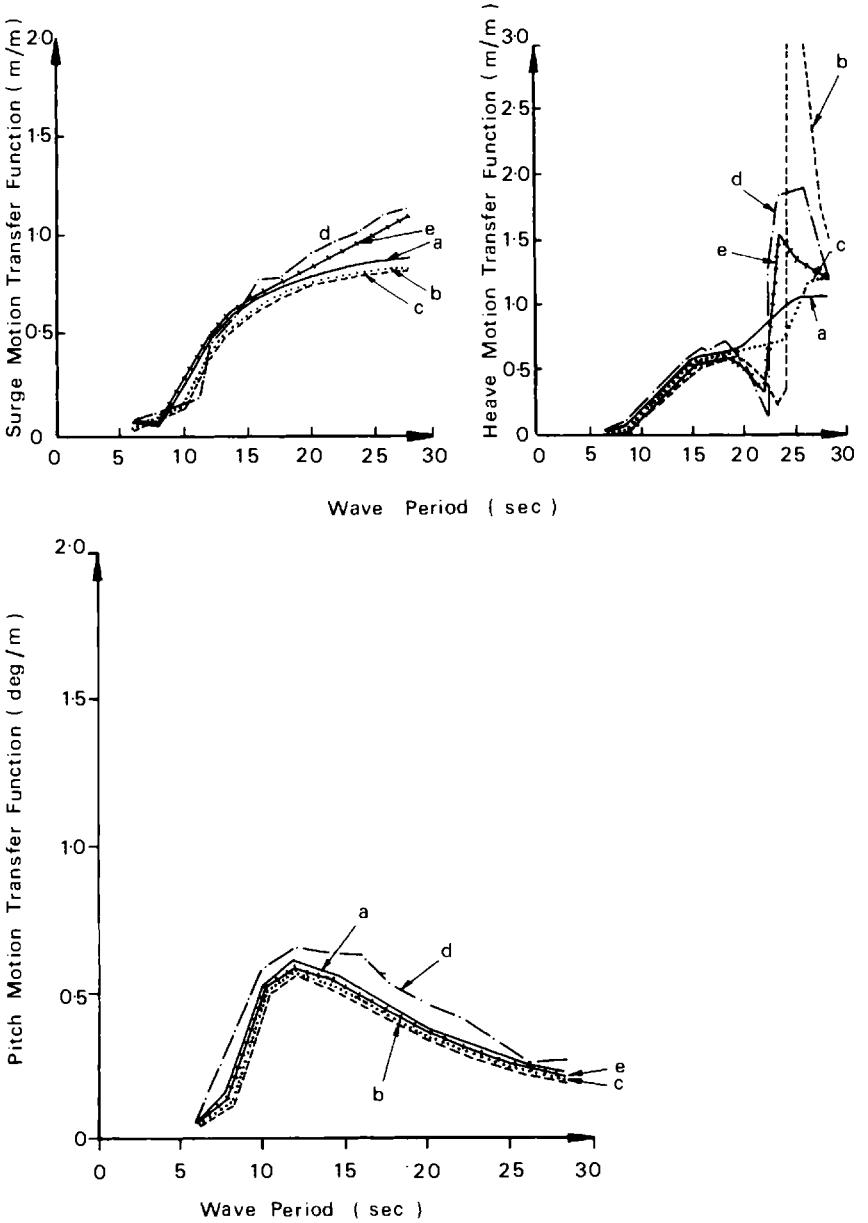

Figure 5.5. Vessel 1 – Takagi semisubmersible head sea data; wave height (wht) 10.24 m. *Key*: a – Morison equation, theory; b – potential flow, theory; c – potential flow (including Morison drag damping), theory; d – experimental data, Takagi model (wht = 2.944 m, depth = 192 m); e – Morison equation, theory (wht = 2.944 m, depth = 192 m)

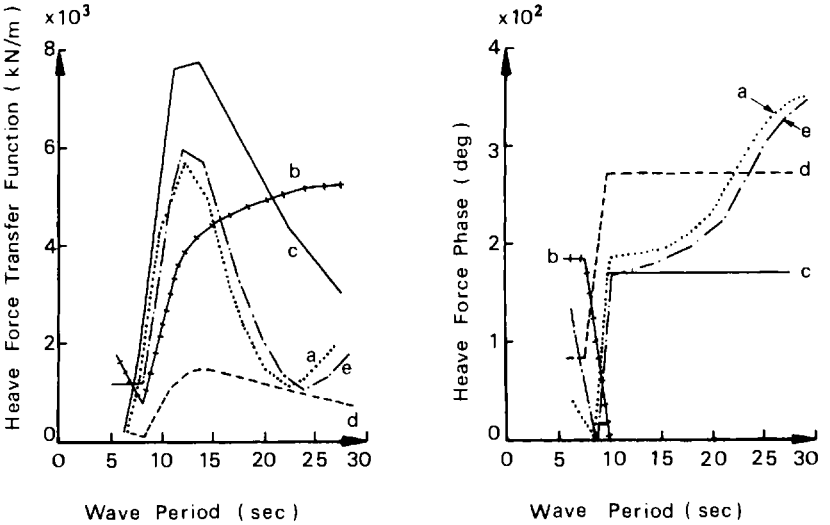

Figure 5.6. Vessel 1 – Takagi semisubmersible head sea data; wave height = 10.24 m. *Key*: a – total force on vessel, Morison equation; b – wave force on surface piercing members, Morison equation; c – inertia force on pontoons, Morison equation; d – drag force on vessel, Morison equation; e – total force on vessel, potential flow and drag force

Another relevant feature of the heave response around the force cancellation period is that the potential flow estimates without the inclusion of non-linear drag and damping agree closely with the Morison based results at small wave heights. When drag and damping effects are included in the potential flow analysis the predicted heave motions are much closer to those from the Morison based method at high wave heights. This is expected because heave motions in the region of the force cancellation will be larger at higher wave heights because of the non-linear influence of drag force terms in the equations of motion.

The theory and test data both indicate heave natural periods at approximately 24 s, as indicated in Table 5.3. However, the resonant heave amplitude predicted by the Morison based method in shallow water differs significantly from the experimental data indicating the inability of the method to predict the level of heave damping. Care should be taken when comparing theoretical data for the deep water case with test data since heave motions are influenced by water depth at large wave periods. However, it should be noted that the potential flow estimate of resonant heave motion is significantly higher than that obtained experimentally, inclusion of drag damping into the method reducing the motions significantly to a similar level to those predicted by the Morison based method. This level is approximately half that obtained experimentally due to the higher wave height used and consequently higher drag damping level. However, the Morison based method still overpredicts the level of damping significantly when using water depth and wave height values corresponding to the experimental tests.

Table 5.3 Natural period and added mass, inertia estimates for prototype semisubmersibles

No.	*Method*	*Natural periods*			**Added masses*			**Added inertias*		
		Heave (s)	*Roll* (s)	*Pitch* (s)	*Surge* $t \times 10^{-4}$	*Sway* $t \times 10^{-4}$	*Heave* $t \times 10^{-4}$	*Roll* $tm^2 \times 10^{-7}$	*Pitch* $tm^2 \times 10^{-7}$	*Yaw* $tm^2 \times 10^{-7}$
1a	E	24.0	52.3†	58.0	–	–	–	–	–	–
1b	M	23.6	56.2	64.9	0.827	1.827	4.256	3.921	4.318	2.371
	P	25.3	58.9	64.9	0.532	5.642	4.618	4.654	4.300	4.685
2	M	19.8	30.1	34.9	0.685	3.389	2.731	2.045	1.239	2.028
	P	21.0	31.3	33.7	0.584	3.637	3.258	2.209	1.016	1.936
3	M	21.8	37.0	49.9	2.633	13.55	11.23	21.15	13.73	19.92
	P	25.4	43.2	51.3	2.143	13.29	17.68	28.66	15.40	16.15
4	M	20.8	47.7	45.7	3.925	21.76	18.65	28.71	27.58	35.17
	P	22.9	55.7	41.6	5.022	19.40	24.72	33.15	27.38	26.40

Notes:
Vessel key as in Table 5.1.
* Average values of potential flow estimates are used.
† Using an experimental value for roll radius of gyration of 33.1 m.
Method
E: experimental data;
M: Morison equation based analysis;
P: potential flow diffraction analysis.

Figure 5.6 presents heave forces calculated by the two methods. Amplitude and phase values are given for the total force on the vessel found from the Morison based method as well as the individual inertia force on the pontoons, wave pressure force on surface piercing members and drag force on the complete vessel. The total force values are compared with the wave exciting force estimates calculated from potential flow including non-linear drag force effects.

The force results underline the relatively small contributions of drag to the total wave force. However, since the two major forces due to wave pressure on the surface piercing members and inertia on the pontoons are 180° out of phase with each other (see Figure 5.6(b)), there is a possibility of the small drag force dominating at some wave periods due to mutual cancellations of the above forces. This phenomenon occurs just below the resonant wave period which for heave is at approximately 24 s.

The potential flow heave force estimates in head seas are in good agreement with those from the Morison based calculation over the entire wave period range when the effects of drag are included. These results show that the Morison equation based approach is valid for semisubmersible vessels with slender members, although the diffraction analysis of such vessels, excluding bracing members, also gives reasonable results. This method is described further in the next section.

5.3 Diffraction analysis

Calculation of wave forces and consequent motions of large floating bodies with dimensions that are greater than 20% of wavelength of incident regular waves must account for modification of the incident wave flow by the floating body. This distortion (or diffraction) of the incident flow can only be fully known by a solution of the governing Laplace equation with the usual free surface and sea bed boundary conditions as well as the additional condition of no flow through the body surface. For bodies of arbitrary geometry, this calculation needs to be done numerically.

There are, in fact, two components with the solution for the motion of a large floating body responding to gravity waves. The first component is due to forces exerted on the body due to its motion in otherwise still water. These forces can be decomposed into two contributions, one proportional to body acceleration, called the added mass force, and the other proportional to body velocity, called the potential damping force. The resultant added mass and potential damping coefficients are used on the left hand side of the equation of motion and the determination of the coefficients is called the radiation wave problem.

The second component is called the scattered wave solution and is concerned with determining forces on a stationary floating body in waves – these forces being on the right hand side of the equation of motion. Both these component problems are addressed below.

The conditions that determine the use of diffraction theory first need to be established. Conventionally, for floating vessels with members of cross-section dimension D, diffraction theory is considered necessary if $D/\lambda > 0.2$ where λ is the incident wave length. However, the ratio of wave

height, H, to wave length, λ, satisfies the condition $H/\lambda < 1/7$ approximately for coherent waves to exist. If both of the above conditions are satisfied, the ratio H/D is smaller than 1. Since wave flow orbital diameters will be equal to or less than H, the wave flow regime around the floating body will not exhibit large scale separated flow. Consequently, drag forces will be small and a potential flow solution of the wave diffraction problem will be representative of reality. However, there is one exception to this argument and this concerns the roll response of ship shape vessels which is considered further in Section 5.4.

It is useful at this stage to explicitly set down the assumptions underlying the solution of diffraction problems. These are:

1. The vessel motions are assumed to be small.
2. The submerged vessel surface is taken to correspond to the instantaneous body surface beneath the still water plane.
3. The vessel response is linear, harmonic loading being due to incident linear sinusoidal waves of small amplitude.
4. Fluid pressures are obtained from the linearized Bernoulli equation, assuming that the wave flow is inviscid and irrotational, the fluid motions being described by a velocity potential.

For space frame structures, diffraction analysis can be adapted to incorporate non-linear drag and drag induced damping forces. This is described further below. A statement of the full wave diffraction problem in three dimensions can be written as follows using an axes system with Oxy in the still water surface and Oz pointing vertically upwards. The governing Laplace equation in terms of the velocity potential, ϕ, is

$$\frac{\partial^2\phi}{\partial x^2} + \frac{\partial^2\phi}{\partial y^2} + \frac{\partial^2\phi}{\partial z^2} = 0 \tag{5.40}$$

with the linearized free surface boundary condition at $z = 0$ of

$$\frac{\partial^2\phi}{\partial t^2} + g\frac{\partial\phi}{\partial z} = 0 \tag{5.41}$$

and the sea bed boundary condition at $z = -d$ of

$$\frac{\partial\phi}{\partial z} = 0 \tag{5.42}$$

together with the no-flow through the immersed body boundary condition of

$$\frac{\partial\phi}{\partial n} = V_n \tag{5.43}$$

at the body surface where n denotes a direction normal to this surface. V_n is the velocity of the body surface in the direction normal to the surface. All the assumptions inherent in the governing equations and the linearized free surface boundary condition thus apply to this linear diffraction problem, that is, irrotational and inviscid flow of small wave amplitude. The solution of the full wave diffraction and radiation problem is stated by writing the

total velocity potential as the sum of incident, scattered and radiated potentials, ϕ_i, ϕ_s and ϕ_r respectively. Thus

$$\phi = \phi_i + \phi_s + \phi_r \tag{5.44}$$

The scattered and radiated wave potentials are found by solving the two corresponding problems separately.

The radiation problem can also be solved by using either boundary integral or boundary element techniques. Only the solution using boundary integral techniques is described here for brevity. The analysis assumes inviscid, irrotational flow and that wave amplitudes are small. The unsteady flow around the floating vessel is calculated by introducing oscillating sources of unknown velocity potential on the vessel submerged surface that is discretized by a mesh of facets with an oscillating source on each facet. Further details on the solution of wave diffraction/radiation problems are given by Eatock Taylor and Waite (1978), Eatock Taylor (1982), Mei (1978) and Shaw (1979).

A Green's function is used to represent the velocity potential of each source which, because of the form of the Green's function, satisfies Laplace's equation, zero flow at the horizontal sea bed, the free surface and radiation boundary conditions.

Now, the solution for scattered wave potential due to the stationary floating body, subjected to incident waves of potential, ϕ_i, is described below. A set of linear simultaneous equations is obtained by equating the flow due to the local source plus the additional flow due to all other sources to the negative of the flow due to the undisturbed wave for each facet on the body surface. Solution of these equations yields the unknown source strengths and, therefore, the velocity potential, ϕ_s, which is used to derive pressures and wave forces by integration over the body surface. Thus the wave force vector, **F**, may be obtained for an incident wave of specified frequency and direction.

The scattered wave problem is associated with waves that are generated by the stationary body boundary in incident waves. Therefore, the scattered wave problem is restricted in the mathematical formulation to outgoing waves only. This requires that the scattered wave potential satisfies the condition

$$\frac{\partial \phi_s}{\partial r} + \frac{1}{c}\frac{\partial \phi_s}{\partial t} = 0 \tag{5.45}$$

where r is radial distance from a point on the body surface and c is wave celerity. This can be written (see Sommerfield, 1949; and Stoker, 1957) as

$$\lim_{r \to \infty} r^{1/2} \left[\frac{\partial \phi_s}{\partial r} - ik\, \phi_s \right] = 0 \tag{5.46}$$

where the factor $r^{1/2}$ takes account of the directional spreading of waves.

Since the incident wave potential, ϕ_i, is known, the boundary condition at the stationary body surface can also be written as

$$\frac{\partial \phi_s}{\partial n} = -\frac{\partial \phi_i}{\partial n} \tag{5.47}$$

Once ϕ_s is obtained as a solution to this problem, wave induced pressures can be obtained from the linearized Bernoulli equation and integrated to obtain forces and moments.

For floating bodies of arbitrary geometry, the scattered wave problem can be solved by simulating the flow using oscillating point sources placed on facets covering the body surface. If the total incident and scattered wave potential is written as

$$\phi = \text{Re}\ \{\phi'(x, y, z)\ e^{-i\omega t}\} \tag{5.48}$$

the spatial variation of potential ϕ' can be split up into its incident and diffracted components:

$$\phi' = \phi'_i + \phi'_s \tag{5.49}$$

Then Lamb (1975) shows that the scattered wave potential may always be represented as a continuous distribution of point sources over the immersed body surface through a summation integral of the form

$$\phi'_s(x, y, z) = \frac{1}{4\pi} \int_S f(\xi, \eta, \zeta)\ G(x, y, z; \xi, \eta, \zeta)\ dS \tag{5.50}$$

where (x, y, z) denotes a point in the fluid with (ξ, η, ζ) denoting a point on the body surface, $f(\xi, \eta, \zeta)$ is the source strength distribution on this surface and dS is a differential area on the body surface. The Green's function $G(x, y, z; \xi, \eta, \zeta)$ must be such that it satisfies the Laplace condition, the radiation condition as well as the sea bed and free surface boundary conditions. Such a function is given by Wehausen and Laitone (1960) and can be written in an infinite series form as

$$G(x, y, z; \xi, \eta, \zeta) = \frac{2\pi(\beta^2 - k^2)}{k^2 d - \beta^2 d + \beta} \cosh[k(z + d)]$$

$$\cosh[k(\eta + d)]\ [y_0(kr) - i\ J_0(kr)]$$

$$+ 4 \sum_{k=1}^{\infty} \frac{\nu_k^2 + \beta^2}{\nu_k^2 d + \beta^2 d - \beta} \cos[\nu_k(z + d)] \cos[\nu_k(\eta + d)]\ K_0(\nu_k r) \tag{5.51}$$

where ν_k are positive roots of equation

$$\nu_k \tan \nu_k d + \beta = 0,$$

$$r = \sqrt{[(x - \xi)^2 + (y - \eta)^2]},$$

$$\beta = k \tanh kd$$

and

$$k = 2\pi/\lambda$$

J_0 and Y_0 denote Bessel functions of the first and second kind, respectively, and of zero order and K_0 denotes the modified Bessel function of the second kind of zero order. The scattered velocity potential, ϕ'_s, is determined by imposing a no flow boundary condition on the body surface. This condition can be implemented by imposing the condition that at an element of the immersed body surface, the flow due to a local source plus the flow due to all other sources on the body surface must be equal and

opposite to the flow at the element due to the undisturbed wave. This can be written mathematically as

$$\tfrac{1}{2} f(x, y, z) - \frac{1}{4\pi} \int_S f(\xi, \eta, \zeta) \cdot \frac{\partial G}{\partial n} (x, y, z; \xi, \eta, \zeta)\, dS$$

$$= -W(x, y, z) \tag{5.52}$$

where the undisturbed incident wave flow is given by

$$W(x, y, z) = \left[n_z \frac{\sinh k(z + d)}{\cosh kd} + i\, n_x \frac{\cosh k(z + d)}{\cosh kd} \right] e^{ikx} \tag{5.53}$$

In Equation (5.52), the factor of $\frac{1}{2}$ in the first term is due to the fact that half the surface source fluid will be streaming into the body's interior volume. A negative sign on the right hand side of this equation defines fluid flow into the surface from the exterior.

Now the unknown source strengths, $f(x, y, z)$, are found by satisfying Equation (5.52) at all points on the body surface. However, since the derivation of $\partial G/\partial n$ is complicated for an arbitrary body, a closed form solution is not possible and a discretized numerical method is adopted instead – see, for example, Garrison and Chow (1972). The submerged surface of the body is divided into a lattice of facets and Equation (5.52) is satisfied at nodal points on each facet to reduce the integral equation to a finite number of simultaneous linear equations. Taking f_i as the source strength at the centroid (x_i, y_i, z_i) of the ith facet of area δS_i, Equation (5.52) can be written as

$$-f_i + \alpha_{ij} f_j = 2W_i \tag{5.54}$$

where

$$\alpha_{ij} = \frac{1}{2\pi} \sum_{j=1}^{N} \frac{\partial G}{\partial n} (x_i, y_i, z_i; \xi_i, \eta_i, \zeta_i)\, \delta S_i \tag{5.55}$$

for a total of N facets with the summation excluded for $i = j$. The derivative of G is evaluated using the equation

$$\frac{\partial G}{\partial n} = \frac{\partial G}{\partial x} n_x + \frac{\partial G}{\partial y} n_y + \frac{\partial G}{\partial z} n_z \tag{5.56}$$

where n_x, n_y and n_z are components of the unit normal vector to the facet surface. Once the coefficient matrix α_{ij} is obtained from Equation (5.55), Equation (5.54) is solved for all f_i by matrix inversion and the scattered potentials obtained through the equation

$$\phi'_{si} = \frac{1}{4\pi} f_j \sum_{j=1}^{N} G(x_i, y_i, z_i; \xi_i, \eta_i, \zeta_i)\, \delta S_i \tag{5.57}$$

Then taking the hydrodynamic pressure as

$$p(x, y, z, t) = -\rho \frac{\partial \phi}{\partial t}$$

$$= \mathrm{Re}\{i\rho\omega\, [\phi'_i(x, y, z) + \phi'_s(x, y, z)]\, e^{-i\omega t} \tag{5.58}$$

the total hydrodynamic forces and moments are given by the integrals

$$\left.\begin{aligned} \mathbf{F}e^{-i\omega t} &= -\int_S p(x, y, z, t)\,\mathbf{n}\,dS \\ \text{and} \\ \mathbf{M}e^{-i\omega t} &= -\int_S p(x, y, z, t)\,(\mathbf{r}\times\mathbf{n})dS \end{aligned}\right\} \tag{5.59}$$

where **n** denotes the unit normal to the surface and **r** denotes the moment arm vector. Numerical values are computed by discretizing these equations and using the scattered wave potential from Equation (5.57).

The numerical integrations defined by Equations (5.55) and (5.57) pose some difficulties due to singularities in the Green's function form. However, the integrals are readily evaluated by using numerical integration schemes designed to cope with singularities. Furthermore, for some so-called 'irregular' wave frequencies, the matrix to be inverted for solving Equation (5.54) becomes non-positive definite and no unique solution of the boundary integral problem is possible. This feature of the solution is not due to the numerical discretization employed but arises inherently from the source distribution representation of the scattered wave potential, see John (1950) and Murphy (1978). Irregular wave frequencies generally correspond to wavelengths which are smaller than the size of the body and are, therefore, usually at frequencies that are too high to be of concern in most wave loading calculations. Boundary integral techniques also suffer from numerical problems when modelling re-entrant structure geometries or structures with small holes or sharp corners – these problems are triggered by numerical problems due to the close proximity of adjacent surface panel sources. Ursell (1981) gives further details on irregular frequencies.

Turning now to the radiated wave problem, the full velocity potential equation (5.44) must satisfy the boundary conditions at the body surface given by

$$\frac{\partial\phi_i}{\partial n} + \frac{\partial\phi_s}{\partial n} + \frac{\partial\phi_r}{\partial n} = V_n \tag{5.60}$$

where V_n is the velocity of the body surface in the direction normal to the surface. This boundary condition can be applied at the mean body surface since the theory is applied for small motions; ϕ, together with its three components, must also satisfy the Laplace equation and the free surface and sea bed boundary conditions. Furthermore, ϕ_s and ϕ_r must satisfy the radiation conditions.

Boundary conditions for the scattering and radiation wave problems can be split up from Equation (5.60) as

$$\frac{\partial\phi_i}{\partial n} + \frac{\partial\phi_s}{\partial n} = 0 \tag{5.61}$$

and

$$\frac{\partial \phi_r}{\partial n} = V_n \tag{5.62}$$

respectively, both being applied on the body surface.

The radiation velocity potential, ϕ_r, is obtained in a similar way to the scattered velocity potential except for the use of a different boundary condition (Equation 5.62), which reflects the fact that ϕ_r arises from body motions in otherwise still water. Thus, at all facets, the source strengths, ϕ_i, are such that the flow due to the local source plus the flow due to all other sources equals the velocity component of the body along the facet normal. This velocity component will depend on the mode of motion (surge, sway, heave, and so on) in which the body is moving. All this can be represented by equating the normal velocity of the fluid and of the jth facet for the vessel moving in its kth mode of motion. This yields the equation

$$\sum_{\text{All } i} \frac{\partial \phi_{ri}}{\partial n_j} \sigma_{ik} = V_{jk} \tag{5.63}$$

where V_{jk} is the normal velocity of the jth facet with the vessel moving in its kth mode of motion. Furthermore, n_j is the normal to the jth facet, $\partial \phi_{ri}/\partial n_j$ is the normal fluid velocity at the jth facet due to a unit source at the ith facet, and σ_{ik} are the unknown source strengths required in the kth mode. Application of Equation (5.63) for all facets produces a system of complex equations to be solved for the source strengths. Once these are known, the pressures at the facets are evaluated and their effects integrated over the vessel surface to yield forces in each mode of motion to unit motion in the kth mode.

Since the wave excitation is harmonic, the response of the floating body will be harmonic and of the form $\mathbf{X}e^{-i\omega t}$ where $\mathbf{X}$ is the complex response amplitude vector.

Solution of the above procedure for the radiated wave force, $\mathbf{F}_r$, yields

$$\mathbf{F}_r(\omega) = \mathbf{G}(\omega)\,\mathbf{X}\,e^{-i\omega t} \tag{5.64}$$

where $\mathbf{G}(\omega)$ is a complex square matrix.

The equation of motion for large floating bodies is given by

$$\mathbf{M}\frac{d^2}{dt^2}(\mathbf{X}\,e^{-i\omega t}) + (\mathbf{K} + \mathbf{K}_m)\,\mathbf{X} = \mathbf{G}(\omega)\,\mathbf{X}\,e^{-i\omega t} + a(\omega)\,\mathbf{F}_\omega(\omega)\,e^{-i\omega t} \tag{5.65}$$

where $\mathbf{F}_\omega(\omega)$ is the complex wave force amplitude vector obtained from Equation (5.59), and $a(\omega)$ is the wave amplitude; $\mathbf{M}$ is the physical mass matrix; $\mathbf{K}$ is the hydrostatic stiffness matrix; and $\mathbf{K}_m$ is the mooring stiffness matrix. The hydrostatic stiffness matrix, $\mathbf{K}$, can be obtained from the hydrostatic pressure integration techniques described in Chapter 3.

The above equation of motion (Equation 5.69) does not contain any viscous flow effects, such as quadratic drag damping, as it is a potential

flow formulation. It is convenient to decompose $\mathbf{G}(\omega)$ into its real and imaginary parts through the equation

$$\mathbf{G}(\omega) = \omega^2 \mathbf{M}_A(\omega) - i\omega \mathbf{B}_p(\omega) \tag{5.66}$$

to yield frequency dependent added mass and damping matrices $\mathbf{M}_A(\omega)$ and $\mathbf{B}_p(\omega)$.

Equation (5.65) now becomes

$$[-\omega^2(\mathbf{M} + \mathbf{M}_A) + i\omega\mathbf{B}_p + (\mathbf{K} + \mathbf{K}_m)]\,\mathbf{X} = \mathbf{F}_\omega \tag{5.67}$$

The above equation forms a set of complex linear algebraic equations which may be readily solved for the motion amplitude vector, $\mathbf{X}$, by

$$\mathbf{X} = \mathbf{A}^{-1}\,\mathbf{F}_\omega \tag{5.68}$$

where

$$\mathbf{A} = [\mathbf{K} + \mathbf{K}_m - \omega^2(\mathbf{M} + \mathbf{M}_A) + i\omega\mathbf{B}_p] \tag{5.69}$$

The hydrodynamic coefficient matrices in Equation (6.67) are frequency dependent and thus a diffraction analysis needs to be carried out for all frequencies at which motions are required.

The exciting force vector $\mathbf{F}_\omega(\omega)$ and the coefficient matrices, $\mathbf{M}_A(\omega)$ and $\mathbf{B}_p(\omega)$, can also be derived using finite element methods in an analogous way to that described for the boundary integral approach described above (Eatock Taylor and Zietsman, 1981).

There is one further point of interest regarding the relationship between the scattered and radiated wave potentials (ϕ_s and ϕ_r) for a floating vessel problem. The use of equations called Haskind relations (see Newman, 1962) enables the scattered wave potential, ϕ_s, to be expressed in terms of the incident and forced wave potentials, ϕ_i and ϕ_r. Thus, once ϕ_r is calculated, ϕ_s need not be computed by diffraction analysis but can instead be derived using the Haskind relations.

The equation of motion for the floating body is often modified to incorporate additional effects not present in the standard linear formulation of the potential flow equations of motion. The equation of motion (6.67) now becomes

$$[-\omega^2(\mathbf{M} + \mathbf{M}_A(\omega)) + i\omega\,\mathbf{B}_p(\omega) + i\omega\,\mathbf{D}(\omega) + \mathbf{K} + \mathbf{K}_m]\,\mathbf{X}(\omega)$$
$$= a(\omega)\,\mathbf{F}_\omega(\omega) + \mathbf{F}_d(\omega) \tag{5.70}$$

where $\mathbf{D}$ and $\mathbf{F}_d$ provide additional sources of damping and excitation respectively. The additional terms are used for diffraction analysis of semisubmersible hull forms where the major pontoons and columns can be included in the submerged surface description, but it is computationally too expensive to include all the bracing members. Terms $\mathbf{D}$ and $\mathbf{F}_d$ are included to take account of the damping contribution of drag forces due to vessel motions on bracing members, and also to account for the direct loading of vessel main members and bracing by drag forces due to wave induced velocities. The linearized damping matrix $\mathbf{D}$ given by

$$\mathbf{D} = \mathbf{B}\,\frac{8}{3\pi}\,|\,\mathbf{X}_{\text{last approximation}}\,| \tag{5.71}$$

accounts for drag force induced damping due to vessel motion. For simplicity, matrix **B** only contains the diagonal terms of the drag force damping matrix derived in Section 5.2. The term $\mathbf{F}_d$ is the force vector due to wave induced drag forces on vessel members and bracings. Terms **D** and $\mathbf{F}_d$ are first found from a Morison equation based analysis as described in Section 5.2. Equation (5.70) is then solved for **X** by matrix inversion with an iterative procedure employed to take account of the non-linear damping term.

In order to illustrate the applications of diffraction analysis for floating vessels, consideration is given first to semisubmersible designs as a continuation of the Morison equation based analysis of Section 5.2. In particular, the respective limitations of Morison and diffraction theory based analyses can be illustrated by analysing three additional semisubmersible designs chosen to cover a wide range of column diameters and displacements. Two twin pontooned designs of small and medium displacement having four circular columns are selected together with a large displacement semisubmersible heavy lift crane vessel (SSCV) with rectangular columns. Dimensions and hydrostatic data for the rigs, denoted vessels 2, 3 and 4, are given in Tables 5.1 and 5.2.

Hydrostatic and hydrodynamic analyses were performed on these vessels in an identical manner to that described for the Takagi semisubmersible in Section 5.2. In all diffraction analyses, between 376 and 440 triangular surface elements were used to define the submerged body boundary in a sufficiently accurate manner. Figure 5.7 shows a typical hydrodynamic mesh for the submerged hull of vessel 4.

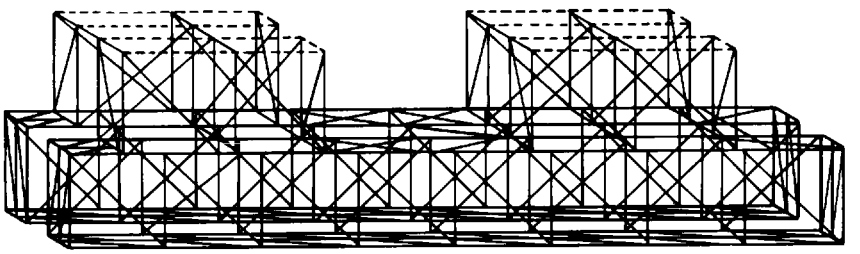

Figure 5.7. Hydrodynamic mesh of Vessel 4 – large displacement semisubmersible

Figures 5.8 and 5.9 present some representative head and beam sea heave motions calculated from the two methods, as well as the diffraction theory calculations including drag damping for vessels 2, 3 and 4 having cross-sectional column dimensions of 12.9, 23.4 and 39 m respectively.

Surge and sway motions calculated by the two methods are not shown here but are in general agreement with each other over the wave period range from 9 to 28 s. At lower periods, however, differences occur for vessels 3 and 4.

Figures 5.8 and 5.9(a) present selected heave motion data in head and beam seas for all three vessels. Vessel 2 with columns of 12.9 m diameter shows agreement between potential flow and the Morison approach for wave periods up to 15 s in head seas. Over the range of heave force

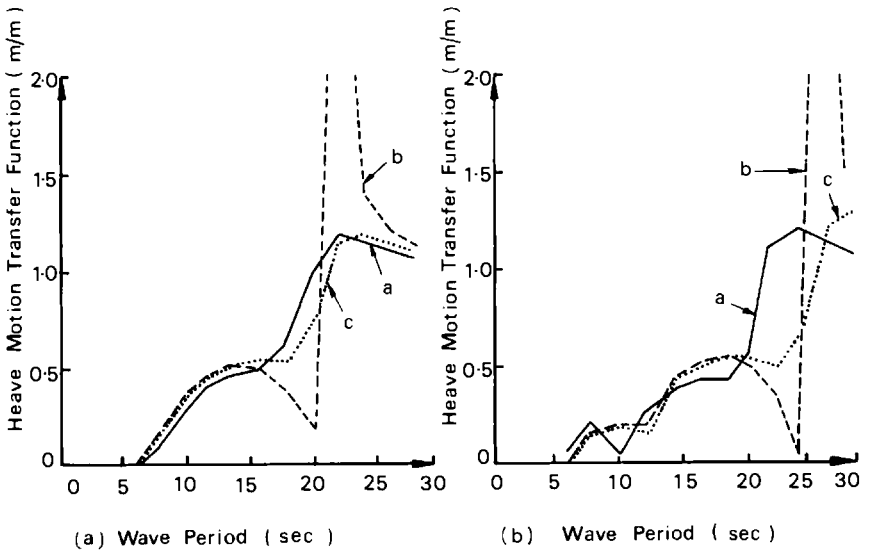

Figure 5.8. Heave motion transfer functions: (a) Vessel 2 – small displacement, head seas; wave height = 10.24 m; (b) Vessel 3 – medium displacement, head seas; wave height = 10.00 m. *Key*: a – Morison equation, theory; b – potential flow, theory; c – potential flow (and Morison drag damping), theory

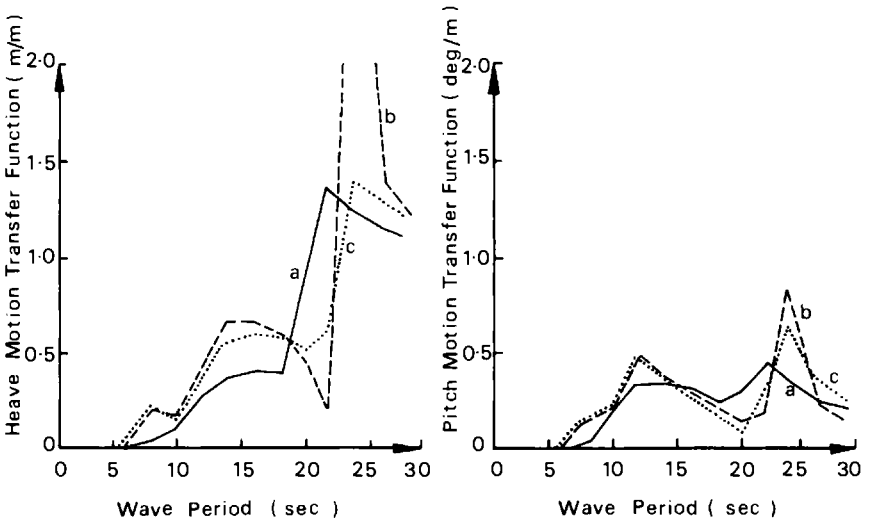

Figure 5.9. Vessel 4 – large displacement semisubmersible, head sea data; wave height = 10.00 m. *Key*: a – Morison equation, theory; b – potential flow, theory; c – potential flow (and Morison drag damping), theory

cancellation from 16 to 19 s, the potential flow method yields significantly lower heave motions for vessel 2 than the potential flow method with drag forces included for the Morison based approach. If results had been calculated for small wave heights using the Morison equation, it is

anticipated that agreement with the potential flow method would have been much closer due to the small non-linear drag force effects. The potential flow method overpredicts the heave resonant amplitude by a factor of two, while the methods that include non-linear damping are in broad agreement. The heave motions of vessel 2 in head seas display the same trends as those of the Takagi semisubmersible and hence the relevant discussion of heave results discussed in Section 5.2 also applies here.

The agreement in head and beam heave results between the two methods for vessels 3 and 4 having columns of dimensions 23.4 and 39 m is not particularly good, especially for the larger vessel see Figures 5.8(b) and Figure 5.9(a). Heave motions below wave periods of 18 s are significantly underpredicted by the Morison based analysis. The reason for this is clearly the wave diffraction and radiation due to the large columns and pontoons of the vessel which are not accounted for in the Morison analysis. Drag effects on the members over the wave period range from 10 to 18 s do reduce the potential flow heave motions to values that are closer to the Morison based predictions, but there are still large discrepancies in the Morison results.

At the heave force cancellation period of approximately 23 s for vessels 3 and 4, the basic potential flow method significantly underpredicts the head and beam sea heave motions since non-linear drag effects are not included. However, the Morison based results do not predict a force cancellation probably because of the high drag forces due to the high wave heights considered. It is believed that the most accurate heave response in this wave period range is obtained from the potential flow method with drag and damping forces included. In the region of heave resonance (above 23 s wave period), similar conclusions apply as for the heave motions of vessel 2.

Figure 5.9(b) presents head sea pitch motion for vessel 4. Here the Morison based estimates are significantly different from the potential flow values, even when drag effects are included. Again, the neglect of wave diffraction by the Morison equation approach is believed to be at fault. At wave periods above 20 s, the Morison based pitch motion estimates of vessel 4 are still in error, though there is agreement in the roll motions.

Table 5.3 presents the natural period estimates and added mass and inertia values for vessels 2, 3 and 4. The added mass and inertia values calculated from the potential flow method have been averaged over the calculated wave period range to give a mean estimate for comparison with the constant values used in the Morison approach. In general there is good agreement between results from the two methods, indicating that the simplification of assuming constant added mass and inertia values made in the Morison method is adequate, although the difficulties of choosing appropriate added mass coefficients still remains.

A review of the above results and those of Section 5.2 indicates that the Morison equation approach is valid for calculating wave induced motions for vessel having D/λ values of less than 0.2. Thus the Morison approach may be used with the Takagi vessel 1 and vessel 2 considered here. However, application of the potential flow method to these vessels does require that drag forces due to vessel motion as well as wave motions are included in the analysis. Inclusion of the drag force due to vessel motion

leads to greater accuracy around resonant wave periods, whereas inclusion of the drag force due to wave particle motion yields more accurate motions in the vicinity of wave cancellation periods.

For vessels 3 and 4 of large displacement and member size, it is clear that the Morison equation approach is inadequate, particularly in estimating heavy motions. In such cases, it is more appropriate to use a full potential flow analysis, though it is essential to include drag forces both due to vessel motion and wave particle velocities.

Attention is now focused on application of diffraction theory to a monohull configuration. An example is taken from a study by Brown *et al.* (1983) that compares model tests on a barge of 1:36 and 1:108 scale with predictions from a diffraction theory analysis. Only the 1:36 scale tests are described briefly here. They were carried out in a complex sea basin that was 18 m square and 1.5 m deep. The 36th scale rectangular barge model was of 2.40 m length, 0.80 m beam and 0.34 m height with a draught of 0.105 m. The mass of the model was 200.8 kg and the model's roll, pitch and yaw moments of inertia about centre of gravity axes were 11.95, 95.05 and 71.81 kg m^2 respectively. The vessel centre of gravity was at 0.111 m above the keel. It was installed with two types of keel edges on the submerged horizontal edges – one being a sharp right angled edge and the other a rounded profile of 40 mm radius.

Measurements of the wave induced motion of the model in all six degrees of freedom were made with both regular and irregular long crested seas. These measurements were reduced to response amplitude operators using the techniques described by Brown *et al.* (1983). This paper also describes the calculation method used for the numerical diffraction analysis which exploits hull symmetry about both vertical axes to enable 156 facets to be used on one-quarter of the hull form. This is, of course, analogous to using 624 facets on the whole hull form.

A selection of test results and comparisons with theory are presented here. Figure 5.10(a) presents the heave response to head seas for both rounded and sharp keel edges and demonstrates that they both agree reasonably well with theory. The discrepancies between theory and tests are believed to be due to experimental errors. Figure 5.10(b) presents the

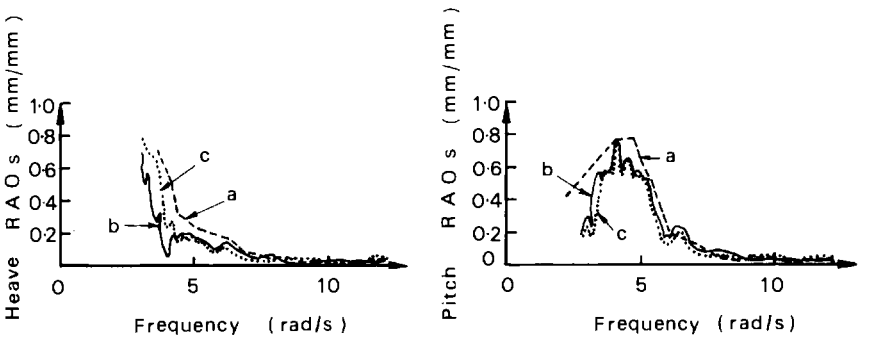

Figure 5.10. Heave and pitch transfer function in head seas for 1:36 scale. RAO is response amplitude operator. *Key*: a – theory; b – data for rounded keel-edge profile; c – data for sharp keel-edge profile

pitch response in head seas. The results for both rounded and sharp keel edges are very close and agree well with theory. The surge response in head seas as well as heave and sway in beam seas show good agreement similar to that presented in Figure 5.10 between the sharp and rounded keel edge profiles and with theory.

The measured roll motion transfer function in beam seas shown in Figure 5.11 shows substantial differences between the sharp and rounded keel edge experimental data, as well as between experiment and theory. The plotted roll responses are centred around the roll resonance frequency (5.8 rad/s for 1:36 scale). Roll motions for the rounded keel edges are seen to be up to 50% greater than those for sharp edges near and above the roll resonance frequency. The physical phenomenon behind these differences is illustrated by the observed changes in local water motions close to the barge in the cases of rounded and sharp keel edges, the latter generating a large amount of turbulence in and under the free surface. Despite the relatively smoother flow observed close to the rounded keel edges during the tests, experiment and theory for this case still disagree substantially at resonance. The roll response data also shows a slight reduction in the roll natural frequency from rounded to sharp keel edge data. This would be consistent with an increase in damping, due to vortex shedding and fluid turbulence induced by the sharp keel edges.

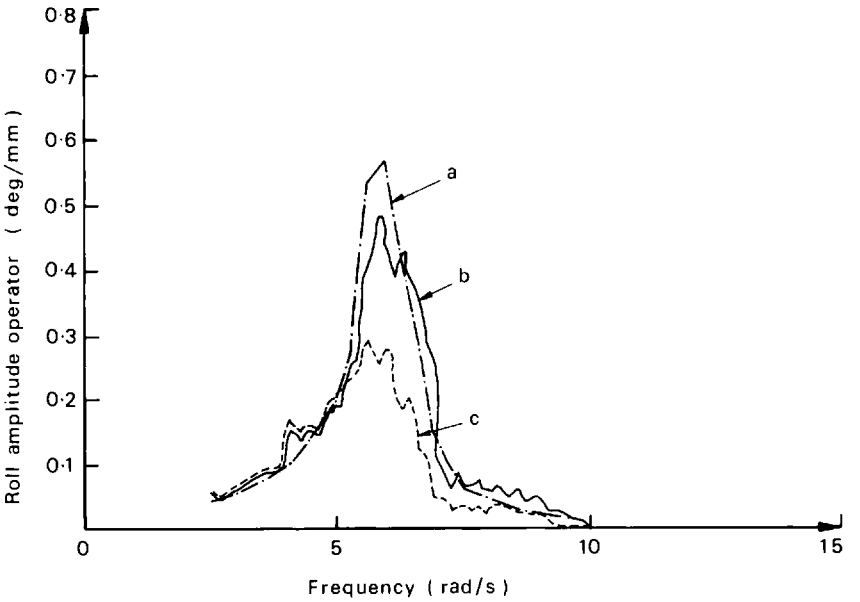

Figure 5.11. Roll transfer function in beam seas for 1:36 scale. *Key*: a – theory; b – data for rounded keel-edge profile; c – data for sharp keel-edge profile

The differences between rounded and sharp keel edge experimental data are also brought out by the plot of roll angle against time displayed in Figure 5.12 for the two conditions. Peak roll angles for the rounded keel edges are approximately double those measured for the sharp keel edges,

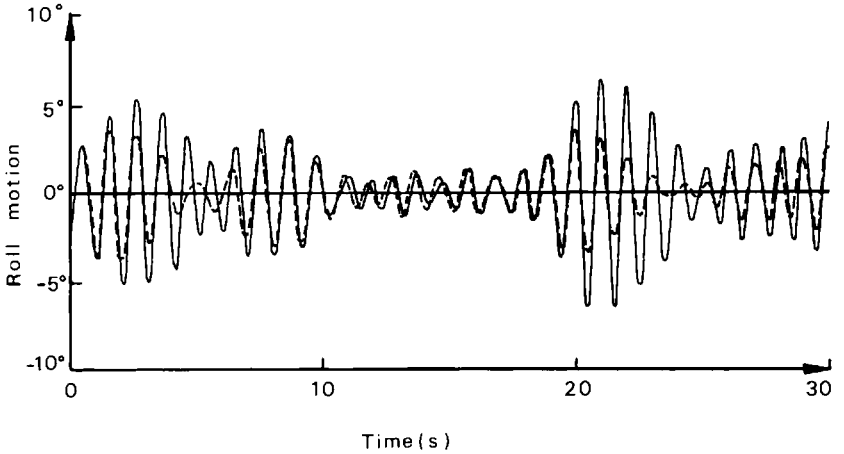

Figure 5.12. Comparison of roll-time history from 1:36 scale tests for two keel-edge profiles (significant wave height = 3.4 cm; characteristic period = 0.9 s). *Key*: — data for rounded keel-edge profiles; --- data for sharp keel-edge profiles

thus illustrating the need for a sound theory to account for the viscous effects at the vessel keel, and to predict the roll motion responses of cargo-carrying barges more accurately. It is worth noting the manner in which the difference between the rounded and sharp keel edge data develops with time. It suggests a vortex shedding or turbulence-generation process which is triggered off by roll motions reaching a particular amplitude. The discrepancy caused by these viscous effects persists for a while before decaying and the triggering process is then repeated.

Additional work, described further in Section 5.4, shows that the observed discrepancies in roll motion can be accommodated by increasing the potential flow radiation damping by approximately 20% of critical damping for the rounded keel edge and 80% of the same for the sharp keel edge. Furthermore, visualization studies of the flow close to the keel edge reveal the presence of strong vortex shedding and consequent vortex movements around the keel. Such vortex shedding is not detected for the rounded keel edges. These studies suggest that the observed discrepancies in roll motions can be predicted by an analytical model which uses point vortices in a background potential flow together with skin-friction calculations to predict the energy dissipated and consequential additional damping due to these viscous effects. Section 5.4 takes these matters further.

5.4 Monohull roll response

The preceding section highlights the inability of potential flow theory to predict the lightly damped roll resonance peak of ship shape vessels. Attempts have been made to predict the magnitude of this roll resonance peak from the very beginning of the development of a scientific basis of naval architecture. These efforts have been motivated by the need to reduce the levels of roll resonance peaks in order to improve vessel sea

keeping and operating effectiveness. A brief review of this work is presented below.

Bilge keels, which are essentially flat plates or similar structures protruding outwards from the submerged vessel corners, have been commonly used to reduce the roll motions of floating vessels. Froude (1874), one of the earliest workers in this area, realized that the total roll damping of a ship, with or without bilge keels, was not proportional to the square of the rate of rolling but was better represented by a combination of linear and square-law terms. Froude's hypothesis was based on experiments performed with a flat plate oscillating in water at various frequencies. Martin (1958) extended these investigations to vary the amplitude of plate oscillation and concluded that the drag on the plate varied with amplitude to a power between 1 and 2.

White (1895) performed experiments on battleships and found that the additional damping produced by fitting bilge keels was linear, rather than square-law in character. He therefore concluded that surface wave radiation must be an important element in bilge keel damping. Bryan (1900) indicated that for ships with fairly large bilge keels, the transverse velocity of the water could be considerably greater than the product of the radius from the roll centre to the bilge keel and the rate of change of roll angle. Bryan also observed that when the ship was rolling, a pressure force would act on the hull ahead of each keel and a suction force behind it, these forces exerting a moment on the vessel that opposed the rolling motion. Other workers include Gawn (1940) and Dalzell (1978) who performed and analysed roll tests on battleships. They found that the test data fitted well to quadratic and cubic variations with roll amplitude.

Over the last two decades a large number of measurements have been made on the roll motions of ships by the 17th Research Committee of the Shipbuilding Research Association of Japan. Kato (1958) developed a method using results of experiments that measured the resistance to rolling of immersed suspended cylinders, and concluded that the frictional damping of ships was insignificant compared to the dominant effects of wave damping. Tanaka (1960) refined the experiments to measure the total resistance to rolling due to eddy making (shedding of vortices from the bilge keels) and friction and hence calculated the resistance due to eddy making alone by subtracting the effects of frictional resistance calculated by Kato's method.

Semiempirical methods based on Tanaka's results have had varying degrees of success in predicting resonant roll motions. For example, Slavesen *et al.* (1970) developed a method using strip theory and a representation of viscous damping to predict vessel roll motions in significantly closer agreement with experimental measurements than the same theory gave without viscous damping. Tanaka has published further work with Ikeda and Himeno (1978) which develops other semiempirical formulae for the roll-damping terms due to friction, wave, eddy and lift components for the hull and bilge keel contributions, with no interaction accounted for between the various terms. The friction term was based on work by Blasius (see, for example, Newman, 1977); the wave-damping term was calculated using strip theory; the eddy-making term was derived from earlier work by Ikeda *et al.* (1977) on two dimensional cylinders of

various cross-section (resulting in rather long and complicated formulae giving a result depending quadratically on roll frequency and amplitude); and the lift and bilge keel contributions were both semianalytical in nature, agreeing reasonably well with experimental results. The authors concluded that the sum of the five damping components showed good agreements with experimental results for ordinary ship forms. However, for ships with high breadth to draught ratios, such as flat-bottomed barges, this method was not always accurate.

Investigations into the motions of flat-bottomed barges have been carried out only recently as these vessels have now come into regular use due to the development of the offshore oil industry. Keuning and Beukelman (1979) performed forced roll-oscillation tests to measure the added mass and damping values of rectangular barges in various water depths, comparing the results with both a strip theory and diffraction model. They indicated that the effects of viscosity played an important role at high wave frequencies, where a growing amount of eddy shedding from the sharp corners could be observed. Surprisingly they found that the sway added mass, and damping coefficients, remained independent of the oscillation amplitude even when there was much vortex shedding, though the roll coefficients were amplitude dependent. Keuning and Beukelman concluded that the predicted damping coefficients were low, especially at higher frequencies where viscous effects were dominant, the damping in roll being particularly difficult to estimate accurately.

Stewart *et al.* (1979) arrived at similar conclusions after comparing roll motion results for full and 1:30 scale models with predictions from commercially available computer programs. They indicated that the results of model tests showed that roll damping was a non-linear phenomenon, the equation of motion being represented by

$$(I + I')\ddot{\theta} + B_1\dot{\theta} + B_2\dot{\theta}^3 + S\theta = F\cos(\omega t + \phi) \tag{5.72}$$

where I and I' are the roll inertia and added inertia, S the roll stiffness, F the roll exciting force to waves of frequency ω, ϕ is a phase angle and B_1 and B_2 are constants. Stewart *et al.* found that the barge roll response per unit wave amplitude decreased with increasing wave height due to increased damping forces and that, in general, the inability of programs to account accurately for the viscous damping in roll led to enormous variations in roll motion predictions close to resonance. By considering an equation of the form of (5.72) a better representation of the roll motions could be found, though they did not know of any theoretical method that existed to calculate appropriate values of B_1 and B_2 for a particular hull form and, therefore, it was always necessary to resort to model tests.

Kaplan *et al.* (1982) proposed a method for representing non-linear contributions to the roll damping based on the concept of cross-flow drag. An expression for the non-linear roll moment due to skegs, bottom and barge sides was derived in which the roll damping was proportional to $|\dot{\theta}|\dot{\theta}$, where θ denotes roll angular velocity. For regular sinusoidal waves this non-linear damping term, B_{NL}, is approximated in an equivalent linear form as

$$B_{NL} \mid \dot{\theta} \mid \dot{\theta} = \frac{8}{3\pi} B_{LL}\, \theta_m \omega_n \dot{\theta} \tag{5.73}$$

where ω_n is the roll natural frequency and θ_m is the roll amplitude.

The non-linear roll motion response of ocean-going barges has been thought to be partially due to features other than the viscous phenomena of vortex shedding and skin friction. Denise (1983) indicates that linear models are inadequate because ocean-going barges have very shallow draught, of the same order of magnitude as the wave amplitudes considered, and hence the basic assumption of small motions required by linear theory is not satisfied. Although a full representation of the additional non-linear effects is difficult, Denise has developed a method to quantify the additional loads due to non-linearities that he refers to as buoyancy-restoring forces and moments. These corrections to the linear forces on the barge cause a non-linear detuning at resonance.

The additional forces primarily apply in the region of the vessel splash zone and depend on the wave profile and relative barge motion. Denise's non-linear model accounts for these effects and he compared his roll motion estimates with model and full scale test data and linear potential flow theory, with and without empirical additions allowing for 'viscous roll damping'. In general, his resonant roll amplitudes agree closely with measured values, the linear potential flow theory consistently overpredicting the motions. However, it is noted that Denise has applied the method only to barges having well rounded keel edges where the effects of vortex shedding would be relatively unimportant. The experimental evidence of Section 5.3 does suggest that a major part of the viscous force acting on a barge with bluff right angle keel edges is due to vortex shedding.

The mechanisms that could contribute to additional damping are described in more detail here and illustrated in Figure 5.13. One of these is associated with the fact that a vessel responding with large roll amplitude violates the assumptions of small motions inherent in linear theory. It is thus entirely possible that non-linear forces arise that modify large angle roll motions without viscosity playing any part in the roll reduction. Two other mechanisms contributing to roll damping are due to the viscous effects of separation and vortex shedding from large changes in hull slope or bilge keels on the vessel, as well as energy dissipation induced by boundary layer friction between the hull and surrounding fluid.

One possible reason for the inability of linear potential flow theory to predict marine vehicle roll motions close to resonance accurately is discussed by Denise (1983). Denise presents a numerical investigation to demonstrate that a linear potential-flow model can be inadequate because the draughts of many marine vehicles are of the same order of magnitude as the wave height. Thus, for large angle roll motions, the vessel keel edges can be displaced through large distances relative to the local wave fluid. The assumptions of linear theory are therefore violated and non-linear force mechanisms must be accounted for.

Denise asserts that by far the most significant non-linearity arises from wave structure interaction in the splash zone. An exact representation of this phenomenon is extremely difficult as it involves second or even third

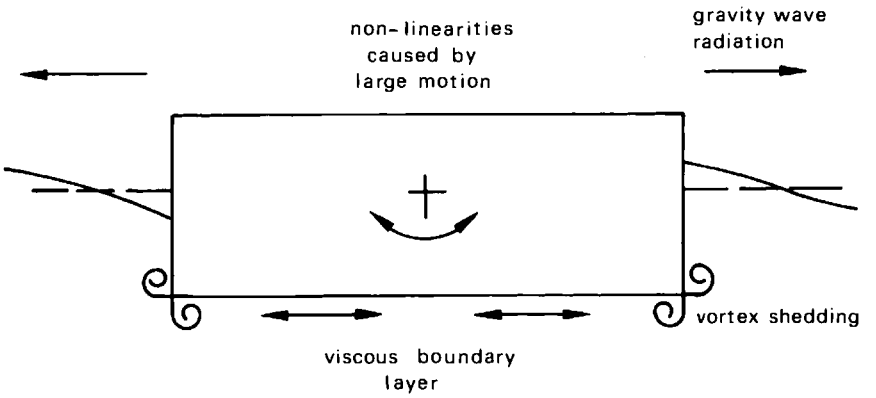

Figure 5.13. Flows associated with a barge in roll motion

order diffraction theory. Denise uses physically realistic assumptions in an attempt to predict the forces caused by non-linear effects. This yields additional force and moment terms in the equations of motion, referred to as the buoyancy restoring force and moment contributions. The buoyancy restoring moment, denoted here by M_{BRM}, is given as

$$M_{BRM} = \int_{S_0} \rho g \xi \, (\mathbf{r} - \mathbf{r}_g) \times \mathbf{n} dS + \int_{S} \rho g \, (\xi + z)(\mathbf{r} - \mathbf{r}_g) \times \mathbf{n} dS \tag{5.74}$$

where ξ is the instantaneous wave elevation, $\mathbf{r}$ is the position of a surface panel, $\mathbf{r}_g$ is the position of the centre of gravity, $\mathbf{n}$ is the unit outward normal, and z is measured vertically from still water level. The first integral is included to subtract the 'hydrostatic' contribution from the linear equation due to the existence of a finite amplitude wave crest and trough. This effect is already included in the second integral of Equation (5.74). In the first term of the expression, integration is performed over the submerged surface, S_0, up to still water level, corresponding to the body fixed in the static position but in the presence of waves. In the second integral the surface, S, corresponds to that of the instantaneous wetted body.

Denise solves the equations of roll motion, including the additional buoyancy restoring force and moment terms, and obtains reasonably good agreement with results of model tests. He concludes that the reductions in roll motion are due to these non-linearities causing a detuning at roll resonance, thus providing an explanation for the discrepancies between present roll motion prediction methods and experimental data. The non-linear effects as presented by Denise are used to deduce predictions for roll motions of the 1:36 scale model test barge described in the

preceding section. No specific calculations have been performed for the test model due to the complicated nature of the theoretical problem.

Another possible cause of the overprediction of roll motions by diffraction theory is the additional damping forces induced by vortex shedding. Attempts have been made to predict these forces by using point vortex distributions to simulate the physics. A brief summary of one typical method is presented below with further details given in Brown and Patel (1985).

The free shear layers that develop from the keel edges are theoretically modelled by point vortices placed in the flow at suitable positions close to the corners of a two dimensional wall-sided block representing the barge in cross-section. A transformation is used to project the exterior of the barge boundary onto a flat plane to simplify the positioning of image vortices in the flow. These image vortices are used to ensure the condition of no fluid flow through the body walls. The transformation from the physical (z) plane to the projected (λ) plane is given by

$$z = -\frac{2s}{\pi}[\sin^{-1}\lambda + \lambda(1 - \lambda^2)^{1/2}] \tag{5.75}$$

where $z(x + iy)$ and $\lambda(a + ib)$ are complex variables, and s is the half-beam of the vessel. In particular, the corners of the barge $z = \pm s + 0i$ transform into the points $\lambda = \pm 1 + 0i$.

A two dimensional oscillating irrotational base flow potential given by

$$w_1 = \frac{4s}{\pi}\lambda\,\theta_m\,\omega\,r\sin\omega t \tag{5.76}$$

for roll of amplitude θ_m, and frequency ω about the roll centre a distance r from the keel is used to represent the rolling motion of the vessel. It can be shown that the base flow potential given by Equation (5.76) satisfies conditions of zero flow at infinity and pure sinusoidal motion at the origin which is at the centre of the barge keel. Furthermore, Equation (5.76) gives realistic base flow velocities in the region of the barge keel edges for roll centres that lie above the barge keel. The vortex shedding model is stepped through time with increments dt, and point vortices are introduced into the base flow close to the points $\lambda = \pm 1$ at each time instant.

These vortices subsequently move under the influence of the base flow and other vortices and images in the flow field. The complex potential for a total of m vortices in the flow is given by

$$w_2 = -\frac{i}{2\pi}\sum_{i=1}^{m}[k_j\log(\lambda - \lambda_j) - k_j\log(\lambda - \bar{\lambda}_j)] \tag{5.77}$$

where k_j and λ_j are the strength and position of the jth vortex and an overbar represents a complex conjugate quantity. Note that Equations (5.75) and (5.76) apply in both the physical and transformed planes as complex potential is invariant with respect to orthogonal transformation.

The complex potential of the complete flow is thus given by

$$w(z) = w(\lambda) = w_1 + w_2 \tag{5.78}$$

Vortex strengths, k, are found by considering the rate of shedding of vorticity in the wake, as used by Stansby (1977) and others, giving

$$\frac{\delta k}{\delta t} = \tfrac{1}{2} U_s^2 \tag{5.79}$$

where U_s is the velocity at the shedding position. The vortex sheet is stepped through time using Eulerian first or second order schemes. For the pth vortex, positions at times $t + \mathrm{d}t$ are found from those at time t using

$$\left.\begin{aligned} \lambda_p(t + \mathrm{d}t) &= \lambda_p(t) + \frac{\mathrm{d}\lambda}{\mathrm{d}t}\lambda_p(t)\mathrm{d}t \\ \lambda_p(t + \mathrm{d}t) &= \lambda_p(t) + \tfrac{1}{2}\left[3\frac{\mathrm{d}\lambda}{\mathrm{d}t}\lambda_p(t) - \frac{\mathrm{d}\lambda}{\mathrm{d}t}\lambda_p(t - \mathrm{d}t)\right]\mathrm{d}t \end{aligned}\right\} \tag{5.80}$$

where $\mathrm{d}\lambda/\mathrm{d}t$ for the vortex is found from the equation of motion of the sheet given by

$$\frac{\mathrm{d}z}{\mathrm{d}t} z_p(t) = \overline{\left(\frac{\mathrm{d}w}{\mathrm{d}z}\lambda_p(t)\right)} \tag{5.81}$$

The term $\mathrm{d}w/\mathrm{d}z$ for the vortex is found from Equation (5.81) as

$$\frac{\mathrm{d}w}{\mathrm{d}z} = \frac{\mathrm{d}w}{\mathrm{d}\lambda}\lambda_p \left|\frac{\mathrm{d}\lambda}{\mathrm{d}z}\right|_{\lambda_p}_{z_p} - \frac{ik_p}{2\pi}\frac{\mathrm{d}^2\lambda(z_p)/\mathrm{d}z^2}{2\mathrm{d}\lambda(z_p)/\mathrm{d}z} \tag{5.82}$$

The last term of this expression arises because λ_p is a vortex position and not a general point in the flow field – for a further dicussion see Clements (1973).

The moment, **M**, induced on the rolling vessel due to the creation and motions of vortices is calculated from a numerical integration of the pressure, p, around the barge cross-section, S, at each time instant using

$$\mathbf{M} = \int_S p(\mathbf{r} \times \mathbf{n})\, L\, \mathrm{d}S \tag{5.83}$$

where $\mathbf{n}$ is the unit normal into the vessel which is of length L. The pressure is found from Bernoulli's equation as

$$p = -\rho\left[\tfrac{1}{2}(u^2 + v^2) + \partial\phi/\partial t\right] \tag{5.84}$$

where

$$\phi = \text{Real}\,\{w\} \tag{5.85}$$

and

$$(u^2 + v^2) = \left(\frac{\mathrm{d}w}{\mathrm{d}z}\right)\overline{\left(\frac{\mathrm{d}w}{\mathrm{d}z}\right)} \tag{5.86}$$

both of which may be obtained using Equation (5.78). Figure 5.14 shows the vortex positions from running the point vortex model for two cycles of vessel roll motion. After a vortex has been shed, a flow reversal leads to

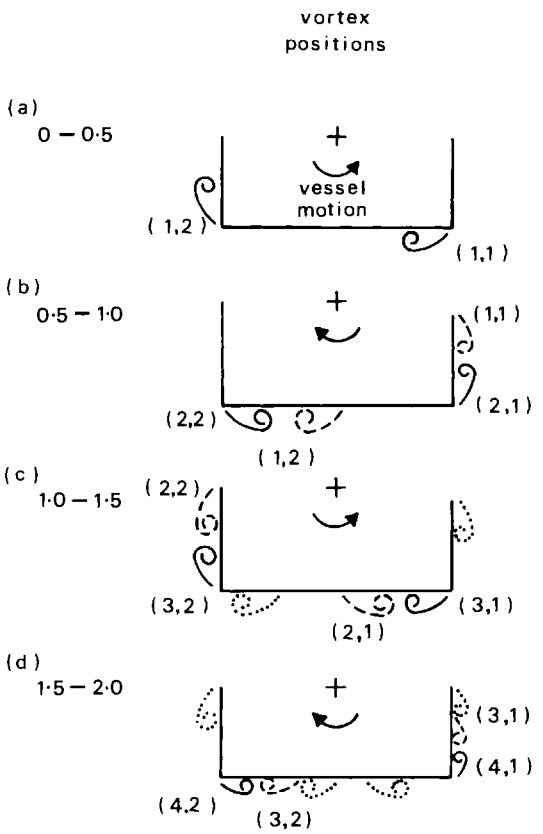

Figure 5.14. Motions at vortices shed from both barge corners over the first two cycles of vessel roll motion

this vortex being swept round the keel edge and a vortex of opposite sign is created on the second face, as shown in Figure 5.14(b). This process continues with the dominant force inducing vortex flow arising from the most recently generated vortices close to each keel edge. The resultant moment, M_{vs}, from integrating surface pressures can be non-dimensionalized by the factor M_D given by

$$M_D = \tfrac{1}{2}\,\rho\, U_m^2 S \tag{5.87}$$

where U_m is the base velocity at the centre of the keel. The functional dependence of M_{vs} obtained from the calculation can be written as

$$M_{vs} = -f_1(\theta_m)\, f_2(r/d)\exp[i(\omega t + \alpha)] \tag{5.88}$$

where α is the phase of the induced moment relative to the wave, and f_1 and f_2 are given by curve fitting to the linearized moment amplitudes close to roll resonance as

$$f_1(\theta_m) = 504.9\,\theta_m^2 - 37.03\,\theta_m + 0.877 \tag{5.89}$$

where θ_m is in radians, and

$$f_2(r/d) = 0.8187(r/d)^3 - 1.501(r/d)^2 + 1.299(r/d) - 0.3474 \quad (5.90)$$

Including (5.88) in the equation of roll motion and ignoring the effects of coupling with the sway mode gives

$$(I + I')\ddot{\theta}_{NL} + \beta\dot{\theta}_{NL} + S\theta_{NL} = a\,M_0 + M_{vs} \quad (5.91)$$

where I and I' are the vessel roll inertia and added inertia, β is the potential flow damping coefficient, S is the roll stiffness, a and M_0 are the wave amplitude and roll wave exciting moment respectively. Assuming harmonic roll motions of the form $\theta_{NL}e^{i\omega t}$ where θ_{NL} is complex allows the solution

$$\theta_{NL} = (a\,M_0 + M_{vs})/[S - \omega^2(I + I') + i\omega\beta] \quad (5.92)$$

A good estimate of M_0 may be obtained using potential flow calculations. Hence

$$\theta_0 = \frac{a\,M_0}{S - \omega^2(I + I') + i\omega\beta} \quad (5.93)$$

and

$$\theta_{NL} = \theta_0 + \frac{M_{vs}}{S - \omega^2(I + I') + i\omega\beta} \quad (5.94)$$

Equation (5.94) may be solved using (5.88) and noting that $|\,\theta_{NL}\,|$ is given by θ_m. Writing the denominator of the last term in Equation (5.94) as $(a + ib)$ allows simplification to

$$\theta_m \exp[i(\omega t + \alpha)] = |\,\theta_0\,| \exp[i(\omega t + \alpha)] - \frac{f_1 f_2}{a + ib} \exp[i(\omega t + \alpha)] \quad (5.95)$$

and hence

$$\theta_m = |\,\theta_0\,| - \frac{f_1 f_2}{(a^2 + b^2)^{1/2}} \exp[i(\alpha - \alpha_1 - \alpha_{ab})] \quad (5.96)$$

where α_{ab} is the argument of $a - ib$ and α_1 is the phase of the roll motion of the barge relative to the wave. It should be noted that the roll phases of the rounded and sharp keel edged vessels are taken to be identical to each other, the validity of this assumption again being confirmed by the results of experimental tests described in Brown *et al.* (1983). Equating the imaginary part of (5.96) to zero gives

$$\sin(\alpha - \alpha_1 + \alpha_{ab}) = 0 \text{ and } \alpha = \alpha_1 - \alpha_{ab} + n\pi \quad (5.97)$$

where n is an integer. Solving for the real part gives

$$\theta_m = |\,\theta_0\,| - f_1 f_2/(a^2 + b^2)^{1/2} \quad (5.98)$$

which is quadratic in θ_m. Hence (5.98) may be solved over a wave frequency range spanning roll resonance, assuming that the functional forms of f_1 and f_2 remain unaltered, to predict the additional reductions in

roll motion due to vortex shedding once the influence of other non-linear phenomena is known. Final results from the vortex shedding analysis are presented later in this section.

Skin friction induced forces on the surface of a ship shape can be readily calculated using the procedures suggested by Schlichting (1968) and Curle (1962). However, the resultant roll damping moments are very small in magnitude and cannot account for the discrepancy between calculated and measured roll angles observed in Figure 5.11.

It is now worth while testing the two remaining possible roll damping mechanisms of higher order roll damping and vortex induced effects against the model test data presented in Figure 5.11. Close to the roll resonant frequency of 6 rad/s, the theoretical estimates overpredict the experimental values by a significant amount. This discrepancy is particularly large for the motions of the barge fitted with sharp keel edges, the potential flow roll estimates being over twice the magnitude of the measured values. The resonant roll motions of the vessel fitted with rounded keel edges are higher than those for the vessel fitted with sharp edges, although they are still significantly lower than the theoretical estimates. It is reasonable to suppose that the tests with the rounded keel edge profile did not trigger any significant effects due to flow separation and consequent vortex shedding. The difference between the linear potential flow theory and round keel edge data must, therefore, be due to higher order potential wave loading. Furthermore, the differences between the data for rounded and sharp keel edge profiles are likely to be entirely due to vortex shedding effects.

Table 5.4 presents the further reductions in regular wave resonant roll motions of the rounded keel edged vessel if vortices were present in the flow, using the vortex shedding theory described earlier. The results are compared with the resonant roll motions of the 1:36 scale sharp keel edge barge. The experimental values $|\theta_r|$ and $|\theta_s|$ indicate that the vessel fitted with sharp keel edges rolls as much as 54% less at resonance than that with rounded keel attachments, both vessels responding to identical sea states.

Table 5.4 Theoretical estimates for reductions in resonant roll motions due to vortex shedding

No.	*Roll centre r/d*	*Wave freq.* ω (rad/s)	*Wave amp.* (cm)	$\lvert\theta_r\rvert$ (deg)	$\lvert\theta_s\rvert$ (deg)	γ_1 (%)	θ_m	γ_2 (%)
1	3.2	5.96	1.33	6.80	3.33	51.0	3.21	52.8
2	3.2	5.96	1.65	7.17	3.91	45.4	3.29	54.0
3	3.2	6.07	1.88	9.11	4.18	54.1	3.68	59.6
4	3.2	5.91	1.90	8.85	4.47	49.5	3.64	58.8

Notes:
$|\theta_r|$: rounded keel edge (1:36 scale barge) roll motion amplitude.
$|\theta_s|$: sharp keel edge (1:36 scale barge) roll motion amplitude.
θ_m: rounded keel edge (1:36 scale barge) + vortex shedding adjustment roll motion amplitude

$$\gamma_1 = \frac{|\theta_r| - |\theta_s|}{|\theta_r|} \times 100\% \qquad \gamma_2 = \frac{|\theta_r| - \theta_m}{|\theta_r|} \times 100\%$$

The theoretical model of vortex shedding applied to the rounded keel edge wave exciting roll moment data as a starting point, but using a roll centre position of $r/d = 3.2$ (corresponding to that measured for the sharp keel vessel), predicts roll motions that are in good agreement with experimentally measured values for the sharp keel edged barge.

It is clear that calculation of roll motion reductions due to vortex shedding requires knowledge of the roll centre position of the vessel in the first place. However, the roll centre cannot be calculated unless the motions of the vessel, including the influence of vortices, are known. This problem is common in many areas of fluid mechanics where separate calculation of the far field inviscid flow and the near field viscous flow leaves the interaction between the two to be included in the analysis. From a strictly academic viewpoint, the interaction needs to be included by incorporating the vortex shedding effects (and those due to the non-linear loading mechanism described earlier) in an extended formulation of the diffraction problem. The motion response analysis that would follow from solution of the diffraction plus vortex shedding forces could then be used to derive motions without prior knowledge of the roll centre position.

However, in order to allow the vortex shedding theory to be used in its present form, it needs to be applied to the rounded keel edge wave exciting roll moment data as a starting point, together with a roll centre position of $r/d = 1.4$, corresponding to that measured from the rounded keel edge tests. This roll centre position is expected to be close to that derived from applying the 'buoyancy restoring moment' non-linearity described earlier so that the theoretically derived value could be used instead.

The roll motion reductions obtained for this case are presented in Figure 5.15. Theory predicts a reduction in resonant roll motion of 28% due to the presence of vortices, whereas measured resonant roll motions for the sharp keel edged vessel are 33% less than the rounded keel edge values. Away from resonance, the experimental data are in reasonable agreement with each other and with predicted values since vortex shedding and non-linear 'buoyancy restoring moment' effects are small due to the much decreased roll amplitudes here.

It is clear from the above that resonant roll motions of ship shape hull forms are influenced by several physical mechanisms in addition to those modelled by linear potential flow theory. For a vessel with well rounded keel edges, skin friction effects appear to be negligibly small but the roll motions for such a vessel are still substantially modified by non-linear wave loading induced by large roll motions. For a vessel with right angled keel edges (equivalent to bilge keels), vortex shedding also contributes to a significant further reduction in roll motion at resonance. This physical mechanism clearly appears as an equivalent damping contribution with the expected large reduction in peak roll angle and a much smaller reduction in the natural frequency as damping increases.

5.5 Design considerations and operability

Ultimately, the analysis methods outlined in the earlier sections of this chapter have to be applied to design floating vessels with sufficient

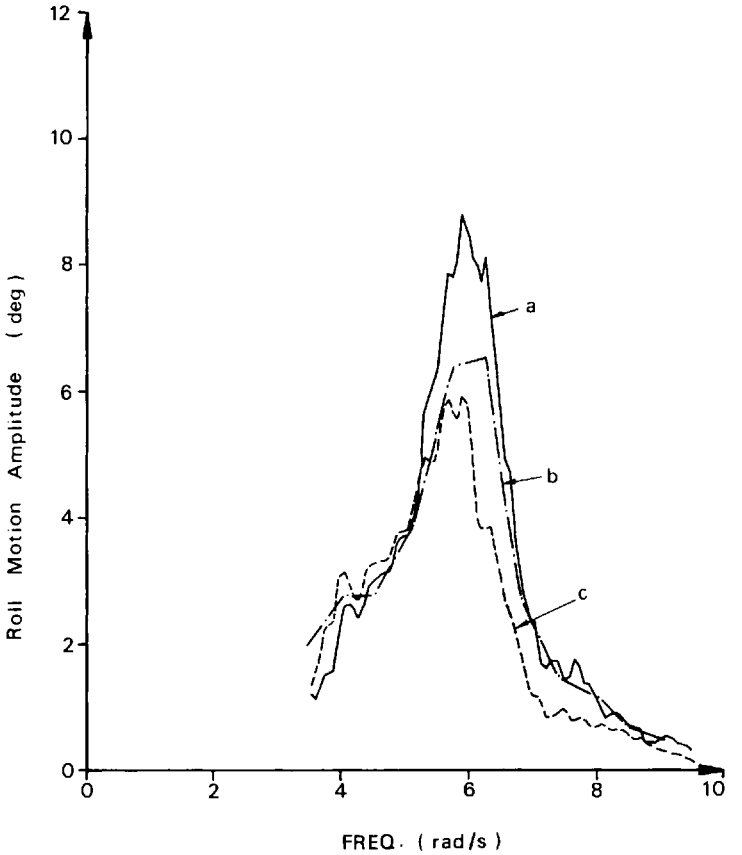

Figure 5.15. Theoretical estimates of reductions in roll due to vortex shedding applied to rounded keel HRS barge compared with sharp keel results (wave amplitude = 1.9 cm). *Key*: a – rounded keel-edge experimental data ($|\theta_r|$); b – sharp keel-edge experimental data ($|\theta_s|$); c – rounded keel-edge experimental data and vortex shedding (θ_m)

operability in ocean environments. Apart from payload capability and low wave induced motions which can be deduced from the hydrostatic and hydrodynamic analysis methods described earlier, the effectiveness of the vessel is also governed by sea worthiness in storms, mooring system integrity, structural strength and fatigue life considerations. These and other features that govern the successful use of a floating vessel are illustrated in this section by examining the performance of a monohull oil production vessel shown in Figure 5.2. The vessel is moored with lines attached to a turret just forward of midships so that the vessel weather vanes. The riser consists of a flexible bundle running from the turret to a submerged tension leg assembly which in turn connects to the manifold on the sea bed.

The vessel houses all the necessary facilities to maintain oil production. It has sufficient oil storage capacity to maintain at least seven days of production at the minimum installed production rate of 40 000 bbls/day.

Oil export is achieved via a loading arm which extends from the barge to a shuttle tanker.

The leading dimensions of the vessel are:

Overall length	231 m
Beam	36 m
Depth (deck to keel)	21 m
Operating draught range	5–16 m
Displacement (in sea water) at the maximum operating draught of 16 m	124 037 t

Limited analyses for vessels of lengths other than 231 m are also presented.

The vessel's hull is similar to that of a large crude carrier with the oil storage tanks located aft of the turret mooring. The turret mooring is located 19.5 m forward of midships (42% of the vessel's length from the bow).

However, these design features do have their complications. The use of a turret mooring does require a complex structure near the vessel's midships where maximum wave induced bending moments are likely. This may lead to structural problems in certain sea states. In addition, the effect of non-uniform loading of the vessel associated with oil storage may introduce high static bending moments which will result in a large and expensive structure. These features are examples of problems that will need to be investigated further.

The distribution of weight within the unit is such that the monohull maitains a 4000 t variable deck payload capacity, together with large fuel oil and fresh water capacities. This allows continuous operation with relatively infrequent supply intervals.

The vessel's general tank arrangement is designed so that perimeter tanks are for ballast and are generally full for all vessel operating conditions. This feature of maintaining full ballast tanks on the perimeter of the vessel serves two purposes:

1. It minimizes the effect of damage in the form of hull penetration on the vessel's stability.
2. The perimeter tanks protect the oil tanks and reduce the risk of pollution and fire as a consequence of damage to the hull.

Ballast tanks are also located at the stern and bow of the unit in order to facilitate trimming of the vessel. The overall process scheme for the unit is designed so that the oil, gas and water components are first separated using a single train process with three separation stages. Excess gas production may be flared if necessary. Produced water is also treated to suitable pollution control standards and then discharged. Alternatively, the produced water may be used for water reinjection. The additional amount of water required for water injection is obtained by lifting and treating sea water. The crude oil production is metered and then either exported immediately or stored in the lower hull oil tanks for later shipment.

The process equipment is located on the main and lower decks, aft of the mooring turret (away from ship utilities and housing quarters) with process items that involve liquid–liquid interfaces such as separators, and oil and water treaters placed as close as possible to the vessel's centre of gravity

with their longitudinal axes parallel to the axis of least significant rotational motion. The limiting motions for process equipment operation are taken as:

Rotational motion	12° double amplitude
Heave displacement	10 m double amplitude
Lateral accelerations	0.2 g m/s^2

The vessel is designed to operate with a range of draughts from 5 to 16 m and maintains adequate initial stability in the above range.

The vessel is turret moored by a system of eight mooring lines. The layout is designed to withstand 100 year storm conditions for a range of water depths from 30 m to 200 m. The mooring lines and associated equipment have the following physical characteristics.

An eight leg system of 89 mm (3.5 inch) diameter and 2.14 m (84.5 inch) gauge length oil rig quality (ORQ) chain having a breaking strength of 6156 kN (1383 kips) and a weight per unit length in air of 1784 N/m (122.2 lb/ft) and 1551 N/m (106.2 lb/ft) in sea water. Each anchor is of the flipper delta high holding type and weighs approximately 15 t.

The applicability of the monohull design is assessed at five depths corresponding to sites A to E as shown below.

Site	*Location* (North Sea)	*Water depth (LAT)*
A	lat 53° 18′N long 3° 45′E	35.0 m
B	lat 56° 12′N long 0° 44′E	79.2 m
C	lat 57° 30′N long 0° E	110.0 m
D	lat 61° 5′N long 1° 24′E	147.0 m
E	lat 61° 20′N long 0° E	170.0 m

These sites correspond to a range of North Sea locations with latitudes of 53° N to 63° N and typify the environmental conditions associated with these geographical locations. Some environmental data is common to all sites reflecting general North Sea conditions. Oilfield data and production requirements are typical of many hydrocarbon accumulations currently being discovered.

The principal aspects investigated for applicability of the monohull floating production system are the mooring system, operability, vessel loading and fatigue.

The mooring pattern has been designed to incorporate a wide 'corridor' for the flexible riser, which is deployed so that mooring lines will not interfere with it and the subsea buoy. The 'worst-case' weather situation is when the wind, current and wave forces apply colinearly in the direction that bisects the riser corridor. Under these circumstances, the vessel rotates on the turret until it is predominantly in head seas. The mooring forces when the vessel is subjected to 100 year storms for this 'worst-case' weather situation have been calculated using a quasi-static mooring analysis (Patel, 1989). The analysis calculates mooring line tensions and vessel restoring forces using the catenary equations. An initial line pretension angle to the horizontal of 50° is assumed. Horizontal vessel

motions due to waves are calculated by linear diffraction analysis and maximum vessel offset and line tension (quasi-static summation of static and dynamic effects) are estimated.

The vessel's operability limits are calculated in terms of significant wave heights of long crested irregular waves of typical sea spectra. The maximum allowable process plant motion or acceleration values are converted to maximum allowable significant motion or accelerations. These are then used with the irregular wave short term response amplitude operator at the appropriate water depth to yield the maximum allowable significant wave height for vessel operations.

To calculate monthly operability for the vessel, weather data have been collected from environmental study reports available for locations close to those defined earlier. In particular, 'average year' monthly significant wave height percentage exceedence figures are documented. Using the weather data together with the maximum operational wave height limits allows the monthly percentage operability at each of the five locations to be determined.

To calculate the overall strength of the vessel and stress range at critical longitudinal positions, it is necessary to estimate the vertical static and hydrodynamic forces acting along the vessel's length. This has been carried out by dividing the vessel into stations, each approximately 6 m long, from stern to bow. Hence the hydrostatic and hydrodynamic load, shear and bending moment values are found at each section and their distribution along the vessel is established. These calculations have been carried out for the fully laden vessel with a draught of 16 m only.

To calculate structural integrity and fatigue life, weather data are required for each of the five locations. In particular the maximum design wave height is needed so that strength requirements may be satisfied, and the distribution and occurrence of wave heights and associated wave periods is required so that fatigue lives may be estimated.

The vessel structural strength is estimated using a maximum permissible bending stress, σ_m, giving the minimum required section modulus, S, as

$$S = \frac{(M_s + M_d)}{\sigma_m} F \tag{5.99}$$

where M_s is the maximum static moment experienced by the vessel, M_d is the maximum moment induced by design wave conditions, and F is an appropriate factor of safety.

The fatigue life of the vessel is calculated for operations at each of the five locations in head, quartering and beam seas, at two positions on the vessel's longitudinal axis, one at the centre line and the other at the mooring turret. The stress range, σ_r, experienced by the vessel to waves of period, T, is calculated from the equation

$$\sigma_r(T) = \frac{M_D(T)\, H\, K}{S} \tag{5.100}$$

where S, is found from Equation (5.99) and K is a stress concentration factor appropriate to the position on the vessel. The dynamic bending moment, M_D, to waves of unit amplitude and period, T, is found once the

annual occurrence of wave period, T, and height, H, for each North Sea location is established. Once the stress range is known a suitable S–N curve may be used to estimate the number of cycles of loading, N_c, required to fatigue the vessel at that stress range. The cumulative damage caused by cyclic loading from waves of various periods can be calculated from a simplified form of Miners' rule given by

$$Y \Sigma (N_a/N_c) = 1 \tag{5.101}$$

where Y is the fatigue life in years, N_a is the number of cycles encountered and summation is performed for all stress ranges experienced annually.

It is noted that the method used to estimate fatigue life is based on highly simplified analysis methods. In a detailed design scenario extensive calculations of a more rigorous nature must be performed. However, the method outlined above gives representative trends for the relative fatigue life of the monohull at different locations.

Figure 5.16 illustrates monthly percentage operability plotted against water depth. As expected, the percentage operability reduces significantly for deep water North Sea latitudes. These operability figures when translated to loss of revenue due to down-time indicate that an accurate assessment of the monthly operability is critical to estimate the feasibility of a monohull, particularly in deeper water.

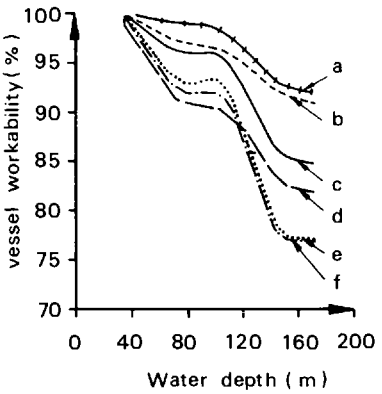

Figure 5.16. Vessel workability against depth for monohull floating production system in head seas. *Key*: a – July; b – May; c – September; d – November; e – January; f – March

Fatigue lives are presented in Table 5.5(a) for the vessel responding in head, quartering and beam seas at each of the five locations. Values have been non-dimensionalized so that results for location E (the deepest and most northerly) are unity, emphasizing the relative magnitudes at different locations. Care should be taken when interpreting the results in Table 5.5(a). In particular, relative fatigue lives should be compared for different locations with the vessel at one heading only – quartering seas, for example. Table 5.5(a) indicates that fatigue life increases as water depth decreases for all three vessel orientations to the waves. The most significant differences occur with the vessel head-on to the wave direction, the fatigue lives being 15 times higher at the shallow water location.

Fatigue life data non-dimensionalized by the head sea values are also presented in Table 5.5(b). The results for locations D and E indicate that the fatigue life of the vessel is approximately five times higher in quartering

Table 5.5 Fatigue life estimates

(a) Non-dimensionalized by location E values

Vessel location	*Depth* (m)	*Position*	*Fatigue life (non-dim)*		
			Head	*Quar.*	*Beam*
A	35.0	Midships	15.8	5.2	6.2
53° 18′N, 3° 45′E		Turret	14.8	4.6	5.9
B	79.0	Midships	2.8	1.8	2.0
56° 12′N, 0° 44′E		Turret	2.8	1.7	1.9
C	110.0	Midships	2.6	1.7	1.8
57° 30′N, 0° 00′E		Turret	2.5	1.7	1.9
D	147.0	Midships	1.0	1.0	1.0
61° 05′N, 1° 24′E		Turret	1.0	1.0	1.0
E	170.0	Midships	1.0	1.0	1.0
61° 20′N, 0° 00′E		Turret	1.0	1.0	1.0

(b) Non-dimensionalized by head sea values

Vessel location	*Depth* (m)	*Position*	*Fatigue life (non-dim)*		
			Head	*Quar.*	*Beam*
A	35.0	Midships	1.0	1.6	0.7
53° 18′N, 3° 45′E		Turret	1.0	1.6	0.4
B	79.0	Midships	1.0	3.2	1.4
56° 12′N, 0° 44′E		Turret	1.0	3.3	0.7
C	110.0	Midships	1.0	3.3	1.4
57° 30′N, 0° 00′E		Turret	1.0	3.4	0.8
D	147.0	Midships	1.0	4.9	2.0
61° 05′N, 1° 24′E		Turret	1.0	5.2	1.1
E	170.0	Midships	1.0	4.9	2.0
61° 20′N, 0° 00′E		Turret	1.0	5.2	1.1

seas than head seas. As fatigue lives could be a problem at these deep water locations it would be advantageous to operate a vessel of 213 m length in quartering seas rather than head seas if fatigue life was of major concern. At the shallow water locations the structural integrity of the vessel is such that fatigue lives are high and the effect of wave directionality is not significant.

These results indicate that fatigue life is a crticial parameter in the design of a monohull Floating Production System, particularly at the deeper water locations of the North Sea. Although the weather vaning ability of the vessel leads to reduced motions and environmental loads, operating the vessel in head seas considerably reduces the fatigue life in deep water locations.

A short study was also carried out to indicate the strong influence on fatigue life of vessel length, by estimating the fatigue lives at the centre section of five monohull floating production systems. The vessels are of equal breadth and depth but vary in length from 120 m to 380 m, and corresponding displacements of 58 500 to 212 000 t.

Figure 5.17 shows the variation of fatigue life with water depth in head seas. The data presented have been non-dimensionalized with respect to the vessel of 231 m length. This vessel has the lowest fatigue life at all water depths because its length is equal to that of frequently occurring waves causing excessive hogging/sagging. Note that vessel 1 has a fatigue life factor greater than 12 and hence does not appear in Figure 5.17.

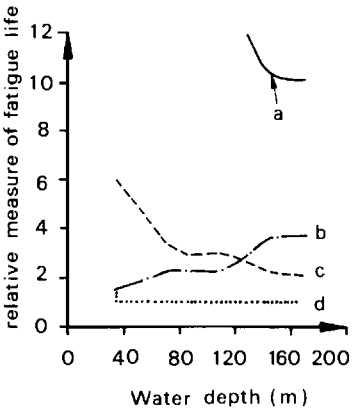

Figure 5.17. Vessel relative fatigue life against depth for monohull floating production system in head seas (data unitized by values for vessel 3). *Key*: a – Vessel 5 (length = 380.0 m); b – Vessel 2 (length = 170.0 m); c – Vessel 4 (length = 300.0 m); d – Vessel 3 (length = 231.0 m)

5.6 Concluding remarks

The methods of analysis given in this chapter and the corresponding effects on vessel structural strength and fatigue life are now sufficiently well proven in comparison with model tests and full scale data to form a reliable basis for engineering design. Both Morison based and diffraction analyses of floating vessels have been researched in depth for first order effects, and attention is now increasingly being focused on second order aspects of vessel interactions with waves – these latter effects are not considered here. One additional feature of first order vessel response that requires further work is the motion and structural response of floating vessels to directional seas. Although the theoretical basis of such methods is well understood, if linearity is assumed for first order calculations, not enough work has been done on producing analysis methods which can be used for design. Yet comparison of full scale data with predictions from the above theories indicates that wave directionality plays an important role in obtaining good agreement between reality and theory.

References

Brown, D. T., Eatock Taylor, R. and Patel, M. H. (1983) Barge motions in random seas – a comparison of theory and experiment. *Journal of Fluid Mechanics*, **129**, 385–407

Brown, D. T. and Patel, M. H. (1985) A theory for vortex shedding from the keels of marine vehicles. *Journal of Engineering Mathematics*, **19**, 265–295

Bryan, G. H. (1900) The action of bilge keels. *Transactions of the Institute of Naval Architects*, **42**, 198

Burke, B. G. (1969) The analysis of motions of semisubmersible drilling vessels in waves. OTC 1024, May

Clements, R. R. (1973) An inviscid model of two dimensional vortex shedding. *Journal of Fluid Mechancis*, **57**, 321–336

Curle, N. (1962) *The Laminar Boundary Layer Equations*, lst edn. Clarendon Press, Oxford, England

Dalzell, J. F. (1978) A note on the form of ship roll damping. *Journal of Ship Research*, **22**, 178–185

Denise, J.- P. F. (1983) On the roll motion of barges. *RINA Suppl. Paper*, **125**, 255, July

Det Norske Veritas (1981) Rules for the classification of mobile offshore units

Eatock Taylor, R. (1982) Analysis of hydrodynamic loads by boundary element methods. In *Developments in Boundary Element Methods – 2* (eds. P. K. Banerjee & R. P. Shaw), p. 211. Applied Science Publishers

Eatock Taylor, R. and Waite, J. B. (1978) The dynamics of offshore structures evaluated by boundary integral techniques. *International Journal of Numerical Methods in Engineering*, **13**, 73–92

Eatock Taylor, R. and Zietsman, J. (1981) Implementation of coupled formulations for hydrodynamic analysis in three dimensions. In *Numerical Methods for Coupled Problems* (eds. E. Hinton, P. Bettess & R. W. Lewis), p. 281, Pineridge

Froude, W. (1874) On the resistance in rolling of ships. *Naval Science*, **3**, 312

Garrison, C. J. and Chow, P. Y. (1972) Wave forces on submerged bodies. *Journal of Waterways, Harbours and Coastal Division*, ASCE, **98**, WW3, 375–392

Gawn, R. W. L. (1940) Rolling experiments with ships and models in still water. *Institute of Naval Architects*, **82**, 46–48

Hooft, J. P. (1971) A mathematical method for determining hydrodynamically induced forces on a semisubmersible. Presented at the Annual Meeting of The Society of Naval Architects and Marine Engineers, New York, 11–12 November

Ikeda, Y., Himeno, Y. and Tanaka, N. (1978) A prediction method for ship roll damping. *Department of Naval Architecture, University of Osaka, Japan, Report No. 00405*

Ikeda, Y., Himeno, Y. and Tanaka, N. (1977) On eddy making component of roll damping force on naked hull. *Journal of the Society of Naval Architects Japan*, **142**, 54

John, F. (1950) On the motion of floating bodies. II. *Communications in Pure and Applied Mathematics*, **3**, 45

Kaplan, P., Jiang, C. W. and Bentson, J. (1982) Hydrodynamic analysis of barge-platform systems in waves. RINA Spring Meeting, Paper 8

Kato, H. (1958) On the frictional resistance to rolling of ships. *Society of Naval Architects, Japan*, **102**, 115

Keuning, J. A. and Beukelman, W. (1979) Hydrodynamic coefficients of rectangular barges in shallow water. *Paper 55, BOSS'79*, Imperial College of Science and Technology, pp. 105–124

Lamb, H. (1975) *Hydrodynamics*, 6th edn. Cambridge University Press, Cambridge

Martin, M. (1958) Roll damping due to bilge keels. *Iowa Institute of Hydraulic Research, Contract Nr. 1611 (01), November*

Matsushima *et al.* (1982) Seakeeping of a Semisubmerged Catamaran (SSC) Vessel. *Journal of the Society of Naval Architects of West Japan*, March

Mei, C. C. (1978) Numerical methods in water wave diffraction and radiation. *Annual Review of Fluid Mechanics*, **10**, 393

Morison, J. R., O'Brian, M. H., Johnson, J. W. and Schaaf, S. A. (1950) The forces exerted by surface waves on piles, *Petroleum Transaction, AIME*, **189**

Murphy, J. E. (1978) Integral equation failure in wave calculations. *Journal of Waterways, Port, Coastal and Ocean Division*, **104**, WW4, 330–334

Natvig, B. J. and Pendered, J. W. (1977) Nonlinear motion response of floating structures to wave excitation. OTC 2796, May

Newman, J. N. (1962) The exciting forces on fixed bodies in waves. *Journal of Ships Research*, **6**, 10–17

Newman, J. N. (1977) *Marine Hydrodynamics*. MIT Press

Ochi, M. K. and Vuolo, R. M. (1971) Seakeeping characteristics of a multi-unit ocean platform. Presented at the Spring Meeting of The Society of Naval Architects and Marine Engineers, Honolulu, 25–28 May

Oo, K. M. and Miller, N. S. (1977) Semisubmersible design: the effect of differing geometries on heaving response and stability, *Transactions of the RINA*, **119**, 97–119

Opstal, G. H. C. van, Hans, D., Salomons, J. W. and Vlies, J. A. van der (1974) MOSAS: A motion and strength analysis sytem for semisubmersibles and floating structures. OTC 2105, May

Patel, M. H. (1989) *Dynamics of Offshore Structures*, Butterworths, London, 392 pp.

Patel, M. H. and Badi, M. N. M. (1980) A calculation method for the wave induced motion response of a semisubmersible vessel – program manual for UCLRIG, *Department of Mechanical Engineering, University College London, Report No. OEG/80/6, July*

Paulling, J. R. (1974) Elastic response of stable platform structures to wave loading. *Proceedings of the International Symposium on the Dynamics of Marine Vehicles and Structures in Waves, Paper 25*, pp. 249–261

Pederson, B., Egeland, O. and Langfeldt, J. M. (1974) Calculation of long term values for motions and structural response of mobile drilling rigs. OTC 1881, May

Pinecemin, M., Planeix, J. M., Huard, G., Dupuis, G. and Duval, G. (1974) An integrated program for the dynamic structural calculation of mobile offshore units. OTC 2052, May

Salvesen, N., Tuck, E. O. and Faltinsen, O. (1970) Ship motions and sea loads. *Transactions of the Society of Naval Architects and Marine Engineers*, **78**, 421

Schlichting, H. (1968) *Boundary Layer Theory*, 6th edn. McGraw-Hill, NY

Shaw, R. P. (1979) Boundary integral equation methods applied to wave problems. In *Developments in Boundary Element Methods – 1* (eds. P. K. Banerjee and R. Butterfield), p. 121, Applied Science Publishers

Sommerfield, A. (1949) *Partial Differential Equations in Physics*. Academic Press, NY, USA

Stansby, P. K. (1977) An inviscid model of vortex shedding from a circular cylinder in steady and oscillatory far flows. *Proceedings of the Institute of Civil Engineers*, **63**, 865–880, December

Stewart, W. P., Ewers, W. A. and Denton, P. J. (1979) Nonlinear barge motion response. Use of physical models in the design of offshore structures. *Paper 23*, Garston, Watford, England

Stoker, J. J. (1957) *Water Waves*, Interscience, NY, USA

Takagi, M., Arai, S., Takezawa, S., Tanaka, K. and Takarada, N. (1985) A comparison of methods for calculating the motion of a semisubmersible. Ocean Engineering. Also in 17th International Towing Tank Conference Report of the Ocean Engineering Committee, 1984

Tanaka, N. (1960) A study of bilge keels (Part 4, On the eddy-making resistance to the rolling of a ship hull). *Society of Naval Architects, Japan*, **109**, 205–212

Tasai, *et al.* (1970) A study on the motion of a semisubmersible catamaran hull in regular waves. *Journal of the Society of Naval Architects of West Japan*, July

Ursell, F. (1981) Irregular frequencies and the motion of floating bodies. *Journal of Mechanics*, **105**, 143

Wehausen, J. V. and Laitone, E. V. (1960) Surface waves. In *Handbuch der Physik*, ed. S. Flugge, Springer-Verlag, Berlin, Vol IX, pp. 446–778 (p. 478)

White, Sir W. (1895) Notes on further experience with first class battleships. *Transactions of the Institute of Naval Architects*, **36**, 127

Chapter 6

Tensioned buoyant platforms

6.1 Introduction

The difficulties of mooring floating platforms by catenary lines, described in the preceding chapter, and the operational need for the virtual elimination of platform vertical motions, has led to the development of platforms moored to the sea bed by vertical tethers which are maintained taut and at high tension by excess buoyancy in the surface platform. This class of floating structures is referred to variously as tension buoyant platforms (TBPs), tension leg platforms (TLPs), vertically moored platforms and tethered production platforms.

The vertical mooring tethers of a TBP introduce a design feature which makes the surface platform highly compliant to horizontal surge and sway wave forces and yaw moments. This ensures that the TBP's natural periods in surge, sway and yaw are well above the range of predominant wave periods. At the same time, the vertical tethers introduce high stiffnesses in heave, roll and pitch which serves to virtually eliminate these modes of motion and also shorten natural periods in these degrees of freedom to be below the periods of predominant wave action.

These characteristic features of the motion of a TBP in waves leads to a number of merits and drawbacks for their use as floating production platforms. The suppression of vertical motion by the tether mooring system provides a stable operating base and simplifies accessibility to sea bed well heads and equipment. The tethered nature of the floating platform also makes its cost less sensitive to water depth, enables early oil production and reduces field abandonment costs. The TBP design also allows for fabrication and outfitting to be completed in a construction yard or inshore location prior to installation. Set against these advantages are the drawbacks of the TBP which requires foundations capable of withstanding large vertically upward forces, coupled with the fact that high tether stresses require careful design and maintenance of these components. A TBP is also more sensitive to mass distribution changes and introduces significant operational limits on total payload.

It is worth providing a brief historical overview of TBP development here. Following the pioneering work of Paulling and Horton (1970), the first sea going prototype was installed offshore Santa Catalina Island, California in 1975 by Deep Oil Technology Inc. (*Oil and Gas Journal*,

1975). The platform was installed in 61 m (200 ft) of water and is shown in Figure 1.7. Tests in a variety of sea states were carried out on this platform in 1975 and 1978. The platform structure and details of these tests are described in a later part of this section.

Two similar moored platform designs were also developed and small scale test structures were installed in offshore locations. Macdonald (1974) describes the installation of a 120 t fully restrained (in all six degrees of freedom), moored structure off the west coast of Scotland between 1963 and 1965. A design similar to that of a TBP was installed in the 1960s by Mitsubishi Heavy Industries of Japan. Since then a large number of engineering and analytical investigations have been carried out on TBP designs. Perret and Webb (1980), Addison and Steinsvik (1976), Roven and Steinsvik (1977), Yashima (1976), Albrecht *et al.* (1978), Capanoglu (1979), Lonergen (1979, 1980), Kitami *et al.* (1982), and Tassini and Panuzzolo (1981) describe a number of engineering studies.

These engineering studies culminated in the decision by Conoco in 1979 to build the first production TBP for drilling and production of hydrocarbons – the site being the North Sea Block 211/27 known as Hutton. This is a location with a water depth of 147 m where a conventional fixed structure would have been adequate. However, it was decided that this would be an opportunity to gain the necessary experience for such a radically different design of platform (TBP) before attempting its use in deeper waters where its application was envisaged. This TBP is known as the Conoco Hutton Platform, Figure 6.1 and Table 6.1 – see Mercier (1982). It produced its first oil in August 1984.

Moving on from the historical overview given above, many research workers have contributed to an understanding of the analysis methods suitable for predicting the behaviour of TBPs. Some of the more notable contributions are reviewed below.

Paulling and Horton (1970) carried out pioneering work on TBPs. They compared a theoretical analysis with experiments at a notional scale of 1/50th on a model platform of three leg configuration. The variation of measured tension amplitude with wave height exhibited non-linear behaviour, although surge motions were shown to behave in a nearly linear fashion. Comparison of model test data with the theoretical solution using quadratic drag coefficients of 1.0 and 1.5 gave a better fit in surge for the higher coefficient. Better agreement with theory was obtained for the tension in the leg at the apex than tensions in the symmetric pair of legs in the base which were underestimated.

The theory utilized linear superposition by considering the structure as an assembly of simple bodies whose individual hydrodynamic properties were known. It was assumed that the hydrodynamic force on the assembled structure was equal to the sum of the forces on the component bodies. The platform dynamic behaviour was assumed to be linear and small amplitude linear wave theory was employed. The quadratic drag force was replaced by an 'equivalent linear' drag force defined as the linear drag force which dissipates the same energy per cycle as the quadratic force, given by

$$C_{DL} = \frac{8\,U_0}{3\pi} C_{DQ} \tag{6.1}$$

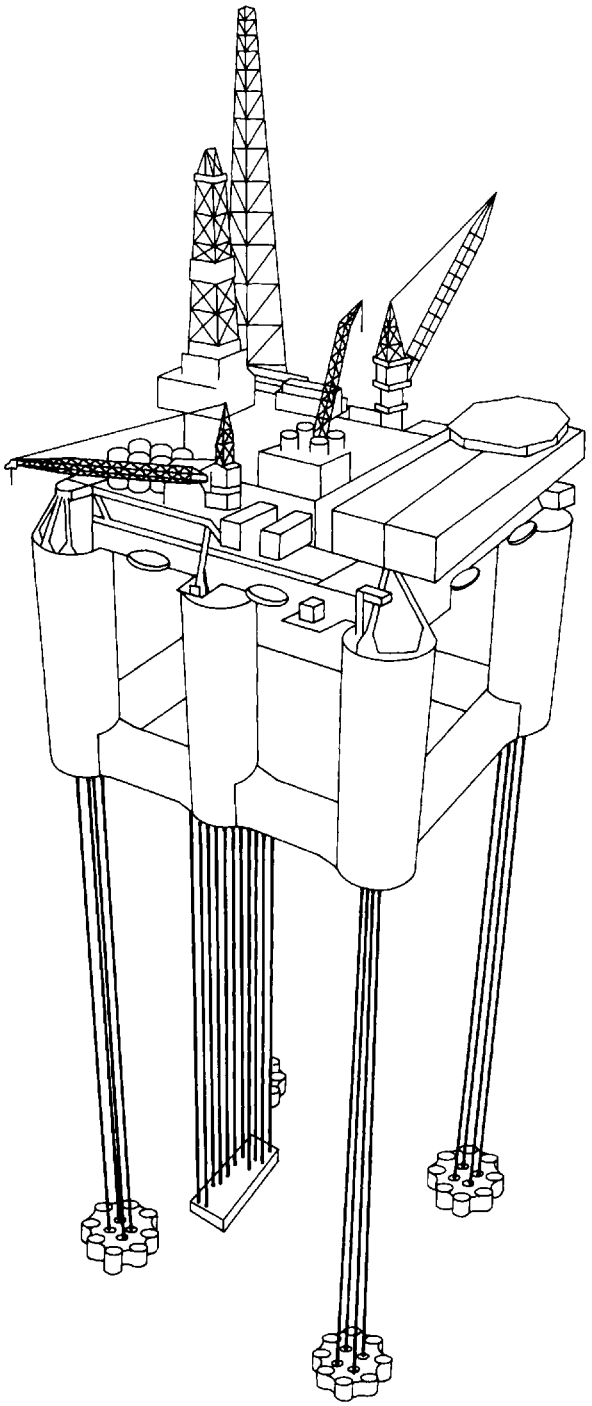

Figure 6.1. Tension leg platform for Hutton Field

Table 6.1 Hutton TBP – principal particulars

Dimensions		
Length	– between column centres	78.0 m
	– overall	95.7 m
Breadth	– between column centres	74.0 m
	– overall	91.7 m
Depth	– keel to weather deck	69.0 m
	– keel to main deck	57.7 m
	– deck	12.5 m
Freeboard	– to underside of deck at MWL	23.3 m
Columns	– 4 corners	17.7 m
	– 2 centre	14.5 m
Pontoons	– height	10.8 m
	– width	8.0 m
Operating conditions		
Draught at MWL		32.2 m
Displacement at MWL		63 300 t
Tension leg pretension at MWL		15 000 t

where C_{DL} and C_{DQ} are the linear and quadratic drag coefficients respectively; and U_0 is the amplitude of the periodic fluid velocity.

The tether legs were considered as simple elastic lines with natural frequencies far removed from wave and structural natural periods. Paulling and Horton considered that the assumption of constant drag and added mass coefficients throughout the structures for all wave frequencies yielded results which were sufficiently accurate for most design purposes. However, a systematic prediction error, which appeared to be a function of wave period, was evident. This was attributed to the frequency dependence of drag and added mass coefficients. The success of the simple theoretical model was thought to be due to the comparatively open platform structure which led to small interference effects between members.

Further to the work by Paulling and Horton (1970), 17 oil companies joined Deep Oil Technology in sponsoring the construction and evaluation of the prototype test platform, *Deep Oil X-1*, described earlier. Horton (1975) describes this project. The test platform, like the scale models used above, was triangular in shape, 40 m on each side and 20 m in height from deck to lower horizontal pontoon. It was considered as a notional one-third scale drilling and production platform or a two-thirds scale production and workover platform. The test site was in 65 m of water 300 m off the Southern Californian coast. There was one tether leg at each corner of the platform. Each leg was made up of 73 mm 6 × 25 (independent wire rope core) steel with 3 mm thick polyethylene coating for corrosion protection. Fifty-one channels of information were monitored including: wave, wind and current excitation, mooring loads, structural member stresses, plat-

form motion, riser pipe stresses and accelerations. These were then compared with the results from wave tank tests by Horton (1975).

Yashima (1976) compared a theoretical model, which was essentially the same as that of Paulling and Horton, with model tests at 1/50th scale. This model was a four column platform with four tethers and no submerged horizontal members. Three types of tether were used, these being 1 mm wire cable, 10 mm polyurethane cable, and 7 mm polyurethane cable – the latter was shown to have non-linear elastic behaviour. Yashima investigated the response of the platform in surge with the tethers statically inclined to the vertical. In addition to wave dynamic effects, he also considered steady state effects and included the coupling of these through the tethers in the analysis.

Reasonable agreement between theory and experiment was obtained, although this was based on rather sparse experimental data. Yashima concluded that less elasticity in the tethers led to greater tension variation. In shallow water the vertical motions would be negligible, but tension variations were large, whereas in deep water the vertical motions would no longer be negligible but the tension variations would be small. For Yashima's model in deep water, the natural periods in surge, sway and yaw would be greater than predominant wave periods so that the response due to waves would have little dependence on the elasticity of the tethers but more on the tether length. However, horizontal displacement by steady state forces would be dependent on the elasticities. The damping was considered important around resonance for pitch and heave, as was viscous damping for this structure. Initial tether tensions had little influence on the wave induced motion of the platform.

Natvig and Pendered (1977) introduced a method for solving the non-linear equation of motion based on a Newton–Raphson technique which was valid for this weakly non-linear system. This was applied to the Aker TPP (Tethered Production Platform). They compared one linearized and two non-linear methods (the Newton–Raphson technique and the time integration Newmark method). Four sources of non-linearity were included in the wave force calculations. Wave forces were calculated at the displaced and rotated structure position and not the mean position; the drag force was calculated using the true relative velocity between the fluid and structure (including current velocity) before squaring; all fluid forces were calculated up to the water surface and not to the still water level; and non-linear mooring forces were included. Natvig and Pendered concluded that in general linearized methods give good results, especially when proper account is taken of the mean drift offset. The platform velocity was found to be the most accurate of the response parameters investigated. The linearized method does not give good results for heave motion with taut moorings but in this case the displacements are small. Although the Newton–Raphson approach compared well with the Newmark method, which was intended as a standard for comparison, it could not be used at resonance in the form presented.

Rainey (1977) advanced a theory to predict Mathieu type instability in the behaviour of tethered buoyant platforms. The possible occurrence of subharmonic oscillations in cross-seas was also investigated. Both of these were considered as very important, and could be masked by scale effects in

model tests. He showed that tethered platforms are prone to dynamic instabilities when subject to single wave-trains at twice the surge or sway natural frequency, and to subharmonic oscillations when subject to orthogonal pairs of wave-trains differing by the surge or sway natural frequency. In each case, the phenomenon is governed by damping for natural oscillations, the motion being particularly serious if the damping ratio is below 0.1. The former effect, being an instability, gives oscillations which will grow until fluid damping reaches a sufficiently high value; the latter effect is a resonance, so again oscillation amplitude is governed by damping. Since fluid damping is always higher in experiments in model test tanks than at full scale, it was considered likely that these effects would be concealed.

Albrecht *et al.* (1978) formulated mathematical models to demonstrate the applicability of numerical techniques for the dynamic behaviour of TBPs with particular attention to the non-linearities owing to the tension rope network. They considered non-vertical networks in which the stiffening characteristics led to non-linear restoring forces which result in non-linear static and dynamic behaviour of the platform.

Beynet *et al.* (1978) described the surge response of the Amoco VMP (Vertically Moored Platform) which is unusual in that the mooring tethers are also the risers, five in each of the four corners. Comparisons between in-house computer programs and model tests for the platform at 1/60th scale were presented as well as separate tests at 1/20th scale for the riser which was fixed at its bottom and oscillated at the top in still water. Superharmonics were evident for the riser response in still water.

Denise and Heaf (1979) presented two mathematical models for the dynamic analysis of TBPs. One was based on linear diffraction–radiation theory using a finite element technique, while the other model employed a non-linear simulation by direct integration in the time domain. Comparison between these two analyses showed that both models gave consistent results.

Non-linearities outlined in the second model were analysed in detail and found to be mostly due to the geometry of the mooring system. Other causes such as variable buoyancy in the splash zone and drag were also investigated but found to be of lesser importance. The influence of these non-linearities on the motion response was found to be quite significant, especially for heave, pitch and roll motions. The mooring line tensions were also influenced but to a lesser extent with variations of the order of 20% from linear analysis results.

Lonergan (1980) performed 19 sets of wave tank tests on a series of TBPs (the Seafox series) including simple structures and detailed models of production platforms over a period from 1975 to 1979. The model scales ranged from 1:250 to 1:150. In certain cases, resonance effects with the tethers were observed. These appeared as high frequency vibrations which were close to the natural frequency in heave and pitch of the platforms. The magnitude of these high frequency vibrations increased with decreasing anchorage stiffness and also with waves of larger period and height. Lonergan concluded that eddy shedding as a result of wave action on the hull members was causing resonance with the structures and their anchorage systems in heave and pitch. The effect of simple resonance on anchor

cable forces for models having natural periods in heave or pitch close to those of shorter wave periods was also observed. For some tests in small waves with a period of twice that of the structure in heave or pitch, the cables completely slackened off resulting in snatching.

This chapter takes the analysis of tensioned buoyant platforms, and describes basic hydrodynamic response prediction methods for TBPs and for the platform tethers. These are then combined to investigate the coupled response of the platform and tethers. Model tests, whether at model or full scale, have always been an invaluable tool in the development of TBP designs. Section 6.5 describes a typical series of such tests and comparisons with theory. Further consideration of the effects of Mathieu instability on TBP performance are described in Section 6.6.

6.2 Platform dynamics

The analysis of a TBP is carried out along the same lines as that of the free floating platforms described in Chapter 5. This analysis method is summarized here for completeness.

A typical TBP structural arrangement with reference axes is shown in Figure 6.2. The surface platform equations of rigid body motions in six degrees of freedom can be written as

$$(\mathbf{M} + \mathbf{M}_A)\ddot{\mathbf{X}} + \mathbf{B}_V \mid \dot{\mathbf{X}} \mid \dot{\mathbf{X}} + \mathbf{B}_p\dot{\mathbf{X}} + (\mathbf{K} + \mathbf{K}_m)\mathbf{X} = \mathbf{F}(t) \qquad (6.2)$$

where $\mathbf{X}$, $\dot{\mathbf{X}}$ and $\ddot{\mathbf{X}}$ are the six component column vectors of displacement, velocity and acceleration in surge, sway, heave, roll, pitch and yaw respectively; $\mathbf{M}$ and $\mathbf{M}_A$ are the (6×6) matrices of physical mass and added mass respectively; $\mathbf{B}_V$ is the (6×6) matrix of drag induced viscous damping; $\mathbf{B}_p$ is the (6×6) matrix of radiation damping; and $\mathbf{K}$ and $\mathbf{K}_m$ are the (6×6) hydrostatic and tether stiffness matrices. The potential damping, $\mathbf{B}_p$, is generally small for TBPs with slender members and is not included in the analysis presented here. $\mathbf{F}(t)$ denotes the 6×1 column vector of wave forces on the surface platform. The coefficient matrices of Equation (6.2) can be evaluated from the given structural data as described below.

The reference axes chosen are principal axes so the physical mass matrix, $\mathbf{M}$, is diagonal with the structure total mass in the first three diagonal positions and the structure moments of inertia for the remaining three diagonal terms. The structure is assumed to be made up of a collection of cylindrical and rectangular elements. The contributions of each element to the added mass, damping and hydrostatic stiffness matrices are computed and then summed for all the elements in the structure.

The general added mass matrix of a circular cylinder with arbitrary end coordinates can be computed by assuming that only the components of acceleration normal to the cylinder axis are significant. Thus, given the cylinder end co-ordinates, diameter and appropriate added mass coefficient, a generalized symmetric added mass matrix can be computed. The calculations can be readily adapted to rectangular elements and discrete non-elongated members.

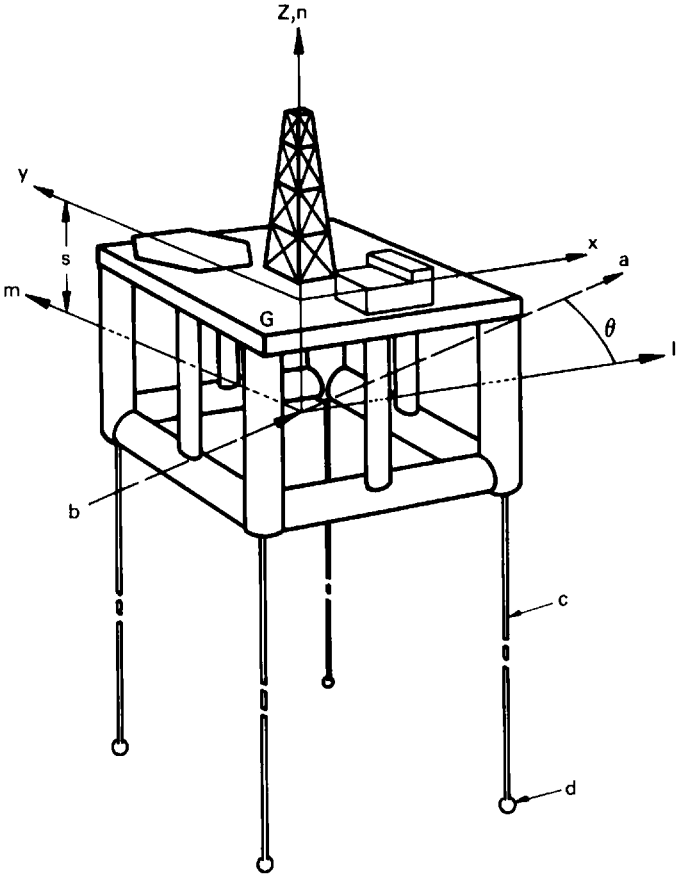

Figure 6.2. TBP reference system. *Key*: a – wave direction; b – origin at still water level; c – tensioned members; d – seabed anchorage

The viscous damping matrix, $\mathbf{B}_V$, for the structure is evaluated in a similar way to $\mathbf{M}_A$ as a sum of the matrices for each individual structural element. Only drag forces normal to the cylinder axis are considered significant, but the non-linear velocity squared proportionality gives an asymmetric damping matrix requiring that all 36 elements have to be evaluated separately. These calculations can also be adapted to apply for rectangular cylinders and non-elongated members.

The contribution of each surface piercing member of the platform to the hydrostatic stiffness will arise only from buoyancy forces in the heave, roll and pitch degrees of freedom. The contribution of each surface piercing member to the hydrostatic stiffness matrix depends only on the magnitude and position of its water plane area. Further details on the procedures for calculating the above coefficient matrices are given in Chapter 5.

The oscillatory wave force column vector on the right hand side of Equation (6.2) is obtained by summing the effects of the wave particle velocities, accelerations and wave pressures (or Froude–Krylov forces) on all the structural members of the surface platform. The wave kinematics are obtained from linear wave theory.

The method for deriving wave forces on the surface platform is also identical to that for semisubmersible space frame structures described in Section 5.2.

The symmetric tether stiffness coefficient matrix, $\mathbf{K}_m$, of Equation (6.2) has still to be derived. In the absence of tether dynamics, an idealized tether stiffness model is usually employed for the platform dynamic analysis. This idealized stiffness is derived by assuming that each mooring cable is weightless and perfectly elastic with a known tension and elastic stiffness. The cable, being weightless, is taken to lie along a straight line joining the two end co-ordinates. The resultant stiffness matrix is evaluated assuming that the surface platform moves through small displacements relative to the cable lengths involved.

Each cable has a constant tension, $\bar{T}$, an elastic stiffness, λ, and is strung between co-ordinates (x_1, y_1, z_1) on the seabed and (x_2, y_2, z_2) at the surface platform; both relative to the platform's principal axes system, $Oxyz$, as shown in Figures 6.2 and 6.3.

The direction cosines are defined as follows:

$$\cos\alpha = \frac{x_2 - x_1}{L};\ \cos\beta = \frac{y_2 - y_1}{L};\ \cos\gamma = \frac{z_2 - z_1}{L} \tag{6.3}$$

where L is the cable length given by

$$L = \sqrt{[(x_2 - x_1)^2 + (y_2 - y_1)^2 + (z_2 - z_1)^2]}$$

To evaluate the cable stiffness matrix, consider that the surface platform translates in the positive x direction through a small distance, δx. Let $a = x_2 - x_1$, $b = y_2 - y_1$, and $c = z_2 - z_1$; then to first order the new cable length becomes

$$L + \delta L = L + \frac{a}{L}\delta x \tag{6.4}$$

Then the additional tension $\delta\bar{T}$ in the cable due to extension δL is

$$\delta\bar{T} = \lambda\delta L = \frac{\lambda(x_2 - x_1)}{L}\delta x \tag{6.5}$$

The resulting restoring force component along the x axis can be written as $\delta\bar{T}_x = (\bar{T} + \delta\bar{T})\cos\alpha_1 - \bar{T}\cos\alpha$, where $\bar{T}$ is the cable tension and α_1 is given by

$$\cos\alpha_1 = \frac{x_2 + \delta x - x_1}{L + \delta L} \tag{6.6}$$

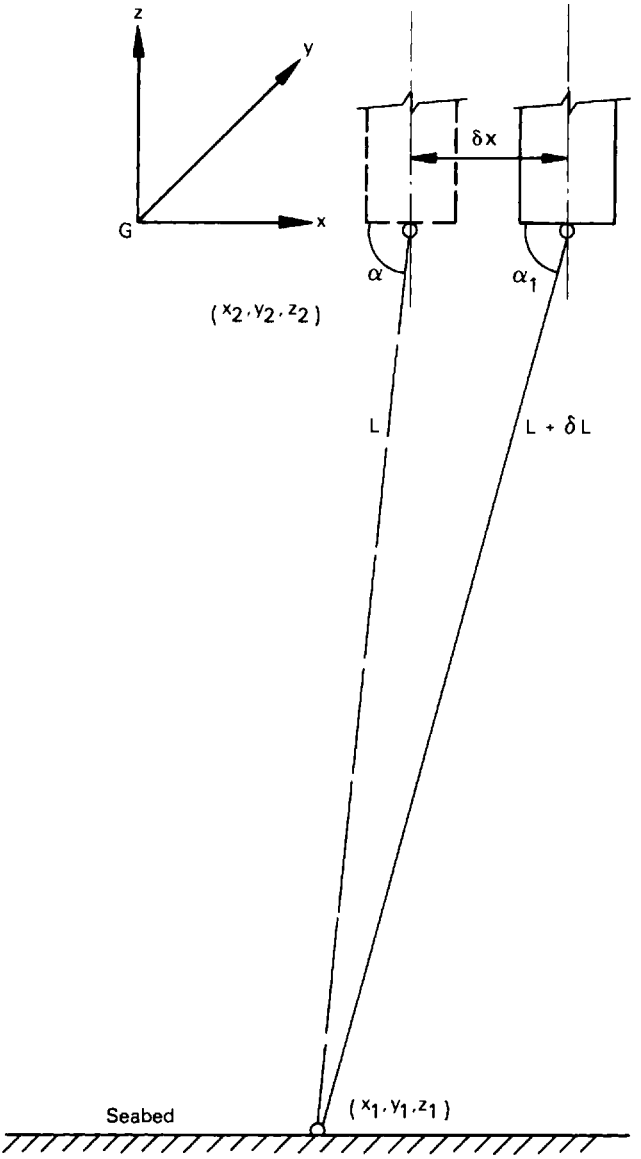

Figure 6.3. Notation for idealized tether stiffness model

Therefore

$$\delta\bar{T}_x = (\bar{T} + \delta\bar{T})\left[\frac{x_2 - x_1}{L}\right]\left[\frac{1 + \dfrac{\delta x}{x_2 - x_1}}{1 + \dfrac{\delta L}{L}}\right] - \frac{\bar{T}(x_2 - x_1)}{L}$$

$$= \bar{T}\cos\alpha\left[\frac{\delta x}{x_2 - x_1} - \frac{\delta L}{L} + \frac{\delta \bar{T}}{T}\right] \tag{6.7}$$

to first order. Since $\delta L = \cos\alpha\ \delta x$

$$\delta \bar{T}_x = \frac{\bar{T}}{L}\cos\alpha\left[\frac{L\delta x}{x_2 - x_1} - \cos\alpha\ \delta x + \frac{\lambda(x_2 - x_1)}{\bar{T}}\delta x\right]$$

$$= \left[\lambda\cos^2\alpha + \frac{\bar{T}}{L}\sin^2\alpha\right]\delta x \tag{6.8}$$

In the limit as $\delta x \to 0$

$$\frac{\delta \bar{T}_x}{\delta x} = \frac{\partial \bar{T}_x}{\partial x} = k_{11} = \lambda\cos^2\alpha + \frac{\bar{T}}{L}\sin^2\alpha \tag{6.9}$$

which is the first term in the (6×6) stiffness matrix $\mathbf{K}_m$. The remaining terms corresponding to the restoring forces due to translations can be derived in a similar fashion in terms of k_{ij} where i, j are row and column numbers respectively. These are given by:

$$\left.\begin{aligned}
k_{21} &= (\lambda + \bar{T}/L)\cos\alpha\cos\beta = k_{12}\\
k_{31} &= (\lambda + \bar{T}/L)\cos\alpha\cos\gamma = k_{13}\\
k_{22} &= \lambda\cos^2\beta + (\bar{T}/L)\sin^2\beta\\
k_{32} &= (\lambda + \bar{T}/L)\cos\beta\cos\gamma = k_{23}\\
k_{33} &= \lambda\cos^2\gamma + (\bar{T}/L)\sin^2\gamma
\end{aligned}\right\} \tag{6.10}$$

The remaining 27 terms corresponding to restoring moments due to translations, restoring forces due to rotations and restoring moments due to rotations can all be expressed in terms of the first nine terms. These are given below for one-half of the matrix below and including the leading diagonal:

$$\left.\begin{aligned}
k_{41} &= k_{31}y_2 - k_{21}z_2\\
k_{51} &= k_{11}z_2 - k_{31}x_2\\
k_{61} &= k_{21}x_2 - k_{11}y_2\\
k_{42} &= k_{32}y_2 - k_{22}z_2\\
k_{52} &= k_{21}z_2 - k_{32}x_2\\
k_{62} &= k_{22}x_2 - k_{21}y_2\\
k_{43} &= k_{33}y_2 - k_{32}z_2\\
k_{53} &= k_{31}z_2 - k_{33}x_2\\
k_{63} &= k_{32}x_2 - k_{31}y_2\\
k_{44} &= k_{33}y_2^2 - 2k_{32}y_2z_2 + k_{22}z_2^2\\
k_{54} &= k_{31}y_2z_2 - k_{21}z_2^2 - k_{33}y_2x_2 + k_{32}x_2z_2\\
k_{64} &= k_{32}x_2y_2 - k_{22}x_2z_2 - k_{31}y_2^2 + k_{21}y_2z_2
\end{aligned}\right\} \tag{6.11}$$

$$\left.\begin{aligned} k_{55} &= k_{11}z_2^2 - 2k_{31}x_2z_2 + k_{33}x_2^2 \\ k_{65} &= k_{21}x_2z_2 - k_{32}x_2^2 - k_{11}y_2z_2 + k_{31}x_2y_2 \\ k_{66} &= k_{22}x_2^2 - 2k_{21}x_2y_2 + k_{11}y_2^2 \end{aligned}\right\}$$

The cable stiffness matrix is computed for each cable in a mooring system and summed to yield a total mooring stiffness matrix, $\mathbf{K}_m$.

The platform response to the applied oscillating wave force vector is then computed by using an iterative technique to account for the non-linear drag damping force. A first approximation diagonal linear damping coefficient matrix is obtained by ignoring all non-diagonal terms in the total mass and stiffness matrices and assuming linear damping to be 10% of critical. The equations of motion are then solved with the first approximation to the damping value. The column vector of these computed velocities is then substituted into the modulus sign in the damping term such that the equation:

$$(\mathbf{M} + \mathbf{M}_A)\,\ddot{\mathbf{X}} + \mathbf{B}_V \frac{8}{3\pi} \left| \dot{\mathbf{X}}_{\text{last approximation}} \right| \dot{\mathbf{X}} + (\mathbf{K} + \mathbf{K}_m)\,\mathbf{X} = \mathbf{F}(t) \tag{6.12}$$

is being solved to obtain a better approximation for the column vector $\mathbf{X}$. The equivalent damping matrix $\mathbf{B}_{eq}$:

$$\mathbf{B}_{eq} = \mathbf{B}_V \frac{8}{3\pi} \left| \dot{\mathbf{X}} \right| \tag{6.13}$$

is a standard result obtained by assuming equal work done at resonance by the non-linear and the equivalent linear damping terms (see Section 5.2).

The iteration is continued until a specified tolerance ($\simeq 1\%$) between successive approximations is achieved. This process converges quickly and can be modified to include the dynamic model for the tethers, in which $\mathbf{K}_m$ can become complex (see Sections 6.3 and 6.4). The convergence is aided by the fact that at wave frequencies the platform motion is inertia dominated, and tether forces, whatever their precise values, remain small compared with the D'Alembert forces required to move the platform. For example, in 120 m of water, typical tether and inertia forces for unit amplitude oscillation of period 10 s are typically 1000 kN and 15 000 kN respectively. Thus the effect of the tethers on the platform is small whereas the platform's effect on the tethers is important.

Figure 6.15 shows a typical TBP surge response for both quasi-static and dynamic tether models at a water depth of 1500 m with 16 tethers, each of mass per unit length 667 kg/m. A conventional surface platform with four vertical columns and four horizontal interconnecting pontoons connected by bracing members, and four tethers per corner is used for the computations. Despite the large difference in the tether restoring forces between quasi-static and dynamic tether models, the corresponding difference in the TBP surge response is much smaller than the variability introduced by other uncertainties such as the values of drag and inertia coefficients.

Vertical TBP motion (heave, roll and pitch) is restrained primarily by the longitudinal stiffness of the tethers leading to high natural frequencies

in these modes for low water depth. However, longitudinal tether stiffness is inversely proportional to depth and so in deep water, heave, roll and pitch natural frequencies will enter the high frequency range of wave excitation leading to the possibility of excessive motions in these modes. This feature could, of course, be counteracted by increasing total tether cross-sectional area while retaining the same total tension and hence the same excess buoyancy requirement in the structure. However, the heavier tethers may then be subject to higher dynamic magnification by platform excitation in the lateral motions.

The equation of motion (6.2) is more difficult to solve for random wave excitation but a number of techniques for stochastic linearization described by De Spanos and Iwan (1978) may be used to linearize the drag force and compute excursion amplitude spectra in an iterative manner.

It is clear that the most important parameter in the solution for a given platform/tether system is the water depth. For horizontal platform motions, tether spring rates decrease in inverse proportion to the water depth, whereas the corresponding drag and inertia forces on the tether increase with water depth. In general terms, the tether's first natural frequency for lateral motions is approximately given by

$$\omega_1^2 \simeq \frac{\pi^2 \bar{T}}{L^2 m_t} \tag{6.14}$$

where $\bar{T}$ is the mean tether tension; m_t is the tether total mass per unit length; and L is the tether length or the approximate TBP deployment water depth. The resonant period for horizontal platform motions increases with the square root of water depth from typically 40 s for 120 m tethers to around 80 s for 500 m tethers. Removing the natural period further from wave periods is desirable for avoiding the possibility of Mathieu excitation at half the wave frequency but the lower tether stiffness does increase the drift displacements caused by wind, current and second order wave forces. This will not necessarily be a problem but little is known of the spectral content of waves at periods greater than 20 s and some possibility of significant second order wave excitation would remain.

6.3 Tether dynamics

It is clear from the above section that the tethered buoyant platform (TBP) is one example of a compliant structure which is heavily dependent on its tensioned vertical tethers for a modification of the platform dynamic characteristics to suit the prevailing wave environment. The platform is very stiff in vertical plane oscillations (heave, roll and pitch) since it is restrained by the longitudinal stiffness of the tethers. Typically, these modes have oscillation periods ranging from 0.5 to 4 s which are outside the band of frequencies where wave energy is significant. On the other hand, horizontal plane motions (surge, sway and yaw) are very compliant with natural periods from 40 s upwards which are again well away from wave frequencies.

Despite the separation of excitation and natural periods, the possibility of interactions between the dynamics of the mooring system and the surface platform can still exist. It is worth noting that in deep water, the tether inertia can be of the order of 6% of that of the surface platform. Furthermore, the natural periods of the taut long tethers are of the order of 5–10 s, well inside the range of wave excitation periods. Up to the present, the analysis of taut mooring systems associated with compliant platforms has tended to be of a quasi-static nature with the tethers idealized as weightless ideal spring elements. It is likely that a more realistic mathematical model of mooring dynamics will reveal a modification of the surface platform response and enable a more accurate assessment of the mooring system internal forces. The latter feature is of great interest in evaluating the fatigue of moorings intended for oil production platforms requiring long service lives.

This section presents three analyses methods for taut vertical mooring systems in order to assess their applicability to compliant offshore platforms. The derivation of the analyses is given together with a description of their comparative performance. The numerical effects of various assumptions are presented and discussed. These possible assumptions are itemized below:

1. The tension in the tether is assumed to be constant along its length although, in fact, self weight may change this to some extent ($\pm 10\%$) in deep water.
2. The tethers are assumed to be pin-jointed to the sea bed and surface structure.
3. The tether dynamics are unaffected by bending forces. This is where TBP tethers differ from the more lightly tensioned marine risers.
4. The tether attachment points to the platform are well below the water line (typically 20–30 m). The tether elements are therefore largely unaffected by wave forces and excited only by the motion of the platform.
5. Fluid forces on tether elements can be modelled by a Morison approach with 'added mass' and non-linear drag forces corresponding to two-dimensional flow around the cylindrical tether cross-section.
6. The tethers move in two dimensions only.

Some of the above assumptions have been used elsewhere (see Wilson and Garbaccio, 1967; Alexander, 1971; and Sluijs and Blok, 1977) and are clearly sensible, whereas others, as pointed out by Folger Whicker (1958); Jain (1980); and Hong (1974) do appear doubtful.

One of the aims of this analysis is to test the validity of assumptions 1 and 5. On a more rigorous level, assumptions 5 and 6 are questionable approximations but they are necessary to obtain an analytical grip on the problem.

Detailed technical studies of catenary mooring systems, as referenced above, have been primarily concerned with the mooring restoring forces exerted by the catenaries on the surface platform as well as with the mooring stresses induced by dynamic excitation due to currents and waves. Less attention has been paid to the dynamics of taut tether systems. Hong (1974) and Connell (1974) apply an analytic 'transmission line' solution

similar to that given in the next section for the dynamics of lightly tensioned taut rope tethers for small oceanographic surface buoys. Richardson and Pinto (1979) have considered the problem of taut TBP cable dynamics but their calculations are restricted to simple analytic models for heavy catenaries with the fluid damping forces neglected in the computations. There is, therefore, a requirement for a taut vertical tether dynamic model which accounts for both the inertia and non-linear fluid damping forces encountered when operating in the ocean environment. Three such models are described here.

6.3.1 Tether linear 'transmission line' model

Consider an element of a tether of mass m_1 per unit length moving in two dimensions with lateral displacement, y, at a vertical coordinate, z, as is shown in Figure 6.4.

By equating all the horizontal force components on the tether element and neglecting bending and second order forces, we obtain

$$m_1 \delta z \, \ddot{y} = T \left[\left[\frac{\partial y}{\partial z} \right]_2 - \left[\frac{\partial y}{\partial z} \right]_1 \right] - \delta z \, w(\dot{y}, \ddot{y}, r) \tag{6.15}$$

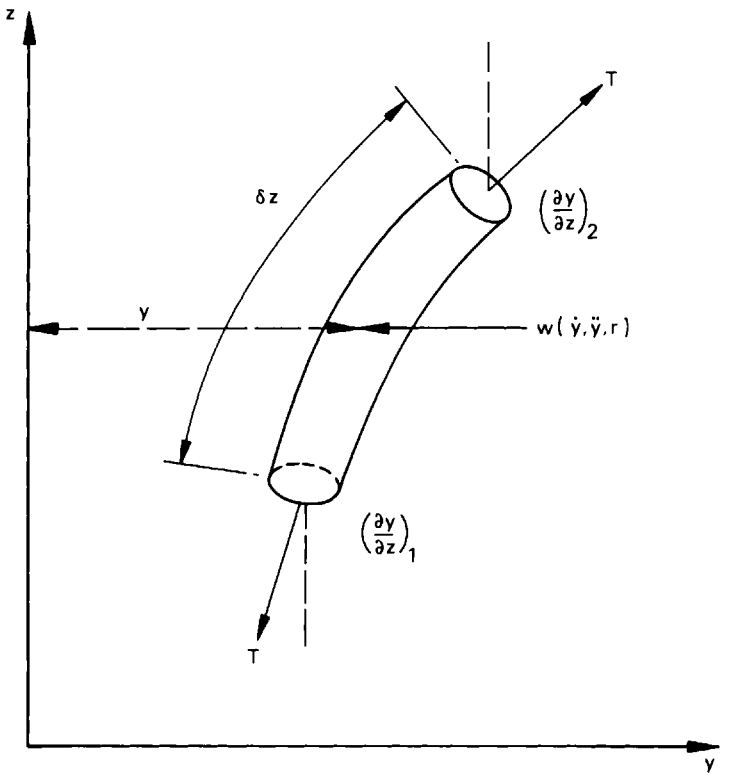

Figure 6.4. Tether element and reference axis system

where $w(\dot{y}, \ddot{y}, r)$ denotes the force per unit length exerted on the tether due to the surrounding fluid flow; r is the radius of the circular tether cross-section; and $\dot{y}$, $\ddot{y}$ are the tether element lateral velocity and acceleration respectively. In the limit, as $\delta z \rightarrow 0$, Equation (6.15) becomes

$$m_1 \ddot{y} + w(\dot{y}, \ddot{y}, r) = T \frac{\partial^2 y}{\partial z^2} \tag{6.16}$$

where the tension T is assumed to be constant along the tether length. Following a conventional hydrodynamics approach, the generalized fluid force $w(\dot{y}, \ddot{y}, r)$ is represented as the sum of an acceleration dependent added mass force and a velocity dependent drag force. Thus:

$$w(\dot{y}, \ddot{y}, r) = m_2 \ddot{y} + \lambda_0 \dot{y} \tag{6.17}$$

where m_2 is a tether added mass per unit length; and λ_0 is a linear drag force constant. By renaming $m = m_1 + m_2$, the following equation:

$$m \ddot{y} + \lambda_0 \dot{y} = T \frac{\partial^2 y}{\partial z^2} \tag{6.18}$$

is obtained. It can be argued that, strictly, the linear drag force constant is incorrect since the drag force can be better represented by a square law for cross-sectional tether dimensions which are small compared with likely relative lateral motions between the tether and fluid. For this case, Equation (6.17) can be replaced by:

$$w(\dot{y}, \ddot{y}, r) = m_2 \ddot{y} + \lambda_0' \mid \dot{y} \mid \dot{y} \tag{6.19}$$

The quadratic drag force model will be used later. It is worth noting here that, in practice, the tether elements can also shed vortices in lateral flows resulting in a very complicated flow regime with significant out-of-plane lift forces exciting the tether into three-dimensional oscillations.

Regardless of the form of the drag force, it will be found helpful, at a later stage, to express Equation (6.16) as a pair of coupled first order partial differential equations. This is easily achieved by introducing a lateral force, f, and lateral velocity, v, such that

$$f = - T \frac{\partial y}{\partial z} \tag{6.20}$$

and

$$v = \frac{\partial y}{\partial t} \tag{6.21}$$

Hence

$$m \dot{v} + w(v, \dot{v}) = - \frac{\partial f}{\partial z} \tag{6.22}$$

and

$$\dot{f} = - T \frac{\partial v}{\partial z} \tag{6.23}$$

In obtaining a solution to Equation (6.18), it is of interest to model the tethers as seen by the platform, that is as a dynamic system to which the surface platform applies a horizontal oscillation with the system responding by exerting a horizontal force amplitude on the platform.

Assuming that the surface platform excites the tether harmonically at the top, a separable solution of the form

$$y(z, t) = \text{Real}[g(z)\, y(i\omega)\, e^{i\omega t}] \tag{6.24}$$

can be postulated with $g(z)$ being a complex function of position.

Substitution in Equation (6.18) gives

$$[-\omega^2 m + i\omega\lambda_0]g(z) = T\, g''(z) \tag{6.25}$$

If

$$k^2 = \frac{\omega^2 m - i\omega\lambda_0}{T} \tag{6.26}$$

then a solution of the form:

$$g(z) = A' \sin kz + B' \cos kz \tag{6.27}$$

is obtained with complex constants A' and B'. The boundary condition of

$$y(0, t) = 0 \tag{6.28}$$

and

$$y(L, t) = \text{Real}[Y_L(i\omega)e^{i\omega t}] \tag{6.29}$$

give $B' = 0$ and

$$A' = \frac{Y_L(i\omega)}{\sin kL}$$

where L is the length of the tether. The solution, therefore, is

$$y(z, t) = \text{Real}\left[\frac{Y_L(i\omega)}{\sin kL} \sin kz\, e^{i\omega t}\right] \tag{6.30}$$

It is now a simple matter to compute the surge forces $f_s(t)$ applied to the platform by the tethers

$$f_s(t) = T\left[\frac{\delta y}{\delta z}\right]_{z=L} \tag{6.31}$$

Thus

$$\frac{F_s(i\omega)}{Y_L(i\omega)} = \frac{T}{L}(kL)\cot(kL) \tag{6.32}$$

Here, the zero frequency 'quasi-static' surge spring stiffness (T/L) is multiplied by a factor $\phi \cot\phi$ where

$$\phi = kL = \omega L \sqrt{\left(\frac{m + \lambda_0/i\omega}{T}\right)} \tag{6.33}$$

Figure 6.5 shows the amplitudes and phase of the tether stiffness dynamic magnification factor ($\phi \cot\phi$) as a function of frequency for a steel tubular tether typical of proposed TBP designs. This tether element is of 500 m length with a mass (m) of 300 kg/m and a constant tension (T) of 10 MN. At zero frequency $\phi \cot\phi$ is, of course, unity and as the frequency increases, the tethers look less like springs and more like dampers. It is clear that the tether behaviour is strongly influenced by assumed levels of damping. Therefore, a damping force proportional to the square of relative velocity between the fluid and the tether will imply that at low amplitudes, the apparently lightly damped tether will behave very differently from the large oscillation amplitude case. The undamped natural frequencies of the tethers are

$$\omega_n = \frac{n\pi}{L}\sqrt{\left(\frac{T}{m}\right)} \qquad n = 1,2,\ldots \tag{6.34}$$

In general, it is important to ensure that tether natural frequencies are above predominant wave excitation frequencies. The tether natural frequencies are primarily dependent on the tether length, L, axial tension, T, and total mass, m. The parameter which has the most influence on the

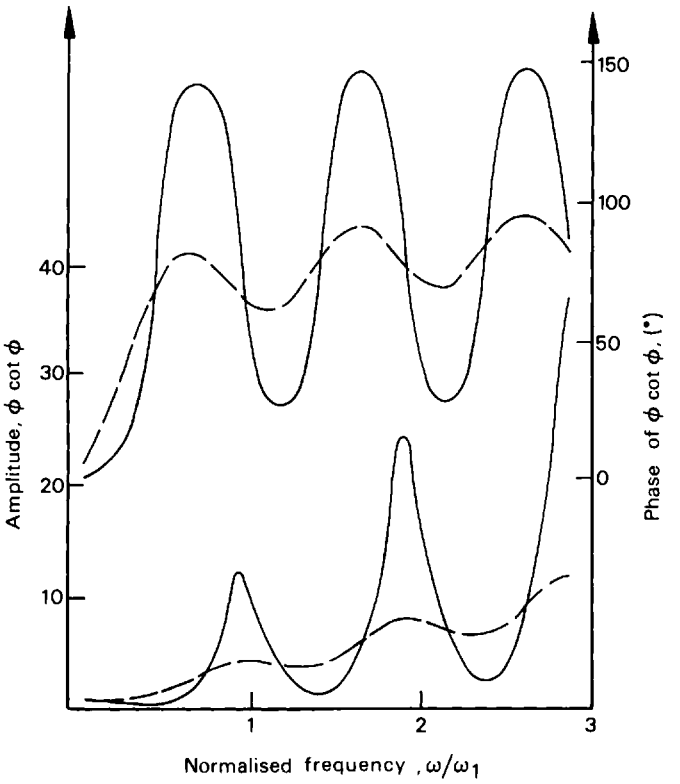

Figure 6.5. Amplitude and phase of $\phi\cot\phi$ for analytic solution. *Key*: — damping coefficient = 0.05 kNs/m; -- damping coefficient = 0.20 kNs/m

natural frequency is the tether length. For a given location this parameter is effectively constant. Therefore, the natural frequencies of the tethers can only be changed by altering the tension or the total mass of the tether. Increases in tension or reductions in tether cross-sectional area are limited to the point at which the axial stress exceeds the yield stress of the tether material.

The linear transmission line tether model can be very useful if an equivalent linear damping value is identifiable. However, modal analysis and finite element dynamic models of the tethers offer possible advantages which are explored in the following sections.

6.3.2 Modal analysis of the tether

This analysis is initiated by decomposing the lateral displacement, y, at any point along a tether into two parts: one, denoted by y_s, representing the 'quasi-static' displacement caused by platform motions and the second, denoted by y_d to account for the dynamic effects caused by tether inertia and damping. Thus:

$$y = y_s + y_d \tag{6.35}$$

where the quasi-static component y_s is

$$y_s = \frac{z}{L} y_L(t) \tag{6.36}$$

for a displacement time history, $y_L(t)$, imposed by the surface platform at the tether top end. Substituting Equations (6.35) and (6.36) into Equation (6.18) gives

$$m\ddot{y}_d + \lambda_0 \dot{y}_d = T\frac{\partial^2 y_d}{\partial z^2} - \frac{mz}{L}\ddot{y}_L(t) - \frac{\lambda_0 z}{L}\dot{y}_L(t) \tag{6.37}$$

Now, the dynamic displacements, $y_d(t)$, are expressed in terms of an infinite set of modal co-ordinates, $q_i(t)$, and the corresponding shape function, $g_i(z)$, which must satisfy the boundary condition of $y_d = 0$ at each end of the tether.

A suitable set of shape functions are given by

$$g_n(z) = \sin k_n z \tag{6.38}$$

where $k_n = \pi n/L$. This leads to

$$y_d(t) = \sum_{n=1}^{\infty} q_n(t) \sin k_n z \tag{6.39}$$

Substituting Equation (6.39) into (6.37), we obtain

$$\sum_{n=1}^{\infty} [m\ddot{q}_n(t) + \lambda_0 \dot{q}_n(t) + k_n^2 T q_n(t)] \sin k_n z = -(m\mathrm{D}^2 + \lambda_0 \mathrm{D})\frac{z}{L} y_L(t) \tag{6.40}$$

where the operator D denotes differentiation with respect to time. By multiplying both sides of this equation by $\sin k_r z$ and integrating with respect to z between the limits 0 and L, we obtain an equation relating the boundary conditions to the excitation of the rth modal co-ordinate. This equation is

$$m\,\ddot{q}_r(t) + \lambda_0 \dot{q}_r(t) + k_r^2\,T\,q_r(t) = 2(mD^2 + \lambda_0 D)\frac{\cos k_r L}{k_r L}\,y_L(t) \qquad (6.41)$$

In this analysis, the horizontal force applied to the platform by the tether dynamics is of interest. This force, f_L, is

$$f_L = T\left[\frac{\partial y}{\partial z}\right]_{z=L} = \frac{T}{L}\,y_L(t) + T\sum_{n=1}^{\infty} k_n q_n(t)\cos k_n L \qquad (6.42)$$

Now, for sinusoidal motion, let

$$\left.\begin{aligned} y_L(t) &= \mathrm{Re}[Y_L(\mathrm{i}\omega)\mathrm{e}^{\mathrm{i}\omega t}] \\ q_n(t) &= \mathrm{Re}[Q_n(\mathrm{i}\omega)\mathrm{e}^{\mathrm{i}\omega t}] \\ f_L(t) &= \mathrm{Re}[F_L(\mathrm{i}\omega)\mathrm{e}^{\mathrm{i}\omega t}] \end{aligned}\right\} \qquad (6.43)$$

Substituting Equation (6.43) into Equations (6.41) and (6.42) gives

$$[-m\omega^2 + \mathrm{i}\omega\lambda_0 + k_r^2 T]\,Q(\mathrm{i}\omega) = 2(-\omega^2 m + \mathrm{i}\omega\lambda_0)\frac{\cos k_r L}{k_r L}\,Y_L(\mathrm{i}\omega) \qquad (6.44)$$

and

$$F_L(\mathrm{i}\omega) = \frac{T}{L}\,Y_L(\mathrm{i}\omega) + T\sum_{n=1}^{\infty} k_n Q_n(\mathrm{i}\omega)\cos k_n L \qquad (6.45)$$

Substituting $Q_n(\mathrm{i}\omega)$ from Equation (6.44) into Equation (6.45) gives

$$\frac{F_L(\mathrm{i}\omega)}{Y_L(\mathrm{i}\omega)} = \frac{T}{L}\left[1 + 2\sum_{n=1}^{\infty}\left\{1 - \frac{k_n^2 T}{-\omega^2 m + \mathrm{i}\omega\lambda_0 + k_n^2 T}\right\}\right] \qquad (6.46)$$

Finally, by using ω_n from Equation (6.34), we obtain

$$\frac{F_L(\mathrm{i}\omega)}{Y_L(\mathrm{i}\omega)} = \frac{T}{L}\left[1 + 2\sum_{n=1}^{\infty}\left\{1 - \frac{1}{1 - \left[\dfrac{\omega}{\omega_n}\right]^2 + \dfrac{\mathrm{i}\omega\lambda_0}{\omega_n^2 m}}\right\}\right] \qquad (6.47)$$

It is usual to truncate the above summation after a finite number of terms and approximate the system dynamics by a specific number of modes. Figure 6.6 shows the amplitudes and phases of the complex $F_L(\mathrm{i}\omega)/Y_L(\mathrm{i}\omega)$ stiffness term for a seven-mode summation in comparison with the exact solution ($\phi\cot\phi$) derived in a preceding section. The agreement is good for low frequencies but it naturally deteriorates at higher excitation frequen-

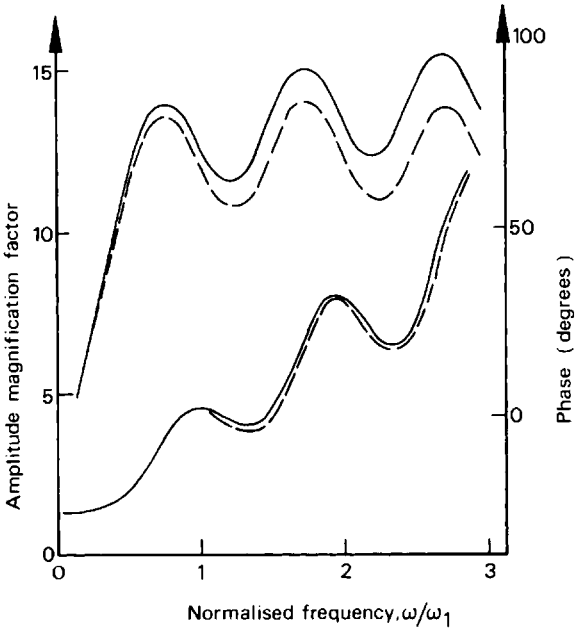

Figure 6.6. Comparative tether performance for analytical and seven-mode model method. *Key*: — analytical solution; -- model solution

cies where the amplitude shows a markedly better quality of agreement with the exact analysis than does the phase.

Modal models can be useful if an approximate time domain model of a linear distributed system is required for simulation as part of an otherwise non-linear system. However, the introduction of non-linear quadratic damping on the tether invalidates the modal decomposition and leads to coupled equations where the velocity of all modes affects the acceleration of all modes. It is much easier to develop a non-linear finite element model if the linear dynamics, which are well modelled by a small number of modes, can be adequately characterized by a reasonable number of finite elements. This model is developed in the next section.

6.3.2 Finite element analysis of the tether

The finite element technique is a powerful dynamic analysis tool which can be used to simulate systems with non-linear and time varying characteristics. It is particularly simple to use in the modelling of transmission line structures such as idealized tethers, shafts and electrical lines since it is exactly equivalent to the lumped mass approach for such systems.

Initially, a frequency domain model of the lumped, linearized tether under constant tension is developed so that its 'force per unit displacement' frequency response can be compared with the analytic solution. If agreement is good, this implies that an adequate number of finite elements are

being used to model the linear dynamics and the model can then be used in the frequency domain to calculate the effects of spatial tension variations due to self weight. A time domain model of the linearized finite element model is also developed and validated against the frequency domain model. This simulation is then used to evaluate the effects of non-linear quadratic damping and to test 'linearization' techniques.

The first order differential equations, Equations (6.22) and (6.23), can be discretized in many different ways, two of which are shown in Figure 6.7. They are physically equivalent and only differ notationally. It is often helpful to use the electrical transmission line analogy for the elements where the equivalences of force to voltage, velocity to current, inertia to inductance, damping to resistance and tension (spring) to capacitance hold. The equivalent electrical systems required to model the tether are also shown in Figure 6.7.

Using the first model, and hence the analogous electrical element of type 1 for simplicity, the equations describing its motion are

$$v_k - v_{k+1} = \delta z \frac{D}{2T}\left[f_{k+1} + f_k\right] \tag{6.48}$$

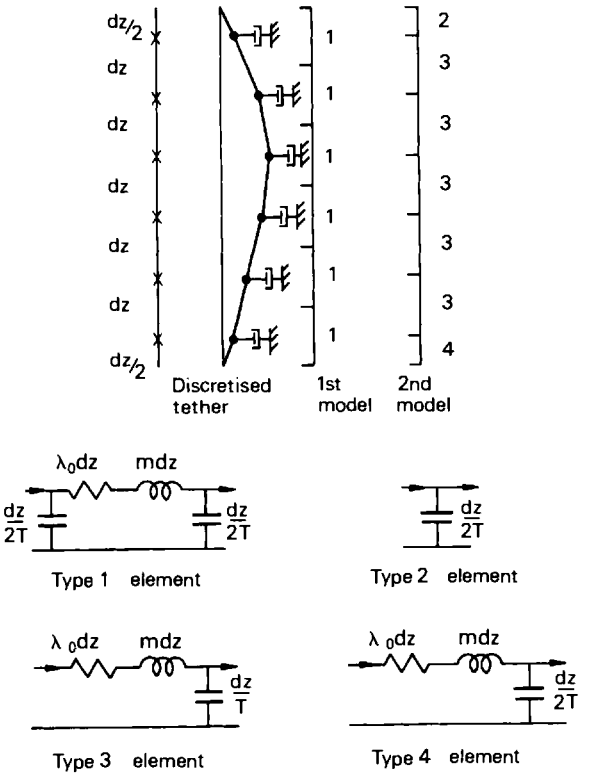

Figure 6.7. Finite element tether models and electrical analogies

$$f_k \left[1 + \frac{\delta z^2}{2T} (\lambda_0 + mD) \right] = f_{k+1} + (\lambda_0 + mD)\, \delta z\, v_k \tag{6.49}$$

where D is the differential operator. These rather complicated equations are not an obvious discretization of Equations (6.22) and (6.23) but are equivalent since they describe the same physical system. Use of the second model leads to simpler equations but at the cost of non-standard end elements.

It is relatively easy to evaluate the element transfer matrix relating the complex amplitudes of f_k, v_k (denoted by $F_k(i\omega)$, $V_k(i\omega)$) to those of their neighbours. Rearranging Equation (6.48), and substituting $i\omega$ for D, the differential operator, gives

$$\begin{bmatrix} V_{k+1}(i\omega) \\ F_{k+1}(i\omega) \end{bmatrix} = \begin{bmatrix} 1 + YZ & Z(2 + YZ) \\ -Y & 1 + YZ \end{bmatrix} \begin{bmatrix} V_k(i\omega) \\ F_k(i\omega) \end{bmatrix} \tag{6.50}$$

where $Y = (i\omega + \lambda_0)\delta z$; and $Z = i\omega\, \delta z/2T$. Renaming Equation (6.50) gives

$$\mathbf{X}_{k+1} = \mathbf{A}\, \mathbf{X}_k \tag{6.51}$$

Values of V_N, F_N, corresponding to the tether lower end, can be evaluated by successive matrix multiplication of V_1, F_1. Thus:

$$\mathbf{X}_N = \mathbf{A}^{N-1}\mathbf{X}_1 \tag{6.52}$$

But $V_N = 0$ so:

$$A_{11}^N V_1 + A_{12}^N F_1 = 0 \tag{6.53}$$

The desired harmonic response ratio, then, is

$$\frac{F_1}{Y_1} = i\omega \frac{F_1}{V_1} = -i\omega \frac{A_{11}^N}{A_{12}^N} \tag{6.54}$$

Figure 6.8 displays the amplitudes and phases of the seven finite element and analytic models. These are in agreement over at least half the frequency range displayed. Higher accuracy could be obtained by dividing the tether into more elements.

Various tests have been performed using a seven-finite-element discretization compared with a modal model which included the first seven tether modes. The finite element technique produced consistently better overall results when compared with the analytic model, although, interestingly enough, the modal analysis demonstrated better agreement in amplitude but significantly greater error in the phase behaviour, leading to greater total distances between approximate and ideal phasors in the complex plane.

The tether tension varies over its length due to its immersed self weight. However, even for a 600 m tether, the tension varies by no more than 10% between the average, top and bottom values. It is easy to quantify the effects of this variation by using the local tension value in place of the average value in the finite element computation of the overall frequency response. Thus

$$\mathbf{X}_{k+1} = \mathbf{A}(k)\, \mathbf{X}_k \tag{6.55}$$

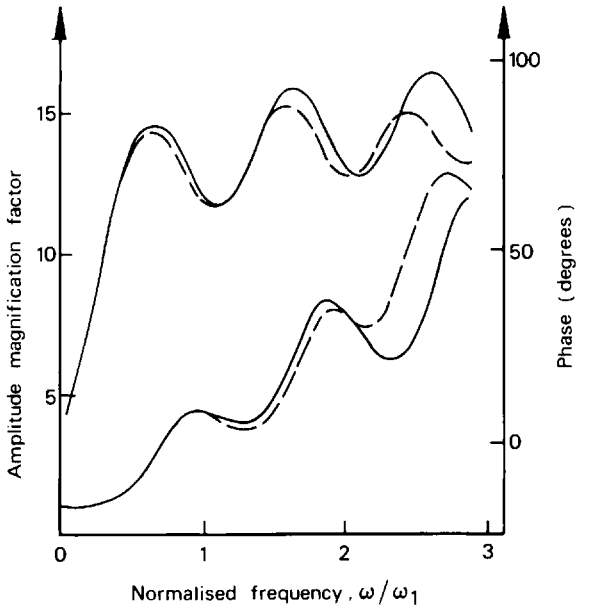

Figure 6.8. Comparative tether response for analytical and seven-finite element model. *Key*: — analytical solution; -- finite element solution

and so

$$\mathbf{X}_N = \left[\prod_{k=1}^{N-1} \mathbf{A}(k) \right] \mathbf{X}_1 \tag{6.56}$$

where $\mathbf{A}(k)$ is the transfer matrix computed from the local tension value. It is found that self weight makes no significant difference to tether frequency response.

A number of linearization techniques are available to quantify the effects of quadratic damping in a frequency domain framework. They can be tested by simulating the finite element time domain non-linear model of the tether with a harmonic velocity time history and comparing the amplitude of the resultant force history at the tether top with that predicted by equivalent linearization with a linear model. The non-linear damping force can be written as

$$R(v_k) = 1/2\ \rho\ d\ C_D \mid v_k \mid v_k \tag{6.57}$$

where ρ is the fluid density, d is the projected area per unit length of the tether cross-section in the direction of motion and C_D is the drag coefficient, generally accepted to be about 1.2 for the Keulegan–Carpenter numbers involved here.

It is desirable to establish an equivalent linear damping for the tethers when they are being used to restrain the motions of a structure such as a TBP. If it is assumed that the tether response will be dominated by the solid body mode and most of the tether velocity is attributable to that

mode, it is reasonable to define an equivalent linear damping factor which permits the same energy dissipation over the length of the tether as the quadratic damping.

The velocity at any point on the tether is given by

$$v(z, t) = \omega\, Y_L \frac{z}{L} \sin\omega t \tag{6.58}$$

and therefore the energy dissipated by a linear damper, λ_l, is

$$\int_0^L \int_0^{2\pi/\omega} \lambda_l\, \omega^2 Y_L^2 \frac{z^2}{L^2} \sin^2\omega t \, dt \, dz = \frac{\pi}{3} \omega\, L\, Y_L^2 \lambda_l \tag{6.59}$$

Similarly, the quadratic damping, λ_q, dissipates:

$$2\int_0^L \int_0^{\pi/\omega} \lambda_q\, \omega^3 Y_L^3 \frac{z^3}{L^3} \sin^3\omega t \, dt \, dz = \tfrac{2}{3}\omega^2\, L\, Y_L^3\, \lambda_q \tag{6.60}$$

and equating these gives:

$$\lambda_l = \frac{2\omega}{\pi} Y_L\, \lambda_q \tag{6.61}$$

Figure 6.9 shows the frequency–amplitude plane contoured with lines of constant error derived from simulation of the harmonically forced non-

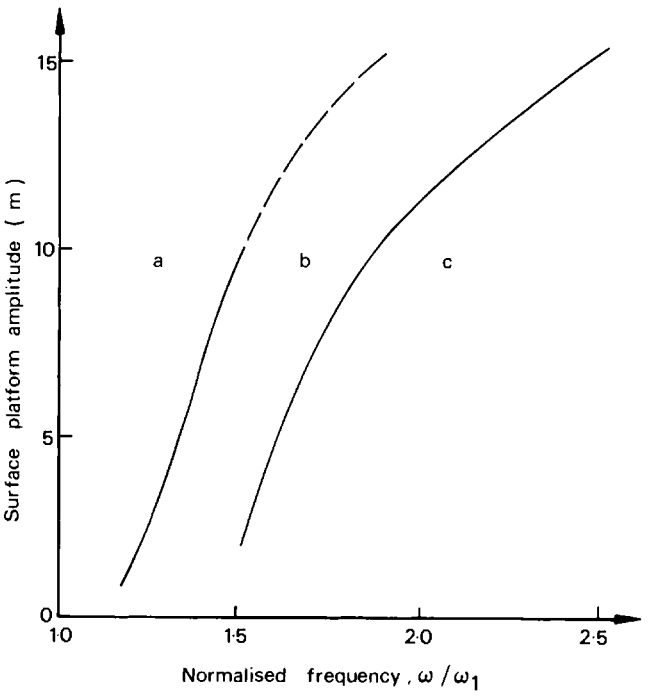

Figure 6.9. Error (t) in equivalent linearization on non-linear drag force for a 600 m tether; $C_D = 1.2$, $\omega_1 = 0.478$ rad/s (13.15 s) ((a) t > 5%; (b) 1% < t < 5%; (c) t < 1%)

linear damped system in comparison with the linearized analysis. The error measure, t, is defined as

$$t = 100 \left| \frac{F_l(i\omega) - F_N(i\omega)}{F_N(i\omega)} \right| \tag{6.62}$$

where $F_N(i\omega)$ is the non-linear force amplitude output at the tether top, and $F_l(i\omega)$is the equivalent linear force output. Clearly, this equivalent linear damping is adequate for the periods and amplitudes of interest in assessing platform dynamics near its resonant frequency. The result implies that the precise form of the damping is irrelevant so long as the correct amount of energy is dissipated per cycle.

A similar technique can be used to define an equivalent damping for each finite element in the frequency domain model. An iterative computation results where the damping at each element is initially assumed to be that predicted by the 'whole tether' linearization, the response is evaluated and the new amplitudes of motion at each segment are used to re-evaluate the damping factors. This technique gives excellent results but is only required at frequencies greater than 0.7 times the first tether natural frequency since it is only at these frequencies that the first and higher modes begin to become significant. Figure 6.9 shows the region in which 'whole tether' linearization is accurate to better than 1% for frequency response.

More complicated stochastic linearization techniques can be used to derive equivalent dampings for use in random seas. This is probably unnecessary for most tether configurations since their behaviour, if dangerous, need not be known very accurately and conservative (low) damping constants can always be assumed. Great mathematical sophistication is certainly not in order given that there is little convincing evidence that quadratic damping is a precise instantaneous model of reality in a random sea.

It is clear from a comparative assessment of the three tether dynamic models presented here that the modal model offers a relatively poor performance for the computational effort involved. On the other hand, the exact and finite element models both offer performance advantages linked to their special characteristics. The more complex finite element model can account for non-ideal tether characteristics such as tension variation and non-linear damping. The simplicity of the exact analytic calculation is also attractive for some purposes since the results presented in this chapter demonstrate that both tension variation and non-linear damping can be reasonably accurately represented by constant tension and equivalent linear damping in a linear tether model which can be used for the investigation of platform dynamics near its resonant frequency.

The great variation in apparent tether stiffness near wave frequencies is relatively unimportant in practice since the horizontal motions of the platform are mainly restrained by inertia in this frequency range. However, the responsiveness of the tethers to excitation by the platform near wave frequencies is disturbingly large and should be investigated thoroughly if TBPs are to be deployed in deep water.

A specific case study of a tether is also considered here using the finite element analysis to investigate tether response for a range of tether frequencies and surface platform excitation amplitudes. The variation with excitation frequency was determined by forcing the tether top with a displacement of unit amplitude at the frequencies of $\omega_1/2$, $3\omega_1/4$, ω_1, ω_2 and ω_3 where ω_n is the nth undamped natural frequency of the tether for lateral motions and is given by Equation (6.34).

The tether properties used in the calculations are a length L = 500 m, outer diameter, D = 0.22 m and inner diameter d = 0.07 m. Coefficients, C_m and C_D, are taken as 1.0 and 1.2, respectively, with a top tether tension of 30 MN. This is the tension value per platform corner; each corner having three tethers with 10 MN top tension. Figure 6.10 displays the variation of lateral deflection amplitude along the tether length and illustrates the development of tether mode shapes as the excitation frequency is increased. Both the calculations from 'whole-tether' and 'element-by-element' linearization are presented. The expected effect of higher modes at larger excitation frequency can be clearly seen. Note the tether displacement amplitude slope for the $\omega_1/2$ frequency at which the restoring force amplitude at the surface platform would be very small. The discrepancy between the 'whole-tether' and 'element-by-element' linearization is dependent on the difference between the distance of the tether oscillation amplitude from the tether rocking mode amplitude; this is consistent with the assumptions embodied in the whole tether linearization.

In all cases, except close to the first natural frequency, the 'whole-tether' linearization is a good approximation to the more exact 'element-by-

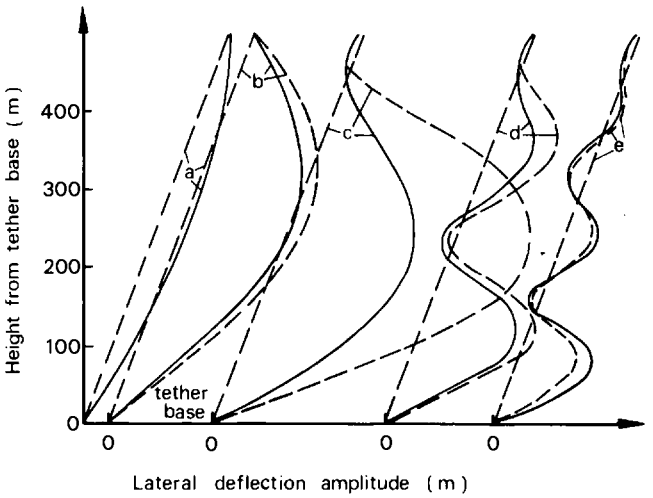

Figure 6.10. Tether amplitude variation with length. (Curves a,b,c,d and e are for excitation frequencies $\omega_1/2$, $3\omega_1/4$, ω_1, ω_2 and ω_3 respectively.) *Key*: — 'element-by-element' linearization; -- quasi-static analysis (straight line); --'whole-tether' linearization (curved line)

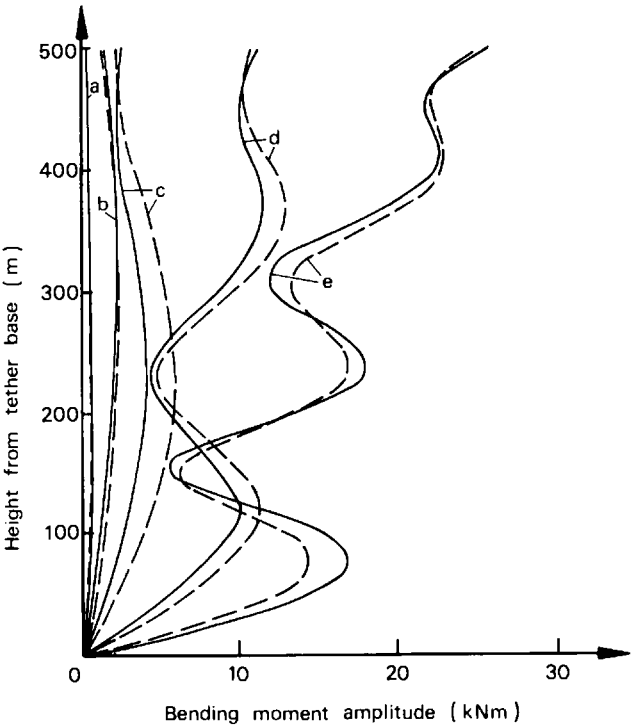

Figure 6.11. Bending moment variation with length. (Curves a,b,c,d and e are for excitation frequencies $\omega_1/2$, $3\omega_1/4$, ω_1, ω_2 and ω_3 respectively.) *Key*: — 'element-by-element' linearization; -- 'whole-tether' linearization

element' linearization technique. Figure 6.11 shows the bending moment amplitudes corresponding to the results of Figure 6.10. Note that the tether bending stiffness has been ignored in the formulation of the tether equations of motion. Since the solutions of these equations are used to derive equivalent bending moments from the tether curvature, non-zero bending moments can be obtained at the surface platform tether connection. The bending moment amplitude can be seen to rise as frequency is increased and the higher mode shapes raise the curvatures in the tether displacements. The difference between 'whole-tether' and 'element-by-element' linearization also remains small throughout the frequency range except around the first natural frequency.

In order to investigate the effect of the drag force non-linearity, the tether dynamic model is used at the first natural frequency for a number of surface vessel displacement amplitudes. Figure 6.12 displays the results for tether displacements. As the surface vessel amplitude is increased, the corresponding increase in tether velocities raises the drag damping coefficient and reduces tether displacement amplitudes. This has the effect of reducing the discrepancy between 'whole-tether' and 'element-by-element'

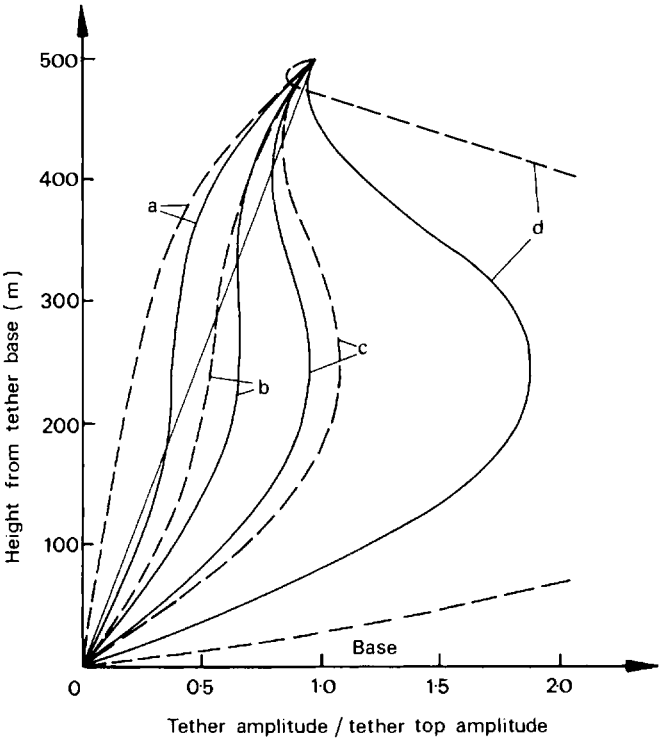

Figure 6.12. Variation of non-dimensionalized tether amplitude with length. (Curves a,b,c and d are for displacement amplitudes of tether top end 10 m, 4 m, 2 m and 0.5 m respectively.) *Key*: — 'element-by-element' linearization; -- 'whole-tether' linearization

tether linearization which only remains significant for surface platform displacement amplitudes in the range 0.5–1.5 m.

Since the surface platform is only influenced by the restoring force amplitude per unit platform amplitude ratio exerted by the tethers, an overall picture of tether dynamic performance can be obtained by plotting this ratio against the platform displacement amplitude in Figure 6.13 for both 'whole-tether' and 'element-by-element' linearization over a range of excitation frequencies. The equivalent idealized tether stiffness from Section 6.2 is indicated. The large effects of tether dynamics on the stiffness value experienced by the surface platform is clear. The frequency of excitation influences the restoring force ratio through the resultant tether mode shapes, whereas the surface platform excitation amplitude shows up through the resultant level of viscous damping affecting the restoring force ratio. The difference between 'whole-tether' and 'element-by-element' linearization is relatively small. Figure 6.14 shows an equivalent plot of the surface platform vessel restoring force amplitude due to the tethers against the surface vessel displacement amplitude. The 'hardening' spring nature of the tether restoring force with increasing surface level displacement amplitude is evident.

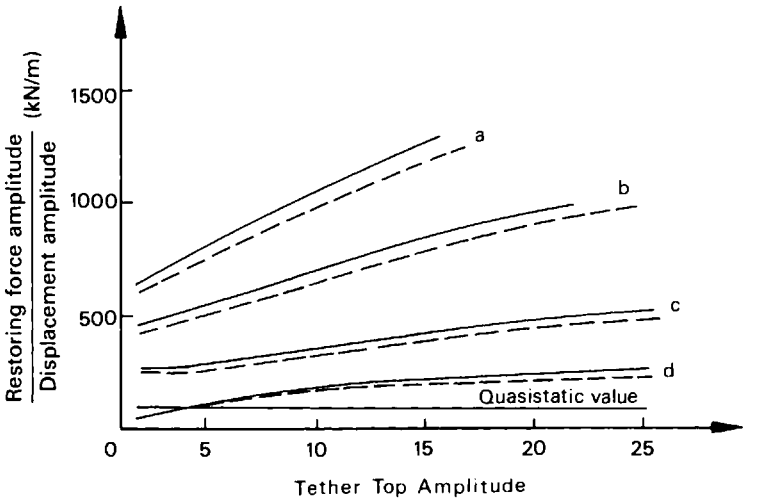

Figure 6.13. Harmonic response ratio variation with tether top displacement amplitude. (Curves a,b,c and d are for excitation frequencies ω_3, ω_2, ω_1 and $\omega_1/2$ respectively.) *Key*: — 'element-by-element' linearization; -- 'whole-tether' linearization

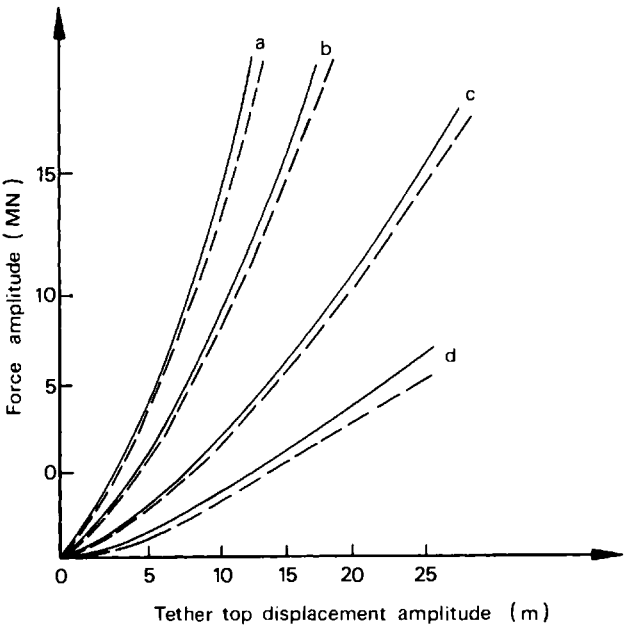

Figure 6.14. Force amplitude against tether top displacement amplitude. (Curves a,b,c and d are for excitation frequencies ω_3, ω_2, ω_1 and $\omega_1/2$ respectively.) *Key*: — 'element-by-element' linearization; -- 'whole-tether' linearization

6.4 Coupling between platform and tether dynamics

A coupled analysis of the TBP and tethers can be carried out in the following manner. First, the finite element model is used to evaluate tether velocities and the restoring force amplitude on the surface platform for each individual platform tether assuming unit surface platform displacement amplitude and taking due account of the tension variations along the tether length due its self-weight. Either the 'whole-tether' or 'element-by-element' drag linearization can be used here.

The tether displacements and equivalent bending moments along the tether are also determined using the equations:

$$Y = \frac{V}{i\omega} \tag{6.63}$$

and

$$\begin{aligned} M &= E\,I\,\frac{\delta y^2}{\delta z^2} \\ &= \frac{\delta}{\delta z}\left[\frac{E\,I}{\bar{T}}\left[\bar{T}\,\frac{\delta y}{\delta z}\right]\right] \\ &= \frac{\delta}{\delta z}\left[\frac{E\,I}{\bar{T}}(-f)\right] \\ &= -E\,I\left[\frac{f_{k+1}-f_k}{\delta z}\right] \end{aligned} \tag{6.64}$$

where $\bar{T}$ is the average tether tension; and EI is the bending stiffness of the tether.

The complex amplitude ratio of the tether restoring force on surface platform to platform displacement at tether top (equivalent to a complex stiffness) arising from the above dynamics calculation for the individual tether is substituted in place of the T/L term in the idealized tether stiffness calculations described in Section 6.2. This yields a (6 × 6) complex tether stiffness matrix which accounts for the orientation of the tether relative to the surface platform (for non-vertical taut tethers) as well as the lateral (to the tether) dynamics of the tether.

The calculation of the surface platform dynamics (through Equation (6.2)) is also altered since the mooring stiffness matrix, $\mathbf{K}_m$, now has complex elements. These complex stiffness elements can be made real by transferring parts of the matrix to equivalent inertia or linear damping components for the harmonic platform displacements. Then the complex stiffness of the moorings may at certain frequencies make the moorings appear as equivalent inertias or dampers to the surface platform. It is to be noted that the complex stiffness matrix, $\mathbf{K}_m$, will be frequency dependent due to the dynamics of the tethers.

The coupled dynamics of the TBP and tethers are computed so as to account for the non-linear damping in both the surface platform and tether motions. Initially, the surface platform's displacement amplitudes are calculated assuming quasi-static tether stiffness. These calculated displacement amplitudes are then inserted into the dynamic tether computations to re-evaluate the tether stiffness and the consequential platform motions. The interaction is only taken through one loop since the high mass and low natural frequency of the surface platform are such that its motions are inertia dominated and influenced only to a much smaller extent by the tether stiffness. Thus the tether stiffnesses affect the platform to a small extent only, whereas the platform motions do affect tether displacements and bending stresses substantially.

The influence of tether dynamics on surface platform motions can be illustrated by using a notional design of the configuration shown in Figure 6.2. This has free floating surface platform displacement of 98 000 t and 500 m long tethers with an excess buoyancy of = 16 000 t. Figure 6.15 displays the platform transfer function in surge with the ratio of platform surge amplitude to unit wave amplitude plotted against wave period for the idealized quasi-static tether model and the dynamic tether models with both 'whole-tether' and 'element-by-element' linearization. For this case, there is no discernible difference between the surface platform motions given by the three tether analyses. Note that the tether first natural period is at 4.84 s for this case.

However, the difference between the quasi-static and dynamic tether models becomes greater for lighter surface platforms and/or longer tethers. Figure 6.15 displays similar data for a platform of 24 000 t displacement in 1500 m water depth with a tether first natural period at 14.53 s and an

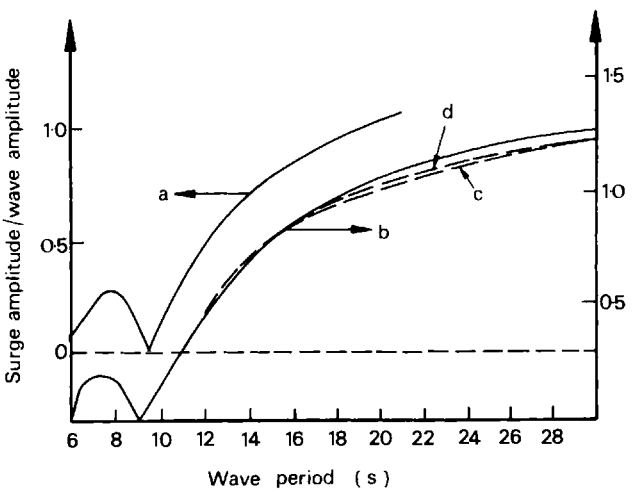

Figure 6.15. TBP surge response with and without effects of dynamic tethers. (Curve a for surface platform displacement 98 000 t with 16 000 t excess buoyancy and 500 m long tethers. Curve b for surface platform displacement 24 000 t with 16 000 t excess buoyancy and 1500 m water depth.) *Key*: full line – quasi-static tether assumptions; dashed line c – 'whole-tether' linearization; dashed line d – 'element-by-element' linearizations

excess buoyancy of 16 000 t. The higher natural period and consequent tether dynamic response shows up in the small difference between the different tether analysis models for the surface motions.

The dynamic analysis of the tethers and a coupled analysis of the platform and tethers yields several results which are common to the majority of tensioned buoyant platforms. These are:

1. The bending stresses induced in the tethers due to their dynamic motions are very small, the highest values occurring in tubular tethers which are relatively short, of large outer diameter and with thin walls. The deflections, however, are quite large at mid-length when the forcing frequency is approximately equal to the tether first lateral natural frequency.
2. The tether dynamics only affect the motion response of the surface platform noticeably if the tethers are long, are of the order of 1500 m or more, have a large mass per unit length and the platform has a relatively small displacement.
3. It is not necessary to use an equivalent damping linearization technique for each finite element of the tether because it is only around the tether first natural frequency that there is any difference between the two techniques, and even then the 'whole-tether' technique gives the more conservative values of bending moment. Furthermore, there is very little difference between the effects of the two on the motion response of a platform, even in the worst cases. The technique of 'each-element' linearization also takes up more computation time depending on the convergence criterion specified.

6.5 Model tests

Tests at model and full scale have played an important role in understanding the behaviour of TBPs in waves and also, of course, in validating analysis methods used in design. This section presents the results of model tests and comparisons with prediction for two TBP designs and for the case of a tether exhibiting dynamic behaviour.

6.5.1 Tests for surface platforms

Two series of test results are presented. The first series of tests were carried out in a tank of water depth 7.6 m (25 ft). Waves were generated by means of a vertical oscillating wedge type wavemaker actuated by hydraulic rams. Testing was carried out using both regular and random waves with results from some of the regular wave tests presented here.

Figure 6.16 shows the configuration of the platform used with full scale dimensions. Tensioning of the tethers was accomplished using constant tension springs at still water for each of the tethers, and clamping the tethers at the specified pretension for the test runs. The tethers comprised of lengths of multi-strand steel cable of 0.125 inch diamter. Ballasting was achieved by pumping water into or out of the columns to obtain the correct buoyancy. A model riser was also attached to the platform.

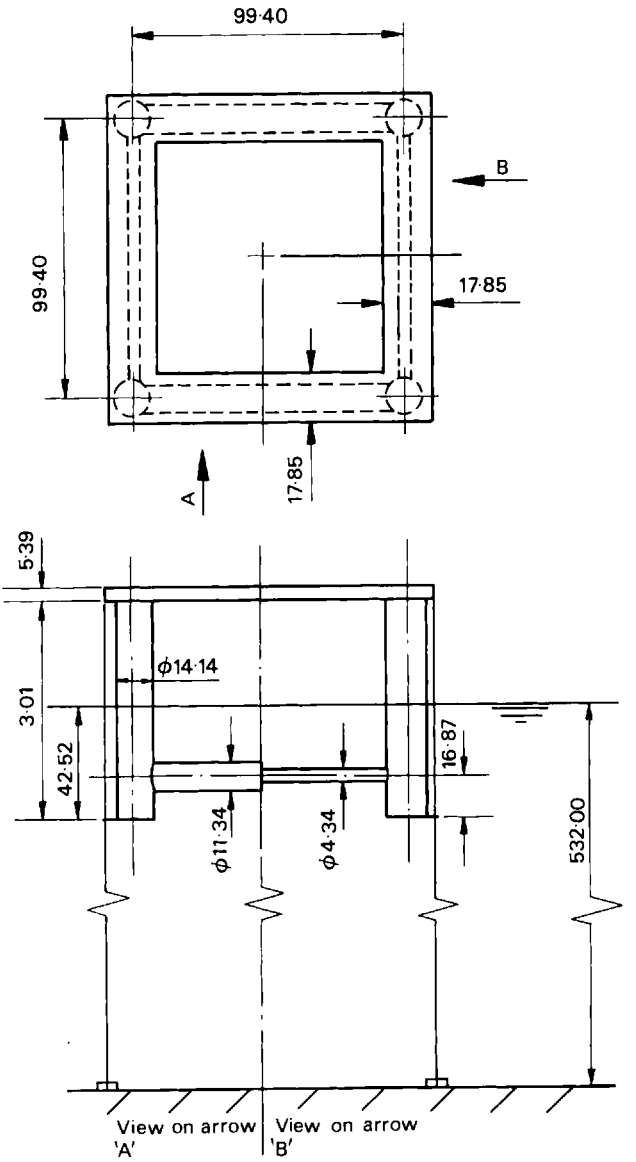

Figure 6.16. Heriot–Watt TBP test model:
Total mass = 32 100 t
Total pretension = 14 944 t
Displacement = 47 044 t
Centre of gravity = 4.20 m below water level
Radii of gyration: k_x = 55.93 m, k_y = 52.7 m, k_z = 67.55 m
Natural periods: heave = 2.98 s, pitch = 2.98 s, roll = 3.14 s, yaw = 84.97 s
surge = 86.78 s, sway = 96.83 s
Tether characteristics (per tether):
axial stiffness = 5762.3 t/m
total weight = 343 t
Full size figures given for 1:70 scale, dimensions in (m)

Tether tensions were measured using strain gauged 'horseshoe' type transducers fixed at the base of the wave tank. Care was taken to ensure that the natural frequencies of the horseshoes were well above vortex shedding and tether natural frequencies. Platform motions were measured using a television monitoring system providing a signal proportional to the displacement of a moving target. Resistance sensing wave probes were used to measure wave heights and to provide a phase angle reference. Typical data sampling rates were 50 samples per second for 1500 samples per channel. Digital time history data were reduced to amplitudes and phases for regular waves using a numerical harmonic analysis and to response spectra through fast Fourier transforms for irregular wave tests.

Figures 6.17 and 6.18 show typical response amplitude operators for surge and tether tension. These are calculated from regular wave test data and shown together with the predicted response from the hydrodynamic analysis described in Section 6.2. Two platform headings are used: 0° and 22.5° (see Figure 6.17 for wave direction). Note that the frequency axes of the diagrams are given for full scale values in rad/s.

Predicted tether tension responses compare well with model tests. Phase angle comparisons are also shown to be good, this being a critical test of computer simulation accuracy. The phase angles are defined relative to the wave elevation on the vertical centre line of the platform in still water with phase angle lag being taken as positive. The observed discrepancies in surge amplitude are probably due to the additional forces generated by the scaled riser installed from the platform during the tests. The horizontal restoring force due to the riser is accounted for in the analysis by the total riser top tension being distributed equally in the four corner tethers, although the horizontal inertia and drag force contributions of the riser are ignored.

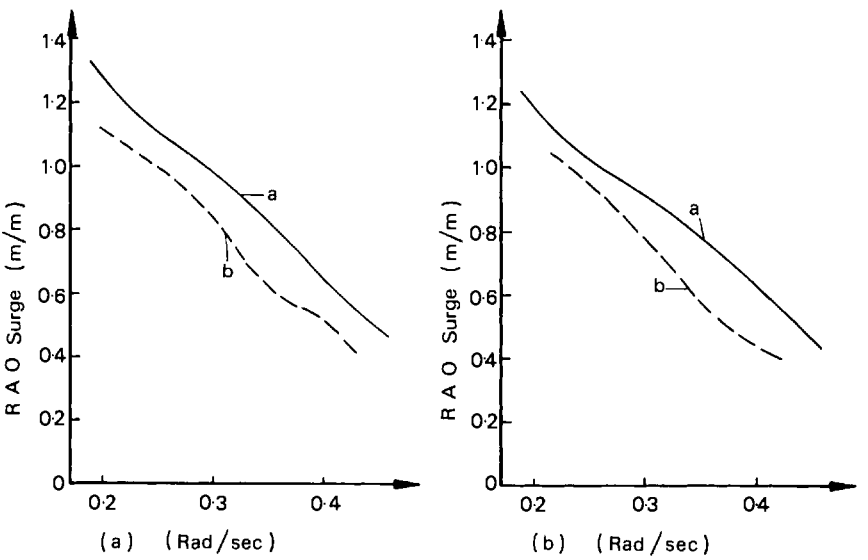

Figure 6.17. Surge motions in waves: (a) 0° platform heading; (b) 22.5° platform heading. *Key*: a – theory; b – regular wave (H = 21–27 m)

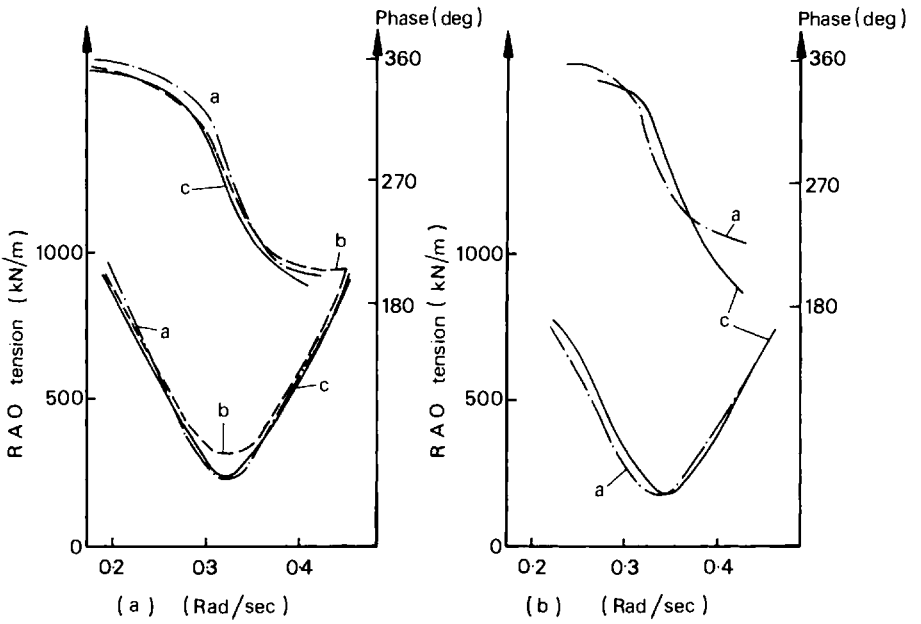

Figure 6.18. Platform tether tensions: (a) 0° platform heading – fore tether; (b) 22.5° platform heading – starboard fore tether. *Key*: a – port; b – starboard; c – theory

Sample time histories for tether tension responses are shown in Figure 6.19. The major response is at wave frequency with a pronounced superharmonic oscillation superimposed on the tether tension variation. The 'relative tension amplitude' is provided for guidance. Figure 6.19 shows that the amplitudes of tether tension increase with incident wave height (at constant wave frequency) in the expected manner. A digital spectral analysis of random wave data from the tests and direct measurements from the regular wave time history data (2.95 rad/s (model scale) trace in Figure 6.19, for example) indicate that a superharmonic frequency of 17.91 rad/s (model scale) is excited in the tethers. Calculations give a tether first natural frequency (at mean tension) of 21.17 rad/s (model scale), whereas the vortex shedding frequency at mid-tether based on half the tether maximum velocity at this station is computed to be 18.03 rad/s (model scale). It is also to be noted, however, that the natural period in heave of the platform is 2.98 s full scale corresponding to 17.64 rad/s frequency at model scale.

The form of the tension response is a combination of the in-line hydrodynamic response of the tether (with vortex shedding), and the force due to the extension of the tether caused by the motion of the platform (predominantly heave for the range of frequencies presented). It is interesting that this form of tension variation is similar to results obtained in oscillatory flow tests on rigid and flexible cylinders by Verley and Every (1977), in which single and grouped stationary slender circular cylinders were subjected to regular waves. A complication arises in these tests, however, due to the proximity of the natural frequencies of tether

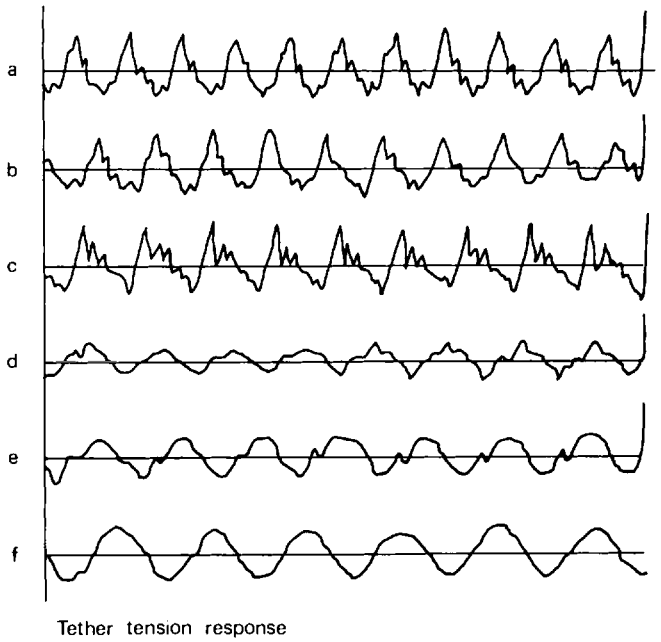

Figure 6.19. Tether tension time histories (starboard aft tether TLP with single tube riser, wave angle = 0°): (a) relative tension amplitude = 0.80, phase = 258°, wave height = 0.362 m, period = 1.77 s; (b) relative tension amplitude = 0.70, phase = 256°, wave height = 0.366 m, period = 1.92 s; (c) relative tension amplitude = 0.64, phase = 281°, wave height = 0.412 m, period = 2.13 s; (d) relative tension amplitude = 0.41, phase = 315°, wave height = 0.346 m, period = 2.40 s; (e) relative tension amplitude = 0.62, phase = 340°, wave height = 0.350 m, period = 2.72 s; (f) relative tension amplitude = 0.89, phase = 347°, wave height = 0.358 m, period = 3.15 s

vibrations, of vortex shedding from a tether and the heave natural frequencies of the platform/tether system – these frequencies being 21.17, 18.03 and 17.64 rad/s, respectively, all at model scale.

At the same time, it has borne in mind that the tension transducers will be most sensitive to platform heave motion induced tensions, with the effects of tether vibrations and vortex shedding only appearing as second order effects on the tension transducer outputs. The actual superharmonic frequency on the tension time histories is measured to be 17.91 rad/s (model scale), suggesting that this feature is primarily induced by platform/tether heave dynamics, although the close proximity of the vortex shedding and tether first natural frequencies are such as to raise the possibility of interaction between the phenomena giving rise to these frequencies.

Similar testing of a TBP was performed by a Norwegian group (Faltinsen *et al.*, 1982). It was felt useful to compare the predicted response of the hydrodynamic analysis presented here with the results of some of these tests. The comparisons cover a wider range of frequencies than those for the first tests and are based on testing in long crested regular waves, in bi-frequency wave-trains as well as in long crested irregular sea states. Only the results of the irregular wave tests are presented here. Details of

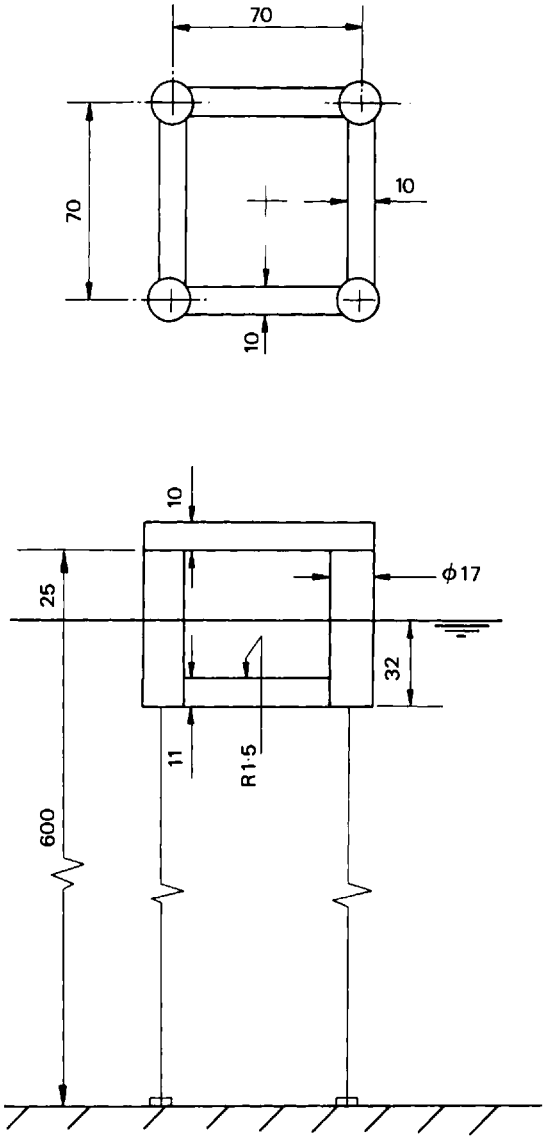

Figure 6.20. Norwegion test model
Total mass = 35 160 t
Total pretension = 17 000 t
Displacement = 52 160 t
Centre of gravity = 3.56 m below water level
Radii of gyration: k_x = 35.1 m, k_y = 35.1 m, k_z = 42.4 m
Natural periods: heave = 2.2 s, pitch = 2.4 s, roll = 2.4 s, yaw = 87.0 s
surge = 107.0 s
Tether characteristics (per tether):
axial stiffness = 8400 t/m
total weight = 925 t
Full size figures given for 1:60 scale, dimensions in m

the platform used for this series of tests is shown in Figure 6.20. The comparisons presented in Figure 6.21 at full scale are for the platform angled at 0 and 45° to the wave direction. The sea has a 12 m significant wave height with a zero-crossing period of 15 s. There is no contribution from wind or current.

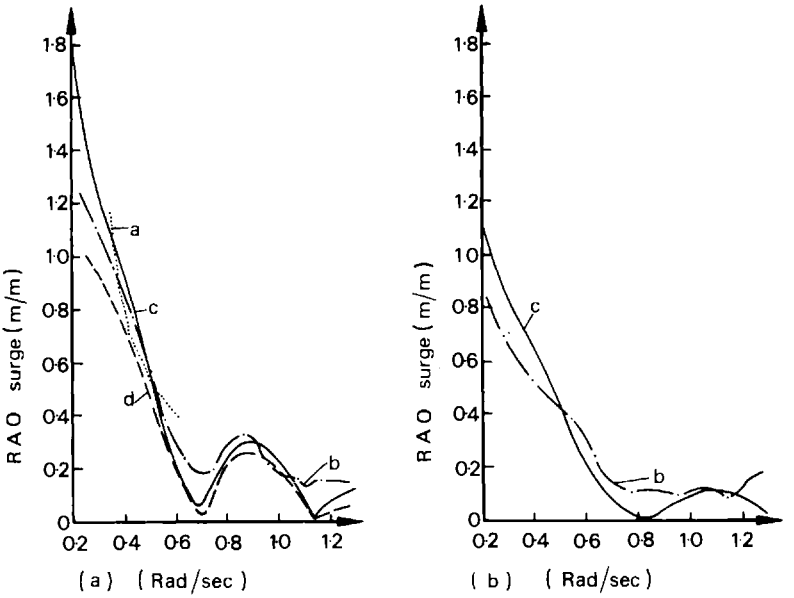

Figure 6.21. Surge motions in waves: (a) 0° platform heading; (b) 22.5° platform heading. *Key*: a – regular wave (H = 12 m); b – random waves (H_s = 12 m); c – theory; d – Norwegian program

The calculated surge response for both headings are in good agreement with the measured data for all frequencies except where minima are predicted. The recorded surge in these cases is greater than calculated. For frequencies over 1.1 rad/s, this might be expected as the wavelength is of the same order as the leading platform dimensions. At around 0.6–0.8 rad/s, the full wave force cancellation does not occur. This cancellation is due to equal and opposite forces induced by wave action on different parts of the platform structure at wave frequencies with wavelengths close to half the platform length. The apparent absence of full wave cancellation is thought to be due to the finite band width of an irregular wave data analysis causing a loss in resolution of the derived response transfer function.

The surge responses were found to be relatively insensitive to the calculated values of added mass and drag forces. However, the prediction of tension amplitude response was found to be strongly dependent on the vertical flow added mass forces on the platform columns for waves of frequencies in the range 0.5–0.8 rad/s. Careful modelling of the column lower end geometry was thus required.

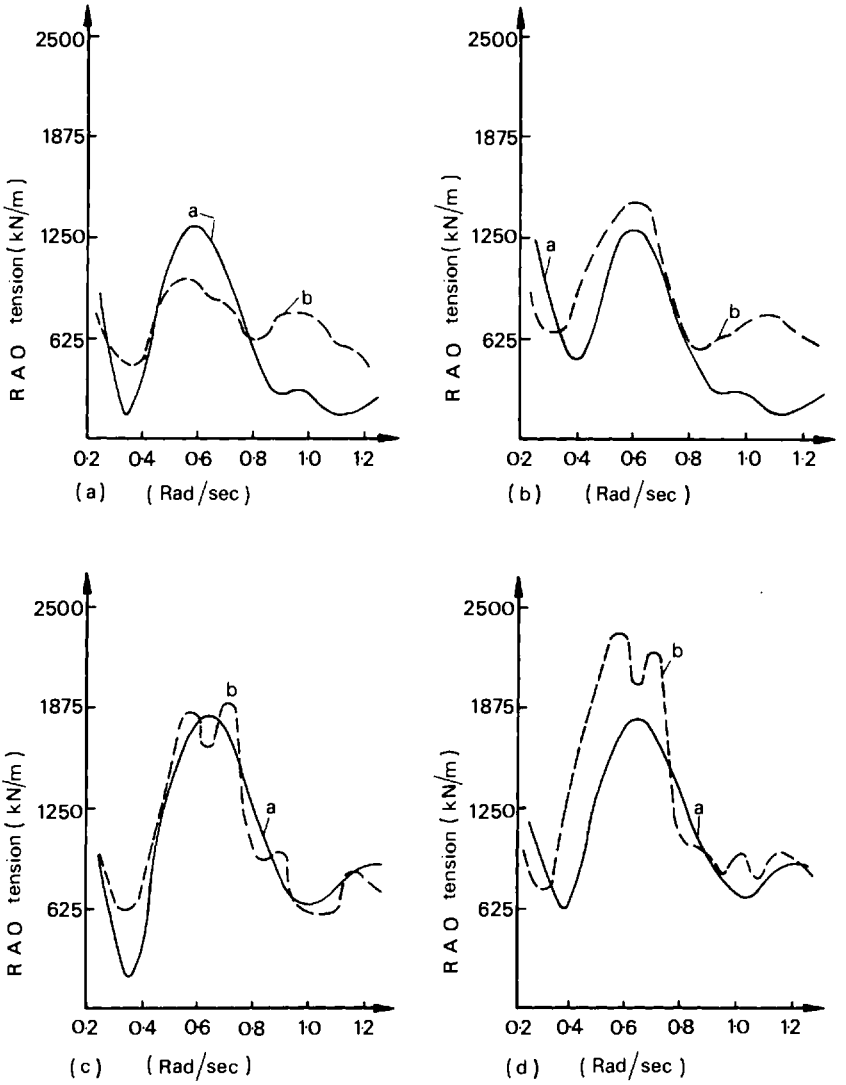

Figure 6.22. Tether tension amplitudes in waves: (a) 0° heading – fore tether; (b) 0° heading – aft tether; (c) 45° heading – fore tether; (d) 45° heading – aft tether. *Key*: a – theory; b – experiment – random waves (H_s = 12 m)

Figure 6.22 shows reasonably good comparison between analysis and model tests for tether tension variations at full scale. For the model tests carried out with a 45° wave direction, the aft tether tension amplitude around a frequency of 0.6 rad/s was greater than that for the fore tethers. The analysis predicts the reverse of this with the fore tether tension amplitudes being slightly larger. This feature is also apparent for the 0° heading case shown in Figure 6.22. The reasons for this are not obvious. Apart from experimental errors, the discrepancy can be ascribed to the

effects of low interference between adjacent members. There is a further discrepancy between predicted and measured tension amplitudes for the 0° heading case at higher wave frequencies. In this frequency range, wave induced pitching moments on the platform contribute a large proportion of the tension magnitudes – suggesting that an incorrect estimate of this moment may lead to the observed discrepancy.

These model test results show generally good agreement with theory, with the exception of high frequency superharmonic tensions vibrations in the tethers. At the scales tested, the amplitudes of these superharmonic vibrations were significant. The proximity of the first tether natural frequency of the platform/tether system raises difficulties in interpreting the underlying physical mechanism causing this superharmonic vibration.

Attention is now focused on using model scale experiments to test the validity of the analysis methods used for tether dynamics. These tests were carried out in a specially constructed 4.5 m deep by 1.5 m square based still water tank. A tether model is mounted on the base of the tank and the tether upper end is excited in surge and heave by an electro-hydraulic servo mechanism. Tether displacements are measured using a television monitoring system described earlier.

A test model of a tether at 1/27th scale (121.5 m; 399 ft full scale length) was constructed using concentric tubes of a Cellulose Acetyl Butyrate material which possessed the properties necessary to scale the tether bending stiffness, with the mass per unit length scaled by using wires running down the centre of the tether. Table 6.2 gives the various scaling rules and dimensions used for the model at high and low tension values.

First, the fundamental first natural frequencies of the tethers were measured in water. The natural frequency of the high tension case was 3.7 Hz (23.25 rad/s) whereas the low tension case yielded 1.13 Hz (7.1 rad/s) both at model scale. For both cases, the damping was measured to be approximately 20% of critical.

Table 6.2 Physical parameters for tether model

		Tether	
Parameter	*Scaling factor*	*Model scale*	*Full scale*
Length	α	4.07 m	110 m
Outside diameter	α	9.5 mm	0.26 m
Tension	$\beta\alpha^3$		
high		160.19 N	875 tf
low		27.49 N	150 tf
Rigidity	$\beta\alpha^5$	0.4424 N/m^2	17.3 MN/m^2
Mass/length	$\beta\alpha^2$	0.0096 kg/m	19 kg/m
Time	$\sqrt{(\alpha)}$		
Velocity	$\sqrt{(\alpha)}$		
Acceleration	1		
Ang. freq.	$1/\sqrt{(\alpha)}$		

Notes:
$\alpha = 27$ length scaling factor.
$\beta = 2.725$ density scaling factor.

The external television cameras were used to measure the in-line displacements of the model at low and high tension. This yielded amplitude and phase information which is presented in Figure 6.23. Figure 6.23(a) shows maximum in-line displacement amplitudes of the model tether at full scale values of 2.7 m top excitation amplitude and 9.12 s period as measured by experiment and calculated from the finite element analysis model (see Section 6.3). For this high tension case, there is minimal deviation from the straight line joining the ends of the tether. Figure 6.23(b) shows the in-line displacement for the low tension case with similar

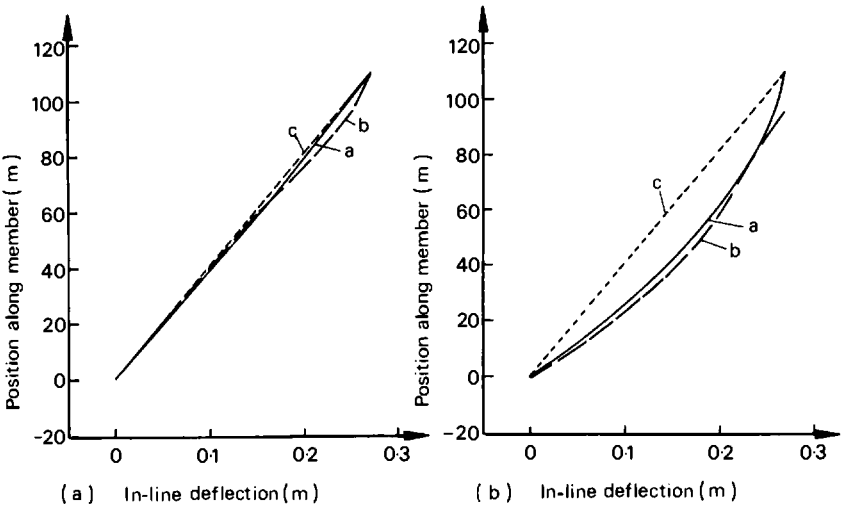

Figure 6.23. Tether amplitude response: (a) high tension (amplitude = 2.7 m, period = 8.93 s); (b) low tension (amplitude = 2.7 m, period = 9.12 s). *Key*: a – experiment; b – theory; c – straight line

values of top excitation (2.7 m amplitude) at 8.93 s period. As is to be expected there is greater bending along the length of the low tension tether. It is seen that the finite element model, described in Section 6.3, compares reasonably well with experiment. The above results demonstrate that there is reasonable agreement between the analysis methods described in Section 6.3 and experimental observations of the dynamics of tethers.

6.6 Mathieu instability

The variations in tether tension due to wave induced vertical forces on a tensioned buoyant platform can lead to the possibility of exciting subharmonic parametric oscillations in platform surge and sway motions. This physical phenomenon can be described in the following way. The longitudinal stiffness of the tethers restrains the vertical motions of the platform against wave excitation forces. The consequential variations in tether tension alter the effective lateral spring stiffness of the platform, leading to the possibility of a Mathieu type of platform excitation in horizontal motions. There is also the possibility that Mathieu type parametric

oscillation in the tether itself could be excited at half the frequency of the wave excitation. In very deep water, this frequency could coincide with the lowest natural lateral tether frequency. Hsu (1975 a,b) has studied such oscillations of a freely hanging string (a riser or unattached tether) with natural frequencies which are much lower than those of a tether and hence more likely to be excited by forcing at half the wave frequency. Hsu has concluded that quadratic damping places strict limits on the oscillation amplitude. On the basis of his work, it seems unlikely that Mathieu excited lateral tether oscillations will be a problem for TBP tethers.

Nevertheless, a methodology for determining the magnitude of maximum platform, parametrically excited oscillations of the platform in still water is developed here. Further consideration of such instabilities for free hanging crane loads is presented in Chapter 7.

Horizontal motions of a TBP are restrained by the horizontal components of the tether tensions and the inertia of the surface platform. In the wave frequency range, up to 20 s period, these inertia forces are dominant in comparison with the tether forces. At larger periods which include the resonant periods of platform horizontal motions, these forces are comparable. In this regime, the tether tension variation induced by restraining the platform heave, roll and pitch motion can, under certain conditions, inject energy into horizontal motions.

The horizontal restraining force, f, can be written as

$$f = -K_0(1 + g(t))\, x(t) \tag{6.65}$$

where x is the horizontal platform motion; t denotes time; K_0 ($= \bar{T}/\mathrm{L}$) is the average value of the horizontal spring; $g(t)$ is its proportional variation caused by heave forces; $\bar{T}$ is the mean tether tension; and L is tether length. Roll and pitch moments will cause equal and opposite tension variations in opposing tethers but will not alter the total surge or sway spring force.

Writing the equation of motion with the time dependent stiffness given:

$$(M_x + M_{ax})\ddot{x} + C_x \mid \dot{x} \mid \dot{x} + K_0\,(1 + g(t))x = f_w(t) \tag{6.66}$$

where M_x and M_{ax} are the physical and hydrodynamic added mass; C_x is the quadratic damping coefficient; and $f_w(t)$ is the wave exciting force.

In sinusoidal waves, this equation represents a Mathieu equation, with a square law damping term and exciting force $f_w(t)$. The classic, linear Mathieu equation has been studied exhaustively and its properties are well known. In canonical form, it is written as

$$\ddot{\psi} + (\delta + \epsilon \cos 2t)\psi = 0 \tag{6.67}$$

In certain areas of the $\delta - \epsilon$ plane, the variable ψ is unstable and grows exponentially without limit, even when linear damping is present. Note that Equation (6.67) can include a linear damping term, $2c\dot{\psi}$, but is returned to the original form by the transformation $\phi = \psi e^{ct}$ so ψ is stable if ϕ grows slower than e^{ct}. The physical reasons for this behaviour are explained later.

Rainey (1977) first used the above equation for the TBP and included forcing and 'equivalent linear' damping terms. Other authors (Hsu, 1975 a, b) have studied Mathieu type instabilities of hanging strings (risers) in a

fluid and have included square law damping effects but excluded the forcing term. Troger and Hsu (1977) subsequently include the forcing term in the analysis. Mathieu type instabilities of rolling ships, with time varying roll stiffness due to heave motion, have also been investigated.

Most of these studies have assumed that the spring variation, $g(t)$, is sinusoidal since analysis is difficult if $g(t)$ is modelled as a zero mean, fairly narrow band Gaussian random process, which is rather closer to reality. However, it is also not proven that sinusoidal spring variation is the worst possible time history and it is conceivable that a random sea could induce a more severe instability instead. A more physical approach to investigate the subharmonic motions is thus employed below.

Instability is the consequence of work being done faster on a system than it can be dissipated. In the case of the Mathieu equation, energy is input by the non-conservative, time varying spring force and dissipated by the damping.

The rate of working, $\bar{P}$, of the spring force over a time period τ is

$$\bar{P} = \left[\frac{1}{\tau}\int_0^{\tau} f(t)\,\dot{x}(t)\,\mathrm{d}t\right]_{\tau\to 0}$$

$$= -\frac{1}{\tau}\int_0^{\tau} K_0\,(1 + g(t))\,x(t)\,\dot{x}(t)\,\mathrm{d}t \tag{6.68}$$

where $f(t)$ is the spring force and; $x(t)$ is the resultant motion.

Integrating by parts yields

$$\bar{P} = \frac{1}{2\tau}\left[K_0(1 + g(\tau))x^2(\tau) - K_0(1 + g(0))x^2(0)\right]$$

$$+ \frac{K_0}{2\tau}\int_0^{\tau} g'(t)x^2(t)\,\mathrm{d}t \tag{6.69}$$

The first term represents the difference in stored energy at the beginning and end of the integration interval, while the second term is caused by the net rate of working of the spring. It is clear that net positive work will be done by the tethers if the rate of change of spring stiffness, $K_0\,g'(t)$, is positive whenever $x^2(t)$ is large. Since $g(t)$ has an upper and lower bound, $g'(t)$ should be negative when $x^2(t)$ is small so it can increase when x is large. If $g(t)$ varies with period p, then energy will be put into motions of period $2\,np$ ($n = 1, 2, 3, \ldots$) and if one of these periods, particularly the first, $2p$, corresponds to the natural frequency

$$\sqrt{[K_0/(M_x + M_{ax})]}\ \text{rad/s}$$

In reality, little is known of the properties of $g(t)$, except that it is bounded by the maximum size of heave force which can be applied to the platform by waves. The response is the result of continuous energy input so the form of the history of $g(t)$ is important as well as its maximum, minimum and average values. It is therefore sensible to treat $g(t)$ as a controllable input to the system and to try to devise some 'worst case' input history, which will always be more destabilizing than any other possible

history. For example, the criteria for selecting the worst case input $g(t)$ could be based on maximum average displacements, largest peak displacements or maximum energy input into the motion. Problems of this type can be solved using the Pontryagin Maximum Principle of optimal control theory (Takahashi *et al.*, 1972). The Maximum Principle indicates that the spring stiffness should be switched between maximum and minimum values, but explicit derivation of the switching times appears extremely difficult, particularly in the non-linear case. A physical argument shows that the stiffness should be switched 'up' near a maximum of $x^2(t)$ and 'down' near the minimum. This is illustrated by a spring force–displacement indicator diagram shown in Figure 6.24.

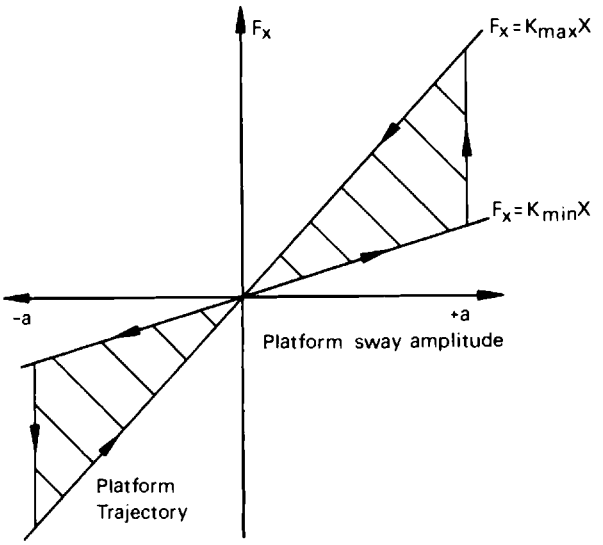

Figure 6.24. Spring force variation during subharmonic oscillations

The strictly optimal solution implies that the switching times are slightly modified by the dynamics and damping levels of the particular platform being considered since the platform motion is dependent on the switching strategy and, on the average, higher frequency motions allow more switchings and hence higher input power. However, these modifications are found to produce trivial changes in the net average energy input.

It is illustrative to consider the switching law in the $x - \dot{x}$ (phase) plane shown by Figure 6.25 for a lightly damped system starting from an initial condition and executing persistently growing oscillations. The spring rate here is high when $x\,\dot{x} < 0$, low when $x\,\dot{x} > 0$, and between switches the platform moves as a square law damped system at approximately its natural frequency. Referring to Figure 6.24, it can be observed that the switching law allows the platform to move away from $x = 0$ against a weak spring and it is forced back by a strong spring. Motions of this nature continue to grow until the energy dissipated by the damping is equal to that injected by the tethers. Figure 6.25 shows trajectories for the motion of the

platform growing up to the limit cycle amplitude from a small initial condition and decaying down to it from a high initial state. The action of an upper bound for the amplitude of this limit cycle will give a measure of maximum platform oscillation amplitude due to this feature.

If the sway spring stiffness switches between values of K_{max} and K_{min} at the maximum and minimum displacements of the platform, as shown in Figure 6.25, the energy input per cycle will be

$$E_{input} = (K_{max} - K_{min})a^2 \tag{6.70}$$

where a is motion amplitude; and K_{max}, K_{min} are maximum and minimum platform stiffnesses. This energy input must balance the energy dissipated

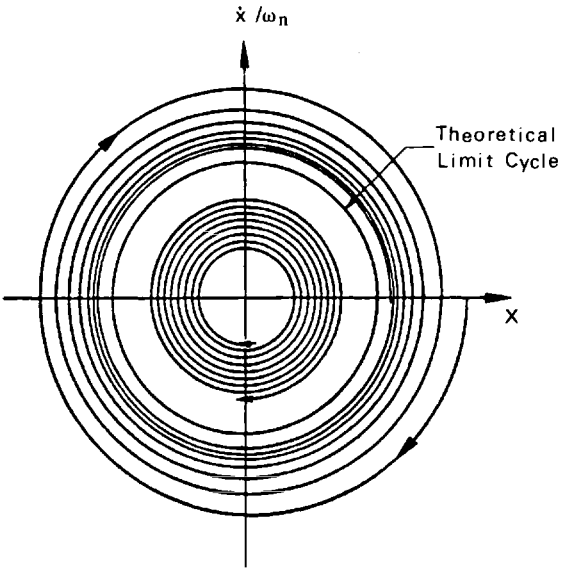

Figure 6.25. A phase plane plot for unstable TBP oscillations

by linear and quadratic damping during the approximately sinusoidal angle. The energy inputs are

$$E_{linear} = \pi\lambda_l a^2\omega \tag{6.71}$$

and

$$E_{quadratic} = \tfrac{8}{3}\lambda_q a^3\omega^2 \tag{6.72}$$

where ω is oscillation frequency; and λ_l, λ_q are linear and quadratic damping coefficients. Equating input and output power leads to an expression for the steady state value

$$a = \frac{3}{8\lambda_q\omega^2}[K_{max} - K_{min} - \pi\lambda_l\omega] \tag{6.73}$$

Using the more optimistic assumption of a sinusoidal spring variation, the energy input per cycle is

$$E_{\text{input}} = \frac{\pi a^2}{4} (K_{\max} - K_{\min}) \sin\theta \tag{6.74}$$

where θ is the phase between the response and the spring variation. Note that there is no steady solution for the amplitude if linear damping only is present. The system is either stable, in which case Mathieu oscillation never occurs, or unstable, resulting in a continuously increasing amplitude. The equation of motion could be solved with the method of slowly varying parameters used by Hsu (1975b) in his study of a square law damped hanging string.

However, $\sin\theta$ in Equation (6.74) is never greater than unity so an upper bound on the energy input and hence the motion amplitude is simple to derive as

$$a = \frac{3\pi}{8\lambda_q \omega^2} \left[\frac{K_{\max} - K_{\min}}{4} - \lambda_l \omega \right] \tag{6.75}$$

This upper bound on the motion amplitude agrees exactly with that derived by Hsu when ω, the frequency of spring variation, is coincident with the natural frequency of oscillation of the platform.

It is interesting to note that the maximum motion amplitude is inversely dependent on the square law drag term, which could be increased by increasing the projected area of the platform below the water line. The oscillation amplitude is also predicted to be inversely proportional to water depth since $K_{\max} = T_{\max}/L$, so if Mathieu oscillations do not affect a shallow water platform, they will not affect similar platforms in deeper water. Substituting typical parameter values for a 40 000 t platform mass and 16 000 t of excess buoyancy in 150 m of water, we obtain a value for amplitude a of 3.8 m if $K_{\max} = 1.1K_{\text{ave}}$, the average stiffness value. The natural period of the platform is 40 s so the spring variation must have a period of 20 s, a period at which there is very little power in the wave spectrum. The variability in stiffness, assumed to be 10%, may be regarded as being conservative since the heave force per unit wave amplitude is 260 tf/m at this frequency, implying that for the platform in question 5 m waves are needed to produce a 10% variation in tether tension and hence the heave spring.

The foregoing stability argument may not seem rigorous since a parametric response is assumed in order that energy input and dissipation can be calculated and the amplitude of motion deduced. It is not proven but it is reasonable to argue that the assumed sinusoidal response is the worst possible from the point of view of energy input. It can be shown by simulation that, for typical parameter values (Figure 6.25), the assumed response is close to the one caused by the time varying spring. Between switches the platform behaves as a square law damped system, perturbed by the known small wave frequency forces.

This decoupling of force and response has made the solution of the 'worst case' problem relatively easy. The Pontryagin Maximum Principle gives conditions that a solution to the true maximum energy input

problems must satisfy but does not provide an explicit solution. It is sometimes possible to derive a solution iteratively from the implicit conditions but this is probably unnecessary since the control law is the same as that derived by naïve analysis with some modification to the switching time. It is found by numerical experiment that the final oscillation amplitude is not changed greatly by small changes in the switching times.

The formal solution via the Maximum Principle is difficult because it requires the solution of the non-linear equations of motion to yield a feedback law for the switching of the spring constant. Another approach to follow is to use Lyapunov stability theory which does not require a solution for the motion.

Lyapunov's second stability theorem is most simply explained geometrically. Consider a set of closed curves enclosing the origin of the x–$\dot{x}$ plane, defined as a potential function $V(x, \dot{x})$ = constant, C. If the phase vector of the TBP system always has components parallel to the negative origin facing gradient of $V(x, \dot{x})$, then once the system state is inside a particular potential level, it will never leave it.

Figure 6.26 illustrates these ideas; the level function is a function of the kinetic and potential energy of the system of the form

$$V = \frac{ax_1^2}{2} + \frac{bx_2^2}{2} \tag{6.76}$$

where $x_1 = x$; $x_2 = \dot{x}$; and a, b are constants.

Thus

$$\nabla V = \begin{bmatrix} ax_1 \\ bx_2 \end{bmatrix} \tag{6.77}$$

Writing Equation (6.66) in terms of x_1, x_2, the position and velocity of the platform, yields

$$\left.\begin{aligned} \dot{x}_1 &= x_2 \\ \dot{x}_2 &= -\frac{K_0}{M_t}(1 + g(t))x_1 - \frac{C_x}{M_t}x_2 \mid x_2 \mid + \frac{f_w}{M_t} \end{aligned}\right\} \tag{6.78}$$

where M_t ($= M_x + M_{ax}$) is the platform's total mass. For stability,

$$\nabla V^T \cdot \dot{\mathbf{x}} \leqslant 0 \tag{6.79}$$

so

$$ax_1x_2 - \frac{b}{M_t}K_0x_1x_2 - \frac{b}{M_t}K_0g(t)x_1x_2\frac{b\lambda_1}{M_t}x_2^2 \mid x_2 \mid + \frac{b}{M_t}f_wx_2 \leqslant 0 \tag{6.80}$$

The parameters a and b can be chosen freely so long as $V(\mathbf{x})$ increases with $\mid \mathbf{x} \mid$ and encloses the origin. So we set

$$a = \frac{bK_0}{M_t} \tag{6.81}$$

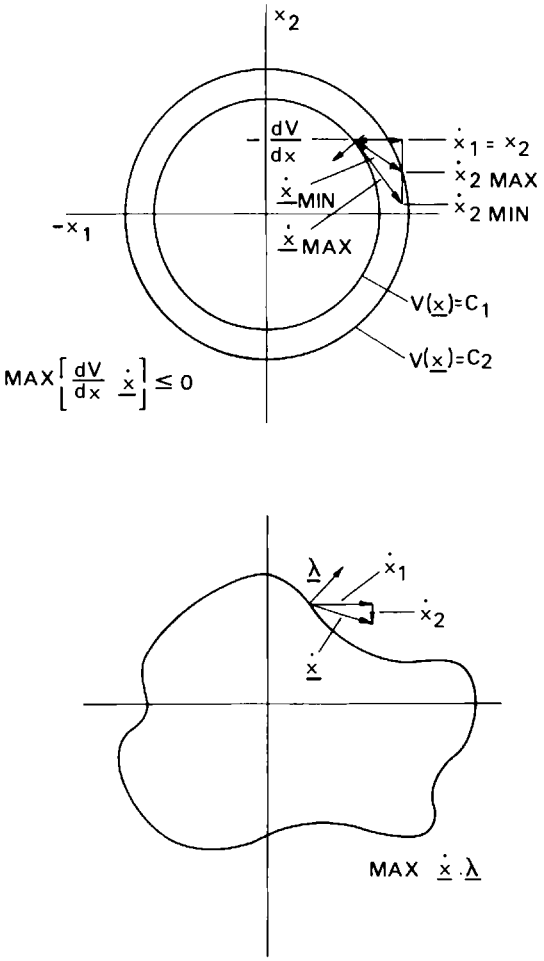

Figure 6.26. Contours of equal energy for the Lyapunov stability theory and the Pontryagin principle

to yield a condition

$$\lambda_1 x_2^2 \mid x_2 \mid \geqslant f_w x_2 - K_0 g(t) x_1 x_2 \tag{6.82}$$

which simply states that rate of energy dissipation must always be greater than energy input by wave forcing and spring variation. Clearly, this criterion is not always satisfied for all $\mid x_1 \mid > x_{1b}$, $\mid x_2 \mid > x_{2b}$ where x_{1b}, x_{2b} are the bounds on position and velocity that we are seeking to establish. This is not because the equation of motion is unstable but, rather, because the Lyapunov function has not been constructed with adequate care. Satisfaction of the Lyapunov criterion is a sufficient condition for stability, but failure to satisfy it is not a sufficient condition for instability.

It is interesting to note that Equation (6.82) implies that the 'worst' $g(t)$ is

$$g = -g_{\max} \operatorname{sgn}(x x_1 x_2) \tag{6.83}$$

which is the condition derived earlier, not surprisingly, given the energy based Lyapunov function. Figure 6.25 illustrates the way in which the phase velocity vector, $\mathbf{x}$, is varied by changing f_w and g. It is clear that for almost all level functions enclosing the origin, the 'worst' $\mathbf{x}$ with the greatest tendency to head up the level function will be obtained with maximum or minimum values of g and f_w.

Lyapunov stability bounds are usually very conservative unless great care is taken over the construction of the potential function. Another factor leading to large stability bounds is that it is difficult to include knowledge of the frequency constraints on the sway force and g, the spring variation. Large excursions might well take place if forces as large as those common at wave frequencies were applied at unrealistically low frequencies. Both Lyapunov and the Maximum Principle suffer from this defect since the time history of the 'worst' possible force is derived, not assumed. Optimal control theory and Lyapunov stability theory are, in fact, two views of the same problem for our purposes (see Figure 6.26), since the solution of the energy maximization problem involves the (implicit) construction of a function, the normals to which indicate the direction in which the system should be controlled (under the constraints on the input) for maximum average rate of energy input. In Lyapunov theory, an arbitrary level function is chosen and the controllable parameters are varied to maximize the rate of change of level, and if this can be made positive then the system can leave the area defined by $V(\mathbf{x}) \leqslant C$.

Neither the Maximum Principle nor Lyapunov stability theory offer an immediate prospect of a flexible routine tool for response analysis of non-linear time varying marine systems. However, they offer a powerful physical insight into the nature of the stability of TBP wave induced motions.

There are several definitive and interesting performance trends that can be deduced from the analysis in this and preceding sections. These trends are:

1. Lateral tether oscillations due to excitation by the surface platform and the consequential internal tether stresses become more important in deep water, particularly if the tethers are heavier for increased longitudinal stiffness.
2. Heave, roll and pitch resonant periods can lie in the region of strong wave excitation in deep water. This effect can be counteracted by increasing the tether cross-sectional area and thus the longitudinal stiffness, although additional excess buoyancy may then be required to avoid lowering the tether lateral motion natural periods further into the wave frequency range.
3. The likelihood and severity of subharmonic Mathieu type excitation is greatest for shallow water TBP deployment. This is because, as water depth increases the change of horizontal spring rate induced by heave forces becomes smaller and the resonant frequency recedes further from typical wave frequencies.

4. From the point of view of susceptibility to parametric excitation, tethered surface platforms of the semisubmersible type constructed from small volume members offer a design advantage over monolithic large volume floating bodies. This is because the large component of quadratic damping for a semisubmersible type of surface platform limits the maximum amplitude for parametric resonance whereas the linear damping typical of large volume structures does not possess this limiting mechanism. A further argument in favour of the semisubmersible type of surface platforms arises from the lower heave excitation associated with the small water plane areas of these structures. The lower heave forces induce smaller spring rate changes and thus reduce the excitation forces in parametric resonance conditions.
5. There is a strong likelihood of tether oscillations being excited by vortex shedding in all water depths. This problem may be aggravated by fluid interference effects between two adjacent tethers being excited by vortex shedding forces. The provision of strakes on the tether surfaces and inter-tether spacers may enable these problems to be bypassed in the design stage. This problem area is investigated further in Chapter 11.

References

Addion, G. D. and Steinsvik, B. (1976) Tethered production platform system'. *Proceedings, Offshore North Sea Conference*, London

Albrecht, H. G., Koenig, D. and Kokkinowrackos, K. (1978) Nonlinear dynamic analysis of tension leg platforms for medium and greater depth. *Offshore Technology Conference*, OTC 3044, pp. 7–15, May

Alexandrov, M. (1971) On the dynamics of cables with application to marine use, *Marine Technology Journal* (SNAME), **8**(1), 84

Annon (1975) New platform begins offshore test, *The Oil and Gas Journal*, 5 May, pp. 59–60

Beynet, P. A., Berman, M. Y. and Von Aschwege, J. (1978) Motion fatigue and the reliability characteristics of a vertically moored platform. *Offshore Technology Conference*, OTC 3304, May

Capanoglu, C. (1979) Tension-leg platform design: interaction of naval architectural and structural design considerations, *Marine Technology*, **16**, No. 4, October 1979, 343–352

Connel, G. M. (1974) Analytical studies of resonances in tautmoored system, OTC 2070, May

Denise, J-p F. and Heaf, N. J. (1979) A comparison between linear and nonlinear response of a proposed tension leg platform. *Offshore Technology Conference*, OTC 3555, pp. 1743–1754

De Spanos, P-T and Iwan, W. D. (1978) Response envelope statistics for nonlinear oscillators with random excitation. *Trans ASME, Journal of Applied Mechanics*, **45**, 170–174

Faltinsen, O. I., Fylling, I. J., van Hooff, R. and Teigen, P. S. (1982) Theoretical and experimental investigation of tension leg platform behaviour. *BOSS 82*, **1**, 411–423

Folger Whicker, L. (1958) Theoretical analysis of the effect of mooring cables in deep water, *David Taylor Ship Model Basin, Report 1221*, March

Hong, S. T. (1974) Tension in a taut line mooring; frequency domain analysis. OTC 2069, May

Horton, E. (1975) Tension leg platform prototype completes Pacific coast test. *Ocean Industry*, pp. 245–247, September

Hsu, C. S. (1975) The response of a parametrically excited hanging string in fluid, *Journal of Sound & Vibration*, **39**(3), 305–316

Hsu, C. S. (1975) Limit cycle oscillations of parametrically excited second order nonlinear systems, *Journal of Applied Mechanics*, March, p. 176–182.

Jain, R. K. (1980) A simple method of calculating the equivalent stiffness in mooring cables, *Applied Oceans Research*, **2**(3), 139

Kitami, E., Ninomiya, M., Katayama, M. and Unoki, K. (1982) Response characteristics of tension leg platform with mechanical damping systems in waves. *Proceedings, 14th Offshore Technology Conference*, OTC 4393, Houston, Texas

Lonergan, J. E. (1979) Development of Seafox tethered buoyant platforms. *Proceedings, Symposium on New Technologies For Exploration of Oil and Gas Resources' Commission of the European Communities*, pp. 970–994, Luxembourg

Lonergan, J. E. (1980) Dynamic behaviour of models of tethered buoyant platforms. *Proceedings, European Offshore Petroleum Conference and Exhibition*, paper EUR 265, pp. 535–544, London, England

MacDonald, R. D. (1974) The design and field testing of the 'Triton' tension leg fixed platform and its future application for petroleum production and processing in deep water. *Proceedings, 6th Offshore Conference* paper OTC 2104, Houston, Texas

Mercier, J. A. (1982) Evolution of tension leg platform technology. Presented at the Third International Conference on the Behaviour of Offshore Structures, Massachusetts Institute of Technology

Natvig, B. J. and Pendered, J. W. (1977) Nonlinear motion response of floating structures to wave excitation. *Offshore Technology Conference*, OTC 2796

Perrett, G. R. and Webb, R. M. (1980) Tethered buoyant platform production system. *Proceedings, 12th Offshore Technology Conference*, OTC 3881, Houston, Texas

Rainey, R. C. T. (1977) The dynamics of tethered platforms. Paper No 6, Spring Meetings, Royal Institution of Naval Architects

Richardson, J. R. and Pinto, U. H. (1979) Dynamics of cable and cable systems for tethered buoyant platforms. *OT-R-7914, NNMI R50*, National Maritime Institute, February

Robren, E. M. Q. and Steinsvik, B. (1978) Deep water resonance problems in the mooring system of the tethered platform. *Proceedings, The International Conference on Offshore Structures Engineering*, Rio de Janeiro

Sluijs, M. F. and Blok, J. J. (1977) The dynamic behaviour of mooring lines, OTC 2881

Takahashi, Y., Rabins, D. and Auslander, D. (1972) *Control*, Addison Wesley, Reading, Massachusetts

Tassini, P. and Paruzzola, A. (1981) A tension leg platform for 1000 m water depth. *Proceedings, Deep Offshore Technology Conference*, Palma de Mallorca, Spain October 1981, volume II, paper 11.2.1.b, pp. 155–162

Troger, H. and Hsu, C. S. (1977) Response of a nonlinear system under combined parametric and forcing excitation. *Journal of Applied Mechanics*, March, pp. 179–181

Verley, R. L. P. and Every, M. J. (1977) Wave induced vibrations on flexible cylinders. OTC 2899

Wilson, B. W. and Garbaccio, D. H. (1967) Dynamics of ship anchor lines in waves and current. *Proceedings of the Conference on Civil Engineering in Oceans*, San Francisco, 6–8 September, p. 277

Chapter 7

Dynamics of crane vessels

7.1 Introduction

The development of oil and gas fields in the North Sea has required activities such as exploration drilling, oil production and well maintenance to be carried out from floating marine vehicles. One particularly critical operation entails lifting and respositioning large loads from cranes mounted on floating vessels. This operation often forms part of the installation of platforms, topside modules and other related tasks. The eventual need for the decommissioning and removal of fixed offshore operations from floating marine vehicles are weather sensitive to some extent. This is primarily due to the motion of the vessel in waves. Crane vessel operations are particularly sensitive to vessel motions since the feasibility of a lift is governed by relatively low maximum permissible values of crane tilt as well as vertical and horizontal crane boom tip accelerations. The weather sensitive nature of crane vessel operations requires that studies are carried out to evaluate vessel operability both from the point of view of design and for providing operational guidance to the lift superintendent.

Consider the dynamics of a crane vessel operating in waves. The vessel hull itself can be regarded as a rigid body with the usual motions in six degrees of freedom. The structural stiffness of the crane housing and boom, the axial stiffness of lifting wires and lateral pendulum swinging motions of the lift mass introduce additional degrees of freedom. These are coupled with the vessel hull motions to generate a complex set of motions where the possibility of large resonant motions would be of concern. Furthermore, combined vertical and lateral oscillatory motions of the crane boom tip can induce large amplitude swinging motions in the suspended load due to excitation of a Mathieu instability. The conditions required for the occurrence of this instability also need to be investigated. Grim (1983) describes some earlier work in this area.

There are several physical parameters that can limit crane operations. One of these arises from the longitudinal bending moment induced by crane operations on the vessel's hull. This bending moment limit is of concern for the structural design of the hull, but the analysis techniques presented in this chapter are based on the assumption that vessel hull and crane tub strength limits on operability exceed those due to wave induced

motions by a wide margin. The analysis required for meeting typical strength requirements for design and certification are not covered here.

Thus the remaining limits of operability on the crane vessel are due to the wave induced motions of the vessel causing the motion of, or forces within, the crane housing, boom and lift hawsers to be outside acceptable bounds. These operability limits can be listed as follows:

1. The crane tilt about the plane of the boom and in a plane perpendicular to that of the boom must not exceed a small value – 3.5° is typical.
2. Inertia force limits within the crane housing and boom may be most conveniently expressed as allowable vertical and horizontal accelerations of the crane boom tip. Allowable horizontal accelerations perpendicular to the plane of the crane boom quantify the lateral force limits on the boom.
3. For certain lifting operations such as pile driving, a maximum allowable absolute motion of the crane hook may impose an operational limit.
4. Wind forces on lifted loads of large surface area may be a limiting factor that needs to be investigated.
5. Other extraneous limits may arise due, for example, to the fact that the vessel mooring or dynamic positioning system must maintain acceptable station keeping during the lift.

Offshore installation duties have been carried out using crane vessels with both semisubmersible and ship shape hull forms. Since wave induced motions are a primary influence on operability, semisubmersible hull forms offer the required low wave induced motions but have a limited payload to displacement ratio. On the other hand, monohull or ship shape hull forms have larger wave induced motions, although these can be reduced by installation of a motion suppression system. Ship shape hull forms do have large deck payload capacity, high transit speeds between work locations and also a low draught in the operating mode. This latter feature is of some importance for load out and installation in shallow water.

This chapter presents mathematical development underlying the consideration of coupling between the motions of the vessel hull and of the hook load through the vertical and lateral elasticities of the crane housing and jib and of the lift wires. The mathematics is illustrated by a case study with results from a typical monohull crane vessel described in Table 7.1 and illustrated in Figure 7.1. Similar calculation techniques would also apply if the vessel hull was of semisubmersible form. The derivation of wave induced forces and resultant motions of the rigid vessel hull are followed by calculations of the coupled motions for the vessel, elastic crane and lift wire assembly and the swinging hook load. The coupled motions that induce vertical and lateral motions of the crane jib are presented. The possible occurrence of dynamic instability due to combined vertical and lateral crane hook motions is also investigated and typical operational criteria are presented for avoiding such instabilities. The impact of all the above on the overall operability is discussed.

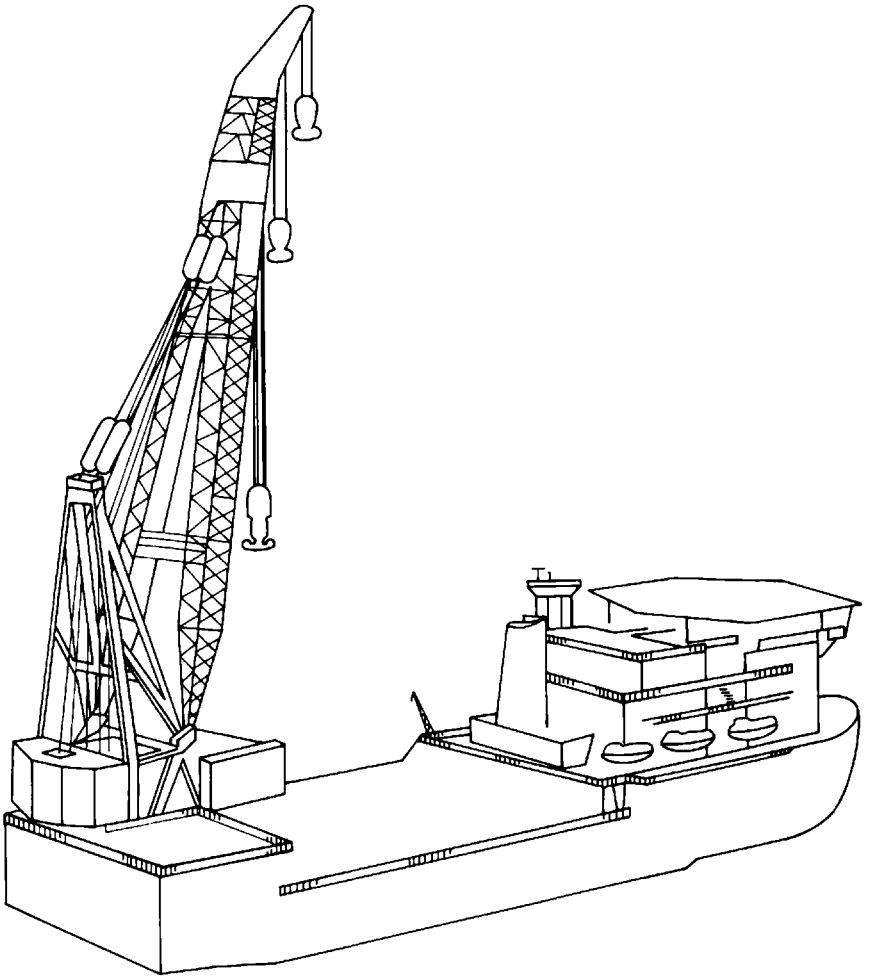

Figure 7.1. Perspective view of crane vessel *McDermott DB50*

7.2 Rigid vessel wave induced forces and motions

Wave induced motions of a monohull vessel have a dominant influence on operability and also form the mechanism through which ocean waves excite elastic vibrations of the crane structure and vertical or swinging oscillations of the suspended crane load.

The equation of motion for a rigid vessel in six degrees of freedom can be written as

$$(\mathbf{M} + \mathbf{M}_A)\,\ddot{\mathbf{X}} + \mathbf{B}_R\,\dot{\mathbf{X}} + \mathbf{B}_V\,\dot{\mathbf{X}} + (\mathbf{K} + \mathbf{K}_m)\,\mathbf{X} = \mathbf{F} \tag{7.1}$$

where $\mathbf{X}$, $\dot{\mathbf{X}}$ and $\ddot{\mathbf{X}}$ are six component column vectors of vessel displacement, velocity and acceleration in surge, heave, sway, roll, yaw and pitch

respectively. The (6 × 6) matrix, $\mathbf{M}$, contains the physical mass of the structure. The added mass matrix, $\mathbf{M}_A$, quantifies the additional mass of fluid entrained with the acceleration of the hull form. The damping coefficients in matrix $\mathbf{B}_R$ are associated with a net outward flux of energy in radiated waves and represent potential damping only. The damping coefficients in $\mathbf{B}_V$ represent a linearization of the quadratic drag damping due to flow separation around the submerged hull. The stiffness matrices, $\mathbf{K}$ and $\mathbf{K}_m$, are due to hydrostatic and mooring restoring forces. The six component column vector, $\mathbf{F}$, contains wave induced forces and moments which are calculated for a stationary body using diffraction theory; see Chapter 5.

Both the fluid structure interaction term coefficients ($\mathbf{M}_A$ and $\mathbf{B}_R$) on the left hand side of Equation (7.1) and the wave induced force ($\mathbf{F}$) on the right hand side are evaluated using a conventional boundary element numerical technique. This method is described further in Chapter 5. For regular wave excitation, Equation (7.1) becomes

$$[-\omega^2(\mathbf{M} + \mathbf{M}_A) + i\omega(\mathbf{B}_R + \mathbf{B}_V) + \mathbf{K} + \mathbf{K}_m]\,\mathbf{X} = A(\omega)\,\mathbf{R}(\omega) \qquad (7.2)$$

in the frequency domain where, for frequency ω, $\mathbf{X}$ are the vector amplitudes of motion, $A(\omega)$ is the wave amplitude, and $\mathbf{R}(\omega)$ is the complex vector of wave induced forces on the vessel. The added mass and radiation damping matrices calculated from the diffraction analysis are functions of wave frequency. Note that the diffraction analysis also yields wave induced forces and moments acting on the vessel which are an essential ingredient to the coupled analyses described in the following sections.

Equation (7.2) is solved for the vessel shown in Figure 7.1 with vessel data given in Table 7.1. Figure 7.2 shows a perspective view of the submerged hull geometry represented by the triangular facets used for the diffraction analysis. A total of 446 facets was used to define the body in a suitably accurate manner.

It is known that wave induced roll and pitch motions of the monohull have a disproportionately large effect on vessel operability by inducing

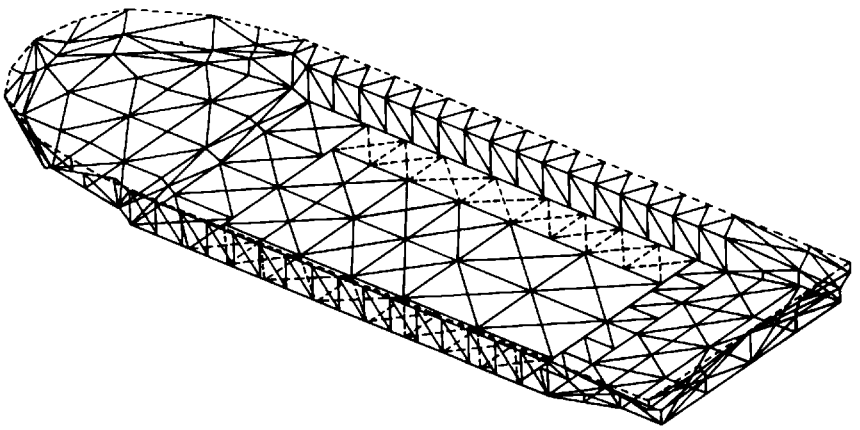

Figure 7.2. Hydrodynamic mesh

Table 7.1 Leading particulars of crane vessel *McDermott DB50*

Displacement (including volume of fluid inside motion suppression tanks)	43 500 t
Length overall	151.5 m
Beam overall	46.0 m
Depth, keel to main cargo deck	12.5 m
Transit draught	4.8 m
Minimum operational draught	5.0 m
Maximum operational draught	8.5 m
Cargo capacity	18 000 t
Cargo area	2935 m^2
Clear cargo height	21 m
Deck load	10 t/m^2
Heavy lift crane:	
boom length	105 m
slewing rate	0.33 rpm (light load) 0.20 rpm (full load)
Main hook maximum static load	4000 t at 37 m
Main hook maximum revolving load	3800 t at 25 m 1100 t at 75 m
Minimum radius (main hook)	21.0 m
Maximum main hook height	93.5 m
Full load hoist speed	2.75 m/min

large accelerations at the crane hook. It is, therefore, worth while considering the installation of a motion suppression system on monohull crane vessels to reduce wave induced roll motions. This has been done for the vessel used to illustrate the study. In the interests of brevity, the motion suppression system is not described here. Its operation on board the vessel is represented within the diffraction analysis by additional degrees of freedom and the full procedure is described in Chapter 10.

Figures 7.3 and 7.4 show heave and pitch wave induced motion responses as a function of wave period for the vessel with no crane load in head seas. The roll and pitch motions are both reduced by the effect of the motion suppression system.

7.3 Coupled motions of vessel and crane load

The wave induced motions of a crane vessel are made up of a complex interaction of the rigid body motions of the hull, elastic deformations of the hull and also of the crane tub, housing and jib, together with vertical stretching of the cable suspending the hook load and swinging pendulum oscillations of the load. All these degrees of freedom pose a cumbersome (but not intractable) problem. However, these degrees of freedom can be significantly reduced by recognizing that the motions and forces at the crane hook will be primarily governed by the relatively low stiffnesses associated with the rigid body motions of the vessel and the vertical or lateral movement of the hook load, with the crane tub and housing playing a small part.

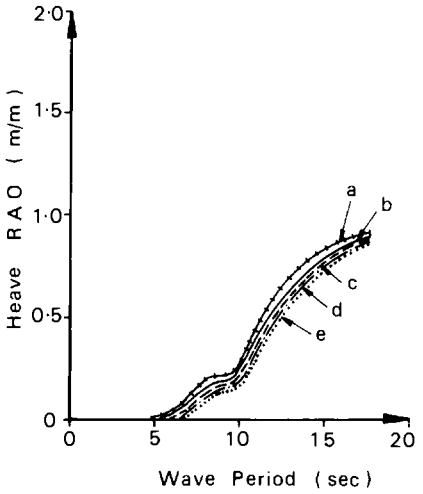

Figure 7.3. Heave motions in head seas (stern lift) for crane load masses of 0 to 4000 t. *Key*: a – crane load = 0.0 t; b – crane load = 500.0 t; c – crane load = 1000.0 t; d – crane load = 2000.0 t; e – crane load = 4000.0 t

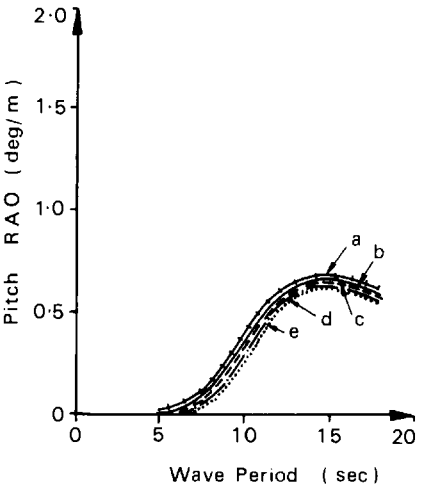

Figure 7.4. Pitch motions in head seas (stern lift) for crane load masses of 0 to 4000 t. *Key*: a – crane load = 0.0 t; b – crane load = 500.0 t; c – crane load = 1000.0 t; d – crane load = 2000.0 t; e – crane load = 4000.0 t

Thus the system may be adequately described by the six rigid body degrees of freedom for vessel motions with the three orthogonal displacements of the lift mass. The equation of motion of this system can be written in nine degrees of freedom as

$$\mathbf{M}'\ddot{\mathbf{Z}}' + \mathbf{B}'\dot{\mathbf{Z}}' + (\mathbf{K}' + \mathbf{K}_c)\mathbf{Z}' = \mathbf{F}'e^{i\omega t} \tag{7.3}$$

where $\mathbf{Z}'$ is the complex vector containing the surge, heave, sway, roll, yaw and pitch motions of the vessel, together with the surge, heave and sway motions of the crane load; $\mathbf{M}'$ combines the physical masses and inertias of the crane load with the added masses and inertias of the vessel calculated by the previously described diffraction analysis; $\mathbf{B}'$ is the total vessel hydrodynamic damping, together with structural damping associated with the crane dynamics. The latter damping is estimated as a small percentage of critical damping – 1% for vertical motions and 5% for horizontal

motions of the crane load; $\mathbf{K}'$ is the combined hydrostatic, and linearized mooring stiffness matrix; $\mathbf{F}'$ is the complex wave exciting force vector evaluated by the diffraction analysis.

The total mass and damping matrices of the coupled system can be written as follows

$$\mathbf{M}' = \left[\begin{array}{c|ccc} (\mathbf{M}+\mathbf{M}_A) & \multicolumn{3}{c}{\mathbf{O}} \\ \hline & m_L & 0 & 0 \\ \mathbf{O} & 0 & m_L & 0 \\ & 0 & 0 & m_L \end{array}\right] \quad \mathbf{B}' = \left[\begin{array}{c|ccc} (\mathbf{B}_R+\mathbf{B}_V) & \multicolumn{3}{c}{\mathbf{O}} \\ \hline & b_1 & 0 & 0 \\ \mathbf{O} & 0 & b_2 & 0 \\ & 0 & 0 & b_1 \end{array}\right] \tag{7.4}$$

where $(\mathbf{M} + \mathbf{M}_A)$ is the (6×6) mass plus added mass matrix of the rigid vessel in the six rigid body degrees of freedom of surge, heave, sway, roll, yaw, and pitch. The remaining three degrees of freedom are crane load surge, heave and sway where the physical mass, m_L, of the crane load remains as a diagonal term. The damping matrix, $\mathbf{B}'$, is made up from the vessel rigid body (6×6) radiation plus linearized drag damping matrix $(\mathbf{B}_R + \mathbf{B}_V)$ together with damping terms b_1 and b_2, taken here as 1% and 5% of critical damping for the horizontal and vertical motions respectively. The matrix, $\mathbf{K}'$, in Equation (7.3) can be written as follows:

$$\mathbf{K}' = \left[\begin{array}{c|ccc} (\mathbf{K}+\mathbf{K}_m) & \multicolumn{3}{c}{\mathbf{O}} \\ \hline & 0 & 0 & 0 \\ \mathbf{O} & 0 & 0 & 0 \\ & 0 & 0 & 0 \end{array}\right] \tag{7.5}$$

and consists of the (6×6) hydrostatic restoring and mooring stiffness matrix, $\mathbf{K}$, in the six vessel rigid body with all remaining terms being zero. The matrix $\mathbf{K}_c$ provides the only source of coupling in the equation between the vessel's rigid body motion and the crane load motions. The matrix $\mathbf{K}_c$ can be written as shown on page 196, where (x', y', z') are the co-ordinates of the crane load suspension point relative to the vessel centre of gravity position; k_c, is the vertical stiffness of the crane structure and load suspension wires with k_t being the transverse stiffness of the swinging load on the suspension lines. In Equation (7.6), terms k_x, k_y and k_z denote the linear hydrostatic plus mooring stiffnesses of the vessel with r_x, r_y and r_z denoting the rotational hydrostatic plus mooring stiffnesses.

For a load mass, m_L, and a suspension line length of L, k_t can be written as

$$k_t = \frac{m_L g}{L} \tag{7.7}$$

$$\mathbf{K}_c = \begin{array}{c} \\ X \\ Y \\ Z \\ \theta_x \\ \theta_y \\ \theta_z \\ X_c \\ Y_c \\ Z_c \end{array} \begin{array}{c} \begin{array}{ccccccccc} X & Y & Z & \theta_x & \theta_y & \theta_z & X_c & Y_c & Z_c \end{array} \\ \left[\begin{array}{ccccccccc} k_x + k_t & 0 & 0 & 0 & z'k_t & -y'k_t & -k_t & 0 & 0 \\ 0 & k_y + k_c & 0 & -z'k_c & 0 & x'k_c & 0 & -k_c & 0 \\ 0 & 0 & k_z + k_t & y'k_t & -x'k_t & 0 & 0 & 0 & -k_t \\ 0 & -z'k_c & y'k_t & \left(\dfrac{r_x + z'^2 \cdot}{k_c + y'^2 k_t}\right) & -x'y'k_t & -x'z'k_c & 0 & z'k_c & -y'k_t \\ z'k_t & 0 & -x'k_t & -x'y'k_t & \left(\dfrac{r_y + x'^2 \cdot}{k_t + z'^2 k_t}\right) & -y'z'k_t & -z'k_t & 0 & x'k_t \\ -y'k_t & x'k_c & 0 & -x'z'k_c & -y'z'k_t & \left(\dfrac{r_z + x'^2 \cdot}{k_c + y'^2 k_t}\right) & y'k_t & -x'k_c & 0 \\ -k_t & 0 & 0 & 0 & -z'k_t & y'k_t & k_t & 0 & 0 \\ 0 & -k_c & 0 & z'k_c & 0 & -x'k_c & 0 & k_c & 0 \\ 0 & 0 & -k_t & -y'k_t & x'k_t & 0 & 0 & 0 & k_t \end{array}\right] \end{array} \tag{7.6}$$

Note:

X = surge	θ_x = roll	X_c = crane load surge
Y = heave	θ_y = yaw	Y_c = crane load heave
Z = sway	θ_z = pitch	Z_c = crane load sway

The wave force vector, $\mathbf{F}'$, may be written as

$$\mathbf{F}' = A(\omega) \begin{bmatrix} \mathbf{R}(\omega) \\ \hline 0 \\ 0 \\ 0 \end{bmatrix}$$

where $A(\omega)\mathbf{R}(\omega)$ is the (6×1) vector of wave induced forces on the rigid vessel. It needs to be emphasized here that the elements of matrices $\mathbf{M}'$, $\mathbf{B}'$ and $\mathbf{F}'$ are obtained from the boundary element numerical analysis described in Chapter 5 and will, therefore, be dependent on incident wave frequency.

The above theory is illustrated by example calculations which address two areas of concern where the coupled motions induce either vertical or lateral oscillations of the hook load. Both phenomena will occur irrespective of the type of lift and the wave direction.

The case of coupled motions inducing vertical oscillations of the hook load is illustrated by considering a stern lift in head seas. Equation (7.3) is solved for a range of wave periods and for crane hood load values of 0, 500, 1000, 2000 and 4000 t with a line length of 90.5 m. Figure 7.3 shows the resultant vessel heave motions and demonstrates that these are not significantly affected by the vertical dynamics. Similarly, Figure 7.4 demonstrates that pitch motions in head seas are only slightly influenced by the vertical dynamics of the hook load. A measure of the vertical inertia

loads in the crane jib and load suspension lines is given by a plot of the relative motion between load and vessel as a function of wave period. This is presented in Figure 7.5 and shows that the inertia loads are small but nevertheless significant in operability considerations. Even for the largest hook loads, the crane dynamics do not approach resonance and, therefore, dynamic magnification effects are negligible. Figure 7.6 illustrates the relative lateral motions of the load (in the vertical plane through the vessel fore and aft centre line) for a stern lift in head seas. For low wave periods, the swinging of the load remains small. However, as the wave period approaches the natural period of the pendulum load the lateral motions increase significantly.

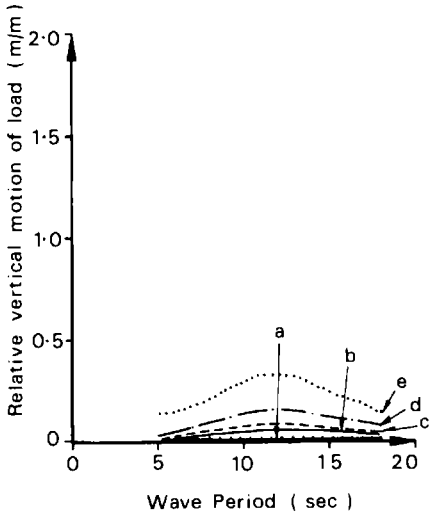

Figure 7.5. Relative vertical motions of crane load (stern lift) for crane load masses of 0 to 4000 t. *Key*: a – crane load = 0.0 t; b – crane load = 500.0 t; c – crane load = 1000.0 t; d – crane load = 2000.0 t; e – crane load = 4000.0 t

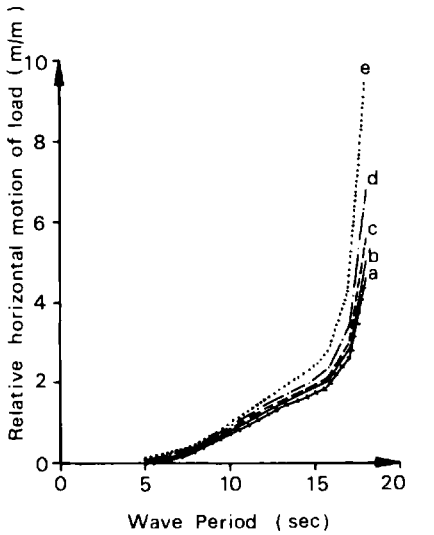

Figure 7.6. Relative horizontal motions of crane load (stern lift) for crane load masses of 0–4000 t (no tugger lines). *Key*: a – crane load = 0.0 t; b – crane load = 500.0 t; c – crane load = 1000.0 t; d – crane load = 2000.0 t; e – crane load = 4000.0 t

The second case of coupled motions exciting swinging hood load motions is illustrated by examining a side lift in beam seas. Equation (7.3) is solved with numerical values derived from vessel data given in Table 7.1 and from the diffraction analysis. Crane load masses of 0, 500, 1000, 2000 and 2500 t are used together with a line length of 90.5 m. The influence of coupling on sway motions of the vessel is very small and is not presented here. Figure 7.7 displays the roll motion of the vessel for the different crane load masses. It is clear that the hook load does not significantly affect the roll motions of the vessel for the case considered. Figure 7.8 presents the relative lateral motion between the suspended mass and the crane jib, as a function of wave period. This yields a measure of side loads on the crane jib. Examination of the diagram and consideration of the suspended mass magnitudes shows that significant lateral loads are applied to the crane jib.

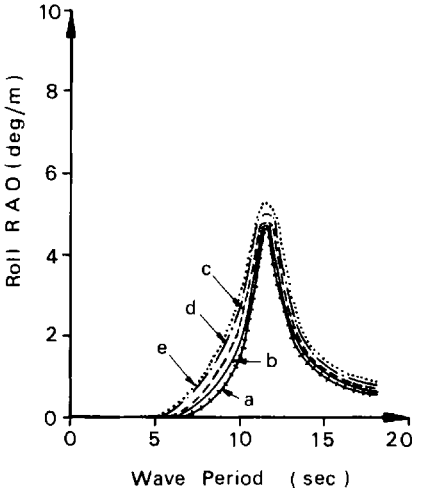

Figure 7.7. Roll motions in beam seas (side lift) for crane load masses of 0–2500 t (no tugger lines). *Key*: a – crane load = 0.0 t; b – crane load = 500.0 t; c – crane load = 1000.0 t; d – crane load = 2000.0 t; e – crane load = 2500.0 t

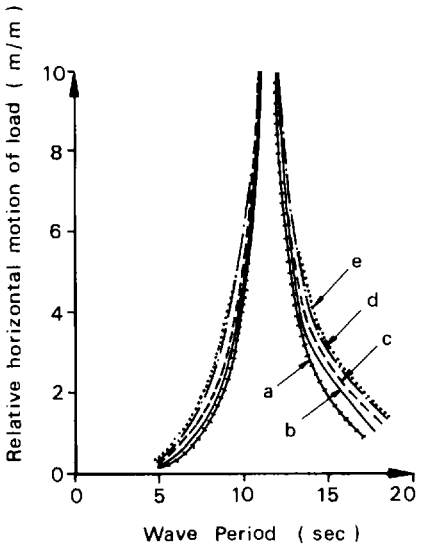

Figure 7.8. Relative horizontal motions of crane load (side lift) in beam seas for crane load masses of 0–2500 t (no tugger lines). *Key*: a – crane load = 0.0 t; b – crane load = 500.0 t; c – crane load = 1000.0 t; d – crane load = 2000.0 t; e – crane load = 2500.0 t

These forces need to be accounted for in the assessment of crane operating loads.

Figure 7.9 shows the roll motions of the ship in beam seas with a side lift of 1500 t and varying line length. This diagram demonstrates the major influence that the load and pendulum length can have on the roll motion of the vessel. This feature is not as operationally significant as it may appear at first sight, since heavy lifts will be carried out with line lengths in the region of 70–100 m.

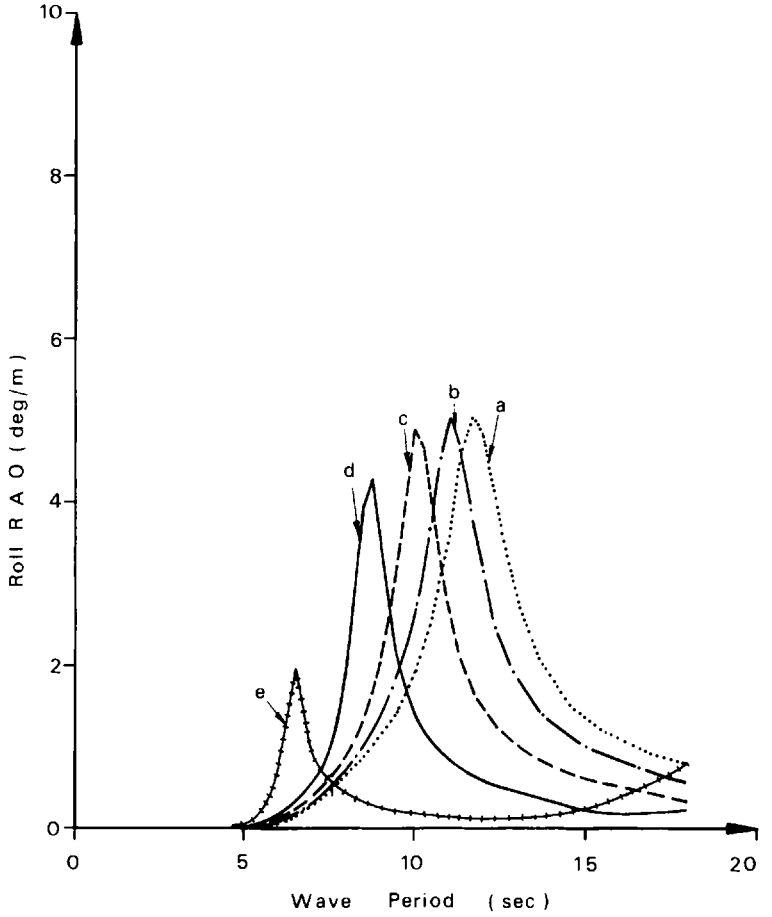

Figure 7.9. Roll motions in beam seas (side lift) for crane line lengths of 20–100 m (crane load = 1500 t) (no tugger lines). *Key*: a – line length = 20.0 m; b – line length = 40.0 m; c – line length = 60.0 m; d – line length = 80.0 m; e – line length = 100.0 m

7.4 Operability limits

The wave induced vessel and hook load motions are only of value operationally if they can be translated into operability limits. In order to do this, however, the regular wave motions calculated in the preceding section

have to be converted into motions and accelerations at specified points around the hull, such as the crane boom tip. The regular wave motions and accelerations have also to be converted into short term responses to long crested irregular waves. These procedures are described below.

In order to calculate accelerations of the crane boom tip for the various lift cases it is necessary to translate the motions of the vessel at its centre of gravity into values applicable to the position of the crane boom tip. To do this, standard equations for coupling the six rigid body modes of motion are used to give the three orthogonal motions per unit wave amplitude, **Y**, at the position of interest. These motions can be converted into regular wave acceleration amplitude operators, **A**, using the equation

$$\mathbf{A} = -\omega^2 \mathbf{Y} \tag{7.9}$$

where ω is the radian frequency of the waves.

Short term responses in irregular waves are calculated using the regular wave response amplitude operators (RAOs) obtained from the solution of the coupled equation of motion (7.3). The vessel response spectrum, $S_r(\omega)$, is obtained by the usual linear system relationship of

$$S_r(\omega) = | R(\omega) |^2 S_w(\omega) \tag{7.10}$$

where $S_w(\omega)$ is the incident wave elevation spectrum and $R(\omega)$ is the appropriate motion or acceleration RAO.

Once the wave elevation and response spectra are known the significant wave height and significant motions (H_w and H_r) can be obtained by using the narrow band spectra relationships

$$\left.\begin{aligned} H_w &\simeq 4\sqrt{(m_w)}, \\ \text{and} \\ H_r &\simeq 4\sqrt{(m_r)} \end{aligned}\right\} \tag{7.11}$$

where m_w and m_r are the areas under the wave elevation and the response spectra respectively. The ratio H_r/H_w is then presented as a short term irregular wave response/amplitude ratio for each of the six vessel motions of surge, heave, sway, roll, yaw and pitch. The ratio is computed for a range of average zero-crossing wave periods.

Several choices of input spectra can be used for these calculations. Among these are the Pierson–Moskowitz, JONSWAP and ISSC forms. These are described further in Chapter 2 and in Patel (1989).

The vessel's operability limits are then calculated in terms of significant wave heights of long crested irregular waves of specified spectra. The maximum allowable crane tilt angle or vertical boom tip acceleration is converted to a maximum allowable significant angle or acceleration. This is then used with the irregular wave short term response amplitude operator (ratio of significant response value to significant wave height) to yield the maximum allowable significant wave height for vessel operations.

This procedure is illustrated first for the crane tilt angle limit. The maximum allowable crane tilt angle, α_{max}, is given by

$$\alpha_{max} = (\alpha - \beta) \tag{7.12}$$

where α is the maximum allowable tilt angle from the vertical, in degrees, and β is the maximum steady crane tilt angle due to side wind, in degrees; β is taken as 0.1° in these calculations. Hence the significant value of the maximum crane tilt angle is given by

$$\alpha_s = \frac{(\alpha - \beta)}{1.86} \tag{7.13}$$

with the constant of proportionality, 1/1.86, being calculated to apply for a storm of 3 h duration. In practice, the taking up and transfer of the load will last rather less time than this and hence the constant of proportionality will be lower than that given, resulting in higher values of α_s.

Using Equation (7.13), the maximum allowable significant wave height for vessel operations is obtained as

$$H_s = \frac{2\alpha_s}{F} \tag{7.14}$$

where F is the greater of the roll or pitch motion short term response amplitude operator of the vessel in degrees per metre.

The maximum significant wave height limit due to maximum vertical crane boom tip acceleration being exceeded is also obtained in a similar manner. For a maximum permissible crane boom tip vertical acceleration of A_{max}, the equivalent maximum significant crane boom tip acceleration, A_s, is given by

$$A_s = \frac{A_{max}}{1.86} \tag{7.15}$$

Then the maximum significant wave height can be derived from the vertical crane boom tip acceleration limit by the equation

$$H_s = \frac{2A_s}{G} \tag{7.16}$$

where G is the crane boom tip vertical acceleration short term response amplitude operator (in $m/s^2/m$). This value will vary with the position of the crane relative to the vessel.

Figures 7.10 and 7.11 show typical operability limits plotted on significant wave height against average zero-crossing period axes. Operability limits due to exceedence of maximum crane tilt and maximum boom tip vertical acceleration are given. Combinations of significant wave height and average zero-crossing period below the lower of the two lines are, therefore, permissible.

The two graphs also present breaking wave height limits which define the maximum value of significant wave height at which the highest one-third of the waves within the irregular sea will have broken. This significant wave height limit is defined as follows. In a regular wave, a breaking wave height limit, H_B, can be written as

$$H_B = \frac{\lambda}{7} \tag{7.17}$$

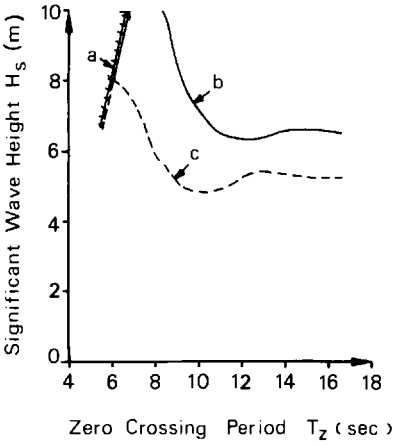

Figure 7.10. Operability significant wave height limits in head seas (100 t stern lift at 40 m radius on whip hook).
Displacement = 34 784 t, draught = 8.5 m;
Vessel KG =10.6 m, Vessel GM = 15.5 m;
Vessel radius of gyration: roll = 11.0 m, pitch = 48.0 m, yaw = 48.0m;
Crane boom tip x,y,z co-ordinates relative to vessel stern deck are −26.2 m, 0 m, 122.7 m.
Key: a – breaking wave limit; b – crane tilt limit (3.5°); c – crane acceleration limit (1.471 m/s^2)

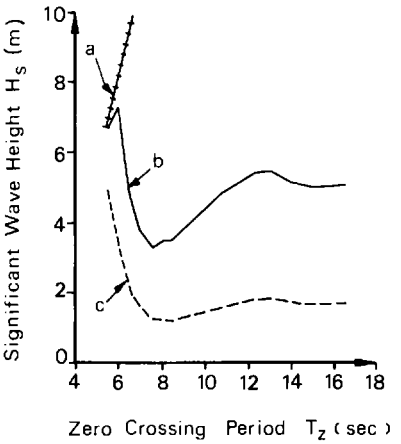

Figure 7.11. Operability significant wave height limits in quartering seas (2700 t side lift at 40 m radius on main hook).
Displacement = 34 784 t, draught = 8.5 m;
Vessel KG =16.7 m, Vessel GM = 11.9 m;
Vessel radius of gyration: roll = 15.2 m, pitch = 52.0 m, yaw = 52.0m;
Crane boom tip x,y,z co-ordinates relative to vessel stern deck are 13.8 m, 40 m, 95.7 m.
Key: a – breaking wave limit; b – crane tilt limit (3.5°); c – crane acceleration limit (0.490 m/s^2)

where λ is the wave length. Writing λ in terms of wave period, T, for deep water gives

$$H_B = \frac{g\,T^2}{14\pi} \tag{7.18}$$

Then an approximation to a significant wave height limit, $(H_s)_{max}$, can be written as

$$(H_s)_{max} = \frac{g\,T_z^2}{14\pi} \tag{7.19}$$

where T_z is an average zero-crossing period. This is the breaking wave limit plotted in Figures 7.10 and 7.11. In conditions where the tilt angle or crane boom tip acceleration induced significant wave height limit exceed the breaking significant wave height limit, the lowest of these limits is taken to apply.

An interesting feature of the dynamics of coupled vertical and lateral motions of the crane hook load is the possibility of exciting unstable large amplitude swinging oscillations through a parametric instability. This can occur due to the oscillatory variation of tension in the suspension lines which is induced by vertical motions of the crane hook.

The fundamental theory underlying such instabilities is described by the Mathieu equation. The development of this theory is comprehensively described by Stoker (1950). This section applies the theory to the crane vessel of Figure 7.1 and demonstrates the derivation of readily usable criteria for ensuring that such unstable hook load swinging motions are avoided during vessel operations.

The equation for lateral motions, z_l, of the crane hook load can be written as

$$m\,\ddot{z}_l + \frac{T}{L}\,z_l = m\,\ddot{z}_j \tag{7.20}$$

where the line tension T is no longer constant, m is the mass of the hook load and L is the suspended line length. The small level of damping is ignored and $\ddot{z}_j$ is the lateral acceleration of the crane jib at the load suspension point. If the vertical motion of the suspension point is of amplitude y_j and radian frequency ω, then, the tension T may be given by

$$T = m\,g + m\,\omega^2\,y_j\cos\omega t \tag{7.21}$$

and the equation of motion becomes

$$\ddot{z}_l + \left[\frac{g}{L} + \frac{\omega^2 y_j}{L}\cos\omega t\right] z_l = 0 \tag{7.22}$$

after division by m. The unstable behaviour is clearly independent of the magnitude of mass m and is only affected by parameters g, L, ω and y_j. It is unnecessary to consider the right hand side of Equation (7.20) if only the stability of the equation is being examined. Therefore this is equated to zero.

A transformation $x = \omega t$ permits Equation (7.22) to be converted to the classical Mathieu equation form of

$$\frac{d^2z}{dx^2} + \left[\frac{g}{L\omega^2} + \frac{y_j}{L}\cos x\right] z = 0 \tag{7.23}$$

and taking

$$\delta = \frac{g}{L\omega^2} \text{ and } \epsilon = \frac{y_j}{L} \tag{7.24}$$

one obtains

$$\frac{d^2z}{dx^2} + [\delta + \epsilon\cos x]\,z = 0 \tag{7.25}$$

Stoker (1950) presents stability diagrams for Equation (7.25) to identify the ranges of δ and ϵ for which unstable and stable solutions will arise.

Since ϵ will be small for the crane vessel problem, a small amplitude approximation to the stability diagram may be used. This diagram is also given by Stoker and is reproduced in Figure 7.12. If the length of the lift wires varies from 10 to 80 m, the wave period from 5 to 15 s and the crane jib vertical motion from 0 to 4 m, then parameters δ and ϵ will vary from 0.078 to 5.59 and 0 to 0.40 respectively. These ranges are represented by a box on Figure 7.12 and indeed show that the crane may operate in two regions (A and B) where the values of parameters δ and ϵ are such that unstable oscillations could arise.

Figure 7.12, however, needs to be transformed into a form which is more suitable for operational use. This has been done in Figure 7.13 which plots the lift wire length, L, against wave period, T, with crane jib vertical amplitudes (y_j) of 1 and 4 m. The first unstable region (A) in Figure 7.12 maps onto Figure 7.13 as a narrow band whose width is governed by the magnitude of y_j. The second unstable region (B) is dominated by the parameter δ being approximately equal to unity and effectively maps as an unstable line except for very short suspended line lengths. In general, the lift superintendent has to be aware that large oscillations of the load may occur when the wave period is an integral multiple of half of the natural period of the pendulum load and that this may occur if the suspended line length and incident wave period were to map onto either of the unstable regions A or B. Note that for small boom tip motion amplitudes, the region

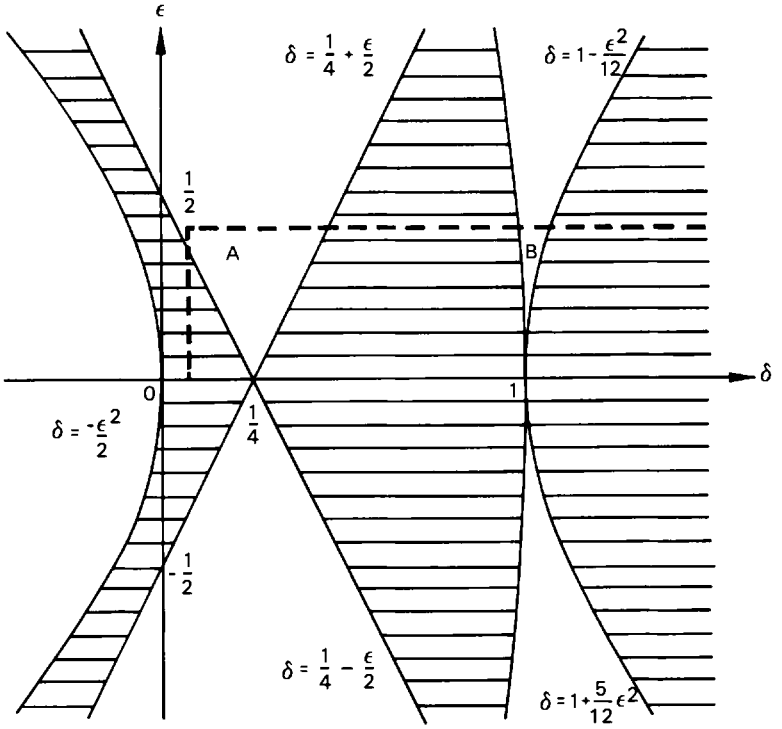

Figure 7.12. Stability diagram for small ϵ (shaded regions are stable)

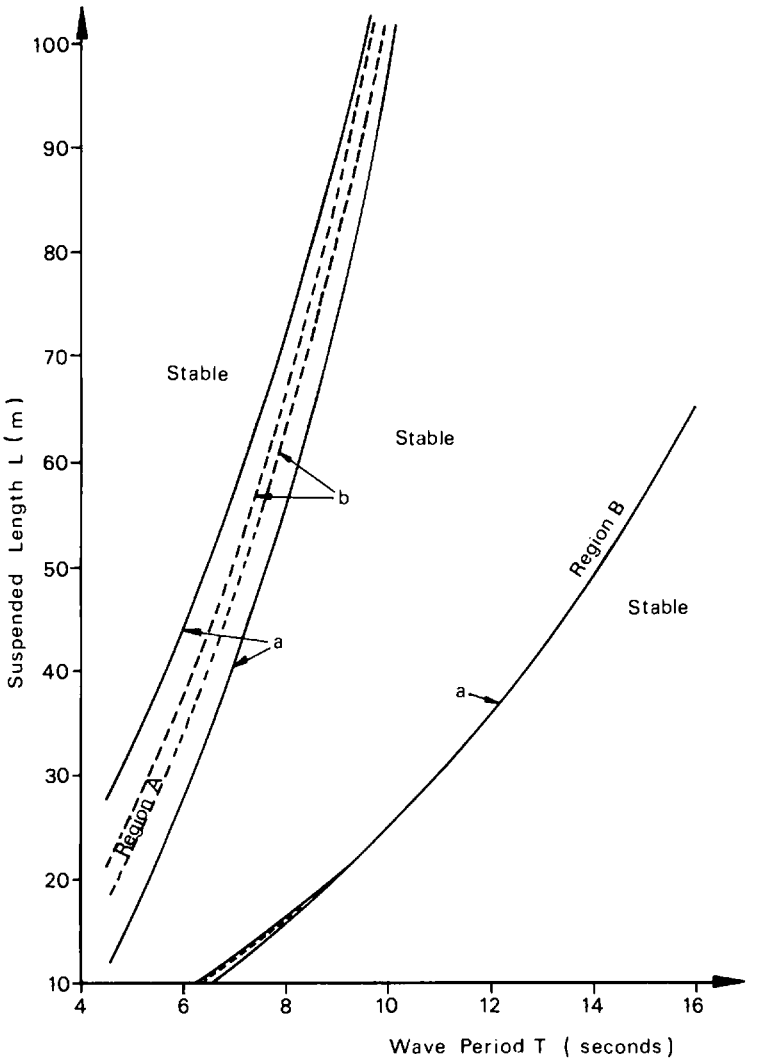

Figure 7.13. Operations advisory diagram for Mathieu instability. *Key*: a – boom tip motion amplitude (z_j) = 4 m; b – boom tip motion amplitude (z_j) = 1 m

of potential unstable motions becomes very small. The existence of load tugger lines reduces the possibility of the instability occurring.

The stability diagram of Figure 7.13 is useful for identifying conditions where 'unstable' swinging hook load oscillations may occur. Clearly, avoiding these conditions during operations is advisable. Nevertheless, the occurrence of Mathieu instability does generally require that regular waves approach the vessel with constant properties over a long period of time. Figure 7.13 shows that the unstable regions are very narrow with respect to wave period. Hence it would be difficult for a real sea state, which has energy distributed over a reasonably wide period range, to excite and

maintain a Mathieu instability. Thus the presence of irregular, directional waves and any non-linear damping within the system does reduce or eliminate the risk of large amplitude swinging hook load motions. Work on Mathieu instabilities for tension leg platforms in Chapter 6 presents further details on this point.

7.5 Transient line tension at lift-off

Transient peaks in crane line tension peaks can occur during load lift off and have to be predicted using a time domain numerical analysis of the vessel dynamics, crane and lift line flexibility and the dynamic behaviour of the floating load delivery barge or of the fixed platform. In order to illustrate this phenomenon the results of four typical lifts carried out by the monohull crane vessel shown in Figure 7.1 are presented. These are

(a) side (port) lift of 2400 t at 40 m radius from a transportation barge;
(b) side (port) lift of 2400 t at 40 m radius from a fixed platform;
(c) stern lift of 4000 t at 37 m radius from a transportation barge;
(d) stern lift of 4000 t at 37 m radius from a fixed platform.

As an example Lloyd's Register's (LR) combined duty and speed factor limits for offshore cranes are used. These factors limit the maximum permissible dynamic line tension to 1.15 and 1.05 of the static load for the 2400 t and 4000 t loads respectively.

The theoretical basis of the numerical analysis is described first. The equation of motion of the crane vessel is given by

$$\mathbf{M}\,\ddot{\mathbf{x}} + \mathbf{D}\,\dot{\mathbf{x}} + \mathbf{K}\,\mathbf{x} = \mathbf{F}(t) \tag{7.26}$$

where $\mathbf{M}$ is the total mass matrix; $\mathbf{D}$ is the equivalent linear damping matrix; $\mathbf{K}$ is the stiffness matrix which incorporates both hydrostatic and mooring stiffnesses; $\mathbf{F}(t)$ is the general disturbing or exciting force vector which may be due, for example, to waves or a crane lift; $\mathbf{x}$, $\dot{\mathbf{x}}$ and $\ddot{\mathbf{x}}$ are the displacement, velocity and acceleration vectors respectively. The displacement vector contains the six rigid body degrees of freedom of the vessel: surge, heave, sway, roll, yaw and pitch.

The property matrices, $\mathbf{M}$, $\mathbf{D}$ and $\mathbf{K}$, are functions of the vessel geometry and the vessel flow field interaction. For the vessel of Figure 7.1, linear hydrodynamic diffraction theory (Chapter 5) is used to generate the added mass, damping and stiffness properties.

For the time domain computation, the dynamics of the load delivery barge should also be included. The vertical equation of motion of the barge when the load and the barge are in contact is given by

$$M_b\,\ddot{z}_b + D_b\,\dot{z}_b + K_b\,z_b = T - m_L g \tag{7.27}$$

where z_b is the vertical displacement of the barge; K_b is the hydrostatic stiffness in heave of the barge; T is the line tension; M_b is the barge total mass of which its added mass component and the damping coefficient, D_b, were also computed using a diffraction analysis; m_L is the mass of the load and associated lifting equipment.

For the results presented here, $\mathbf{F}(t)$ consists of the crane lift forces only. The crane lift induced roll moment is assumed to be counteracted by a crane moment compensation system. The equations of motion of the crane vessel and the delivery barge are solved by numerical integration using conventional techniques. The load on the vessel is due to the line tension at the crane boom tip which is given by

$$T = k_c [w(t) + z_c - z_b] \tag{7.28}$$

where k_c is the crane stiffness; z_c is the vertical displacement of the crane tip; $w(t)$ is the crane wind up. Table 7.2 lists the major parameters used in

Table 7.2 Major simulation parameters

Crane vessel draught		8.5m
Load delivery barge	length	91.44 m
	beam	27.43 m
	total mass	40 856 t
	heave damping	3120 kNs/m
Estimated crane stiffness	revolving mode	20 531 kN/m
	tied back mode	45 665 kN/m
	damping	$0.04\sqrt{(k_c m_L)}$
Load wind up rate		2.75 m/min
Line pretensions (% of $m_L g$)	Lift A	80%
	Lift B	90%
	Lift C	80%
	Lift D	95%
Simulation time step		0.05 s
Plotting time step		0.50 s

Table 7.3 Results for analysis of transient line tensions

Lift label	*Lift load* t^{-1}	*Lift radius* m^{-1}	*Lift type*	*Line pretension at start of lift off as % of static load*	*Maximum line tension* kN^{-1}	*Minimum required LR combined duty and speed factor*
A	2400	40	SI/TB	80	25 250	1.072
B	2400	40	SI/FP	90	25 510	1.083
C	4000	37	ST/TB	80	40 050	1.021
D	4000	37	ST/FP	95	40 950	1.044

Notes:
SI: Side lift;
ST: Stern lift;
TB: Transportation barge;
FP: Fixed platform.

the numerical computation described here. The simulations are carried out in the time domain using a time step of 0.05 s and using the maximum crane wind up rate of 2.75 m/min. Figure 7.14 presents a typical time history plot of line tension during the lift off phase for the lift *D* described in Table 7.3. This table also presents the lift off maximum tension data from calculations for all four lifts. It can be observed that in the cases examined, which are typical of the most severe lifts, line tensions do remain below the allowable LR combined duty and speed factors by reasonable margins. The level of dynamic line tensions may be further reduced by lowering the permissible crane wind up rate to less than 2.75 m/min.

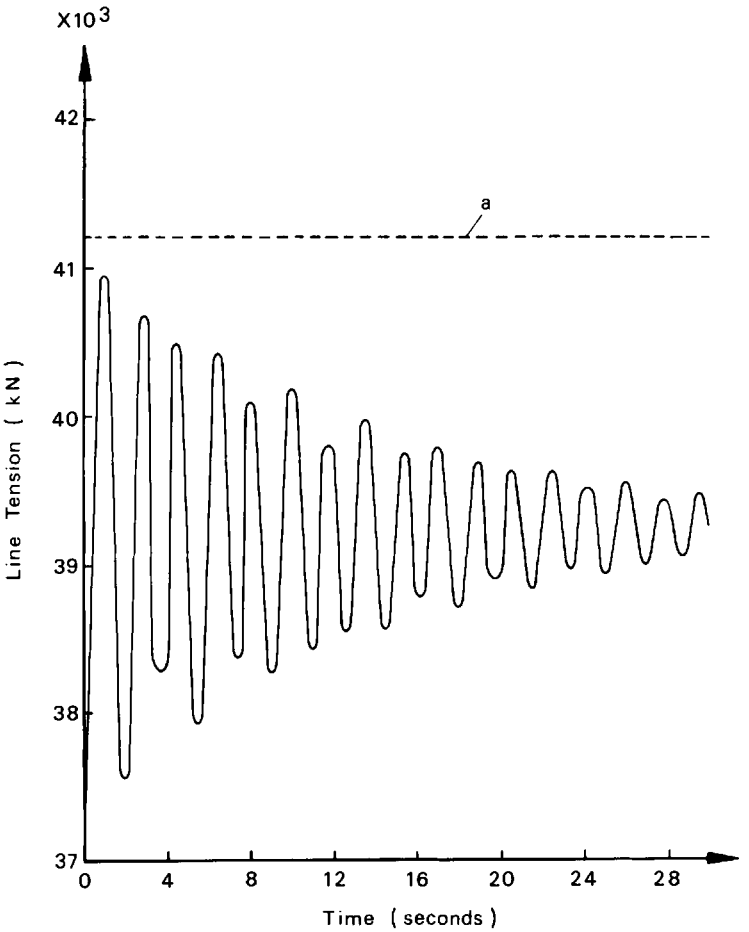

Figure 7.14. Line tension for 4000 t stern lift from a fixed platform. *Key*: a – maximum allowable tension

References

Grim, O. (1983) Crane ships in a seaway: movements of the ship and load. *Jahrbuch der Schiffbautechnischen, Gesellschaft*, **77**, 237–245

Patel, M. H. (1989) *Dynamics of Offshore Structures*. Butterworths, London, 392 pp

Stoker, J. J. (1950) *Nonlinear Vibrations in Mechanical and Electrical Systems*. Interscience Publishers, New York

Chapter 8

Tandem hull floating vessels

8.1 Introduction

Considerations of the hydrodynamics of semisubmersibles, tensioned leg platforms and ship shape hulls in the preceding chapters have illustrated the substantial differences in performance directly related to the open space frame or the ship shape nature of vessel hull forms. Over recent years, the offshore industry has substantially broadened the duties required from these two types of hull forms. They have been used as drilling platforms, crane vessels, diving and maintenance support vessels, for marine transportation of very large structures and, lately, for oil production.

These applications have required the vessels to carry reasonably large deck payloads and exhibit low wave induced motions. Requirements of cruising speed have been secondary to the above and to those of station keeping and survival in very heavy seas. The importance of low wave induced motions, for oil drilling or production activities, for example, has necessitated the use of semisubmersibles, whereas high payload requirements have tended to require ship shape hull forms.

However, an unusual floating vessel design, which can be regarded as a hybrid of monohull and semisubmersible hull shapes can offer a combination of the low wave induced motions and high payload advantages of both these hull forms. The tandem hull vessel consists of a surface piercing hull separated by a small distance from a fully submerged hull directly below it. The gap between the hulls is substantially open, with the hulls connected by short vertical bracing members of circular or rectangular cross-section. Figure 8.1 shows a perspective view of a typical tandem hull design with an upper hull of 124.0 m length, 32.68 m beam and 5.37 m draught. A lower hull of 124.0 m length, 32.68 m beam and 10.4 m depth is connected to the upper hull by rectangular members bridging a gap of 4.0 m height. For this particular vessel, there are 12 inter-gap members, each of 11.25 m length and 3.44 m width. The tandem hull veseel is of 58 745 t displacement with a 19.77 m total draught.

The three major performance requirements for a floating production platform are high payload capacity for process plant and oil storage, low motion response to waves and low construction cost. Both semisubmer-

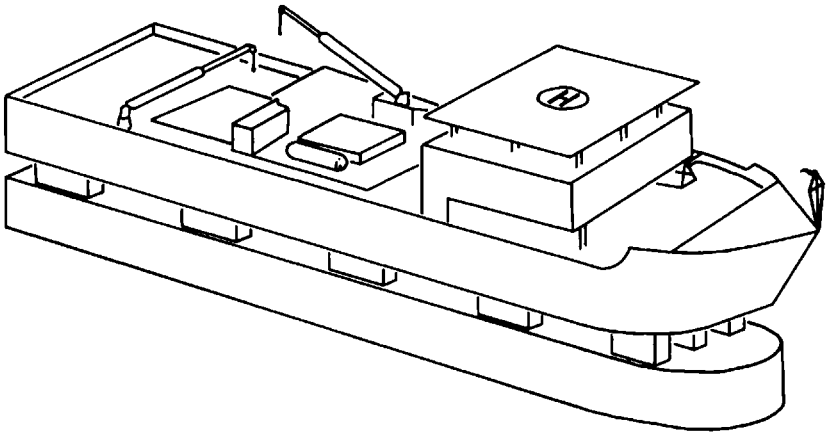

Figure 8.1. Perspective view of a tandem hull vessel

sibles and monohull vessels have shortcomings when viewed against these criteria. Semisubmersibles have low wave induced motion characteristics but suffer from low payload capacity and high construction cost. Monohull vessels, on the other hand, offer high payload capacity and low construction cost but have higher wave induced motions than semisubmersibles. The low wave induced motions of semisubmersibles are due to the open 'space frame' pontoon/column configuration which allows inertia and pressure induced wave forces to partially cancel each other, thereby reducing the level of wave forces on the vessel. The low waterplane area of a semisubmersible also gives rise to high natural periods which are helpful to vessel motions at predominant wave periods. In contrast, a monohull vessel achieves its high load carrying capacity due to its large waterplane area, but this contributes to its relatively higher wave induced motions. The tandem hull platform combines the beneficial design features of both conventional monohull vessels and semisubmersibles to satisfy the needs of both high payload capacity and low wave induced motion characteristics.

However, the emergence of these special purpose hull configurations requires a unified technical approach to such designs – both to place them within the contest of all marine vehicles and to enable better understanding of their hydrodynamic behaviour. This chapter attempts to provide this for the tandem hull form in a floating production platform application where deck payload capacity and low wave induced motions of the stationary vessel are the primary design goals. The chapter presents a survey of 23 vessels whose leading dimensions, payloads and displacements are used to define non-dimensional ratios for each vessel with the ratios plotted against each other to reveal some interesting generic variations.

A simplified hydrodynamic analysis is then derived for wave induced heave forces and motions for typical semisubmersible, tandem and monohull vessels to illustrate their hydrodynamic behaviour. The simplified analysis is complemented by a more representative diffraction theory based hydrodynamic analysis of the hull form to yield wave induced

motions and inter-hull forces. The analyses results are compared with model tests at 1/75th scale for both wave induced motions and inter-hull forces. The theory and model tests are used to deduce principal features of the tandem hull's hydrodynamic behaviour in waves.

8.2 Hybrid hull characteristics

A survey of 23 designs falling within seven distinct vessel types is presented here. The vessel types are described further below.

Type 1 consists of semisubmersibles with pontoons that are deeply submerged and vertical columns that connect the deck to the pontoons through the water surface. The resultant small water plane area coupled with low wave induced forces due to deep pontoon submergence leads to low wave induced vessel motions. However, semisubmersibles have limited deck payload capacity due to low stability from the small water plane area and because of the large separation between centres of gravity and buoyancy. Vessel type 2 is the special purpose tensioned buoyant platform used for hydrocarbon production. Types 3 and 4 are crane vessels of semisubmersible (as in type 1 above) and conventional monohull form respectively. Vessel types 5 and 7 consist of conventional cargo carriers and naval ships respectively. These vessels have large water plane areas and submerged volumes that are close to the water surface compared to the hull shapes of type 1. Thus such hulls tend to have higher load carrying capacity but poorer wave induced motion characteristics. Vessel type 6 is the special purpose tandem hull form being considered in this chapter.

Table 8.1 lists these vessels together with their displacements, overall lengths, water plane areas, normal loaded or operating draughts, submerged pontoon depths, if any, and payloads, with some of the data obtained from several sources such as Greenham (1986) and Moore (1986). Due to possible inconsistencies in definition of payload, the values presented for this parameter must be viewed with caution, particularly for crane vessels. No payload data are included for naval ships for the same reason. If the water plane area of a monohull is not directly available, it has been calculated using a coefficient of fineness of water plane area of 0.9 – this is characteristic of tanker type vessels with long parallel sides. The displacements of commercial cargo carriers are calculated assuming that the ratio of summer dead-weight to displacement is equal to 0.86. Tanker 2 is selected to be a monohull vessel with a displacement close to that of the type 6 tandem hull vessel.

Since the small water plane area and deeper draught of a semisubmersible vessel contributes to its low wave induced motion response, two non-dimensional ratios incorporating these parameters can be written as the water plane area ratio:

$$R_1 = \frac{A}{V^{2/3}} \tag{8.1}$$

Table 8.1 Vessel data

Type		*Vessel*	*Displacement* (t)	*Overall length, L* (m)	*Water plane Area A* (sq m)	*Draught D* (m)	*Dimension c* (m) *Fig.8.5*	*Payload P* (t)
1	A	Aker H3	19 636	108.2	305	21.3	14.6	4500
	B	GVA 4000	25 790	80.6	523	20.5	13.0	4020
	C	GVA 5000	33 600	98.6	726	22.5	14.5	6900
	D	GVA 10000	63 900	82.4	853	24.5	13.5	9300
	E	BS 8000	40 813	113.0	681	23.0	12.5	8000
	F	Western Pacesetter	19 680	79.3	463	18.3	12.2	5428
	G	Semiflex II	45 250	150.0	486	50.0	47.0	10 000
	H	Penta 7000	19 710	97.0x	433	22.5	13.5	8000
2	I	Hutton Tension Leg Platform	63 300	95.7	1320	33.2	22.2	7950
3	J	Derrick Barge 102	175 000	153.9	5034	26.6	13.0	29 000
	K	HD GL 100	90 000		3706	12.0	12.0	33 500
4	L	ITM *Mariner*	5300	95.5	2450	2.0	2.0	900
	M	ITM *Challenger*	44 128	140.8	5457	8.5	8.5	6500
5	N	Bulk Carrier	155 440	245.0+	9271	16.9	16.9	46 820@
	O	Tanker 1	277 579	310.0+	17 183	19.4	19.4	92 062@
	P	Tanker 2	61 150	214.9+	6430	12.3	12.3	16 726@
6	Q	Tandem Hull	59 200	130.5	3561	19.8	5.5	15 000
7	R	Aircraft Carrier	24 284	208.8*	5149	8.7	8.7	
	S	Invincible	16 257	192.8*	4772	7.3	7.3	
	T	Type 82	6198	149.3*	2257	5.2	5.2	
	U	Type 42	3556	119.5*	1538	5.8	5.8	
	V	Type 21	2794	109.7*	1254	6.0	6.0	
	W	Fleet Tanker	36 578	197.5	4550	11.1	11.1	

Notes:
x Length across apexes;
* Length at waterline;
+ Length between perpendiculars;
@ Based on net tonnage.

1: semisubmersible drilling or production vessels; 2: tension leg platform; 3: semisubmersible crane vessels; 4: monohull crane vessels; 5: commercial cargo carriers; 6: tandem hull; 7: naval vessels

and the draught ratio:

$$R_2 = \frac{D}{V^{1/3}} \tag{8.2}$$

where A is the surface hull water plane area; V is the total hull volume; and D is the total draught of the vessel.

Three further ratios which incorporate the water plane area, displaced volume and the leading dimensions of the vessel can be written as the length ratio

$$R_3 = \frac{L}{V^{1/3}} \tag{8.3}$$

the area ratio:

$$R_4 = \frac{1}{R_1 R_3} = \frac{V}{AL} \tag{8.4}$$

and the lower hull depth ratio:

$$R_5 = \frac{c}{V^{1/3}} \tag{8.5}$$

where L is the overall length; c is the hull draught for a monohull, the upper hull draught for the tandem hull, or the depth of submergence of the pontoon upper surface for a semisubmersible (see Figure 8.5).

A further ratio can be written as lower hull depth to length ratio:

$$R_6 = \frac{R_5}{R_3} = \frac{c}{L} \tag{8.6}$$

A payload to draught non-dimensional ratio can also be written as

$$R_7 = \frac{1}{D}\left[\frac{P}{\rho}\right]^{1/3} \tag{8.7}$$

where P is the vessel payload; and ρ is sea water density.

The ratios defined above are calculated from Table 8.1 and plotted in various ways. Three representative variations are presented here with Figure 8.2 giving area ratio (R_4) plotted against water plane ratio (R_1) for all the surveyed vessels. The distribution of plotted points clearly shows distinct clusters corresponding to semisubmersibles including the tensioned buoyant platform and those due to monohulls. The hybrid nature of the tandem hull, as a vessel configuration midway between the semisubmersible and monohull, is clearly evident in Figure 8.2 with data for the tandem hull lying between the semisubmersible and monohull clusters.

Figure 8.3 shows the lower hull depth ratio (R_6) plotted against water plane ratio. Once again, the distribution of points reflects the high pontoon submergence of semisubmersible vessels which are all within a band of high values of R_6 from 0.12 to 0.32. For monohulls, however, this ratio is approximately 0.05 with the tandem hull (type 6) showing up in a distinctly different position from the general trend. Furthermore, the differing demands of higher stability placed on crane vessels are evident since the point clusters for both semisubmersible and monohull crane vessels are skewed towards higher values of ratio R_1 which correspond to greater hydrostatic stability.

Figure 8.4 presents payload to draught ratio against the water plane ratio. Naval vessels are excluded from this curve due to the absence of

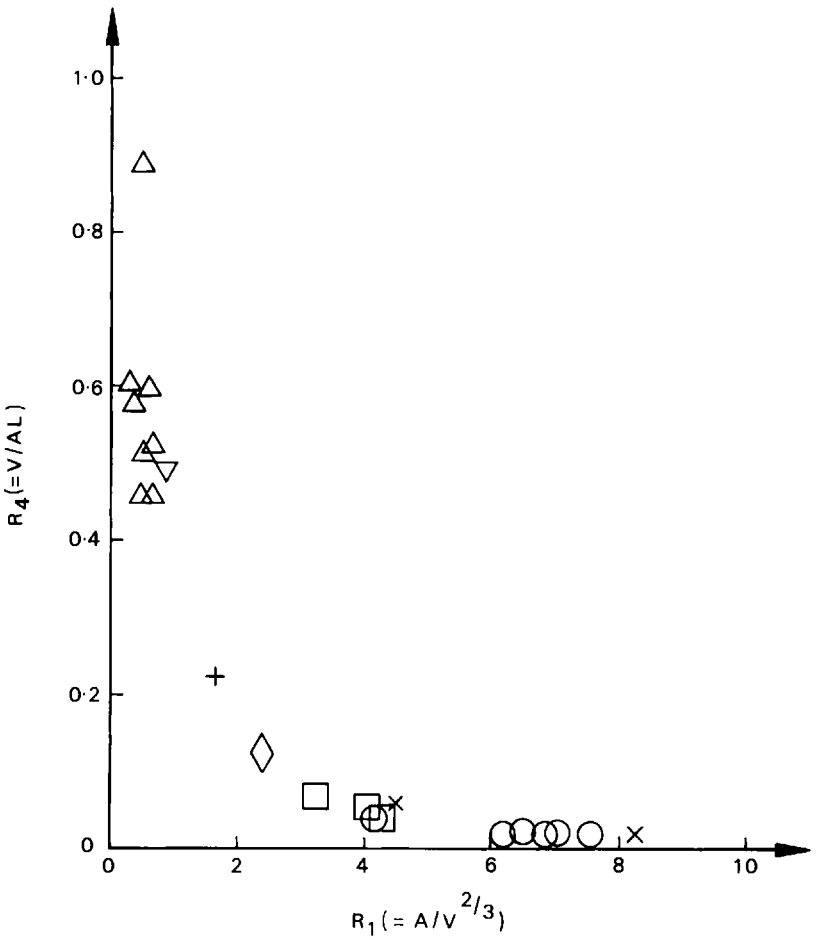

Figure 8.2. Area ratio against water plane ratio for surveyed marine vehicles. *Key*: △ Type 1, semisubmersible; ▽ Type 2, Hutton tension buoyant platform; + Type 3, semisubmersible crane vessels; × Type 4, ship shape crane vessels; □ Type 5, cargo vessels; ◊ Type 6, tandem hull; ○ Type 7, naval vessels

payload data. The tensioned buoyant platform has a smaller value of R_7 due to the excess buoyancy required to maintain the vertical mooring tethers in tension since the excess buoyancy reduces the payload capacity compared to a freely floating vessel. The distribution of points presented here shows an interesting, approximately straight line relationship between the ratios. Once again, the tandem hull lies midway between the semisubmersible and monohull point clusters.

8.3 Simplified wave induced motions analysis

The difference in the ratios of leading parameters for semisubmersible and monohull vessels is reflected in the substantially different wave loading

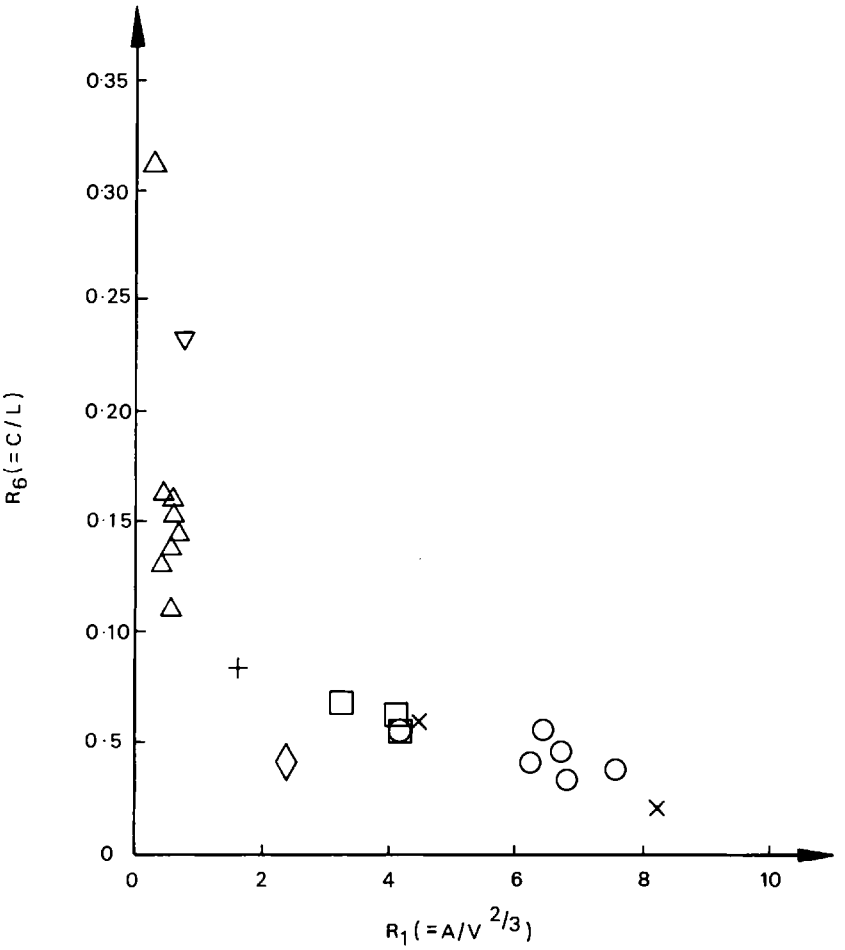

Figure 8.3. Lower hull depth to length ratio against water plane ratio. *Key*: △ Type 1, semisubmersible; ▽ Type 2, Hutton tension buoyant platform; + Type 3, semisubmersible crane vessels; × Type 4, ship shape crane vessels; □ Type 5, cargo vessels; ◊ Type 6, tandem hull; ○ Type 7, naval vessels

mechanisms for such designs, which in turn leads to different methods of hydrodynamic analysis.

Semisubmersible vessels consist of a space frame of slender cylindrical members incorporating vertical surface piercing columns which connect deeply submerged horizontal pontoons to a deck structure with appropriate bracing to stiffen the structure. The low wave induced motions of semisubmersibles are primarily due to low wave induced forces and high heave, roll and pitch natural periods due to the low water plane area and low hydrostatic stiffness. The low wave induced forces are due to the deeply submerged pontoons being in the region of lower wave velocities and accelerations since wave energy decays rapidly with depth. However, force cancellation plays an even greater role in the occurrence of low wave

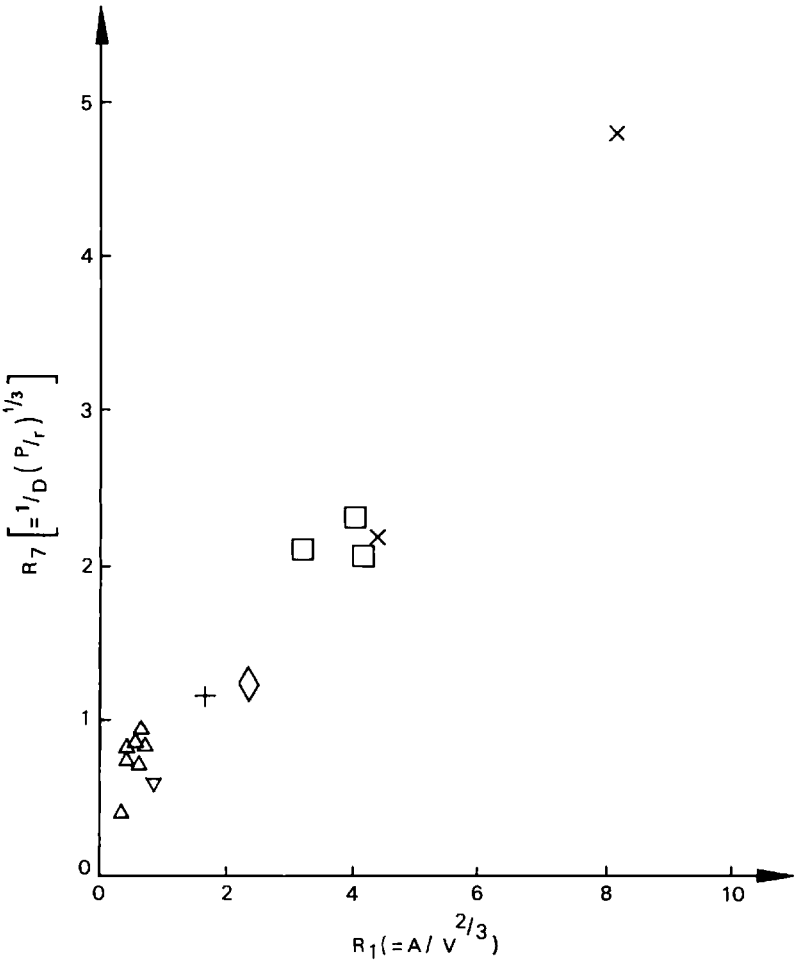

Figure 8.4. Payload to draught ratio against water plane ratio: *Key*: △ Type 1, semisubmersible; ▽ Type 2, Hutton tension buoyant platform; + Type 3, semisubmersible crane vessels; × Type 4, ship shape crane vessels; □ Type 5, cargo vessels; ◊ Type 6, tandem hull;

induced forces. Such cancellation arises from two sources – the first occurs because, for some specific wave periods, a wave length can straddle or be some multiple of the vessel length which leads to zero pitch or roll moments. The second source of wave cancellation arises for vertical forces, say, if vertical wave induced pressure forces on the submerged pontoons are 180° out of phase with pressure forces on surface piercing columns leading to a smaller net force amplitude than the forces on the pontoons or columns on their own.

For a monohull, on the other hand, a vessel length straddling a wave length is the only source of wave cancellation and occurs for the vessel in head or stern seas only since such vessels are normally long compared to their beam. Also, monohulls generally have low natural periods in heave,

roll and pitch which are much more likely to be within the periods of typical wave action.

The above differences continue into methods of analysis. The slender space frame structure of a conventional semisubmersible permits the assumption that wave properties are not influenced by the presence of the members. Consequently, a Morison equation based approach (see Chapter 5) can be used for vessel motions analysis with drag forces included in the formulation and linearized during solution of the equations of motion.

The large submerged volume typical of a tandem hull or a monohull is such that the hull will interact with incident waves in a complex manner depending on the hull shape. Wave and vessel motion induced surface pressures on the hull can then only be deduced from a solution of the linearized wave problem with no flow boundary conditions satisfied at the free surface, the sea bed and the vessel hull. Chapter 5 presents the formulation of such a boundary integral hydrodynamic analysis technique. This boundary integral technique is used subsequently to predict wave induced forces and motions for a tandem hull.

However, in order to illustrate the physical principles underlying hydrodynamic behaviour of these vessels, a simpler analysis is presented here, which, brings out the most significant features of the governing physics despite the simplifying assumptions used.

Consider heave motion of a generic multi-hull vessel of the configuration shown in Figure 8.5. The vessel has dimension, b, perpendicular to the paper. It can represent a monohull vessel if dimensions a and d are taken as zero. A simple four column semisubmersible vessel can be invoked by setting a at an appropriate value and s equal to zero, whereas the twin hull tandem vessel is modelled by setting dimension a equal to zero and s at an appropriate value to represent the inter-hull structure.

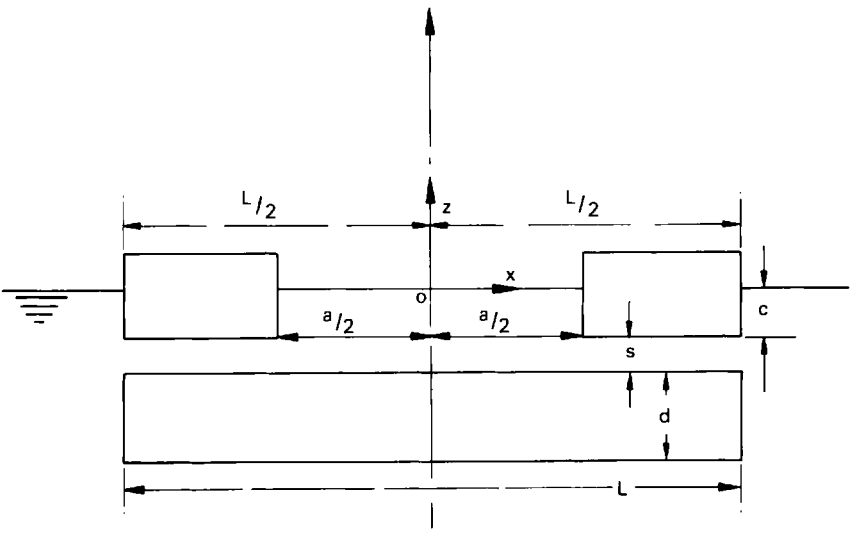

Figure 8.5. Side view of multi-hull vessel

The following simplifying assumptions are used:

1. The submerged and surface piercing hulls are treated as rectangular boxes having the same vertical centre line.
2. Wave diffraction effects are ignored, including the linear damping due to gravity wave radiation from the hulls. Drag forces due to wave velocities are also neglected, permitting the undamped dynamic motion response to be calculated.
3. Deep water linear gravity wave theory is used.
4. Inter-hull bracing members are assumed to be of small volume. Wave forces on such members are neglected in comparison with wave forces on the hulls.

The multi-hulled vessel of Figure 8.5 in head seas will experience two types of wave induced heave force cancellation periods. These are values of wave period at which the heave force amplitude will become zero. Two mechanisms give rise to such cancellation periods:

1. The first is associated with a complete wavelength or a specific multiple of a wavelength straddling the vessel length in head seas. At this period, the total heave force on the vessel will become zero.
2. The second cancellation period is associated with wave forces on the upper and lower hulls. These forces are 180° out of phase with each other and at a particular wave period will cancel out in magnitude to give zero heave force amplitude.

The effects of both cancellation periods can be quantified by deriving an expression for vertical wave force on the vessel.

Now the velocity potential, Q, for a deep water linear wave is

$$Q = \frac{\omega H}{2k} e^{kz} \cos(kx - \omega t) \tag{8.8}$$

where ω is wave frequency; H is wave height; k is wave number; t is time and the axes system Oxz is defined in Figure 8.5.

Now the pressure force, F_p, on the upper hull can be readily derived as

$$F_p = \int_{a/2}^{L/2} -\rho \frac{\partial Q}{\partial t} \cdot b\,dx + \int_{-L/2}^{-a/2} -\rho \frac{\partial Q}{\partial t} \cdot b\,dx$$

$$= \frac{\rho g H b}{k} e^{-kc} \left[\sin \frac{kL}{2} - \sin \frac{ka}{2} \right] \sin \omega t \tag{8.9}$$

where g is the acceleration due to gravity.

Next, the vertical inertia force, F_i, on the lower hull is calculated as

$$F_i = \int_{-L/2}^{L/2} \rho \, [C_m + 1] \cdot b \, d \frac{\partial^2 Q}{\partial z \partial t} \cdot dx$$

where C_m is the added mass coefficient for the lower hull in vertical motion.

Taking $C'_m = C_m + 1$

$$F_i = -\frac{\rho C'_m b d \omega^2 H}{k} \exp[-k(c + s + d/2)] \sin\frac{kL}{2} \sin\omega t \tag{8.10}$$

with the wave fluid acceleration calculated at the centre of the submerged hull. Therefore, the total vertical wave force on the hulls is

$$\begin{aligned} F &= F_p + F_i \\ &= \rho g \frac{H}{2} A \exp(-kc) \left\{ \frac{2}{k(L-a)} \left(1 - \frac{\sin ka/2}{\sin kL/2}\right) \right. \\ &\quad \left. - \frac{2d}{L-a} C'_m \exp\{-k[s + (d/2)]\} \right\} \cdot \sin\frac{kL}{2} \sin\omega t \end{aligned} \tag{8.11}$$

using $\omega^2 = gK$ and a water plane area of $A = b(L - a)$. For the hull shape of Figure 8.5, it can be shown that

$$\frac{d}{L-a} = R_4 - R_6 \tag{8.12}$$

enabling Equation (8.11) to be written as

$$\begin{aligned} F = \rho g \frac{H}{2} A \exp(-kc) & \underbrace{\left\{ \frac{2}{k(L-a)} \left(1 - \frac{\sin ka/2}{\sin kL/2}\right) \right.}_{X} \\ & \underbrace{\left. - 2C'_m (R_4 - R_6) \exp\{-k[s + (d/2)]\} \right\}}_{Y} \cdot \sin\frac{kL}{2} \sin\omega t \end{aligned} \tag{8.13}$$

Equation (8.13) for vertical wave induced force illustrates the source of the two force cancellation mechanisms. The zeroes of the $\sin(kL/2)$ term denote the occurrence of cancellation associated with a whole wavelength straddling the hull length. This occurs for vessel hull configurations where term a is zero or very small so that term $\sin(ka/2)$ is approximately zero. The total force can also go to zero, however, when terms X and Y are equal in magnitude, corresponding to the case when the wave force on the upper hull is 180° out of phase and equal in magnitude to the wave force on the lower hull. Note that even when the magnitudes are not equal, the opposite signs of terms X and Y mean that the total heave force is lowered due to wave cancellation.

Now Equation (8.13) can be used to deduce the vertical wave force amplitude on various vessel designs. For a single surface hull, $a = d = 0$ and $R_4 - R_6 = 0$. This leads to the disappearance of one source wave force cancellation due to term Y vanishing in Equation (8.13). For semisubmersibles, the horizontal separation of vertical surface piercing columns plays a part in wave force cancellation. This feature is illustrated by the role played by term a in Equation (8.13). A conventional four column semisubmersible can be represented by choosing a value of a just

smaller than that of L and taking s as zero. On the other hand, a tandem hulled vessel can be represented by taking a as zero. In this latter case, the wave force equation reduces to a simpler expression but the two force cancellation mechanisms are still present.

For all three semisubmersible, tandem hull and monohull vessels, a wave force cancellation will occur when the vessel length, L, and dimension, a, are multiples of the incident wavelength. However, in practice this is too restrictive since such force cancellation for wave periods of interest occur for vessel lengths that are unrealistically high. Therefore, the presence of wave force cancellation due to out of phase forces on submerged and surface piercing hulls is of much more interest. For a tandem hull vessel, this cancellation is exact for the condition.

$$f(k) = \frac{(L - a)\exp\{-k[s + (d/2)]\}}{1 - [\sin(ka/2)/\sin(kL/2)]} = \frac{1}{C'_m (R_4 - R_6)} \tag{8.14}$$

where $f(k)$ can be called a cancellation function.

If this transcendental Equation (8.14) is satisfied for specific values of k (and therefore wave period, T), force cancellation will lead to a zero wave force amplitude. The values of wave period at which exact force cancellations occur are primarily influenced by the vessel's ratio of submerged longitudinal cross-sectional area to the water plane area (area ratio, $R_4 = V/AL$) and the lower hull depth to length ratio, R_6, although the length scales a, d and s also play a progressively less important part.

Now for a tandem hull with $a = 0$, it can readily be shown that the left hand side of Equation (8.14) has a maximum value of

$$\frac{2L}{e(2s + d)} \tag{8.15}$$

at a wave number k, and period, T, of

$$k = \frac{1}{s + (d/2)} \text{ or } T = 2\pi \sqrt{\left[\frac{s + (d/2)}{g}\right]} \tag{8.16}$$

Then from Equations (8.14) and (8.15), a condition for wave force cancellation due to opposing forces on the submerged and surface piercing hull can be written as

$$\frac{2L}{e(2s + d)} < \frac{1}{C'_m (R_4 - R_6)} \tag{8.17}$$

or

$$\frac{s}{L} > \frac{C'_m}{e}(R_4 - R_6) - \frac{d}{2L} \tag{8.18}$$

Expressions for heave natural period of the vessel of Figure 8.5 can also be readily derived as

$$T_h = 2\pi \sqrt{\left[\frac{\rho(Ac + Ldb + C_m Ldb)}{\rho g A}\right]}$$

$$= 2\pi \sqrt{\left\{\frac{L}{g}\left[R_6 + (R_4 - R_6)\, C'_m\right]\right\}} \tag{8.19}$$

and, consequently, the undamped heave motion amplitude, Z, may be written as

$$Z = \frac{F_a\, e^{i\omega t}}{\rho A\left[g - L\left\{R_6 + (R_4 - R_6)\, C'_m\right\}\omega^2\right]} \tag{8.20}$$

where F_a is the total vertical wave force amplitude.

Finally, an expression for vessel longitudinal stability is required to permit examination of vessel load carrying capacity when balanced against the force cancellation feature. For simplicity, only the multi-hull vessel with $a = 0$ is considered and the distance of the longitudinal metacentre, M, above the keel, K, is evaluated.

Thus, taking B as the centre of buoyancy

$$KM = KB + BM$$

$$= (d + c)\left[\tfrac{1}{2} + \frac{cs}{(d + c)^2}\right] + \frac{L^2}{12(d + c)}$$

Therefore

$$\frac{KM}{(d + c)} = \tfrac{1}{2} + \frac{1}{12\, R_4^2} + \frac{R_6}{R_4^2} = \tfrac{1}{2} + \frac{1}{12\, R_4^2}\left[1 + \frac{12\, R_6 s}{L}\right] \tag{8.21}$$

Equations (8.19), (8.20) and (8.21) for heave natural period, motion response and stability reinforce the point that ratios R_4 and R_6 play a key role in the motions as well as load carrying capacity of marine vessels.

In order to illustrate the implications of the equations derived above, the various functions are examined for four vessel designs ranging from a typical four column, twin pontooned semisubmersible to a conventional ship shape hull. The leading particulars of these vessels are listed in Table 8.3, together with the non-dimensional ratios R_4 and R_6. The semisubmersible design, the tandem hull 1 and the ship shape hull have numerical values very close to the data presented in Table 8.1. An additional hull shape, called tandem hull 2, is introduced to investigate hull behaviour over a wider range of ratios R_4 and for a different value of ratio s/L.

In particular, Equation (8.14) is investigated. A cancellation function, $f(k)$, defined by the left hand side of Equation (8.14), is plotted against wave period, T, in Figure 8.6 for the three twin hull designs. The right hand side of Equation (8.14) is a constant term for each design and is equal to 0.868, 2.387 and 4.785 for the semisubmersible, tandem hull 2 and tandem hull 1 respectively. These constant values are denoted in Figure 8.6 by the horizontal full lines. Furthermore, Equation (8.18) identifies a condition for inter-hull force cancellation to occur for a tandem hull. Figure 8.6 illustrates this point where the condition of Equation (8.18) is not satisfied for tandem hull 1 implying that Equation (8.14) has no solution for this case since the $f(k) = 4.785$ line does not intersect the $f(k)$ curve for tandem hull 1. In the case of tandem hull 2, there are two

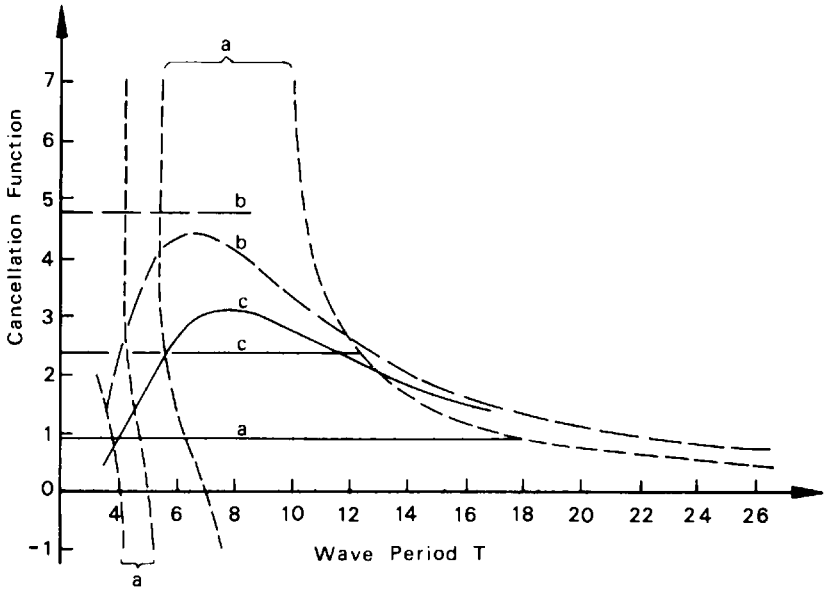

Figure 8.6. Cancellation function: *Key*: a – semisubmersible; b – tandem hull 1; c – tandem hull 2

solutions corresponding to $f(k) = 2.387$ – these being at wave periods of 5.50 and 11.60 s.

For the semisubmersible vessel, however, the effect of the $\sin(ka/2)$ term due to separation of the surface piercing columns is to change the shape of the $f(k)$ curve such that solutions corresponding to interhull cancellation periods will always arise. Thus, Figure 8.6 shows that for $f(k) = 0.868$, such cancellations occur at wave periods of 3.64, 4.53, 6.23 and 18.50 s.

At the same time, satisfying the condition of $\sin(kL/2) = 0$ leads to wave straddling cancellation periods. These are listed in Table 8.2 and labelled as W together with inter-hull cancellation periods which are labelled as F. Figure 8.7 shows the position of W and F marked for tandem hulls 1 and 2. For a ship shape vessel, inter-hull cancellations will not arise. On the other hand, for a semisubmersible the combination of $\sin(ka/2)$ and $\sin(kL/2)$ terms means that pure wave straddling cancellations will not occur – all the cancellations being given by Equation (8.14).

Figure 8.7 illustrates the resultant heave force amplitudes, non-dimensionalized with respect to $\rho gHA/2$ as functions of wave period. Curves are presented for all four vessels and indicate the zeroes in force magnitudes due to the cancellations described above. For wave periods above 16 s, the drop in wave force from ship shape vessel through the tandem hulls to the semisubmersible illustrates the role of the inter-hull cancellations in being able to reduce wave induced forces. For wave periods below 16 s, the reduction in wave forces continues for the ship shape and tandem hull designs. The semisubmersible, on the other hand,

Table 8.2 Summary of cancellation periods

Semisubmersible		*Tandem hull 2*		*Tandem hull 1*		*Ship*	
Period/s	*Type*	*Period/s*	*Type*	*Period/s*	*Type*	*Period/s*	*Type*
18.50	F	11.60	F	8.91	W	9.50	W
6.23	F	8.91	W	6.30	W	6.71	W
4.53	F	6.30	W	5.15	W	5.48	W
3.64	F	5.50	F	4.46	W	4.75	W
		5.15	W	3.99	W	4.25	W
		4.46	W			3.88	W
		3.99	W				

Notes:
F: inter-hull force cancellation periods; and W: wave straddling force cancellation periods.

shows an increase in force amplitude here due to the fact that forces on the column and hulls can reinforce each other as well as cancel. It should be noted that the absolute magnitude of these forces is small for a semisubmersible but so is its sensitivity to these forces due to its small water plane area and thus heave stiffness.

Equations (8.19) and (8.20) also show that only the ratios R_4 and R_6 appear within the equations and influence the natural period and wave induced heave motion response. In the expression for natural period, the ratio $(R_4 - R_6)$ is largest for semisubmersibles reducing to zero for a ship shape. This mirrors the natural period variation across the range of designs listed in Table 8.3.

As mentioned earlier, the payload capacity of offshore marine vessels is of importance. The expression for $(kM)/(d + c)$ in Equation (8.21) is a measure of the stability of the vessel and, therefore, its payload capacity.

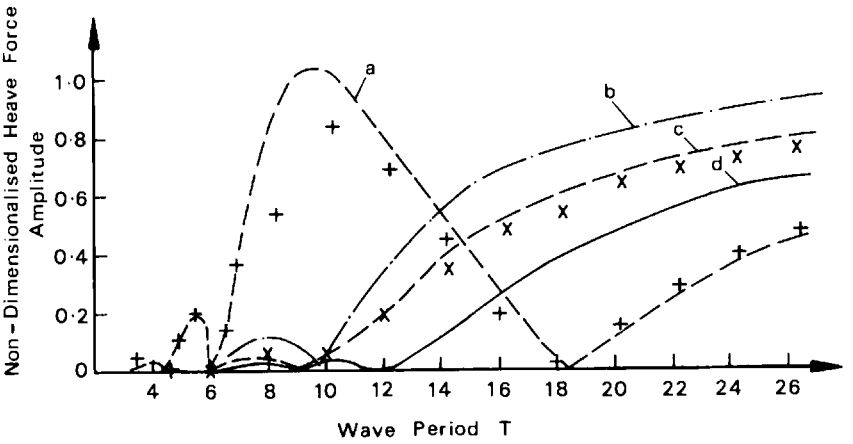

Figure 8.7. Non-dimensionalized heave force amplitude: *Key*: a – semisubmersible (simple calculation); b – ship (simple calculation); c – tandem hull 1 (simple calculation); d – tandem hull 2 (simple calculation); + – semisubmersible (full method); × – tandem hull 1 (full method)

Table 8.3 Vessel particulars and results for hand calculations

Vessel	Vessel data							Non-dimensional ratios		Heave nat. period	KM
	L(m)	d(m)	a(m)	c(m)	s(m)	V(m^3)	A(m^2)	R_4	R_6	T_h/s	$(d + c)$
1	73.6	7.5	57.2	12.5	0	24 352	524	0.631	0.170	19.79	–
2	124.0	20.8	0	5.5	5	97 836	3720	0.212	0.0444	15.21	2.386
3	124.0	10.4	0	5.5	4	59 148	3720	0.128	0.0444	11.25	5.696
4	140.8	0	0	8.5	0	43 052	5457	0.0604	0.0604	5.85	23.343

Notes:
1: four column semisubmersible; 2: tandem hull 2; 3: tandem hull 1; and 4: ship shape vessel.

Equation (8.21) applies only for $a = 0$ (ships and tandem hulls 1 and 2) but shows up the strong sensitivity to the value of ratio R_4. Table 8.3 presents values for the designs considered here and shows that the stability, and thus payload capacity, reduces sharply as the force cancellation characteristics are improved. A practical design would need to compromise between the demands of motion response and payload capacity through stability.

One feature of engineering concern in tandem hull design is the magnitude of inter-hull forces. These are measured during the model tests described later. At this stage, however, it is worth while to extend the simplified analysis developed here to yield an expression for the vertical component (compression positive) of inter-hull force. This can be written as

$$F_g = \tfrac{1}{2}\,[F_p - (F_i - \rho C_m L b d\ddot{Z})] - \tfrac{1}{2}\,[m_u - m_l]\ddot{Z} - \tfrac{1}{2}\,\rho g A\, Z \qquad (8.22)$$

with F_p and F_i obtained from Equations (8.9) and (8.10) and $\ddot{Z}$ obtained from Equation (8.20). This expression includes the effects of direct wave force in the first term and the inertia force due to the differential physical mass of the upper and lower tandem hulls in the second term. Numerical values from Equation (8.22) are used subsequently for Section 8.6.

The validity of the approximate results derived from the simplified analysis has been confirmed by computing the heave force amplitudes of two of the designs (the semisubmersible and tandem hull 1) using more detailed calculations which incorporate fewer simplifying assumptions. The wave induced heave force for the semisubmersible has been calculated using a Morison equation approach which is described in further detail in Chapter 5. A boundary integral brief analysis, described in the following section and in more detail in Chapter 5, is used for tandem hull 1. Figure 8.7 shows an acceptable level of agreement between the simplified analyses and the more detailed calculations for the two hull forms, suggesting at least that the simplified analysis can be regarded as being adequate for preliminary design.

8.4 Dynamic analysis of tandem hulls

Figure 8.1 shows the geometry of a tandem hull design (hull B) for use as a floating offshore oil production platform. Hydrodynamic analysis of a tandem hull poses two problems. A boundary integral diffraction analysis is required for such a large hull structure but the correct surface facet representation of the inter-hull geometry is difficult to achieve and is likely to require a large number of facets and be prone to numerical errors associated with sources on adjacent or opposing facets being in close proximity. Additionally, drag forces may be significant and, therefore, need to be calculated for the smaller inter-hull members.

The difficulty in boundary integral analysis of the inter-hull gap structure is resolved by using a single equivalent inter-hull structure for the analysis. This structure is of the same plan area and aspect ratio as the individual members and is placed amidships and on the centre line of the vessel. Figure 8.8 shows the equivalent inter-hull structure. It is also shown later that drag forces on the inter-hull members are negligibly small compared to inertia forces and can, therefore, be ignored.

The complex amplitudes of wave and motion dependent forces acting on the tandem hull are evaluated by a conventional boundary integral numerical analysis for the six rigid body degrees of freedom of the vessel. A mesh generation program represents the surface of the vessel with a large number of triangular facets; the inter-hull connecting structures are modelled by a single column in the diffraction analysis (see Figure 8.8).

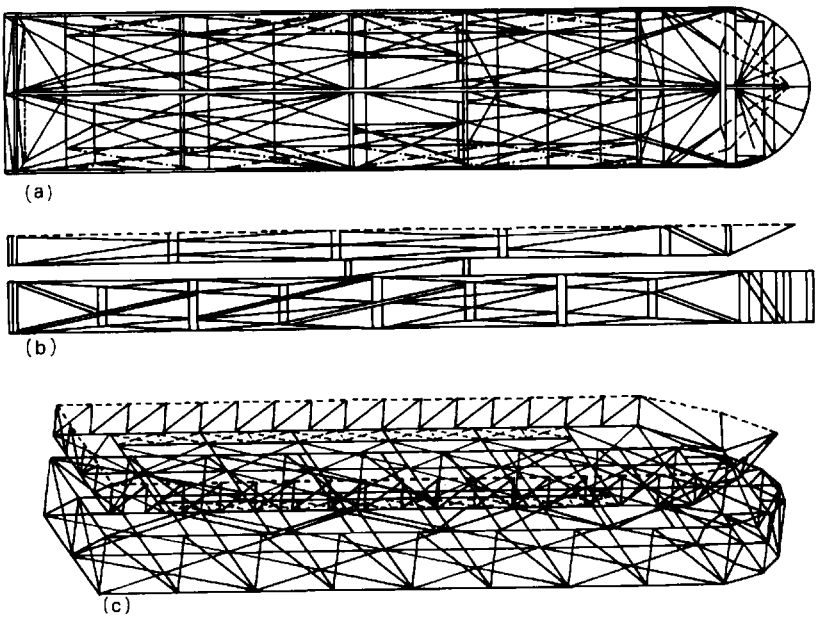

Figure 8.8. Tandem-hull facet for diffraction analysis. (a) view from underside; (b) side view; (c) perspective view (denser mesh than (a) and (b))

The boundary integral analysis with the formulation given in Chapter 5 is used to derive the coefficient matrices of the governing equation of motion

$$\{-\omega^2 [\mathbf{M} + \mathbf{M}_A(\omega)] + i\omega \mathbf{N}(\omega) + \mathbf{K}'\} \mathbf{X}(i\omega) = (H/2) \mathbf{R}(i\omega) \qquad (8.23)$$

where $\mathbf{M}$ is the physical mass matrix; $\mathbf{M}_A(\omega)$ and $\mathbf{N}(\omega)$ are frequency dependent added mass and radiation; $\mathbf{K}'$ is the vessel hydrostatic stiffness matrix; $\mathbf{R}(i\omega)$ is the exciting force vector and ω is the wave frequency. The amplitudes of motion, $\mathbf{X}(i\omega)$, are evaluated by matrix inversion. The solution of Equation (8.23) is further modified to include typically 2.2, 8 and 10% of critical damping in the heave, roll and pitch degrees of freedom, respectively, to represent the additional effects of viscous damping that are not accounted for in the formulation of the diffraction analysis. These additional levels of damping have been estimated from model tests of the tandem vessel.

The results of the diffraction analysis are also used to obtain estimates of inter-hull force. This is done by summing the incident wave and vessel motion induced pressure forces on all the facets of the upper and inter-hull structure separately from the pressure forces on the lower hull only. Then the total inter-hull force (or more specifically the force at the lower end of the inter-hull members) can be written as

$$F_{gL} = \tfrac{1}{2}\left[\sum_{\substack{j \\ \text{facets on upper hull and gap}}} p_j f_j \cdot m'_j - \sum_{\substack{j \\ \text{facets on lower hull}}} p_j f_j \cdot m'_j \right] - \tfrac{1}{2}(m_u - m_l)\, \ddot{Z} - \tfrac{1}{2} K'_L Z_L \qquad (8.24)$$

for the three linear modes of motion (L) corresponding to vessel surge, sway and heave. Here, p_j is the pressure at facet j of area f_j; m'_j is the normal vector to facet j; and m_u, m_l are the masses of the upper and lower hull respectively. K'_L is the vessel stiffness in the Lth mode of motion and Z_L is the motion in that mode.

An approximate evaluation of drag forces on the inter-hull structure is presented below to confirm that drag forces on inter-hull members are small in comparison with inertia forces on the whole vessel. Wave induced horizontal particle velocities around the inter-hull structure were calculated from linear wave theory and the consequent drag forces on the inter-hull members were evaluated using the Morison equation. This procedure was repeated for a wave period range from 7 to 16 s at 2 m wave height and for wave heights of 2, 6 and 12 m at 12 s period. In all cases considered, wave induced drag forces on the inter-hull members were less than 2% of the total wave exciting force on the vessel. Despite the fact that wave diffraction effects were ignored in the calculation of wave velocities incident on the inter-hull members, the level of the drag forces is considered small enough to be ignored.

Predictions of vessel wave induced motions and interhull forces from the above theories were validated by model tests at 1/75th scale. A model of the tandem hull vessel shown in Figure 8.1 was used to determine the vessel wave induced motions and also to measure forces in the gap structure in the vertical and fore and aft directions.

The tandem hull scale model was tested in two configurations. The first configuration, tandem hull A, had a 130.5 m long lower hull that was 6.50 m longer than the 124.0 m upper hull and protruded ahead of the bow of the upper hull. The second tandem hull configuration, B, was tested and had a lower hull that had been shortened by 6.50 m such that the upper and lower hulls were of the same length. The shape of the upper hull and gap structure were identical for both hulls. Table 8.4 describes the full scale principal particulars of both hulls, and Figures 8.1 and 8.8(c) show perspective views of tandem hull B.

Table 8.4 Summary of vessel data (all displacements for fresh water conditions)

Dimensions		*Tandem hull A*	*Tandem hull B*
Displacement (t)		60 955	58 745
Lower hull	Length (m)	130.5	124.0
	Width (m)	32.68	32.68
	Height (m)	10.4	10.4
	Displacement (t)	43 222	41 012
Surface piercing hull	Length (m)	124.0	124.0
	Width (m)	30.0	30.0
	Draught (m)	5.37	5.37
	Displacement (t)	17 576	17 576
	Water plane area (m^2)	3 031	3 031
Total draught (m)		19.77	19.77
Gap height (m)		4.0	4.0
Non-dimensional Ratios	R_4	0.1582	0.1525
	R_6	0.0756	0.0756
Height of CG above keel (m)		9.19	9.19
Radius of gyration in pitch (m)		41.9	41.9

The test model was designed to Froude number scaling and care was taken to ensure that the mass distributions of the upper and lower hulls were separately representative of the proposed full scale design. The model was moored by a soft catenary system in head seas. The second test model, *b*, had an internal aluminium frame installed which connected the upper and lower hulls. The frame was mounted with load cells to detect wave induced inter-hull forces in the vertical and fore and aft directions.

The results of the model tests are presented in Figures 8.9–8.12. Figures 8.9, 8.10 and 8.11 present model wave induced motion in heave, pitch and surge, respectively, as functions of wave period. Figure 8.12 presents the corresponding inter-hull vertical and fore and aft force amplitudes per unit wave amplitude, again as functions of wave period.

Figures 8.9–8.12 also present predictions based on both the simplified analysis of Section 8.3 (using an added mass coefficient, C_m, of 1.25) and on the more detailed diffraction theory described in Section 8.4. Since both tandem hulls A and B had non-rectangular bow shapes, as shown in Figure 8.8, the simplified hydrodynamic analysis for these hulls is carried out by assuming equivalent rectangular hulls of equal volume and by modifying the integration limits of Equation (8.10) to accommodate an equivalent

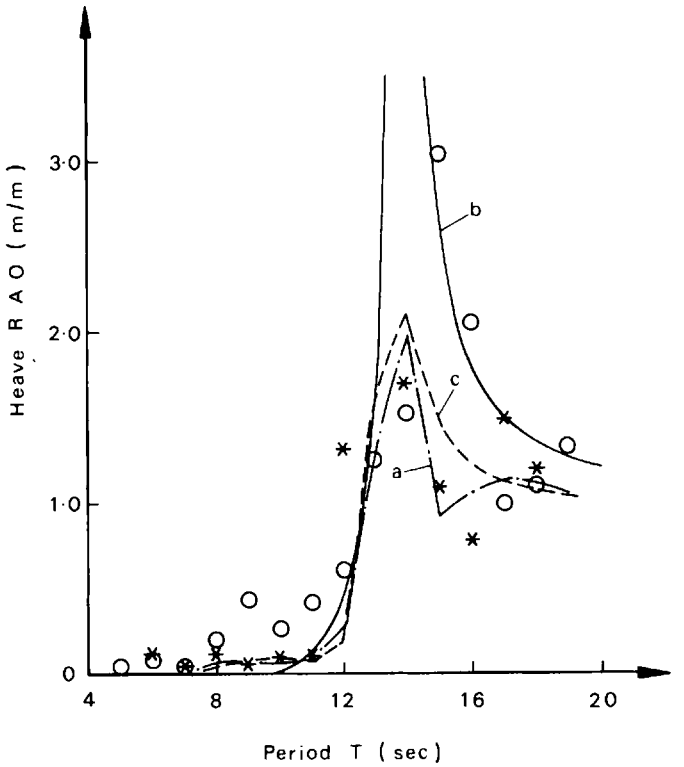

Figure 8.9. Heave motion in head seas. *Key*: a – Hull A (diffraction theory); b – Hull B (simplified analysis); c – Hull B (diffraction theory); O – Hull A (model test); * – Hull B (model test)

lower hull length. Figures 8.9 and 8.10 show generally reasonable agreement in overall trends between the diffraction theory analysis and model tests for heave and pitch motions. The tandem hull motions are characterized by low motion amplitudes for wave periods up to 12.5 s with high resonant peaks for wave periods around 14 s. There is some disagreement between theory and tests for heave motion of tandem hull A in the wave period range from 9 to 11 s. This is believed to be due to the effect of the lower hull bow protruding ahead of the upper hull and causing incident waves to exhibit complex local breaking and slamming effects. These were observed during the tests with tandem hull A but were absent for tandem hull B with its shortened lower hull bow.

Figure 8.11 presents surge motions in head seas for tandem hulls A and B. The diffraction analyses are in close agreement but again the tandem hull A model test data are at significantly higher values than those for tandem hull *B*. The effects of complex wave interactions associated with the protruding lower hull are again believed to be responsible for this. Surge motion data above 15 s are influenced by mooring system resonance (not modelled in the dynamic analysis) and are, therefore, not presented in Figure 8.11.

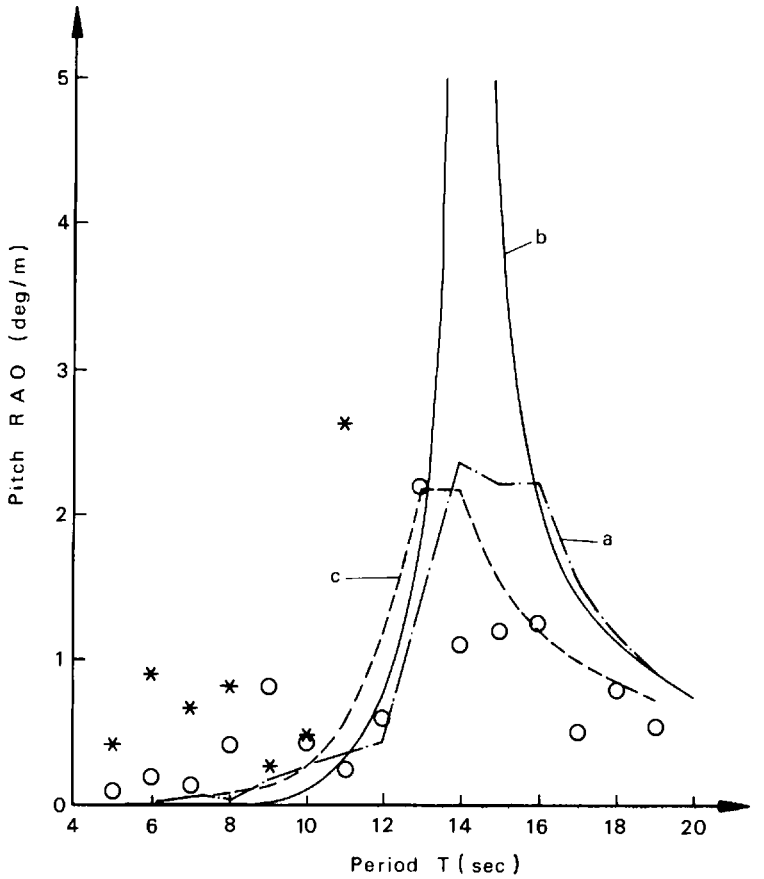

Figure 8.10. Pitch motion in head seas. *Key*: a – Hull A (diffraction theory); b – Hull B (simplified analysis); c – Hull B (diffraction theory); O – Hull A (model test); * – Hull B (model test)

Figure 8.12 presents predicted and measured data for inter-hull forces on tandem hull B. There is reasonable agreement between the two. In particular, the influence of wave induced forces on vertical inter-hull forces below 11 s is clearly distinguishable from tandem hull motion induced inter-hull inertia forces above 10 s period. The fore and aft inter-hull forces are very small compared to vertical forces.

Figures 8.9 and 8.12 also demonstrate the extent to which the simplified hydrodynamic analysis models overall trends for heave and vertical inter-hull forces as obtained from the more representative diffraction analysis and model tests. The discrepancy at heave and pitch natural periods is due to the assumption of undamped motions in the simplified analysis, although the motion response and force at the low period cancellation region are well represented. It is instructive to note the difference in motion response exhibited by tandem hulls A and B with tandem hull A having the lower water plane area ratio corresponding to a

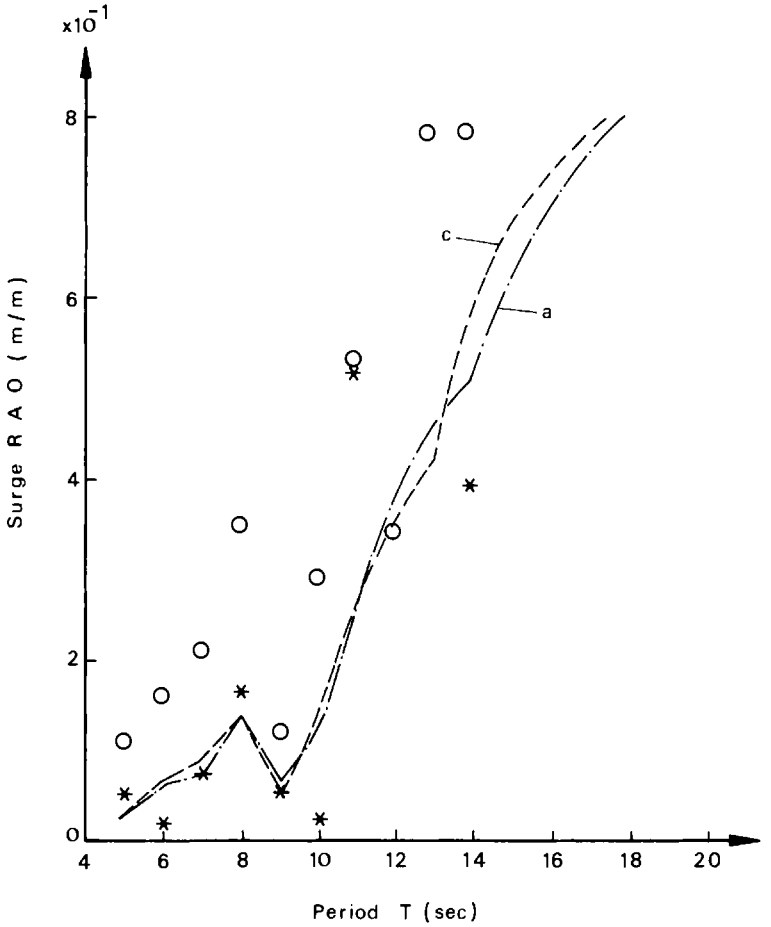

Figure 8.11. Surge motion in head seas. *Key*: a – Hull A (diffraction theory); c – Hull B (diffraction theory); O – Hull A (model test); * – Hull B (model test)

greater submerged volume. This leads to reduced heave and pitch natural periods for tandem hull B. The remaining difference in motion response seems to arise from wave interactions with the protruding lower hull bow of tandem hull A. Removal of this feature reduces the wave induced motions of the tandem hull (B).

It is necessary to point out one further feature of the behaviour of the tandem hulls that was observed in the model tests. Although only the test data for low (2 m) wave heights are presented here, the data for large wave heights showed up significant non-linear behaviour which had the primary effect of substantially reducing the values of peak resonant response per unit wave amplitude. Thus the peak values of motions and forces presented in Figure 8.9–8.12 can not be used for estimating the maximum values of these parameters in waves of large height. The additional model test data for large wave height are not presented here.

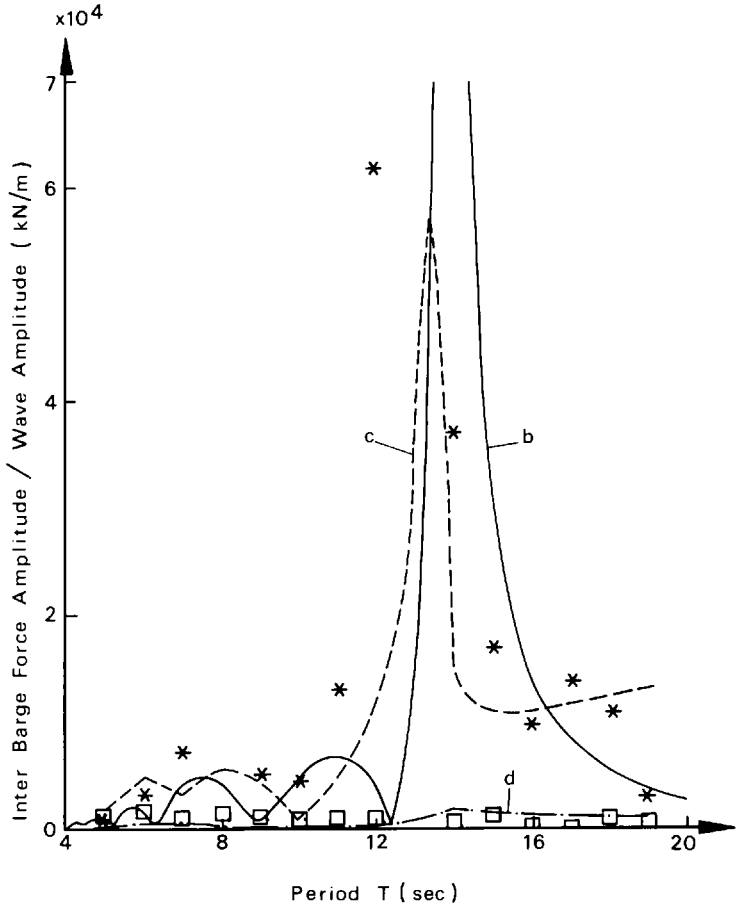

Figure 8.12. Inter-hull force amplitudes in head seas for Hull B. *Key*: * – vertical force (model tests); b – vertical force (simplified analysis); c – vertical force (diffraction theory); d – horizontal force (diffraction theory); □ – horizontal force (model tests)

8.5 Design considerations

The above comparisons between theory and model tests lead on to the equations for wave induced forces, motions and stability derived in Section 8.3. These simple equations clearly demonstrate that the heave motions and stability of stationary marine vessels operating in waves are primarily governed by the area ratio R_4 and a further length ratio, R_6, defined in Equations (8.4) and (8.6), respectively, although vessel length L, and depth (through variables s and d) also have some influence.

By appropriate choice of these ratios, the heave force function can be shaped to contain zeros due to both inter-hull wave cancellation effects as well as wave straddling cancellations. The selection of wave periods at which force cancellation occurs has a predominant effect on the motion

response. Selection of the above parameters also fixes the natural period and the stability of the vessel. The former has an influence on heave motion and must, therefore, be included with consideration of force cancellation wave periods. It is apparent from the equations that selection of parameters for low motion response conflicts with the parameters required for high stability to attain a useful deck payload capacity. However, the stability parameter varies rapidly with ratio R_4, whereas the motion response is not quite so sensitive. This characteristic offers the possibility of carrying out a preliminary vessel design using the simplified hydrodynamic analysis to attain just enough stability to cope with the required payload and thereby obtain the best resultant low wave induced heave motions.

The material presented in this chapter thus offers two opportunities for tandem hull vessel design. The first, as mentioned above, is the possibility of optimizing a vessel's payload and motions performance in the early stages of preliminary design by selecting leading particulars as described here. A second opportunity arises because low heave motion response is strongly dependent on the occurrence of wave force cancellation periods. The techniques presented here can be used to establish the occurrence of multiple wave force cancellations over a larger period range than obtained with the vessels examined here.

The tandem hull vessel shown in Figures 8.1 and 8.8 is one design which balances the need for adequate payload capacity from an oil production vessel with low wave induced motions in the frequently occurring operating wave period range of up to 12.5 s. Above this wave period, the occurrence of heave and pitch resonant peaks and the consequently larger motions offer further advantages. These are due to the fact that for the much rarer occurrence of severe storms, with their characteristic high periods, larger vessel motions lead to better sea keeping in terms of water on deck and general damage to deck equipment. Thus the freeboard requirements, deck production equipment durability and general vessel survivability are improved while providing a production platform which exhibits very low wave induced motions at the much more frequently occurring operating wave period values.

References

Greenham, D. (1986) *Jane's Merchant Ships 1985–86*, Jane's Publishing Co. Ltd, 238 City Road, London EC1V 2PU

Moore, J. (1986) *Jane's Fighting Ships 1985–86*, Jane's Publishing Co. Ltd, 238 City Road, London EC1V 2PU

Chapter 9

Articulated structures

9.1 Introduction

One of the obvious ways in which compliance can be introduced into an offshore structure is by the use of articulated (or universal) joints allowing one part of a structure to rotate relative to another. Many examples of structures with such joints are found in the oceans. The most common of these are loading/mooring towers which are placed on the sea bed with a gravity or piled base and a universal joint permitting rotation relative to the base in all vertical planes. The towers are held upright by excess buoyancy and can rotate in pitch and roll in response to wave excitation and mooring tanker loads. Similar, but more complex, configurations are used for mooring tankers as part of a permanent mooring or storage facility. Such single anchor legged moorings (SALMs) also have joints connecting the upper part of the slender tower structure to the tanker bow allowing it to pitch, heave and yaw about the mooring leg.

Clearly, these fully or partially floating structures with articulated joints pose interesting problems in dynamics which are associated with the additional degrees of freedom created due to the articulations. In general, articulations on structures where one segment is stiffly connected to the sea bed do not pose insurmountable dynamic problems during design and operation. The articulations serve to reduce system motions and, more importantly, reduce wave induced and mooring loads on such structures.

However, articulated structures do not always offer performance improvements. In the case of fully floating structures with articulations, substantial apparent performance advantages during normal operation can be won at the cost of major and unacceptable occurrences of catastrophic instabilities in off-design conditions. It is instructive to examine the hydrostatics and hydrodynamics of one such floating structure with jointed segments to illustrate these substantial apparent merits but unacceptable draw backs. The analysis methods used here can, however, be applied to a wide class of structures with jointed segments. In particular, Section 9.4 of this chapter illustrates techniques which should be used to investigate potential catastrophic (in the mathematical sense) behaviour of fully floating structures with articulated joints.

In principle, such catastrophic behaviour can also occur, as a special case, for conventional semisubmersibles. Section 9.7 extends the treatment

given in Section 9.4 to investigate the dynamical effects of such behaviour.

The structure considered in detail in this chapter is a semisubmersible with articulated columns. This design can be considered to be an extension of conventional rigid semisubmersible designs but in order to put the design into context, the essential performance related structure features of a rigid semisubmersible are considered here first. Chapter 5 gives considerable additional information on semisubmersible and monohull dynamic response.

Semisubmersibles are floating platforms with a geometry that is substantially different from the conventional ship shape, or monohull form. A typical modern rigid semisubmersible consists of submerged pontoons which are connected to the deck by several large diameter columns together with bracing members. A semisubmersible possesses low wave induced motions because a large proportion of its submerged volume is at a deep draught where wave pressures have rapidly decayed with depth. The small water plane area of the vessel and large submerged volume yield long natural periods in heave, roll and pitch. These periods are above the periods of predominant wave action, further contributing to a reduction of the motions. The hydrostatic stability of a semisubmersible is strongly dependent on large inter-column spacings which yield large second moments of water plane area about the principal axis of the water plane. Because of their smaller water plane, semisubmersibles have limited deck payload capacity when compared with monohulls.

Semisubmersibles are viable contenders for production platforms, especially in deep water locations, if their payload capacity could be increased and their wave induced motions could be further reduced. The latter would decrease the amount of time the vessel had to be disconnected from the well due to bad weather, thus minimizing production down-time.

The payload and motions of a rigid semisubmersible could potentially be improved by increasing the span and draught of the vessel. However, the increased vessel size would increase wave loading, so necessitating a stronger and heavier structure. This would increase the cost of the vessel and limit the payload, thus establishing a performance limiting design loop. Such a constraint may be avoided by using an articulated column semisubmersible such as the one illustrated in Figure 9.1. Vessels of this type are further described by Biewer (1971), Noble *et al.* (1984) and in the patents of Biewer (1974) and Interig Ltd (1984). The articulations would allow an increased span (or pitch radius) and draught, and yet the wave loads on the vessel would not increase significantly (if at all) due to the compliance.

The articulated column semisubmersible exhibits similar geometrical features to a rigid semisubmersible. It consists of a hexagonal star shaped submerged pontoon base connected to a deck by an inner ring of surface piercing columns. There is an outer ring of surface piercing columns which are connected to the pontoon base by universal joints about which they are free to rotate in all vertical planes through the joint.

This chapter describes the theoretical development of methods to analyse the hydrostatic and hydrodynamic behaviour of articulated column semisubmersibles. The theory is complemented by model tests specifically designed to compare the wave induced motion response of the articulated

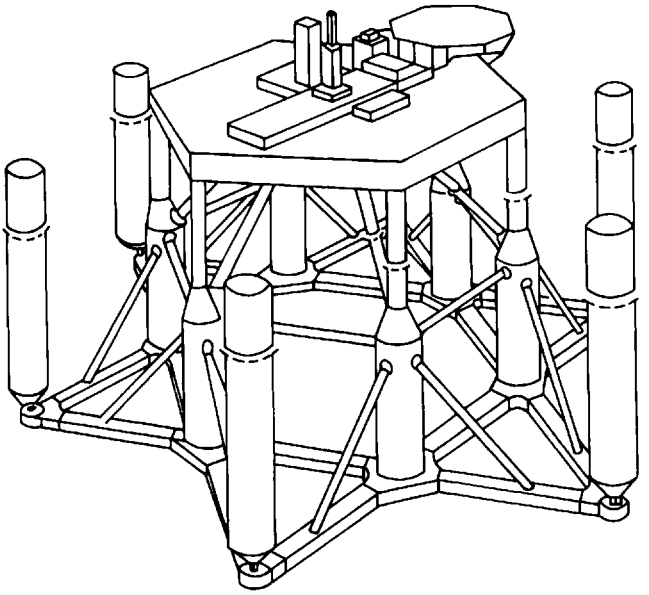

Figure 9.1. Perspective view of an articulated-column semisubmersible

column semisubmersible with that of an equivalent rigid vessel. Various aspects of the design and engineering of an articulated column semisubmersible are discussed.

9.2 Design criteria

The primary design objective for a floating oil production platform is to maximize the payload while maintaining hydrostatic stability and yet minimizing vessel motion response to waves. These requirements conflict to a certain extent but they play a dominant role in defining the primary characteristics of a semisubmersible. The metacentric height (GM) is often used as a measaure of the hydrostatic stability of a floating vessel. It is defined by the equation (Ramsey (1961), Clayton *et al.* (1982))

$$GM = \frac{I_{\text{wpa}}}{V} - c \tag{9.1}$$

where I_{wpa} is the second moment of water plane area about the horizontal axis of rotation; V is the submerged volume of the vessel; c is the vertical distance between the centres of buoyancy and gravity. The vessel is stable if GM is positive, with the magnitude of GM quantifying the extent of stability.

Most ocean waves have periods between 4 and 20 s. An important hydrodynamic consideration is to ensure that the heave natural period of the vessel lies outside this wave period range to avoid large motions

associated with resonance. The heave natural period (T_h) is given approximately by

$$T_h = 2\pi\left(\frac{\rho V + M_a}{\rho g A_{wpa}}\right)^{1/2} \tag{9.2}$$

where ρ is the sea water density; M_a is the vessel's heave added mass; g represents gravitational acceleration; and A_{wpa} is the water plane area.

Consider the implications of Equations (9.1) and (9.2) on the geometry of a semisubmersible. The large payload requirement ensures that V is large to support the weight and that the position of the centre of gravity above the keel is high because of the position of the payload. Most wave energy is confined to within half a wavelength of the surface. Therefore, to ensure good motion response, the vessel must be as 'transparent' as possible at the water line and the major buoyancy contributing components of the hull (the pontoons) must be as deeply submerged as possible. This implies a low water plane area and a low centre of buoyancy. This situation is ideal when considering the heave natural period as it is desirable to have a large displacement together with a small water plane area. However, to satisfy stability requirements with this small waterplane area, the column spacing must be large enough to ensure that the second moment of waterplane area is sufficient to maintain adequate hydrostatic stability. The limiting factor in column spacing is the fact that increasing the latter leads to increased structural steel weight – often at the expense of the payload. Thus the final configuration of a semisubmersible will be a compromise between obtaining good motion characteristics, an adequate payload and a reasonably efficient structural layout.

By using such considerations, it is possible to examine the effect of a desirable increase in payload and the possible design changes that must be made to retain sufficient stability and structural strength. Consider the design changes required to generate an increase in payload. The consequent increase in buoyancy force can be obtained by using larger or deeper columns. The increased payload will require more stability which can be attained by larger columns or by moving the columns further away from the geometric centre. In the former case, larger wave forces are experienced by the structure and also the heave natural period may lie within the encountered wave spectrum. Projecting the columns further from the vessel centre requires additional bracing at deck level due to the increase in bending moments. In either case, a heavier structure results which requires a further increase in buoyancy and consequently more stability. Thus the designer is trapped in a design loop which limits the vessel's payload and motions performance.

An articulated column semisubmersible, such as the one shown in Figure 9.1, presents an opportunity to break out of these design limitations. Because the articulated columns are only connected to the vessel at their base by universal joints, the articulated column spacing may be increased without any increase in structural weight at deck level. The resulting increase in stability leads to significantly higher payloads compared with those for rigid semisubmersibles. The increased stability allows the vessel draught to be increased, thus improving the motion characteristics further.

It also allows for columns supporting the deck to be smaller, making the vessel more 'transparent' at the waterline, and ensures an acceptably high heave natural period. The compliance of the articulations has the effect of reducing the horizontal wave forces transmitted to the vessel and thus reduces structural steel weight.

The articulated columns also contribute to some curious features of the large angle hydrostatics. The articulated columns normally remain upright in still water due to their excess buoyancy over self weight. However, when the vessel heels, the emerging articulated columns lose buoyancy until at some heel angle the self weight is no longer supported by its buoyancy. In this condition, the articulation will assume a stable equilibrium position which is inclined at some angle to the vertical and will, therefore, alter the overall hydrostatic stability of the vessel substantially.

Apparently, this feature does not pose a problem if the small angle hydrostatic stability of the vessel is considered. However, deeper consideration of the vessel's stability at large angles shows that it leads to an unacceptable catastrophic instability which implies that the vessel, in its present form, would not be usable.

Both the small angle classical and larger angle stability aspects are examined in this chapter.

9.3 Classical hydrostatics

The hydrostatic stability of marine vehicles floating at the air–water interface has been fully investigated and extensively documented in naval architecture literature. Ramsey (1961) presented an early unified treatment of the theory. These theoretical investigations and results have been concerned with the hydrostatic stability of marine vehicles which can be regarded as rigid bodies in the context of the hydrostatics calculations. The presence of articulated segments on a floating vessel requires that the theory of hydrostatic stability for rigid vessels be extended to account for this feature.

9.3.1 Small angle hydrostatics

Consider an arbitrary rigid body from which are mounted a number of articulated appendages each of which cuts through the waterplane area and has sufficient excess buoyancy (above self weight) to remain in a vertical equilibrium position. Figure 9.2 shows a sketch of the body with a waterplane area of A_w and just one of the articulated appendages mounted at position (x_i, y_i, z_i) with a waterplane area of A_i. The articulation is assumed to be universal such that the appendage is free to move in all vertical planes through (x_i, y_i, z_i). When the floating body is at rest, the net forces due to buoyancy and weight (with positive excess buoyancy) exerted by the articulated members are transmitted through the joint into the main structure with no modification. This implies that the centre of buoyancy position is not influenced by whether or not the articulations are consi-

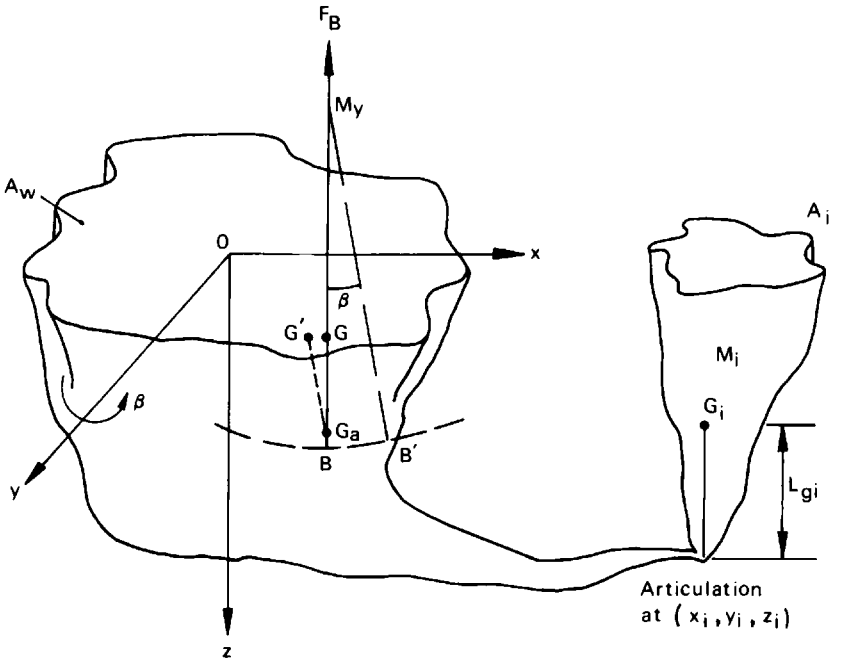

Figure 9.2. An arbitrary rigid body with an articulated appendage

dered rigid, although the orientation of the articulated member relative to the body will influence both the centre of buoyancy and centre of gravity positions.

As a result of a small rotation, β, about the *Oy* axis, the rigid body will have emerging and submerging wedges contributing to the hydrostatic forces, whereas the articulated members will submerge or emerge vertically as cross-sections with local waterplane area, A_i. There will be an additional shift in centre of buoyancy due to the change of position of the submerged volumes in the rotated articulations. Furthermore, this rotation will induce asymmetric articulation waterplane areas about the *Oy* axis, thus causing a shift in the centre of flotation which will induce a deficit in submerged volume and a consequent parallel sinkage with increasing angle of inclination, β.

The deficit in submerged volume is given by taking the difference of submerged volumes before and after a small rotation β about the *Oy* axis. This gives

$$\int_{A_w} z\mathrm{d}A_w + \sum_i \int_{A_w} z_{ai}\mathrm{d}A_w = \int_{A_w} (z - x\beta)\mathrm{d}A_w + \sum_i \int_{A_w} [z_{ai} - (x_i + L_i\beta)\beta]\mathrm{d}A_w \tag{9.3}$$

where $z_{ai} = z(x, y)$ describes the submerged shape of articulated member i and L_i is the draught of the member pivot. For symmetric dispositions of rigid and articulated members about the Oy axis

$$\int_{A_w} x \mathrm{d}A_w = 0 \tag{9.4}$$

and

$$\sum_i \int_{A_w} x_i \mathrm{d}A_w = 0 \tag{9.5}$$

Then from Equation (9.3), the deficit of volume is

$$\beta^2 \sum_i L_i A_i \tag{9.6}$$

where A_i is the waterplane area of articulation number i. The parallel sinkage, p, is

$$p = \frac{\Sigma L_i A_i}{A_w + \Sigma_i A_i} \beta^2 \tag{9.7}$$

Thus the presence of symmetric articulations does shift the centre of flotation and induces a second order parallel sinkage. Turning now to the position of the centre of buoyancy, the co-ordinates of the centre of buoyancy before inclination can be given by Equations (9.8) to (9.10) below with the effects of the articulations included.

Thus

$$\bar{x} = \frac{1}{V}\left[\int_{A_w} xz \mathrm{d}A_w + \sum_i \int_{A_i} x z_{ai} \mathrm{d}A_i\right] \tag{9.8}$$

$$\bar{y} = \frac{1}{V}\left[\int_{A_w} yz \mathrm{d}A_w + \sum_i \int_{A_i} y z_{ai} \mathrm{d}A_i\right] \tag{9.9}$$

$$\bar{z} = \frac{1}{V}\left[\int_{A_w} \tfrac{1}{2} z^2 \mathrm{d}A_w + \sum_i \int_{A_i} \tfrac{1}{2} z_{ai}^2 \mathrm{d}A_i\right] \tag{9.10}$$

After small rotation, β, the centre of buoyancy, B, will be at co-ordinates given by

$$\bar{x}' = \frac{1}{V}\left[\int_{A_w} x(z - x\beta)\mathrm{d}A_w + \sum_i \int_{A_i} (x_i + L_i\beta)(p - x_i\beta)\mathrm{d}A_i + \sum_i \int_{A_i} (x_i + L_{bi}\beta) z_{ai} \mathrm{d}A_i\right] \tag{9.11}$$

$$\bar{y}' = \frac{1}{V}\left[\int_{A_w} y(z - x\beta)\mathrm{d}A_w + \sum_i \int_{A_i} y(p - x_i\beta)\mathrm{d}A_i + \sum_i \int yz_{ai}\mathrm{d}A + \sum_i \int_{A_w} yz_{ai}\mathrm{d}A_i\right] \tag{9.12}$$

and

$$\bar{z}' = \frac{1}{V}\left[\int_{A_w} \tfrac{1}{2}(z + x\beta)(z - x\beta)\mathrm{d}A_w + \sum_i \int_{A_w} \tfrac{1}{2}\{z_{ai} + p + (x_i + L_i\beta)\beta\}\{z_{ai} + p - (x_i + L_i\beta)\beta\}\mathrm{d}A_i\right] \tag{9.13}$$

where L_{bi} is the distance of the articulation centre of buoyancy above the pivot. Then, from Equations (9.10) and (9.13), the vertical movement of the centre of buoyancy is given by

$$\bar{z} - \bar{z}' = \frac{\beta^2}{2V}\left[\int_{A_w} x^2\mathrm{d}A_w + \sum_i \int_{A_i} x_i^2\mathrm{d}A_i\right] \tag{9.14}$$

by neglecting cubic and higher powers of β. This equation simplifies to

$$\bar{z} - \bar{z}' = \frac{\beta^2}{2V}\left[\int_{A_w} x^2\mathrm{d}A_w + \sum_i x_i^2 A_i\right] \tag{9.15}$$

which is also of second order for small β, and is positive. Thus the surface of buoyancy for a rigid body with articulations is similar to that of the rigid body, that is, horizontal at B and concave upwards.

In the same way as before, for small β, B and B' must lie in the same plane perpendicular to Oy. Thus

$$\bar{y} = \bar{y}' \tag{9.16}$$

and using Equations (9.9) and (9.12):

$$\beta\int_{A_w} xy\mathrm{d}A_w + \beta\sum_i x_i \int_{A_i} y\mathrm{d}A_i - p\sum_i \int_{A_i} y\mathrm{d}A_i = 0 \tag{9.17}$$

Again, if the articulated member waterplane areas are symmetric about the Ox axis, then

$$\sum_i x_i \int_{A_i} y\mathrm{d}A_i = 0 \tag{9.18}$$

so that

$$\int_{A_w} xy\mathrm{d}A_w = 0 \tag{9.19}$$

and Ox, Oy still remain principal axes of the total vessel waterplane area.

Now using Figure 9.2 and Equations (9.18) and (9. 11), we get

$$BM_y = \frac{BB'}{\beta} = \frac{\bar{x} - \bar{x}'}{\beta}$$

$$= \frac{1}{\beta V}\left[\int_{A_w} \beta x^2\mathrm{d}A_w - \sum_i p x_i A_i - \sum_i \beta p L_i A_i + \sum_i \beta x_i^2 A_i + \sum_i \beta^2 x_i L_i A_i - \sum_i \beta L_{bi} V_i\right] \tag{9.20}$$

where V_i is the initial submerged volume of the ith articulation. For initial symmetry of waterplane areas:

$$\sum_i p x_i A_i = 0$$

and

$$\sum_i \beta^2 x_i L_i A_i = 0$$

Therefore

$$BM_y = \frac{1}{V}\left[\int_{A_w} x^2 \mathrm{d}A_w + \sum_i x_i \int_{A_i} x \mathrm{d}A_i - \sum_i L_{bi} V_i\right] \tag{9.21}$$

if β^2 and higher powers are ignored.

If $I_{yy} = \int_{A_w} x^2 \mathrm{d}A_w$, for the rigid part of the body,

and

$$I_{ay} = \sum_i x_i \int_{A_i} x \mathrm{d}A_i \tag{9.22}$$

is due to the articulations, then

$$BM_y = \frac{I_{yy} + I_{ay}}{V} - \frac{\Sigma_i L_{bi} V_i}{V} \tag{9.23}$$

Similarly,

$$BM_x = \frac{I_{xx} + I_{ax}}{V} - \frac{\Sigma_i L_{bi} V_i}{V} \tag{9.24}$$

where

$$I_{ax} = \sum_i y_i \int_{A_w} y \mathrm{d}A_i. \tag{9.25}$$

Unlike a conventional rigid body, however, the articulated vehicle also has an inherent horizontal shift in the centre of gravity position due to rotation of the articulations. This shift contributes to additional stability by increasing the effective value of GM, as illustrated in Figure 9.2. The horizontal shift in centre of gravity position GG' can be obtained by taking moments of forces due to mass about an axis through G perpendicular to the Oxz plane. This gives

$$MgGG' = g\sum m_i L_{gi} \beta + g\sum m_i s_i \tag{9.26}$$

where M is the total vessel mass; m_i are the masses of each articulated member with its local centre of gravity position, G_i, at a distance of L_{gi} above the articulation point (x_i, y_i, z_i) and a horizontal distance of s_i from the vertical through G. The second term on the right hand side of Equation (9.26) is zero for articulations that are symmetrically disposed about the vessel planes of symmetry. Thus the increment in metacentric height due to gravity shift can be written for small β as

$$GG_a = \frac{GG'}{\beta} = \frac{\Sigma_i m_i L_{gi}}{M} \tag{9.27}$$

and the effective metacentric height can be written as

$$\begin{aligned} G_aM_y &= BM_y - BG = GG_a \\ &= \frac{I_{yy} + I_{ay}}{V} + \frac{\Sigma_i m_i L_{gi}}{\rho V} - \frac{\Sigma_i L_{bi} V_i}{V} = BG \end{aligned} \tag{9.28}$$

where BG is the distance between the centres of buoyancy and gravity at zero angle of inclination.

It is of interest to quantify the effects of articulated appendages by comparing the relative influence on distance BM of rigid and articulated members of equivalent waterplane area.

For a rectangular waterplane section of dimensions b and d, with its centroid a distance D (parallel to dimension d) away from the vessel axis, the rigid body second moment of waterplane area is

$$I_{ry} = \int_{A_w} x^2 \mathrm{d}A_w = \frac{bd^3}{12} + bd \cdot D^2 \tag{9.29}$$

whereas the articulated member value is

$$\begin{aligned} I_{ay} &= x_i \int_{A_i} x \mathrm{d}A_i \\ &= D \int_{D-d/2}^{D+d/2} bx \mathrm{d}x = bd \cdot D^2 \end{aligned} \tag{9.30}$$

It is clear that the effect of the articulation is to remove the $bd^3/12$ term from the second moment of waterplane area. For large D (i.e. $D \gg d$), this term is small and does not influence the value of the overall second moment of area unduly.

Similarly, for the circular waterplane area, of radius r at a distance D from the vessel axis, the rigid and articulated results are

$$I_{ry} = \int_{A_w} x^2 \mathrm{d}A_w = \frac{\pi r^4}{4} + \pi r^2 \cdot D^2 \tag{9.31}$$

and

$$I_{ay} = \pi r^2 \cdot D^2 \tag{9.32}$$

Then for the rectangular waterplane area

$$\frac{I_{ay}}{I_{ry}} = \frac{1}{1 + \dfrac{d^2}{12D^2}} \tag{9.33}$$

and for the circular waterplane area

$$\frac{I_{ay}}{I_{ry}} = \frac{1}{1 + \dfrac{r^2}{4D^2}} \tag{9.34}$$

Figure 9.3 shows a plot of I_{ay}/I_{ry} as a function of D/d and $D/2r$ to illustrate the strong influence of this ratio on the second moment of area ratio. Note that Equation (9.28) contains terms due to shifts in the centres of gravity and buoyancy for the articulations. These cause a net reduction in stability which is much greater than the reductions shown in Figure 9.3 due to second moments of articulation waterplane areas.

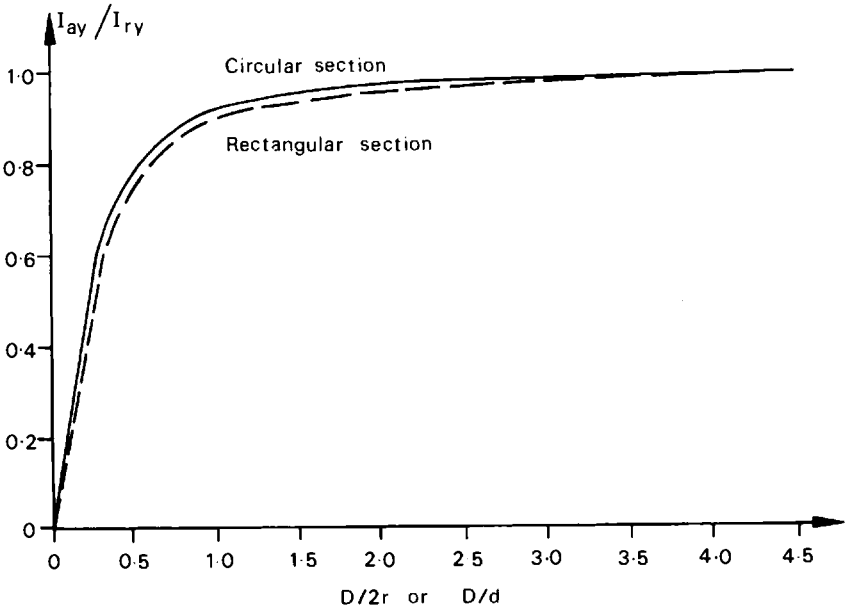

Figure 9.3. Ratios of articulated to rigid waterplane areas

9.3.2 Large angle results

Using conventional rigid body hydrostatic analysis for large angles, it can readily be shown that the distance between the centre of buoyancy, B, and metacentre, M, can be written as

$$BM = \frac{[I_R + \Sigma_i I_i]}{V} + \frac{\frac{1}{2}[I_R + \Sigma_i I_i]\tan^2\beta}{V} \tag{9.35}$$

for finite angle β. This relationship is referred to as the wall sided formula. Figure 9.4 shows a schematic cross-sectional representation of the vessel shown in Figure 9.1. The ith column pair shown in Figure 9.4 have radii r_i, water plane area $A_i(=\pi r_i^2)$ at a distance D_i from axis AA'; I_R is the second moment of water plane area of the centre body R; and I_i is the second moment of water plane area of the pair of columns about an axis through O perpendicular to the plane of the diagram.

For the case when columns C and C' are articulated at Q and Q' (see Figure 9.4), an inclination, β, will induce a rotation of angle β in each of the columns so that they, in fact, remain vertical with their axes at right angles to the waterplane. Figure 9.4 illustrates the new positions of the articulated columns perpendicular to the inclined vessel waterline $S_\beta S_\beta'$.

Now

$$UV = L_i \tan\beta$$

and

$$OU = D_i - L_i \tan\beta$$

Therefore

$$OR = (D_i - L_i \tan\beta)\cos\beta \tag{9.36}$$

Also

$$QT = L_i + L_i \tan\beta$$

Therefore

$$QR = (L_i + D_i \tan\beta)\cos\beta$$

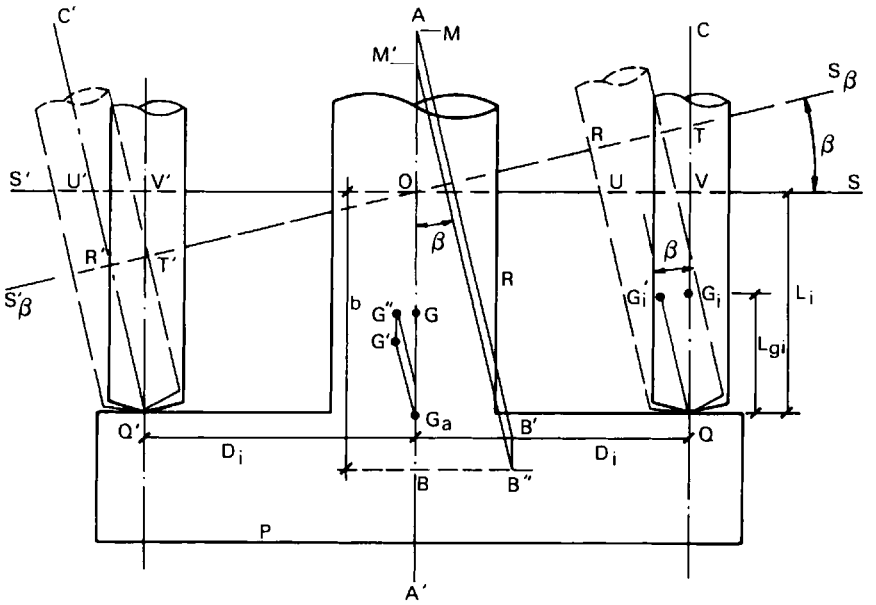

Figure 9.4. The semiflex with articulated columns

So that

$$QR - QV = (L_i + D_i \tan\beta) \cos\beta - L_i$$

Similarly,

$$U'V' = L_i \tan\beta$$

$$OU' = D_i + L_i \tan\beta$$

$$OR' = (D_i + L_i \tan\beta) \cos\beta \tag{9.37}$$

and

$$Q'V' - Q'R' = L_i - (L_i - D_i \tan\beta) \cos\beta$$

As the vessel shown in Figure 9.4 inclines, the submerged volume deficit between zero inclination and angle β is given by

$$A[U'R' - UR] = 2A_iL_i \sin\beta \tan\beta$$

for each column pair. The total volume deficit is, therefore,

$$\sum_i A_iL_i \sin\beta \tan\beta$$

and the parallel sinkage is

$$p = \frac{\Sigma_i L_i A_i}{A_w + \Sigma_i A_i} \sin\beta \tan\beta = k \sin\beta \tan\beta$$

where

$$k = \frac{\Sigma_i L_i A_i}{A_w + \Sigma_i A_i}$$

Taking moments of submerging and emerging volumes about an axis through O perpendicular to the plane of the diagram gives

$$V \cdot BB'' = I_R \tan\beta + (1/2) \sum_i \pi r_i^2 \left[(QR - QV) \left\{ OR \cos\beta + \frac{(QR - QV)}{2} \sin\beta \right\} \right] - \sum_i 2L_{bi}V_i \sin_B - \sum_i 2pA_iL_i \tan\beta \cos^2\beta \tag{9.38}$$

using volume integrations which are not included here.

Thus

$$V \cdot BB'' = I_R \tan\beta + \tfrac{1}{2} \sum_i \pi r_i^2 \left[(L_i + D_i \tan\beta) \cos\beta - L_i \right\} \{D_i - L_i \tan\beta) \cos^2\beta + \tfrac{1}{2} < (L_i - D_i \tan\beta)\cos\beta - L_i > \sin\beta \} + (L_i - D_i \tan\beta) \cos\beta] \} (D_i + L_i \tan\beta) \cos^2\beta$$

$$+ \tfrac{1}{2} < L_i - (L_i - D_i \tan\beta) \cos\beta > \sin\beta\}$$

$$- \sum_i 2L_{bi}L_i \sin\beta - 2pL_i \tan\beta \cos^2\beta]$$

after multiplying out and simplifying, this reduces to

$$BB'' = \frac{1}{V}[I_R \tan\beta + \tfrac{1}{2}\sum \pi r_i^2 \sin^2\beta + D_i^2 \sin\beta$$

$$(1 + \cos^2\beta) - 2L_{bi}L_i \sin\beta - 2pL_i \tan\beta \cos^2\beta\}] \quad (9.39)$$

Similarly, by taking moments of volume about an axis through O perpendicular to the plane of the diagram and integrating we get

$$V \cdot B''B' = \tfrac{1}{2} I_R \tan^2\beta + \tfrac{1}{2}\sum_i \pi r_i^2 [QR - QV)$$

$$\{b + OR \sin\beta - \tfrac{1}{2}(QR - QV) \cos\beta\} - (Q'V' - Q'R')$$

$$\{b + OR' \sin\beta + \tfrac{1}{2}(Q'V'' - Q'R') \cos\beta\}]$$

$$- \sum_i 2L_{bi}V_i (1 - \cos\beta) + \sum_i 2pA_i[b - L_i \sin^2\beta$$

$$+ \frac{p}{2} \cos\beta] \quad (9.40)$$

with b denoting the distance OB shown in Figure 9.4.

Therefore

$$VB''B' = \tfrac{1}{2} I_R \tan^2\beta + \tfrac{1}{2}\sum_i \pi r_i^2 [(L_i + D_i \tan\beta) \cos\beta - L_i]$$

$$\{b + D_i - L_i \tan\beta) \cos\beta \sin\beta - \tfrac{1}{2} < (L_i + D_i \tan\beta) \cos\beta$$

$$- L_i > \cos\beta\} - \{L_i - (L_i - D_i \tan\beta) \cos\beta\}\{b - (D_i$$

$$+ L_i \tan\beta) \cos\beta \sin\beta + \tfrac{1}{2} < L_i - (L_i - D_i \tan\beta) \cos\beta >$$

$$\cos\beta - 2L_{bi}L_i (1 - \cos\beta) + 2p(b - L_i \sin^2\beta + \tfrac{1}{2}L \cos\beta)] \quad (9.41)$$

Again after multiplying out and simplifying, we get

$$V \cdot B''B' = \tfrac{1}{2} I_R \tan^2\beta + \tfrac{1}{2}\sum_i \pi r_i^2 (D_i^2 - L_i^2) \sin^2\beta \cos\beta$$

$$+ 2L_i^2(1 - \cos\beta) - 2bL_i + 2bL_i \cos\beta - 2L_{bi}L(1 - \cos\beta)$$

$$+ 2p(b - L_i \sin^2\beta + \frac{p}{2} \cos\beta) \quad (9.42)$$

Then

$$BM = \frac{BB''}{\tan\beta} + B'B'' \tag{9.43}$$

$$= \frac{1}{V}[I_R + \tfrac{1}{2} I_R \tan^2\beta] + \frac{1}{2V}\sum_i \pi r_i^2[L_i^2 \sin^2\beta \cos\beta + D_i^2 \cos\beta(1 + \cos^2\beta) + (D_i^2 - L_i^2)\sin^2\beta \cos\beta + 2L_i^2(1 - \cos\beta) - 2bL_i + 2bL_i \cos\beta\ 2L_{bi}L_i - 2L_i k \sin^2\beta \cos\beta + 2k \sin\beta \tan\beta(b - L_i \sin^2\beta + \tfrac{1}{2} k \sin^2\beta)]$$

$$= \frac{1}{V}[I_R + \tfrac{1}{2} I_R \tan^2\beta] + \frac{1}{V}\sum_i A_i[D_i^2 \cos\beta + L_i(L_i - b)(1 - \cos\beta) - L_{bi}L_i - L_i k \sin^2\beta \cos\beta + k \sin\beta \tan\beta(b - L_i \sin^2\beta + \tfrac{1}{2} k \sin^2\beta) \tag{9.44}$$

An identical result can be obtained if the moments of volume are taken about an axis through B and perpendicular to plane $S_\beta S_{\beta'}$. The expression in Equation (9.44) shows the contributions of the rigid central waterplane cutting member (with second moment of area, I_R) and of the articulated columns such as C and C'. This expression is equivalent to the small angle result of Equation (9.20) when $\beta \to 0$.

It is interesting to note the effects of distances L_i and b on the large angle hydrostatics. The $D_i^2 \cos\beta$ term is generally dominant for large D_i but the additional modification to BM at high angles is eliminated if $L_i = b$. Furthermore, this modification changes sign depending on $L_i > b$ or $L_i < b$.

The $L_{bi}L_i$ term causes a constant and significant reduction in BM due to movement of the articulation submerged volumes, whereas the terms due to parallel sinkage change the BM values by small amounts.

The movement of the position of the centre of gravity due to the articulated columns must be considered for its effect in increasing the metacentric height. For the large angle problem, Figure 9.4 illustrates the horizontal shift of G to G'' together with a vertical downward shift to G'.

The effective increase in metacentric height, then, is

$$GG_a = \frac{GG''}{\tan\beta} + G'G'' \tag{9.45}$$

The effects of each pair of columns i can be summed to give a total horizontal shift of the centre of gravity as

$$GG' = \frac{\Sigma_i m_i L_{gi}(1 - \cos\beta)}{M} \tag{9.46}$$

where m_i is the mass of each of the columns; L_{gi} is the vertical distance between the column centre of gravity and the point of articulation at zero angle of inclination; M is the total vessel mass.

In a similar manner, the vertical shift in the centre of gravity position is obtained as

$$GG' = \frac{\Sigma_i m_i L_{gi}(1 - \cos\beta)}{M} \tag{9.47}$$

Then the net increment in GM is obtained via Equation (9.45) as

$$GG_a = \frac{\Sigma_i m_i L_{gi}}{M} \tag{9.48}$$

with the contributions of $\cos\beta$ cancelling out. The total metacentric height can then be

$$\begin{aligned} G_aM_y &= BM_y - BG + GG_a \\ &= \frac{1}{V}[I_R + \tfrac{1}{2} I_R \tan^2\beta] + \frac{1}{V}\sum_i A_i[D_i^2 \cos\beta \\ &\quad + L_i(L_i - b)(1 - \cos\beta) - L_{bi}L_i - L_i k \sin^2\beta \cos\beta \\ &\quad + k \sin\beta \tan\beta(b - L_i \sin^2\beta + \tfrac{1}{2} k \sin^2\beta)] + \frac{\Sigma_i m_i L_{gi}}{M} - BG \end{aligned} \tag{9.49}$$

The influence of articulations on the hydrostatics of a floating body is illustrated by numerical values for an articulated column pair and submerged pontoon arrangement shown in Figure 9.4. Numerical values of $D_i = 64.95$ m, $L_i = 42$ m, $b = 31.1$ m, $r_i = 3.5$ m are taken from data for a proposed vessel (Figure 9.1) of 30 750 t displacement. Only the BM contribution due to the articulated columns is considered first to highlight the difference between the articulated and rigid body hydrostatics.

Figure 9.5 displays the variation of BM as a function of angle of inclination, β. The rigid equivalent value is compared with the value arising from the articulated columns.

The BM contribution from the rigid column arises in the conventionally accepted manner, whereas the BM contribution of the articulated columns starts from a lower value due to the net effect of the shift in total vessel centres of buoyancy due to articulation rotation. This feature is not as

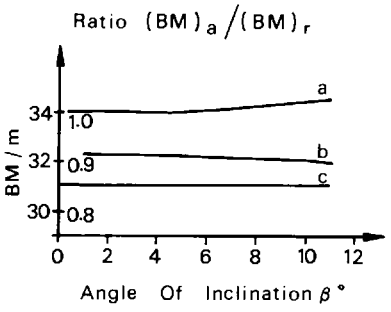

Figure 9.5. Distances BM as functions of angle of inclination β. *Key*: a – rigid BM; b – $(BM)_a/(BM)_r$ ratio; c – articulated vessel BM

much of a drawback as it appears at first sight because the existence of articulations allows the values of D_i to be large without significant structural penalties and, therefore, the base BM (for $\beta = 0°$) has a large value.

Figure 9.5 also displays the ratio of articulated to rigid BM value which tends to fall off more rapidly with angle due to the increase in rigid column BM with angle of inclination.

Figure 9.6 displays the variation in righting moment arm GZ with angle of inclination β. These curves include the effective increase in metacentric height which occurs in the presence of the articulations. Despite this feature, the articulated columns contribute a smaller righting moment arm than the equivalent rigid columns. Figure 9.6 also displays the ratio of articulated to equivalent rigid body GZ value. Values of $m_i = 657$ t and $L_{gi} = 21$ m are assumed for each articulated column.

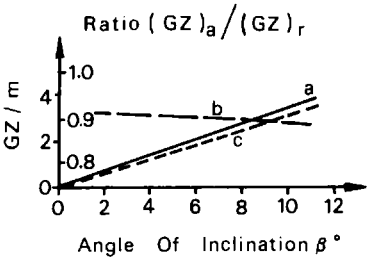

Figure 9.6. Righting moment arms as functions of angle of inclination β. *Key*: a – rigid vessel GZ; b – $(GZ)_a/(GZ)_r$ ratio; c – articulated vessel GZ

The extension of the theory of conventional rigid body hydrostatic stability to non-rigid bodies with articulated members shows that the presence of the articulations reduces the stability by a relatively small proportion for articulated member waterplane areas that are well separated from the principal axes of the waterplane. The stability reduction is primarily due to the movements of the centres of buoyancy and gravity induced by rotation of the articulations.

The predictions of the above analysis have been verified against model tests at 1:100 scale (see Section 9.5). Figure 9.7 gives a comparison of predicted and measured data.

A different method of analysis can be employed for hydrostatic analysis by using the variation of tension in the articulating columns as they emerge or submerge from the water surface. Consider an arbitrary body with each of i articulated columns on the body replaced by a tension T_i acting vertically upwards. Vertical equilibrium is given by

$$m_r g = F_{br}(\beta) + \sum_i T_i(\beta) \tag{9.50}$$

where m_r and F_{br} are respectively the mass of, and buoyancy force on, the rigid part of the body. Both F_{br} and T_i are functions of the angle of inclination of the body, β.

If the body undergoes a rotation, β about a horizontal axis through the centroid of the water plane area, the centre of gravity co-ordinate vector $(\mathbf{x}_{gr})$ of the rigid body moves to $\mathbf{x}'_{gr}$ and its centre of buoyancy $\mathbf{x}_{br}$ moves to $\mathbf{x}'_{br}$. Note that the centre of gravity does not move with respect to the rigid

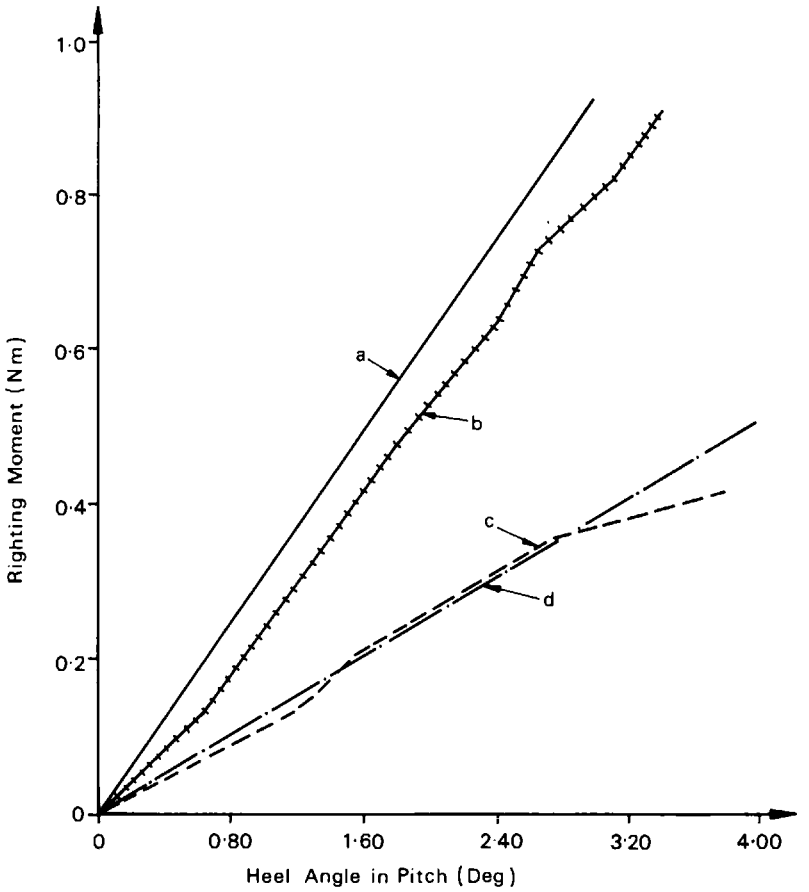

Figure 9.7. Comparison of righting moment curves for the articulated-column semisubmersible. *Key*: a – rigid vessel (theoretical); b – rigid vessel (experimental); c – articulated vessel (experimental); d – articulated vessel (theoretical)

body but it does move with respect to a fixed axes system. The co-ordinates of the articulation pivot move from $\mathbf{x}_i$ to $\mathbf{x}'_i$.

Resolving moments to find the net restoring moment, M_R, gives

$$\mathbf{M}_R(\beta) = \mathbf{x}'_{gr}(\beta) \times m_T g\mathbf{k} - \mathbf{x}'_{br}(\beta) \times F_{br}(\beta)\mathbf{k} - \sum_i \mathbf{x}'_i(\beta) \times T_i(\beta)\mathbf{k} \quad (9.51)$$

where $\mathbf{k}$ is the unit vector along the vertical (z) axis. This equation is true provided that vertical equilibrium (Equation (9.50)) is satisfied.

The tension, T_i, is a function of the depth of the pivot and hence the angle of inclination, β. The theory presented in Section 9.6 demonstrates that the joint tension varies linearly with pivot depth for an articulated column – the relation being bounded by constant minimum and maximum tensions. Maximum tension is reached when a column is completely submerged, whereas the minimum tension arises when an emerging

column's buoyancy force no longer balances its self weight and leads to the column resting in a non-vertical equilibrium position. It is important, in terms of hydrostatic stability, to maximize the range in which the tension is a linear function of draught since both the maximum and minimum tensions represent a loss in the restoring moment contribution of an articulated member. The maximum tension may be increased by increasing the articulated column length. The vessel heel angle at which non-vertical articulation equilibrium positions arise may be increased by lowering the mass and centre of gravity position of the articulated column.

Large angle restoring moments have been evaluated numerically using the tension method for the articulated vessel shown in Figure 9.1. The vessel was modelled by cylindrical volume elements consisting of slender circular and rectangular cylinders whose individual submerged volumes were summed to obtain F_{br}. The vessel was rotated an angle β and its draught was adjusted iteratively by calculating the new submerged volume and tensions at each step until Equation (9.50) was satisfied. Then the restoring moment was calculated using Equation (9.51). The results of these calculations are presented in Section 9.4.

One of the problems associated with the tension method occurs when modelling the rigid part of the vessel and complex deck structure with volume elements. This is because, especially at large angles of inclination, it is difficult to determine the submerged volume and its centroid due to the way the water plane cuts complex element shapes and intersections. Chapter 3 describes a pressure integration technique for hydrostatic analysis which overcomes this problem by expressing all hydrostatic properties in terms of surface pressure integrals. Integration of pressure over the submerged body then yields hydrostatic forces and moments.

Using the above methods, Figures 9.8 and 9.9 present large angle restoring (or righting) moments for the full vessel shown in Figure 9.1. Details of dimensions and other vessel properties are given in Table 9.1.

Table 9.1 Articulated column semisubmersible dimensions

Inner column pitch radius	43.3 m
Outer column pitch radius	75 m
Inner column buoyancy chamber diameter	8.2 m
Articulated column diameter	7 m
Inner pontoon (within inner column pitch circle) cross-sectional dimensions	5 m width × 3 m depth
Draught	50 m
Height of top of inner column buoyancy chamber above keel	38 m
Height of underside of deck above keel	65 m
Height of top of articulated column above keel	64 m
Height of pivot above keel	8 m
Displacement (in sea water)	30 526 t
Vessel GM (in sea water)	11 m
Articulated column static tension (in sea water)	6867 kN
VCG of rigid part of vessel above keel	28.8 m
VCG of articulated column above keel	28 m
Deck support bracing diameter	2.5 m
Lower hull bracing diameter	1.6 m
Outer pontoon cross-sectional dimensions	3 m width × 3 m depth

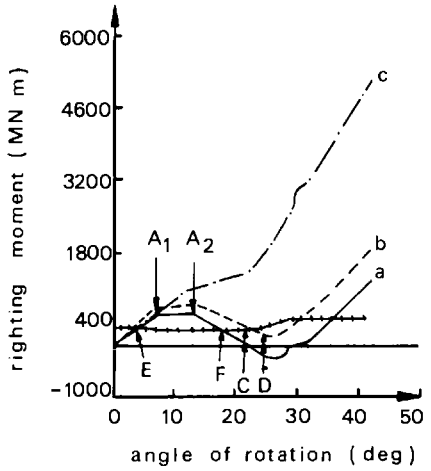

Figure 9.8. Large-angle righting moment curves for the articulated-column semisubmersible: (a) h = 11 m, articulation centre of gravity = 16.6 m above pivot; (b) h = 13 m, articulation centre of gravity = 16.6 m above pivot; (c) h = 11 m, equivalent rigid vessel; (A_1 – first articulated-column instability; A_2 – second articulated-column instability; B – articulated-column immersed; C – possible articulated-column joint failure; D – deck immersed); E – survival wind heeling moment (wind speed = 51 m/s)

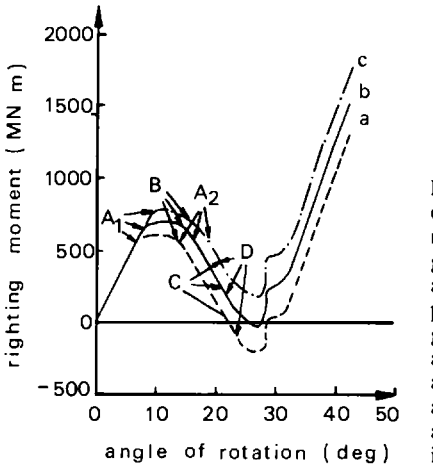

Figure 9.9. Large roll-angle righting moment curves for the articulated-column semisubmersible: (a) h = 11 m, articulation centre of gravity = 16.6 m above pivot; (b) h = 11 m, articulation centre of gravity = 15.0 m above pivot; (c) h = 11 m, articulation centre of gravity = 13.5 m above pivot; (A_1 – first articulated-column instability; A_2 – second articulated-column instability; B – articulated-column immersed; C – possible articulated-column joint failure; D – deck immersed

Five curves illustrate the effects of vessel initial metacentric height (*GM*) and articulated column centre of gravity. The vessel geometry and static tensions are the same for all five cases.

Figure 9.8 also illustrates the large angle restoring moment of the vessel with the articulated columns held rigid. The rigid vessel has an initial *GM* of 11 m and at small angles there is little difference between the rigid and articulated vessels. However, at rotations beyond 7°, the respective restoring moment curves diverge considerably. The restoring moment for the equivalent rigid vessel increases monotonically with rotation. In contrast, the restoring moment for the articulated vessel falls rapidly after the first articulated column inclines to a non-vertical equilibrium position and does not increase until after deck submergence commences. Thus the rigid vessel is substantially more stable than the articulated vessel at larger angles of heel.

There are several features of interest in the curves: A_1 and A_2 indicate the points where one or more articulated columns have become non-vertical; B denotes the point at which one or more articulated columns have immersed; and D indicates that the deck has immersed; the point C signifies a strong possibility of joint failure as a result of the exceptionally large angle of inclination of the articulation from the vertical.

All the curves exhibit the same general features. There is a reasonably linear increase in the restoring moment up to approximately 8–10°, at which point the first articulated column inclines away from the vertical. This leads to a large loss in restoring moment which causes the curves to level out and then to decrease rapidly. The decrease in restoring moment is reinforced further each time a column submerges or moves to an inclined equilibrium position. The decrease in restoring moment is eventually arrested by the submergence of the deck which generates an increasing restoring moment.

To maximize the area under the restoring moment curve, and hence the stability, it is desirable to increase the initial GM and to lower the centre of gravities of the columns – the latter change delaying the critical event of non-vertical column equilibrium positions. The other alternative is to increase the tension at the joint. However, care must be taken to ensure that the tension is not too high and that column natural periods are still outside the expected wave spectrum.

The hydrostatic stability of a vessel is important because it provides a restoring moment to oppose any disturbing moments that may act on the rig. The most obvious of these is the disturbing moment due to wind loading. The wind heeling moment (M_w) is calculated by

$$M_w(\beta) = \sum_{i=1}^{n'} \tfrac{1}{2} \rho_a v^2 C_{si} C_{hi} A_{pi} l_i \tag{9.52}$$

where ρ_a is the air density; C_{si} is a shape coefficient associated with the ith vessel member (of a total of n' members); C_{hi} is a height coefficient which accounts for the effects of the atmospheric boundary layer; v is the wind velocity; A_{pi} is the projected area of the ith member normal to the wind velocity; and l_i is the moment arm which is the distance from the centroid of A_{pi} to the centre of lateral resistance of the vessel (International Maritime Organisation, 1980).

Figure 9.8 presents wind heeling moment as a function of angle of rotation. The positions of vessel equilibrium are located where the wind heeling moment curve intersects the positive gradient of the restoring moment curve. For example, points E and G are stable, whereas the intersection at F is unstable. The presence of stable and unstable intersections between the restoring moment and wind heeling curves leads to unusual physical behaviour at large angles of inclination.

A typical restoring moment curve ($OA'B'$) for an equivalent rigid vessel is shown Figure 9.10. Although the restoring moment is positive for all angles of heel shown, the vessel is only stable between the points O and A'. For stability to be maintained the vessel must be able to generate a hydrostatic restoring moment equal in magnitude, and of opposite sense, to an applied overturning moment. Anywhere between the points O and

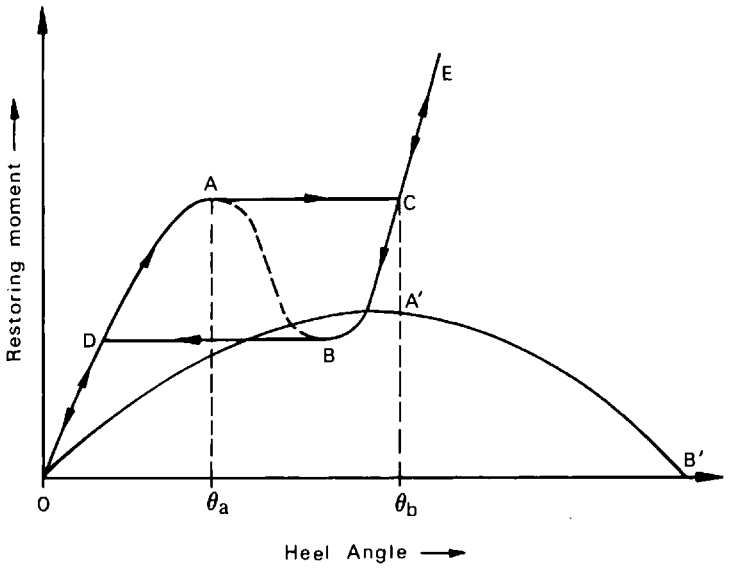

Figure 9.10. Large-angle stability curve for articulated and rigid vessels

A', the restoring moment will be in equilibrium with the overturning moment. For disturbing moments that are higher than the level of A', the vessel restoring moment will not be able to counteract the overturning moment, thus causing the vessel to become unstable and capsize.

Figure 9.10 also illustrates a representative restoring moment curve (based on Figures 9.8 and 9.9) for the articulated vessel. The point A identifies a local maximum in restoring moment – the curve beyond this point, shown by the broken line, decreases to point B as emerging and submerging articulated members contribute to a loss in restoring moment. The change of gradient beyond B is caused by the submerging buoyant deck generating additional restoring moment.

If an overturning moment, the magnitude of which is in the range OA, is applied to the vessel, a positive hydrostatic stiffness (restoring moment per unit rotation) will ensure that stability is maintained. If the vessel were to be released from such a position, it would oscillate about the equilibrium position until the motions were damped. Now consider the consequence of an increased overturning moment such that it intersects the restoring moment curve at A. Here the effective stiffness of the system is zero (as it changes from positive to negative). This represents a static instability and is characterized by the appearance of an adjacent position of equilibrium at the point C. To arrive at this second position of stable equilibrium, the vessel cannot follow the computed curve along line AB. In this region, the hydrostatic restoring moment is less than the overturning moment and, furthermore, the effective stiffness is negative – the latter implying that the vessel is unstable between angles θ_a and θ_b. A new equilibrium position is then established at point C, with the vessel moving rapidly from the angle of heel θ_a and θ_b in a very short space of time. Further increases in

overturning moment result in the curve CE being followed beyond this point. During reductions in overturning moments, the positive stiffness ensures that the point of stable equilibrium will pass through C to the point B. This point is analogous to A during increasing overturning moment in that it represents a change from positive to negative stiffness. Again, on the point of a static instability, an adjacent position of equilibrium appears at D, from which further reduction in overturning moment results in a return to the origin, O. Thus, in applying and removing an overturning moment to the vessel, large angle behaviour in the form of a hysteresis cycle results. If the point B is located at a negative restoring moment value, a feature illustrated in some of the curves in Figures 9.8 and 9.9, then its adjacent equilibrium point, D, will also occur at a negative restoring moment. The curves presented here can be extended to negative angles of heel by taking successive mirror images in the horizontal and vertical axes.

9.4 Catastrophic instability at large angles

An essential aid to the classification of static instabilities is provided by catastrophe theory for discrete conservative systems governed by a potential function (Thompson, 1982). The topological concept of structural stability has been invoked to argue that the experimentally observable forms of instability depend on the number of operational control parameters. The restoring moment, or potential, is governed by a single control parameter, the angle of heel. The variation of potential as a function of a control parameter will exhibit maxima and minima corresponding to unstable and stable states of equilibrium. However, the occurrence of a horizontal point of inflection, such as the line AC in Figure 9.10, cannot be expected. The point A is a critical point termed the fold or limit point; similarly AC is called the fold line. The occurrence of a critical point is assigned a probability of zero. This simple energy transformation involving a single control parameter is termed a fold catastrophe – this is the simplest of the seven elementary catastrophes.

Such large angle catastrophic behaviour has been further investigated by numerical time domain simulations of the dynamics of an articulated column semisubmersible subjected to a suddenly applied disturbing couple. The equation of motion for such a system in terms of heel angle θ is

$$I\frac{d^2\theta}{dt^2} + \lambda\frac{d\theta}{dt} + R(\theta) = D(t) \tag{9.53}$$

where I is the total rotational moment of inertia; λ is the equivalent linear damping coefficient; $R(\theta)$ is the large angle restoring moment; $D(t)$ is the applied disturbing couple; and t is time.

I and λ were evaluated by the standard methods described in Chapter 5 for the articulated vessel (Table 9.1) and $R(\theta)$ was obtained by digitizing the large angle restoring moment curve for the vessel with a metacentric height of 13 m, as shown in Figure 9.8. The applied disturbing couple was taken to be constant for all time after its application.

The equation of motion (9.53) was solved numerically using a fourth order Runge–Kutta–Nyström Method (Kreyszig, 1979). This involves a Taylor's series expansion where fifth and higher order terms are neglected.

A disturbing moment of 686.7 MNm was applied to the vessel which was initially on an even keel. Figure 9.8 illustrates that this disturbing couple gives two stable equilibrium positions corresponding to heel angles of 6.5 and 33°, respectively, and an unstable equilibrium position at 15.5°. A static analysis would suggest that the vessel would heel to 6.5° when this couple was applied. However, the dynamic analysis illustrates a far more alarming behaviour. Figure 9.11 shows the heel angle time history following application of the disturbing couple at zero time. Because of the dynamic overshoot the vessel heels over beyond the first equilibrium position and beyond the critical point (*A* in Figure 9.10). Once it has overshot the critical point it follows the fold line and heels over to the

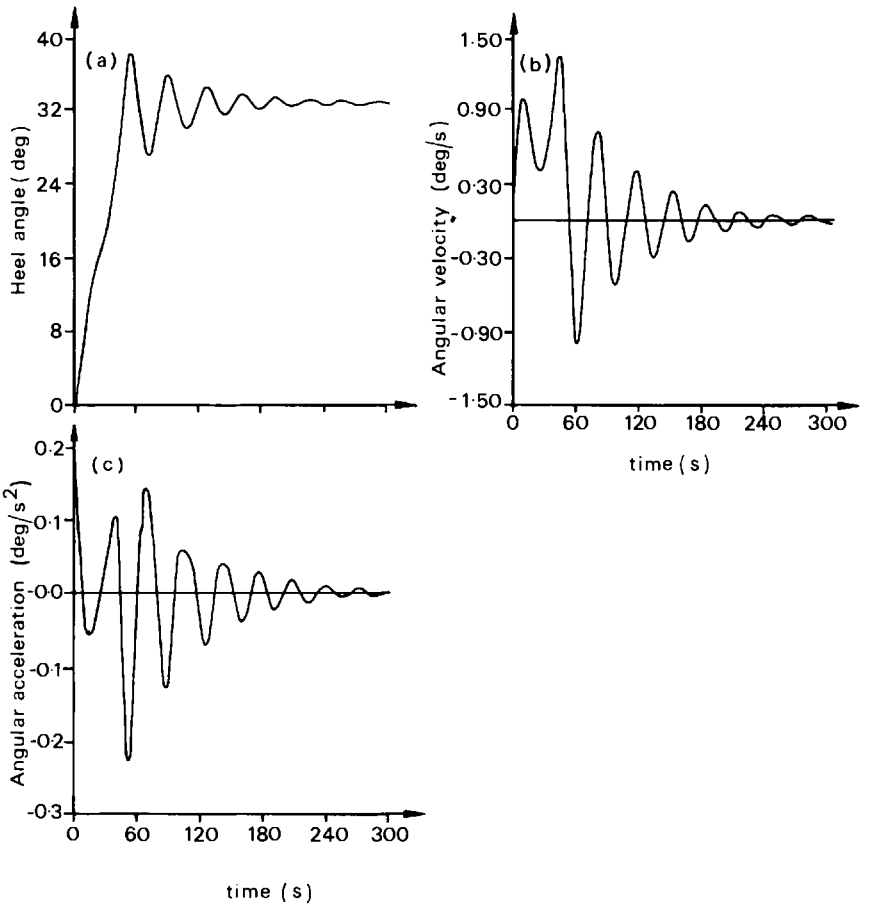

Figure 9.11. Time history of the articulated-column semisubmersible. *Key*: a – heel angle (disturbing couple = 686.7 MNm); b – angular velocity (disturbing couple = 686.7 MNm); c – angular acceleration (disturbing couple = 686.7 MNm)

second equilibrium position (at point C in Figure 9.10). The vessel then oscillates at a heel angle of 33° until it comes to rest. Figure 9.11(b) and (c) illustrate the corresponding angular velocity and angular acceleration time histories.

There are several alarming features due to the catastrophe. The first is the magnitude of the maximum heel angle reached, which is almost 39°, and the final equilibrium position of 33°. These angles are exceptionally large and, for a floating vessel, would almost certainly lead to down flooding with the eventual capsize of the vessel. Yet the first equilibrium position of 6.5° would be acceptable. Fortunately, the vessel does not experience exceptionally large velocities and accelerations during transition between its stable states. This is due to the fact that its rotational moment of inertia is large with respect to the magnitude of the applied couple and the natural period is high. For example, at the time of first impact with the still water surface, the deck edge experiences a velocity of 1.10 m/s and an acceleration of 0.09 m/s^2. However, the consequent structural loads will still be significant due to the large deck mass and the small initial impact area.

It is worth noting that the magnitude of the disturbing couple is not unrealistic in that it is equivalent to the disturbing moment resulting from the complete flooding of an empty 15 m section of an articulated column. Further damage stability calculations were carried out using the tension method. These results show that the flooding of an articulated column with 1000 t of sea water would result in a heel angle of approximately 14.5° and the complete loss of an articulated column would result in a heel angle of approximately 9°. In terms of dynamic stability considerations and the catastrophe phenomenon, these heel angles would be unacceptable.

Figure 9.12((a)–(f)) shows phase space trajectories for six disturbing couples of increasing magnitude. It illustrates the transition between two stable states characteristic of a fold catastrophe. The first disturbing couple of 294.3 MNm results in the vessel following a smooth path to a stable focus at an angle of 2.9°, as illustrated in Figure 9.12(a). The phase space trajectory plotted in Figure 9.12(b) is the result of a disturbing couple of 657.3 MNm. The effects of a non-linear hydrostatic stiffness are clearly evident. The initial overshoot of 15° is beyond the critical angle, however, vessel dynamics just manage to offset a change in equilibrium state. The magnitude of the initial overshoot in comparison with subsequent oscillations signifies the closeness of the instability. When the disturbing moment was increased to 659.7 MNm (an increase of 0.4% from the previous value), this was sufficient to induce transition to a new equilibrium position. Figure 9.12(c) illustrates that the vessel almost comes to rest before transition – the point at which the trajectory would have intersected the line $x = 0$ is a saddle point. However, the vessel heels over through a series of unstable equilibrium states until it oscillates about its stable equilibrium position at an angle of 32.5°. Subsequently, the applied couple is increased through 686.7, 833.9 and 981 MNm (Figure 9.12(d)–(f)). As the couple is increased the final resting angle increases. Higher initial couples result in the disappearance of the saddle point.

The above work demonstrates that the stability curve of the articulated vessel is very limiting. From the point of view of certification, the

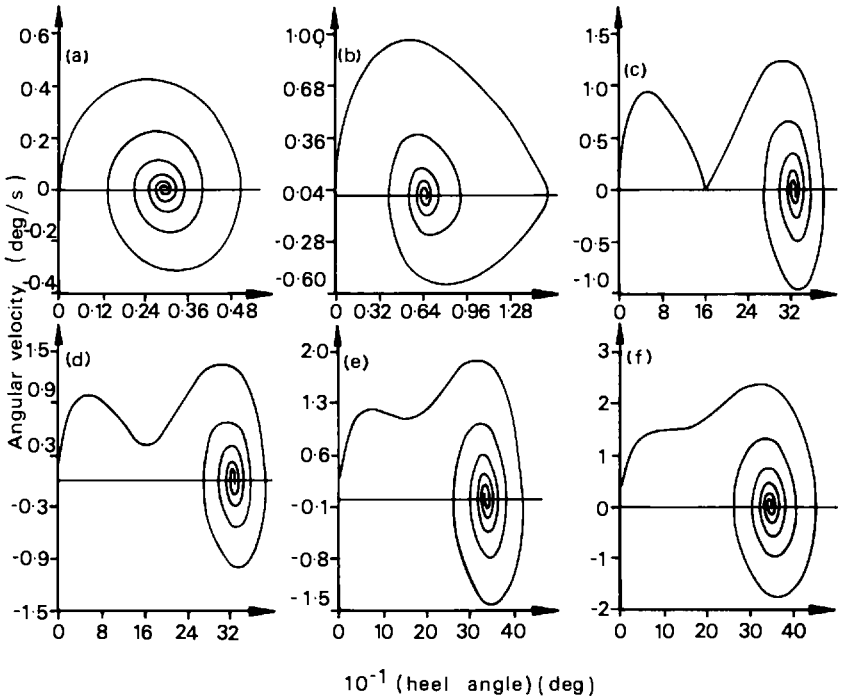

Figure 9.12. Phase-space trajectories. *Key*: a – disturbing couple = 294.3 MNm; b – disturbing couple = 657.3 MNm; c – disturbing couple = 659.7 MNm; d – disturbing couple = 686.7 MNm; e – disturbing couple = 833.9 MNm; f – disturbing couple = 981.0 MNm

conventional requirements of sufficient area ratio between righting to disturbing moments up to a second intercept of the moment curves (or up to a downflooding angle if this is smaller) and an angle range for positive stability can, in theory, be met. However, for this vessel, damage to an articulated column leading to flooding or other like events would induce occurrence of the catastrophic instability. It is clear that conventional certification requirements for hydrostatic stability would need to be extended or rethought for articulated column vessels, particularly for damage stability. In practical terms, the occurrence of a rapidly changing angle of heel (movement along the fold lines AC in Figure 9.10) would lead to complete loss of the vessel as a result of structural failures induced by transient accelerations at large angles and water slam loads during this motion. Furthermore, the rapid (or catastrophic) onset of this sudden change in angle of heel would lead, in all probability, to heavy loss of life.

9.5 Hydrodynamic response

A general hydrodynamic analysis for the articulated column semisubmersible would need to be formulated in 18 degrees of freedom – 6 for the

rigid body motions of the primary vessel and 12 degrees of freedom to describe the angular motions in two perpendicular vertical planes for each of the six articulated columns. There are several drawbacks to this approach. First, even a frequency domain solution of the 18 degrees of freedom problem is complicated. Despite the complexity, such a calculation cannot take articulated member non-linear behaviour into account. The additional difficulty of an 18 degree of freedom non-linear time domain analysis is similarly not justified by the quality of vessel behaviour prediction that it would yield.

However, the 1:100 scale model tests described later do indicate that the articulated and its equivalent rigid vessel yield very similar motion responses to waves. Furthermore, for a small motion amplitude, linear, frequency domain hydrodynamic analysis, the articulated columns move through small angles and can thus be assumed to be rigidly connected to the vessel. These two features have prompted the development of a two step analysis of the articulated column semisubmersible. The motion of the overall vessel is obtained from a linear analysis of an equivalent rigid vessel, whereas motions of the articulated column are obtained from a separate non-linear analysis of an articulated column with a fixed pivot. The former analysis is briefly described first.

The general equation of motion for a rigid semisubmersible is of the form

$$(M + M_a)\ddot{\mathbf{x}} + D|\dot{\mathbf{x}}|\dot{\mathbf{x}} + (K + K_m)\mathbf{x} = \sum_i \mathbf{F}_i(t), \tag{9.54}$$

where M and M_a are the mass and added mass matrices; D is the damping matrix; K and K_m are the hydrostatic and mooring stiffness matrices; and $\mathbf{F}_i$ is the wave exciting force vector acting on the ith member; $\mathbf{x}$, $\dot{\mathbf{x}}$ and $\ddot{\mathbf{x}}$ are the displacement, velocity and acceleration vectors containing the six rigid body degrees of freedom (surge, sway, heave, roll, pitch and yaw). The solution procedure for this equation is described further in Chapter 5 and is not repeated here. Figures 9.13, 9.14 and 9.15 illustrate the heave, pitch and surge responses of the articulated vessel obtained from the solution. However, this equivalent rigid vessel analysis yields no information on the behaviour of the articulated columns or about the forces at the universal joints.

The behaviour of a representative articulated column is examined, first in its static and still water dynamic behaviour. Consider a slender articulated column of radius r, mass M_c, submerged length L_s and a centre of gravity distance L_g from the pivot. It has a second moment of inertia, I_c, about the pivot, an added mass coefficient, C_m, and a drag coefficient, C_d, associated with flow normal to its axis.

Assuming that the column is statically inclined at an angle γ from the vertical axis and resolving forces vertically gives

$$T' + M_c g = (\rho g \pi r^2 L_s)/\cos\gamma \tag{9.55}$$

where T' is the tension at the pivot. Taking moments about the pivot gives

$$M_c g L_g \sin\gamma = (\rho g \pi r^2 L_g^2 \sin\gamma)/(2\cos^2\gamma) \tag{9.56}$$

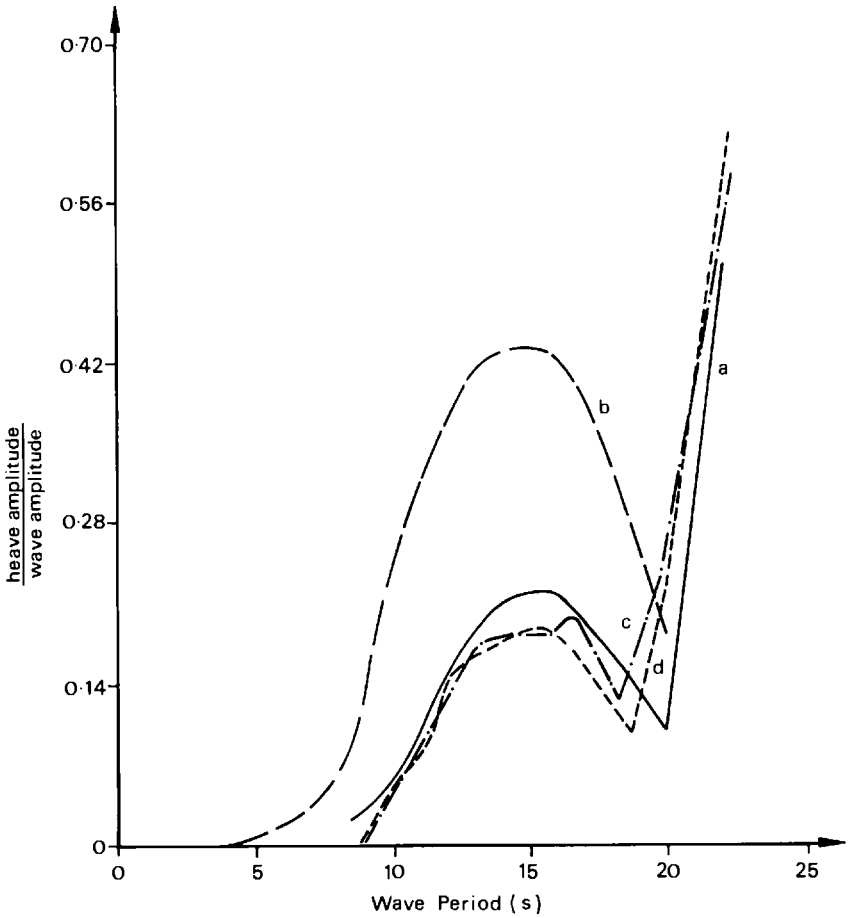

Figure 9.13. Articulated-column semisubmersible heave response in head seas of 6 m wave height. *Key*: a – rigid vessel (theoretical); b – typical semisubmersible heave RAOs; c – articulated vessel (experimental); d – rigid vessel (experimental)

Re-arranging (9.56)

$$\cos\gamma = \sqrt{\left(\frac{p\pi r^2 L_s^2}{2m_c L_g}\right)} \tag{9.57}$$

Below a certain critical draught, the column no longer takes up a vertical position. It assumes an equilibrium position at some angle to the vertical. The critical submerged length L_c is given by

$$L_c = \sqrt{\left(\frac{2M_c L_g}{p\pi r^2}\right)} \tag{9.58}$$

When the column is at a non-vertical equilibrium position, the tension is given by

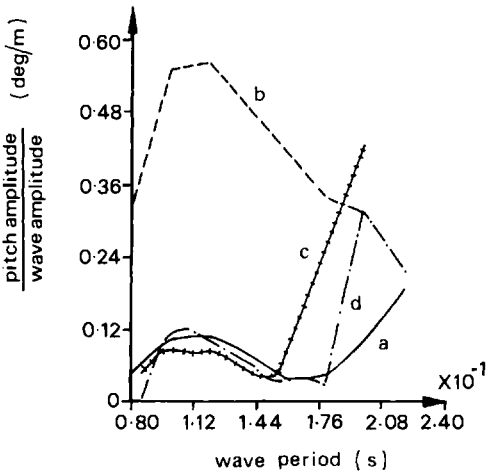

Figure 9.14. Articulated-column semisubmersible pitch response in head seas of 6 m wave height. *Key*: a – rigid vessel (theoretical); b – typical semisubmersible RAOs; c – rigid vessel (experimental); d – articulated vessel (experimental)

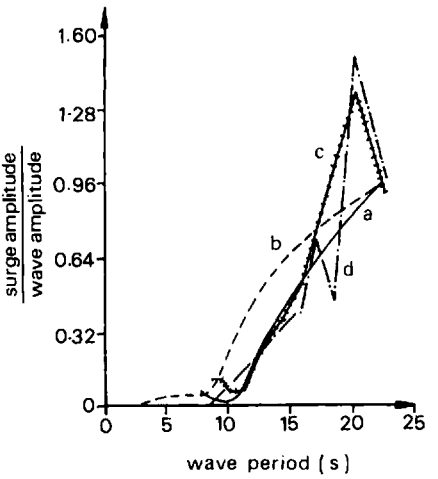

Figure 9.15. Articulated-column semisubmersible surge response in head seas of 6 m wave height. *Key*: a – rigid vessel (theoretical); b – typical semisubmersible surge RAOs; c – rigid vessel (experimental); d – articulated vessel (experimental)

$$T' = \sqrt{[(2\rho\pi r^2 M_c L_g) - M_c g]} \tag{9.59}$$

which is constant and independent of the submerged length.

Now consider the articulated column when it is in its initial vertical attitude. The column is given a small rotational displacement, α, about the pivot. Resolving moments about the pivot and ignoring any damping gives

$$(I_c + I_a)\ddot{\alpha} + (\tfrac{1}{2}\rho g\pi r^2 L_s^2 - M_c g L_g)\sin\alpha = 0 \tag{9.60}$$

where I_a is the added inertia of the column about the pivot, given by

$$I_a = \rho C_m \pi r^2 \tfrac{1}{3} L_s^2 \tag{9.61}$$

Because the rotation α is small, $\sin\alpha \simeq \alpha$ and Equation (9.60) has the form

$$\ddot{\alpha} + \omega_n^2\alpha = 0 \tag{9.62}$$

where ω_n is the angular natural frequency. Hence the natural period of the column, T_c, is given by

$$T_c = 2\pi \sqrt{\left(\frac{I_c + I_c}{\frac{1}{2}\rho g\pi r^2 L^2 s - M_c g L_g}\right)} \tag{9.63}$$

Turning now to the column response to waves, the equation of motion for a column with a fixed base pivot and subjected to wave action can be written as

$$(I_c + I_a)\ddot{\alpha} + B|\dot{\alpha}|\dot{\alpha} + (\tfrac{1}{2}\rho g\pi r^2 L_b^2 - M_c L_g g)\alpha = M_\alpha \tag{9.64}$$

where B is the rotational viscous damping term; L_b is the instantaneous distance of the centre of buoyancy from the pivot; and M_α is the wave induced overturning moment. The rotational viscous damping term is given by

$$B = \tfrac{1}{4}\rho C_d r L^4 s \tag{9.65}$$

where C_d is the drag coefficient whose value is a function of Reynolds number. The left hand side of the equation contains a non-linear drag term, a time variant stiffness due to the instantaneous submerged length and a non-linear overturning moment, M_α. All such non-linear information would be lost in a linear solution.

The overturning moment, M_α, is evaluated by integrating the wave force given by Morison's equation over the submerged length of the column. The small additional moment due to the wave pressure force acting on the base of the column is also included. The Morison equation states that the incremental wave forces, δf, acting on a moving cylinder section of length δL is given by

$$\delta f = \{\rho r C_d|u - \dot{x}|(u - \dot{x}) + \rho\pi r^2(\mathrm{d}u/\mathrm{d}t) + \rho\pi r^2 C_m[(\mathrm{d}u/\mathrm{d}t) - \ddot{x}]\}\delta L, \tag{9.66}$$

where u and $\mathrm{d}u/\mathrm{d}t$ are the instantaneous normal velocity and acceleration of the undisturbed wave flow; $\dot{x}$ and $\ddot{x}$ are the normal velocity and acceleration of the cylinder; C_m is the added mass coefficient which has a value of 1 for long circular cylinders. The wave flow field was calculated using Stokes' fifth order gravity wave theory (Skjelbreia *et al.*, 1960).

Equation (9.64) is solved in the time domain by using a Newmark algorithm and assuming a constant average acceleration between time steps (Bathe, 1982). Time histories of tilt angle are obtained from solution of the governing equation with forces at the pivot evaluated by considering static and dynamic equilibrium of the column at any instant in time.

Figure 9.16 gives the resultant column tilt response to waves as a function of wave period. Furthermore, the horizontal reaction force amplitude at the pivot and the horizontal wave force amplitude on an articulated column are compared in Figure 9.17 for two different wave heights. This shows that the component transmitted to the rigid part of the

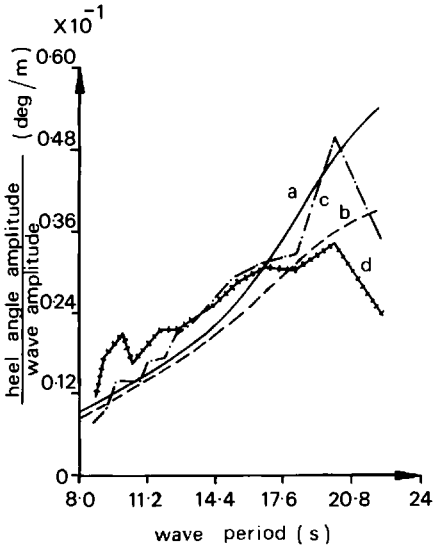

Figure 9.16. Articulated-column response (column diameter = 7 m; draught = 42 m; C_d = 1.2; C_m = 1.0). *Key*: a – theoretical (wave height = 6 m); b – theoretical (wave height = 12 m); c – experimental (wave height = 6 m); d – experimental (wave height = 12 m)

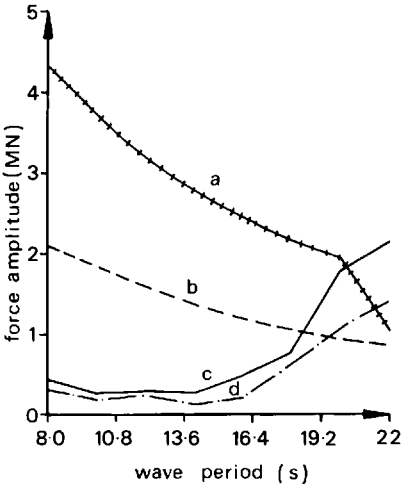

Figure 9.17. Articulated-column horizontal force (column diameter = 7 m; draught = 42 m; C_d = 1.2; C_m = 1.0). *Key*: a – force on rigid column (wave height = 12 m); b – force on rigid column (wave height = 6 m); c – force at pivot (wave height = 12 m); d – force at pivot (wave height = 6 m)

vessel is less than the hydrodynamic force on the column at wave periods away from resonance, in particular below 20 s. It can be seen that for a large part of the lower wave period range, the ratio of the two forces is less than 20%. This would be of benefit to the structural design. The reduction in horizontal force transmitted to the rigid vessel at lower wave periods will also help to reduce horizontal motion response. However, it should be noted that at these lower periods the motions are already small due to the fact that the wave forces are relatively small and the vessel displacement is large.

In order to ensure sufficient hydrostatic stability, it is desirable to maximize the static tension in the articulated column by increasing the excess buoyancy and minimizing the distance of the centre of gravity from

the pivot. However, both these objectives also lower the natural period of the column. It is preferable that the tilt natural period lies outside the wave spectrum in order to avoid large column motions which may result in collision with the deck. It can be seen that dynamic and hydrostatic considerations conflict and there must be a compromise between the two.

The theoretical prediction from the equivalent rigid vessel and articulated column analyses described above have been compared with model tests of the vessel at 1:100 scale. The test model was designed to ensure that pre-selected mass distribution could be obtained for the rigid and articulated segments and that the model could be operated either with the columns held rigid or moving freely. Motion measurements were carried out in waves of both the central rigid platform and the angular motions of the articulated columns.

Still water hydrostatic inclining tests, with the results shown in Figure 9.7, confirmed the validity of the hydrostatic restoring moment predictions given in Section 9.3. Regular wave motion response tests were also performed for the vessel with columns held rigid and allowed to move freely, and these demonstrated that the differences between the two are negligibly small. This justifies the assumptions used in the analysis methods. Figure 9.13 presents a comparison of the articulated and rigid vessel heave RAO in head seas. This shows that the articulated compliance has no significant effect on the vertical motion of the vessel. The most important feature of the amplitude response curve is the magnitude of the secondary peak. This indicates that the vessel heave amplitude will be 20% of the incident wave amplitude, in comparison with most existing semisubmersibles which heave between 40 and 50% of wave amplitude. Figure 9.14 shows the pitch response to be of the order of 0.1°/m and shows good comparison between calculated and measured rigid vessel responses. In this example, rigid and articulated vessel responses are also very similar.

Figure 9.15 illustrates small differences between articulated and rigid vessel surge response amplitudes. Overall, articulated columns do reduce horizontal motions, particularly at low wave periods (8 and 9 s), although the reductions are not substantial. Discrepant experimental points for the pitch and surge results at periods above 16.5 s are due to the influence of the mooring lines. The theoretical results have been obtained for a free vessel.

Figure 9.16 illustrates measured and predicted articulated column tilt angle amplitudes per unit wave amplitude as a function of wave period in 6 and 12 m waves. Results are presented for a column of 7 m diameter and 42 m draught. Curves for both wave heights indicate a similar response with tilt angle amplitudes increasing in the vicinity of the column natural period (23.0 s, full scale). Increasing the wave height from 6 to 12 m illustrates non-linearities in the response above wave periods of 18 s. Experiment and theory compare well, particularly at the smaller wave height, suggesting that the column response is not strongly influenced by motion of the pivot.

It is clear from the work presented here that the introduction of articulations complicates the hydrostatic stability of a semisubmersible. When comparing the articulated vessel with the equivalent rigid vessel, some small angle stability is lost as a direct result of articulating the

columns. However, the vessel does possess high initial stability due to the large column spacings. The large angle hydrostatics (Figures 9.8 and 9.9) exhibit large restoring moment losses due to the behaviour of articulations at lower draughts. The form of the restoring moment curve is alarming and would be of major concern to certifying authorities (Department of Energy, 1988; Det Norske Veritas, 1987). Note that large amounts of energy would be required to rotate the vessel up to the point where instabilities occur due to the large initial metacentric height. Nevertheless, such energy inputs are not unrealistic. Further dynamic stability considerations have shown that the vessel exhibits behaviour which is qualitatively predicted by the mathematics of classical catastrophe theory. It is certain that the stability requirements applied to articulated column semisubmersibles would have to be re-assessed and that in its present form the vessel would be unacceptable as a working design. Nevertheless, the articulated column semisubmersible at normal operating conditions offers exceptional motion response characteristics in all its degrees of freedom.

An interesting feature of the effect of articulations is the considerable reduction in the magnitude of forces transmitted to the main platform due to the columns being articulated. This is shown in Figure 9.17 which presents the horizontal wave induced force on the articulated column and the horizontal shear force at the pivot. For wave periods up to 18 s, the shear force is much less than the wave force. If the articulation were held rigid, the shear force would be equal in magnitude to the wave force. Furthermore, this would induce a bending moment at the column base. This is relieved by articulating the column. For wave periods up to 16 s the ratio of pivot shear force to horizontal wave force is less than 20%.

The articulated column semisubmersible offers potentially exceptional motion response characteristics but it appears at the cost of severe catastrophic instability in heel and pitch at large angles. It is clear that the same feature of the vessel design which gives it exceptionally good motion response during normal operations also causes the catastrophic instability at large angles. There is, therefore, no apparent design refinement that could maintain a significant motion response advantage during normal operations with acceptable behaviour at large angles of inclination.

9.6 Rigid vessels with inflected righting moment curves

The catastrophically unstable behaviour described in the above section is not confined to vessels with joints but can also arise, in a weaker form, in rigid vessels where the righting moment with heel angle variations has a point of inflection within it.

This section describes the dynamics of roll motion of such vessels in greater detail. One of the most common causes of inflected righting moment curves is the installation of sponsons around the hulls of rigid vessels. This feature usually arises because of the demands of high deck payload for offshore oil drilling, production or support duties together with the increasingly stringent hydrostatic stability requirements of certifying authorities.

This section demonstrates the occurrence of such inflectional righting moments for a four column semisubmersible installed with sponsons on the columns at the water line. A polynomial approximation to the hydrostatic moment against roll angle variation is used within the governing equations to deduce vessel behaviour under static overturning moments, when oscillating in free vibrations and when excited by wave induced roll moments. These analyses are used to deduce salient features of vessel behaviour due to the presence of inflections in the righting moment curves. Solutions of the governing equations derived from a time domain integration are also used to illustrate vessel behaviour. The section concludes with a discussion of the implications of such inflection induced behaviour on vessel safety.

9.6.1 Calculation of righting moment curves

A four column semisubmersible with sponsons is used as the example vessel. Figure 9.18 gives a perspective view of the vessel hull and Table 9.2 gives principal particulars. A surface pressure integration technique (see

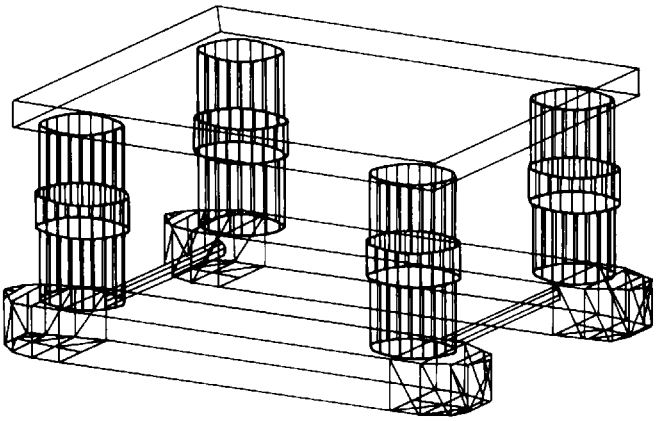

Figure 9.18. Conventional four-column semisubmersible with sponsons

Table 9.2 Four column semisubmersible data

Displacement (in sea water)	25 585 t
Draught	20.5 m
Roll metacentric height	1.98 m
Column diameter	12.92 m
Column pitch radius	38.69 m
Pontoon dimensions	73.64L m
Sponson width/diameter	16.00W m
Sponson height	7.50D m
Height of underside of sponson	
Above keel	18.0 m
Deck dimensions ($L \times W \times D$)	70 × 70 × 4 m
Height of underside of deck above keel	33.0 m
Bracing diameter	2.0 m

Chapter 3) is utilized to yield hydrostatic righting moment against angle of heel curve shown in Figure 9.19. It is important to point out here that the addition of sponsons on rigid conventional vessels will not necessarily generate an inflected righting moment curve. The presence and precise shape of the inflection does depend on the vessel geometry, weight distribution and the sponson geometry. Nevertheless, in configurations where the inflection does occur, the restoring moment is represented by a spring which is effectively linear for small rotations, softens and then hardens with increasing rotation. Furthermore, the restoring moment, $R(\phi)$, is an odd function so that $R(\phi) = -R(-\phi)$ where ϕ is the angle of rotation. Thus $R(\phi)$ may be approximated by the series in odd powers of ϕ given by

$$R(\phi) = \alpha\phi + \beta\phi^3 + \gamma\phi^5 + \ldots \tag{9.67}$$

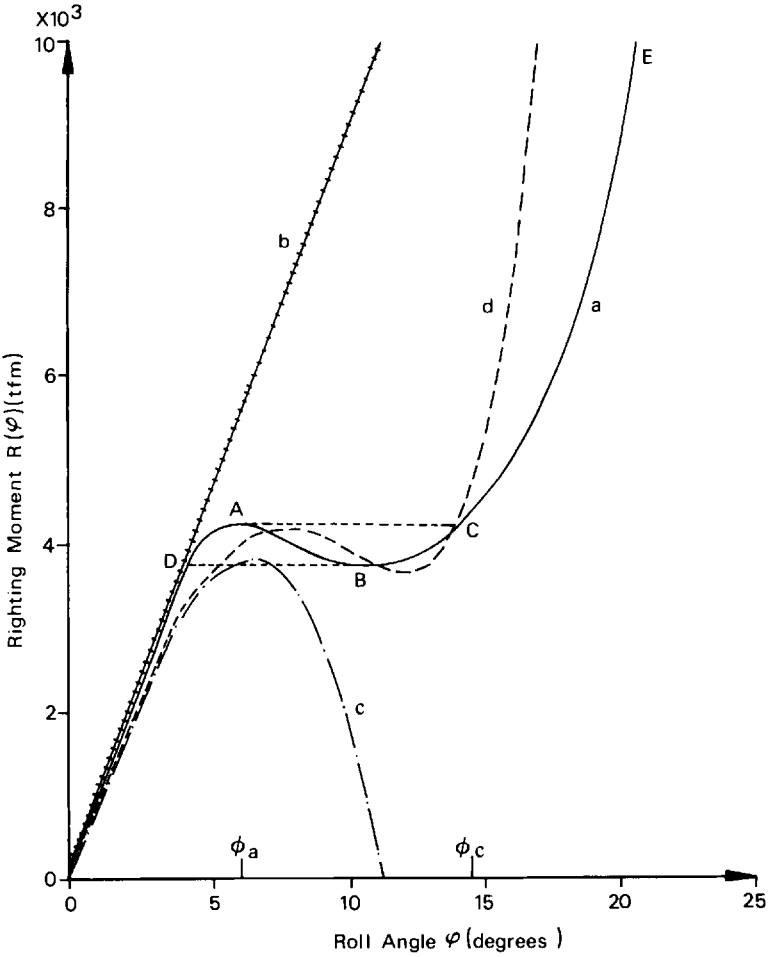

Figure 9.19. Roll righting moment for a semisubmersible with sponsons: *Key:* a – actual righting moment; b – linear approximation; c – cubic approximation; d – pentic approximation

Considerable work has been done on systems with non-linear springs (Stoker, 1950; Jordan and Smith, 1977; and Nayfeh and Mook, 1979) where the restoring force or moment is represented by just the first two terms of the above series. However, it can readily be shown that it is necessary to include the third term of the series in order to model the local maximum and minimum. Thus $R(\phi)$ may be approximated by the first three terms of the series with the local maximum and minimum given by the roots of the equation

$$5\gamma\phi^4 + 3\beta\phi^2 + \alpha = 0 \tag{9.68}$$

This chapter only considers the case where α is positive and β and γ are relatively small. In order for an inflectional point to exist, β and γ must be of opposite sign. If β and γ were of the same sign, then the restoring moment may be represented by a continuously hardening or continuously softening spring – depending on the sign of β and γ. This section is only concerned with inflectional curves and hence the case where β and γ are of opposite sign.

Figure 9.19 illustrates an approximate fit of the pentic equation (first three terms of the series) to the calculated restoring moment curve for the semisubmersible shown in Figure 9.18 and with numerical data given in Table 9.2. The linear approximation (first term of the series) and the cubic approximation (first two terms of the series) are also plotted. These curves indicate that a fifth order polynomial adequately models the local maximum and minimum whereas any lower order fit is not sufficiently representative. The coefficients of the curve fit are; $\alpha = 0.009\,461\,16$, $\beta = -0.244\,598\,9$, $\gamma = 2.339\,526\,80$ and $\lambda = 0.017\,767\,33$ (tonne metre second units). Note that the righting moments presented here are calculated using static conditions and are time invariant. In practice, the restoring moments will be time dependent due to changes in the vessel's submerged volume during wave action. However, it is reasonable to assume that a static analysis will generate the mean restoring moment.

9.6.2 Dynamic analysis

The general equation of roll motion for a marine vehicle is

$$I\ddot{\phi} + D\dot{\phi} + R(\phi) = M_r(t) \tag{9.69}$$

where ϕ is the roll angle; I is the total (physical plus added) inertia; D is the equivalent linear damping; R is the restoring moment; and M_r is the roll exciting moment. This equation assumes no coupling between roll and any other degrees of freedom and that the total inertia is effectively constant. The non-linear quadratic component of the damping associated with viscous forces has been linearized and combined with the damping due to radiation forces to form the equivalent linear damping. The reader is referred to work by Dalzell (1978) and Brown and Patel (1985) where non-linear damping is considered. This aspect of the roll equation of motion is not considered here.

If the restoring moment $R(\phi)$ can be approximated by the first three terms of the series given in Equation (9.67), then the roll equation of

motion (9.69) becomes

$$\ddot{\phi} + \lambda\dot{\phi} + \alpha\phi + \beta\phi^3 = \gamma\phi^5 + m_r(t) \tag{9.70}$$

where α, β and γ now include the total inertia; and m_r is the roll exciting moment divided by the total inertia; λ is the linearized damping coefficient divided by the total inertia.

An examination of Equation (9.70) will enable the effect of the local minimum and maximum in restoring moment on the behaviour of the vessel in roll to be deduced. Unfortunately, exact closed form analytical solutions of Equation (9.70) do not exist. It may only be solved by approximate methods depending on the form of m_r or by numerical methods.

This section uses both approximate methods and numerical integration to solve Equation (9.70). A Runge–Kutta–Nyström method is used for the numerical integration (Kreyszig, 1979). Jones and Lee (1985) have used numerical methods for the solution of non-linear systems with some success.

9.6.2.1 Free motions

The homogeneous or free equation of motion merits investigation as it yields useful information of a qualitative character on the system. The free system is described by the equation

$$\ddot{\phi} + \lambda\dot{\phi} + \alpha\phi + \beta\phi^3 + \gamma\phi^5 = 0 \tag{9.71}$$

This equation cannot be solved directly but it may be transformed to the phase plane to yield energy curves. Substituting the following relationships:

$$\frac{d\phi}{dt} = v; \qquad \frac{d^2\phi}{dt^2} = v\frac{dv}{d\phi} \tag{9.72}$$

into Equation (9.71) gives

$$-v\frac{dv}{d\phi} = \alpha\phi + \beta\phi^3 + \gamma\phi^5 + \lambda v \tag{9.73}$$

This equation may be integrated to give the energy integral equation:

$$\frac{v^2}{2} + P(\phi) = h_0 - \int \lambda v d\phi \tag{9.74}$$

where

$$P(\phi) = \frac{\alpha\phi^2}{2} + \frac{\beta\phi^4}{4} + \frac{\gamma\phi^6}{6} \tag{9.75}$$

and h_0 is the initial total energy of the system. Equation (9.74) states that the sum of the kinetic and potential energies is equal to the total energy at any instant. If the system is conservative, that is, there is no damping, then the total energy would always equal the initial energy. The integral term of Equation (9.74) represents energy dissipated by damping ($\lambda > 0$) which tends to h_0 as time tends to infinity. Thus the system will tend to a

stationary equilibrium position unless more energy is injected by external forces. In the phase plane, all equilibrium points lie on the angular displacement axis. As ϕ and v tend to zero the phase space trajectories of the free undamped system are ellipses about the origin similar to those for the linear system. The phase space trajectories of the non-linear system with no damping presented in Figure 9.20 were obtained using the values of coefficients α, β and γ given in Section 9.6.1. Each closed path represents a constant energy trajectory with greater energy further from the origin. These closed paths represent periodic solutions where the system will oscillate indefinitely. In practice the trajectory will spiral towards the equilibrium position at the origin as energy is dissipated by positive damping.

Depending on the values of β and γ, solutions of $P(\phi) = h_0$ will determine whether or not the non-linear systems's maximum angular

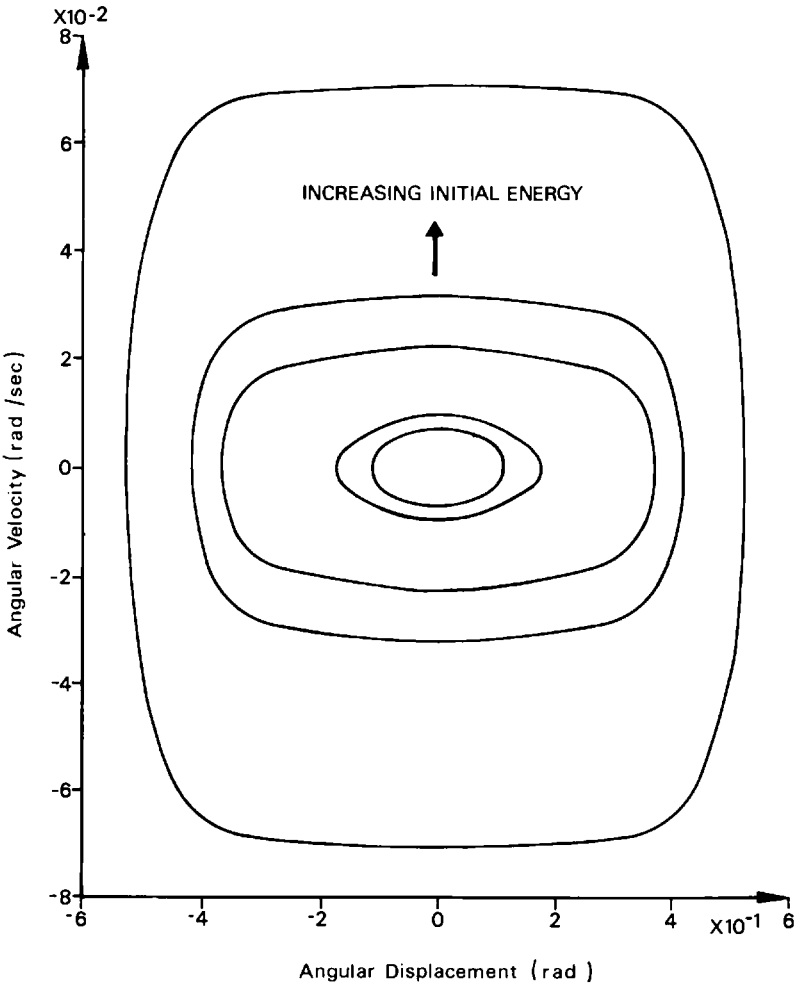

Figure 9.20. Phase-space trajectory for the non-linear system with zero damping

displacement is greater than the maximum angular displacement for the linear system. For the semisubmersible vessel example presented here with $h_0 = 0.0005$, the non-linear terms had the effect of increasing the maximum angular displacement. The non-linearity in the restoring moment also modifies the periodicity of the motion. If the phase space trajectory is a closed curve, then $v(t) = v(t + T)$ and $(t) = (t + T)$ where T is the period of motion. The period T may be calculated by the integral

$$T = \int \frac{d\phi}{[2(h_0 - P(\phi)]^{1/2}} \tag{9.76}$$

which, for a linear system, gives $T = 2\pi/\sqrt{(\alpha)}$. Examination of the homogenous system shows that both the amplitude and the periodicity of the motion are affected by the non-linear restoring moment. Furthermore, the introduction of non-linear terms make the period of motion dependent on the amplitude of oscillation. This will become evident later.

9.6.2.2 Equilibrium positions

Marine vessels rely on their hydrostatic stability to counteract applied moments which may build up to a constant value. While such a moment is applied, the vessel maintains a new equilibrium position governed by its hydrostatic stability. The build up of the applied moment may be instantaneous such as the moment induced by the loss of a crane load or more gradual such as an increase in the wind overturning moment.

If the restoring moment curve of the vessel is monotonic in the range of interest, then there is only one equilibrium position given by the point where the restoring moment equals the applied moment. However, if there is a local maximum and minimum in the restoring moment curve, then there exists a range of applied moments where there are three possible equilibrium positions.

For example, if a roll moment of 4000 tfm was applied to the four column semisubmersible, then Figure 9.19 shows that there are three possible equilibrium angles of approximately 4.4°, 8.0° and 13.1°. This would be a major source of alarm to certifying authorities because although the first equilibrium position would be acceptable, the second two would not. Since all three positions are the result of the same applied moment, uncertainty about which position would actually be achieved casts severe doubts on the vessel's safety.

If an overturning moment, the magnitude of which is in the range of OA (see Figure 9.19), is applied to the vessel, a positive hydrostatic stiffness (righting moment per unit rotation) will ensure that stability is maintained. Releasing such a moment would result in the vessel oscillating about its initial equilibrium position until the motions were damped out. If the overturning moment is increased so that it intersects the righting moment curve at A, the effective stiffness will be zero (as it changes over from positive to negative). This represents a static instability and is characterized by the appearance of an adjacent position of equilibrium, the point C. During transition to this position of stable equilibrium, the vessel will not follow the computed curve along line AB. In the heel angle range from A to C, the righting moment will be less than the overturning moment and,

furthermore, the effective stiffness is negative (in the region from A to B), both of which imply that the vessel would be unstable. The vessel will rotate rapidly from an angle of γ_a (6°) to eventually settle at ϕ_c (14.3°). Further increases in overturning moment result in the curve CE being followed. As the overturning moment is reduced, the positive effective stiffness ensures that the locus of stable equilibrium will pass through C to point B. This point is analogous to A when the overturning moment was increasing, in that it represents a change from positive to negative stiffness (although this time it is a minimum point). Again, on the point of a static instability, an adjacent position of stable equilibrium appears at D from which further reductions in overturning moment results in a return to the initial equilibrium position, O. Thus, in applying and removing an overturning moment to the vessel, the angle of heel will follow a hysteresis loop. Such a righting moment curve will cause a vessel to behave in a manner which exhibits the features of a fold catastrophe (Zeeman, 1977; and Thompson, 1982). The point A is a critical point termed the fold or limit point – similarly, AC is called the fold line.

So far nothing has been said about the stability of the equilibrium points. If the angular displacement, ϕ, is re-expressed in terms of a small perturbation, ϵ, about the equilibrium position, ϕ_s, then

$$\phi = \phi_s + \epsilon \tag{9.77}$$

where ϕ_s is given by solution of s

$$m_s = \alpha\phi_s + \beta\phi_s^3 + \gamma\phi_s^5 \tag{9.78}$$

m_s is the applied moment. Substituting (9.77) and (9.78) into the equation of motion (9.70) with $m_r(t) = m_s$ yields the variational equation

$$\ddot{\epsilon} + \lambda\dot{\epsilon} + (\alpha + 3\beta\phi_s^2 + 5\gamma\phi_s^4)\epsilon = 0 \tag{9.79}$$

where second and higher order terms in ϕ have been neglected. Using this equation the stability of the three equilibrium positions associated with the applied moment m_s may be investigated.

Since the damping is positive, the variational equation and hence the equilibrium position is stable if

$$\left.\begin{aligned} &\alpha = 3\beta\phi_s^2 + 5\gamma\phi_s^4 > 0 \\ &\text{or} \\ &\frac{dR(\phi)}{d\phi}\bigg|_{\phi=\phi_s} > 0 \end{aligned}\right\} \tag{9.80}$$

Thus the equilibrium position is stable if the restoring moment gradient about the equilibrium position is positive. So although the four column semisubmersible has three equilibrium positions (4.4°, 8.0° and 13.1° respectively) when a moment of 4000 tfm is applied to it, Figure 9.19 shows that the positions corresponding to 4.4° and 13.1° are stable, while the position corresponding to 8° is unstable. As a consequence of Equation (9.80), one of the equilibrium positions has been eliminated. The equilibrium position finally obtained would depend on the dynamics of the system. The governing equation for this is solved by numerical integration

in the time domain for the four column semisubmersible whose restoring moment curve is shown in Figure 9.19. In the time domain solution, the actual restoring moment is used rather than the truncated series approximation. Inertia and damping coefficients were obtained by a slender member discretization described in Chapter 5.

Two cases are considered. The first is where the applied moment builds up slowly and, in the second case, the moment is applied instantaneously. In the case where the moment is applied slowly, the vessel tends to settle at the first equilibrium position. However, the situation is very different for the instantaneously applied moment. Figures 9.21((a)–(f)) show the phase trajectories for increasing roll moments applied to the four column semisubmersible. Figure 9.21(a) shows the phase trajectory spiralling into the only equilibrium position (2.27°) associated with the applied moment of 19.62 MNm. Similarly for an applied moment of 35.32 MNm, the vessel heel angle spirals in towards its only equilibrium position at 4°. However, the phase trajectory (Figure 9.21(b)) shows that the vessel rotates beyond the local maximum point and then returns. The next applied moment of 37.28 MNm has three equilibrium positions – two of them being very near the local minimum point. Figure 9.21(c) shows that the phase trajectory circumvents the highest equilibrium position near 12° and heads towards the unstable equilibrium position at 9.2°. The phase trajectory diverges away from the unstable equilibrium position and converges on to the first stable equilibrium position at 4.2°. A small increase in the applied moment to 38.26 MNm results in the phase trajectory converging on the last equilibrium position near 12.5° (see Figure 9.21(d)). Further increases in moment result in convergence on the last equilibrium position (see Figure 9.21(e)) until the applied moment is large enough to have only one equilibrium position (Figure 9.21(f)).

The phase trajectories shown in Figures 9.21((a)–(f)) were calculated with the four column semisubmersible initially at rest and on an even keel. However, the vessel may not be at rest or on a even keel at the instant of the application of the disturbing moment because of oscillatory roll motion within a seaway. Figure 9.22((a)–(e)) show the phase trajectories for an applied moment of 37.5 MNm with a range of initial conditions. The moment of 37.5 MNm has three equilibrium positions. Depending on the initial conditions the vessel either settles at 4.2° or 12.2°.

Of the three equilibrium positions that occur for a range of restoring moments in the region of the point of inflection, one is unstable. The final resting position of the vessel may be either of the two remaining equilibrium positions. The final position depends on the dynamics of the system. This is a major concern because the first equilibrium position is generally acceptable while the last equilibrium position is almost certainly not acceptable. Yet both remain feasible.

Figure 9.21. Phase trajectory for a semisubmersible with sponsons: (a) overturning moment = 2000 tfm; (b) overturning moment = 3600 tfm; (c) overturning moment = 3800 tfm; (d) overturning moment = 4000 tfm; (e) overturning moment = 3900 tfm; (f) overturning moment = 5000 tfm

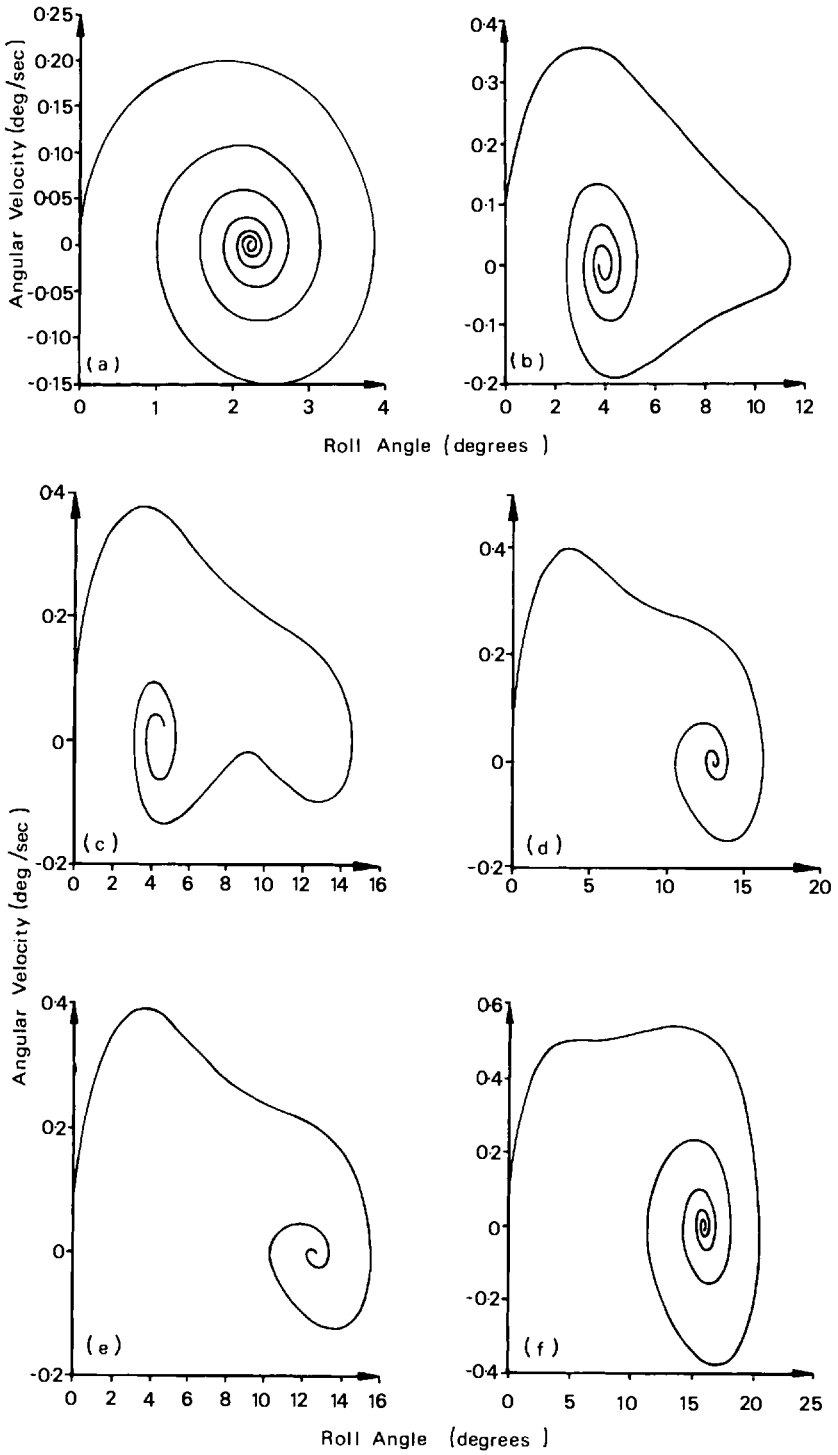
Angular Velocity (deg/sec)
0·25
0·20
0·15
0·10
0·05
0
-0·05
-0·10
-0·15
(a)
0 1 2 3 4
0·4
0·3
0·2
0·1
0
-0·1
-0·2
(b)
0 2 4 6 8 10 12
Roll Angle (degrees)
0·4
0·2
0
-0·2
(c)
0 2 4 6 8 10 12 14 16
0·4
0·2
0
-0·2
(d)
0 5 10 15 20
Angular Velocity (deg/sec)
0·4
0·2
0
-0·2
(e)
0 2 4 6 8 10 12 14 16
0·6
0·4
0·2
0
-0·2
-0·4
(f)
0 5 10 15 20 25
Roll Angle (degrees)

9.6.2.3 Motions with harmonic excitation

Wave loading is the dominant source of harmonic excitation of a marine vessel. The equation of roll motion with regular wave loading in beam seas can be written as

$$\ddot{\phi} = m_0(\omega)\cos(\omega t + \psi) - \lambda\dot{\phi} - \alpha\phi - \beta\phi^3 - \gamma\dot{\phi}^5 \tag{9.81}$$

where m_0 and ω are the amplitude and frequency of roll exciting moment respectively; and ψ is a phase shift between the response and the wave induced roll moment. In general, m_0 is a function of ω. Equation (9.81) does not have an exact solution although an approximate solution method based on an iterative approach has been proposed by Duffing (Stoker, 1950).

If β and γ are reasonably small then let the first approximate solution of ϕ be

$$\phi_0 = A\cos\omega t \tag{9.82}$$

where A is the unknown amplitude of oscillation. Now, substituting Equation (9.82) into (9.81) and using trigonometric identities gives

$$\ddot{\phi}_1 = m_0\cos(\omega t + \psi) + \omega\lambda A\sin\omega t - \left[(\alpha A + \frac{3\beta A^3}{4} + \frac{5\gamma A^5}{8}\cos\omega t + \left[\frac{\beta A^3}{4} + \frac{5\gamma A^5}{16}\right]\cos 3\omega t + \frac{\gamma A^5}{16}\cos 5\omega t\right] \tag{9.83}$$

Integrating and retaining the periodic solution gives

$$\phi_1 = \frac{-m_0}{\omega^2}\cos(\omega t + \psi) - \frac{\lambda A}{w}\sin\omega t + \left[\frac{1}{\omega}(\alpha A + \frac{3\beta A^3}{4} + \frac{5\gamma A^3}{8}\right] + \cos\omega t + \frac{1}{9\omega^2}\left[\frac{\beta A^3}{4} + \frac{5\gamma A^5}{16}\right]\cos 3\omega t + \left[\frac{\gamma A^5}{400\omega^2}\cos 5\omega t\right] \tag{9.84}$$

This is the next approximation to the solution of ϕ. Note that higher harmonics are appearing in the solution. The iteration may be continued by substituting Equation (9.84) into (9.81) and integrating to obtain the next approximate solution of ϕ.

The amplitude of oscillation, A, still remains unknown. However, if Equation (9.82) is a good approximation to the solution then

$$A = \frac{-m_0}{\omega^2}\cos\psi + \frac{1}{\omega^2}\left[\alpha A + \frac{3\beta A^3}{4} + \frac{5\gamma A^5}{8}\right] \tag{9.85}$$

and

$$0 = -\omega\lambda A + m_0\sin\psi \tag{9.86}$$

Eliminating ψ gives

$$\left[\alpha A + \frac{3\beta A^3}{4} + \frac{5\gamma A^5}{8} - \omega^2 A\right])^2 + \omega^2\lambda^2 A^2 = m_0^2 \tag{9.87}$$

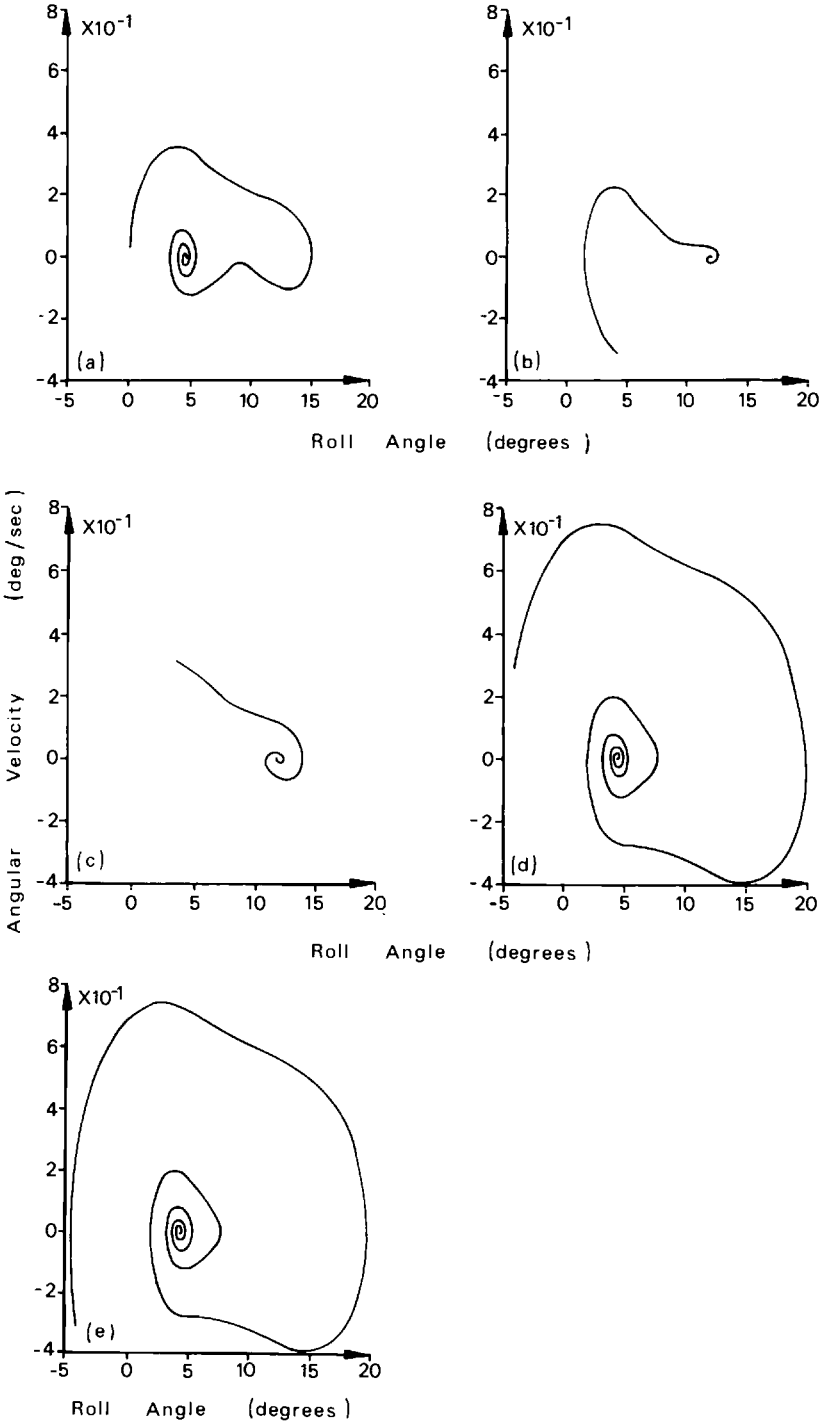

Figure 9.22. Various phase trajectories for an overturning moment of 37.5 MNm applied to a semisubmersible with sponsons

The amplitude of oscillation, A, can now be found by solving Equation (9.87). It is instructive to note that A is now a more complex function of ω and the equation coefficients compared with the solution of A for the linear stiffness case. This complexity is explored further below. Consider the undamped case. Equation (9.87) now becomes

$$\omega^2 = \alpha + \frac{3\beta A^2}{4} + \frac{5\gamma A^4}{8} - \frac{m_0}{A} \tag{9.88}$$

Figure 9.23 illustrates the above relationship as a plot of the magnitude of oscillation ($|A|$) against frequency for the case where β and γ are less than zero. If β and γ were both greater than zero the curves would bend to the right instead of the left. This case represents a softening spring and shows all the classical features of the response curve of a system with a non-linear spring. For a range of frequencies less than $\sqrt{\alpha}$, the response curve folds over, implying that there are two values of $|A|$ for a given frequency. This leads to jump phenomena in the system response, further discussed by Stoker (1950) and Nayfeh and Mook (1979).

Figure 9.24 illustrates the case where β is less than zero and γ is greater than zero. This represents a spring which softens and then hardens. Near the frequency $\sqrt{\alpha}$, the response curve bends to the left as the spring softens and then folds over to the right as the spring hardens. If β was greater than zero and γ was less than zero the response curve would do the opposite.

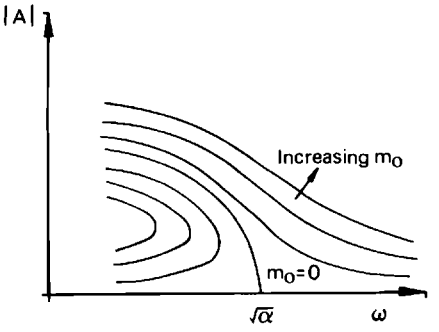

Figure 9.23. Response curve for system with softening spring

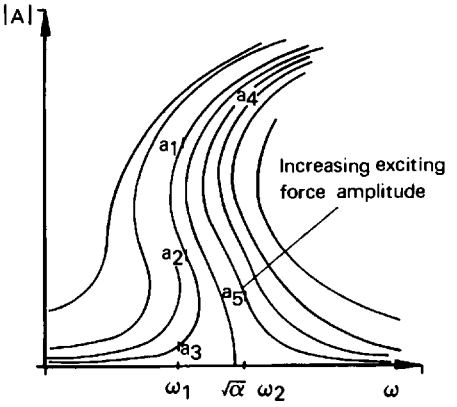

Figure 9.24. Response curve for system with softening and then hardening spring

The response curve of Figure 9.24, which is associated with a local minimum and maximum in the restoring moment, exhibits features not found in the response curve of Figure 9.23 which is for a conventional restoring moment variation. The response curve of Figure 9.24 shows that for a range of frequencies on either side of $\sqrt{\alpha}$, multiple solutions exist for $|A|$. Thus, frequency ω_1 has solutions for $|A|$ at a_1, a_2 and a_3, and ω_2 has solutions at a_4 and a_5. This feature leads to more complex jump phenomena and is in direct contrast to the response curve of Figure 9.23 where multiple solutions of $|A|$ exist only on one side of the frequency $\sqrt{\alpha}$.

So far the response curves have been obtained for undamped motions which lead to unbounded curves at resonance. The response curves with damping are given by Equation (9.87). However, if the damping is small then the damped response curve is close to the undamped curve but bounded. A typical damped response curve with a small amount of damping is represented by the dashed line in Figure 9.25.

Since there are multiple solutions of $|A|$ for frequencies near $\sqrt{a}$, jump phenomena will occur as the response amplitude, $|A|$, jumps from one stable solution to another.

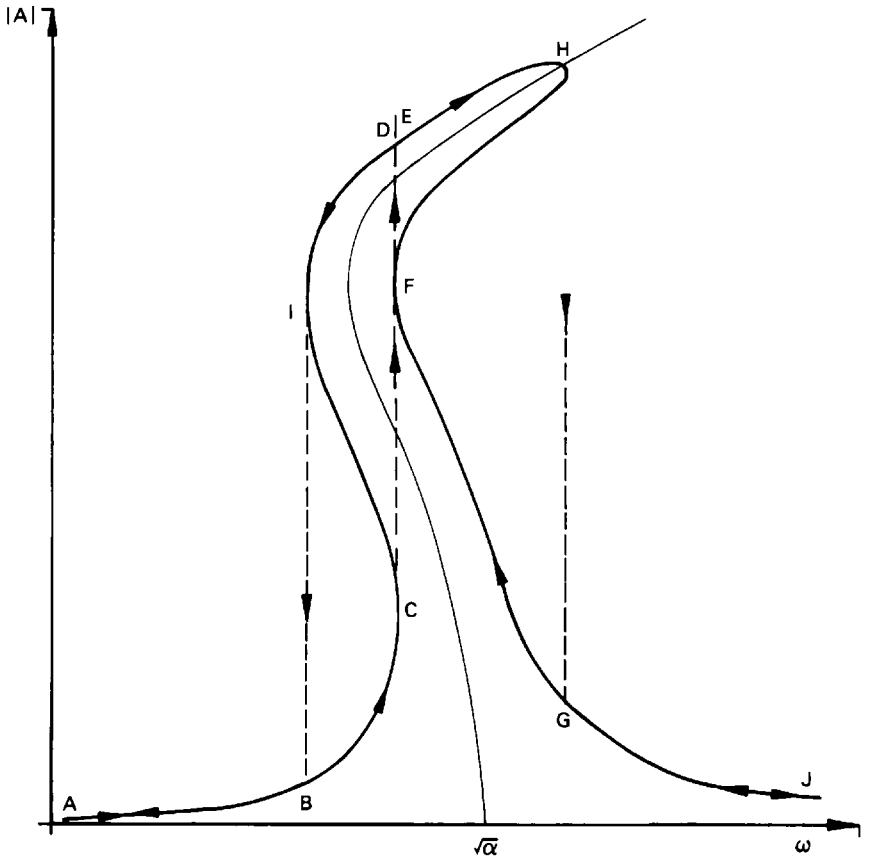

Figure 9.25. System response with increasing and decreasing frequencies of excitation

Figure 9.25 shows the damped response curve of a system for a softening and then hardening spring with a slowly increasing excitation frequency at a constant force amplitude. As the frequency is increased from a value at point A, the response will follow the path ABC until the point C is reached. The response cannot follow the path CI as the frequency is increasing and therefore the response must 'jump' to point D. A further increase in frequency causes the response to follow path DEH until H is reached. Again the increasing frequency means that the response must drop to G. Further increase of frequency results in the path GJ being followed.

Now, if the frequency is decreased from a value J, then the response will follow the path JGF until point F is reached. Using similar arguments to those given above, the decreasing frequency results in the path $FEDIBA$ being followed. Thus there is a hysteresis in the response associated with increasing or decreasing frequency.

If the frequency at C was the same as the frequency at F then a bifurcation would occur. If the frequency was increased from its value, C, it is possible for the response to follow one of two paths. The response may jump to E and then follow the path EH or it may jump to F and follow the path FG. It is likely that the latter would occur since the jump from C to E must pass through F and the latter path represents a smaller response. However, the former path is still possible and would represent a phenomenon described by catastrophe theory (Thompson, 1982; Poston and Stewart, 1978).

These jump phenomena have been created by increasing and decreasing the excitation frequency while maintaining constant amplitude of excitation. The same jump phenomena would also occur if the frequency was held constant and the amplitude of excitation was varied. This would cause the system to move to a new response curve associated with the amplitude of excitation (see Figures 9.23 and 9.24).

Two paths on the response curve of Figure 9.25 are never followed due to the jump phenomena. These are the paths IC and FH. Thus there exist two regions in the response curves where the solutions of $|A|$ are unstable. The stability of the solutions of Equation (9.68) may be investigated by generating a variational equation using the method described earlier. In this case the variational equation has time variant periodic coefficients. The stability of the variational equation may be investigated by Floquet's theory which is given in detail by Stoker (1950) and hence is not presented here.

9.6.3 Vessel design implications

It has been demonstrated that points of inflection can occur within the righting moment against angle of heel curve for a conventional semisubmersible when fitted with sponsons. These may be avoided by dispensing with the sponsons or by altering the hull geometry and vessel weight distribution.

The local minima and maxima in an inflected restoring moment curve lead to phenomena which are not present in a linear system or one in which the restoring moment is monotonic in the range of interest. The impact on the stability and operating safety of the vessel clearly depends on the

magnitude and range of the inflection when compared with the full righting moment curve.

In the case of the four column semisubmersible, the local inflection is relatively small and may be acceptable. However, for other vessels such as the articulated semisubmersible, the range and magnitude of the inflection is so great that the vessel is unlikely to meet acceptable hydrostatic stability requirements. From the certifying authorities' point of view, it is easier to adopt the conservative approach of not allowing localized maxima or minima in the righting moment curve and avoid involvement with specific decisions on phenomena that have uncertain consequences. Indeed, this is the case with current draft proposals on stability criteria (Department of Energy, 1986).

Figure 9.24 illustrates the dynamic wave induced roll response of a typical vessel with such a softening and then hardening hydrostatic spring stiffness. The amplitude of oscillation is a complicated function of frequency. Also there are multiple solutions for the response amplitude at a given frequency on either side of the linear system's natural frequency. Some of these solutions are unstable. As a consequence of these multiple solutions, complex jump phenomena will occur as the frequency or amplitude of excitation is increased or decreased.

This chapter demonstrates that wave induced harmonic excitation of vessels with inflected righting moment curves can lead to increased response amplitudes when compared to an equivalent linear righting moment. If the vessel's roll natural frequency lies in the range of expected excitation frequencies, then a complex response is observed with jump phenomena occurring around the natural frequency. This may lead to unacceptable vessel motions.

Fortunately, semisubmersible roll natural periods lie well outside the expected wave period range, although such vessels may be susceptible to very long period swells. For monohulls, however, the roll natural period invariably lies in the expected wave period range. If such a vessel has an inflected righting moment curve, wave induced roll motions due to the inflection and any consequential jump phenomena need to be fully investigated.

Another point of concern for vessels with inflected righting moment curves is the assessment of the likely heel angle to be attained by the vessel in conditions where two or more equilibrium heel angles exist. The worst case approach of selecting the largest equilibrium heel angle may be unduly conservative and make the design unacceptable. A more realistic assessment of such equilibrium heel angles may be made using the time domain integration approach used in part of the work presented here.

This section has only considered the effects of inflectional righting moment curves for intact vessels at operating draughts. It is possible that changes in vessel draught (such as transit draught for a semisubmersible) or damage due to flooding or a cargo shift may generate inflectional righting moment curves whose further effects need to be examined in the light of this work.

References

Bathe, K. J. (1982) *Finite Element Procedures in Engineering Analysis*. Prentice Hall, pp. 499–556

Biewer, F. N. (1974) (Inventor) Stably buoyed floating offshore device. United States Patent No 3837309

Biewer, F. N., Buland, R. N. and Macan, J. J. (1971) The articulated column semisubmersible, OTC Paper 1419. *Third Annual Offshore Technology Conference, Houston, Texas, April*

Brown, D. T. and Patel, M. H. (1985) A theory for vortex shedding from the keels of marine vehicles. *Journal of Engineering Mathematics*, **19** (4)

Dalzell, J. F. (1978) A note on the form of ship roll damping. *Journal of Ship Research*, **22** (3), 178–85

Department of Energy (1986) *Offshore Installations: Guidance on Design and Construction*, Part II, Section 4.3, Stability (mobile units). HMSO, London

Det Norske Veritas (1987) Rules for the design, construction and inspection of offshore structures

Interig Ltd (UK) (1984) Semisubmersible marine platform, UK Patent No GB 2141076, Published 12 December

International Maritime Organisation (1980) *Code for the Construction and Equipment of Mobile Offshore Drilling Units*. London

Jones, D. J. and Lee, B. H. K. (1985) Time marching numerical solution of the dynamic response of nonlinear systems. *Aeronautical Note NAE-AN-25, NRC No 24131*, National Research Council Canada

Jordan, D. W. and Smith, P. (1977) *Nonlinear Ordinary Differential Equations*. Oxford University Press

Kreyszig, E. (1979) *Advanced Engineering Mathematics*, 4th edn. John Wiley and Sons, NY

Nayfeh, A. H. and Mook, D. T. (1979) *Nonlinear Oscillations*. John Wiley and Sons, NY

Noble, P., McDowall, J. and Munson, M. (1984) Floating offshore production systems for ice infested waters. *RINA Developments In Floating Production Systems, RINA*, March

Poston, T. and Stewart, I. N. (1978) *Catastrophe Theory and its Applications*. Pitman, London

Ramsey, A. S. (1961), *Hydrostatics*, 2nd edn. Cambridge University Press, Cambridge

Skjelbreia, L. S. and Hendrickson, J. (1960) Fifth order gravity wave theory. *Proceedings of the 7th Conference on Coastal Engineering*, The Hague, pp. 184–196

Stoker, J. J. (1950) *Nonlinear Vibrations*. Interscience, NY

Thompson, J. M. T. (1982) *Instabilities and Catastrophes in Science and Engineering*. John Wiley and Sons, NY

Zeeman, E. C. (1977) A catastrophe model for the stability of ships, *Catastrophe Theory – Selected Papers 1972–77*. Addison-Wesley, London

Chapter 10

Floating vessels with trapped air cavities

10.1 General considerations

The introduction of trapped air cavities within the open bottom tanks of a floating vessel offers an interesting method of modifying wave induced forces acting on the vessel, and its resultant motions. The trapped air introduces a pneumatic compliance with the air's compressibility producing a variation in the hull's buoyant volume as a function of vessel motion and wave action. This compliance modifies the dynamic behaviour of the vessel and can be used to reduce wave induced motions of semisubmersible and ship shape vessels and to reduce dynamic tether forces on tensioned buoyant platforms. The pneumatic compliance is used in a passive mode for the above applications but it can also be used in an active manner (by varying the volume of trapped air) to reduce wave induced motions or to counteract disturbing forces due to vessel operation (such as on-board crane lifting).

This chapter is concerned with exploring the mechanics of both passive and active pneumatic compliances in modifying and improving the wave induced motions and internal forces on a variety of floating vessels.

In practice, pneumatic compliance on a floating vessel is achieved through the use of open bottom tanks mounted at the vessel water line and extending some distance above and below still water level. In calm water, the internal water surface is at the same level as external still water, with a volume of air at atmospheric pressure trapped between the internal water level and the boundary of the containing tank. Such air tanks may be mounted along both beams of a monohull vessel or they may be mounted around the vertical surface piercing columns of semisubmersible vessels or tension buoyant platforms. Each air cavity is connected by a valve to atmosphere. The air can be trapped by closing the valve or, alternatively, by leaving the valve open – the air can then flow freely in and out, thereby eliminating the effects of fluctuating air pressures on the vessel. In some cases, the trapped air can be pressurized, with the internal water level being lowered to generate forces and moments to counteract loads on the vessel due to cargo transfer or on-board crane operation. Figures 10.1 and 10.2 show a typical installation of these air tanks on a semisubmersible vessel, whereas Figure 10.3 illustrates an application on a ship shape vessel.

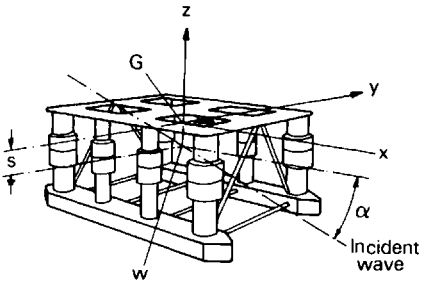

Figure 10.1. Perspective view of a semisubmersible with air tanks and reference axes system

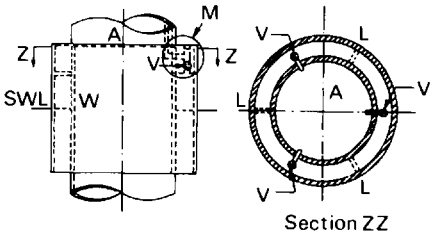

Figure 10.2. Schematic views of air tank on semisubmersible vessel. *Key*:
A – vessel column; W – internal water level in the tanks in calm water;
L – partial bulkheads dividing air tanks;
V – valves connecting the air volumes to atmosphere; M – manned access space.

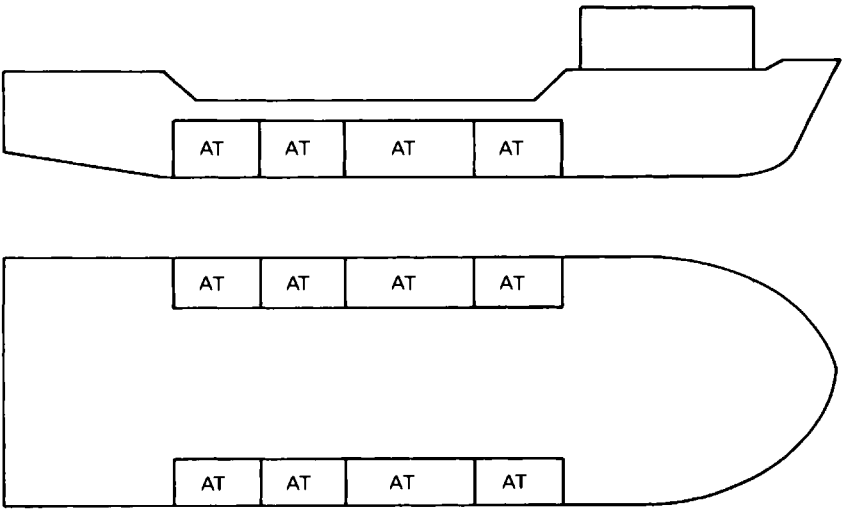

Figure 10.3 Monohull vessel. *Key*: AT – air tank

These pneumatic compliances introduce additional dynamic systems. Linked by the trapped air pressures to their host vessel, the behaviour of these systems is governed by the water column masses under the trapped air volumes, and the consequent added masses, radiation and viscous damping together with the stiffnesses of the water columns and the trapped air volumes. These dynamic systems interact with the essentially rigid six degrees of freedom of the vessel to substantially modify vessel hydrostatic

stiffnesses and the total wave induced foces acting on the vessel. These modifications can be designed to reduce wave induced forces and motions of the vessel.

For a monohull vessel, when the valves connecting the trapped air spaces to atmosphere are closed, the compressibility of the air volume increases the effective hydrostatic stiffness of the hull and thus shortens its heave, pitch and roll natural periods. Thus by opening or closing the trapped air vent valves, the vessel can exhibit two selectable natural periods in each of these degrees of freedom. This is particularly effective for wave excited roll motions since the pneumatic compliance can be designed with a significant shift in roll natural period so that roll resonance can be largely avoided by opening or closing the vent valves as a function of incident wave frequency. In addition, motion of the water columns within the submerged sections of the open bottom tanks yields additional viscous damping which serves to reduce vessel motions further.

Open bottom tanks on a semisubmersible vessel operate in a rather different manner to reduce wave induced heave motions. This is necessary because semisubmersibles on oil drilling or exploration duty operate on sea bed well heads through drill strings and marine risers. Low heave motion of the vessel to wave permits smaller relative movement between the vessel and riser and, therefore, enhances vessel operability.

The wave induced heave force on semisubmersibles arises from three sources. These are inertia loading on submerged horizontal pontoons, unbalanced wave pressure forces on the submerged sections of vertical surface piercing columns and drag forces on main and bracing members. For most wave periods of significant energy, the heave force is inertia dominated – implying that the net vertical force is 180° out of phase with local wave elevation. Conversely, wave pressure on the base of the columns is in phase with wave elevation and if the amplitudes of these forces are equal, a heave force cancellation occurs. At a specific cancellation period, the vertical drag force is then the only contributor to the net heave force.

Adopting a system which generates an oscillating force which is in phase with wave elevation would reduce the net heave force on a semisubmersible and, consequently, the wave induced motion response. Bottom opening tanks trapping volumes of air above their internal water levels offer just such a system. During wave action, the water column in an open bottom tank is excited by the wave pressure force. As with structural columns, this wave induced force is in phase with local wave elevation. The compressibility of the trapped air volume generates a vertical force which is transmitted to the vessel via the tank air pressure. Thus two dynamic systems, the vessel and water column, are coupled in stiffness through the trapped air volumes. The oscillating vertical force generated by the 'air spring' is in phase with the wave pressure force on the water column and hence serves to reduce the net heave force on the vessel. It is shown later that this mechanism also reduces net pitching and rolling moments.

The principles of operation of pneumatic compliances on both monohull and semisubmersible vessels shows that the hydrostatic stiffness contribution of the trapped air and water column beneath it play a crucial role in modifying the dynamics of the vessel. A consistent and accurate definition

of the air stiffness contribution is thus important for the dynamic analysis of the vessel. Furthermore, national certifying agencies require that any proposed vessel design meets minimum safety criteria associated with all its operations including the criterion of adequate hydrostatic stability to withstand overturning moments due to wind or due to a limited amount of flooding caused by damage. The stability criteria demanded by certifying agencies are becoming increasingly stricter and require that the stability contributions of trapped air volumes on advanced vessel designs be fully investigated.

Section 10.2 of this chapter presents a theory for calculating the air stiffness of an individual air volume and the associated water column. This is then extended to incorporate the stiffness of a number of air volumes and columns into equations to describe the overall hydrostatic stability of the vessel. The theory is applied to air volumes whose equilibrium pressure (at even vessel keel) is at, or above, one atmosphere. Results from theory are verified by comparison with model test data for a monohull vessel and semisubmersible mounted with trapped air volumes.

This is followed by consideration of the coupled dynamics of semisubmersibles and ship shape hull forms and their passive pneumatic compliances. The role of these passive compliances in reducing the dynamic tensions in tensioned buoyant platform tethers are then described. The last section of the chapter examines the performance of active compliances in reducing the wave induced motions of a semisubmersible vessel and in compensating for the disturbing forces due to the operation of a crane on a floating vessel. This latter application is illustrated by description of a practical application on an offshore crane vessel.

10.2 Hydrostatic analysis

10.2.1 Air tanks at mean atmospheric pressure

Figure 10.4 illustrates an open bottom tank where for $s = 0$, the trapped air pressure for Figure 10.4(a) equals one atmosphere. Consider this tank being give a small downward displacement, z in still water. This corre-

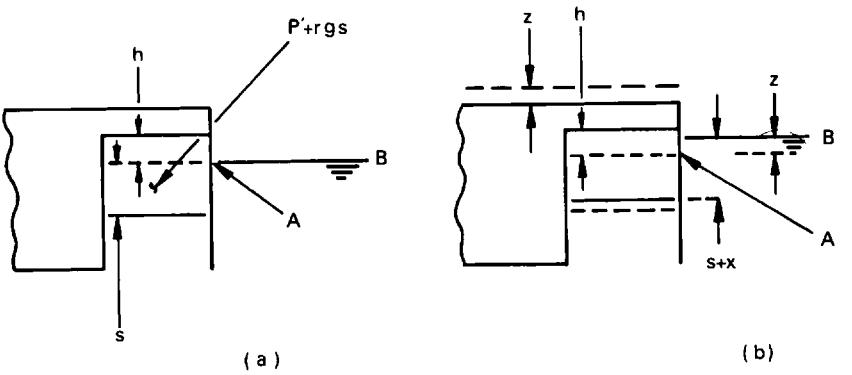

Figure 10.4. Open bottom tank notation

sponds to the external still water level, initially at draught line A, rising a distance, z, to B. If the open bottom air tank valves are closed, the compression of the air volume will only permit the internal water level in the tank to rise through a distance smaller than z such that the difference in level between external and internal water levels is x.

The using a pressure/volume gas law relationship for a polytropic process (Rogers and Mayhew, 1976), we get the pressure, P, and volume, V, before and after a displacement of the tank internal water level as

$$(PV^n)_{\text{before displacement}} = (PV^n)_{\text{after displacement}} \tag{10.1}$$

where n is the gas law index. This gives

$$P'[Ah]^n = [P' + \rho g x][A(h - z + x)]^n \tag{10.2}$$

where P' is atmospheric pressure; A is the plan area of the air tank; h is the air height within the tank; g is the acceleration due to gravity; and ρ is water density; x is the difference between the external water level and the tank water level due to displacement, z , of the tank or of the external water level.

Taking $P' = \rho g H$, dividing by $\rho g H(Ah)^n$ and rearranging gives

$$x = H\left[1 + \frac{x}{h} - \frac{z}{h}\right]^{-n} - H \tag{10.3}$$

where H is the water gauge height equal to atmospheric pressure.

Differentiating with respect to z yields

$$\frac{dx}{dz} = -nH\left[1 + \frac{x}{h} - \frac{z}{h}\right]^{-n-1} \cdot \left[\frac{1}{h}\frac{dx}{dz} - \frac{1}{h}\right] \tag{10.4}$$

and since x and z are small displacements, terms x/h and z/h can be neglected. The above equation can then be written as

$$\frac{dx}{dz} = -\frac{nH}{h}\left[\frac{dx}{dz} - 1\right] \tag{10.5}$$

and hence

$$\frac{dx}{dz} = \left[\frac{1}{1 + \dfrac{h}{nH}}\right] \tag{10.6}$$

The resultant stiffness of the tank due to internal trapped air is

$$\frac{dF}{dz} = \rho g A \frac{dx}{dz}$$

$$= \frac{\rho g A}{\left[1 + \dfrac{h}{nH}\right]} \tag{10.7}$$

where dF is the vertical force on the air tank. The index n equals 1 if the air volume behaves isothermally in compression and equals 1.398 (the ratio of constant pressure and constant volume specific heat capacities) if the air volume behaves adiabatically. Also $H = 10.077$ m for $P' = 1.013\ 25$ bar ($101\ 325\ N/m^2$) and $\rho = 1025\ kg/m^3$.

It should be noted that the air stiffness equals ρgA if h is zero, that is, in the absence of an air spring, and tends to zero if h becomes very large, corresponding to a large volume.

For a typical air height of 2 m and assuming adiabatic conditions, the right hand side of Equation (10.7) becomes $0.8757\ \rho gA$, whereas if the air volume behaves isothermally, this becomes $0.8344\ \rho gA$. The air stiffness correction factor above is only slightly sensitive to choice of the index of expansion or compression, n. The rate at which the air volume is compressed and decompressed by wave action indicates that an adiabatic process is occurring and n should be taken as 1.398. On the other hand, if the vessel is being inclined slowly, the air process would be closer to isothermal conditions and n should be taken as 1.0. In realistic conditions, n seems to take a value between 1.0 and 1.398 as shown later.

The relationship for air volume and water column stiffness can also be derived by separately considering the stiffnesses of the air volume and the water column below it.

The stiffness of the air volume in isolation can be derived by introducing perturbations of δP and δV to the polytropic gas law to yield

$$P_0 V_0^n = (P_0 + \delta P)(V_0 + \delta V)^n \tag{10.8}$$

where P_0 and V_0 are the initial pressure and volume of the air space. Dividing the above equation by V_0^n, expanding binomially and neglecting all higher order quantities yields

$$\frac{\delta P}{\delta V} = -\frac{nP_0}{V_0} \tag{10.9}$$

which can be written in terms of stiffness, k_a, for an air column of plan area, A, and height, h, in terms of the equation

$$k_a = \frac{dF}{dx} = \frac{nP_0 A}{h} \tag{10.10}$$

with the sign change arising from transforming air pressure, P_0, to a restoring force, dF. Also the stiffness of the water column, k_c, in the earth's gravitational field is

$$k_c = \rho gA \tag{10.11}$$

Since the air volume and water column stiffness act in series, the total stiffness may readily be deduced as being identical to that given by Equation (10.7).

10.2.2 Air tanks with mean pressure greater than atmospheric pressure

In this case, the air tanks are taken to contain an air pressure above atmospheric pressure in the initial undisturbed condition. Thus, in Figure

10.4(a), the internal water level is at a finite distance, s, below external water level corresponding to an absolute pressure of $(P' + \rho gs)$ within the open bottom tank. It is assumed that the vessel is at an even keel with the excess force due to the air pressure distributed symmetrically around the vessel plan.

Now, in a similar manner to that developed above, consider the vessel being given a small downward displacement, z, as in Figure 10.4(b). This is equivalent to the external water level rising by a small distance, z, from the initial draught line, A. The internal water level will, however, rise a distance smaller than z due to the trapped air volume being compressed. The difference between the internal and external water levels is defined as $(s + x)$ where x is a small, unknown distance.

Now, applying Equation (10.1) gives

$$[P' + \rho gs][A(h + s)]^n = [P' + \rho g(s + x)] \cdot [A(h + s - z + x)]^n \tag{10.12}$$

Using $P' = \rho gH$, dividing by $\rho gA^n\,[H + s][h + s]$, rearranging and differentiating with respect to z yields

$$\frac{dx}{dz} = -n[H + s]\left[1 + \frac{x}{h + s}\frac{z}{h + s}\right]^{-n-1} \cdot \frac{1}{(h + s)}\left[\frac{dx}{dz} - 1\right] \tag{10.13}$$

Since x and z are small, $x/(h + s)$ and $z/(x + s)$ can be neglected. Then, by rearranging, we get

$$\frac{dx}{dz} = \frac{1 + \dfrac{s}{H}}{\left[1 + \dfrac{h}{nH} + \dfrac{(n + 1)s}{nH}\right]} \tag{10.14}$$

Then

$$\frac{dF}{dz} = \rho gA\,\frac{1 + \dfrac{s}{H}}{\left[1 + \dfrac{h}{nH} + \dfrac{(n + 1)}{n}\dfrac{s}{H}\right]} = \rho gA \cdot Q \tag{10.15}$$

with an air stiffness factor, Q, being used for brevity. The effect of the initial pressure head is summarized in Table 10.1 which shows that depressing tank water levels reduces the combined stiffness arising from the air cavity and water column.

10.2.3 Application to hydrostatic stability

The foregoing derivation of air stiffness for an isolated air volume and water column can be incorporated into conventional naval architecture in two ways. It is common practice for marine vehicle stability to be calculated on the basis of the submerged hull volume, centre of volume (buoyancy) and water plane area prior to a correction being applied to account for the centre of gravity shift due to movement of free surface within tanks on board the vessel (see Ramsey, 1961, for further details). It

Table 10.1 Air stiffness correction factors

Gas law index	*Air stiffness correction factor, Q*				
	$s = 0\ m$	$s = 2\ m$	$s = 4\ m$	$s = 6\ m$	$s = 8\ m$
Isothermal process $n = 1.00$	0.8344	0.7512	0.7012	0.6677	0.6438
Adiabatic process $n = 1.398$	0.8757	0.8085	0.7664	0.7375	0.7165

Notes:
$H = 10.077$ m;
$h = 2.00$ m;
$\rho = 1025$ kg/m^3.

is, therefore, also possible for the stability of a vessel with air volumes and water columns to be calculated assuming it to be a rigid vessel with an impermeable boundary at the base of the water columns, provided that a correction is then applied to account for the fact that the trapped air spring is softer than an identical hard hull surface. The correction for the water column free surface would still need to be applied.

A second approach may also be taken by calculating the hydrostatic righting moment due to angle of heel from first principles for the primary rigid vessel together with the additional effects of the air tanks. Both these approaches are examined below. First, however, the air correction terms for a whole hull are derived.

Consider open bottom tanks of rectangular plan form installed along both beams of a monohull vessel of beam b and length L. The tanks are also of length L and width c each, with the distance from the tank centre lines to vessel fore and aft centre line being $(b - c)/2$.

The increment in BM (distance between centre of buoyancy and metacentre) due to solid water plane area corresponding to the plan area of the air tanks is

$$\mathrm{d}(BM)_{\text{solid}} = \frac{2}{D_r}\left[\frac{Lc^3}{12} + \frac{Lc(b-c)^2}{4}\right] = \frac{1}{D_r}\left[\underbrace{\frac{Lc^3}{}}_{Y} + \underbrace{\frac{Lc(b-c)^2}{2}}_{Z}\right] \tag{10.16}$$

where B is the position of the centre of buoyancy including the water columns in open bottom tanks; M is the transverse metacentre; and D_r is a reference displaced volume which may be the vessel displaced volume including or excluding the volume of the water columns in the open bottom tanks. Here, term Y is due to the second moment of area of the water plane about an axis through its own centroid, whereas term Z arises because the tank water plane area centroid is offset from the centroid of the total vessel water plane area.

The increment in BM due to the air tanks may be calculated as follows.

Consider the vessel undergoing a small rotation (angle β) in roll. The submergence and emergence of starboard and port air tanks, respectively, is given by $\beta(b - c)/2$. The moment induced by the resultant force due to the air springs in port and starboard air tanks is then given by

$$2\rho g \cdot Lc \frac{\left[1 + \frac{s}{H}\right]}{\left[1 + \frac{h}{nH} + \left(\frac{n+1}{n}\right)\frac{s}{H}\right]} \frac{\beta(b-c)^2}{4} \tag{10.17}$$

This corresponds to an effective BM increase which is given by

$$d(BM)_{\text{air tanks}} = \frac{\textit{Righting moment}}{\rho g D_r \cdot \beta}$$

$$= \frac{Lc(b-c)^2}{2D_r} \frac{\left[1 + \frac{s}{H}\right]}{\left[1 + \frac{s}{nH} + \left(\frac{n+1}{n}\right)\frac{s}{H}\right]} \tag{10.18}$$

Then the reduction in BM (or GM) due to replacement of solid hull with air tanks is given by

$$d(BM)_{\text{solid}} - d(BM)_{\text{air tanks}} = GM_{\text{loss}}$$

$$= \frac{Lc(b-c)^2}{2D_r}\left[\frac{1}{1 + \frac{n(H+s)}{(h+s)}}\right] \tag{10.19}$$

Term Y in Equation (10.16) is not included in the above expression since it would normally already be accounted for in the free surface corrections for the water columns. Only Equation (10.19) is required for calculating metacentric height corrections during design studies. Note that the choice of reference displaced volume D_r, alters the magnitude of reduction in BM or GM. Such effects are examined further below.

Also, the correction to the tonnes per centimetre immersion (TCM 1 cm) can be readily written as

$$[TCM\ 1\ \text{cm}]_{\text{loss}} = \frac{2\rho Lc}{100\,000}\left[\frac{1}{1 + \frac{n(H+s)}{(h+s)}}\right] \tag{10.20}$$

where ρ is in kg m^{-3} and the 100 000 accounts for the formula units.

The second approach for evaluating the hydrostatic stability of a marine vehicle with trapped air cavities is to calculate hydrostatic righting moments. This can be done from first principles or by submerged volume considerations using an extension of conventional naval architecture. Both of these are presented below with the two approaches being used to deduce hydrostatic righting moments with and without the air tanks being activated, that is, with the valves connecting the air spaces to atmosphere in the closed and open position respectively.

Results for the latter case with valves open can be deduced from conventional hydrostatic analysis with the volume of the trapped air and water column below it excluded from the submerged vessel volume.

However, all such solid body calculations are based on taking moments of an inclining submerged solid volume. In this procedure, the submerged volume is assumed to have an impermeable boundary – the only volume changes occurring close to the free surface in the shapes of emerging and submerging wedges. So the $BM = I/D$ formula of conventional naval architecture can strictly only be applied for solid shapes with an impermeable submerged boundary.

For open bottom tanks with trapped air volumes, the vessel boundary is no longer impermeable. As the vessel inclines, the submerged volume can eject or take up additional volumes of water from the open bottom tanks due to the effect of trapped air above the water columns (as illustrated in Figure 10.5(a)). There are two methods of converting this physical phenomenon into an equation to yield the increase in hydrostatic righting moments due to the presence of trapped air volumes. Both of these are applied below.

Figure 10.5(a) shows the cross-section of a vessel with open bottom tanks (and valves closed). If the vessel is inclined through a small angle, β, then the internal water levels in the port tanks fall while those in the starboard tanks rise relative to the tank sides. The additional pressure

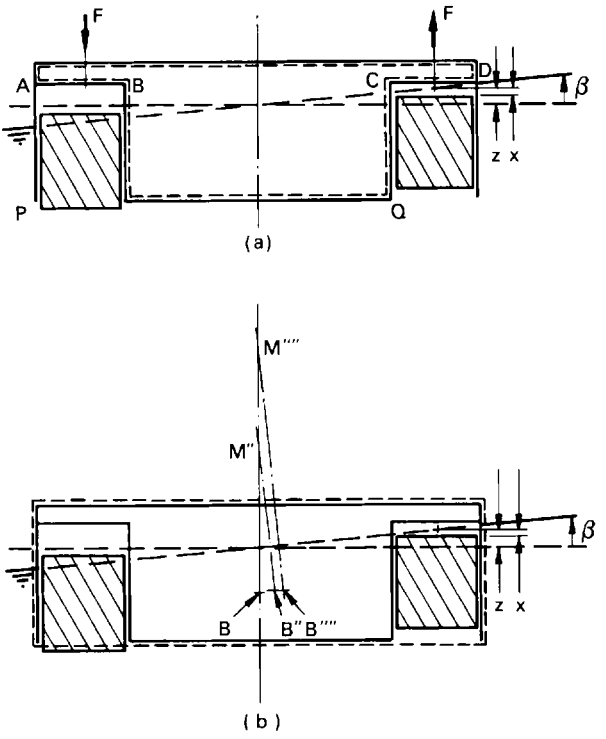

Figure 10.5. Cross-section of ship shape vessel with air tanks; B″ and M″ are centre of buoyancy and transverse metacentre position respectively at heel angle β for vessel excluding water columns in open bottom tanks. B″″ and M″″ are centre of buoyancy and transverse metacentre position respectively at heel angle β for vessel including water columns in open bottom tanks

induced forces due to these water level changes act on horizontal bulkheads AB and CD of the tanks.

The force per unit depression (or elevation) of the tank water level, or the stiffness of the air and water column in vertical motion is given by Equation (10.7). This relationship applies for a mean pressure of one atmosphere in the air cavities. For a small heel angle, β, the depression and elevation of the centre lines of the port and starboard tanks, respectively, are $(b - c)\beta/2$.

The magnitude of restoring moment generated by the forces on the top of the air tank tops (see Figure 10.5(a)) is then

$$= \rho g \cdot (\mathrm{d}I) \cdot \beta \tag{10.21}$$

where

$$(\mathrm{d}I) = \underbrace{2A \frac{(b - c)^2}{4}}_{\text{equivalent } I/D \text{ value}} \cdot \underbrace{\frac{1}{\left[1 + \dfrac{h}{nH}\right]}}_{\text{air correction}} \tag{10.22}$$

constitutes an equivalent 'second moment of water plane area' due to the presence of the tanks.

A righting moment, M_r', for the vessel without the effects of open bottom tanks can then be written as

$$M_r' = \rho g D' \left[\frac{I'}{D'} - B'G'\right] \beta \tag{10.23}$$

where I' is the transverse second moment of water plane area of the vessel excluding air tanks; D' is the vessel displacement excluding water columns in the open bottom tanks; B' is the vessel centre of buoyancy excluding the open bottom tanks; and G' is the position of the centre of gravity of the vessel excluding water columns in open bottom tanks.

Also the total righting moment M_r of the vessel with open bottom tank valves closed is

$$M_r = \rho g D' \left[\frac{I'}{D'} - B'G'\right] \beta + \rho g(\mathrm{d}I)\beta - \rho g(D - D')B'G'\beta \tag{10.24}$$

where $\mathrm{d}I$ is the effective increment in second moment of water plane area due to the air tanks; and D is the vessel displacement including water columns in open bottom tanks. The last term in the above expression accounts for the fact that inclination of the water columns in the open bottom tanks with the vessel leads to a moment couple which is proportional to the initial weight of water columns and the moment arm $B'G'$.

Then the change in righting moment due to the open bottom tanks is given by

$$M_r - M_r' = \rho g(\mathrm{d}I)\beta - \rho g(D - D')B'G'\beta \tag{10.25}$$

This restoring moment can be converted to an effective metacentric height (GM) increase in two ways:

1. The submerged volume of the vessel excluding the open bottom tanks can be used as the reference volume to convert the above equation into an expression for increase in GM.
2. Alternatively, the righting moments experienced by the vessel without and with open bottom tanks can be converted into corresponding GM values by using the appropriate submerged volumes without and with the open bottom tanks.

These approaches give different values for the increase in GM but are consistent if the same procedure is used to convert righting moment to GM values and vice versa.

Approach (1) yields a GM increase of

$$\mathrm{d}(GM) = \frac{(\mathrm{d}I)}{D} - \left[1 - \frac{D'}{D}\right] B'G' \tag{10.26}$$

whereas approach (2) yields

$$\mathrm{d}(GM) = \frac{I' + (\mathrm{d}I)}{D} - \frac{I'}{D'} \tag{10.27}$$

Note that the length of water column that enters the bottom of the open bottom tanks per unit rise of the open bottom tanks relative to local external water level will be given by

$$\frac{\mathrm{d}z - \mathrm{d}x}{\mathrm{d}z} = 1 - \frac{\mathrm{d}x}{\mathrm{d}z} = \frac{\dfrac{h}{nH}}{1 + \dfrac{h}{nH}} = \frac{1}{1 + \dfrac{nH}{h}} \tag{10.28}$$

The above results for hydrostatic righting moments can also be obtained from the conventional approach of taking moments of volumes provided that water column lengths emerging or being drawn into the base of the open bottom tanks are correctly accounted for.

Consider the vessel Figure 10.5(b) with an effective boundary to the vessel denoted by the short dashed line which includes the open bottom tanks. The increment in BM due to the open bottom tanks can then be obtained by taking moments of volume in the horizontal direction.

In Figure 10.5(b), B is the centre of buoyancy of the vessel at zero heel angle and B'' is the centre of buoyancy position at heel angle β for the solid vessel excluding the open bottom tanks; B'''' is a further centre of buoyancy position of the vessel if the effective buoyancy changes due to the open bottom tanks are accounted for.

If the vessel inclines through a small angle, β, the magnitude of the change in external water level at the centre line of each of the open bottom tanks will be $(b - c)\beta/2$ and, therefore, the height of water column that will enter or exit from the open bottom tanks will be

$$\frac{(b - c)}{2} \cdot \left[\frac{1}{1 + \dfrac{nH}{h}}\right] \tag{10.29}$$

Then taking moments of added volumes induced by submergence or emergence of the hull at the free surface less the volumes of the water columns entering or leaving the tanks from their open bottoms yields the equation

$$B''B'''' \cdot D = 2\left[\frac{Lc^3}{12} + A\frac{(b-c)^2}{4}\right]\beta - 2\frac{(b-c)^2}{4}\left[\frac{1}{1+\dfrac{nH}{h}}\right]\beta \tag{10.30}$$

giving

$$B''B'''' \cdot D = 2\frac{Lc^3}{12}\beta + A\frac{(b-c)^2}{4}\left[\frac{1}{1+\dfrac{h}{nH}}\right]\beta \tag{10.31}$$

The above moment increase may be reduced by a correction for the effects of free surface within the open bottom tanks. This removes the first term on the right hand side of Equation (10.31) after which we get

$$M''M'''' = 2A\frac{(b-c)^2}{4}\left[\frac{1}{1+\dfrac{h}{nH}}\right]\beta$$

$$= (\mathrm{d}I)\,\beta \tag{10.32}$$

where M'' and M'''' are metacentre positions corresponding to centre of buoyancy positions B'' and B''''.

The righting moment for the vessel with trapped air valves open is given, as before, by Equation (10.23). The corresponding righting moment with valves closed is

$$M_r = \rho g D\left[\frac{I' + (\mathrm{d}I)}{D'} - BG\right]\beta \tag{10.33}$$

where all of the above variables have been defined earlier. The terms BG and $B'G'$ corresponds to the distances between centres of buoyancy and gravity for the open bottom tanks included and excluded respectively. Since the inclusion of open bottom tanks corresponds to including a weight of water which is directly and exactly supported by its own buoyancy, the shift in centre of buoyancy and centre of gravity due to the inclusion of the tanks will be identical leading to $BG = B'G'$.

The the change in righting moment is

$$M_r - M_r' = \rho g(\mathrm{d}I)\beta - \rho g(D - D') \cdot BG \cdot \beta \tag{10.34}$$

which is the same result as obtained in Equation (10.25).

10.2.4 Verification with model test data

The theory derived above needs to be verified using model tests. The results of this for a monohull and a semisubmersible configuration are presented here.

A significant source of difficulty arises in maintaining dynamic similarity between model and full scale for the behaviour of the stationary vessel in gravity waves. Since both Reybolds number (R_e) and Froude number (F_r) influence the flow around the vessel in waves, these need to be modelled for similarity. Another important parameter characterizing the flow is the amplitude of fluid motion relative to body size. This is usually expressed as the Keulegan–Carpenter number, K_C.

In maintaining similarity of the ratio of inertia to gravity forces (Froude number) for a linear scale force, α, model time scales by a factor $1/\sqrt{(\alpha)}$ of prototype time. Having established the scaling relationship for time, it follows that model scale and prototype Keulegan–Carpenter numbers will be similar. To ensure equal ratios of inertia to viscous forces (Reynolds number) requires kinematic viscosity to scale by a factor of $\alpha^{3/2}$ from prototype to model. The physical impossibility of this means that there is no satisfactory answer to the dilemma and the Reynolds number disparity has to be accepted.

The presence of a pneumatic compliance introduces an additional scaling requirement, that is, dynamic similarity between model and prototype air spring forces. Now, the model scale air force may be written as

$$(F_{air})_m = \frac{-nP'_m A_m^3 (\delta x)_m}{h_m} \tag{10.35}$$

where P_m, is the ambient pressure at model scale with the suffix m referring to model scale values. Furthermore, using the suffix p for prototype scale, the initial air height, h_p, compliant water plane area, A_p, and the displacement, δx, of the water columns may be scaled by the relationships

$$h_p = h_m, \; A_p = \alpha^2 A_m \text{ and } (\delta x)_p = \alpha(\delta x)_m \tag{10.36}$$

Now, to maintain dynamic similarity, the ratio of air forces must equal α^3. However, the above equation gives

$$\frac{(F_{air})_p}{(F_{air})_m} = \frac{\alpha^2 P'_p}{P'_m} \tag{10.37}$$

Reducing atmospheric pressure for model purposes is not a practical consideration but it is possible to increase the model scale air volume, such that

$$V_p = \alpha^2 V_m \tag{10.38}$$

This could be achieved by adjusting either the compliant water plane area or initial air height, or both. The latter would involve the use of air reservoirs situated on the deck. A second option would be to increase air tank wall thicknesses in order to reduce the compliant water plane area while maintaining the outer diameter, and hence horizontal wave loading, constant. This method would conflict with scaling of the water columns and increase hydrodynamic forces on the vessel. For some of the work presented here, air tanks are used to achieve correct air stiffness scaling whereas for the rest direct comparisons are made by using an artificially high (78 times) atmospheric pressure in the calculations.

Tests were carried out on two scale models. The first was a 78th scale model of a drill ship of 24 273 t displacement, 128.0 m overall length, 33.77 m beam, 15.91 m overall depth and 9.52 m draught. The vessel was mounted with air tanks inside sponsons on both beams of the vessel. Each air tank was of the same depth and draught as the vessel and of 4.78 m width running along 106.35 m of the length of the vessel. The tanks on each beam of the vessel wave partitioned into four smaller tanks. Table 10.2 gives a summary of principal dimensions of the hull and air tanks.

A 78th scale model of a twin potooned, eight column semisubmersible with bracing members was used as the second vessel. The vessel had a prototype scale displacement of 22 743 t and an overall length, breadth and height of 97.0 m, 74.4 m and 41.0 m, respectively, with an operating draught of 26.33 m. The principal dimensions are listed in Table 10.2.

Both the ship shape and semisubmersible vessel were subjected to inclining tests which were carried out in three stages. First each model was ballasted down to float at even keel. The position of the vessel centre of gravity was measured by suspending the models from these pairs of lifting points. Static heeling moments were then applied to the vessels and the

Table 10.2 Vessel and open bottom tank particulars – full scale values

Dimensions			*Monohull*	*Semisubmersible*
Displacement			10 779	22 743
Pontoon	Length (m)		–	97.00
	Width (m)		–	11.62
	(Height (m)		–	6.47
Surface piercing hull	Length (m)		114.57	–
	Width (m)		33.77	–
Draught (m)			4.84	26.33
Vessel depth (m)			15.91	41.03
Column diameter (m)	Inner		–	6.44
	Outer		–	8.92
Column spacing	Longitudinal (m)	inner	–	25.50
		outer	–	76.28
	Transverse (m)		–	62.78
Cylindrical bracing diameter (m)			–	1.50
Height of CG above keel (m)			13.86	13.1
Open bottom tanks	Total height (m)		14.35	11.8
	Tank depth below SWL (m)		4.84	6.77
	Height of air column (m)		9.57	5.03
Tank plan areas	On inner columns (m^2)		–	24.84
	On outer columns (m^2)		–	52.88
	On each beam of vessel (m^2)		115.30	–
Distance betwen tank centre line and longitudinal centre line (m)			14.49	31.39

consequent angle of inclination measured with air tank valves open and then with these valves closed. Overturning moments were applied to the vessels by shifting a known mass on the vessel in a transverse direction through a known distance. This permitted the moment to be applied without altering the height of the centre of gravity of the vessel above the keel (the KG value). Heel and pitch angles were measured by a pointer and scale arrangement with an accuracy of $\pm$ 0.3°.

The semisubmersible vessel was tested for small angles of heel (up to 7°) with the trapped air volumes being geometrically scaled only. For large angles, however, emergence of the base of the open bottom tanks above still water level will cause the water columns within such tanks to drain out. In order to demonstrate this feature and to verify the applicability of the theory to it, the ship shape vessel was also tested for large angles of heel of up to 35°. This could not be done at a large draught since the remaining vessel free board was insufficient to prevent the deck edge from submerging and flooding the vessel at large heel angles. The large angle tests were, therefore, carried out for a small draught of 3.74 m (full scale). Furthermore, in order to limit the overturning moments that needed to be applied to the model at large angles of heel with air space valves closed, only valves to one of the air tanks (of plan area 115.30) m^2, full scale) on each beam were closed during the tests, with the remaining valves being kept open. In this configuration, the ship model was tested up to large angles of heel using two values for the trapped air volumes. The first correspond to simple geometric scaling of the trapped air volumes which resulted in the model scale air stiffness being too high. In the second test, the trapped air volumes were increased by using supplementary air reservoirs external to the model which permitted the air stiffness to be scaled correctly.

The results of the inclining tests for the ship shape and semisubmersible vessel are presented in Figures 10.6 and 10.7 respectively.

The theory developed in the earlier sections was implemented for the two vessels with the dimensions and principal particulars listed in Table 10.2. It uses an ambient pressure that is higher than atmospheric (by the model scale factor) to account for the requirements of the scaling rules. The slopes of the righting moment curves at zero angle of heel are compared by evaluating predicted and measured metacentric heights. Note that the metacentric heights are evaluated by using the submerged volume of the vessel excluding the air space and water column volumes. These are listed in Table 10.3 for both vessels. The theoretical predictions are listed for both isothermal and adiabatic air processes. The overturning moments are plotted together with measured data on Figures 10.6 and 10.7.

Figure 10.6 presents monohull inclining moment against angle of heel using both geometric and air stiffness scaling of the trapped air volumes. The curve for trapped air valves open to atmosphere shows the characteristic features of a conventional righting moment variation with first an increase and then a reduction in the slope of the curve as angle of heel increases. With the trapped air valves closed, the sharp drop in righting moment due to loss of water column in the emerging open bottom tanks can also be observed. This feature of the righting moment is analogous to down flooding in conventional naval architecture. The resultant drop in righting moment must be accounted for within calculations at large angles

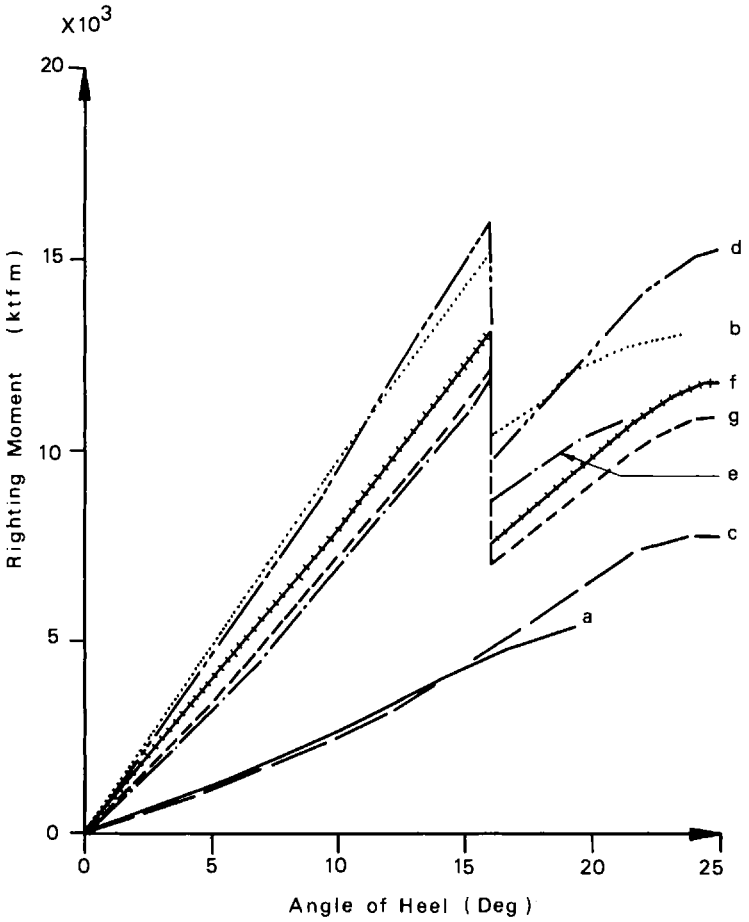

Figure 10.6. Restoring moment against angle of heel for ship shape vessel. *Key*: a – experiment, valves open; b – experiment, valves closed with geometric scaling; c – theory, valves open; d – theory, valves closed with geometric scaling for n = 1.000 and 1.398; e – experiment, valves closed with air stiffness scaling; f – theory, valves closed with air stiffness scaling for n = 1.398; g – theory, valves closed with air stiffness for n = 1.000

of heel. The theory presented in Figure 10.6 incorporates large angle effects using the pressure integration technique presented in Chapter 3. The use of geometric or air stiffness scaled trapped air volumes leads to differing righting moment curve slopes due to the resultant change in air stiffness. The predicted and measured righting moments of Figure 10.6 show reasonably good agreement.

Corresponding results for the semisubmersible are presented in Figure 10.7 for three conditions. Two of these correspond to all tanks open and all valves closed. An intermediate condition is also presented which corresponds to the vales on the central four columns being closed, together with valves on one of the three segmented tanks in each of the four corner columns being closed. Theoretical predictions are presented for both

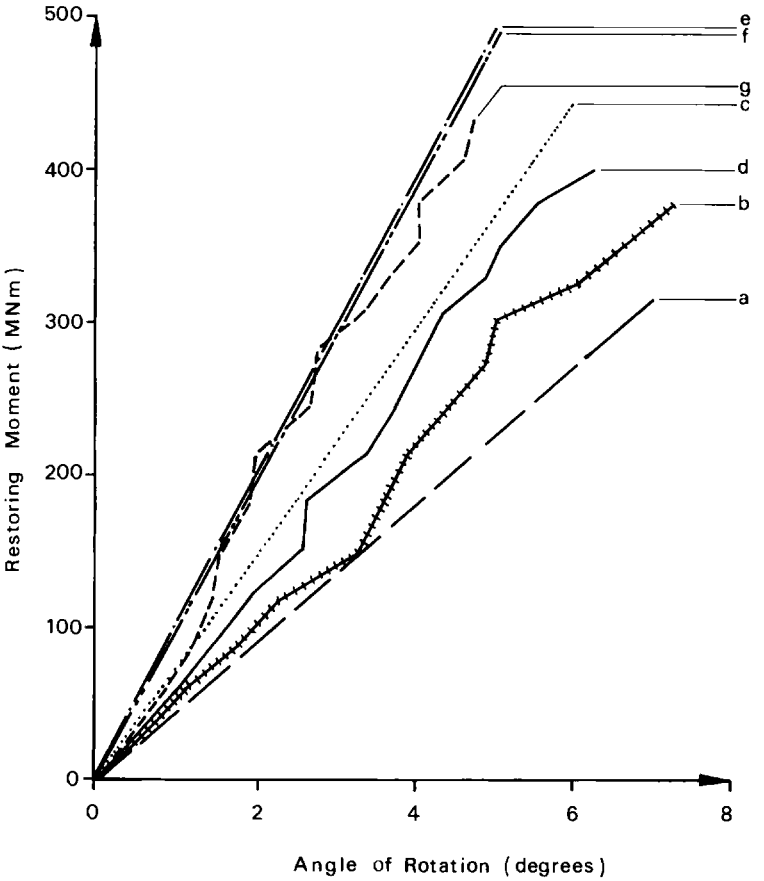

Figure 10.7. Restoring moment against angle of heel for semisubmersible vessel. *Key*: a – theory, valves open; b – experiment, valves open; c – theory, state 2; d – experiment, state 2; e – theory, valves closed for n = 1.398; f – theory, valves closed for n = 1.000; g – experiment, valves closed

isothermal and adiabatic conditions. It should be pointed out here that for both the ship shape and semisubmersible vessel the results predicted by theory do depend on the measured vessel centre of gravity position, to which the restoring moment is quite sensitive. This is the only significant source of error in the comparisons between tests and theory.

10.2.5 Design considerations

The theoretical expressions and model test data presented in this paper raise the question of whether the air compression and rarefraction process behaves in an isothermal or adiabatic manner. If it is assumed that the air temperature in the chambers can equalize during each compression and expansion then the process is isothermal, in which case the polytropic constant, n, should be 1.0. Alternatively, if the assumption of no heat

Table 10.3 Predicted and measured metacentric height – full scale values

Vessel	*Conditions*	*Metacentric heights (m)*					
		Roll			*Pitch*		
		Theory		*Model tests*	*Theory*		*Model tests*
		Isothermal	*Adiabatic*		*Isothermal*	*Adiabatic*	
Monohull	All vales open	1.34	1.34	1.42	–	–	–
Air stiffness scaling	All valves closed for 2 tanks	3.78	4.15	3.61	–	–	–
Monohull	All valves open	1.34	1.34	1.42	–	–	–
Geometric scaling	Valves closed for 2 tanks	5.03	5.03	5.35	270.42	270.42	268.22
Semisubmersible	All valves open	11.42	11.42	12.12	12.69	12.69	–
	All valves closed	24.75	24.79	23.94	26.83	26.88	
Geometric scaling	All inner column and 1 segment of outer columns closed	18.72	18.75	17.60	17.86	17.89	–

transfer to or from the air volume is applied, then an adiabatic process exists and n equals 1.398, the ratio of specific heat capacities at constant pressure and constant volume. The analysis of Sections 10.2.1, 10.2.2 and Table 10.1 shows that, for vessels at full scale, the choice of index of compression or expansion does not alter the air stiffness dramatically but the changes are still significant. It is reasonable to believe that for the vessel responding to wave action, the air stiffness should be based on an adiabatic process since the wave frequencies present in a typical wave spectrum are high enough to prevent temperature equalization between the air volume and surroundings. On the other hand, for the inclining tests carried out in this work, an isothermal air process should occur since the time scale for each test was of the order of 30 min.

The model tests presented here are carried out with Froude number scaling, which means that for correct scaling of the force from trapped air volumes, the model scale atmospheric pressure needs to be reduced by the linear scale factor 78. Since this is not possible tests on the ship model have been carried out in two ways – firstly using geometric trapped air volume scaling and secondly obtaining correctly scaled trapped air stiffness by increasing the trapped air volume of the model by the scale factor. Note that geometric scaling of the trapped air volumes substantially reduces the relative effects of the trapped air process on the righting moment and, therefore, makes it impossible to use the comparison of theory with model tests to determine whether the trapped air process is isothermal or adiabatic. As an example, for the semisubmersible vessel at model scale, the increment in stiffness due to compression and expansion of the trapped air volumes being considered adiabatic rather than isothermal is only

0.2%, whereas at full scale this increment is 9.5%. Figure 10.6 presents large angle righting moment curves for the geometrically scaled and air stiffness scaled trapped air volumes. The agreement between theory and model tests is good. The drop in righting moment due to dewatering of the emerging tanks is also correctly predicted. The theory is implemented in this latter case by applying the righting moment equation for the open bottom tanks on one beam of the vessel only and taking due account of the resultant change in draught and centre of flotation position of the asymmetrically buoyant vessel. It can be seen from the comparison between theory and tests for the air stiffness scaled case in Figure 10.6 that the trapped air volume appears to be behaving isothermally. This is to be expected since the righting moment tests were carried out over time scales which were long enough for a large degree of temperature equalization to occur between the trapped air and its surroundings.

Nevertheless, even with representative air stiffness the difference in stiffness increment between isothermal and adiabatic air processes is reasonably small. From the point of view of certification, since the isothermal air process leads to lower righting moments, it would be conservative to assume this for assessing stability criteria.

The theory presented earlier demonstrates that a consistent relationship may be defined for the hydrostatic righting moment contributions of open bottom tanks by using either first principles or conventional consideration of moments of submerged volume. However, the definition of equivalent increase in GM is dependent on selection of the reference displaced volume of the vessel. This displaced volume can be selected to be either:

(a) the displaced volume around the 'hard' submerged boundary of the vessel and excluding the open bottom tanks, as in Figure 10.5(a), when considering both valves open and valves closed cases; or
(b) the displaced volume around the outer envelope of the ship and including the open bottom tanks, as in Figure 10.5(b), when the valves are closed but using the definition in (a) above when the valves are open.

In either case, calculations of change in righting moments from GM values must reflect the reference volumes used to derive such lengths in the first place. These righting moments will then yield consistent results.

Furthermore, calculations in terms of moment arms (called GZ in conventional naval architecture) also require that the displaced volume for conversion of righting or disturbing moments to GZ values is kept consistent in all the calculations such that the magnitudes of righting and disturbing moments remain unchanged.

10.3 Semisubmersible vessels

This section describes the mechanics of incorporating passive open bottom air tanks for improving the motion response in waves of semisubmersible vessels. Section 10.1 describes the basic mechanism for ocean waves exerting heave forces on semisubmersible vessels and the way in which

trapped air in open bottom tanks modifies this mechanism. This can be further illustrated by example calculations on the semisubmersible vessel shown in Figure 10.1. The annular open bottom tanks on this vessel are subdivided by radial bulkheads (Figure 10.2). These tanks' subdivisions can be used to illustrate the operation of the tanks by progressively activating their action. If all the valves are open, the vessel can be regarded as being in a condition known as state 0. When all chambers on the four inner columns are closed, the vessel is in an operational mode called state 1. Closure of each of the three independent chambers on the four outer columns in addition to the four inner columns corresponds to system states 2, 3 and 4, such that state 4 represents the maximum compliant water plane area. Figure 10.8 shows calculated progressive heave force reductions as the magnitude of the active compliant water plane area increases. The actual wave induced forces on the rigid vessel (that is, the drag, inertia and wave pressure forces) are equal for all the states. However, the force presented here includes the air spring force which accounts for the appreciable reduction of the secondary peaks. Thus, at a given frequency it is possible to reduce the net heave force and, therefore, motion response.

A hydrodynamic analysis for calculating the wave induced motion response of a conventional semisubmersible vessel in its six rigid body degrees of freedom is used as a starting point for the theoretical work described here – see Chapter 5 for further details.

Figure 10.1 shows the reference axis system used in the calculation. The *Gxz* axes are taken in the vessel's fore and aft vertical plane of symmetry with the centre of gravity taken as the origin and the *Gz* axis vertically upwards. For vessels with lateral symmetry about the *Gxz* plane, these correspond to principal axes.

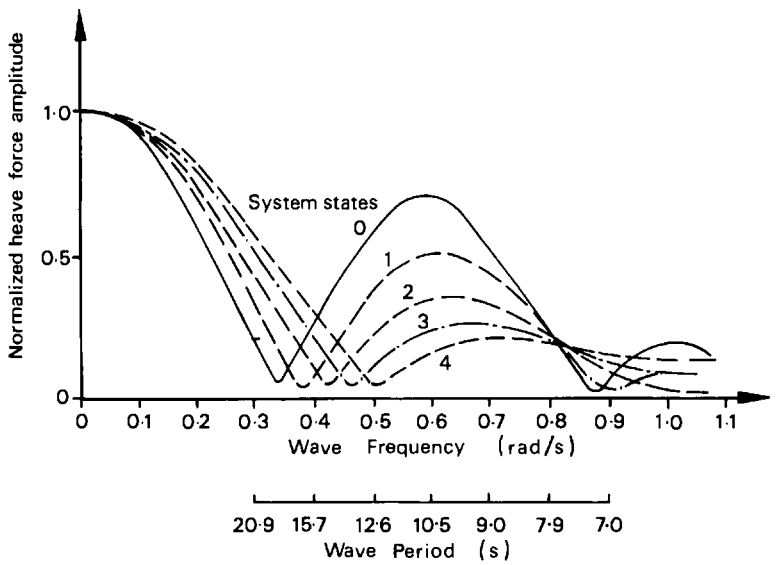

Figure 10.8. The effects of system states on the net heave force

The semisubmersible model is based on a Morison formulation. The resultant rigid body equation of motion for the vessel in six degrees of freedom is rewritten here for convenience:

$$(\mathbf{M} + \mathbf{M}_A)\ddot{\mathbf{X}} + \mathbf{B}|\dot{\mathbf{X}}|\dot{\mathbf{X}} + (\mathbf{K} + \mathbf{K}_M)\mathbf{X} = \mathbf{F}(t) \tag{10.39}$$

where $\mathbf{X}$, $\dot{\mathbf{X}}$ and $\ddot{\mathbf{X}}$ are the six component column vectors of displacement, velocity and acceleration in surge, sway, heave, roll, pitch and yaw respectively; $\mathbf{M}$ and $\mathbf{M}_A$ are the (6×6) matrices of structure mass and added mass respectively; $\mathbf{B}$ is a (6×6) matrix representing the non-linear drag induced damping contribution; $\mathbf{K}$ and $\mathbf{K}_M$ are (6×6) stiffness matrices contributed by hydrostatic and mooring restoring forces respectively; and $\mathbf{F}(t)$ is the wave force.

All the remaining details of the analysis are given in Chapter 5. This rigid body analysis in six degrees of freedom is now extended to a multi-degree of freedom solution.

The air tanks are considered as part of the vessel structure but the water columns are treated as individual degrees of freedom. The added mass of the water columns is calculated by assuming the added volume for a vertical cylinder to be equal to that of a hemisphere of equal radius. If r_1 is the radius of a column leg, and r_2 is the inner radius of a heave can, then the added mass of a water column is expressed as

$$m_a = \tfrac{2}{3}\rho\pi(r_2^3 - r_1^3) \tag{10.40}$$

Damping is taken to be 10% of critical and the hydrostatic stiffness is calculated as if the water column were a solid annulus. The wave force on the water column is calculated to be the force resulting from changes in wave dynamic pressure evaluated at the base of each column.

The equations of motion can then be written as

$$\begin{bmatrix} \mathbf{m}_1 \; (6 \times 6) & 0 \\ 0 & \mathbf{m}_2 \; (q \times q) \end{bmatrix} \ddot{\mathbf{X}} + \begin{bmatrix} \mathbf{b}_1 \; (6 \times 6) & 0 \\ 0 & 0 \end{bmatrix} |\dot{\mathbf{X}}|\dot{\mathbf{X}} + \begin{bmatrix} 0 & 0 \\ 0 & \mathbf{b}_2 \; (q \times q) \end{bmatrix} \dot{\mathbf{X}}$$

$$+ \begin{bmatrix} \mathbf{k}_{H_1} \; (6 \times 6) & 0 \\ 0 & \mathbf{k}_{H_2} \; (q \times q) \end{bmatrix} \mathbf{X} + \begin{bmatrix} \mathbf{k}_{a_3} \; (6 \times 6) & \mathbf{k}_{a_2} \; (6 \times q) \\ \mathbf{k}_{a_3} \; (q \times 6) & \mathbf{k}_{a_4} \; (q \times q) \end{bmatrix} \mathbf{X} = \mathbf{F}(6 + q \times 1) \tag{10.41}$$

where $\mathbf{m}_1$ contains the vessel mass and added mass matrices; $\mathbf{b}_1$ and $\mathbf{k}_{H_1}$ are the vessel damping and hydrostatic stiffness matrices; and q is the number of air tanks. The restoring forces contributed by the mooring stiffness matrix, $\mathbf{F}$ are the vessel wave forces in surge, sway, heave, roll, pitch and yaw, respectively, the remaining q being the forces on each water column.

The terms $\mathbf{m}_2$, $\mathbf{b}_2$ and $\mathbf{k}_{H_2}$ are the mass and added mass, damping and hydrostatic stiffness matrices for the water columns (in which only the leading diagonal terms are non-zero).

In Equation (10.41), equivalent linearization of the vessel damping term is included, although the water column damping is taken to be linear. The additional stiffness matrix, $\mathbf{k}$, represents the restoring force contributed by the compression and expansion of the air above each water column.

10.3.1 Pneumatic stiffness and hydrostatics

Equation (10.41) represents the equation of motion for a $6 + m$ degree of freedom system, its formulation is more clearly illustrated by considering a two degree of freedom solution in which one vessel motion is coupled in stiffness with a single water column.

A simple mass, spring and damper idealisation of such a system is illustrated in Figure 10.9. The equations of motion can be written in matrix form as,

$$\begin{bmatrix} m_1 & 0 \\ 0 & m_2 \end{bmatrix}\begin{pmatrix} \ddot{x}_1 \\ \ddot{x}_2 \end{pmatrix} + \begin{bmatrix} b_1 & 0 \\ 0 & b_2 \end{bmatrix}\begin{pmatrix} \dot{x}_1 \\ \dot{x}_2 \end{pmatrix} + \begin{bmatrix} k_1 + k_c' & -k_c \\ -k_c & k_2 + k_c' \end{bmatrix}\begin{pmatrix} x_1 \\ x_2 \end{pmatrix} = \begin{pmatrix} f_1 \\ f_2 \end{pmatrix} \tag{10.42}$$

assuming there is no damping in the air volume.

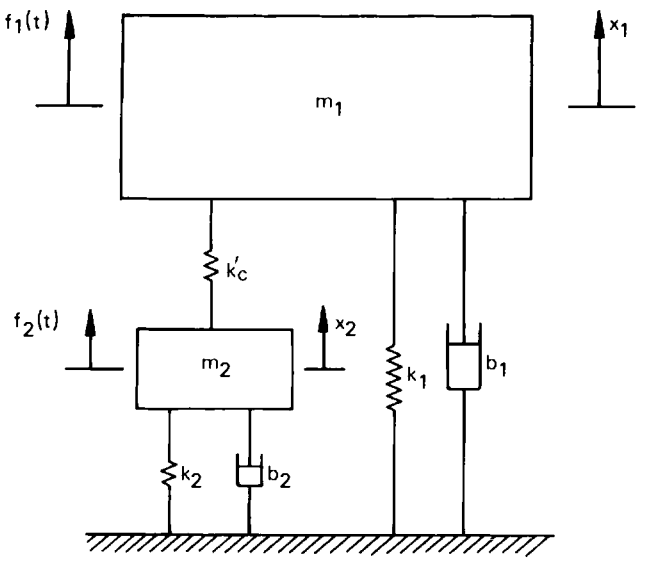

Figure 10.9. Two degrees of freedom mass, spring and damper idealization

If the coupling stiffness, k_c', is set equal to zero, the systems are uncoupled yielding two independent differential equations which can be solved for x_1 and x_2; k_c' is derived by considering the compression and expansion process in the trapped air volumes. Using the work of Section

10.2, the force, F, per relative displacement, x, between the vessel and water column can be writen as

$$\frac{dF}{dx} = -\frac{nP_0A}{h} \tag{10.43}$$

where h is the height of the air volume; A is it's cross-sectional area in plan; P_0 is atmospheric pressure; and n is the gas law index. The value for air stiffness is based on an adiabatic process since wave frequencies present in a typical wave spectrum are considered high enough to prevent temperature equlization between the air volume and surroundings.

Now by using the expression for linear air spring restoring force (Equation 10.43) the air stiffness matrix can be derived. The air springs only affect motions acting in the vertical plane, they have no influence on vessel surge, sway or yaw motions. Referring to Equation (10.41) the partitions of the air stiffness matric, k_a, are

$$\mathbf{k}_a = \begin{bmatrix} 0 & 0 & 0 & 0 & 0 & 0 \\ 0 & 0 & 0 & 0 & 0 & 0 \\ 0 & 0 & k_{33} & k_{34} & k_{35} & 0 \\ 0 & 0 & k_{43} & k_{44} & k_{45} & 0 \\ 0 & 0 & k_{53} & k_{54} & k_{55} & 0 \\ 0 & 0 & 0 & 0 & 0 & 0 \end{bmatrix} \tag{10.44}$$

where

$$k_{33} = \sum_{i=1}^{q} nP_0A_i/h_i,\ k_{44} = \sum_{i=1}^{q} nP_0A_iy_i^2/h_i,\ k_{55} = \sum_{i=1}^{q} nP_0A_ix_i^2/h_i,$$

$$k_{43} = k_{34} = \sum_{i=1}^{q} nP_0A_iy_i/h_i,\ k_{53} = k_{35} = \sum_{i=1}^{q} -nP_0A_ix_i/h_i$$

$$k_{54} = k_{45} = \sum_{i=1}^{q} -nP_0A_ix_iy_i/h_i \tag{10.45}$$

With the notation $c_i = nP_0A_i/h_i$ $(i = 1, q)$, $d_i = -nP_0A_iy_i/h_i$ $(i = 1, q)$, and $e_i = nP_0A_ix_i/h_i$ $(i = 1, q)$, and assuming for simplification that $q = 4$, the partition $\mathbf{k}_{a_2}$ can be written as

$$\mathbf{k}_{a_2} = \begin{bmatrix} 0 & 0 & 0 & 0 \\ 0 & 0 & 0 & 0 \\ -c_1 & -c_2 & -c_3 & -c_4 \\ d_1 & d_2 & d_3 & d_4 \\ e_1 & e_2 & e_3 & e_4 \\ 0 & 0 & 0 & 0 \end{bmatrix} \tag{10.46}$$

and by symmetry $\mathbf{k}_{a_3} = \mathbf{k}_{a_2}^{\mathrm{T}}$

Finally

$$\mathbf{k}_{a_4} = \begin{bmatrix} c_1 & 0 & 0 & 0 \\ 0 & c_2 & 0 & 0 \\ 0 & 0 & c_3 & 0 \\ 0 & 0 & 0 & c_4 \end{bmatrix} \tag{10.47}$$

The full governing equation can then be written as

$$(\mathbf{M} + \mathbf{M}_A)\ddot{\mathbf{X}} + \mathbf{B}_A|\dot{\mathbf{X}}|\dot{\mathbf{X}} + \mathbf{B}_B\dot{\mathbf{X}} + (\mathbf{K} + \mathbf{K}_a)\mathbf{X} = \mathbf{F}(t) \tag{10.48}$$

with the mooring system stiffness excluded; $\mathbf{B}_A$ contains the vessel damping matrix and $\mathbf{B}_B$ represents the linear water column damping terms. Assuming small amplitude sinusoidal motions Equation (10.48) can be re-arranged to give

$$[-\omega^2(\mathbf{M} + \mathbf{M}_A) - i\omega(8/3\pi)\mathbf{B}_A|_{\mathbf{X}_{0_{\text{last approx}}}}| - i\omega\mathbf{B}_B + \mathbf{K} + \mathbf{K}_{aa}]\mathbf{X}_0 = \mathbf{F}_0(\omega) \tag{10.49}$$

which can be solved for $\mathbf{X}$ using standard matrix manipulation to yield the motion response amplitudes and phases in all $6 + q$ degrees of freedom.

The results of the above analysis have been validated against model tests on a $\frac{1}{78}$th model of the configuration shown in Figure 10.1. The scaling laws used are described further in Section 10.2. The inability of scaling atmospheric pressure by the appropriate amount has required that in comparing model tests results with theory, an artificially high atmospheric pressure (by the scale factor 78) is used.

The results of the theory described above and model test results are presented in Figures 10.10 to 10.13.

Figure 10.10 compares experimental and theoretical heave RAOs for the modified vessel in 0.06 m (model scale) head seas. The heave amplitudes are non-dimensionalized with respect to wave amplitude and are plotted

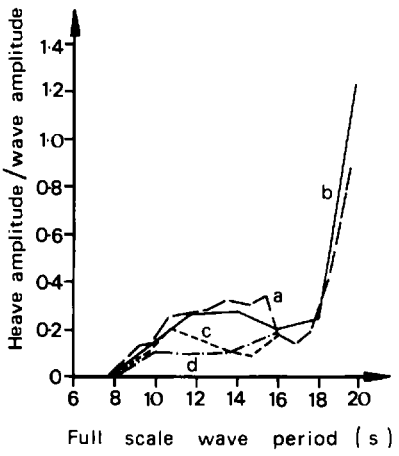

Figure 10.10. Modified vessel heave RAOs in 0.06 m head seas. *Key*: a – state 0, experiment; b – state 0, theory; c – optimum, experiment; d – optimum, theory

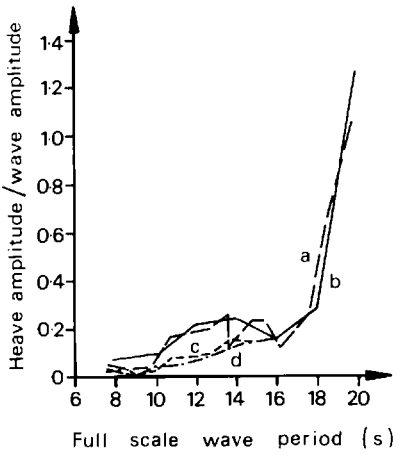

Figure 10.11. Modified vessel heave RAOs in 0.06 m beam seas. *Key*: a – State 0, experiment; b – state 0, theory; c – optimum, experiment; d – optimum, theory

against full scale wave period. The motion suppression capabilities are clearly evident. With an optimized heave response less than 20% of the wave height, for periods up to 16 s the motion has been reduced by up to 50% in the centre of the period range.

Figure 10.11 indicates that heave motion is further reduced in beam seas. Also, roll motions are reduced, as seen in Figure 10.12. When a vessel of this design is in a beam sea the predominant structural members tend to possess the same moment arm relative to the axis of rotation. The air spring restoring forces oscillate in phase with each other and act with the same moment arm as the main vertical hydrodynamic forces, reducing beam sea responses more effectively than those in head seas, for which vertical forces along the pontoon length are more sensitive to changes in wavelength and prone to cancellations.

A comparison of measured regular and irregular wave heave amplitude transfer functions for states 0 and 4 is presented in Figure 10.13. The shift in cancellation frequency and suppressed amplitude response are clearly shown. The high frequency response of the compliant vessel is slightly worse than the state 0 response. At these frequencies state 4 is not the optimum operating condition, the motion could be reduced in an alternative state.

The vessel response in a number of wave spectra (Houmb and Overvik, 1976; and Spidsoe and Sigbjornsson, 1980) can be illustrated by short term response curves such as those presented in Figure 10.14. These curves were formed by generating response amplitude spectra through calculated response amplitude operators (Pedersen *et al.*, 1973). Figure 10.14 indicates that appreciable reductions in heave motions can be obtained in sea states possessing average wave periods of up to 10 s.

Motion suppression using pneumatic compliance is an attractive feature because it has the potential to reduce the motions down-time of a semisubmersible being used for drilling or production purposes. An indirect advantage of the annular tanks retro-fitted to column legs arises from their protection of the stabilizing columns in the vicinity of still water

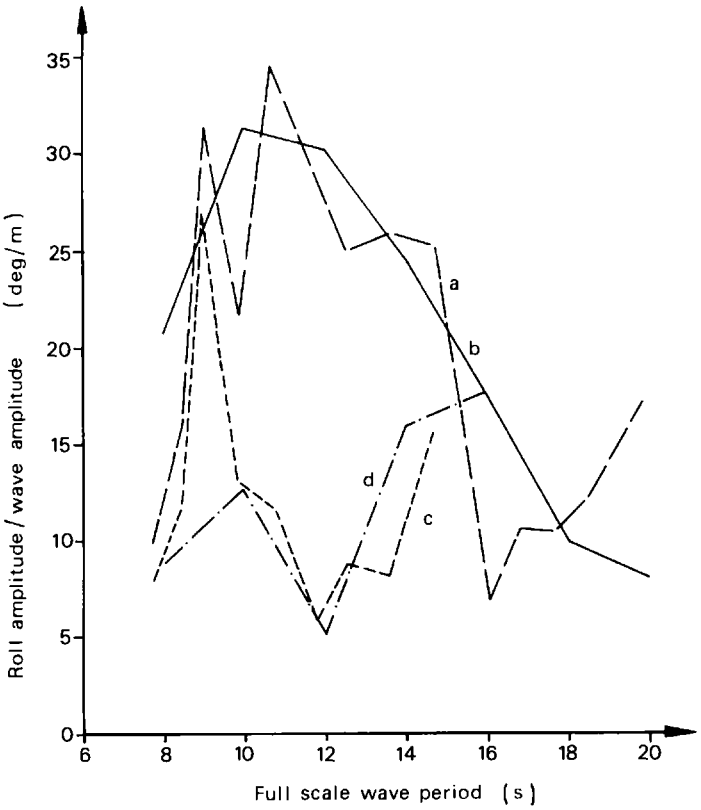

Figure 10.12. Modified vessel roll RAOs in 0.06 m beam seas. *Key*: a – State 0, experiment; b – State 0, theory; c – optimum, experiment; d – optimum, theory

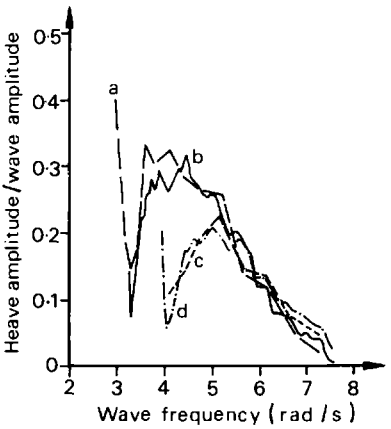

Figure 10.13. Heave amplitude transfer function in a head sea JONSWAP spectrum of 0.03 m significant wave height. *Key*:
a – regular waves, State 0; b – irregular waves, State 0; c – regular waves, State 4;
d – irregular waves, State 4

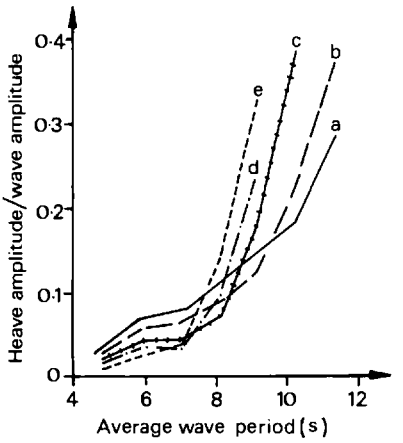

Figure 10.14. Short term heave responses in beam seas for JONSWAP wave spectra. *Key*: a – State 0; b – State 1; c – State 2; d – State 3; e – State 4

level. A collision and breach of the tanks at this level would only affect tank operations and not flood the basic vessel. The system described possesses a simple on/off, manually operated valve system with no active control mechanism. This makes it fail-safe and at any instant it is possible to revert to conventional vessel stability and motion response.

The only penalties of such a system are increased structural weight (although this is only a small fraction of vessel displacement) and slightly higher surge, drift and mooring forces, as well as a small increase in internal forces within transverse bracing members.

10.4 Tensioned buoyant platforms

The tensioned buoyant platform (TBP) is a form of vertically restrained (but horizontally compliant) floating platform that has been described extensively in Chapter 6.

One of the major design problems associated with TBPs is the high level of cyclic tether stresses induced by wave forces on the surface platform. High cyclic stresses reduce the fatigue life of the tethers and also require high pretensions such that the tethers never become slack. These factors complicate the TBP design and usually lead to substantially increased structural weight. It is of fundamental importance to the design that the vessel's geometry is optmized so that the induced tether cyclic stresses are minimized. This optimization is often difficult to achieve satisfactorily because it is constrained by other practical considerations (see Mercier 1982, for example).

The physical mechanism through which vertical wave forces are exerted on tensioned buoyant platforms are such that a large proportion of the local forces exerted on one part of the structure can be cancelled out by opposing forces acting on other parts of the submerged structure. This feature can be illustrated by separating out the heave wave forces in beam seas acting on the pontoons and the columns of the design shown in Figure 10.15. The separate pontoon and column forces, together with the total

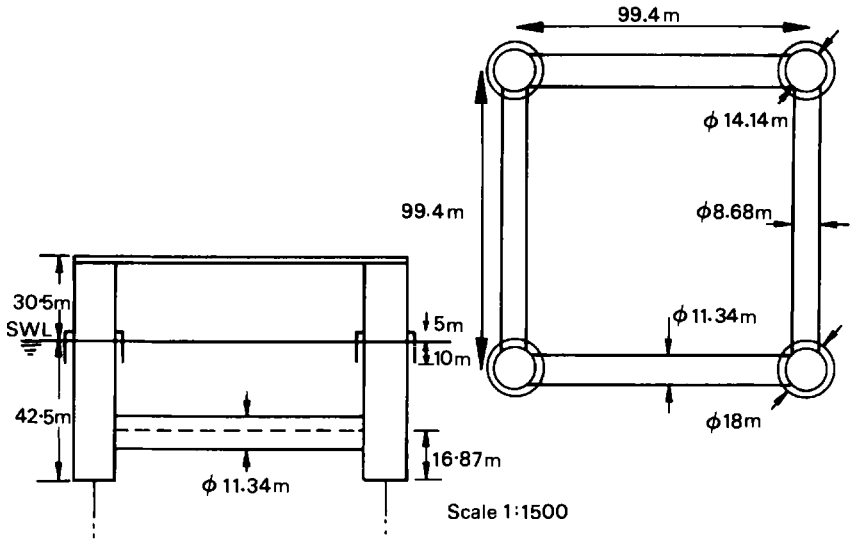

Figure 10.15. Four column TBP

force, are plotted in Figure 10.16(a) as a function of wave period. Curve a denotes the vertical inertia force amplitude acting on the pontoons – this force being 180° out of phase with wave elevation for wave periods between 11 and 18 s. Curve b shows the variation of unbalanced vertical wave pressure force amplitude acting on the surface piercing columns. This force is in phase with wave elevation for large wave periods. Curve c shows

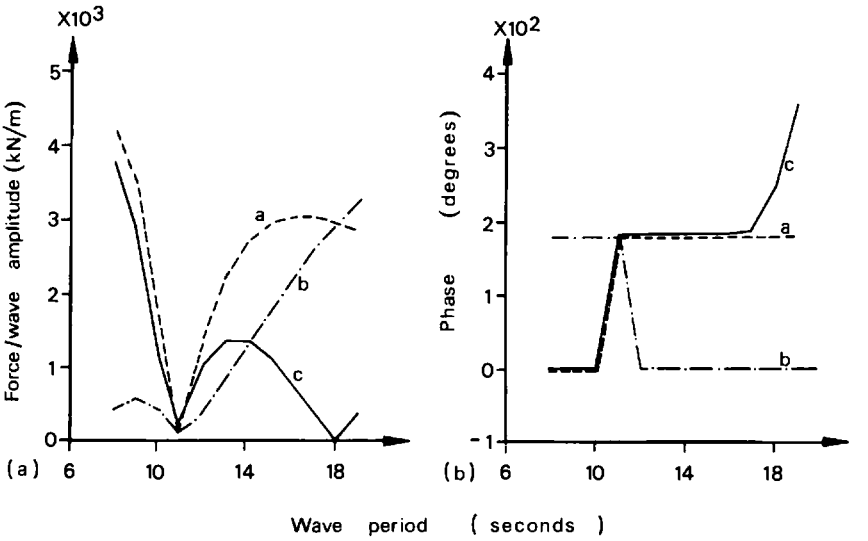

Figure 10.16. Four column tensioned buoyant platform heave wave in beam seas: (a) forces; (b) force phases. *Key*: a – pontoon; b – column; c – total

the variation of total vertical wave force with period and illustrates how the opposing effects of forces denoted by a, and b cancel each other out – this cancellation being complete at wave periods of 11 and 18 s. Note also that the total vertical wave force on the platform is out of phase with wave elevation over a period range of from 11 s to 18 s (Figure 10.16(b)).

This is analogous to the mechanism that operates with semisubmersibles, but differs in detail due to the specific geometry of TBPs. Again as with semisbmersibles, open bottom tanks with trapped air can serve to reduce total vertical wave induced force amplitudes and thus axial tether forces on the platform. Figure 10.17 shows a typical platform layout with configuration details of given in Table 10.4. Figure 10.2 gives a more detailed view of an open bottom air tank.

Now the hydrodynamic analysis of the TBP with open bottom tanks is very similar to that of the semisbmersible except for the inclusion of a tether stiffness matrix. The matrix equation of motion for a TBP, analogous to Equation (10.41) for a semisubmersible, can be written as

$$\begin{bmatrix} \mathbf{M}'_p & \mathbf{0} \\ \mathbf{0} & \mathbf{M}_c \end{bmatrix} \begin{bmatrix} \ddot{\mathbf{x}}_p \\ \ddot{\mathbf{x}}_c \end{bmatrix} + \begin{bmatrix} \mathbf{D}'_p & \mathbf{0} \\ \mathbf{0} & \mathbf{D}_c \end{bmatrix} \begin{bmatrix} \dot{\mathbf{x}}_p \\ \dot{\mathbf{x}}_c \end{bmatrix} + \begin{bmatrix} (\mathbf{K}'_{ph} + \mathbf{K}_{pt}) & \mathbf{0} \\ 0 & \mathbf{K}_c \end{bmatrix} \begin{bmatrix} \mathbf{x}_p \\ \mathbf{x}_c \end{bmatrix}$$

$$+ \mathbf{K}_a \begin{bmatrix} \mathbf{x}_p \\ \mathbf{x}_c \end{bmatrix} = \begin{bmatrix} \mathbf{F}'_p(t) \\ \mathbf{F}_c(t) \end{bmatrix} \tag{10.50}$$

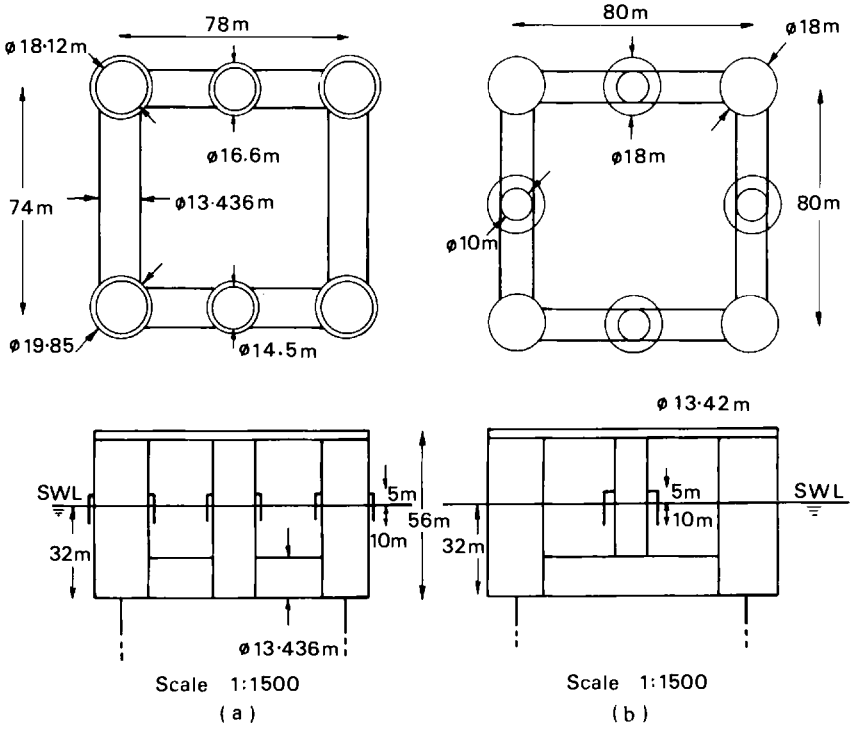

Figure 10.17. Six and eight column tensioned buoyant platforms with open bottom tanks

Table 10.4 Summary of TBP data

	4 column TBP	*6 column TBP*	*8 column TBP*
Displacement (t)	47 700	74 360	73 750
Vertical centre of gravity above keel	38.32 m	28 m	28 m
Draught	42.5 m	32 m	32 m
Outer column spacing	99.4 m	78 m lth 74 m wth	80 m
Outer column radius	7.07 m	9.06 m	9 m
Outer column tank radius	9 m	9.925 m	
Inner column radius		7.25 m	5 m
Inner column tank radius		8.3 m	8 m or 9 m
Cable axial stiffness (kN/m)	56 528.8	258 307.7	258 303.7
Cable pretension (t)	3750	4000	4000
Air tank height above SWL	5 m	5 m	5 m
Air tank depth below SWL	10 m	10 m	10 m
Water depth	500 m	150 m	150 m
Natural periods for TBP with air tanks (s)			
surge	93.7	60.8	61.3
sway	103.8	60.1	61.3
heave	2.9	1.8	1.8
roll	3.2	1.8	1.7
pitch	3.0	1.8	1.7
yaw	91.8	49.9	48.9
Water columns	4.4	4.4 oc 4.3 cc	4.2 or 4.3

Notes:
oc = outer air tanks;
cc = centre air tanks.

The notation used here is different from that of Equation (10.41). Here $\mathbf{M}_c$ is the water column total mass matrix; $\mathbf{D}_c$ is the water column damping matrix; $\mathbf{K}_c$ is the water column hydrostatic stiffness matrix; $\mathbf{F}_c(t)$ is the wave exciting force vector acting on the water columns; $\mathbf{M}'_p$, $\mathbf{D}'_p$ and $\mathbf{K}'_{ph}$ are the corresponding mass, damping and hydrostatic stiffness matrices for the platform; $\mathbf{K}_{pt}$ is the tether stiffness matrix; and $\mathbf{x}_p$ is the (6×1) vector of platform displacements in surge, sway, heave, roll, pitch and yaw; $\mathbf{x}_c$ are the water column displacements. The only coupling between the water columns and the vessel is through the fully populated pneumatic stiffness matrix, $\mathbf{K}_a$. All the submatrices associated with the vessel are of order 6 and if there are 'q' air tanks, then all the square submatrices associated with the water columns are of order q. The pneumatic stiffness matrix, $\mathbf{K}_a$, is of order '$q + 6$'.

This equation of motion can be rewritten as

$$\mathbf{M}\ddot{\mathbf{x}} + \mathbf{D}\dot{\mathbf{x}} + \mathbf{K}\mathbf{x} = F(t)$$

where

$$\mathbf{M} = \begin{bmatrix} \mathbf{M}'_p & \mathbf{0} \\ \mathbf{0} & \mathbf{M}_c \end{bmatrix} \quad \mathbf{D} = \begin{bmatrix} \mathbf{D}'_p & \mathbf{0} \\ \mathbf{0} & \mathbf{D}_c \end{bmatrix}$$

$$\mathbf{K} = \mathbf{K}_a + \begin{bmatrix} \mathbf{K}'_{ph} + \mathbf{K}_{pt} & \mathbf{0} \\ \mathbf{0} & \mathbf{K}_c \end{bmatrix} \quad \mathbf{F} = \begin{bmatrix} \mathbf{F}'_p(t) \\ \mathbf{F}_c(t) \end{bmatrix} \tag{10.51}$$

$$\mathbf{x} = \begin{bmatrix} \mathbf{x}_p \\ \mathbf{x}_c \end{bmatrix} \quad \dot{\mathbf{x}} = \begin{bmatrix} \dot{\mathbf{x}}_p \\ \dot{\mathbf{x}}_c \end{bmatrix} \quad \ddot{\mathbf{x}} = \begin{bmatrix} \ddot{\mathbf{x}}_p \\ \ddot{\mathbf{x}}_c \end{bmatrix}$$

Although, the water column dynamics is incorporated into matrix Equations (10.50) and (10.51), it is instructive to examine the equation of motion for a single column in vertical motion, z_c. The equation can be written as

$$(\rho Ad + m_a)\ddot{z}_c + \dot{c}z_c + \rho g A z_c = (p_{wave} - p)\, A \tag{10.52}$$

where A is the plan area of the column; m_a is the added mass; c is the linear damping coefficient; p_{wave} is the oscillatory wave pressure; p is the instantaneous pressure of the trapped air; and ρ is water density. From linear wave theory p_{wave} is given by

$$p_{wave} = \rho \frac{H}{2} e^{-ikx} \left[\frac{\cosh k\,(z' + d)}{\cosh kd} \right] e^{i\omega t} \tag{10.53}$$

where z' is vertically up from still water level; d is the water depth; k is the wave number; H is the wave height; and ω is wave frequency.

If the pitch (α), roll (β) and heave (z_p) motions of the rig are also taken into account and substituted into the adiabatic gas law relationship,

$$pV^{\gamma} = p_0(Ah)^{\gamma} = \text{constant} \tag{10.54}$$

then

$$p = p_0 \left[1 - \left(\frac{z_c + l_x\alpha - l_y\beta - z_p}{h} \right) \right]^{-\gamma} \tag{10.55}$$

where h is the height of the trapped air column; and (l_x, l_y) are the co-ordinates of the tank vertical centre line in the G_{xy} plane.

Substituting Equations (10.53) and (10.55) into Equation (10.52) gives

$$(\rho Ad + m_a)\ddot{z}_c + c\dot{z}_c + \rho g A z_c + p_0 A \left[1 - \left(\frac{z_c + l_x x - l_y\beta - z_p}{h} \right) \right]^{-\gamma}$$

$$= A\rho g \frac{H}{2} a^{ik(l_x \cos\theta + l_y \sin\theta)} \left[\frac{\cosh(k(D - d))}{\cosh kD} \right] e^{i\omega t} \tag{10.56}$$

where θ is the angle of the incident wave with respect to the x axis. This equation of motion may be linearized by expanding the pneumatic term

and neglecting the higher order terms. The linear equation of motion for the water column then is

$$(\rho Ad + m_a)\ddot{z}_c + c\dot{z}_c + \rho g A z_c + \frac{\gamma p_0 A}{h}[z_c + l_x\alpha - l_y\beta - z_p]$$

$$= \rho g \frac{H}{2} A a \exp[-ik(l_x \cos\theta + l_y \sin\theta)] \left[\frac{\cosh k(D-d)}{\cosh kD}\right] e^{i\omega t} \quad (10.57)$$

The above equation for a single water column is coupled to the platform motions α, β and z_p through the pneumatic stiffness term. It is sensible, therefore, to solve the full platform and water column system of equations and this has been done for three candidate TBPs to illustrate the influence of open bottom tanks on platform motions and tether tensions. Figures 10.15 and 10.17 show the four column, six column and eight column TBPs used for this purpose. The air tanks are positioned on the columns shown – with Figure 10.2 showing details of air tank layout. Table 10.4 gives numerical data on the platform.

Figure 10.18 shows the four column TBP's most loaded tether tension amplitude operator (TAO) as a function of wave period in beam and quartering seas for the platform with and without cans. There is a considerable reduction in the TAO in beam seas for wave periods up to 16 s. This reduction also occurs in quartering seas for wave periods between 9 and 16 s. For periods greater than 16 s the cans increase the TAO. Similarly, Figure 10.19 shows the six column TBP's most loaded tether TAO against wave period for the platform with and without tanks in head and quartering seas. In a similar manner to the four column TBP, there is considerable reduction in the TAO for wave periods around 9–13 s due to the addition of the open bottom tanks. However, the tanks increase the TAO for wave periods greater than 14 s.

These reductions in tether TAO are due to the oscillating water column below the trapped air exerting a force on the platform which opposes the inertia dominated vertical wave exciting forces. In seas of larger wave periods the vertical wave force on the column tends to dominate. This force is in phase with the tank forces, which in turn leads to increased tether tensions. The point at which the exciting force changes over from being dominated by inertia forces on the pontoons to being dominated by column forces depends on the platform geometry, in particular the column to pontoon volume ratio. The tanks may always be deactivated by releasing the trapped air inside the cans. This would return the vessel to very nearly its behaviour prior to tank installation.

Figure 10.18(b) shows an increase in the TAO for the four column TBP in quartering seas of around 8 s wave period. This is because the vessel's geometry is such that the vertical wave exciting forces are in phase with the tank forces and hence increase tether tensions.

Figure 10.20 illustrates the most loaded tether TAO against wave period for the eight column TBP in head and quartering seas. There are three curves on each graph. The first curve gives the TAO for the TBP without open bottom tanks. The second two curves give the TAOs for the vessel with 9 m and 8 m diameter tanks, respectively, on the centre columns.

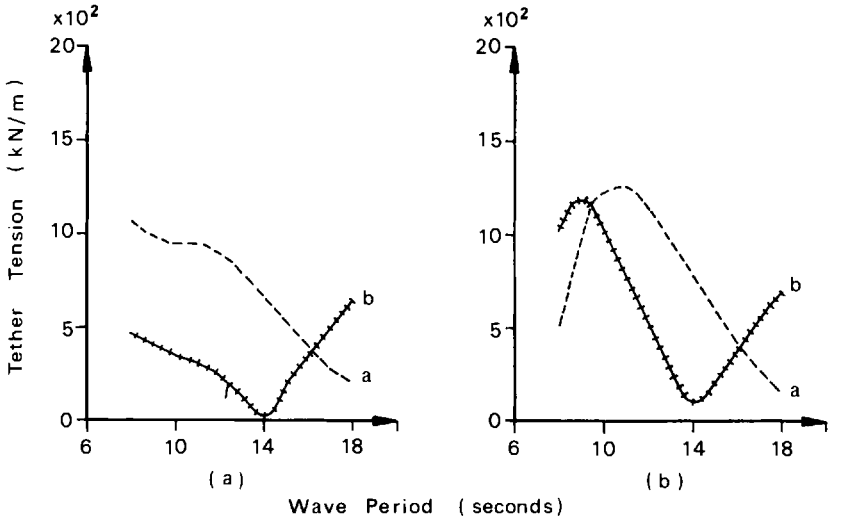

Figure 10.18. Four column tensioned buoyant platform port bow tether tension amplitude per unit wave amplitude: (a) beam seas; (b) quartering seas. *Key*: a – no air tanks; b – air tanks on all columns

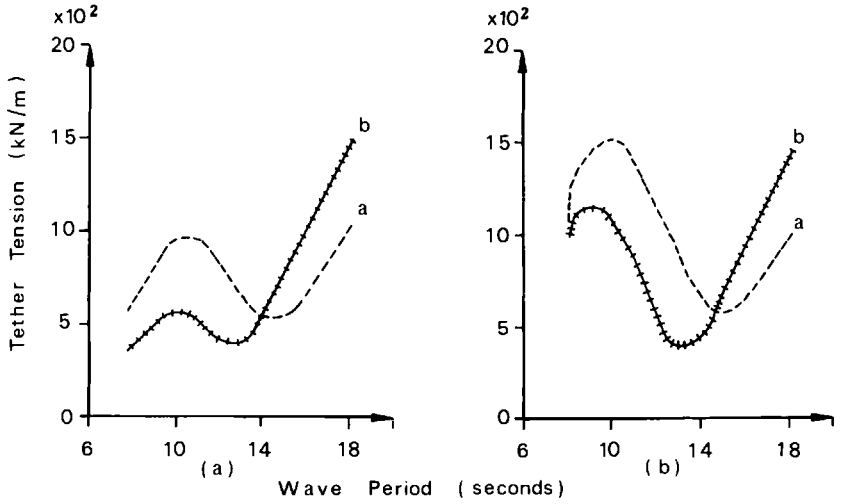

Figure 10.19. Six column tensioned buoyant platform port bow tether tension amplitude per unit wave amplitude: (a) head seas; (b) quartering seas. *Key*: a – no air tanks; b – air tanks on all columns

There is a large reduction in the TAO for wave periods between 8 and 13 s. The amount of reduction depends on the tank diameter since forces due to the tanks are proportional to their plan areas. Subdivision of the tanks into smaller compartments would allow more control since the plan area could be changed by opening or shutting valves to selected compartments.

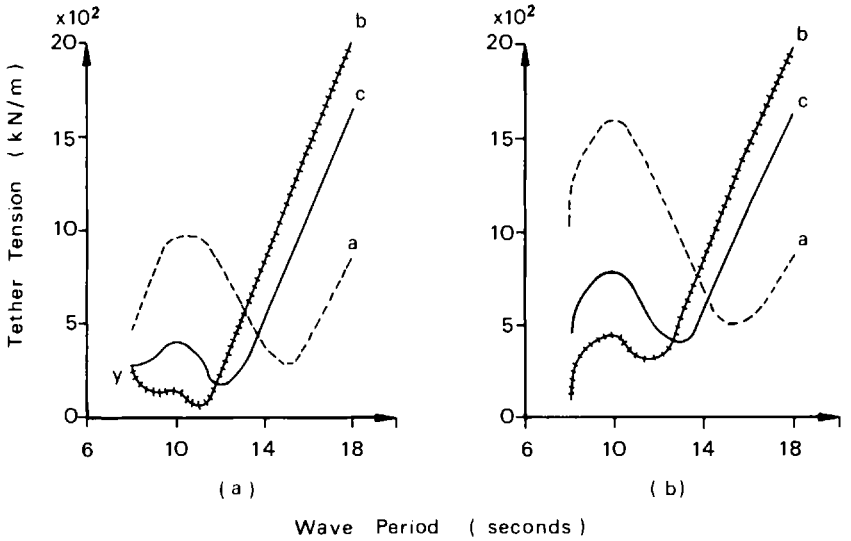

Figure 10.20. Eight column tensioned buoyant platform port bow tether tension amplitude per unit wave amplitude: (a) head seas; (b) quartering seas. *Key*: a – no air tanks; b – 9 m air tanks on centre columns; c – 8 m air tanks on centre columns

An additional feature which influences trapped air behaviour arises from the spatial phase shift experienced by tanks with spacings comparable to incident wave lengths. For practice TBP configurations, the phase shift only plays an important part at low wave periods. However, TBP column spacings and air tank layouts can be designed such that the wave induced pitching or rolling moment amplitudes acting on the tanks are 180° out of phase with the wave induced pitching or rolling moments on the rest of the platform. This, in fact, occurred for the TBPs analysed here for wave periods around 9 s in most seeea states. Although this pitch or roll moment amplitude cancellation only occurs over a narrow wave period range, it can be advantageous to the platform design if the cancellation coincides with a pitch or roll moment amplitude maxima.

The regular wave results have been used to calculate short term TAOs for seas modelled by the JONSWAP wave elevation spectra $S_W(\omega)$ given in Spidsoe and Sigbjornsson (1980). The corresponding tether tension spectrum, $S_T(\omega)$, is given by the usual linear system relationship of

$$S_T(\omega) = [T(\omega)]^2 S_W(\omega) \tag{10.58}$$

where $T(\omega)$ is the tether TAO at frequency ω. The areas under the wave elevation and tether tension spectra (M_W and M_T respectively) were evaluated numerically and then converted into significant wave heights (H_W) and significant tether tensions (H_T) using the relationships:

$$H_W = 4\sqrt{(M_W)} \quad \text{and} \quad H_T = \sqrt{(M_T)} \tag{10.59}$$

The significant tether TAO is given by the ratio H_T/H_W. Figures 10.21 and 10.22 present the significant tether TAO based on the results given in Figures 10.18(a) and 10.19(b) respectively. For the four column TBP,

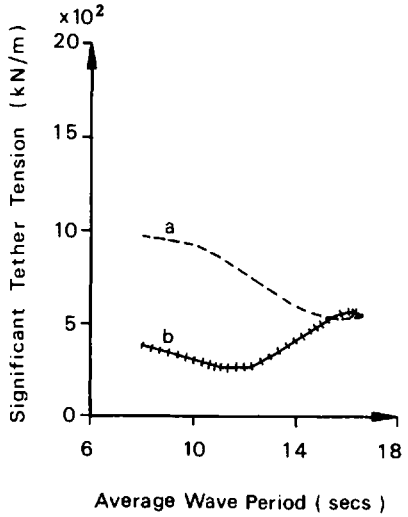

Figure 10.21. Four column tensioned buoyant platform port bow tether significant peak to peak tension per unit significant wave height in beam seas. *Key*: a – no air tanks; b – air tanks on all columns

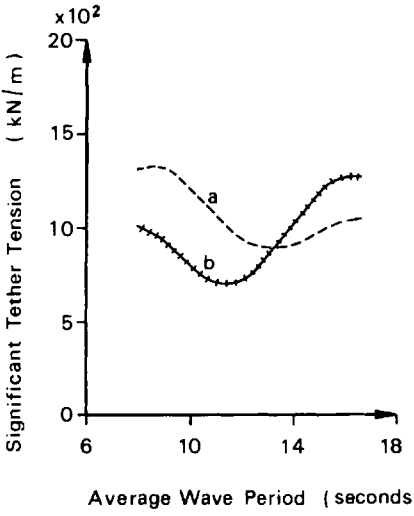

Figure 10.22. Six column tensioned buoyant platform significant peak to peak tether tension per unit significant wave height for tether on port bow in quartering seas. *Key*: a – no air tanks; b – air tanks on all columns

there is a reduction in TAO for beam seas with average wave periods between 8 and 16 s due to the addition of the tanks. Similarly, there is a reduction due to the tanks for the six column TBP's TAO in quartering seas for average wave periods between 8 and 13 s. These results show that the general characteristics of the regular frequency results apply to seas modelled by narrow banded spectra.

The addition of the open bottom tanks will affect the surge, sway and yaw motions of the TBP. Figure 10.23 presents a typical surge response amplitude operator against wave period for the eight column TBP in head seas. It can be seen that the tanks do not have a significant effect on these motions.

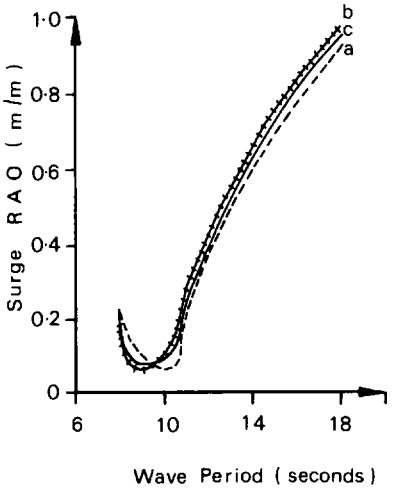

Figure 10.23. Eight column tensioned buoyant platform surge response amplitude operator in head seas. *Key*: a – no air tanks; b – with air tanks (9 m); c – with air tanks (8 m)

The results presented here show that the inclusion of trapped air devices on the columns of a tensioned buoyant platform offers significant reductions in tether tension amplitudes. These reductions can have a far reaching impact on the overall platform design including the choices of tether static pre-tensions and platform strength, among others.

The designer of a TBP is conventionally faced with the task of optimizing a specific platform hull for all likely incident wave conditions. However, the inclusion of trapped air tanks offers the fundamentally different approach of operating a variable geometry platform. The variable geometry arises from the fact that the platform can be operated with the air tank valves open or shut – each condition offering optimum platform performance over a specific wave period range. This mode of operation can be simply attained by valves connecting the trapped air spaces to atmosphere and designed to operate in the fully open or fully shut condition.

Open bottom tanks offer some secondary advantages irrespective of whether they are operated in the fully passive mode (permanently trapped air volumes) or the 'variable geometry' mode (cans with valves which can be opened or shut in). They offer excellent column damage protection and serve to reduce internal oscillating vertical forces within the structure, although horizontal forces on the columns are increased slightly.

10.5 Ship shape hull forms

Open bottom tanks with trapped air on both beams of a ship shape vessel (see Figure 10.3) can be used to reduce the wave induced roll motions of a vessel. The tanks do not, however, modify the heave and pitch motions appreciably because the wave forces inducing these two motions are several orders of magnitude higher than the forces exerted by the air tanks.

Methods of reducing the rolling motions of ships have been pursued since the last century. Some ship stabilizing systems in current use do rely directly on forward motion to generate the necessary forces, whereas a large proportion of vessels used in offshore applications are required to maintain station during operation and can only utilize wave action to modify the vessel's roll response.

A brief overview of roll reduction systems is worth giving at this point.

Watts (1883, 1885) pesented papers on a free surface absorber for roll motion reduction to the Institution of Naval Architects. Although the method was of limited success, it prompted further work by Frahm (1911) on an anti-rolling device utilizing a U-tube configuration. Existing stabilization devices include bilge keels, gyroscopes, active and fixed fins, active and passive tanks and moving weight systems (see Rawson and Tupper, 1976; and Bhattacharyya, 1978). The tank configurations currently in use are all of similar design, extending athwartships and consisting of columns of water that oscillate due to motion of the vessel. By restricting the internal fluid motion, the system can be tuned to the roll natural frequency (Seatek Corporation, 1981), enabling reductions in resonant roll amplitudes.

The use of U-tubes and bottom opening tanks fitted with venting valves has also been investigated with the aim of reducing semisubmersible motions (Bassiouny and Miller, 1982). The latter method was suggested in the early 1900s and uses constricted air flow as a stabilizing damper for ships. The principal reason for this not being extensively developed, however, was that difficulties were encountered in tuning the device at relatively shallow draughts. There were additional problems with both types of device as they were fitted internally to the vessel and, therefore, the presence of an internal waterplane caused a reduction in hydrostatic stability.

On ship shape hull forms, the open bottom tanks for pneumatic compliance are usually mounted along both beams of the vessel, as shown by the hull centre-section cut out at Figure 10.24. Each of the tanks is fitted with a vent valve (or valves) on its upper surface, allowing unrestricted flow of air to and from atmosphere. The valves are either open or closed, with no further control of the air flow being maintained in any form. When the valves are closed, a volume of air is trapped above the internal water level in each tank, the compressibility of the trapped air volume increasing the effective hydrostatic stiffness of the hull in heave, roll and pitch and thus shortening the vessel natural periods in these modes. Hence by opening or closing the vent valves, the vessel can exercise two combinations of natural periods.

In particular, the pneumatic compliance allows a shift in roll natural period which provides the means to avoid resonance by suitable opening or closing of the vent valves depending on incident wave frequencies. As stated earlier, resonant roll motions of monohull vessels are commonly encountered since the roll natural period is almost always in the range of predominant wave periods. Use of open bottom tanks allows the possibility of readily changing the vessel's resonant roll period. In addition, the motions of the water columns within the lower sections of the open bottom tanks generate damping forces which serve to reduce motions further. With a conventional monohull, no convenient and rapid change in roll

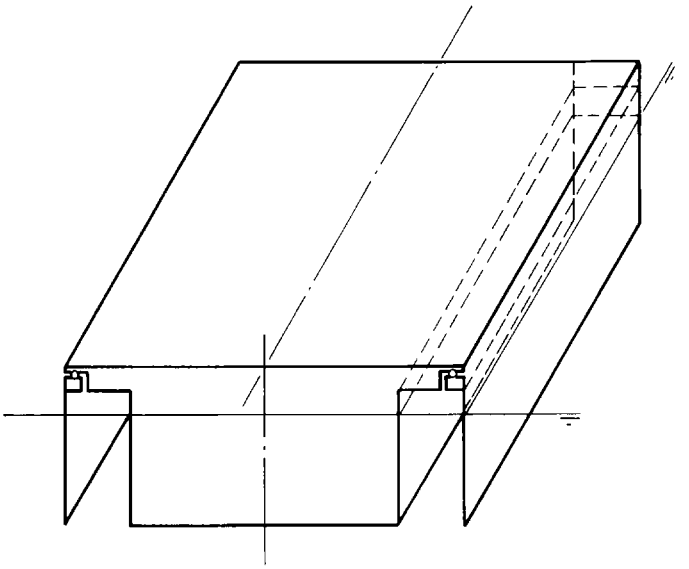

Figure 10.24. Centre section of a monohull with open bottom tanks

natural period is possible and furthermore, resonant roll motions are higher since no additional damping due to water column motions can be utilized.

The equations of motion for a ship shape vessel are identical to those of semisubmersible hull forms described above except that the coefficients have to be obtained using a potential flow diffraction analysis.

The rigid body equation of motion for a ship shape vessel in six degrees of freedom can be written as

$$(\mathbf{M} + \mathbf{M}_A)\ddot{\mathbf{X}} + \mathbf{B}_R\dot{\mathbf{X}} + \mathbf{B}_V|\dot{\mathbf{X}}|\dot{\mathbf{X}} + (\mathbf{K} + \mathbf{K}_m)\mathbf{X} = \mathbf{F} \qquad (10.60)$$

where $\mathbf{X}$, $\dot{\mathbf{X}}$ and $\ddot{\mathbf{X}}$ are six component column vectors of vessel displacement, velocity and acceleration in surge, sway, heave, roll, pitch and yaw respectively. The (6×6) matrix, $\mathbf{M}$, contains the physical mass of the structure, with $\mathbf{M}_A$ being the added mass matrix.

The damping co-efficients in matrix $\mathbf{B}_R$ are associated with a net outward flux of energy in radiated waves and thus represent damping due to the fluid motion only. The viscous damping co-efficients in $\mathbf{B}_V$ are induced by drag forces. The stiffness matrices, $\mathbf{K}$ and $\mathbf{K}_m$, are due to hydrostatic and mooring restoring forces. The six component column vector, $\mathbf{F}$, contains wave induced forces and moments which may be calculated using diffraction theory.

The introduction of pneumatic compliance requires the analysis to be extended for the additional degrees of freedom representing the vertical displacements of each of the water columns. This is done in an identical manner to that used for semisubmersibles and tensioned buoyant platforms in the earlier subsection. It yields the matrix equation

$$\left[\begin{array}{c|c} \mathbf{m}_1 & \mathbf{0} \\ \hline \mathbf{0} & \mathbf{m}_2 \end{array}\right] \ddot{\mathbf{X}} + \left[\begin{array}{c|c} \mathbf{b}_1 & \mathbf{0} \\ \hline \mathbf{0} & \mathbf{b}_2 \end{array}\right] \dot{\mathbf{X}} + \left[\begin{array}{c|c} \mathbf{b}_V & \mathbf{0} \\ \hline \mathbf{0} & \mathbf{0} \end{array}\right] |\dot{\mathbf{X}}|\dot{\mathbf{X}} + \left[\begin{array}{c|c} \mathbf{k}_{h_1} & \mathbf{0} \\ \hline \mathbf{0} & \mathbf{k}_{h_2} \end{array}\right] \mathbf{X} +$$

$$\left[\begin{array}{c|c} \mathbf{k}_m & \mathbf{0} \\ \hline \mathbf{0} & \mathbf{0} \end{array}\right] \mathbf{X} + \left[\begin{array}{c|c} \mathbf{k}_{a_1} & \mathbf{k}_{a_2} \\ \hline \mathbf{k}_{a_3} & \mathbf{k}_{a_4} \end{array}\right] \mathbf{X} = \mathbf{F} \qquad (10.61)$$

where $\mathbf{m}_1$, $\mathbf{b}_1$, $\mathbf{b}_v$, $\mathbf{k}_{h_1}$ and $\mathbf{k}_m$ are (6×6) matrices of vessel mass physical and added masses), radiation damping, viscous damping, hydrostatic stiffness and mooring stiffness respectively. The matrices $\mathbf{m}_2$, $\mathbf{b}_2$ and $\mathbf{k}_{h_2}$ represent the $(q \times q)$ water column mass, radiation damping and hydrostatic stiffness, respectively, for q water columns mounted on the vessel. The air stiffness matric has been expressed by four submatrices which will be discussed in more detail later.

The fluid structure interaction terms associated with the added mass, damping, hydrostatic stiffness and wave exciting forces on the rigid structure needs to be derived using a diffraction analysis. This is based on a conventional boundary element numerical technique. The method uses a linear potential-flow analysis formulated for inviscid, irrotational flow. The submerged vessel surface is represented by a mesh of triangular facets. The application of the no-flow boundary condition at each facet then yields a system of equations that need to be solved for the source strengths. Once these are known, the pressures at the facets are evaluated and their effects integrated over the vessel surface to yield hydrodynamic forces. This technique is described further in Chapter 5.

The pneumatic stiffness coupling terms of Equation (10.61) contributed by the trapped air volumes have already been calculated in Section 10.3.

The potential flow analysis of a ship shape vessel also needs to be extended to incorporate the additional degrees of freedom associated with the vertical displacement of each water column in the same manner as for the semisubmersible vessel. As with conventional rigid vessels, the added mass and radiation damping forces on the water columns are obtained from the forces induced by unit amplitude water column motion in still water – the radiation problem. The forces exerted on a stationary column by incident waves are obtained by solving the alternative diffraction problem. Chapter 5 describes this procedure in further detail. Equation (10.61) can then be readily solved.

Results from the above theory are presented in conjunction with test data obtained from a $\frac{1}{78}$th scale model of the ship shape hull of principal particulars given in Table 10.5.

Figure 10.25(a) and (b) compare experimental and theoretical heave response amplitude operators (RAOs) obtained in a regular wave head sea. Results with and without the pneumatic compliance (valves closed and open) are presented. At wave periods above 9 s, the theoretical and measured heave motions are in agreement with each other, the difference being explained by standing wave effects associated with the test tank. The heave motions with valves closed are slightly higher than those with valves open due to the increased vertical wave forces on the vessel. At wave periods between 6 and 9 s, the predicted results in heave for the vessel with valves open are significantly higher than for measured valves. This is believed to be due to additional viscous damping within the model tests

Table 10.5 Vessel and open bottom tank particulars – full scale values

Particulars			*Monohull*
Displacement (t)			24 273
Pontoon	Length (m)		–
	Width (m)		–
	Height (m)		–
Surface piercing hull	Length (m)		128.00
	Width (m)		33.77
Draught (m)			9.52
Vessel depth (m)			15.91
Column diameter (m)	Inner		–
	Outer		–
Column spacing	Longitudinal (m)	inner	–
		outer	–
	Transverse (m)		–
Cylindrical bracing diameter (m)			–
Height of CG above keel (m)			7.33
Open bottom tanks	Total height (m)		14.28
	Tank depth below SWL (m)		9.52
	Height of air column (m)		4.76
Tank plan areas	On inner columns (m^2)		–
	On outer columns (m^2)		–
	On each beam of vessel (m^2)		394
Distance between tank vessel and longitudinal centre line (m)			16.89

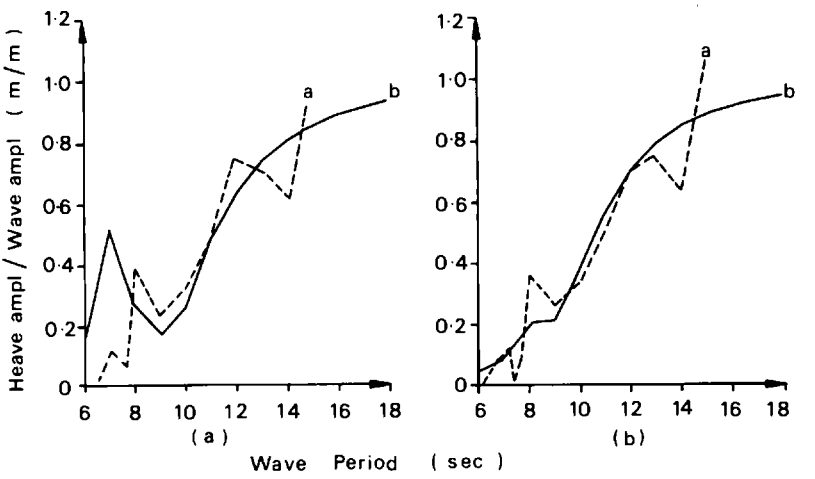

Figure 10.25. Monohull head sea heave RAOs: (a) valves open; (b) valves closed. *Key*: a – experimental; b – theory

that is not represented in the inviscid potential-flow theory. However, the low wave period heave motions for the vessel with valves closed are broadly in agreement with each other.

Measured and predicted pitch motions for the monohull in head seas are presented in Figure 10.26(a) and (b). The pneumatic compliance does not noticeably shorten the pitch natural period because of the comparative magnitudes of second moments of compliant and 'hard' waterplane areas about the vessel's transverse mid-section. Theoretical predictions are in close agreement with measured values at low wave periods, though the agreement is less good at longer wave periods.

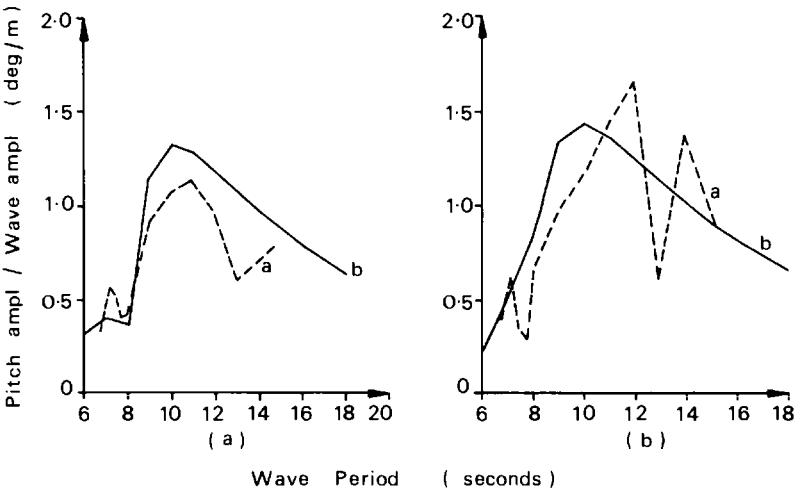

Figure 10.26. Monohull head sea pitch RAOs: (a) valves open; (b) valves closed. *Key:* a – experimental; b – theory

Measured and calculated roll RAOs (roll amplitude per unit wave amplitude) are presented in Figure 10.27(a) and (b). Because the tanks are sited along the vessel beams, their air springs generate a larger increase in effective stiffness in roll than they do in heave or pitch. The shift in roll natural period gives the suppression system a two phase operating strategy, the valves controlling the venting of the trapped air being either open or closed depending on incident wave frequency. By choosing the appropriate operating condition (that is, either opening or closing the valves), the effects of resonance on roll response can be appreciably reduced for a particular incident wave spectrum.

There is a discrepancy between predicted and measured resonant roll amplitudes with the valves open and closed. This suggests that the flow in and out of the open bottom tanks and around the vessel is more heavily damped than calculated by potential-flow theory, implying that wave radiation is not the only source of damping. Viscous drag, such as that due to water column motion inside the tanks, is likely to provide additional damping.

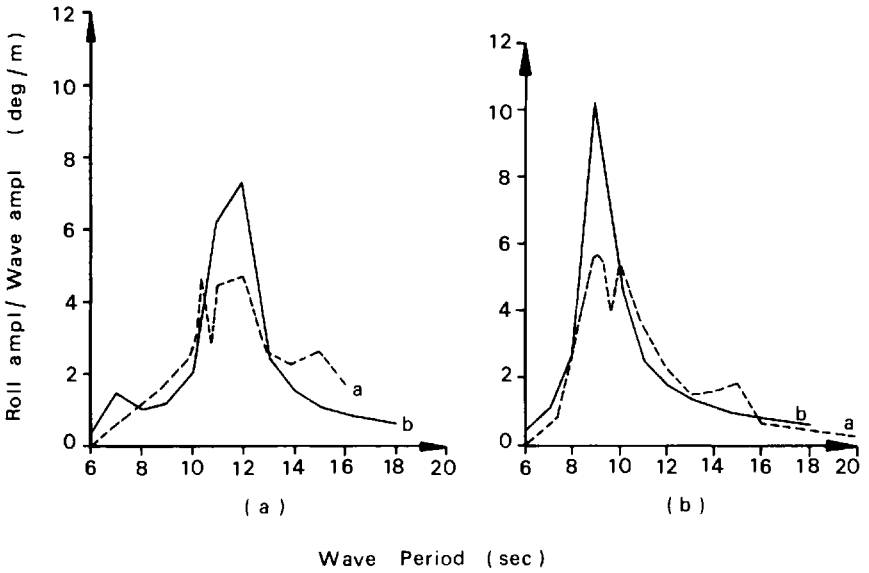

Figure 10.27. Monohull beam sea roll RAOs: (a) valves open; (b) valves closed. *Key*: a – experimental; b – theory

10.6 Active control of trapped air volumes

10.6.1 Motion reduction in waves

The passive use of open bottom tanks, as described earlier, may be extended to an active system by controlling the mass of air trapped inside the air tanks. This is done by blowing to or venting from each of the trapped air volumes by a pneumatic power and control system. Thus, unlike the passive system, the active system requires the valves connecting the tanks to the air reservoirs to open and close within a wave cycle. The changing air masses and the consequent pressure variations exert a heave force and pitch and roll moments on the vessel. By controlling the air masses, these generated forces can be used to counteract wave induced forces and moments and hence reduce motions.

This section examines the use of active air tanks for controlling the heave motions of semisubmersibles. This is done both by means of analysis and computer based simulations of system performance. The results of such calculations are verified by comparisons with model tests at $\frac{1}{78}$th scale. The development of a mathematical model to describe the behaviour of an actively controlled vessel requires that the governing equations for vessel hydrodynamics in the usal six rigid body degrees of freedom need to be extended to account for the additional degrees of freedom due to vertical motions of water columns within the tanks. These equations of motion have to incorporate the thermodynamics of air flows within the system as

well as the spring constants associated with compression and rarefaction of the trapped air. Furthermore, time domain simulations of total system performance heave to include the characteristics of the pneumatic air power equipment (centrifugal blowers and pipe work, for example), control valves, actuators and the control strategy to be used during operation. The above need to be accounted for in order to obtain realistic estimates of system performance and hence its value.

The theory underlying the analysis of a semisubmersible with attached air tanks is illustrated by two approaches. A simplified frequency domain approach is used to demonstrate the reduction of steady state heave motions of a semisubmersible in regular waves. The analysis is then extended to a time domain simulation and its results compared with data from model tests.

10.6.1.1 Frequency domain analysis

A fundamental understanding of the mechanisms which govern semisubmersible heave motions are best illustrated by a simplified frequency domain analysis. Consider the simplest of semisubmersible designs shown in Figure 10.28 with dimensions in Table 10.6(b). The vessel consists of two large parallel pontoons interconnected by relatively small bracing members. Each pontoon has two vertical larger diameter columns which are connected to the deck. The typical heave response of such a vessel shows little sensitivity to the direction of incident waves. Thus, if only head seas are considered and taking account of port-starboard symmetry, the semisubmersible may be idealized as two columns connected by a pontoon, as shown in Figure 10.28, which also illustrates two open bottom tanks attached to each column. This section extends the passive use of trapped air in these open bottom tanks to an active system where the mass of air trapped by each tank is allowed to vary with time. Thus an additional force is exerted on the vessel due to resultant pressure changes which are a consequence of the variations in trapped air masses. By controlling the mass of air in each tank, forces can be exerted on the vessel which oppose external exciting forces and hence reduce the vessel motions.

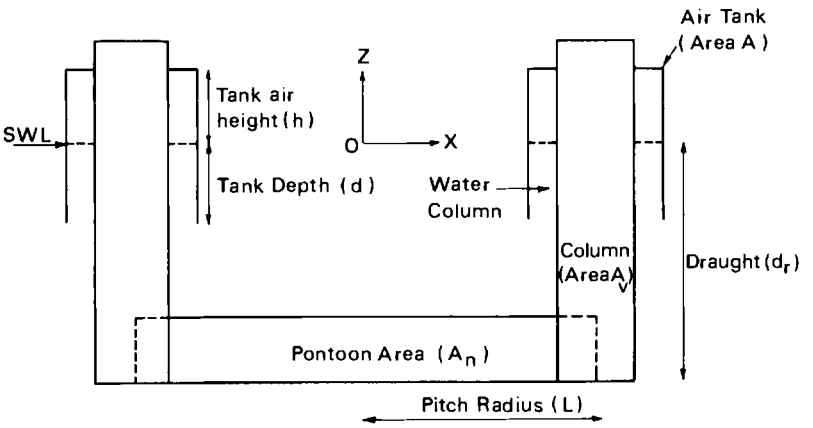

Figure 10.28. An idealized two column semisubmersible

Table 10.6 Semisubmersible data for active control

	Ideal 4 column semisubmersible (A)	*4 column semisubmersible (B)*	*8 column semisubmersible (full scale) (C)*
Displacement (t)	30 200	26 000	22 834
Draught (m)	25.00	20.71	26.47
Pontoon length (m)	90.60	80.56	97.00
Pontoon width × ht (m)	12.8 dia	16.00 × 7.5	11.62 × 6.47
Corner column dia. (m)	10.6	12.0	8.92
Inner column dia. (m)	–	–	6.44
Corner column longitudinal spacing (m)	80.0	54.72	76.28
Inner column longitudinal spacing (m)	–	–	25.50
Pontoon transverse spacing (m)	80.0	54.72	62.78
Bracing diameter (m)	–	2.0	1.5
Corner tank inner diameter (m)	13.0	15.00	6.06
Corner tank outer diameter (m)	–	15.10	6.16
Corner tank air ht(m)	5.0	4.3	5.12
Corner tank depth below SWL (m)	5.0	5.7	6.91
Height of deck above keel (m)	–	–	41.03
Unmodified vessel heave natural periods (s)	23.93	21.99	21.04
Vessel heave natural periods with passive air tanks (s)	20.83	18.58	17.86* 17.29+

* = theory;
+ = experimental

Now consider the equations of vertical motion for the idealized vessel and the water columns shown in Figure 10.30. In this case it is assumed that the disturbing force is due to regular head sea waves, although in principle the disturbing force may be due to any source. The system has three degrees of freedom: the vertical displacement of the vessel (z_1) and the vertical displacements of the water columns (z_2 and z_3) in the bow and stern open bottom tanks respectively. The system has two controllable input variables – the masses of air ($m_f(t)$ and $m_r(t)$) in the forward (bow) tank and the rear (stern) tank respectively.

The following assumptions have been made.

1. The model consists of slender cylinders with respect to incident wave length and the column spacing to diameter ratio is large.

2. Wave forces acting on the vessel and on water columns are evaluated using deep water linear wave theory and Morison's equation. The drag force component of Morison's equation has been neglected and the effects of bracing have been ignored.
3. Vessel and water column displacements are small relative to tank trapped air heights. Perturbations of the trapped air masses are also assumed small.
4. Each water column behaves like a rigid body. The trapped air is assumed ideal and undergoes changes governed by a polytropic process.

Using linearized air stiffness, as derived in Section 10.2, the equation of motion for the semisubmersible can be written as

$$\begin{bmatrix} 2\rho[A_v d_r + L(1 + C_m)A_h] & 0 & 0 \\ 0 & \rho Ad + M_{wc} & 0 \\ 0 & 0 & \rho Ad + M_{wc} \end{bmatrix} \begin{bmatrix} \ddot{z}_1 \\ \ddot{z}_2 \\ \ddot{z}_3 \end{bmatrix}$$

$$+ \begin{bmatrix} c_1 & 0 & 0 \\ 0 & c_2 & 0 \\ 0 & 0 & c_3 \end{bmatrix} \begin{bmatrix} \dot{z}_1 \\ \dot{z}_2 \\ \dot{z}_3 \end{bmatrix} + \begin{bmatrix} 2\rho gA & 0 & 0 \\ 0 & \rho gA & 0 \\ 0 & 0 & \rho gA \end{bmatrix} \begin{bmatrix} z_1 \\ z_2 \\ z_3 \end{bmatrix}$$

$$+ Q \begin{bmatrix} m_f + m_r & -m_f & -m_r \\ -m_f & m_f & 0 \\ -m_r & 0 & m_r \end{bmatrix} \begin{bmatrix} z_1 \\ z_2 \\ z_3 \end{bmatrix}$$

$$= \rho gH \begin{bmatrix} e^{-kd_r}(A_v \cos kL - A_h(1 + C_m)\sin kL) \\ \frac{A}{2} e^{-kd} e^{-ikL} \\ \frac{A}{2} e^{-kd} e^{ikL} \end{bmatrix} e^{i\omega t}$$

$$+ hQ \begin{bmatrix} m_f + m_r \\ -m_f \\ -m_r \end{bmatrix} - \begin{bmatrix} 2p_0 A \\ -p_0 A \\ -p_0 A \end{bmatrix} \tag{10.62}$$

or

$$\mathbf{M}'\ddot{\mathbf{Z}}' + \mathbf{C}'\dot{\mathbf{Z}}' + \mathbf{K}_c'\mathbf{Z}' + Q\mathbf{K}_m(t)\mathbf{Z}' = \mathbf{F}_0 e^{i\omega t} + \mathbf{W}'(t) - \mathbf{H}' \tag{10.63}$$

in matrix notation, where

$$Q = \frac{RT}{h^2}$$

$\mathbf{M}'$ contains the total mass of the vessel and the water columns; the elements of the damping matrix, $\mathbf{C}'$, are estimated as a prescribed

percentage of critical damping; $\mathbf{K}_c'$ is the hydrostatic stiffness matrix; $\mathbf{K}_m$ is the pneumatic stiffness matrix associated with the trapped air in each tank. The first element of the exciting force vector, $\mathbf{F}_0$, is the vertical wave exciting force on the rig. It consists of the summation of the pressure force acting at the bases of columns and the inertia force acting on the pontoon. The remaining elements of $\mathbf{F}_0$ are the forces acting on the water column bases due to pressure changes associated with incident waves; $\mathbf{W}'$ is vector of tank pressure forces acting on the vessel and water columns; $\mathbf{W}'$ is a result of variations in air masses trapped inside the tank, $\mathbf{H}'$ is a constant vector which exists because $\mathbf{W}'$ is expressed in terms of air masses.

The equation of motion (10.63) is too complicated in its present form to solve analytically. Fortunately, $\mathbf{K}_m$ and $\mathbf{W}'(t)$ are known since they are functions of the inputs, $m_f(t)$ and $m_r(t)$, and Equation (10.63) may be solved by using conventional numerical methods. From the control point of view, m_f and m_r may be functions of the state of the system or they may be independently specified.

In order to obtain a frequency domain solution, it is assumed that during active motion suppression, the tank air masses fluctuate harmonically about a mean (m_0) at the same frequency as the wave and with a known controlled amplitude and phase shift with respect to wave elevation at the centre of the vessel. The air masses can then be expressed as

$$\left.\begin{aligned} m_f(t) &= m_0 + Ee^{ia}e^{i\omega t} \\ m_r(t) &= m_0 + Ee^{ib}e^{i\omega t} \end{aligned}\right\} \tag{10.64}$$

where E is the amplitude of the air mass perturbation; and a and b are known phase shifts.

The time variant stiffness $\mathbf{K}_m$ can now be written as

$$\mathbf{K}_m = m_0\begin{bmatrix} 2 & -1 & -1 \\ -1 & 1 & 0 \\ -1 & 0 & 1 \end{bmatrix} + E\begin{bmatrix} e^{ia}+e^{ib} & -e^{ia} & -e^{ib} \\ -e^{ia} & e^{ia} & 0 \\ -e^{ib} & 0 & e^{ib} \end{bmatrix} e^{i\omega t} \tag{10.65}$$

Substituting the above into the equation of motion (10.63) gives

$$\mathbf{M}'\ddot{\mathbf{Z}}' + \mathbf{C}'\dot{\mathbf{Z}} + (\mathbf{K}_c' + Q\mathbf{K}_{m0})\mathbf{Z}' + Q\mathbf{K}_{mt}\,e^{i\omega t}\mathbf{Z}' = (\mathbf{F}_0 + \mathbf{W}_t)\,e^{i\omega t} \tag{10.66}$$

If the air tank system is passive then $\mathbf{K}_{mt}$ and $\mathbf{W}_t$ are zero and the equation of motion becomes a set of second order linear differential equations with constant coefficients. However, if the system is active then the equations are complicated by the time variant stiffness term. If the air mass perturbation is small, then $\mathbf{K}_{mt}$ may be assumed to be negligible. The equation of motion can then be solved by writing the displacement, $\mathbf{Z}'$, as

$$\mathbf{Z}' = \mathbf{X}\,e^{i\omega t} \tag{10.67}$$

and substituting into Equation (10.66) with $\mathbf{K}_{mt}$ taken as zero to yield

$$[\mathbf{K}_c' + Q\mathbf{K}_{m0} - \omega^2\mathbf{M}' + i\omega\mathbf{C}']\,\mathbf{X} = \mathbf{F}_0 + \mathbf{W}_t \tag{10.68}$$

$\mathbf{X}$ can now be obtained by using a standard complex matrix inversion technique.

Although this simplified analysis is concerned with excitation of the system by a sinusoidal disturbing force, it is indicative of the way pneumatic compliance may be used to counteract a general exciting force or moment and thus suppress excessive vessel motions.

10.6.1.2 Time domain simulation

The general equation of motion of a floating vessel with attached open bottom air tanks is

$$\mathbf{M}\ddot{\mathbf{Z}} + \mathbf{C}\dot{\mathbf{Z}} + \mathbf{K}_c\mathbf{Z} + \mathbf{K}_p(t)\mathbf{Z} = \mathbf{F}(t) + \mathbf{W}(t) - \mathbf{H} \tag{10.69}$$

where $\mathbf{M}$ is the mass matrix; $\mathbf{C}$ is the equivalent linear damping matrix; $\mathbf{K}$ is the stiffness matrix which incorporate both hydrodynamic and mooring stiffnesses; $\mathbf{K}_p$ is the time variant pneumatic stiffness matrix; $\mathbf{F}(t)$ is the general disturbing or exciting wave forces vector; $\mathbf{W}(t)$ is the force vector exerted on the vessel due to air pressures inside the tank; $\mathbf{H}$ is a constant force vector which exists due to the fact that $\mathbf{W}(t)$ is expressed as a function of the air mass inside each tank; $\mathbf{Z}$, $\dot{\mathbf{Z}}$ and $\ddot{\mathbf{Z}}$ are the displacement, velocity and acceleration vectors respectively. The displacement vector contains the six rigid body degrees of freedom of the vessel surge, sway, heave, roll, pitch and yaw and q additional degrees of freedom associated with the displacement of the q water column contained within the air tanks.

The equation of motion (10.69) can be then re-expressed as

$$\begin{aligned}\ddot{\mathbf{Z}} &= \mathbf{M}^{-1}[\mathbf{F}(t) + \mathbf{W}(t) - \mathbf{H} - \mathbf{C}\dot{\mathbf{Z}} - \mathbf{K}_c\mathbf{Z} - \mathbf{K}_p(t)\mathbf{Z}] \\ &= f(t, \mathbf{Z}, \dot{\mathbf{Z}})\end{aligned} \tag{10.70}$$

and integrated numerically using a fourth order Runge–Kutta–Nyström method (Kreyszig, 1979). This involves a Taylor's series expansion where fifth and higher order terms are neglected. The terms $\mathbf{W}(t)$ and $\mathbf{K}_p(t)$ are functions of the tank air masses which are related to the system state or external parameters via a chosen control strategy. The above procedure needs to be implemented in a computer program to allow simulation studies to be performed.

Apart from the six rigid body degrees of freedom of the vessel and q water column displacements there are another q variables which describe the system. These are associated with the mass of air (m_i) trapped in the ith air tank, which has two effects on the system. The first is that it influences the pneumatic stiffness matrix $\mathbf{K}_p$ found in Equation (10.69). In general $\mathbf{K}_p$ is given by

$$\mathbf{K}_p = \begin{bmatrix} 0 & 0 & 0 & 0 & 0 & 0 & 0 & 0 & 0 \\ 0 & 0 & 0 & 0 & 0 & 0 & 0 & 0 & 0 \\ 0 & 0 & \sum_{i=1}^{q} k_i & \sum_{i=1}^{q} k_i y_i & -\sum_{i=1}^{q} k_i x_i & 0 & -k_1 & -k_2 & -k_q \\ 0 & 0 & -\sum_{i=1}^{q} k_i y_i & \sum_{i=1}^{q} y_i^2 k_i & -\sum_{i=1}^{q} x_i y_i k_i & 0 & -y_1 k_1 & -y_2 k_2 & -y_q k_q \\ 0 & 0 & -\sum_{i=1}^{q} k_i x_i & -\sum_{i=1}^{q} x_i y_i k_i & \sum_{i=1}^{q} x_i^2 k_i & 0 & x_1 k_1 & x_2 k_2 & x_q k_q \\ 0 & 0 & 0 & 0 & 0 & 0 & 0 & 0 & 0 \\ 0 & 0 & -k_1 & -y_1 k_1 & x_1 k_1 & 0 & k_1 & 0 & 0 \\ 0 & 0 & -k_2 & -y_2 k_2 & x_2 k_2 & 0 & 0 & k_2 & 0 \\ 0 & 0 & -k_q & -y_q k_q & x_q k_q & 0 & 0 & 0 & k_q \end{bmatrix} \tag{10.71}$$

where x_i and y_i are the horizontal co-ordinates of the centre of each air tank. The degrees of freedom are the six rigid body freedoms of surge, sway, heave, roll, pitch and yaw followed by water level displacement in q open bottom tanks. The constant k_i is given by

$$k_i = \frac{nRTm_i}{h_i^2} \tag{10.72}$$

which is the linearized stiffness coefficient expressed in terms of the tank's trapped air mass m_i and the air height h_i. The trapped air also exerts a vertical force on the vessel due to the varying pressures associated with the changing air masses. This is represented by the vector $\mathbf{W}(t)$ in Equation (10.70). In terms of individual air masses, $\mathbf{W}(t)$ is given by

$$\mathbf{W}(t)^{\mathrm{T}} = RT \left[0\ 0 \sum_{i=1}^{q} \frac{m_i}{h_i} \sum_{i=1}^{q} y_i \frac{m_i}{h_i} \sum_{i=1}^{q} x_i \frac{m_i}{h_i} 0 \frac{m_1}{h_1} \frac{m_2}{h_2} \frac{m_q}{h_q} \right] \tag{10.73}$$

and consequently the constant vector, $\mathbf{H}$, is given by

$$\mathrm{H}^{\mathrm{T}} = \left[0\ 0 \sum_{i=1}^{q} p_0 A_i \sum_{i=1}^{q} y_i p_0 A_i \sum_{i=1}^{q} x_i p_0 A_i\ 0\ -p_0 A_i\ -p_0 A_2\ -p_0 A_q \right] \tag{10.74}$$

where A_i is the cross-sectional area of the ith air tank. When the mass of air in each tank is constant then $\mathbf{W}$ equals the constant vector, $\mathbf{H}$, and the pneumatic stiffness, $\mathbf{K}_p$, is also constant.

Experimental investigation of active control

Tests were performed on the model of the type shown in Figure 10.1 in a wave tank. The equipment used consisted of a microcomputer with an

analogue to digital convertor, a digital to analogue converter and a real time programmable clock. This equipment was used to log heave motion of the model, the air pressure inside the tanks and to control the valve position. This experimental set up is illustrated schematically in Figure 10.29. Air pressures inside the tanks were measured using a pressure transducer. The heave motion of the model was measured by a light source at the centre of the model and a camera system which gave a voltage proportional to the vertical position of the light source. The high and low pressure air reservoirs were supplied by a rotary compressor.

The scaling rules used for the tests are identical to those described in Section 10.2. The passive air volumes were modelled to ensure correct scaling of resultant air stiffnesses using Froude number similarity, despite the fact that the ambient pressure at model scale was one atmosphere.

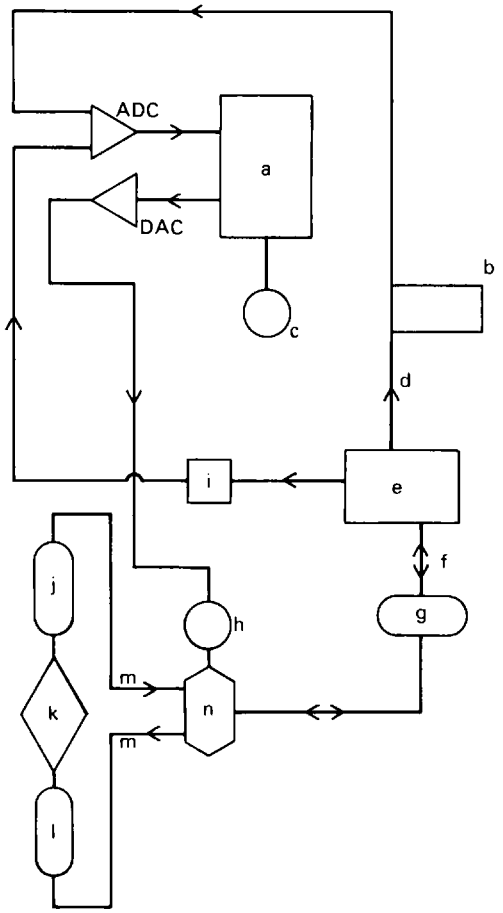

Figure 10.29. Schematic diagram of experimental layout. Lines represent electrical signal paths unless otherwise indicated. *Key*: a – DEC LSI 11/03 microcomputer; b – camera system; c – real time clock; d – displacement; e – model; f – air flow; g – reservoir for scaling purposes; h – positional servo unit; i – pressure transducer; j – high pressure reservoir; k – compressor; l – low pressure reservoir; m – air flow; n – valve

Such scaling was achieved by using large air reservoirs attached to the tank air volumes on the test model – the total model scale trapped air volume being larger by a multiple of the scale factor. Thus the pressure variations used to achieve active control were scaled correctly. However, the individual components and their mechanical properties, the valve and its response time, for example, were not scaled because of the difficulty of such a task.

A valve had to be specifically designed for these tests. It consisted of a rotating, electrically driven spindle mounted in a cylindrical housing with air inlets and outlets on its circumference. The valve spindle was installed with diametrical passages with a shape designed to proportionally increase the flow area as a function of spindle angle of rotation. The valve permits connection of the model vessel's air tanks to the low pressure, or high pressure reservoirs, or to seal the tanks when in its centre position.

10.6.1.3 Control algorithm

Ultimately, the object of introducing pneumatic compliance is to reduce vertical motion of the vessel by controlling the mass of air in each tank. This is done in effect by controlling the mass flow rate ($\dot{m}_i$) associated with each tank. In general, $\dot{m}_i$ will be a function of the state of the system, the rate of change of the state of the system and a function of parameters external to the system. Thus

$$\dot{m}_i = f(\mathbf{X}_s, \dot{\mathbf{X}}_s, \mathbf{E}) \tag{10.75}$$

where $\mathbf{X}_s$ is the state vector; and $\mathbf{E}$ is a vector of external parameters. The state vector contains

$$\mathbf{X}_s^T = [\mathbf{Z}^T, \dot{\mathbf{Z}}^T, \mathbf{m}^T] \tag{10.76}$$

where $\mathbf{Z}$ is the displacement vector; $\dot{\mathbf{Z}}$ is the velocity vector; and $\mathbf{m}$ is the vector containing the masses of air trapped in each tank. If the control is linear, then Equation (10.75) has the form

$$\dot{m}_i = \mathbf{p}_i^T \mathbf{X}_s(t) + \mathbf{q}_i^T \mathbf{X}_s(t) + \mathbf{r}_i^T \mathbf{E}(t) \tag{10.77}$$

where $\mathbf{p}_i$, $\mathbf{q}_i$ and $\mathbf{r}_i$ are constant vectors associated with the ith tank. It is evident that the number of different feasible permutations of $\mathbf{p}_i$, $\mathbf{q}_i$ and $\mathbf{r}_i$ are large. However, by considering the nature of the disturbing force, a suitable control strategy can be derived.

The general featues of a control algorithm for the model tests are described earlier. In practice, difficulties often arise in the implementation because of insufficient information on the state of the system and a shortage of available energy which is needed to achieve the controller's demands. These points are best illustrated by using these experiments as an example. Here only the heave displacement is measured. Thus any control algorithm requiring the velocity or acceleration is demanding information that is not directly available. This information would then have to be obtained indirectly using approximate methods. In addition, the amount of energy available is limited to the compressor and reservoir capacity.

In the experiments, the mass of air in the air tanks was not directly controllable. However, by controlling the air flow between the low and high pressure reservoirs and the air tank the mass of air trapped inside the

tank could be controlled by valve position. Thus these experiments utilized the control strategy that

$$\beta = k_e z \tag{10.78}$$

where β is the valve position; z is the heave displacement of the vessel; and k_e is the experimental constant of proportionality. The controller was set so that when the vessel displaced downwards the low pressure model port opened.

Equation (10.78) reflects the desired control strategy but this had to be adjusted for the experiments in order to allow for the time response of the valve. Thus, the following control strategy was utilized:

If

$$0 < |k_e z| < \frac{\beta_m}{3} \quad \text{then } |\beta| = 0$$

If

$$\frac{\beta_m}{3} < |k_e z| < \frac{2\beta_m}{3} \quad \text{then } |\beta| = \frac{\beta_m}{2}$$

If

$$\frac{2\beta_m}{3} < |k_e z| \quad \text{then } |\beta| = \beta_m \tag{10.79}$$

where sign $(k_e z)$ = sign (β). This control strategy ensures that the valve is either closed, half-open or fully open depending on the range in which k_{ez} falls. In the experiments, large valves of k_e were used so that the valve tended to be either closed or fully open over a large part of the wave cycle.

10.6.1.4 Frequency domain results

The heave motion of a semisubmersible tends to be the limiting criterion in determining whether the vessel can continue to operate. For ocean wave periods of between 4 andf 9 s, the semisubmersible has sufficiently low response so that heave motion does not impose an operational limit. Heave motions become greater in wave periods from 9 to 15 s, making it worth while to consider implementing active control to reduce motions in this period range and thereby reduce vessel down-time.

The heave response of the idealized four columns semisubmersible (Table 10.6) was investigated using the simplified frequency domain analysis. Figure 10.30 shows the heave response of the vessel with and without motion suppression tanks in waves of 2 m height. The results show that there is a significant reduction in heave response due to the passive tanks for wave periods less than 19 s. The question is whether these reductions can be enhanced further by actively controlling the mass of air in each tank. The simplified frequency domain analysis allows the mass of air in each tank to vary sinusoidally by an amount, E, about a mean air mass (m_0). These air mass variations are related to wave elevation at the centre of the semisubmersible by phase shifts a and b (see Equation 10.64).

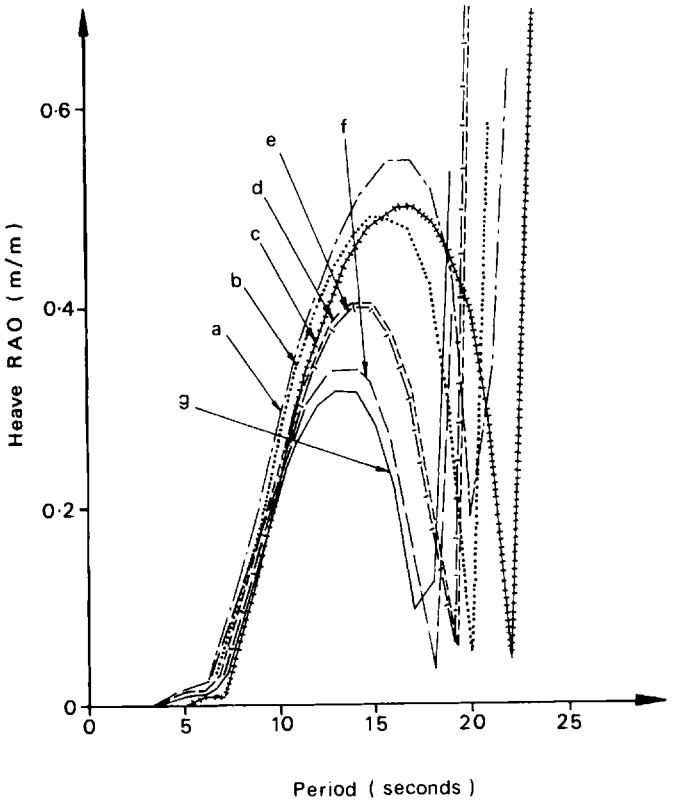

Figure 10.30. Ideal active control of a four column semisubmersible in head seas of 2 m wave height. *Key*: a – 10% control, Phase = 180°; b – 10% control, Phase = 135°; c – no air tanks; d – 10% control, Phase = 90°; e – passive air tanks; f – 10% control, phase = 45°; g – 10% control, phase = 0°

Figure 10.30 presents results from the simplified frequency domain analysis for active control of air masses in the open bottom tanks. The vessel is subjected to waves of 2 m height and the controlling air mass perturbation is set at 10% of the mean air mass with the perturbation phase angles, a and b, set to be equal. This strategy is subsequently referred to as 10% control.

The air mass phases vary from 0 to 180°. Further reductions in heave motions are obtained for phases of less than 90°. The largest reductions are obtained for zero phase when the air masses exert a force on the vessel which is out of phase with the wave exciting inertia force. Active control has no effect if the phase is 90° and the system effectively behaves as if it is passive. However Figure 10.32 shows that if the phase is greater than 90°, the tanks contribute to the wave exciting forces rather than opposing them, thus increasing the total force and hence motions. These results demonstrate that the phase of the control signal is critical to the performance of active control. Lags of up to 90° are permissible with some benefit.

However, increasing log does reduce overall performance. In practice there will always be some lag between the desired and achieved mass flow rates.

Figure 10.31 shows that increasing the amount of control with zero phase reduces the heave response considerably. This is due to the fact that increasing the amount of control increases the tank force and hence reduces net vertical force. However, as wave height increases, wave forces increase in magnitude whereas tank forces generated by active control remain constant for a given amount of control. Therefore, as wave height increases, the amount of reduction in heave response will reduce.

The simplified frequency domain analysis has shown that heave motion reductions are possible with active control for wave periods of between 10 and 15 s, provided that the air mass is varied in phase with wave elevation at the centre of the vessel. For wave periods of interest, the heave response is effectively in phase with wave elevation. Thus the simplified frequency domain analysis has identified the control strategy where the mass of air (m) trapped in the tanks must be proportional to the vessel's heave displacement (z) to yield

$$m = kz \tag{10.80}$$

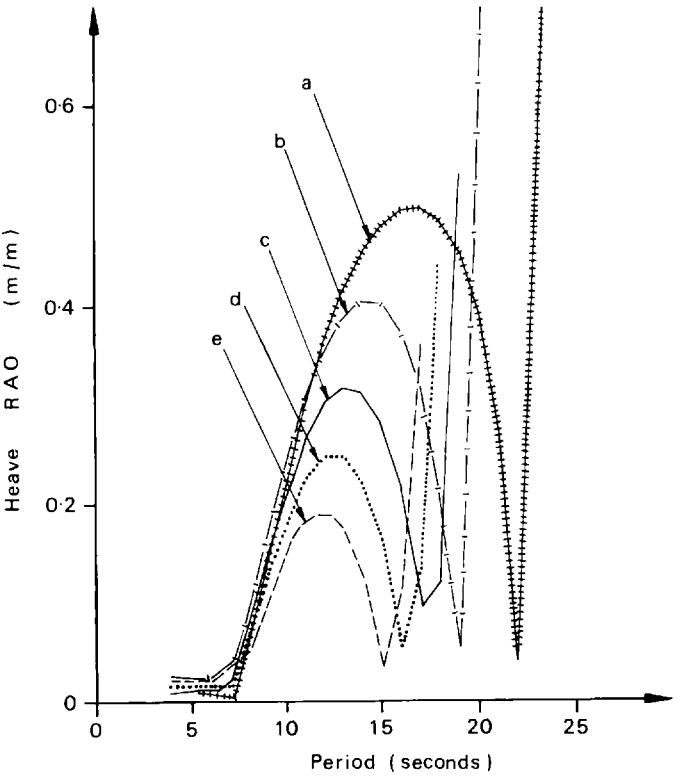

Figure 10.31. Ideal active control of a four column semisubmersible in head seas of 2 m wave height. *Key*: a – no air tanks; b – passive air tanks; c – 10% control, zero phase; d – 20% control, zero phase; e – 30% control, zero phase

The constant of proportionality (k) is taken to be the control constant. Since the mass of trapped air is related to the force exerted by the air on the vessel, the basis of operation of this control strategy is clear. Since semisubmersible wave exciting heave forces are out of phase with wave elevation at typical wave frequencies, the tanks are further reducing motions by generating forces which oppose wave exciting forces. Thus for wave frequencies where inertia forces dominate, the control strategy is given by Equation (10.80).

In practice, it is easier to control the mass flow rate and so the control strategy suggested by (10.80) becomes

$$\dot{m} = k \frac{\mathrm{d}z}{\mathrm{d}t} \tag{10.81}$$

that is, the mass flow rate in and out of the tanks is proportional to the vessel's heave velocity.

10.6.1.5 Time domain simulation results

The results presented so far have been calculated by the simplified frequency domain analysis. The time domain analysis has been used to investigate the control strategy suggested by the simplified frequency domain analysis where the mass flow rate into each open bottom tank is proportional to the vessel's heave velocity. Figure 10.32 shows the effect that the constant of proportionality, k, has on heave response in regular waves. The control constant was increased from 0 kg/m (the passive system) to 75 kg/m. Increasing the control constant increases the amount of heave motion reduction and correspondingly increases the desired mass flow rates. The larger reductions occur with increasing wave periods. This is because the wave exciting force per unit wave amplitude tends to decrease with wave period for waves between 10 and 20 s. Hence the net resultant force reduces with increasing wave period. When the control constant is negative, the motions deteriorate as the pressures inside the cans no longer generate forces which oppose the wave exciting forces. These results suggest that for any given wave frequency, the amount of heave reduction is approximately proportional to the control constant and hence to the maximum flow rates. This is illustrated in Figure 10.35 where the normalized heave response and the maximum air mass flow rates have been plotted against the control constant for a wave of 14 s period and 10 m height. These results suggest that, provided the mass flow rates are achievable, then it would be possible to reduce the heave response to very small magnitudes if so required.

Figure 10.33 shows that for a 10% reduction in heave at 14 s, a maximum mass flow rate per tank of approximately 30 kg/s is required. Furthermore, this flow rate has to vary sinusoidally with a period of 14 s. These numbers are typical of the requirements of active control and, therefore, raise questions regarding the practicality of utilizing active control for reduction of heave motions. The flow rates are large, which would imply large air reservoirs and compressors together with large ducting. The control valves would need to have exceptionally fast response times. Any build-up of air in the tanks has to be avoided. All these

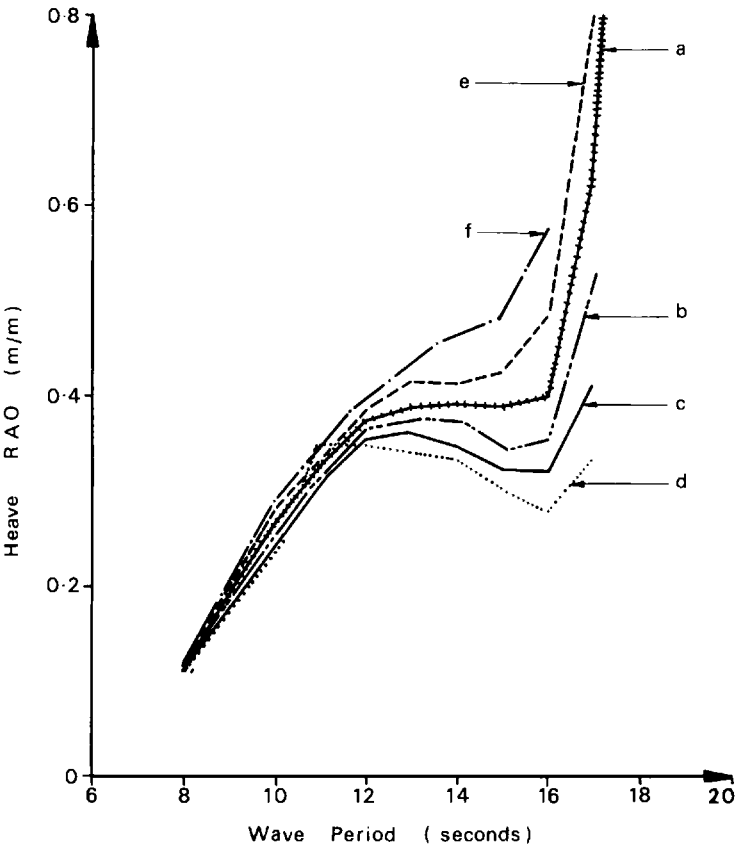

Figure 10.32. A comparison of the heave response of a four column semisubmersible with active control in head seas of 10 m wave height. *Key*: a – 0 kg/m; b – 25 kg/m; c – 50 kg/m; d – 75 kg/m; e – −25 kg/m; f – −50 kg/m

requirements need pneumatic components with high performance specifications. Real components would introduce phase lags into the system which would be detrimental to the performance of the system.

Figure 10.34 shows the calculated and measured heave response of the eight column semisubmersible (Figure 10.1 and Table 10.6(c)) without tanks and with passive tanks. It can be seen that the introduction of the passive tanks reduces the heave of the vessel considerably for wave periods between 10 and 15 s. Figure 10.36 also shows the experimental results of the vessel without tanks and with passive tanks in beam seas. There is reasonable agreement between experiment and theory. The predicted heave response of the vessel with active control together with measured data in beam seas of 1.9 m and 6 m wave heights are also presented in Figure 10.36. Some reduction in the heave motions of the vessel can be seen for waves between 10 and 14 s period. It is in this wave period range that the heave response is out of phase with the dominant wave forces and therefore this is the optimum region for active control. However, it is in

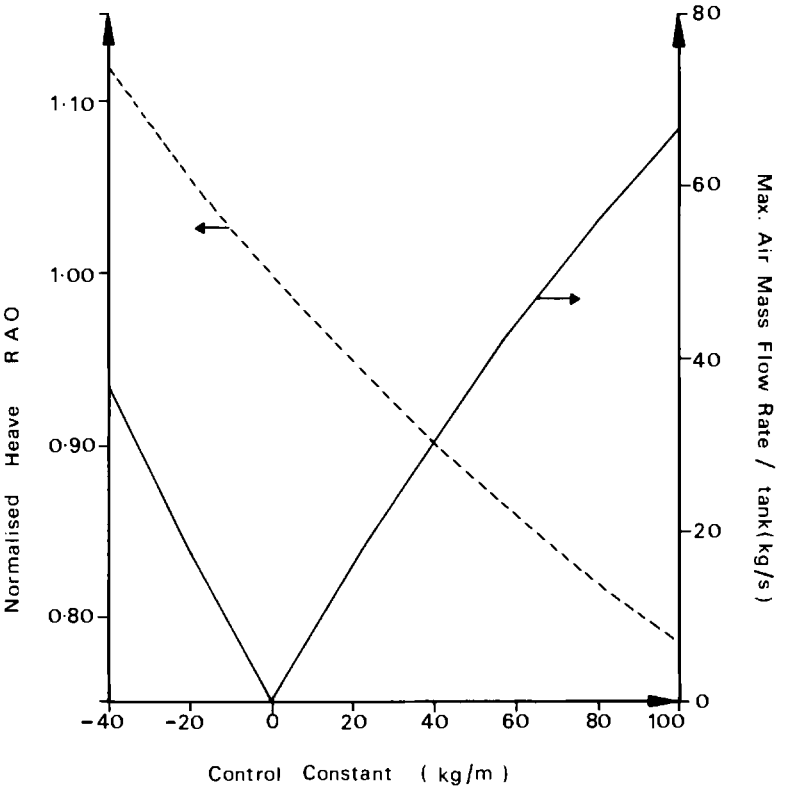

Figure 10.33. Normalized heave response and air mass flow rates due to ideal control (wave period = 14 s; wave height = 10 m (head seas))

this wave period range that forces are a maximum. Therefore, large flow rates, and hence large tanks, are required for any significant heave reductions.

As the wave period increases further, the wave forces reduce and active control becomes more effective. This is evidenced by the large reductions in motions due to active control in the longer wave periods. There is good agreement between the predicted active system performance and the experimental active system in waves of 1.9 m height. This is because the demanded flow rates, and hence masses of air, are proportional to wave height. At lower wave heights, the demanded air masses generated by the controller in the experiment are within the capability of pneumatic equipment. However, in the 6 m high waves the experimental pneumatic equipment does not have the capcacity to achieve the demanded air masses. Hence there is little reduction in the heave response.

The work presented in this section shows that, unlike passive use of the air tanks, active control involves changing the amount of trapped air inside the tanks within a wave cycle. However, the active system is inherently more complex, although the above work demonstrates both theoretically and experimentally that it is possible to actively control a semisubmer-

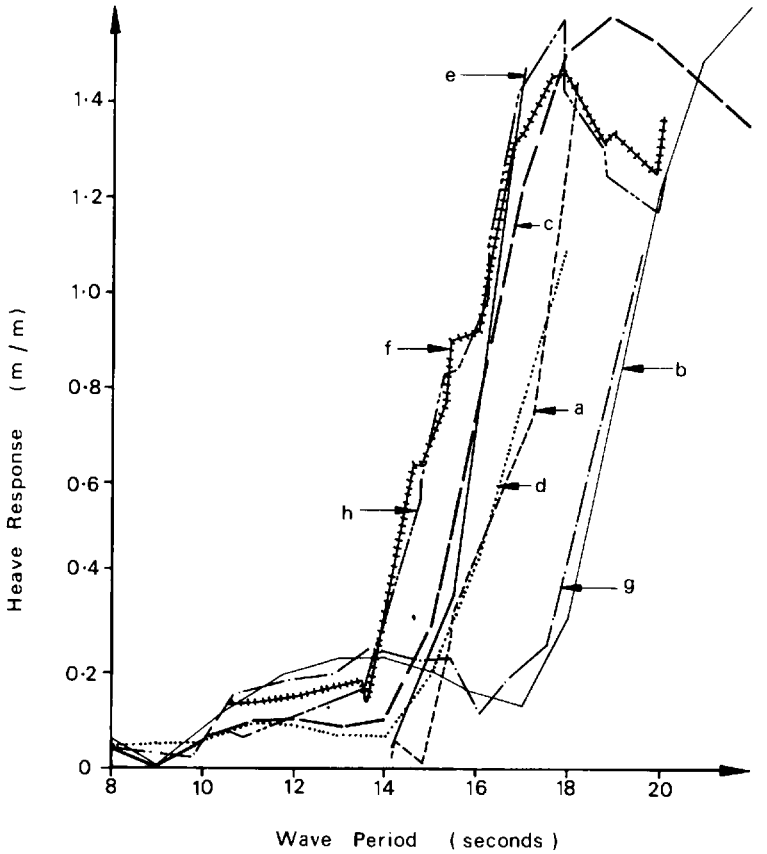

Figure 10.34. Heave response of an eight column semisubmersible in beam seas. Active control constant = 60 kg/m. *Key*: a – experimental – active air tanks, 1.9 m wave height; b – theory – unmodified vessel, 6 m wave height; c – theory – passive air tanks, 6 m wave height; d – theory – active air tanks, 6 m wave height; e – experimental – passive air tanks, 1.9 m wave height; f – experimental – passive air tanks, 6 m wave height; g – experimental – active air tanks, 1.9 m wave height; h – experimental – active air tanks, 6 m wave height

sible's heave motions using pneumatic compliances in the form of trapped air in open bottom tanks. The amount of heave reduction depends on the size and efficiency of the pneumatic equipment. For significant heave motion reductions in high waves, large pneumatic equipment is required. The installation of such equipment would be at the expense of available payload. This is unlikely to be acceptable to the vessel operator since the payload capability of a semisubmersible is already a limiting criterion in its utilisation.

Nevertheless, this work illustrates the characteristics of actively controlled pneumatic compliances and points the way towards the use of such active control for compensating out-of-balance operating forces on an offshore work vessel. Such an application is described in the next section.

10.6.2 Crane compensation

The construction and installation phases of most offshore facilities require the use of a crane vessel – usually to place pre-fabricated topside modules on to a supporting jacket structure. There are two main classes of crane vessel in current use. These are the large displacement semisubmersible and the monohull barge. There are operational advantages associated with both types of vessel. The semisubmersible has inherently low wave induced motion characteristics and large clear deck areas. The monohull vessel offers improved manoeuvrability and a relatively high transit speed. It is also capable of operating in shallow waters because of its low draught. This enables the monohull vessel to collect its load from a sheltered inshore site and transport it to more exposed offshore location, thus disposing of the need for a transportation barge. Further details of crane vessels and their coupled dynamics with the crane load hook are given in Chapter 7.

The lifting and repositioning of a crane load induces large disturbing forces and moments which need to be compensated for so that the vessel's mean attitude in heel or trim remains close to level. This is normally achieved by either ballast transfer or by the use of free flooding/gravity discharge tanks. The disadvantage of ballast transfer is that it is slow due to the limited capacity of pumps. Free flooding/gravity discharge tanks are faster but suffer from poor controllability and therefore considerable care has to be exercised in their use. An alternative is to use a pneumatic system. This has an inherently fast response time, is easily controlled and has a relatively small plant size.

This section describes the design, analysis and performance of a pneumatic crane compensation system developed by the authors and installed on the monohull crane vessel *DB50* (formerly *Challenger*). The vessel was constructed by North East Shipbuilders Ltd and is now operated by McDermott Inc. A comprehensive description of the vessel's features is given in *The Motorship* and Figure 7.1 gives a perspective view.

The pneumatic system, based on open bottom tanks, was analysed and designed using the mathematical methods described earlier. The most important tool in the design procedure was a real time numerical simulation which allowed an assessment of individual system components and then the system overall performance. This simulation is described further in this section.

The pneumatic crane compensation system consists of a set of open bottom tanks. Each tank has an inlet and vent butterfly valves which connect the internal trapped air mass to a pneumatic supply and atmosphere respectively. Figure 10.35 shows a schematic view of the open bottom tank.

These tanks are also used as passive roll suppression devices as described in Section 10.5. This dual role of the pneumatic crane compensation system as a motion suppression device is important since it overcomes one of the main disadvantages of monohull crane vessels – excessive roll motions in moderate sea states.

At the core of the pneumatic crane compensation system is the active operation of the open bottom tanks which involves controlling the mass of

Table 10.7 Monohull crane vessel *DB50* data

Displacement	34 424 t
Length overall	151.5 m
Beam overall	46.0 m
Depth, keel to deck	12.5 m
Draught	8.5 m
Radius of gyration in roll	11 m
Radius of gyration in pitch	48 m
Longitudinal centre of gravity from stern	67.81 m
Vertical centre of gravity from keel	9.96 m
Longitudinal metacentric height (no MST in use)	244.9 m
Transverse metacentric height (no MST in use)	15.5 m
Number of centrifugal blowers	3
Air height	2 m
Small MST cross-sectional area	118 m^2
Large MST cross-sectional area	165 m^2
MST centre to vessel longitudinal centreline	16.4 m
Heave added mass	88 500 t
Roll added inertia	3 530 000 tm^2
Pitch added inertia	136 000 000 tm^2
Small MST water column added mass	576 t
Large MST water column added mass	937 t
Heave damping	23 100 kNs/m
Roll damping	95 100 kNms
Pitch damping	12 600 000 kNms
Small MST water column damping	18 kNs/m
Large MST water column damping	34 kNs/m

Note:
MST = motion suppression tank.

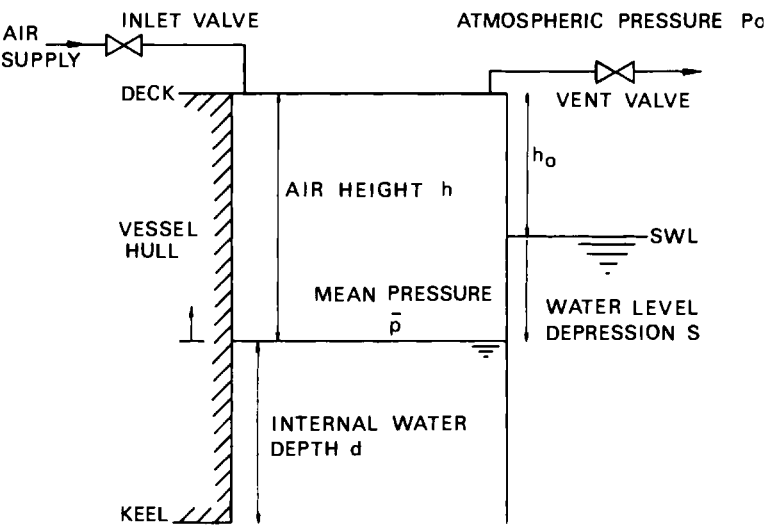

Figure 10.35. Motion suppression tanks

air trapped in each tank. This is achieved by regulating the air mass flow rate into the tank using the inlet and vent valves. The changing air masses and consequent pressure variations exert a heave force as well as pitch and roll moments on the vessel. By actively controlling the trapped air masses inside the open bottom tanks, the generated pneumatic forces are used to counteract any disturbing forces and moments, thus reducing the vessel's heave, pitch and roll motions.

Large disturbing moments associated with load movements such as crane slewing induce large angles of heel and trim if they are not reacted by ballast redistribution or by the vessel's hydrostatic stiffness. The introduction of an active pneumatic system provides an additional mechanism for the compensation of disturbing moments by pumping air in and out of open bottom tanks. Monohull crane vessels have sufficient heave and pitch hydrostatic stiffness in order to cope with a typical lift. Their roll hydrostatic stiffness, however, is inadequate for reacting the roll moment induced by the crane load. Thus, these vessels require some other means to reduce the induced roll angle.

Consider the monohull crane vessel *DB50* whose profile and general arrangement is shown in Figure 10.36. The dimensions of the vessel are

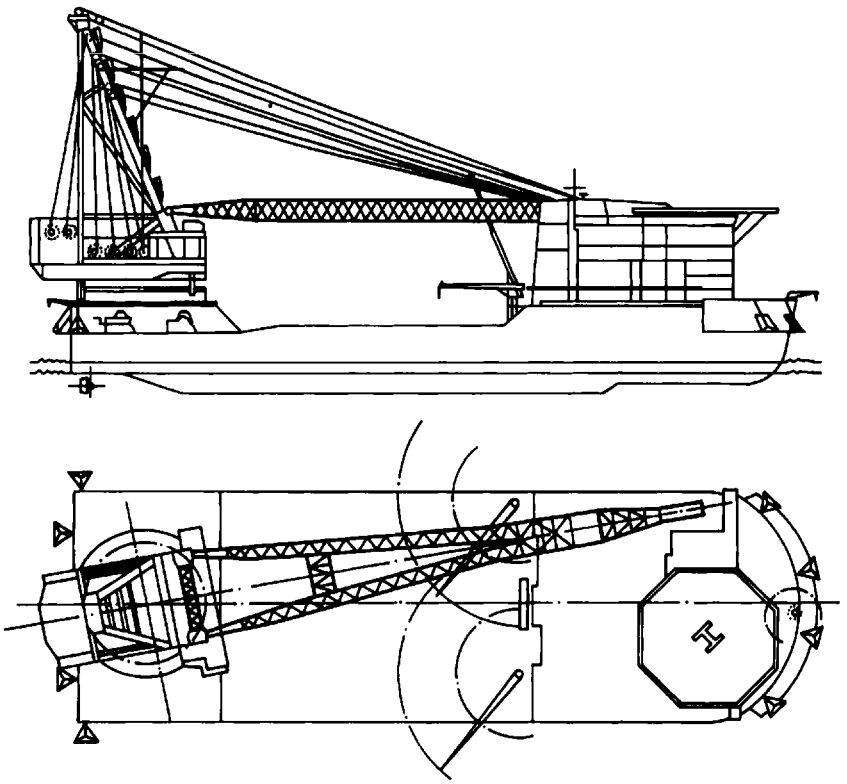

Figure 10.36. General arrangement of crane vessel *DB50*

given in Table 10.7. The vessel has open bottom tanks which run along its port and starboard mid-section. Hydraulic shell doors are located at the bottom of the motion suppression tanks which are opened when the tanks are in use. A schematic view of the pneumatic crane compensation system installed on the *DB50* is given in Figure 10.37. The main components of the system, apart from the open bottom tanks, are the control valves, the pneumatic supply unit and the control panel.

The pneumatic supply unit consists of three identical SGR55 centrifugal blowers manufactured by The Bryan Donkin Company Ltd. Each blower is capable of delivering up to 32 500 m^3 of free air per hour at a pressure of 1.8 bar absolute. The blowers are installed with automatic inlet guide vane control systems and anti-surge units. The inlet guide vane control systems maintain a variable delivery at a constant preset pressure. However, the guide vanes are only able to operate successfully down to a fraction of the maximum flow rate. If the flow rate drawn is less than this minimum controllable value, the automatic anti-surge system opens a relief value which vents the excess air to atmosphere. Thus, the anit-surge units prevent the blowers from operating with volume flow rates below the critical surge volume flow rate. This is important because a surging compressor results in violent oscillations in the power input, pressure

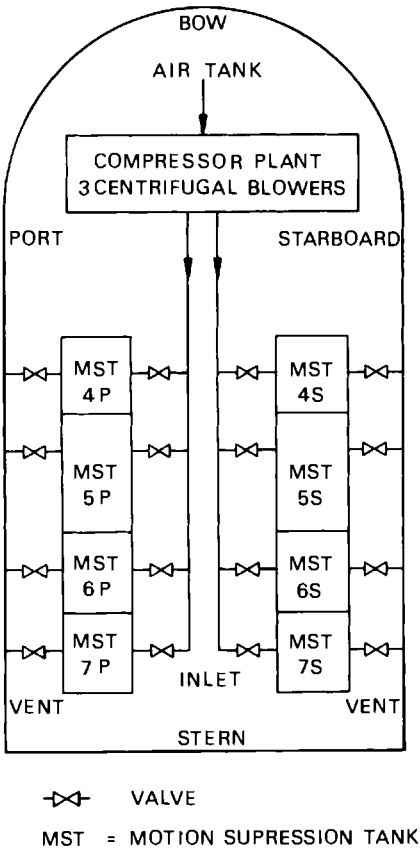

Figure 10.37. Monohull crane vessel pneumatic crane compensation system layout

difference and volume flow, which can damage both the blower and the rest of the pneumatic crane compensation system. When the demanded flow rate increases again, the above systems bring the blower on line and control the delivery. Non-return valves on the blower outlets prevent air from being blown back from a running machine to a stationary one. A typical blower operating curve is shown in Figure 10.38 for an inlet temperature of 15 °C. Note that the operating curve is a function of inlet temperature.

The air flow into and out of each motion suppression tank is controlled by 400 mm (16 inch) diameter butterfly valves. Each valve is operated by a pneumatic double acting spring return actuator (spring to close) with valve position controlled by a electro pneumatic positioner. The flow rate through a butterfly valve is a non-linear function of the pressure drop across the valve and valve position. This function is characterized by the empirical formula

$$\dot{m}_v = 9.698 \times 10^{-8} \times L_v(\theta) \sqrt{(p_2 \Delta p)} \text{ t/s} \qquad (10.82)$$

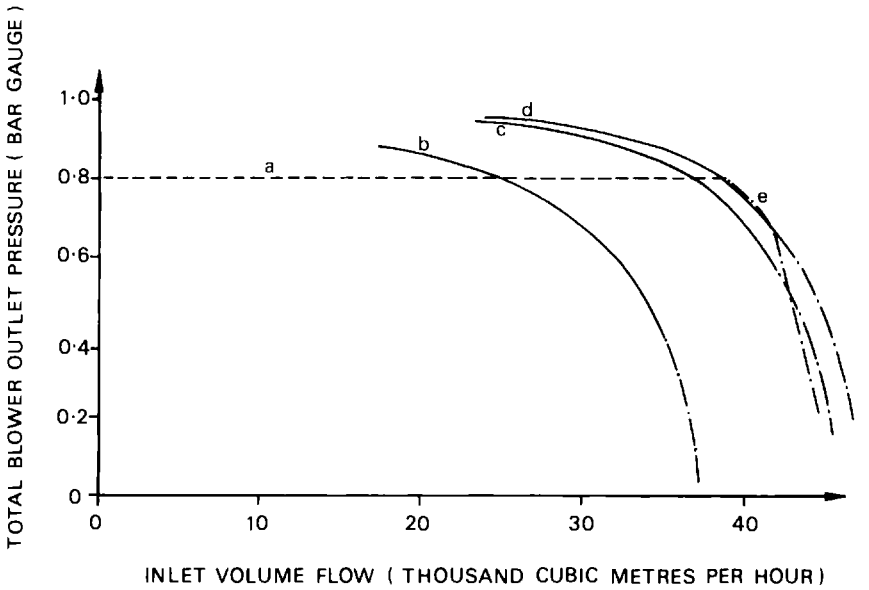

Figure 10.38. Centrifugal blower pressure-flow curves. *Key*: a – blower operating line; b – IGV angle = 50°; c – IGV angle = 10°; d – IGV angle = 0°; e – motor rating limit

where $\dot{m}_v$ is the mass flow rate through the valve; Δp is the pressure drop across the valve in kN/m^2; p_2 is the downstream pressure in kN/m^2; L_v is the valve lift and is a non-linear function of valve position, θ. This is illustrated in Figure 10.39 which shows L_v against θ for a 400 mm diameter butterfly valve. The choice of valve diameter was based on the large flow rates expected with the operation of the pneumatic crane compensation system. All pipework uses a minimum diameter of 400 mm. Typical valve response times are 10.4 s (8.65°) to open and 5.5 s (16.4°/s) to close. This disparity in response time is due to a spring mechanism which automa-

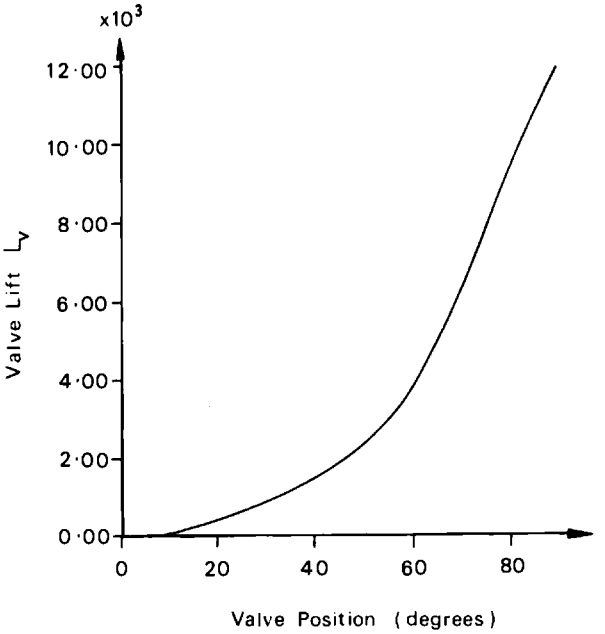

Figure 10.39. 400 mm diameter butterfly valve flow characteristics

tically closes the valve if there is a loss of pneumatic supply or control signal to the actuator.

At the core of the pneumatic crane compensation system is the controller, which is supplied with information signals giving crane induced forces and moments, vessel attitude and inclination in heel and trim, valve positions and motion suppression tank water levels and internal pressures. The controller generates valve position control signals for all the motion suppression tanks based on the net vertical force and pitch and roll moments acting on the vessel.

In the case of *DB50*, the controller is a human operator with a control panel. The control panel displays all the above information. However, since only the crane induced roll moment needs to be counteracted on the *DB50*, the principles of operation are simpler, thus making manual control feasible.

For manual control, the operator sees two strip recorder levels on the control panel. One strip recorder level represents the crane roll moment and the second gives the pneumatic roll moment generated by the motion suppression tank internal pressures. The strip recorder levels are calibrated so that when they are level the two roll moments cancel. The operator adjusts the pneumatic roll moment by controlling the motion suppression tanks' inlet and vent valve positions using throttles located on the control panel. The throttles are potentiometer devices whose analogue output signals are valve position control signals.

The use of the pneumatic crane moment compensation system on the *DB50* is best illustrated by the following example. As the crane boom slews

from the vessel's longitudinal centre line to port, the controller opens the inlet valves to the port motion suppression tanks. Air flows into the port tanks which increases the tank pressures. The operator maintains the vessel on an even keel by adjustment of the relative position of the port tank's inlet and vent valves. Once the crane boom is directly pointed to port, the crane induced roll moment and motion suppression tank pressures have reached their maximum values. As the crane boom slews back to the vessel's longitudinal centre line, the crane induced roll moment reduces and hence air is vented from the port motion suppression tanks.

The number of tanks in operation is dictated by the maximum crane roll moment and the vessel's draught. The latter governs the maximum motion suppression tank internal pressure which is set to be such that the internal water level is approximately 1 m above the keel. For example, the maximum internal tank pressure is 0.75 bar gauge for a vessel draught of 8.5 m. Increasing this pressure further will eventually lead to air venting from the bottom of the tanks.

At an operating draught of 8.5 m, the pneumatic crane compensation system installed on the *DB50* can counteract a maximum crane roll moment of 65 412 tfm by only using the tanks along one side of the vessel. Maximum crane roll moments in the range of 65 412 tfm to 130 825 tfm are compensated for by pre-charging the motion suppression tanks on the opposite side of the load swivel and using water ballast to maintain the vessel on an even keel.

An important consideration for any design is the degree of redundancy and the consequences of failure. The pneumatic crane compensation system has a high degree of redundancy and numerous fail-safe features.

10.6.2.1 Real time system simulation

The equation of motion of the vessel (Equation 10.63) together with the control system (Equation (10.75)) was integrated numerically in the time domain. $\mathbf{F}_0 e^{i\omega t}$ is replaced by a discrete time history and $\mathbf{W}(t)$ and $\mathbf{K}_m(t)$ are functions of the motion suppression tank air masses which are related to the system state or external parameters via the chosen control strategy. The simulation also includes empirical models of real components of the pneumatic system such as the centrifugal blowers and valves. This simulation proved to be of considerable value during the design process of the pneumatic crane compensation system since it allowed an assessment of system performance.

The simulation has one special feature. It has the facility to run in real time at a frequency of 2 Hz and to accept analogue input signals which are transformed to digital signals via an analogue to digital convertor. A spare set of valve throttles from the control panel used on the *DB50*, together with a video display replicating the actual control panel formed part of the simulator. This allowed human operator control to be simulated and thus permitted assessment of a human controller's performance.

Results from the simulator which illustrate the main performance characteristics of the system are presented in the next section. It is useful, however, to compare manual control with a controller which utilizes a similar control strategy. For the purposes of simplification, active control is restricted to either port or starboard slewing lifts. The port lift controller is

described below. The sign convention used is one where positive roll angle and moment makes the vessel's port side rise and the starboard side fall. The active controller obtains the crane roll moment and the pneumatic roll moment. The former is calculated from sensors giving the crane's position and line tension. The pneumatic roll moment is calculated from the tank pressures. An out of balance or error roll moment is calculated by summing the crane roll moment and the pneumatic roll moment. If the error roll moment is negative then port inlet valves are opened and port vent valves are closed. If the error roll moment is positive then port vent valves are opened and port inlet valves are closed.

The above control strategy operates between the two extremes of valves open or valves closed. It relies on the slow response time of the valves (which is of order 10 s) to alleviate excessive valve actuation. This may be further alleviated by incorporating a deadband of width ϵ into the controller. If the error poll moment (∇) falls in the deadband then the desired valve positions are not adjusted. This control procedure is outlined below:

If $\nabla < -\epsilon/2$	Open port inlet valves, close port vent valves	
If $\nabla > \epsilon/2$	Close port inlet valves, open port vent valves	
If $-\epsilon/2 \ll \nabla \ll \epsilon/2$	Continue	(10.83)

The choice of deadband must not be large enough to generate large vessel roll angles. In this case, a relatively small deadband of 200 kNm was used.

10.6.2.2 System performance and results

Results from the simulation are presented here for a lift where the crane slews 180° to port. The load starts above the vessel's deck and finishes over the vessel's stern. This operation is carried out in a period of ten minutes with a hook load of 2500 t. The roll moment induced by the 2500 t load together with the slew rate of 180° in 10 min represents the maximum capacity of the pneumatic crane compensation system. Table 10.8 gives the crane moment time history for the 2500 t lift. Intermediate moment values were obtained by linear interpolation. This time history approximates a constant slew rate of 18°/min. The roll moment reaches a maximum and then falls. Note that the pitch moment steadily increases.

Table 10.8 2500 t port slewing lift moment time history

Position	*Time* (s)	*Roll moment* (kNm)	*Pitch moment* (kNm)
1	0	0	0
2	10	0	0
3	110	−323 062	−86 564
4	210	−559 560	−323 062
5	310	−646 124	−646 124
6	410	−559 560	−969 186
7	510	−323 062	−1 205 684
8	610	0	−1 292 248
9	710	0	−1 292 248

The requirement for maintaining the vessel on an even keel is due to operational limits of the crane. The maximum inclination the crane can sustain is 3° for loads less that 3000 t. This reduces to 1.5° for heavier loads. These operational limits are typical of heavy lift cranes. Without the pneumatic crane compensation system, the maximum roll angle is just over 4.8° with a pitch angle of 0.43° for the 2500 t slewing lift. This inclination is well beyond the crane's operational limits and therefore demonstrates the need to compensate for the crane roll moment. The pitch angle steadily increases to a maximum of 0.86°.

Figure 10.40(a) presents the roll time history for the 2500 t lift with active control. It can be seen that the active controller has kept the roll angle to less than 0.2°. Transients are observed in the roll response which illustrates the effects of rapid changes in the slew rate. Another interesting feature is that between 150 and 300 s, the pneumatic crane moment compensation system is operating at its maximum capacity. Between 150 and 210 s the crane induced roll moment increases at a rate which exceeds the crane compensation system's capacity and the roll angle steadily increases. After 210 s the rate of change of crane roll moment slows down and the crane compensation system, still operating at maximum capacity, catches up. Hence there is a steady reduction in roll angle between 210 and 300 s.

Figure 10.40 also shows the achieved inlet and vent valve positions for the port bow motion suppression tank during the 2500 t lift. The inlet valve position increases until it is fully open at approximately 150 s. It remains fully open until 300 s while the system is operating at its maximum capacity. The vent valve remains closed during this period. Once the maximum crane moment has been reached at 310 s the inlet valve closes and remains virtually closed for the rest of the time history. The vent valve starts to open once the maximum crane moment has been reached; it opens in steps with each step corresponding to a constant rate of change of crane moment. Towards the end of the lift, the vent valve rapidly opens in order to return the tank pressure to atmosphere. It can be seen that the slow response time of the valves prevents them from oscillating between their open and closed positions.

Figure 10.40 also shows the time history of the net air mass flow rate into the port bow motion suppression tank during the 2500 t lift. The air mass flow rate is positive as the tank is pressurized until the crane roll moment is a maximum. After this point the air mass flow rate is negative as the tank is vented. Between 150 and 200 s the air mass flow rate into the tank steadily falls as the tank pressure builds up. Steps in the mass flow rate out of the tank are observed. These correspond to constant rates of change of crane moment.

The above results have been for the 2500 t lift with active control but with no deadband. Results for the same lift but with a deadband of 200 kNm are not shown here but show that most small variations in valve positions are suppressed, especially during the period when the valves are virtually closed.

Figure 10.41 shows the roll time history for the 2500 t lift using manual control with one of the authors as the operator. To a certain extent the

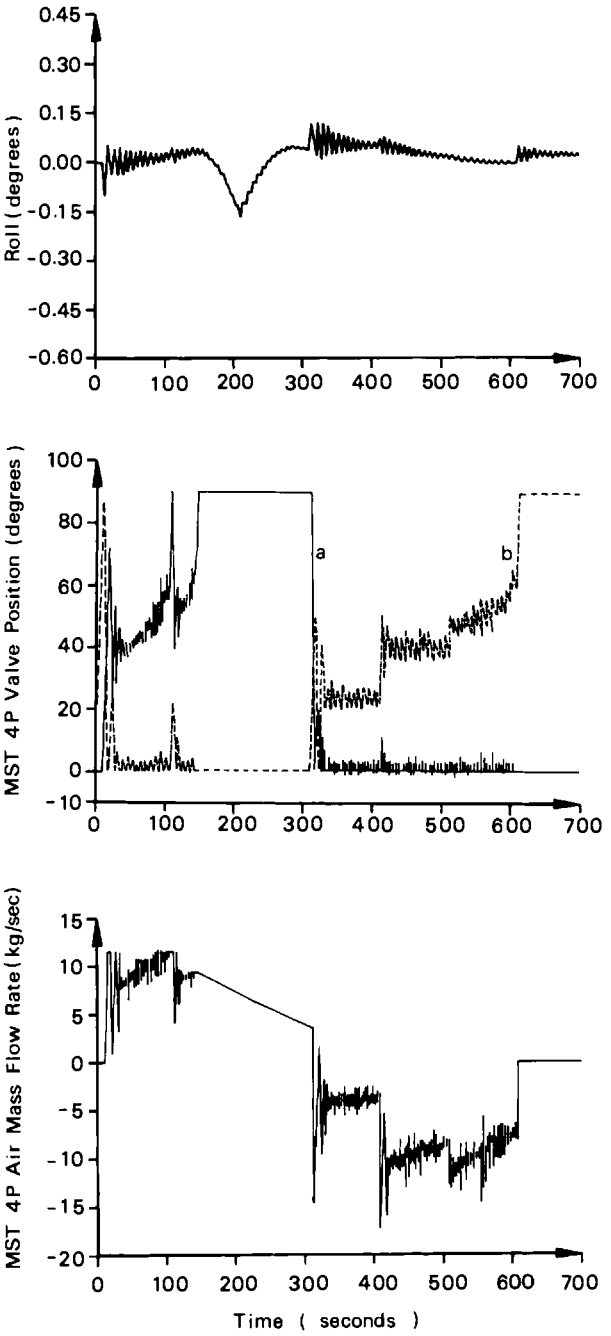

Figure 10.40. 2500 t lift time history active control. *Key*: a – inlet; b – vent

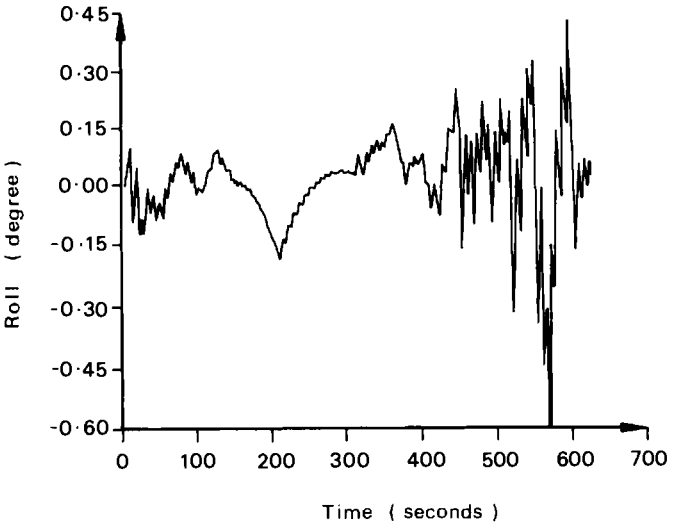

Figure 10.41. 2500 t lift roll time history manual control

performance of an operator depends on the individual. However, some comparisons can be made with active control. The performance of the system with manual control is comparable with the actively controlled results for the first 400 s. Manual control is more difficult in regions of relatively rapid decreases in crane roll moment. This is mainly due to difficulties experienced in trying to control the release of air from a finite volume. However, roll angles are still kept to less than 0.6°, which is well within operational limits. Table 10.9 lists the lifts performed by *DB50* during trials.

Table 10.9 Lifts performed during sea trials of monohull crane vessel *DB50*

Load (t)	*Hook radius* (m)	*Max. crane roll moment* (tm)	*Crane rotation*	*Max. roll angle* (deg)	*Max. pitch angle* (deg)	*Duration* (min)	*No. of blowers operating*
550	50	41 111	stern → port beam → stern → stbd beam → stern	0.2	0.4	113	2
858	77	50 337	stern → 30° to port → stern → 30° to stbd → stern	< 0.2	0.4	48	2
2970	40	129 866	stern → stbd beam → bow → stbd beam	< 1.0	0.9	15+16+10	2

References

Bassiouny, H. A. and Miller, N. S. (1982) An examination of the problems associated with the stabilization of semisubmersibles. *Proceedings of the RINA Symposium on Semisubmersibles: The New Generations*, Royal Institution of Naval Architects

Bhattacharyya, R. (1978) *Dynamics of Marine Vehicles*. John Wiley and Sons, NY, pp. 278–307

Frahm, H. (1911) Results of trials of the anti-rolling tanks at sea. *Transactions of the INA*, **53**, 183–216

Houmb, O. G. and Overvik, T. (1976) Parameterization of wave spectra and long term joint distribution of wave height and period. *BOSS '76*, Trondheim, Norway, Vol. 1

Kreysig, E. (1988) *Advanced Engineering Mathematics*, 6th edn. John Wiley & Sons, NY

Mercier, J. A. (1982) Evolution of tension leg platform technology, Presented at the Third International Conference on Behaviour of Offshore Structures (BOSS 82), Massachusetts Institute of Technology

Pedersen, B., Egeland, O. and Langfeldt, J. N. (1973) Calculation of long term values for motions and structural response of mobile drilling rigs. OTC paper 1881, *5th Annual Offshore Technology Conference, Houston, Texas*

Ramsey, A. S. (1961) *Hydrostatics*, 2nd edn (reprinted). Cambridge University Press

Rawson, K. J. and Tupper, E. C. (1976) *Basic Ship Theory*. Longman, Vol. 2, pp. 454–463, London

Rogers, G. R. C. and Mayhew, Y. R. (1976) *Engineering Thermodynamics*, Work and Heat Transfer. Longman, London

Seatek Corporation (1981) *New Semisubmersible Design*. 7394 Calle Real, Goleta, California 93117

Spidsoe, N. and Sigbjornsson, R. (1980) On the reliability of standard wave spectra in structural response analysis. *Engineering Structures*, **2**, 2, 123–135

The Motorship (1988) July, *McDermott Crane Barge No. 50*, pp. 23–31

Watts, P. (1883) On a method of reducing the rolling of ships at sea. *Transactions of the INA*, **24**, 165–191

Watts, P. (1885) On the use of water chambers for reducing the rolling of ships at sea. *Transactions of the Institution of Naval Architects* **26**, 30–49

Chapter 11

Vertical marine risers

11.1 Introduction

The operation of fixed and floating offshore structures requires the use of pipe connections between surface facilities and the sea bed. Pipes bridging the vertical separation between surface vessel and sea bed are called marine risers and are of two fundamental types. Since the 1950s, drilling operations from fixed and floating offshore structures has been carried out by using jointed steel pipes of between 0.204 m (8 inch) and 0.762 m (30 inch) external diameter to act as a conduit for the drill pipe penetrating the sea bed. Such drilling risers connect the surface platform to the subsea well head. Drilling mud at high pressure is transported to the drill face through the hollow drill pipe and returns to the surface vessel through the annulus between the drill pipe and drilling riser. Marine risers are also used to transport oil and gas from production fields for processing up to a surface platform and back down for export through a subsea pipeline or a tanker loading system. Vertical steel marine risers used for drilling or production break down into two categories. Fixed offshore structures tend to use risers which are clamped at intervals to structural members of the platform along their vertical run up to the surface. On the other hand, floating or compliant offshore structures tend to use freely strung risers which are only connected at the surface vessel and sea bed. Such risers have to be held up with a sufficiently high tension at their top to prevent buckling due to self weight of their very slender geometry. They also need to have heave compensating slip joints at their top end to take up the relative motion between the moving surface vessel and stationary sea bed.

Vertical steel risers are examples of highly compliant slender structures which have to be carefully analysed during design to ensure that the pipes have acceptable levels of deformations, stresses and fatigue lives due to forces induced by currents, waves and surface vessel motions. The presence of internal hydrostatic pressure and external sea water pressure has a fundamental effect on the governing equations for these tubular structures. Vertical risers are compliant but are themselves operated from floating compliant platforms whose operational effectivenss is directly related to the structural integrity of their risers. This chapter is concerned with presenting an overview of analysis methods and design considerations for vertical steel risers.

A brief literature survey of analysis methods and design techniques used in marine risers is presented first. Morgan (1974–1976) presents an interesting description of the historical development of marine riser technology and describes all the fundamental features that govern vertical steel riser design and selection. Most analysis work on steel risers has been carried out to determine lateral motions and corresponding stresses due to forces induced by ocean currents, waves and surface vessel motions. Gardner and Kotch (1976), Sparks (1979), Patel *et al.* (1984), McIver and Lunn (1983), McNamara *et al.* (1986) and Wang (1983) present some typical analysis methods. The role of internal and external hydrostatic pressure in modifying the governing equations of motions was first identified by Young and Fowler (1978). The resultant concept of effective tension has now been incorporated generally into design methods for vertical steel risers. Vertical steel risers at high water depths are also susceptible to axial vibrations. These have been investigated by Sparks *et al.* (1982) and Miller and Young (1985).

11.2 Governing equations

A vertical marine riser may be regarded as a hollow 'beam column'. The difference between a column subjected to lateral loading and a marine riser is that the riser is subjected to both internal and external hydrostatic pressure as well as axial and lateral loadings.

If the riser is simply considered as a beam column then the governing differential equation used for lateral static deflection is

$$\frac{d^2}{dy^2}\left(EI\frac{d^2x}{dy^2}\right) - T(y)\frac{d^2x}{dy^2} - w\frac{dx}{dy} = f \tag{11.1}$$

where EI is the riser bending stiffness; T is axial tension in the riser pipe wall; w is the weight per unit length of riser and contents; and f is the lateral force per unit length. The co-ordinate system used is shown in Figure 11.1 with y measured from the bottom of the riser and positive upwards, while x denotes horizontal riser deflection from a vertical through the riser base.

If, however, the hydrostatic pressure is included in the analysis, a slightly different form of Equation (11.1) is arrived at. The force due to the hydrostatic external pressure distribution which exists around the riser, and also the force due to internal pressure (which is related to well head pressure) are resolved into horizontal and vertical force components and incorporated into the governing equation for static deflection to give

$$\frac{d^2}{dy^2}\left(EI\frac{d^2x}{dy^2}\right) - [T(y) + A_o p_o - A_i p_i]\frac{d^2x}{dy^2}$$

$$- (\gamma_s A_s - \gamma_o A_o + \gamma_i A_i)\frac{dx}{dy} = f \tag{11.2}$$

where the additional terms are the external hydrostatic pressure around the riser, p_o; the internal hydrostatic pressure, p_i; with A_o being the

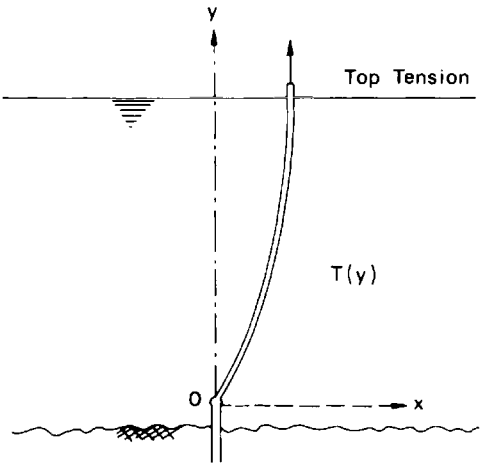

Figure 11.1. Conventional vertical riser notation

cross-sectional area of riser bore and wall; A_i, the cross-sectional area of riser bore only; A_s, the cross-sectional area of riser wall; γ_i is the specific weight of fluid in the riser bore; γ_o is the specific weight of fluid surrounding the riser tube (sea water); and γ_s is the specific weight of riser pipe wall material.

Equation (11.2) will be drived later but is valid for small deflections only, that is, for offset angles less than 10° from the vertical, and thus the error is applying this equation to a vertical steel riser is usually negligible. Some interesting points concerning the effects of pressure on the riser may be deduced by further consideration of the second term in Equation (11.2). The $(A_o p_o - A_i p_i)$ term comes from the lateral effect of external and internal hydrostatic pressure. Its effect is similar to that of the actual tension in the riser wall since this term also multiplies the second derivative of displacement, x. The pressure term does not modify the actual riser axial tension or the resultant direct stress in the riser wall. For this reason, the collection of parameters that multiply the second derivative is sometimes called 'effective tension', T_e, given by

$$T_e = T + A_o p_o - A_i p_i \tag{11.3}$$

The concept of effective tension is a convenient mathematical grouping of parameters that have a similar effect. Equation (11.3) demonstrates that the effect of external hydrostatic pressure is similar to that of a tensile axial force, while the internal pressure influences riser behaviour as would a compressive force. The term $(\gamma_s A_s + \gamma_i A_i - \gamma_o A_o)$ is equivalent to the corresponding term w in Equation (11.1).

Now, the differential equation describing the static behaviour of a marine riser of arbitrary geometry is derived using the notation of Figure 11.2 and the element of Figure 11.3. The analysis is restricted to two dimensions for simplicity. The static forces acting on the pipe element of Figure 11.3 can be listed as follows:

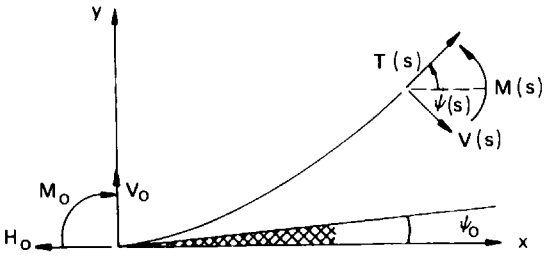

Figure 11.2. Notation for a riser of arbitrary geometry

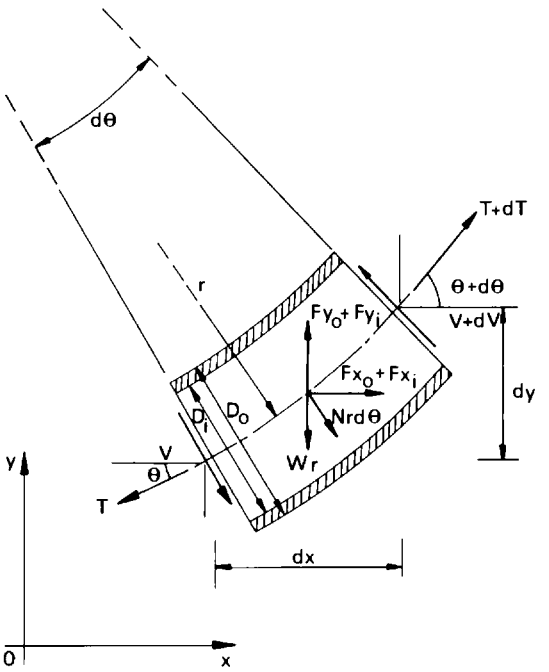

Figure 11.3. Riser element

(a) an axial tension and shear force within the pipe wall material;
(b) a horizontal force due to the resultant external and internal hydrostatic pressures, called $(F_{xo} + F_{xi})$;
(c) a vertical force due to the resultant of external and internal hydrostatic pressures $(F_{yo} + F_{yi})$;
(d) a drag force due to steady current. The velocity vector is resolved into component normal and tangential to the element, with only the normal component assumed to exert a distributed force of N per unit length;
(e) the weight of the element (W_R) acting vertically downwards.

Summing components of force in the y direction for the element in figure 11.3 yields the equation

$$(T + dT)\sin(\theta + d\theta) - T\sin\theta - (V + dV)\cos(\theta + d\theta) + V\cos\theta + (F_{yo} + F_{yi}) - W_R - N\cos\theta\, r\, d\theta = 0 \quad (11.4)$$

where W_R is the element weight. Similarly, summing forces in the x direction yields

$$(T + dT)\cos(\theta + d\theta) - T\cos\theta + (V + dV)\sin(\theta + d\theta) - V\sin\theta + (F_{xo} + F_{xi}) + N\sin\theta\, r\, d\theta = 0 \quad (11.5)$$

These equations can be simplified for small $d\theta$ to

$$(T\cos\theta + V\sin\theta)\, d\theta + dT\sin\theta - dV\cos\theta + (F_{yo} + F_{yi}) - W_R - N\cos\theta\, r\, d\theta = 0 \quad (11.6)$$

and

$$-(T\sin\theta - V\cos\theta)\, d\theta + dT\cos\theta + dV\sin\theta + (F_{xo} + F_{xi}) + N\sin\theta\, r\, d\theta = 0 \quad (11.7)$$

Combining these expressions gives

$$T\, d\theta - dV + (F_{yi} + F_{yo} - W_R)\cos\theta - (F_{xo} + F_{xi})\sin\theta - N\, r\, d\theta = 0 \quad (11.8)$$

Continuing with the above analysis requires that the forces on a cylindrical element due to internal and external hydrostatic pressure (F_{xo}, F_{xi}, F_{yo}, F_{yi}) be defined. This is done using the derivation presented below:

A hollow cylindrical member submerged in a fluid and containing a fluid within itself will experience a force due to the external and internal hydrostatic pressures of both fluids acting on the surfaces of the cylinder. An element of the cylinder is shown in Figure 11.4. The resultant force is obtained by finding the force on an arbitrary section of the element (shaded portion of Figure 11.4), and resolving it into components before integrating to obtain the total force on the element. Note that only the force on the curved walls of the cylinder due to hydrostatic pressure is evaluated. The force on the end cross-sections is not considered here since the cylinder is taken to be very long and the end cross-section will usually terminate to a coupling such that hydrostatic pressure will not act on the cylinder cross-sections. Furthermore, the axes system used in Figure 11.4 is such that the hydrostatic pressure is taken to increase linearly along the vertical axis.

Angle ϕ is used to describe position on the circumference of the element to be analysed. Initially, only external pressure is considered in the derivation. Forces due to internal pressure can be readily deduced from those due to external pressure by a simple reversal of signs and change of diameter.

As shown in Figure 11.4, the length, ds, of any strip on the cylinder circumference parallel to its axis is given by

$$ds = (r + \tfrac{1}{2} D\cos\phi)\, d\theta \quad (11.9)$$

where r is the element radius of curvature; D is the diameter of the pressure bearing surface; θ and ϕ are defined in Figure 11.4. If the

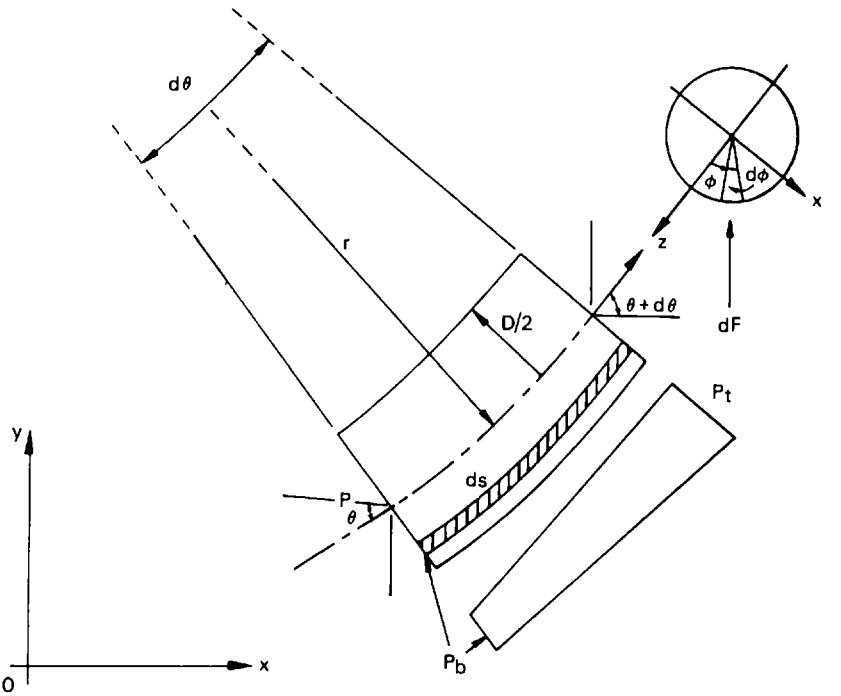

Figure 11.4. Pressure integration variables

hydrostatic pressure on the centre line of the element at its lower end is p, then the pressure, P_b, at various levels along the bottom surface is given by

$$p_b = p - \tfrac{1}{2}\gamma D \cos\theta \cdot \sin\phi$$

where γ is the weight per unit volume of the fluid medium. Also the corresponding pressure p_t at the top of the element is hydrostatic, and given by the equation

$$p_t = p_b - \gamma \cdot \cos\theta \, ds \tag{11.10}$$

since

$$\cos\theta = \frac{dy}{ds}$$

The area of section of element described by arc $d\phi$ is given by

$$dA = \tfrac{1}{2} D \cdot ds \cdot d\phi \tag{11.11}$$

The force which acts on this section of the element is then

$$dF = \tfrac{1}{2}(p_b + p_t)\, dA \tag{11.12}$$

Substituting the expressions derived for dA, p_b, p_t into (11.12) gives

$$\left.\begin{aligned} dF &= \tfrac{1}{2}(p_b + p_b - \gamma\, ds \cos\theta)\,(\tfrac{1}{2} D \cdot ds \cdot d\phi) \\ dF &= (p - \tfrac{1}{2}\gamma D \cos\theta \cdot \sin\phi - \tfrac{1}{2}\gamma\, ds \sin\theta)\,(\tfrac{1}{2} D\, ds\, d\phi) \end{aligned}\right\} \tag{11.13}$$

Replacing (11.9) for ds leads to

$$\left.\begin{aligned} dF = \{p - \tfrac{1}{2}\gamma D\cos\theta \cdot \sin\phi - \tfrac{1}{2}\gamma(r + \tfrac{1}{2}D\cos\phi)\, d\theta \sin\theta\} \\ \cdot (\tfrac{1}{2}r + \tfrac{1}{4}D\cos\phi)\, D \cdot d\theta \cdot d\phi \end{aligned}\right\} \quad (11.14)$$

Expanding the individual terms gives

$$\begin{aligned} dF = {} & [\tfrac{1}{2}p\, D\, r\, d\theta - \tfrac{1}{4}\gamma\, D\, r^2 \sin(d\theta)^2]\, d\phi \\ & + [\tfrac{1}{4}p\, D^2\, d\theta + \tfrac{1}{4}\gamma\, D^2\, r\, 2\cos\theta\, d\theta - \tfrac{1}{4}\gamma\, D^2\, r \sin\theta\, (d\theta)^2] \sin\phi\, d\phi \\ & + [\tfrac{1}{8}\gamma\, D^3 \cos\theta\, d\theta - \tfrac{1}{8}\gamma\, D^3 \sin\theta\, (d\theta)^2] \sin^2\phi\, d\phi \end{aligned} \quad (11.15)$$

The differential force may be resolved into its three directional components – F_x, F_y and F_z along the x, y and z axes respectively. In this case, the analysis is restricted to two dimensions and since there is no deformation out of the x–y plane, the resultant force in the z direction is taken as zero, i.e.

$$F_z = 0.0$$

$$dF_x = -dF \sin\theta \sin\phi \quad (11.16)$$

$$dF_y = dF \cos\theta \quad (11.17)$$

$$dF_x = \int_{\phi=0}^{\phi=2\pi} -dF \sin\theta \sin\phi \quad (11.18)$$

$$dF_y = \int_{\phi=0}^{\phi=2\pi} dF \cos\theta \sin\phi \quad (11.19)$$

Therefore

$$\begin{aligned} F_x = {} & -[\tfrac{1}{2}p\, D\, r \sin\theta\, d\theta - \tfrac{1}{4}\gamma r^2 D \sin^2\theta\, (d\theta)^2] \int_{\phi=0}^{2\pi} \sin\phi\, d\phi \\ & - [\tfrac{1}{4}p\, D^2 \sin\theta\, d\theta + \tfrac{1}{4}\gamma\, D^2 r \sin\theta \cos\theta\, d\theta - \tfrac{1}{4}\gamma\, D^2 r \sin^2\theta\, (d\theta)^2] \\ & \times \int_{\phi=0}^{2\pi} \sin^2\phi d\phi - [\tfrac{1}{8}\gamma\, D^3 \cos\theta \sin\theta\, d\theta - \tfrac{1}{16}\gamma\, D^3 \sin\theta\, (d\theta)^2] \int_{\phi=0}^{2\pi} \sin^3\phi d\phi \end{aligned}$$

This gives the force in the x direction on a curved element as

$$F_x = -[pA + r\gamma A\, (\cos\theta - \sin\theta\, d\theta)] \sin\theta\, d\theta \quad (11.20)$$

When the force due to internal pressure is considered, it's form will be the same but of opposite sign. Combining the effects of internal and external pressure for the most general case gives:

$$\begin{aligned} (F_{xo} + F_{xi}) = {} & [(p_i A_i - p_o A_o) + r(\gamma_i A_i - \gamma_o A_o) \\ & (\cos\theta - \sin\theta\, d\theta)] \sin\theta\, d\theta \end{aligned} \quad (11.21)$$

where p_o, p_i are the external and internal pressures respectively at the level of the bottom of the element centre line.

The vertical force F_y is obtained in a similar way. Before the integration is performed, the expression for the force in the vertical direction appears as

$$F_y = [\tfrac{1}{2} p\, D\, r\, d\theta - \tfrac{1}{4} \gamma\, D\, r^2 \sin\theta\, (d\theta)^2] \cos\theta \left\{ \int_0^{2\pi} \sin\phi\, d\phi \right.$$

$$+ \{\tfrac{1}{4} p\, D^2\, d\theta + \tfrac{1}{4} \gamma\, D^2\, r \cos\theta\, d\theta - \tfrac{1}{4} \gamma\, D^2\, r \sin\theta\, (d\theta)^2] \cos\theta$$

$$\times \int_0^{2\pi} \sin^2\phi\, d\phi + [\tfrac{1}{8} \gamma\, D^3 \cos\theta\, d\theta$$

$$- \tfrac{1}{8} \gamma\, D^3 \sin\theta\, (d\theta)^2] \cos\theta \int_0^{2\pi} \sin^3\phi d\phi \qquad (11.22)$$

Thus Equation (11.22) becomes

$$F_y = [p\, A + r\, \gamma\, A\, (\cos\theta - \sin\theta\, d\theta)] \cos\theta\, d\theta \qquad (11.23)$$

As before, the effect of including the internal pressure acting on the element can be seen quite easily. The final expression for the vertical force on a curved inclined element due to both internal and external pressure is given by;

$$(F_{yo} + F_{yi}) = [(p_o A_o - p_i A_i) + r(\gamma_o A_o - \gamma_i A_i)$$
$$(\cos\theta - 1\sin\theta\, d\theta)] \cos\theta\, d\theta \qquad (11.24)$$

Substituting the above expressions, Equations (11.21) and (11.24), for the resultant horizontal $(F_{xo} + F_{xi})$ and vertical forces, $(F_{yo} + F_{yi})$ due to internal and external hydrostatic pressure together with equations for the element weight and drag force into Equation (11.6) yields

$$T \cdot d\theta - dV - [(p_i A_i - p_o A_o) + r(\gamma_i A_i - \gamma_o A_o)(\cos\theta$$
$$- \sin\theta\, d\theta)] \cos^2\theta\, d\theta - W_R \cos\theta - [(p_i A_i - p_o A_o) + r(\gamma_i A_i$$
$$- \gamma_o A_o)(\cos\theta - \sin\theta\, d\theta)] \sin^2\theta\, d\theta - N\, r\, d\theta = 0 \qquad (11.25)$$

and after simplification this becomes

$$[T + p_o A_o - p_i A_i]\, d\theta - dV + \{(\cos\theta - \sin\theta\, d\theta)(\gamma_o A_o - \gamma_i A_i)$$
$$- \gamma_s A_s \cos\theta - N\}\, r\, d\theta = 0 \qquad (11.26)$$

with $W_R = \gamma_s A_s\, r d\theta$ where γ_s is the weight per unit volume of the pipe material and A_s is the pipe wall area of cross-section. It is of interest at this stage to rewrite Equation (11.26) for a nearly vertical pipe. This can be done by using ϕ as the angle between the pipe element and the vertical such that $\phi = \pi/2 - \theta$ and $d\phi = -d\theta$.

Then, Equation (11.26) can be rewritten in terms of ϕ as

$$-[(T + p_o A_o - p_i A_i]\, d\phi - dV - \{(\sin\phi + \cos\phi\, d\phi)$$
$$(\gamma_o A_o - \gamma_i A_i) - \gamma_s A_s \sin\phi - N\}\, r\, d\phi = 0 \qquad (11.27)$$

Now for small ϕ, the expressions

$$\cos\phi = 1,\ \sin\phi = -\frac{dx}{dy},\ r\, d\phi = -dy,\ \frac{d\phi}{dy} = -\frac{d^2x}{dy^2}$$

are substituted into Equation (11.27). After neglecting products of differentials, dividing by dy and using the small deflection equation

$$\frac{dV}{dy} = \frac{d^2}{dy^2}\left(EI\frac{d^2x}{dy^2}\right)$$

the equation becomes

$$\frac{d^2}{dy^2}\left\{EI\frac{d^2x}{dy^2}\right\} - \underbrace{(T + p_o A_o - p_i A_i)}_{A}\underbrace{\left\{1 + \left(\frac{dx}{dy}\right)^2\right\}^{-1}}_{B}\frac{d^2x}{dy^2}$$

$$\underbrace{- (\gamma_s A_s - \gamma_o A_o + \gamma_i A_i)\frac{dx}{dy}}_{D} = \underbrace{N\left\{1 + \left(\frac{dx}{dy}\right)^2\right\}^{1/2}}_{C} \qquad (11.28)$$

Note that term A in the above equation arises from the lateral effects of internal and external pressure and is the source of the concept of effective tension outlined earlier. Terms B and C, on the other hand, are due to the effects of riser orientation. Now because small deflections are assumed in vertical riser analysis, terms B and C in Equation (2.29) may be equated to one to give

$$\frac{d^2}{dy^2}\left(EI\frac{d^2x}{dy^2}\right) - (T + p_o A_o - p_i A_i)\frac{d^2x}{dy^2} - (\gamma_s A_s - \gamma_o A_o + \gamma_i A_i)\frac{dx}{dy} = N \qquad (11.29)$$

which is of similar form to Equation (11.2).

11.3 Methods of analysis

A typical finite element analysis method used for vertical marine risers is described here. There are, however, some special features of such vertical marine risers that have to be accounted for in any analysis. These are discussed briefly first.

It is important to distinguish between the tension and non-tension contributing riser internal contents. Since the marine riser is a long, slender structure with relatively small bending stiffness, it needs to be kept in tension to prevent buckling collapse. Thus a tension is applied to the riser at its top; and it is the weight in air of the riser pipe, associated choke and kill lines and the vertical force due to internal and external hydrostatic pressure on a non-vertical pipe segment or buoyancy module which cause a variation in tension along the riser's length. The weight of the separately tensioned drill pipe and the riser fluid contents do not directly affect the tension variation. However, the non-tension contributing elements in a riser cross-section must be accounted for when computing an effective lateral force component (coefficient A in Equation (11.28)).

For deep water risers, the top tension requirement to prevent buckling collapse can become excessive. In order to reduce top tension, buoyancy modules can be attached along the length of the riser. The distribution of buoyancy modules influences the tension variation in the riser thus altering its structural response and internal stresses. However, the increase in diameter of a riser cross-section due to buoyancy modules also increases current and wave forces. This introduces considerable scope for optimizing the intensity and distribution of buoyancy modules in deep water applications.

11.3.1 Static analysis

The finite element analysis presented here is based on a governing equation of the form given by Equation (11.28) which is restricted for the moment to vertical risers by neglecting coefficients B and C in Equation (11.28). The description of the analysis is also restricted to two dimensions for simplicity. The vertical riser pipe is idealized as an assembly of beam elements, as shown in Figure 11.5. Each element possesses six degrees of freedom, two translations and one rotation at each end. Consequently, the numerical computation is two dimensional with all external forces on the riser, including forces due to current and waves, acting in one plane.

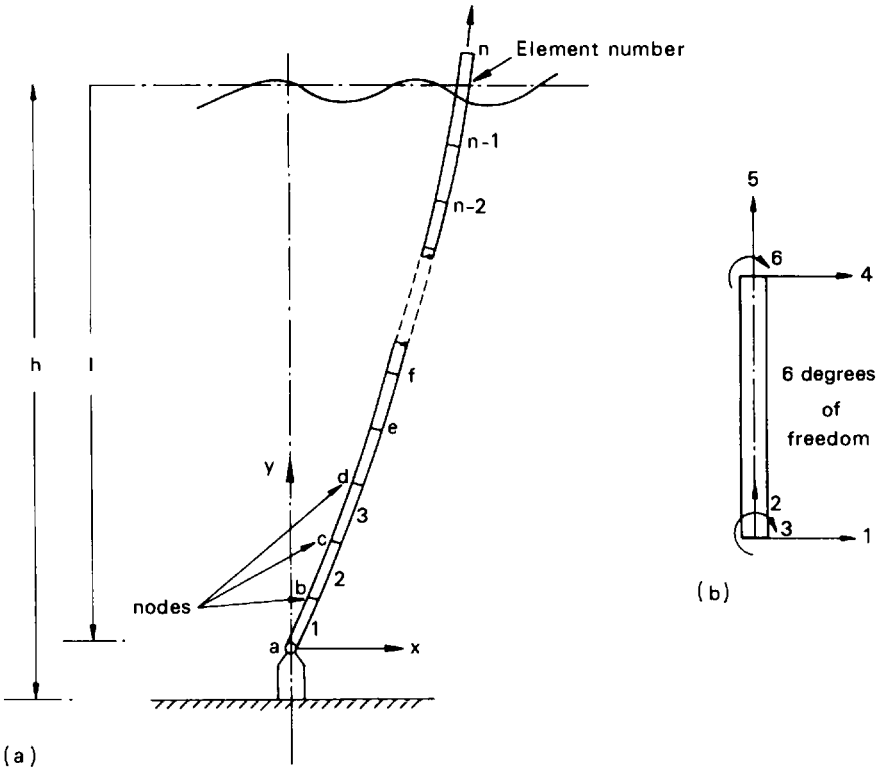

Figure 11.5. Element and global node description for a finite element idealization of a vertical riser: (a) riser element nodes; (b) single beam element

The current loading q per unit length along the riser due to a lateral drag force is

$$q = \tfrac{1}{2}\rho_o C_D d\,|U_c|\,U_c \tag{11.30}$$

where ρ_o is the density of sea water, C_D is a drag coefficient, d is an effective riser external diameter, and U_c is the current velocity. The variation of current velocity with depth needs to be known.

A static analysis can also be used to relate riser deflections and stresses to current and wave loadings in a quasi-static manner. For a known regular wave height and period, the current velocity, U_c, can be superimposed on to the horizontal component of the wave particle velocity, U_w, at any instant. The quasi-static hydrodynamic loading can then be written as

$$q = \tfrac{1}{2}\rho_o C_D d\,|U_c + U_w|\,(U_c + U_w) + \tfrac{1}{4}\rho_o \pi d^2(1 + C_m)\,\dot{U}_w \tag{11.31}$$

where $\dot{U}_w$ is the horizontal local component of wave particle acceleration; and C_m is an applicable added mass coefficient.

The total stiffness matrix, $\mathbf{S}_m$, for each beam element is derived as the sum of the standard elastic stiffness matrix, $\mathbf{S}_e$, and a geometric stiffness matrix, $\mathbf{S}_g$, which is a function of deflected element geometry and axial force on the element. Thus

$$\mathbf{S}_m = \mathbf{S}_e + \mathbf{S}_g \tag{11.32}$$

For an element of length L and an 'effective' axial tension T', S_m in member axes is given by the sum of

$$\mathbf{S}_e = \frac{EI}{L^3}\begin{bmatrix} AL^2/I & & & & \text{symmetric} & & \\ 0 & 12 & & & & & \\ 0 & 6L & 4L^2 & & & & \\ -AL^2/I & 0 & 0 & AL^2/I & & & \\ 0 & -12 & -6L & 0 & 12 & & \\ 0 & 6L & 2L^2 & 0 & -6L & 4L^2 & \end{bmatrix} \tag{11.33}$$

and

$$\mathbf{S}_g = \frac{T'}{L}\begin{bmatrix} 0 & & & & & & \\ 0 & 6/5 & & & & & \\ 0 & L/10 & 2L^2/15 & & \text{symmetric} & & \\ 0 & 0 & 0 & 0 & & & \\ 0 & -6/5 & -L/10 & 0 & 6/5 & & \\ 0 & L/10 & -L^2/30 & 0 & -L/10 & 2L^2/15 & \end{bmatrix} \tag{11.34}$$

where A is the area of steel cross-section; E is Young's modulus; and I is an appropriate second moment of area. The local effective axial tension, T', is

calculated by accounting for the modification due to hydrostatic pressures in the surrounding fluid, as described earlier.

The fixed end action vectors, $\mathbf{A}_{mL}$, are obtained by using an assumed shape function, $N(x)$, in conjunction with a total lateral load distribution, $w(x)$. This load is due to both the hydrodynamic loading, q, and an effective lateral load derived from term D in governing Equation (2.29), with dx/dy obtained from an initially assumed undeflected riser configuration. Thus

$$\mathbf{A}_{mL} = -\int_0^l w(x)N(x)\,dx \tag{11.35}$$

where x is the vertical distance from the bottom ball joint and l is the total riser length. The final static member and actions $\mathbf{A}_m$ are then obtained from:

$$\mathbf{A}_m = \mathbf{A}_{mL} + \mathbf{S}_m\,\mathbf{D}_m \tag{11.36}$$

where $\mathbf{D}_m$ is the nodal displacement matrix. These combined end actions are applied incrementally in order to account for the changes in term D and the non-linear behaviour caused by large deflections of the riser pipe. Thus $\mathbf{A}_m$ is divided into a specified number of equal increments, $\Delta\mathbf{A}_m$, which are applied progressively to obtain the incremental displacements, ΔD, through the equation

$$\Delta\mathbf{D} = \mathbf{S}^{-1}\,\Delta\mathbf{A}_m \tag{11.37}$$

where $\mathbf{D}$ and $\mathbf{S}$ are the overall displacement and overall stiffness matrices in global co-ordinates. The overall stiffness matrix is re-evaluated after each load increment to account for the change in geometry due to large deflections.

The static analysis is executed in different ways depending on the type of dynamic analysis which is to follow. For frequency-domain dynamic analysis, the effects of current are considered in the preceding static analysis. However, the non-linear time-domain method requires that the steady current, unsteady wave velocities and riser velocity be summed before applying the non-linear square-law drag force. For this reason, the static analysis preceding the time-domain dynamic analysis only accounts for self weight, buoyancy and pressure forces on the riser and excludes the current velocity. The loading due to current is then accounted for in the time-domain dynamic analysis.

11.3.2 Dynamic analysis

The differential equation of motion for a system with many degrees of freedom and having a mass matrix $\mathbf{M}_T$ can be written as:

$$\mathbf{M}_T\ddot{\mathbf{D}} + \mathbf{C}\dot{\mathbf{D}} + \mathbf{S}\mathbf{D} = \mathbf{F} \tag{11.38}$$

where $\mathbf{D}$ is the matrix of nodal displacements; and $\mathbf{C}$ and $\mathbf{S}$ are the structural damping matrix and the overall stiffness matrix respectively; all are defined in global riser axes.

The external force matrix **F** due to wave action on the system is obtained from a modified form of Morison's equation:

$$\mathbf{F} = \rho_o \mathbf{V}\dot{\mathbf{U}} + \rho_o \mathbf{V}\, C_m(\dot{\mathbf{U}} - \ddot{\mathbf{D}}) + \mathbf{B}\,|\mathbf{U} - \dot{\mathbf{D}}|\,(\mathbf{U} - \dot{\mathbf{D}}) \tag{11.39}$$

where **V** is the vector of elemental volumes; **B** is the matrix of hydrodynamic drag coefficients; and **U** and $\dot{\mathbf{U}}$ are the horizontal components of wave particle velocities and accelerations. It is assumed here that the fluid induced forces on a structure are given by the linear superposition of a drag force and an inertia force. The first two terms of Equation (11.39) signify Froude–Krylov and added mass forces, respectively, while the last term describes the drag force.

By substituting Equation (11.39) into (11.38) and replacing $[\mathbf{M} + \rho_o C_m \mathbf{V}]$ by $\mathbf{M}_T$, $\rho_o(1 + C_m)\mathbf{V}$ by $\mathbf{M}_H$ and re-arranging we get:

$$\mathbf{M}_T\ddot{\mathbf{D}} + \mathbf{C}\dot{\mathbf{D}} + \mathbf{S}\mathbf{D} = \mathbf{M}_H\dot{\mathbf{U}} + \mathbf{B}\,|\mathbf{U} - \dot{\mathbf{D}}|\,(\mathbf{U} - \dot{\mathbf{D}}) \tag{11.40}$$

The above matrix equation cannot be used directly for incorporating the boundary condition at the surface vessel which requires that the riser top end must follow the surge motion of the surface platform. This known horizontal riser nodal translation at the surface (denoted by suffix B) can be separated from all other unknown degrees of freedom (denoted by suffix A), through the following matrix partitioning:

$$\begin{bmatrix} \mathbf{M}_{T\,AA} & \mathbf{M}_{T\,AB} \\ \mathbf{M}_{T\,BA} & \mathbf{M}_{T\,BB} \end{bmatrix} \begin{bmatrix} \ddot{\mathbf{D}}_A \\ \ddot{\mathbf{D}}_B \end{bmatrix} + \begin{bmatrix} \mathbf{C}_{AA} & \mathbf{C}_{AB} \\ \mathbf{C}_{BA} & \mathbf{C}_{BB} \end{bmatrix} \begin{bmatrix} \dot{\mathbf{D}}_A \\ \dot{\mathbf{D}}_B \end{bmatrix} + \begin{bmatrix} \mathbf{S}_{AA} & \mathbf{S}_{AB} \\ \mathbf{S}_{BA} & \mathbf{S}_{BB} \end{bmatrix} \begin{bmatrix} \mathbf{D}_A \\ \mathbf{D}_B \end{bmatrix}$$

$$= \begin{bmatrix} \mathbf{M}_{H\,AA} & \mathbf{M}_{H\,AB} \\ \mathbf{M}_{H\,BA} & \mathbf{M}_{H\,BB} \end{bmatrix} \begin{bmatrix} \dot{\mathbf{U}}_A \\ \dot{\mathbf{U}}_B \end{bmatrix} + \begin{bmatrix} \mathbf{B}_{AA} & \mathbf{B}_{AB} \\ \mathbf{B}_{BA} & \mathbf{B}_{BB} \end{bmatrix}$$

$$\times \begin{bmatrix} |\mathbf{U}_A - \dot{\mathbf{D}}_A| \cdot (\mathbf{U}_A - \dot{\mathbf{D}}_A) \\ |\mathbf{U}_B - \dot{\mathbf{D}}_B| \cdot (\mathbf{U}_B - \dot{\mathbf{D}}_B) \end{bmatrix} + \begin{bmatrix} 0 \\ \mathbf{F}_B \end{bmatrix} \tag{11.41}$$

Here, $\mathbf{F}_B$ is a force required to cause the specified surge motion at the surface. The dynamic response of the riser structure in terms of the remaining degrees of freedom can be obtained solely from the upper set of equations from (11.41), which do not contain $\mathbf{F}_B$.

11.3.2.1 Element property formulation

In the formulation of the beam element mass matrix, the lumped mass or the consistent mass approach may be used. In the former, the entire mass is assumed to be concentrated at nodes where the translational degrees of freedom are defined. For such a system, the mass matrix has a diagonal form. Off-diagonal terms disappear since the acceleration of any nodal point mass would only produce an inertia force at that point. The consistent mass formulation, however, makes use of the finite-element concept and requires that the mass matrix be computed from the same shape functions that are used in deriving the stiffness matrix. Coupling due to off-diagonal terms exists, and rotational as well as translational degrees of freedom need to be considered.

In theory, this consistent mass approach can lead to greater accuracy, although this improvement is believed to be small. On the other hand, the

lumped mass formulation is easier to apply because fewer degrees of freedom are involved, leading to a simpler definition of element properties. The lumped mass formulation is chosen for this analysis because the advantages of a small improvement in accuracy for the consistent mass approach are outweighed by the additional computational effort entailed in its implementation.

It having been noted that off-diagonal terms of $\mathbf{M}_H$, $\mathbf{M}_T$ and $\mathbf{B}$ are zero for the lumped mass formulation, the following equations are obtained from (11.48):

$$\mathbf{M}_{T\,AA}\ddot{\mathbf{D}}_A + \mathbf{C}_{AA}\dot{\mathbf{D}}_A + \mathbf{S}_{AA}\mathbf{D}_A = \mathbf{M}_{H\,AA}\dot{\mathbf{U}}_A + \mathbf{B}_{AA}\,|(\mathbf{U}_A - \dot{\mathbf{D}}_A)|$$
$$(\mathbf{U}_A - \dot{\mathbf{D}}_A) - \mathbf{C}_{AB}\dot{\mathbf{D}} - \mathbf{S}_{AB}\mathbf{D}_B \qquad (11.42)$$

At the end of the static analysis, the stiffness matrix of the structure in its deformed position is available. In modelling the dynamic response about this mean statically deflected shape, the stiffness matrix is assumed to remain constant throughout the dynamic analysis.

In the lumped mass approach, all the rotational degrees of freedom need to be substructured out. Since vertical wave forces are not significant for the riser system, the vertical translation degrees of freedom can also be eliminated. This feature can lead to a substantial reduction in computer time and storage in the dynamic analysis. The horizontal degrees of freedom having been segregated, the force-deflection equations can be written in partitioned for as:

$$\begin{bmatrix} \mathbf{S}_{HH} & \mathbf{S}_{HN} \\ \mathbf{S}_{NH} & \mathbf{S}_{NN} \end{bmatrix} \begin{bmatrix} \mathbf{D}_H \\ \mathbf{D}_N \end{bmatrix} = \begin{bmatrix} \mathbf{F}_H \\ 0 \end{bmatrix} \qquad (11.43)$$

where subscripts H and N denote the horizontal and the other group of vertical and rotational degrees of freedom respectively.

From equation (11.43)

$$\mathbf{D}_N = -\mathbf{S}_{NN}^{-1}\,\mathbf{S}_{NH}\,\mathbf{D}_H \qquad (11.44)$$

The condensed stiffness matrix suitable for use in the equations of motion is then

$$\mathbf{S}_{HH}^{*} = \mathbf{S}_{HH} - \mathbf{S}_{HN}\,\mathbf{S}_{NN}^{-1}\,\mathbf{S}_{NH} \qquad (11.45)$$

The matrix is further partitioned to separate out the top surge degree of freedom:

$$\mathbf{S}_{HH}^{*} = \begin{bmatrix} \mathbf{S}_{AA} & \mathbf{S}_{AB} \\ \mathbf{S}_{BA} & \mathbf{S}_{BB} \end{bmatrix} \qquad (11.46)$$

where subscript B denotes the vessel motion as before.

The mass matrix for each element is built up by concentrating half of the total mass of mud, pipes and buoyancy material at each end of the element. For a fully submerged vertical element, the added mass associated with unit horizontal body acceleration is $\rho_o C_m V$, where C_m is the added mass coefficient. Taking half the added mass to be lumped at each node, the added mass submatrix for each element is

$$\begin{bmatrix} \frac{1}{2}\rho_o C_m V & 0 \\ 0 & \frac{1}{2}\rho_o C_m V \end{bmatrix} \tag{11.47}$$

This added mass matrix and the real mass matrix are summed together to give the total mass matrix $\mathbf{M}_{T\,AA}$.

The manner in which the partially submerged element at the water surface is idealized depends on the amount by which the element is wetted at the mean sea level. If the wetted length L_s is less than half the element length, all the added mass is lumped at the lower node and the element submatrix becomes

$$\begin{bmatrix} \rho_o C_m A_x L_s & 0 \\ 0 & 0 \end{bmatrix} \tag{11.48}$$

where A_x is the total cross-sectional area of the riser element, including buoyancy elements when present. Should L_s be greater than half the element length L, the added mass associated with the lower half of the element is concentrated at the lower node, while the rest of the hydrodynamic effects are taken to act on the top node. The element submatrix for such a situation is

$$\begin{bmatrix} \frac{1}{2}\rho_o C_m A_x L & 0 \\ 0 & \rho_o C_m A_x (L_s - L/2) \end{bmatrix} \tag{11.49}$$

For the riser structure, this appears to be a simple and logical way to treat the element at the water surface in the lumped mass formulation. The hydrodynamic mass matrix $\mathbf{M}_{H\,AA}$, which includes Froude–Krylov forces, is built up from element submatrices in a similar manner. The submatrices corresponding to Equations (11.48) and (11.49) respectively are

$$\begin{bmatrix} \rho_o(1 + C_m)A_x L_s & 0 \\ 0 & 0 \end{bmatrix} \tag{11.50}$$

$$\begin{bmatrix} \rho_o(1 + C_m)A_x L_s & 0 \\ 0 & \rho_o(1 + C_m)A_x(L_s - L/2) \end{bmatrix} \tag{11.51}$$

Due to the unit relative horizontal velocity $(U - \dot{D})$, the horizontal drag force on a full submerged element is $(1/2)\rho_o C_D L d$. The hydrodynamic damping submatrix for such an element is

$$\begin{bmatrix} \frac{1}{4}\rho_o C_D L d & 0 \\ 0 & \frac{1}{4}\rho_o C_D L d \end{bmatrix} \tag{11.52}$$

The corresponding submatrices for a partially immersed element are:

$$\begin{bmatrix} \frac{1}{2}\rho_o C_D L_s d & 0 \\ 0 & 0 \end{bmatrix}, \text{ for } L_s \leqslant L/2 \tag{11.53}$$

and

$$\begin{bmatrix} \frac{1}{4}\rho_o C_D L d & 0 \\ 0 & \frac{1}{2}\rho_o C_D (L_s - L/2) d \end{bmatrix}, \text{ for } L_s > L/2 \tag{11.54}$$

The structural damping matrix may be explicitly defined as

$$\mathbf{C} = \alpha_o \mathbf{M}_T + \alpha_1 \mathbf{S} \tag{11.55}$$

To obtain the coefficients α_o and α_1, the damping ratios, ζ_1 and ζ_2, in any two modes need to be specified. An eigen-value analysis is carried out to find the natural frequencies corresponding to the two modes chosen.

For Rayleigh damping:

$$\begin{bmatrix} \zeta_1 \\ \zeta_2 \end{bmatrix} = \tfrac{1}{2} \begin{bmatrix} \dfrac{1}{\omega_1} & \omega_1 \\ \dfrac{1}{\omega_2} & \omega_2 \end{bmatrix} \begin{bmatrix} \alpha_0 \\ \alpha_1 \end{bmatrix} \tag{11.56}$$

From Equation (11.55)

$$\alpha_0 = \frac{2(\zeta_1\omega_2 - \zeta_2\omega_1)}{\dfrac{\omega_2}{\omega_1} - \dfrac{\omega_1}{\omega_2}} \tag{11.57}$$

$$\alpha_1 = \frac{2(\zeta_1/\omega_2 - \zeta_2/\omega_1)}{\dfrac{\omega_2}{\omega_1} - \dfrac{\omega_1}{\omega_2}} \tag{11.58}$$

A damping ratio of 5% in the first two modes is usually chosen for all the analyses carried out in this work. The actual level of structural damping that should be specified is rather unclear in current literature.

11.3.2.2 Solution in the frequency domain

A linearized form of the equation of motion may be obtained by replacing the drag term in Equation (11.42) with a suitable equivalent linear damping term which is proportional to the relative velocity $(\mathbf{U}_w - \mathbf{D}_A)$. For such a linear system

$$\begin{aligned} &\mathbf{M}_{T\,AA}\ddot{\mathbf{D}}_A + (\mathbf{C}_{AA} + \mathbf{B}_{eq\,AA})\dot{\mathbf{D}}_A + \mathbf{S}_{AA}\mathbf{D}_A \\ &= \mathbf{M}_{H\,AA}\dot{\mathbf{U}} + \mathbf{B}_{eq\,AA}\mathbf{U} - \mathbf{C}_{AB}\dot{\mathbf{D}}_B - \mathbf{S}_{AB}\mathbf{D}_B \end{aligned} \tag{11.59}$$

Since the current velocity imposed is not sinusoidal, only the wave particle velocity $\mathbf{U}_w$ and the structure velocity $\mathbf{D}_A$ can be included in the fluid interaction term. The stiffness matrix in the frequency analysis will therefore be obtained from the final statically deformed shape caused by current and riser internal forces.

From linear wave theory, the elevation ξ of a single wave train may be represented by

$$\xi = r\cos(ky - \omega t) \tag{11.60}$$

The corresponding horizontal wave particle velocities and accelerations are given by

$$U_w = \omega r \frac{\cos(x - l + h)k}{\sinh kh} \cos(ky - \omega t) \tag{11.61}$$

$$\dot{\mathbf{U}}_w = \frac{\omega^2 r \cos(x - l + h)k}{\sinh kh} \sin(ky - \omega t) \tag{11.62}$$

Rewriting Equation (11.61) in complex form gives

$$U_w = \mathrm{Re}\left[\omega r \frac{\cos(x - l + h)}{\sinh kh} e^{iky}\, e^{-i\omega t}\right] \tag{11.63}$$

or

$$\mathrm{Re}(U'_w)\, e^{-i\omega t} \tag{11.64}$$

where U'_w is a complex amplitude. Similarly,

$$\dot{\mathbf{U}}_w = \mathrm{Re}(-i\omega U'_w\, e^{-i\omega t}) \tag{11.65}$$

In the steady state, the response of the system represented by Equation (11.59) to a sinusoidal wave will also be proportional to $e^{-i\omega t}$. Thus

$$\mathbf{D}_A = \mathrm{Re}(\mathbf{D}'_A\, e^{-i\omega t}) \tag{11.66}$$

where $\mathbf{D}'_A$ is complex.

Differentiating Equation (11.66) and substituting Equations (11.64) and (11.65) into (11.59) gives

$$[\mathbf{S}_{AA} - \mathbf{M}_{T\,AA}\,\omega^2 - i\omega(\mathbf{C}_{AA} + \mathbf{B}_{eq\,AA})]\mathbf{D}'_A = \mathbf{M}_{H\,AA}(-i\omega\mathbf{U}_w) + \mathbf{B}_{eq\,AA}\mathbf{U}'_w = \mathbf{F}' \tag{11.67}$$

where $\mathbf{F}'$ is a complex forcing function; and $\mathbf{B}_{eq}$ is an equivalent damping matrix described in the following section.

Since the matrix $\mathbf{B}_{eq}$ contains a term in $\dot{\mathbf{D}}$, available only from the final solution, an iterative calculation scheme needs to be derived. Starting from a trial solution for the velocities $\dot{\mathbf{D}}$, $\mathbf{B}_{eq}$ is estimated and the simultaneous complex Equations (11.67) are solved for a new set of displacements and velocities $\mathbf{D}_A$ and $\dot{\mathbf{D}}_A$. These velocities are compared with the original values ($\dot{\mathbf{D}}$) and the whole calculation is repeated with a better estimate of $\mathbf{B}_{eq}$ until the real and imaginary parts of $\dot{\mathbf{D}}$ and $\dot{\mathbf{D}}_A$ differ by a small specified tolerance.

In order to proceed with the frequency domain solution the equivalent linear damping needs to be determined. Since 'damping' forces are responsible for the dissipation of energy in a vibratory system, the obvious, and most common, way of obtaining $\mathbf{B}_{eq}$ is to equate the work done by the linearized and the non-linear forces such that

$$\mathbf{B}_{eq}(\mathbf{U} - \dot{\mathbf{D}}) \equiv \mathbf{B} \mid (\mathbf{U} - \dot{\mathbf{D}}) \mid (\mathbf{U} - \dot{\mathbf{D}}) \tag{11.68}$$

For the purpose of illustration, a convenient node where y is assumed to be zero is chosen. From Equation (11.61), the wave particle velocity is

$$U = R \cos\omega t \tag{11.69}$$

where

$$R = \frac{\omega r \cosh k(x - l + h)}{\sinh kh}$$

Let the corresponding riser nodal velocity be defined by

$$\dot{\mathbf{D}} = Q\cos(\omega t - \phi) \tag{11.70}$$

where Q is the amplitude of vibration velocity and ϕ is an arbitrary phase difference. The relative velocity is

$$(U - \dot{D}) = R\cos\omega t - Q\cos(\omega t - \phi) = R_T\cos(\omega t - \Psi)$$

where

$$R_T = (R^2 - 2RQ\cos\phi + Q^2)^{1/2} \tag{11.71}$$

$$\tan\Psi = \frac{-Q\sin\phi}{R - Q\cos\phi}$$

The work done by the damping force $B \mid (U - \dot{D}) \mid (U - \dot{D})$ over an elemental displacement dD may be written as

$$dW = B \mid R_T\cos(\omega t - \Psi) \mid R_T\cos(\omega t - \Psi) \times Q\cos(\omega t - \phi)\, d(\omega t) \tag{11.72}$$

On substituting β for $(\omega t - \Psi)$, we can express the work done over a complete wave period by this non-linear term as

$$\begin{aligned} W &= \int_{-\Psi}^{2\pi-\Psi} B \mid R_T\cos\beta \mid R_T\cos\beta \times Q\cos(\beta + \Psi - \phi)\, d\beta \\ &= \int_{-\Psi}^{2\pi-\Psi} B \mid R_T\cos\beta \mid R_T\cos\beta\, Q\cos(\beta + \gamma)\, d\beta \\ &= \tfrac{8}{3} Q\, B\, R_T^2\cos\gamma \end{aligned} \tag{11.73}$$

by splitting up the limits of integration to account for the modulus sign, and assuming that $\gamma = (\Psi - \phi)$ is time independent. The work done by an equivalent linearized damping force $B_{eq}(U - \dot{D})$ over a wave cycle is readily obtained from

$$\begin{aligned} W &= \int_0^{2\pi} B_{eq}\, R_T\cos(\omega t - \Psi)\, Q\cos(\omega t - \phi)\, d(\omega t) \\ &= \pi\, Q\, B_{eq}\, R_T\cos\gamma \end{aligned} \tag{11.74}$$

Finally, equating the work done by the two damping terms gives

$$B_{eq} = \frac{8}{3\pi} B\, R_T$$

Hence, the damping coefficient can be used in Equation (11.67):

$$\mathbf{B}_{eq} = \frac{8}{3\pi}\mathbf{B}\,|(\mathbf{U} - \dot{\mathbf{D}})_{max}| \tag{11.75}$$

To ensure that Equations (11.67) converge rapidly to the final solution, a reasonably accurate initial estimate of the displacements $\mathbf{D}$ (and thus the velocities $\dot{\mathbf{D}}$) is required for evaluating the equivalent damping matrix from

the total mass matrix and the diagonal terms of the stiffness matrix. Then, assuming a damping ratio of 10%, the initial estimate of $\mathbf{B}_{eq}$ is taken to be:

$$B_{eq} = 0.2 \begin{bmatrix} (M_{T\,AA}^{11} S_{AA}^{11})^{1/2} & 0 & 0 \\ 0 & (M_{T\,AA}^{22} S_{AA}^{22})^{1/2} & 0 \\ & & (M_{T\,AA}^{NN} S_{AA}^{NN})^{1/2} \end{bmatrix} \quad (11.76)$$

This matrix is substituted into Equations (11.67), which are subsequently solved for the initial trial solution. This method leads to rapid convergence with only two or three iterations required for forcing frequencies away from the structure resonant frequencies. Up to 10 iterations may be necessary at and around resonance frequencies.

11.3.2.3 Time series analysis

The basic method of analysis here involves integrating Equation (11.38) through discrete steps in time and accounting for the non-linear drag loading without a linearization approximation.

In the equation of motion (Equation (11.40)), the generalized fluid velocity can be decomposed into the static current velocity $\mathbf{U}_c$ and a wave particle velocity $\mathbf{U}_w$. Thus Equation (11.40) becomes:

$$\mathbf{M}_T\ddot{\mathbf{D}} + \mathbf{C}\dot{\mathbf{D}} + \mathbf{S}\mathbf{D} = \mathbf{M}_H\dot{\mathbf{U}}_w + \mathbf{B}\,|(\mathbf{U}_w + \mathbf{U}_c - \dot{\mathbf{D}})| \times (\mathbf{U}_w + \mathbf{U}_c - \dot{\mathbf{D}}) \quad (11.77)$$

where $\dot{\mathbf{U}}_c$ is taken to be zero for the current velocity. The requirement to sum the current and wave velocities before applying the resultant loading through the square-law relationship requires that the current velocity be ignored in the static analysis that precedes this time-domain calculation.

The time step integration of the equation of motion also allows irregular wave sequences (and the corresponding surface vessel surge responses) to generate dynamic excitation forces on the riser. This wave sequence can be specified in two ways. A wave elevation spectrum of the incident irregular wave can be used to compute the corresponding spectra of the subsurface wave velocities and acceleration as well as the spectrum of surface vessel surge motions. These spectra can be Fourier transformed to generate corresponding time series of these quantities for use in the dynamic analysis. However, this procedure is cumbersome and computationally time-consuming. Therefore, a simple alternative method is usually employed. The incident wave elevation is specified as a 'frequency comb' sum of individual sinusoidal components with randomly distributed phase angles. The subsurface wave kinematics and surface vessel surge response are then readily computed by summing the effects of all the sinusoidal components in the wave spectrum.

The numerical time step integration technique proposed by Newmark is used with the following relations

$$\dot{\mathbf{D}}_{t+\Delta t} = \dot{\mathbf{D}}_t + [(1 - \delta)\ddot{\mathbf{D}}_t + \delta\ddot{\mathbf{D}}_{t+\Delta t}]\Delta t$$

$$\mathbf{D}_{t+\Delta t} = \mathbf{D}_t + \dot{\mathbf{D}}_t\Delta t + [(\tfrac{1}{2} - \beta)\ddot{\mathbf{D}}_t + \beta'\ddot{\mathbf{D}}_{t+\Delta t}]\,\Delta t^2 \quad (11.78)$$

where β' and δ are parameters which can be varied to achieve an

acceptable integration accuracy and stability. Subscript t denotes the variable at the beginning of the time interval Δt.

The direct integration analysis does rely on selection of an appropriate time step which must be small enough to obtain sufficient accuracy, although a time step smaller than necessary would reflect on the cost of the solution. Bathe and Wilson (1976) have analysed the stability and accuracy of various numerical integration schemes and suggested that, for reasonable accuracy, the time step-to-period ratio be not more than 1/6 for the highest significant mode. In its standard form, the Newmark technique is unconditionally stable.

The two parameters δ and β' introduced in Equation (11.78) indicate how the acceleration is modelled over the time interval. $\delta = 1/2$ and $\beta' = 1/6$ correspond to a linearly varying acceleration. Newmark's original scheme which is pursued here uses $\delta = 1/2$ and $\beta' = 1/4$ and gives a constant-average-acceleration based integration scheme. Using these latter values in Equation (2.86) and rearranging gives

$$\ddot{\mathbf{D}}_{t+\Delta t} = \frac{4}{(\Delta t^2)} [\mathbf{D}_{t+\Delta t} - \mathbf{D}_t - (\Delta t)\dot{\mathbf{D}}_t] - \ddot{\mathbf{D}}_t$$

$$\dot{\mathbf{D}}_{t+\Delta t} = \frac{2}{\Delta t} [\ddot{\mathbf{D}}_{t+\Delta t} - \ddot{\mathbf{D}}_t] - \dot{\mathbf{D}}_t \tag{11.79}$$

Then expressing Equation (11.77) explicitly at instant $(t + \Delta t)$ and using the lumped-mass approach with the top vessel surge motion duly separated as in Equation (11.42), we get

$$\begin{aligned}
&\mathbf{M}_{\mathrm{T\,AA}}\ddot{\mathbf{D}}_{\mathrm{A},\,t+\Delta t} + \mathbf{C}_{\mathrm{AA}}\dot{\mathbf{D}}_{\mathrm{A},\,t+\Delta t} + \mathbf{S}_{\mathrm{AA}}\mathbf{D}_{\mathrm{A},t+\Delta t} = \mathbf{M}_{\mathrm{H\,AA}}\dot{\mathbf{U}}_{\mathrm{WA},\,t+\Delta t} \\
&+ \mathbf{B}_{\mathrm{AA}} |(\mathbf{U}_{\mathrm{WA}} + \mathbf{U}_{\mathrm{CA}} - \dot{\mathbf{D}}_{\mathrm{A}})|_{t+\Delta t} \times (\mathbf{U}_{\mathrm{WA}} + \mathbf{U}_{\mathrm{CA}} - \dot{\mathbf{D}}_{\mathrm{A}})_{t+\Delta t} \\
&- \mathbf{C}_{\mathrm{AB}}\dot{\mathbf{D}}_{\mathrm{B},t+\Delta t} - \mathbf{S}_{\mathrm{AB}}\mathbf{D}_{\mathrm{B},t+\Delta t}
\end{aligned} \tag{11.80}$$

Substituting Equations (11.79) into (11.80) and rearranging gives:

$$\begin{aligned}
&\left[\frac{4}{(\Delta t)^2}\mathbf{M}_{\mathrm{T\,AA}} + \frac{2}{(\Delta t)}\mathbf{C}_{\mathrm{AA}} + \mathbf{S}_{\mathrm{AA}}\right]\mathbf{D}_{\mathrm{A},\,t+\Delta t} \\
&= \mathbf{M}_{\mathrm{H\,AA}}\dot{\mathbf{U}}_{\mathrm{WA},\,t+\Delta t} + \mathbf{B}_{\mathrm{AA}} |(\mathbf{U}_{\mathrm{WA}} + \mathbf{U}_{\mathrm{CA}} - \dot{\mathbf{D}}_{\mathrm{A}})|_{t+\Delta t} \\
&\quad \times (\mathbf{U}_{\mathrm{WA}} + \mathbf{U}_{\mathrm{CA}} - \dot{\mathbf{D}}_{\mathrm{A}})_{t+\Delta t} - \mathbf{C}_{\mathrm{AB}}\dot{\mathbf{D}}_{\mathrm{B},\,t+\Delta t} \\
&\quad - \mathbf{S}_{\mathrm{AB}}\mathbf{D}_{\mathrm{B},\,t+\Delta t}\left[\frac{4}{\Delta t}\mathbf{M}_{\mathrm{T\,AA}} + \mathbf{D}_{\mathrm{AA}}\right]\dot{\mathbf{D}}_{\mathrm{A},\,t} \\
&\quad + \left[\frac{4}{(\Delta t)^2}\mathbf{M}_{\mathrm{T\,AA}} + \frac{2}{(\Delta t)}\mathbf{C}_{\mathrm{AA}}\right]\mathbf{D}_{\mathrm{A},\,t} + \mathbf{M}_{\mathrm{T\,AA}}\ddot{\mathbf{D}}_{\mathrm{A},\,t} = \mathbf{F}_{t+\Delta t}
\end{aligned} \tag{11.81}$$

This is the basic equation used in the time step integration scheme.

The solution scheme assumes that displacement, velocity and acceleration vectors at time zero, denoted by subscript 0, are known and the solution is required from time zero to time τ. The given time span τ is subdivided into equal time intervals Δt (where $\Delta t = \tau$ divided by the

number of time intervals). The algorithm calculates the solution at the next required time from known information at the previous time steps. The process is repeated until the solution at all discrete time point is known.

To initialize the numerical solution, the acceleration corresponding to zero time is derived from the reduced form of Equation (11.81) giving

$$\ddot{\mathbf{D}}_A = \mathbf{M}_{T\,AA}^{-1}\left[\mathbf{M}_{H\,AA}\dot{\mathbf{U}}_{WA_0} + \mathbf{B}_{AA}\,|(\mathbf{U}_{WA} + \mathbf{U}_{CA})_0| \times (\mathbf{U}_{WA} + \mathbf{U}_{CA})_0 - \mathbf{C}_{AB}\dot{\mathbf{D}}_{B_0} - \mathbf{S}_{AB}\mathbf{D}_{B_0}\right] \tag{11.82}$$

In arriving at Equation (11.82) the unknown value of velocity $\dot{\mathbf{D}}_{A,\,t+\Delta t}$ of the forcing vector of Equation (11.81) has been approximated to $\dot{\mathbf{D}}_{A,\,t}$. The approximation gives an acceptable degree of accuracy provided the time step chosen is sufficiently small. An alternative approach to this would require an elaborate iterative scheme with a significantly greater computation effort.

From the set of simultaneous Equations (11.81) the displacements are simply obtained from

$$\mathbf{D}_{A,\,t+\Delta t} = \mathbf{J}^{-1}\mathbf{F}_{t+\Delta t} \tag{11.83}$$

where

$$\mathbf{J} = \frac{4}{\Delta t^2}\mathbf{M}_{T\,AA} + \frac{2}{\Delta t}\mathbf{C}_{AA} + \mathbf{S}_{AA} \tag{11.84}$$

The inversion of matrix $\mathbf{J}$ in the above equation can be made more efficient by the use of banded equation solvers as suggested by Bathe and Wilson (1976). However, $\mathbf{J}$ is independent of time and needs to be inverted once only.

When $\mathbf{D}_{A,\,t+\Delta t}$ is known, the accelerations and velocities at $(t + \Delta t)$ are derived from Equations (11.79).

11.3.3. Typical results

Finite element calculations of the type presented here can be validated by a number of methods.

For the static analysis, the finite element formulation can be checked by comparison with the analytic result for an idealized weightless tensioned beam. A typical such comparison is shown in Table 11.1. Such comparisons can confirm the validity of the computational procedure as well as indicating the number of finite elements required for an acceptable level of accuracy.

The American Petroleum Institute Committee on the Standardization of Offshore Structures defined a set of test risers as a basis for comparing the performance of riser analysis methods for both static and dynamic loadings. Nine anonymous participants to this study submitted solutions for the various test cases and *API Bulletin 2J* (1977) gives the overall comparisons. Table 11.2 gives the input data for one of the API test cases, and Table 11.3 displays the corresponding static analyses results. These are displayed in terms of maximum bending stress value and position, maximum total stress (axial plus peak bending), as well as upper and lower riser angles from the vertical. Results of the analysis presented here are given in Table

Table 11.1 Results of static analyses of API cases (mean figures from the *API Bulletin 2J* are quoted below each solution in parentheses)

Case	Max. bending stress Value (ksi)	Location* (ft)	Max. total stress (ksi)	Angles from vertical (deg) Lower BJ	Top
500-0-1	3.99	104	5.46	3.64	0.44
	(2.53)	(111)	(4.34)	(2.94)	(0.82)
500-0-2	1.62	104	6.98	2.58	0.96
	(0.94)	(115)	(6.80)	(2.20)	(1.21)
500-20-1S	5.92	442	9.43	4.35	−1.17
	(5.86)	(461)	(9.51)	(3.66)	(−0.79)
500-20-2S	3.90	442	10.381	2.79	0.04
	(4.27)	(463)	(10.54)	(2.51)	(0.24)

Notes:
ksi is kilo pounds force per square inch; BJ is ball joint.

* Above lower ball joint.

Table 11.2 Ten element idealization of weightless tensioned 500 ft beam

Parameters:	
Total length	152.4 m
Applied tension	54.422 tf
Uniform load intensity*	6.035×10^{-3} t/m

Results:	*Analytical solution*	*FE idealization*
Slope at ends (rad)	0.007 1	0.007 1
Maximum moments (tf-m)	0.863 1	0.868 9
Lateral displacements (m)		
Node		
1,11	0.0	0.0
2,10	0.104 4	0.104 4
3,9	0.191 4	0.191 3
4,8	0.254 9	0.254 8
5,7	0.293 3	0.293 1
6	0.306 1	0.306 0

*Equivalent to load caused by 0.5 m/s current.

11.3 with the mean values from the nine API test cases displayed in parentheses. It is clear from these comparisons that results from the *API Bulletin* and the present method agree reasonably well.

The frequency domain and time domain dynamic analyses presented here have also been compared with the dynamic analyses in the API bulletin. Figures 11.6 and 11.7 show typical results for one of the API test risers; the plotted API values are the maximum and minimum of the combined results from the nine calculations compiled in the bulletin. The

Table 11.3 Input parameters for API cases

Distance from mean sea level to riser support ring	15.24 m
Distance from sea floor to bottom ball joint	9.144 m
Water depth	152.4 m
Riser pipe outer diameter	0.406 4 m
Riser pipe wall thickness	0.015 87 m
Choke line outer diameter	0.101 6 m
Choke line wall thickness	0.016 51 m
Kill line outer diameter	0.101 6 m
Kill line wall thickness	0.016 51 m
Buoyancy material outer diameter	0.609 6 m
Modulus of elasticity of riser pipe	2.1×10^7 t/m^2
Density of sea water	1.025 t/m^3
Density of mud	1.438 t/m^3
Drag coefficient	0.7
Added mass coefficient	1.5
Effective diameter for wave/current load	0.660 4 m
Density of buoyancy material	0.160 2 t/m^3
Current at surface	0.257 4 m/s
Surface vessel static offset	4.572 m
Weight per unit length of riser joint in air	0.2565 tf/m
Wave height	6.096 m
Wave period	9 s
Vessel surge amplitude	0.609 6 m
Vessel surge phase angle	15°

frequency domain analysis is computed conventionally using a regular wave period of 9 s and wave height of 6.096 m. The time domain analysis uses a single frequency 'comb' to produce equivalent data but with the non-linear drag force due to current and wave velocities included in the calculations. It should be emphasized that none of the results published in the API bulletin has to our knowledge been directly validated by measurements on full scale risers. Nevertheless, this comparison gives an indication of agreement between the other methods and the analysis presented here.

11.3.3.1 Influence of non-linearity on structural response

A comparison of the time domain and frequency domain analyses presented in Figures 11.6 and 11.7 gives an indication of the effects of nonlinear fluid loading on the riser response. A static current profile is included, and so time domain and frequency domain results differ markedly owing to the effect of the square law drag force with and without linarization. However, the frequency domain results are at lower values for the induced stresses.

The finite element analysis and the frequency domain and time domain solutions outlined in this section attempt to balance the small computing cost advantages of linearization against the additional accuracy available from the non-linear time domain calculation. The frequency domain analysis uses the linearization approximation of equal energy dissipation between non-linear damping and equivalent linear damping in the solution. An alternative linearization technique for frequency domain analysis has been tested by Krolikowski and Gray (1980). It is based on a statistical minimization of mean squared error between the non-linear damping force

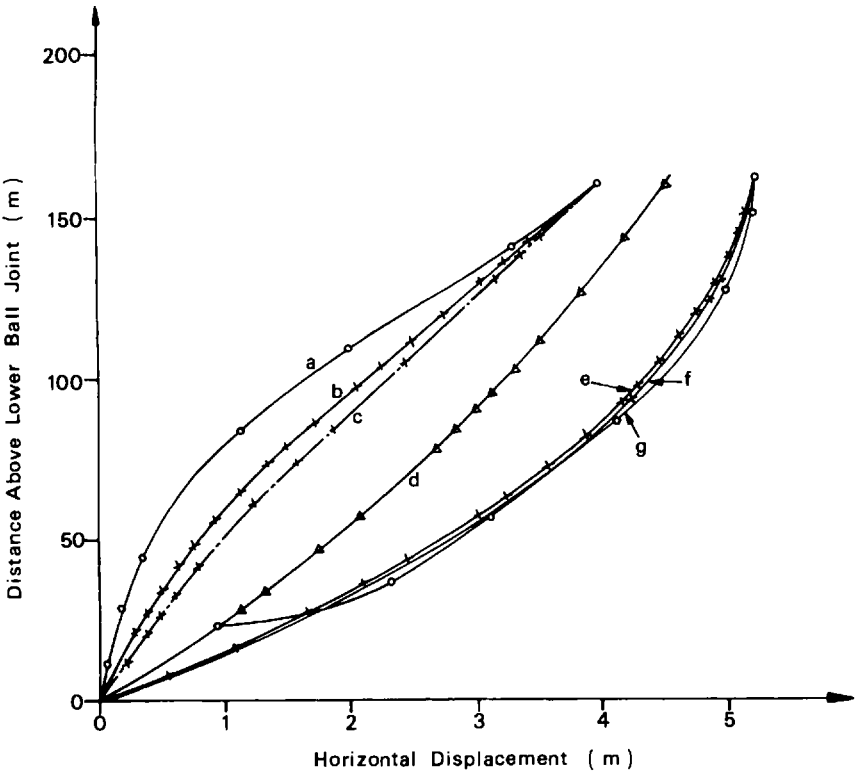

Figure 11.6. Displacement and stresses for a marine riser compared with API case 500-20-1D. *Key*: d – static values; a,g – API results envelope; c,e – frequency domain analysis envelope; b,f – time domain analysis envelope

and its linear representation used in the analysis. The statistical approach uses linearization at the discrete frequency components of a wave spectrum to arrive at a global linearized damping force with a least squares minimized error. This technique allows a frequency domain method to be applied over a wider frequency range, in contrast to the linearization method used in the analysis presented here which is used for regular waves only.

The technique of linearization by least squares minimization is not followed up in the frequency domain analysis presented here. This is because both riser methods developed here have been aimed at computing riser motions and stresses, the latter for feeding into fatigue calculations based on linear elastic theory or fracture mechanics. The fracture mechanics approach demands that representative stress time histories for a marine riser in waves be known in detail, particularly in terms of the sequences of stress cycles that are likely to occur. A computationally efficient time domain analysis is capable of producing this information, whereas frequency domain analyses, whatever their level of sophistication in linearization, operate in the freqeuncy domain where the phase information which governs wave sequencing is lost.

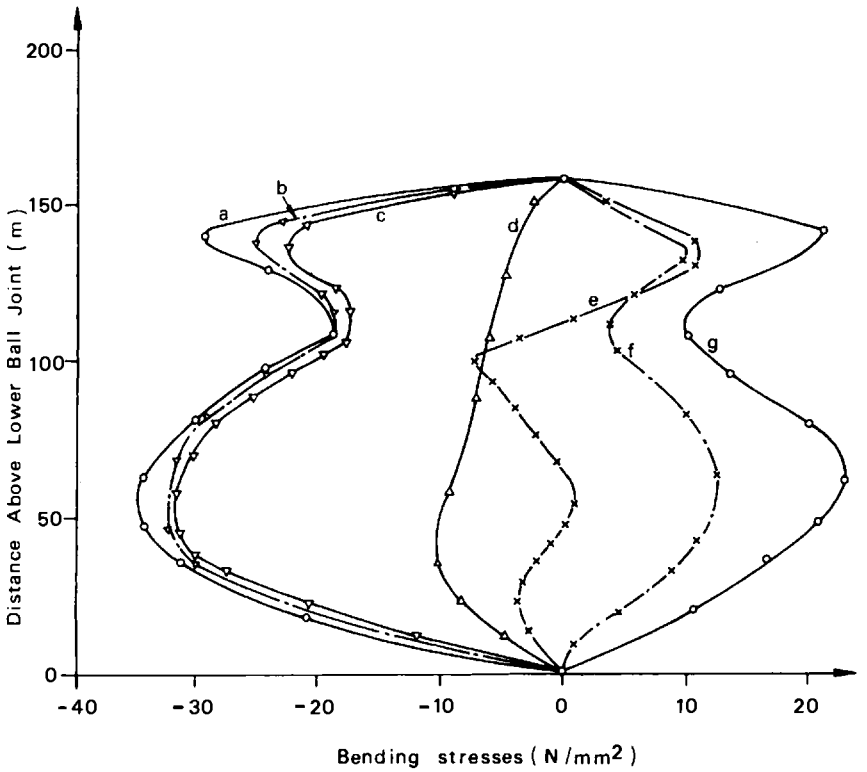

Figure 11.7. Displacement and stresses for a marine riser compared with API case 500-20-1D. *Key*: d – static values; a,g – API results envelope; c,e – frequency domain analysis envelope; b,f – time domain analysis envelope

A further feature which has prompted the use of an efficient time domain analysis for riser calculations is based on the comparative performance of the frequency domain and time domain analyses which shows that there are substantial difference in peak stresses between the two analyses. These discrepancies may be reduced by a more sophisticated linearization technique in the frequency domain analyses, but the discrepancies do highlight the importance of modelling the non-linear fluid loading on the riser cross-section in a physically representative manner.

An additional problem associated with marine risers occurs in the analysis of multi-tube production risers of complex cross-sectional geometries. These may be made up of a central structural riser with a number of large diameter satellite flow lines or as a bundle or array of low lines. The beam finite element analysis techniques described in this paper need to be extended to these production risers. Patel and Sarohia (1982) suggest one solution by equivalencing a production riser of complex cross-section to a simpler single-tube marine riser, which is then used for the finite element analysis. This approach is sufficient for a global riser analysis, but it needs to be used with care when localised riser fluid forces or member stresses

are required. Krolikowsky (1981) presents an alternative frequency domain approach.

11.4 Vortex shedding effects

It was Strouhal (1878) who found Aeolian tones generated by a wire were proportional to the wind speed, V, divided by the wire thickness, D. Later Rayleigh (1896) proved that the vortex shedding frequency was not only a function of V/D but also of Reynolds number ($\mathrm{Re} = VD/\nu$) where ν is kinematic viscosity. Figure 11.8 shows the variation of Strouhal number, S, with Reynolds number for a smooth stationary circular cylinder as determined by more recent researchers. Absolute values of S have been shown to depend also on cylinder surface roughness, length to diameter ratios and turbulence levels – see Sarpkaya and Isaacson (1981).

The physical mechanism of vortex shedding from bluff cylinders is as follows. A particle flows towards the leading edge of the cylinder, the pressure in the fluid particle rises from the free stream pressure to the stagnation pressure. The high pressure near the leading edge impels the developing boundary layers around both sides of the cylinder. However, the pressure forces are not sufficient to force the boundary layers around the back side of bluff cylinders at high Reynolds numbers. Near the widest section of the cylinder, the boundary layers separate from each side of the cylinder surface and form two free shear layers that trail aft in the flow. These two free shear layers bound the wake. Since the innermost portion of the free shear layers moves much more slowly than the outermost portion of the layers which are in contact with the free stream, the free shear layers tend to roll up into discrete, swirling vortices. A regular pattern of vortices is formed in the wake which can interact with the cylinder motion and is the source of vortex induced vibrations.

The major regimes of vortex shedding from a circular cylinder are given in Figure 11.9, adapted from Lienhard (1966). The vortex sheet evolves constantly as it flows downstream of the cylinder with the lateral to streamwise spacing necking down to a minimum a short distance downstream of the cylinder, before increasing – see Scraeffer and Eskanazi (1959). It has been shown that the wake can be strongly three dimensional – see Humphreys (1960) and Roshko (1953).

11.4.1 Vortex induced vibrations

Vortex induced forces that act along the in-line and transverse direction to the excitation flow give rise to additional riser response. Considerable work has been done to investigate these effects in steady flow, Chryssostomidis and Patrikalakis (1984), Every *et al.* (1981), Griffin *et al.* (1973), (1980), (1984), Hall (1981), Jacobsen *et al.* (1984), King *et al.*(1973), Pelzer and Rooney (1984), Schafer (1984), Syck (1981), Tsahalis (1984). However, the flow around a riser will generally vary with time and axial location owing to the oscillatory and depth decaying nature of waves, possibly complicated by surface vessel motions.

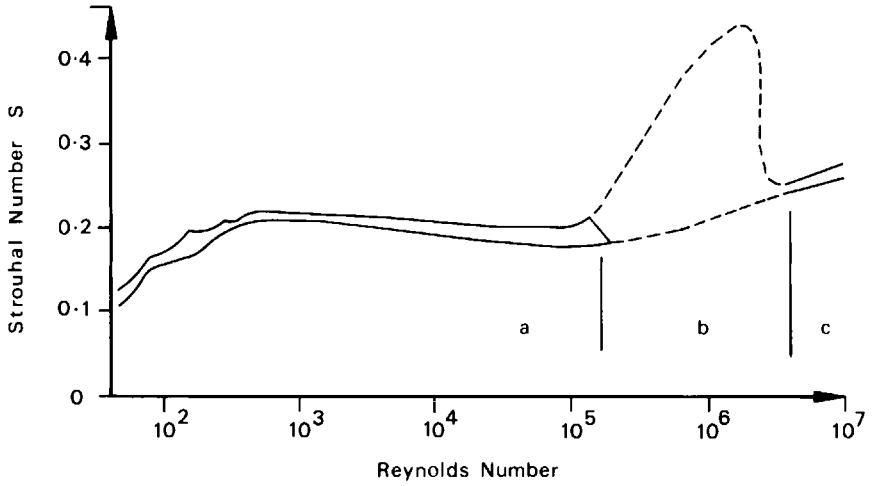

Figure 11.8. Strouhal number variation for stationary circular cylinders. *Key*: a – laminar; b – transition; c – turbulent

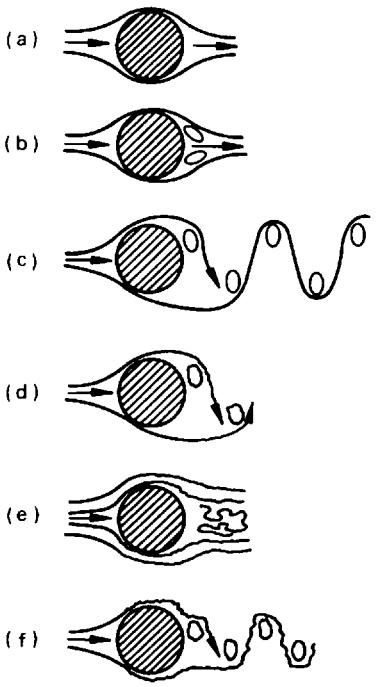

Figure 11.9. Regimes of fluid flow across circular cylinders:
(a) $Re < 5$
(regime of unseparated flow)
(b) $5 \text{ to } 15 < Re < 40$
(a fixed pair of FOPPL vortices in wake)
(c) $40 < Re < 90$ and $90 < Re < 150$
(two regions in which vortex street is laminar)
(d) $150 < Re < 300$
(transition range to turbulence in vortex)
$300 < Re < 3 < 10^5$
(vortex street is fully turbulent)
(e) $3 \times 10^5 < Re < 3.5 \times 10^6$
(laminar boundary layer has undergone turbulent transition and wake is narrower and disorganised)
(f) $3.5 \times 10^6 < Re$
(re-establishment of turbulent vortex street)

Griffin and Ramberg (1982), Blevins (1977), King (1977), Sarpkaya (1979), Sarpkaya and Isaacson (1981), Shaw (1979), and Simpson (1978) give comprehensive reivews of the state of the art in respect of vortex shedding and associated vibrations. The CIRIA report (1978) presents a

background and some example solutions for simplified vortex induced vibration problems.

Many of the theories that have been developed to predict the vortex induced oscillations of bluff cylindrical members attempt to include physical phenomena underlying the fluid mechanics of vortex behaviour and the structural member response to the consequent loading.

The first of these is lock-on of vortex shedding frequencies (determined by the Strouhal relationship) to a natural frequency of the cylinder. Thus

$$\left.\begin{array}{l} f_v = f_n \text{ at lock-on} \\ \text{and} \\ f_v = f_s\, SV/D_s \text{ otherwise} \end{array}\right\} \tag{11.85}$$

The following parameters are of major importance in determining the amplitude of vibrations and the range of lock-on or synchronization for a given body:

$$\text{Reduced damping, } k_s = \frac{2m\delta}{\rho D_s^2} \tag{11.86}$$

$$\text{Reduced velocity, } V_r = V/(f_n\, D_s) \tag{11.87}$$

The reduced damping is the product of the logarithmic decrement of structural damping (it does not incude fluid damping) and the mass density of the structure relative to the fluid.

The reduced velocity may be used to determine the existence and degree of vortex induced vibration. For transverse vibrations of a cylindrical bluff body, it has been shown from experiment in water by many researchers that excitation begins when the reduced velocity reaches a value of between 3.5 and 5.0. A peak occurs around 6.0 and decay to no vibration at around 8.0–12.0 (see Figure 11.10 from Parkinson *et al.* (1968) and Figure 11.11 from Griffin and Ramberg (1982)). For in-line oscillations, the onset of vibration occurs at reduced velocities around 1.0 to 1.5 for the case where two vortices of opposing sign are shed symmetrically and continues to a reduced velocity of about 2.5, when a stream of alternating vortices is formed. Vibration ceases for the in-line case at a reduced velocity of 3.0–3.5 – see Figure 11.12 from Dean *et al.* (1977).

It has been shown for right circular cylinders in uniform flow, that there is a relationship between the maximum possible amplitude of transverse vibrations and the reduced damping which applies for flexible and flexibly mounted rigid cylinders. Various workers give this relationship as follows and as compared in Figure 11.13.

Griffin *et al.* (1973) give

$$\frac{Y_{max}}{D} = \frac{1.29\,\gamma}{[1 + 0.43\,(2\pi S^2\, k_s)]^{3.35}} \tag{11.88}$$

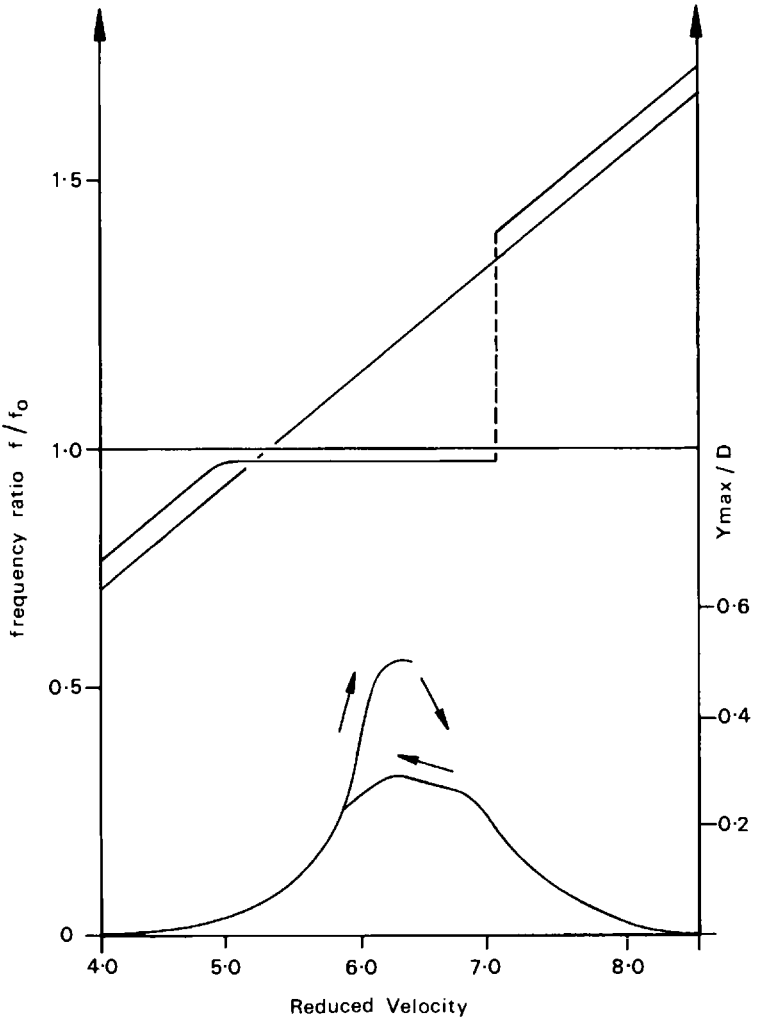

Figure 11.10. Resonance of a rigid right cylinder

Blevins (1977) gives

$$\frac{Y_{max}}{D} = \frac{0.07\,\gamma}{(1.9 + k_s)\,S^2}\left[0.3 + \frac{0.72}{(1.9 + k_s)\,S}\right]^{1/2} \tag{11.89}$$

Iwan (1975) gives

$$\frac{Y_{max}}{D} = \frac{\gamma}{[1 + 9.6\,(k_s/\pi)^{1.8}]} \tag{11.90}$$

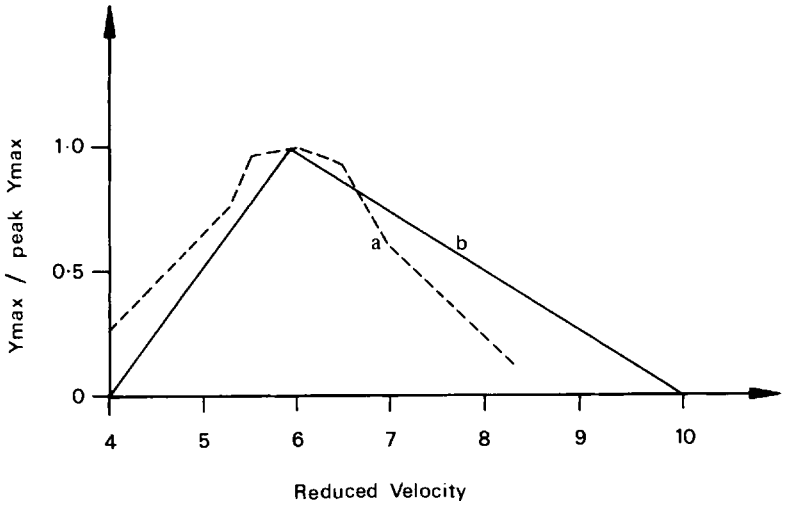

Figure 11.11. Transverse oscillations of a circular cylinder (adapted from Griffin and Ramberg, 1982). *Key*: a – experimental data; b – triangular function used

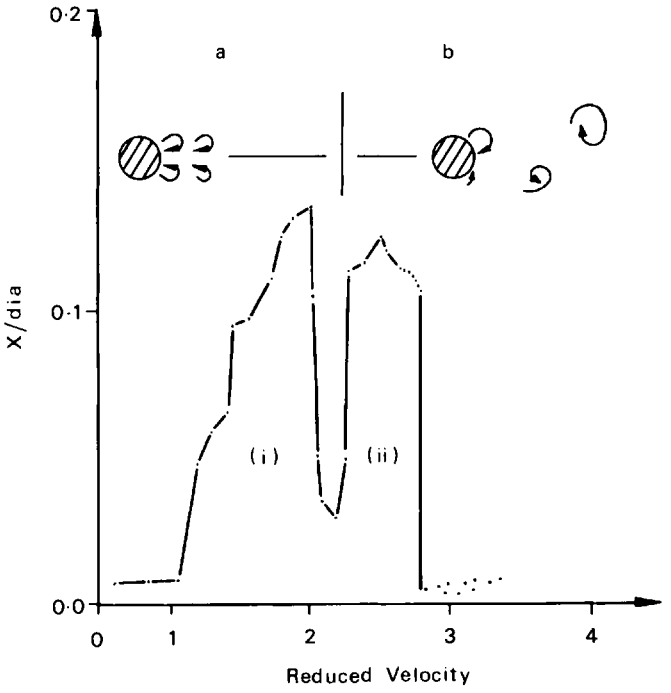

Figure 11.12. In-line oscillations of a circular cylinder. *Key*: a – symmetric vortex shedding; b – asymmetric vortex shedding; (i) first instability reading, (ii) second instability reading

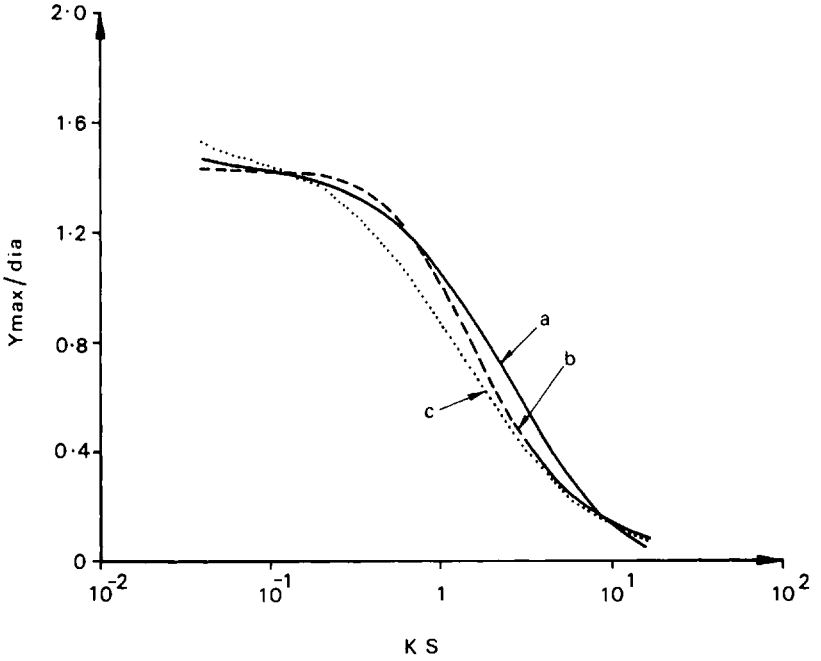

Figure 11.13. Maximum cross-flow vibration amplitude using equations by various authors for circular cables. *Key*: a – Griffin *et al.*; b – Sarpkaya; c – Blevins

where a geometric function of mode shape

$$\gamma = \xi_{max}\,(x/L)\left[\frac{\int_0^L \xi^2\,(x)\,dx}{\int_0^L \xi^4\,(x)\,dx}\right] \tag{11.91}$$

is used to collapse the data for the different modes of response for the systems shown in Figure 11.14; ξ_{max} is the maximum value of the modal shape ξ over the span extending form $x = 0$ to $x = L$.

11.4.2 Analysis models

The non-linear, wake oscillator model initially proposed by Bishop and Hassan (1964)) and pursued by others including Blevins (1977) and Hartlen and Currie (1970) is based on a modified Van der Pol equation. This has been developed because it exhibits many of the features of interaction between the structure and its wake at resonance. Model parameters must be determined from curve fitting of experimental data. Some success has

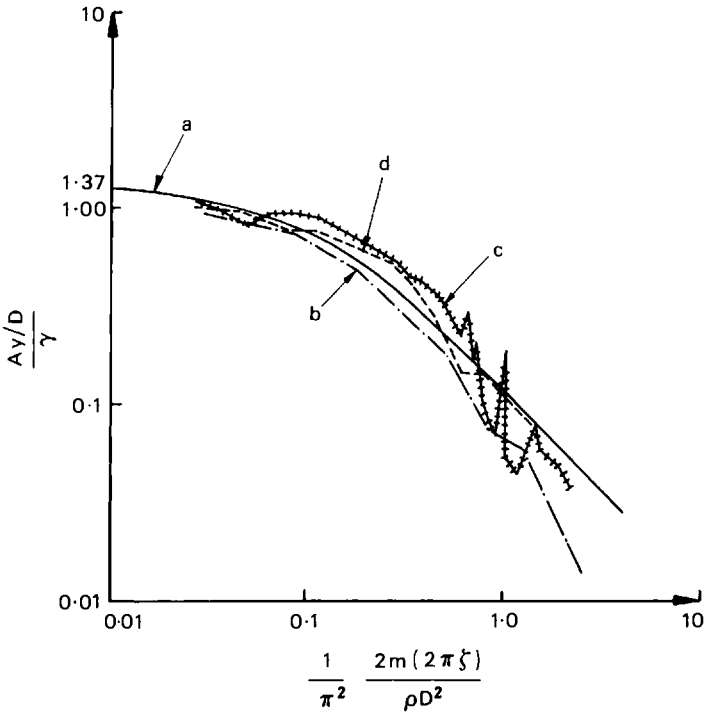

Figure 11.14. Normalized maximum amplitude of response versus mass ratio damping parameter. *Key*: a – theory; b – rigid cylinder experiments; c – pivoted rod experiments; d – cable experiments

been achieved using this method for steady flow. Nordgren (1982) applied Iwan and Belvins' (1974) version of this model, with riser equations derived from the theory of elastic rods. He applied a strip theory approach with the vortex model acting only on the portion of the riser exposed to a current which varied with depth. It is not apparent that this analysis accounted for the effects of the limited spatial extent of lock-on and the fluid damping of inactive elements.

The correlation model developed by Blevins and Burton (1976) and Kennedy and Vandiver (1979) is a specialized dynamic analysis using random vibration theory based on a representative span-wise correlation and cylinder amplitude dependence of vortex induced forces. Experimental data on correlation lengths and lift functions or resonant cylinder vibration amplitudes are used to determine model parameters. This approach is useful in making predictions of non-resonant response condition which may occur at low amplitudes of vibration where it is probably superior to the wake oscillator model. However, existing data is limited to steady flow conditions for stationary cylinders. The validity for straightforward extensions to non-steady flow conditions is questionable, especially in respect of correlation length parameters. Whitney and Nickel (1983) applied this method to uniform and sheared flows. Their results for

uniform flow compare well with laboratory and field tests. However, they were not able to conclusively validate their predictions for sheared flow.

Empirical models based on measured fluid dynamic force coefficients have been used to predict resonant transverse vibrations in steady and harmonic flow – see Sarpkaya and Isaacson (1981), Rajabi (1979) and Zedan and Rajabi (1981). Rajabi *et al.* (1981) applied empirical correlations for lift coefficients and shedding frequencies to an analytic frequency domain model for vortex induced vibration of risers. It assumes lock-on with one mode and perfect vortex correlation along the length. It makes use of the relationship between a lift amplification parameter C_L/C_{Lo} and KC/KC^*, where, KC^* is Keulegan–Carpenter number KC at perfect synchronisation, with KC defined as $V_{max}T/D$; KC/KC^* is equal to the corresponding ratio of reduced velocities V_r/V_r^*; C_{Lo} is the lift coefficient of a stationary cylinder and is a function of Reynolds number. This relationship, shown in Figure 11.15, is analogous to that of Y_{max}/D versus V_r shown in Figure 11.11. Apparently this model takes no account of the influence of one mode upon another nor of the consequences of the limited capital extent of lock-on.

A statistical vortex shedding linear model based upon flow oscillator governing equations has been developed by Benaroya and Lepore (1983). This uses a variation of the Hartlen and Currie (1970) uniform flow model developed by Landl (1975) which introduces a fifth order fluid dynamic damping term to account for the hysteresis effect and the cases of soft and hard excitation. Hard excitation refers to a reduced velocity range for which two stable states are possible for one value of reduced velocity; the poistion of rest and a vibration of finite amplitude. To get an oscillation from rest in this case, it is necessary for an external disturbance to exceed a

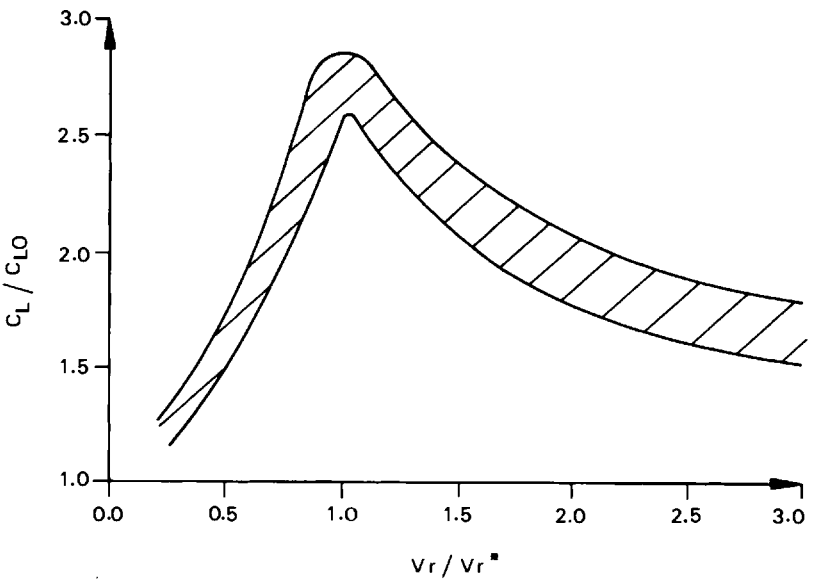

Figure 11.15. Lift amplitude correlation

certain displacement threshold. In the case of soft excitation, the rest position is unstable so that an oscillation is always generated. The statistical model assumes perfect span-wise correlation of the flow and, therefore, is not in this form fully applicable to the varying flow cases to which risers are generally subjected.

Other methods such as discrete vortex models and numerical solutions of the time depedent Navier–Stokes equations in the presence of an oscillating cylinder are computationally expensive for the results obtainable. Sarpkaya and Shoaff (1979) developed a comprehensive discrete vortex model based on potential flow and boundary layer interaction, redicretization and the shear layers, and circulation dissipation to determine the characteristics of an impulsively started flow. The evolution of the flow from start to large times, lift and drag forces, Strouhal number, oscillations of the stagnation and separation points and the vortex street characteristics, were all calculated and found to be in good agreement with experiment. This numerical model was then applied to flow about a transversely oscillating cylinder. It produced many of the experimentally observed features of the lock-on phenomenon. Apparently, it took about three hours of computer time on a CDC-6600 to reach a steady state equivalent to a simulated time of 400 s. While such a model provides a useful tool for numerical experiments to investigate the underlying physics of vortex shedding and associated vibration, it does not in this form provide a method of simulating the vortex induced vibration response of tethers or risers for engineering design purposes.

The method favoured by Lyons and Patel (1986) for application to the dynamics of marine risers and tethers invokes the following assumptions:

1. The vortex shedding phenomenon is dependent on instantaneous relative flow velocity.
2. Transverse vibration is approximated to begin at a reduced velocity of 4, reach a maximum at 6 and cease beyond 10.
3. The amplitudes of vibration for each mode may be calculated with a scheme devised by Iwan (1981) described below where the regions of excitation are those defined in (b).
4. Regions exciting higher modes do not excite lower modes, i.e. modal priority of higher modes occurs.
5. The drag coefficient, which will vary with time and along the length, is fixed at 2.0 for computational simplicity.
6. The added mass coefficient, which is also likely to vary with time and along the length, is fixed at 1.0.
7. Similarly the Strouhal number is fixed at 0.2.
8. For pinned-end numbers, all higher natural frequencies are integer multiples of the fundamental natural frequency. Although it is likely that buoyancy dependent effective tension, which varies along the length, and added mass will have some effect on natural frequencies and mode shapes.
9. Lock-on frequencies do not vary from the natural frequencies of the member.
10. The mode shapes are given by $\xi = \sin(n\pi x/L)$.
11. For all such modes, the mode shape factor, I_n, has a value of 1.155.

Iwan's scheme presents a simple analytical model for the vortex induced transverse oscillation of non-uniform structures in which the effects of lock-on and fluid damping of inactive elements are accounted for. The theory is based on a modal decomposition approach. The appropriate equations used are given below. Figure 11.16 shows the solution scheme graphically.

The amplitude of locked-on oscillation of the structure is given by

$$Y_n(x) = D_s F_n I_n^{-1/2} \xi_n(x) \tag{11.92}$$

where D_s is the cylinder diameter and the modal shape factor is

$$I_n = \frac{\int_0^L m(x)\, \xi_n^4(x)\, dx}{\int_0^L m(x)\, \xi_n^2(x)\, dx} \tag{11.93}$$

The amplification factor is taken to be

$$F_n = (1 + 9.6\, (\mu_r^n\, \zeta_n^s)^{1.8})^{-1} \tag{11.94}$$

where ζ_n^s is the effective damping, although expressions by other authors may be used as in Figure 11.13. A particularly important parameter is the effective mass ratio,

$$\mu_r^n = \frac{\nu_n}{(\rho\pi\, D_s^2/4)} \tag{11.95}$$

in which the effective mass is given by

$$\nu_n = \frac{\int_0^L m(x)\, \xi_n^2(x)\, dx}{\int_0^L s(x)\, \xi_n^2(x)\, dx} \tag{11.96}$$

where

$$s(x) = \begin{cases} 1 & \text{for those portions of the structure where vortex shedding is locked on to the structural motion} \\ 0 & \text{otherwise} \end{cases}$$

The effect of the position of locked-on regions determined by this parameter on the amplitude of vibration is demonstrated in Figure 11.17 for the first mode of vibration. It is clearly seen that the amplitude of vibration is greater when the region of excitation is near the centre (antinode) and increases with the extent of the excited region. Similar effects result for all other modes.

Figure 11.16 presents a flow chart of the implementation of the time domain theoretical model. Relative velocities along the length are calcu-

Y = function (x, t, top amplitude and period)

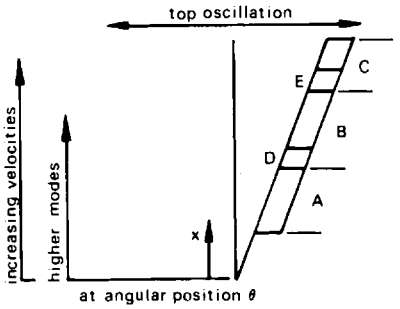

excited regions A, B, C, defined by $4 < V_r < 10$; $V_r = V/f_n d$; overlaps D. E attributed to higher modes B and C respectively

START: For angular position θ, mode n

$\zeta_n^s = \zeta_n^l$ initial condition

$$\nu_n = \frac{\int_0^l m(x)\xi_n^2(x)\,dx}{\int_0^l s(x)\xi_n^2(x)\,dx}$$

$s(x) = 1$ locked on
$= 0$ otherwise

$$\mu_r^n = \frac{\nu_n}{\rho\pi D_s^2/4}$$

$$\phi_n = \frac{2D_s}{3\pi} \frac{\int_0^l [C_D(x)\rho D(x)][1 - s(x)]|\xi_n(x)|^3\,dx}{\left[\int_0^l m(x)\xi_n^1(x)\,dx\right]^{1/2}\left[\int_0^l m(x)\xi_n^2(x)\,dx\right]^{1/2}}$$

$$F_n = \left(1 + 9.6\left(\mu_r^n \zeta_n^s\right)^{1.3}\right)^{-1}$$

gives maximum possible for structure (need to modify for V_r)

$\zeta_n^s = \zeta_n^l + F\phi_n$

N

Convergence for ζ_n^s?

Y

$$\left(\frac{Y_n(x)}{D_s}\right)_{\max} = F_n I_n^{-1/2} \xi_n(x)$$

to modify for V_r

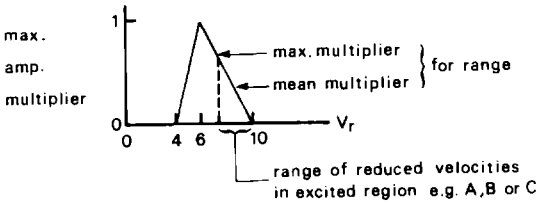

$$\left(\frac{Y_n(x)}{D_s}\right)_{\text{possible}} = \left(\frac{Y_n(x)}{D_s}\right)_{\max} \times \text{maximum amplitude multiplier}$$

GOTO START for next mode

GOTO START for next angular position

Figure 11.16. Transverse vortex-induced vibration production scheme

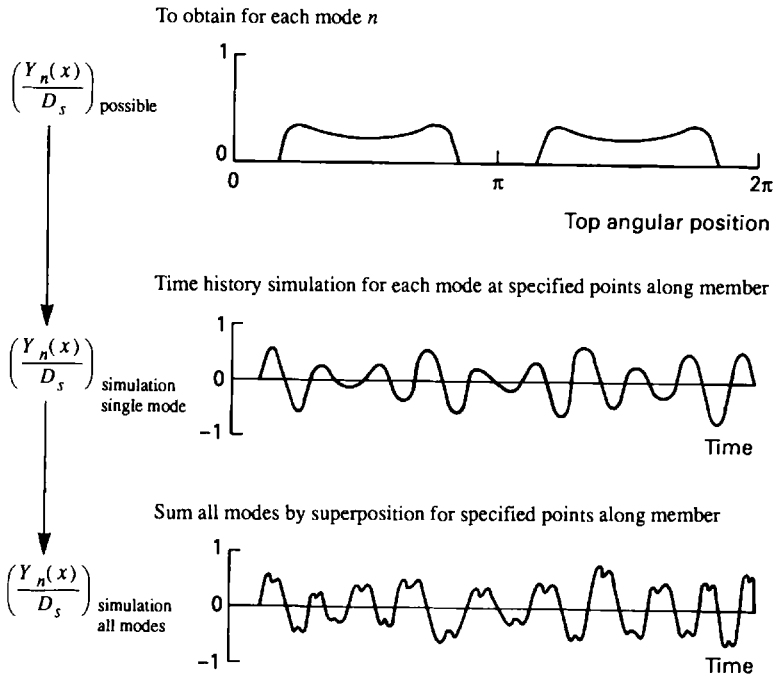

Figure 11.16. (*continued*)

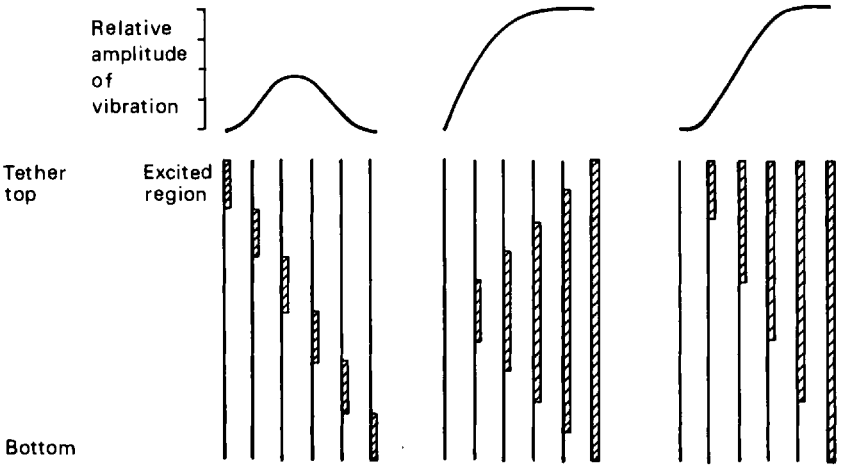

Figure 11.17. Variation of amplitude of vibration with extent of excited region for first mode of pinned-end sinusoidal vibrations

lated and the extent of regions of corrected vortex shedding excitation are identified for incremental time steps. Iwan's method is implemented for the length of the member in each mode which is excited to obtain the modal amplitude. Since this amplitude is the peak resonant amplitude, it is necessary to modify it to determine the amplitude of vibration at the reduced velocities in the region of excitation. Use is made of assumption (b) above. From this an amplitude multiplier is determined, by which the peak resonant amplitude is modified dependent on the range of reduced velocities in the excited region. The method utilizes the maximum reduced velocity in each region of excitation. The amplitude values for each mode are constructed into time histories which are then superimposed to obtain the overall member vibration time history. During vortex induced vibration of a particular mode, the member amplitude is set at the value given by the above procedure. When this mode is inactive, however, its vibration is taken to be due to its damped motion in still water from the vortex induced vibration during its last active condition. This time history procedure thus accounts for the following features:

(a) decay of vibration using the member structural and viscous damping in still water, ζ_n^T;
(b) phase of vibration changes randomly if a mode has a period of inactivity;
(c) vibration amplitude for any mode not being lower than that due to decay from a previous event.

The value of drag coefficient has been fixed within the computation to permit a simplified implementation with good agreement with measurements. In reality, the drag coefficient is a function of Reynolds number and of vibration amplitude. Griffin and Ramberg (1982) give this function from the results of full scale measurements in current flow as

$$\left.\begin{aligned} C_D/C_{Do} &= 1 + 1.16/(W_r - 1)^{0.65} \quad \text{for } W_r > 1 \\ \text{and} \\ C_D/C_{Do} &= 1 \quad \text{for } W_r < 1 \end{aligned}\right\} \tag{11.97}$$

where the wake stability parameter, $W_r = (1 + 2Y/D)/(V_r S)$.

King (1977) compares the relationships between steady drag coefficient and Strouhal number with Reynolds number variation as shown in Figure 11.18.

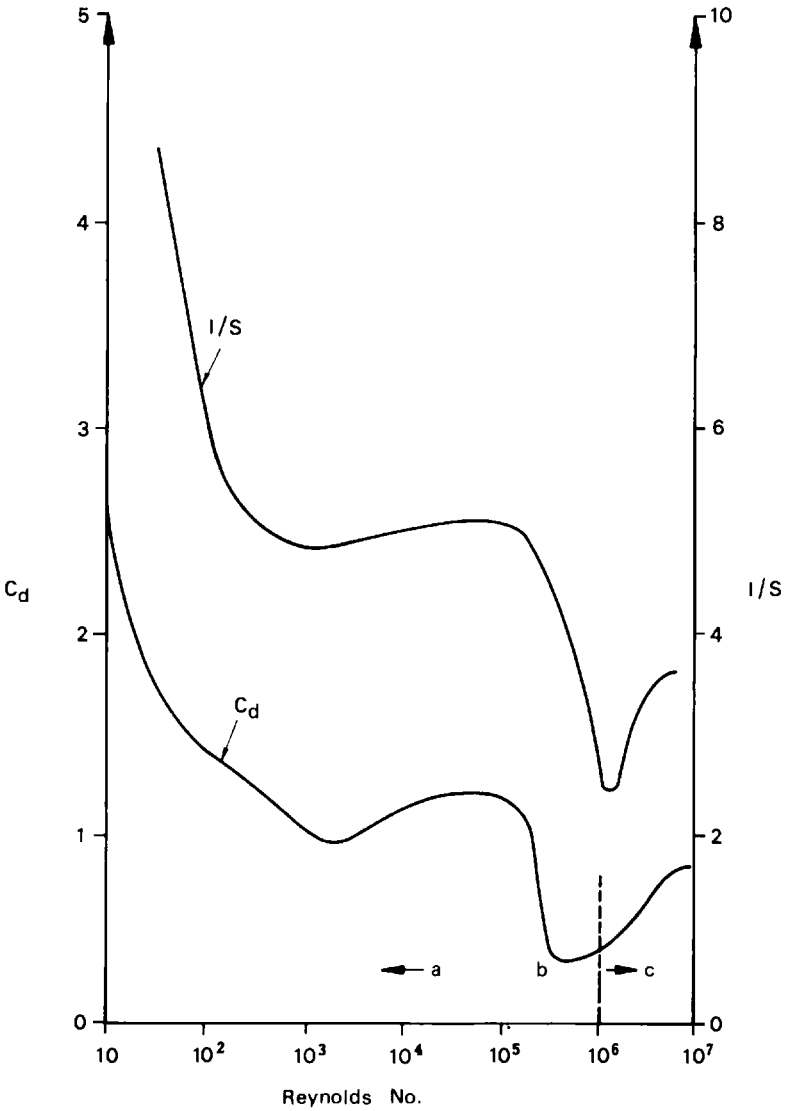

Figure 11.18. General relationships between Strouhal number, steady drag coefficient and Reynold's number. *Key*: a – subcritical; b – critical; c – supercritical

The definition of drag coefficient to be used remains an unclear area but the above equations may be used within this method to incorporate a more refined variation of drag coefficient. Values of C_D/C_{Do} of up to 4.5 have been demonstrated. The situation is complicated for multi-riser bundles. Depending upon the configuration, the entrained fluid may often result in riser behaviour as if it were a single body. Drag coefficients for bundled risers have been obtained by Demirbilik and Halvorsen (1985).

11.4.3 Vortex vibration suppression

In order to reduce or avoid troublesome vortex induced vibrations, there are two approaches which may be adopted. One may consider altering the riser physical properties to increase k_s or changing the natural frequencies so as to avoid vortex shedding frequencies. This approach is often not possible because of other design constraints. The second approach is to attach some form of flow spoiling or damping device along the riser length. For practical purposes, while they may reduce the vibrations their attachment and riser deployment is often unsatisfactory and their service performance variable due to marine fouling and mechanical failure.

Flow spoiling devices can be categorized into three main groups:

(a) those which affect the separation lines or separated shear layers;
(b) those which affect the entrainment layers;
(c) those which act as near wake stabilizers and inhibit the switching of the confluence point of the entrainment layers.

These devices are discussed in detail by Zdravkovitch (1981) and Every *et al.* (1982). They include splitter plates, fairings, guide plates and vanes. These have the disadvantage that they are unidirectional in action and can cause large lateral forces when the flow is at an angle to the design direction. Since this is often the case in the offshore environment it is beneficial to allow them to 'weathervane'. In its simplest form this can comprise flags along the riser length. However, these may wrap themselves around the riser. A more sophisticated design is the use of a series of rotatable aerofoil-shaped sections. These may also provide the advantage of reduced steady drag force. Omni-directional performance may also be obtained by the use of helical strakes as commonly used in chimneys. However, they have the disadvantage of increasing the steady drag force.

Similarly, perforated shrouds, and shrouds of vertical slats offer suppresion with somewhat less of a drag penalty. Investigations have also been made into the vortex suppression capabilities of plumes of rising air bubbles disrupting the flow around the riser with success, but this is probably only viable as a temporary measure.

An interesting proposal for riser vibration suppression is the nutation damper. This device has been used successfully in spacecraft. It is essentially a torus which is part filled with a sloshing liquid. Its damping characteristics are shown by Modi *et al.* (1986) to be sensitive to the physical properties of the liquid used, its height in the torus, damper

geometry and dynamical parameters representing amplitude and frequency. Advantages include requirement for only a few dampers along the riser length with minimal increase in steady drag, with optimal reduction in vibration when placed at anti-nodes of maximum vibration.

11.5 Design considerations

Whether the riser be for drilling or production duty, the fitness for purpose of the design is determined by the estimates of its likely loading conditions. These conditions include environmental forces and if applicable surface support motions. Confident estimates of these are essential. They are not limited to static behaviour, but should include dynamic response. For rigid risers the likely causes of failure are local material yielding and Euler column buckling.

The design of all types of tensioned risers is affected by:

(a) motions of the surface facility;
(b) tensioner stroke limits and response rates;
(c) bottom connection angle limits;
(d) distribution of buoyancy modules.

Additionally, drilling risers are particularly affected by:

(a) mud weight;
(b) drill string tension;
(c) possible abnormal gas pressure;

while production risers are particularly affected by:

(a) buoyancy modules for the free-standing mode;
(b) drag of multiple piping;
(c) rigidity of multiple piping;
(d) installation, repair and maintenance procedures.

11.5.1 Sources of failure

It is important to understand the likely causes of riser failure when designing a riser system. Almost inevitably this understanding comes from past experience. Morgan (1974–1976) indicates the following for tensioned risers:

Response	*Cause*
1. Buckling	Failure to predict multiple curvature Failure to predict high curvature Inadequate top tension available Inadequate tensioner rate Excessive bending in free-hanging condition Failure of buoyancy modules
2. Ball joint damage Drill string fatigue BOP fatigue damage Blowout risk	Drill bit, collars, casing causing mechanical damage as a result of excessive joint angle
3. Riser/conductor failure	Excessive bending moment due to vessel excursion and BOP weight
4. Emergency disconnect failure	Excessive bending causing binding
5. Riser to supplementary buoy over-stressing	Out-of-phase dynamics of system elements
6. Conductor pipe failure and BOP stack collapse	Resonant excitation of BOP

11.5.2 Riser top tension and supplementary buoyancy

A truly vertical riser connected at the sea bed has no buoyancy force. This is because buoyancy is the resultant net force acting vertically on a body and if there is no horizontal surface on which the hydrostatic pressures may act, the resultant force is zero. However, disconnect the riser from the sea bed or incline it and it will exhibit a buoyancy force. Generally for risers the combined effects of self weight and buoyancy yields a net negative force which is destabilizing in that the riser will continue to move away from the vertical unless restrained. This restraint is provided by means of top tensioning which may be aided by the use of supplementary buoyancy modules along the riser length.

Near optimum choice of top tension can be arrived at by calculating the sum of the reduction in bending stress and the increase in axial stress with increase in top tension (see Figure 11.19). Care must be taken to ensure that the lateral component of top tension does not result in excessive horizontal deflection of the bottom BOP stack, Figure 11.20. The moment due to the BOP weight and its eccentricity may lead to bending failure of the sea bed conductor column. Reduction in top tension requirement is particularly advantageous in very deep water. Care must be taken to ensure that such reductions do not lead to local compression which is more likely to occur near the sea bed.

Buoyancy modules in use include air-filled cans in which the volume of air may be controlled from the surface and so alter the buoyancy available. Other forms do not offer this control but have cost advantages in certain cases. Materials for these include cellular polystyrene, cellular vinyls, cellular silicones, cellular acetate, synthetic foams which may contain spheres of various amterials, and foamed aluminium. Some of these materials can deteriorate with time resulting in a change in buoyancy.

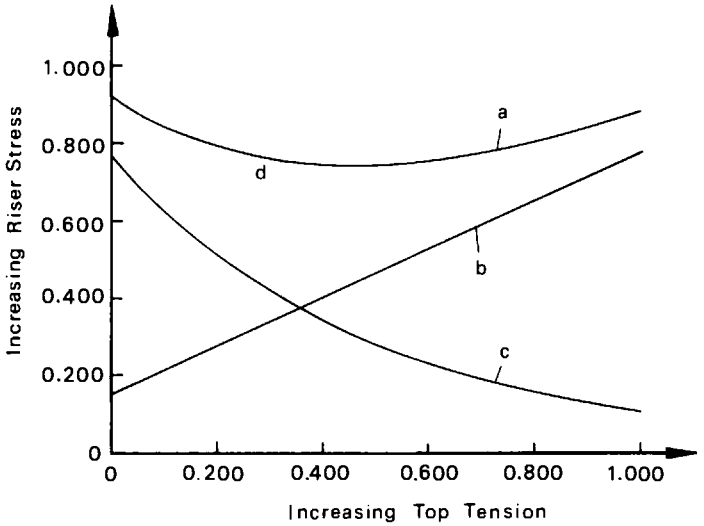

Figure 11.19. Aid to optimizing riser top tension: (a) combined axial and bending stress; (b) axial stress = T/A; (c) bending stress = M_c/I; (d) minimal combined stress

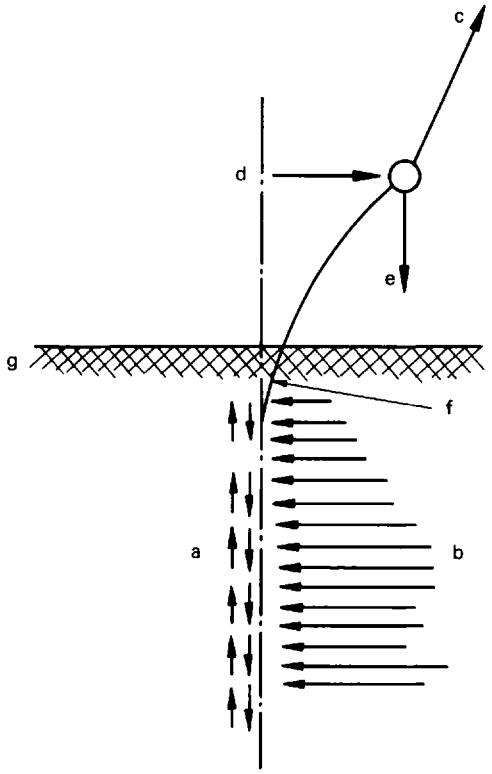

Figure 11.20. BOP eccentricity resulting in bending of the conductor column. *Key*: a – non-linear shear transfer properties of soil; b – non-linear resistance of soil to displacement; c – riser tension; d – wave and current forces; e – BOP weight; f – deflection of conductor; g – mudline

References

American Petroleum Institute (1977) *Comparison of Marine Drilling Riser Analysis*. API Bulletin 2J, 1st edn, January

Bathe, K. J. and Wilson, E. L. (1976) *Numerical Methods of Finite Element Analysis*. Prentice Hall, Englewood Cliffs, NJ

Benaroya, H. and Lepore, J. A. (1983) Statistical flow-oscillator modelling of vortex shedding. *Journal of Sound and Vibration*, **86**(2), 159–179

Bishop, R. E. D. and Hassan, A. Y. (1964) The lift and drag forces on a circular cylinder in a flowing field. *Proceedings of The Royal Society (London, Ser A*, **277**, 51–75

Blevins, R. D. and Burton, T. E. (1976) Fluid forces induced by vortex shedding. *Journal of Fluid Engineering*, pp. 19–26, March

Blevins, R. D. (1977) *Flow Induced Vibration*. Van Nostrand Reinhold, NY

Chyssostomidis, C. and Patrikalakis, N. M. (1984) A comparison of theoretical and experimental prediction of the vortex induced response of marine risers. *Proceedings of the 3rd International Offshore Mechanics and Arctic Engineering Symposium, ASME*, Volume 1, pp. 318–327

Cowan, R. and Andris, R. P. (1977) Total pipe laying system dynamics. *Proceedings of the 1977 Offshore Technology Conference, Houston, Texas*, OTC 2914

Dean, R. B., Milligan, R. W. and Wooton, L. R. (1977) *An Experimental Study of Flow Induced Vibration*. EEC Report 4, Atkins Research and Development, Epsom, UK

Demirbilek, Z. and Holvosen, T. (1985) Hydrodynamic forces on multi-tube production risers exposed to currents and waves. *Proceedings of the 4th Offshore Mechanics and Arctic Engineering Symposium*, pp. 363–370

Every, M. J., King, R. and Griffin, O. M. (1981) Hydrodynamic loads on flexible marine structures due to vortex shedding, *ASME, Journal of Energy Resources Technology*, **104**, 330–336, December

Gardner, T. N. and Kotch, M. A. (1976) Dynamic analysis of riser and caissons by the finite element method. *Proceedings of the 1976 Offshore Technology Conference, Houston, Texas*, OTC 2651

Griffin, O. M., Pattison, J. H., Skop, R. A., Ramberg, S. E. and Meggitt, D. J. (1980) Vortex excited vibrations of marine cables. *Journal of Waterways: Post Coastal and Ocean Division*, **106**, 183–205

Griffin, O. M. and Ramberg, S. E. (1982) Some recent studies of vortex shedding with application to marine tubulars and risers. *ASME*, **104**, 2–13, March

Griffin, O. M., Skop, R. A. and Koopman, G. H. (1973) The vortex excited resonant vibrations of circular cylinders. *Journal of Sound and Vibration*, **31**(2), 235–249

Griffin, O. M. and Vandiver, J. K. (1984) Vortex induced strumming vibrations of marine cables with attached masses. *Proceedings of the 3rd International Offshore Mechanics and Arctic Engineering Symposium*, Volume 1, pp. 300–309

Hall, S. A. (1981) Vortex induced vibrations of structures, PhD Thesis, California Institute of Technology

Hallam, M. G., Heaf, N. J. and Wooton, R. L. (1978) *Dynamics of Marine Structures*. Construction Industry Research and Information Association (CIRIA) Report UR8, London, pp. 175–206

Hartlen, R. T. and Currie, I. G. (1970) Lift oscillation model for vortex induced vibration. *Journal of Engineering, Mechanical Division, ASCE*, **96**, 577–591

Humphreys, J. S. (1960) On a circular cylinder in a steady wind at transition Reynolds numbers. *Journal of Fluid Mechanics*, **9**, pp. 603–612

Iwan, W. D. (1975) The vortex induced oscillation of elastic structural elements. *ASCE, Journal of Engineering for Industry*, **91**, 1378–1382, November

Iwan, W. D. (1981) The vortex induced oscillation of non-uniform structural systems. *Journal of Sound and Vibration*, **79**(2), 291–301

Iwan, W. D. and Blevins, R. (1974) A model of vortex induced oscillation of structures. *Journal of Applied Mechanics*, **41**, 581–586, September

Jacobsen, V., Nielsen, R. and Fines, S. (1984) Vibration of offshore pipelines exposed to current and wave action. *Proceedings of the 3rd International Offshore Mechanics and Arctic Engineering Symposium*, Volume 1, pp. 291–299

Kennedy, M. and Vandiver, J. K. (1979) A random vibration model for cable strumming predictions. *Civil Engineering in the Oceans*, **IV**, ASCE, pp. 273–292

King, R. (1977) A review of vortex shedding research and its application. *Ocean Engineering*, **4**, 141–171

King, R., Prosser, M. H. and Johns, D. J. (1973) On vortex excitation of model piles in water. *Journal of Sound and Vibration*, **29**(2), 169–188

Kirk, C. L. and Etok, E. U. (1979) Wave induced random oscillations of pipe lines during laying, *Applied Ocean Research*, **1**, (1)

Krolikowski, L. P. (1981) Modern production risers, Pt 9 – The frequency domain method for production riser analysis. *Petroleum Engineering International*, July, p. 88.

Krolikowski, L. P. and Gray, T. A. (1980) An improved linearisation technique for frequency domain riser analysis. *Proceedings of the 1980 Offshore Technology Conference, Houston, Texas*, OTC 3777

Landl, R. (1975) A mathematical model for vortex excited vibration of bluff bodies. *Journal of Sound and Vibration*, **42**(2), 219–234

Leinhard, J. H. (1966) *Synopsis of Lift, Drag and Vortex Frequency Data for Rigid Circular Cylinders*. Washington State University, College of Engineering, Research Division Bulletin 300

Lyons, G. J. and Patel, M. H. (1986) A prediction technique for vortex induced transverse response of marine risers and tethers. *Journal of Sound and Vibration*, **111**, 467–487

McNamara, J. F., O'Brien, P. J. and Gilroy, S. G. (0000) Non-linear analysis of flexible risers using hybrid finite elements. *Fifth International Offshore Mechanics and Arctic Engineering (OMAE) Symposium*, Volume III, Tokyo

McIver, D. B. and Lunn, T. S. (1983) Improvements to frequency domain riser programs. *Proceedings of the 1983 Offshore Technology Conference, Houston, Texas*, OTC 4550

Miller, J. E. and Young, R. D. (1985) Influence of mud column dynamics on top tension of suspended deepwater drilling risers. *Proceedings of the Offshore Technology Conference, Houston, Texas*, OTC 5015

Modi, V. J., Welt, F. and Irani, M. B. (1986) On the nutation damping of fluid structure interaction instabilities and its application to marine riser design. *Proceedings of the 1986 Offshore Mechanics and Ocean Engineering Symposium*, Tokyo, Volume III

Morgan, G. W. (1974–6) Applied mechanics of marine riser systems. *Petroleum Engineer*, Parts I–VIII, October 1974–May 1976

Nordgren, R. P. (1982) Dynamic analysis of marine risers with vortex excitation, *Journal of Energy Resources Technology*, **104**, 14–19, March

Patel, M. H. and Sarohia, S. (1982) On the dynamics of production risers. *Proceedings of the Third International Conference on Behaviour of Offshore Structures (BOSS 82)*, Volume 1, Massachusetts Institute of Technology

Patel, M. H., Sarohia, S. and Ng, K. F. (1984) Finite element analysis of the marine riser. *Engineering Structures*, **6**, 175–184

Pelzer, R. D. and Rooney, D. M. (1984) Near wake properties of a strumming marine cable: an experimental study. *Proceedings of the 3rd International Offshore Mechanics and Arctic Engineering Symposium*, Volume 1, pp. 310–317

Rajabi, F. (1979) Hydroelastic oscillation of smooth and rough cylinders in harmonic flow. PhD Thesis, Naval Postgraduate School, Monterey, Ca

Rajabi, F., Zedan, M. F. and Mangiavacchi, A. (1984) Vortex shedding induced dynamic response of marine risers. *Journal of Energy Resources Technology*, **106**, 214–221, June

Rayleigh, Lord. (1896) *Theory of Sound*, London Macmillan, 2nd edn

Sarpkaya, T. (1979) Vortex induced oscillations, a selective review. *Journal of Applied Mechanics*, **46**, 241–258

Sarpkaya, T. and Isaacson, M. (1981) *Mechanics of Wave Forces on Offshore Structures*. Van Nostrand Reinhold, NY

Sarpkaya, T. and Shoaff, R. L. (1979) *A Discrete Vortex Analysis of Flow about Stationary and Transversely Oscillating Circular Cylinders*. Technology Report No NPS-69LS79011, Naval Postgraduate School, Monterey, Ca

Schafer, B. (1984) Dynamical modelling of wind induced vibrations of overhead lines. *International Journal of Nonlinear Mechanics*, **19**(5), 455–467

Schlichting, H. (1968) *Boundary Layer Theory*, 6th edn. McGraw-Hill Book Co., NY

Scraeffer, J. W. and Eskanzi, S. (1959) An analysis of the vortex street generated in a viscous fluid. *Journal of Fluid Mechanics*, **6**, 241–260

Shapiro, A. H. (1953) *The Dynamics and Thermodynamics of Compressible Fluid Flow*, Volume I, Ronald Press Co., NY

Shaw, T. L. (ed.) (1979) *Mechanics of Wave Induced Forces on Cylinders*. Pitman, London

Shotbolt, K. (1983) The influence of production-riser design on the configuration and operation of semisubmersible floating production systems. *Proceedings Offshore Europe Symposium*, Aberdeen, 6–9 September

Simpson, A. S. (1978) Cables: dynamic stability aspects – a review. *Department of Aeronautics Engineering, University of Bristol, Symposium of Mechanics of Wave-induced Forces on Cylinders*, 3–6 September

Sparks, C. P. (1979) Mechanical behaviour of marine risers mode of influence of principal parameters. *Proceedings of the Winter Annual Meeting of the American Society of Mechanical Engineers*, 2–7 December, OED Volume 7, NY

Sparks, C. P., Cabillic, J. P. and Schawann, J. C. (1982) Longitudinal resonant behaviour of very deep water risers. *Proceedings of the 1983 Offshore Technology Conference, Houston, Texas*, OTC 4317

Strouhal, V. (1878) Uber eine besondere Art der Tonerregung. *Ann. Physik* (Leipzig)

Tsahalis, D. T. (1984) Vortex induced vibrations of a flexible cylinder near a plane boundary exposed to steady and wave induced currents. *Journal of Energy Resources Technology*, **106**, 206–213, June

Wang, E. (1983) Analysis of two 13,200-ft riser systems using a three dimensional riser program. *Proceedings of the 1983 Offshore Technology Conference*, Houston, Texas, OTC 4563

Whitney, A. K. and Nikkel, K. G. (1983) Effects of shear flow on vortex shedding induced vibration of marine risers, *Proceedings of the 15th Offshore Technology Conference*, OTC 4595, pp. 127–137, May

Young, R. D. and Fowler, O. O. (1978) Mathematics of marine risers. *The Energy Technology Conference and Exhibition*, November 1978, Houston, Texas

Zdravkovich, M. M. (1981) Review and classification of various aerodynamic and hydrodynamic means for suppressing vortex shedding. *Journal of Wind Engineering and Industrial Aerodynamics*, **7**, 145–189

Zedan, M. F. and Rajabi, F. (1981) Lift forces on cylinders undergoing hydroelastic oscillations in waves and two dimensional harmonic flow. *Proceedings of NHL International Symposium on Hydrodynamics in Ocean Engineering*, Volume 1, pp. 239–62

Appendix – Results of linear wave theory

This section contains results from linear wave theory. Sarpkaya and Isaacson (1981) and Patel (1989) give further details on linear wave theory.

The axes system used here has the origin at the still water level with the horizontal co-ordinate, x, positive in the direction of the wave propagation and the vertical co-ordinate, z, positive away from the sea bed.

The following notation is used for the wave parameters:

c = wave speed or celerity
d = water depth
k = wave number ($k = 2\pi/L$)
H = wave height
L = wave length
T = wave period ($T = 2\pi/\omega$)
ω = wave circular frequency
θ = wave phase angle ($\theta = k[x - ct] = kx - \omega t$)
s = vertical co-ordinate ($s = z + d$)

Results of linear wave theory

Velocity potential	$\phi = \dfrac{\pi H}{kT}\dfrac{\cosh(ks)}{\sinh(kd)}\sin\theta$
	$= \dfrac{gH}{2\omega}\dfrac{\cosh(ks)}{\cosh(kd)}\sin\theta$
Dispersion relation	$c^2 = \dfrac{\omega^2}{k^2} = \dfrac{g}{k}\tanh(kd)$
Surface elevation	$\eta = \dfrac{H}{2}\cos\theta$
Horizontal particle displacement	$\xi = -\dfrac{H}{2}\dfrac{\cosh(ks)}{\sinh(kd)}\sin\theta$
Vertical particle displacement	$\zeta = \dfrac{H}{2}\dfrac{\sinh(ks)}{\sinh(kd)}\cos\theta$
Horizontal particle velocity	$u = \dfrac{\pi H}{T}\dfrac{\cosh(ks)}{\sinh(kd)}\cos\theta$
Vertical particle velocity	$w = \dfrac{\pi H}{T}\dfrac{\sinh(ks)}{\sinh(kd)}\sin\theta$
Horizontal particle acceleration	$\dfrac{\partial u}{\partial t} = \dfrac{2\pi^2 H}{T^2}\dfrac{\cosh(ks)}{\sinh(kd)}\sin\theta$
Vertical particle acceleration	$\dfrac{\partial w}{\partial t} = -\dfrac{2\pi^2 H}{T^2}\dfrac{\sinh(ks)}{\sinh(kd)}\cos\theta$
Pressure	$p = -\rho g z + \frac{1}{2}\rho g H\dfrac{\cosh(ks)}{\cosh(kd)}\cos\theta$
Group velocity	$c_G = \frac{1}{2}\left[1 + \dfrac{2kd}{\sinh(2kd)}\right]c$
Average energy density	$E = \frac{1}{8}\rho g h^2$

Shallow and deep water approximations to linear wave theory

	Shallow water	*Deep water*
Range of validity	$kd < \frac{\pi}{10}$	$kd > \pi$
	$\frac{d}{L} < \frac{1}{20}$	$\frac{d}{L} > \frac{1}{2}$
	$\frac{d}{gT^2} < 0.0025$	$\frac{d}{gT^2} > 0.08$
Velocity potential	$\phi = \frac{\pi H}{k^2 T d} \sin\theta$	$\phi = \frac{\pi H}{kT} e^{kz} \sin\theta$
	$= \frac{gH}{2\omega} \sin\theta$	$= \frac{gH}{2\omega} e^{kz} \sin\theta$
Dispersion relation	$c^2 = \frac{\omega^2}{k^2} = gd$	$c^2 = c_0^2 = \frac{\omega^2}{k^2} = \frac{g}{k}$
Wave length	$L = T\sqrt{(gd)}$	$L = L_0 = gT^2/2\pi$
Surface elevation	$\eta = \frac{H}{2} \cos\theta$	$\eta = \frac{H}{2} \cos\theta$
Horizontal particle displacement	$\xi = -\frac{H}{2kd} \sin\theta$	$\xi = -\frac{H}{2} e^{kz} \sin\theta$
Vertical particle displacement	$\zeta = \frac{H}{2}\left(1 + \frac{z}{d}\right) \cos\theta$	$\zeta = \frac{H}{2} e^{kz} \cos\theta$
Horizontal particle velocity	$u = \frac{\pi H}{T(kd)} \cos\theta$	$u = \frac{\pi H}{T} e^{kz} \cos\theta$
Vertical partical velocity	$w = \frac{\pi H}{T}\left(1 + \frac{z}{d}\right) \sin\theta$	$w = \frac{\pi H}{T} e^{kz} \sin\theta$

	Shallow water	*Deep water*
Horizontal particle acceleration	$\frac{\partial u}{\partial t} = \frac{2\pi^2 H}{T^2(kd)} \sin\theta$	$\frac{\partial u}{\partial t} = \frac{2\pi^2 H}{T^2} e^{kz} \sin\theta$
Vertical particle acceleration	$\frac{\partial w}{\partial t} = \frac{2\pi^2 H}{T^2}\left(1 + \frac{z}{d}\right) \cos\theta$	$\frac{\partial w}{\partial t} = -\frac{2\pi^2 H}{T^2} e^{kz} \cos\theta$
Pressure	$p = -\rho g z + \frac{1}{2} \rho g H \cos\theta$	$p = -\rho g z + \frac{1}{2} \rho g H e^{kz} \cos\theta$
Group velocity	$c_G = c$	$c_G = \frac{1}{2} c$
Average energy density	$E = \frac{1}{8} \rho g H^2$	$E = \frac{1}{8} \rho g H^2$

References

Sarpkaya, T. and Isaacson, M. (1981) *Mechanics of Wave Forces on Offshore Structures*. Van Nostrand Reinhold, NY

Patel, M. H. (1989) *Dynamics of Offshore Structures*. Butterworths, London

Index